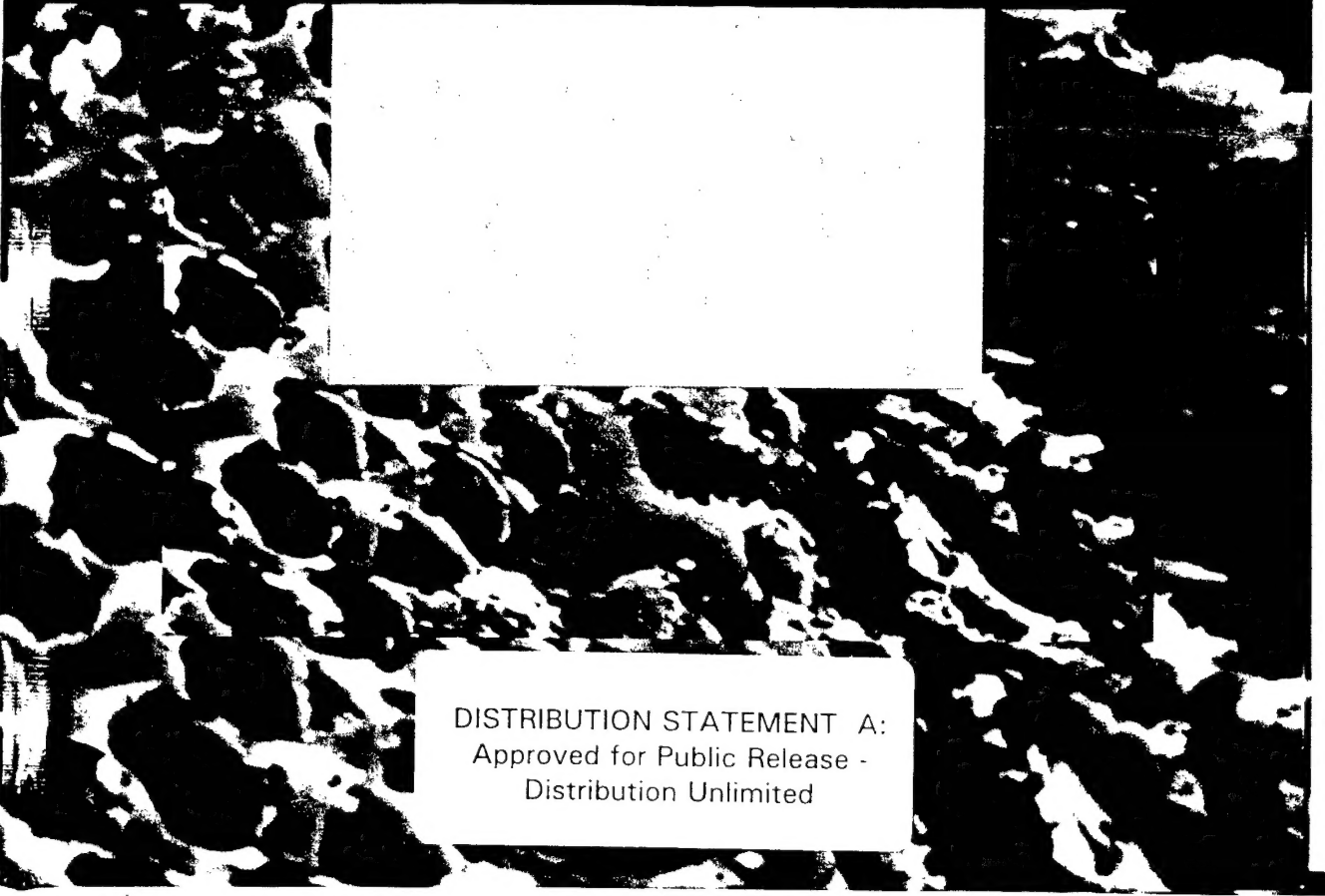


# **PROGRESS IN DURABILITY ANALYSIS OF COMPOSITE SYSTEMS**

**KENNETH L. REIFSNIDER, DAVID A. DILLARD AND ALBERT H. CARDON, EDITORS**



**DISTRIBUTION STATEMENT A:**  
Approved for Public Release -  
Distribution Unlimited

# REPORT DOCUMENTATION PAGE

Form Approved  
OMB No. 0704-0188

Public reporting burden for this collection of information is estimated to average 1 hour per response, including the time for reviewing instructions, searching existing data sources, gathering and maintaining the data needed, and completing and reviewing the collection of information. Send comments regarding this burden estimate or any other aspect of this collection of information, including suggestions for reducing this burden, to Washington Headquarters Services, Directorate for Information Operations and Reports, 1215 Jefferson Davis Highway, Suite 1204, Arlington, VA 22202-4302, and to the Office of Management and Budget, Paperwork Reduction Project (0704-0188), Washington, DC 20503.

1. AGENCY USE ONLY (Leave blank)	2. REPORT DATE	3. REPORT TYPE AND DATES COVERED	
	1 Feb. 99	Final	14 Aug. 97 - 28 Aug. 98
4. TITLE AND SUBTITLE  The Third International Conference on Progress in Durability Analysis of Composite Systems			5. FUNDING NUMBERS G N00014-97-1-0760
6. AUTHOR(S) Kenneth L. Reifsnider			
7. PERFORMING ORGANIZATION NAME(S) AND ADDRESS(ES) Virginia Polytechnic Institute and State University Office of Sponsored Programs 301 Burruss Hall Blacksburg, VA 24061			8. PERFORMING ORGANIZATION REPORT NUMBER 4-30710
9. SPONSORING/MONITORING AGENCY NAME(S) AND ADDRESS(ES) Office of Naval Research Ballston Centre Tower One 800 North Quincy Street Arlington, VA 22217-5660			10. SPONSORING/MONITORING AGENCY REPORT NUMBER
11. SUPPLEMENTARY NOTES  This report is delayed because of the lateness of the publication of the Conference Proceedings.			
12a. DISTRIBUTION/AVAILABILITY STATEMENT  unlimited		12b. DISTRIBUTION CODE	
13. ABSTRACT (Maximum 200 words)  Composite materials are widely used in a variety of applied technologies including transportation, off-shore, power, electronics, communications, sports equipment, and infrastructure industries. In the last few years, these applications have matured in many ways. For example, polymer composites are increasingly used in primary and man-rated structures. A controlling feature of the general use of composite systems is their damage tolerance, durability, and reliability. That is the subject of the present book.  The papers in this volume were generated as a result of the Third International Conference on Progress in Durability Analysis of Composite Systems, held on 14-17 September 1997 on the campus of Virginia Polytechnic Institute and State University in Blacksburg, Virginia. Delegates from 19 countries and more than a dozen universities and a like number of industries participated in the conference.			
14. SUBJECT TERMS Durability of composites for marine applications; physical and chemical aging processes in high temperature applications; applications of damage mechanics to durability; infrastructure applications, manufacturing, processing and durability; emerging technologies and case studies.			15. NUMBER OF PAGES 358
			16. PRICE CODE
17. SECURITY CLASSIFICATION OF REPORT none	18. SECURITY CLASSIFICATION OF THIS PAGE none	19. SECURITY CLASSIFICATION OF ABSTRACT none	20. LIMITATION OF ABSTRACT unlimited

PROCEEDINGS OF THE THIRD INTERNATIONAL CONFERENCE ON PROGRESS IN  
DURABILITY ANALYSIS OF COMPOSITE SYSTEMS/BLACKSBURG/VIRGINIA  
USA/14-17 SEPTEMBER 1997

# Progress in Durability Analysis of Composite Systems

*Edited by*

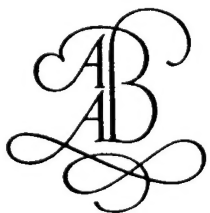
Kenneth L. Reifsnider & David A. Dillard

*Virginia Polytechnic Institute and State University, Blacksburg, Va., USA*

Albert H. Cardon

*Free University of Brussels, Belgium*

19990205 002



A.A.BALKEMA/ROTTERDAM/BROOKFIELD/1998

DTIC QUALITY INSPECTED 2

*The texts of the various papers in this volume were set individually by typists under the supervision of each of the authors concerned.*

Authorization to photocopy items for internal or personal use, or the internal or personal use of specific clients, is granted by A.A.Balkema, Rotterdam, provided that the base fee of US\$ 1.50 per copy, plus US\$ 0.10 per page is paid directly to Copyright Clearance Center, 222 Rosewood Drive, Danvers, MA 01923, USA. For those organizations that have been granted a photocopy license by CCC, a separate system of payment has been arranged. The fee code for users of the Transactional Reporting Service is: 90 5410 960 2/98 US\$ 1.50 + US\$ 0.10.

Published by

A.A.Balkema, P.O.Box 1675, 3000 BR Rotterdam, Netherlands  
Fax: +31.10.413.5947; E-mail: [balkema@balkema.nl](mailto:balkema@balkema.nl); Internet site: <http://www.balkema.nl>  
A.A.Balkema Publishers, Old Post Road, Brookfield, VT 05036-9704, USA  
Fax: 802.276.3837; E-mail: [info@ashgate.com](mailto:info@ashgate.com)

ISBN 90 5410 960 2  
© 1998 A.A.Balkema, Rotterdam  
Printed in the Netherlands

## Table of contents

Preface	IX
Organization	XI
<b>1 Durability of composites for marine applications</b>	
Effect of seawater on the interfacial strength and durability of polymer composites <i>W.L.Bradley, C.A.Wood, B.A.Pratt &amp; C.S.Chatawanich</i>	3
Characterizing the durability of PVDF and PPS for extended use in marine environments <i>D.Kranbuehl, W.Newby-Mahler, J.Garrett, A.Meyer, J.Warner, R.Gittleson, A.Ebersole, J.Rogozinski, D.Hood, S.Case, K.Reifsnider &amp; A.Loos</i>	11
Composites underwater <i>P.Davies, D.Choqueuse, F.Mazéas</i>	19
Fluids effects in polymeric composites – An overview <i>Y.J.Weitsman</i>	25
Effects of moisture and loading mode on transverse cracking of GFRP laminates <i>J.J.L.Morais &amp; A.T.Marques</i>	31
Flexible risers with composite armor for deep water oil and gas production <i>M.D.Kalman &amp; J.R.Belcher</i>	41
<b>2 Physical and chemical aging processes in high temperature applications</b>	
The effect of physical aging on the durability of carbon fiber reinforced PEI <i>A.D'Amore, G.Caprino, L.Nicolais &amp; G.Marino</i>	51
Mechanism-based modeling of long-term degradation <i>H.L.McManus, B.J.Foch &amp; R.A.Cunningham</i>	63
Thermal and mechanical durability of graphite-fiber-reinforced PMR-15 composites <i>K.J.Bowles</i>	71
Environmental effects on the Mode I fracture and fatigue of bonded composites <i>L.M.Butkus, R.V.Valentin &amp; W.S.Johnson</i>	77

---

### **3 Applications of damage mechanics to durability**

Damage modeling of composite structures: Static and dynamic approach <i>Y.Chevalier, M.Louzar, M.Chafra &amp; G.A.Maugin</i>	87
Prediction of transverse cracking in CFRP laminates with interlaminar resin layers <i>S.Ogihara, N.Takeda &amp; A.Kobayashi</i>	95
Damage characterization of elastomeric composites using X-ray attenuation <i>C.Bathias, K.Le Gorju, P.Houël &amp; Y.N'Faly Bérété</i>	103
Damage initiation and progression in notched unidirectional composites <i>C.L.Chow &amp; F.Yang</i>	111
Recent developments in damage mechanics of composite materials <i>R.Talreja</i>	119
The role of interphasial inhomogeneities on failure mechanism of fiber-reinforced composites <i>G.C.Papanicolaou, P.A.Kakavas &amp; N.K.Anifantis</i>	129
Influence of interfacial strength on micro- and macroscopic fatigue behavior of longitudinal glass fiber reinforced polypropylene <i>E.K.Gamstedt, L.A.Berglund &amp; T.Peij</i>	137
Creep-damage interaction in composites <i>V.Tamuzs, J.Andersons, K.Aniskevich &amp; J.Korsgaard</i>	143

### **4 Infrastructure applications**

Composite infrastructure applications: Concept, design and durability control and prediction <i>P.Hamelin</i>	153
Instantaneous damage kinetic of composite pipes and moisture effect <i>D.Perreux &amp; C.Suri</i>	159
Mechanical behavior of multiaxial reinforced composites sun light degraded <i>F.Segovia, C.Ferrer, V.Amigó, M.Salvador &amp; C.Bloem</i>	167
The effects of cyclic moisture aging on a glass/vinyl ester composite system <i>K.Garcia, M.D.Hayes, N.Verghese &amp; J.J.Lesko</i>	173
Polymer composites for infrastructure <i>A.Zureick</i>	181
Applications of composite materials in the oil industry: Case studies <i>F.Dal Maso &amp; P.Odru</i>	185

### **5 Manufacturing, processing and durability**

Aging analyses of polymer composites through time-temperature equivalence <i>J.C.Sefaris</i>	193
Influence of matrix ductility and fibre architecture on the repeated impact response of glass-fibre-reinforced composites <i>B.A.G.Schrauwen &amp; T.Peij</i>	203

Reliability methods for structural composite applications in vehicle suspensions <i>P.T. MacLellan &amp; J.R. Gentry</i>	211
Durability in the life cycle of polymer composites <i>Y. Leterrier, Y. Wyser &amp; J.-A. E. Månsen</i>	219
Environmental stress cracking in polyimide composites and adhesives <i>D.A. Dillard, A.P.C. Furrow, H. Parvatareddy, T.L. St. Clair &amp; J. Hinkley</i>	227
Affordable processing of composite structures for the civilian infrastructure <i>J.L. Kardos, B. Khomami, P. Ramachandran, B. Yang &amp; R. Shepard</i>	235
Improved adhesive performance through surface treatment <i>M.A. Gaynes, J.M. Spalik &amp; H. Shaukatullah</i>	241

## **6 Emerging technologies and case studies**

Characterization and prediction of nonlinear VE-VP behaviour of CRP under cyclic loading by using a neuro-fuzzy model <i>Y. Qin, R. Guedes &amp; A.H. Cardon</i>	249
In-situ SEM/micro-line methods for microscopic deformation and damage evolution analysis of composites <i>N. Takeda &amp; S. Ogihara</i>	255
Micromechanically based constitutive models for damage evolution in composite laminates <i>P. Gudmundson</i>	263

## **Technical posters**

A predictive method for the nonlinear viscoelastic characterization of carbon/epoxy fibre composites <i>G.C. Papanicolaou &amp; S.P. Zaoutsos</i>	271
Time-dependent behaviour of T300/5208 under creep, relaxation and ramp loading <i>R.M. Guedes, A.T. Marques &amp; A. Cardon</i>	279
Reliability-based optimization of a laminated cylinder subject to a given axial load and pressure <i>A. Béakou</i>	285
Comparison of methodologies for prediction of long-term properties of GRP pipes <i>A.T. Marques &amp; F. Martins de Brito</i>	289
Evaluation of damage accumulation of glass fibre reinforced chemically bonded ceramics (CBC) using the resonalyser technique <i>P. Bauweraerts, J. Wastiels, X. Wu, S. Faingnet &amp; A. Edelstein</i>	295
Prediction of tensile fatigue life for unidirectional CFRP <i>Y. Miyano, M. Nakada, H. Kudoh &amp; R. Muki</i>	303
Effect of acid-base properties of sized carbon fibers on fiber/epoxy matrix adhesion <i>N. Dilsiz &amp; J.P. Wightman</i>	309

---

Prediction of long term behaviour of graphite-bismaléimide composites: Assessment of residual stresses <i>A.Vinet, D.Gamby &amp; M.C.Lafarie-Frenot</i>	315
Life prediction for continuous fiber reinforced composites under stochastic fatigue loading based on the Critical Element Concept <i>R.Carmine &amp; N.Himmel</i>	319
Probabilistic approach for residual compressive strength of CFRP laminates, following low velocity impact <i>G.C.Papanicolaou, A.V.Pournaras, D.E.Mouzakis, J.Karger-Kocsis &amp; D.A.Bofilios</i>	325
Fatigue behavior of angle-ply AS4/PEEK composite <i>X.R.Xiao &amp; I.Al-Hmouz</i>	331
Moisture detection in composite materials using infrared thermography <i>J.C.Kneip, X.J.Gong &amp; S.Aivazzadeh</i>	339
Crack growth prediction in composites using the dual boundary element method <i>P.Sollero, S.G.Mendonça &amp; M.H.Aliabadi</i>	343
Estimation of carrying capacity of aviation engine parts from composite materials <i>T.D.Karimbayev, A.A.Lupov, D.I.Nicolayev &amp; A.N.Zavyalov</i>	349
Author index	357

## Preface

Composite materials are widely used in a variety of applied technologies including transportation, off-shore, power, electronics, communications, sports equipment, and infrastructure industries. In the last few years, these applications have matured in many ways. For example, polymer composites are increasingly used in primary and man-rated structures. A controlling feature of the general use of composite systems is their damage tolerance, durability, and reliability. That is the subject of the present book.

The papers in this volume were generated as a result of the Third International Conference on Progress in Durability Analysis of Composite Systems, held on 14-17 September 1997 on the campus of Virginia Polytechnic Institute and State University in Blacksburg, Virginia. Delegates from 19 countries and more than a dozen universities and a like number of industries participated in the conference. The first two such conferences were organized by Prof. Albert Cardon and held at the Free University (VUB) in Brussels, Belgium. The present conference continued the traditions of limited attendance, extended discussions, and a focused effort to advance the field of durability analysis. Support for the Conference was provided by Virginia Polytechnic Institute and State University (through the NSF Center for High Performance Polymeric Adhesives and Composites, Virginia Institute for Material Systems, Center for Composite Materials and Structures, Materials Response Group, and the Department of Engineering Science and Mechanics), the Free University of Brussels, the Air Force Office of Scientific Research, the Office of Naval Research, and the National Science Foundation. The local host committee consisted of: Ken Reifsnider, General Co-Chair; David Dillard, Program Chairman; John Dillard, Industrial Chairman; Mike Hyer, Events Chairman; and Al Loos, Posters and Displays Chairman. The Organizing Committee and International Scientific Advisory Committee are listed below. On behalf of all of the authors and conference participants, the contribution of all of these individuals to the success of the conference is gratefully acknowledged. Special thanks also goes to Mrs Shelia Collins who served as conference coordinator, and who contributed in so many ways to the planning and execution of the conference. A fourth conference is in the planning stages.

## Organization

### ORGANIZING COMMITTEE

*Chairman*

Albert H. Cardon, VUB, Brussels, Belgium

*Conference Chairman*

Ken Reifsnider, Virginia Tech, Blacksburg, Virginia, USA

*Conference Co-Chairmen*

Steve Johnson, Georgia Tech, Atlanta, Georgia, USA  
Ramesh Talreja, Georgia Tech, Atlanta, Georgia, USA  
Hiroshi Fukuda, Science University, Tokyo, Japan  
Norbert Himmel, University of Kaiserslautern, Germany  
Ralph Stotesberry, DuPont Corp., Richmond, Virginia, USA  
Bill Long, Babcock and Wilcox Corp., Lynchburg, Virginia, USA

### INTERNATIONAL SCIENTIFIC COMMITTEE

R.Adams, UK	K.Schulte, Germany
J.A. Manson, Switzerland	A.Torres-Marques, Portugal
T.Blażcinski, Poland	Z.Hashin, Israel
L.Nicolais, Italy	A.Vautrin, France
V.Tamuz, Latvia	L.Berglund, Sweden
G.Papanicolaou, Greece	G.Verchery, France
H.Brinson, USA	P.Hogg, UK
C.Roy, Canada	A.Vlot, Netherlands
O.Brueller, Germany	M.Tuttle, USA

---

## 1 Durability of composites for marine applications

## Effect of seawater on the interfacial strength and durability of polymer composites

W.L. Bradley, C.A. Wood, B.A. Pratt & C.S. Chatawanich

*Department of Mechanical Engineering and Offshore Technology Research Center, Texas A&M University,  
College Station, Tex., USA*

**ABSTRACT:** The effect of absorbed moisture on the fiber/matrix interfacial strength and 90° ply strength have been studied for E-glass and carbon fiber reinforced epoxy. In-situ observations of fracture in an environmental scanning electron microscope with associated calculations indicating reductions in ply stress at debonding ranging from 0% to 30%, with 70% at the reduction attributed to a weaker interface and the balance due to changes in the residual thermal stresses. Burst tests and low-cycle fatigue tests using internal pressure in filament wound tubes gave only a 6% reduction in burst strength for seawater saturated specimens compared to unaged specimens, but a more significant reduction in the low-cycle fatigue behavior was noted. The effect of moisture was apparently to plasticize the matrix, giving more viscoelastic deformation and to reduce the strain to failure in the glass fibers.

### 1 INTRODUCTION

The prospect of large oil reserves at 2000m of ocean depth has created a significant interest in the possibility of using polymeric composite tubulars for both drilling risers and production risers. The higher specific strength of polymeric composite material systems can potentially allow conventional equipment designed for drilling and oil production using floating ships and platforms for depths of greater than 500m to be used at these greater depths by reducing the hanging weight of the tubulars. The potential use of polymeric matrix composites for offshore applications has been recently reviewed (Gibson, 1993) and the economic feasibility of using polymeric composite tubulars for production risers has already been demonstrated (Tamarelle and Sparks, 1987).

Polymeric matrix composites are known to have excellent fatigue resistance, do not corrode, and can be tailored to give optimal combinations of stiffness, strength, and thermal expansion by proper ply sequencing. The two technical obstacles to the use of polymeric composite materials for offshore risers are joining and long-term durability. While polymeric composite materials do not corrode like metals, they do absorb moisture, generally 1-3% of the weight of the matrix. This absorbed moisture strength of the glass fibers (carbon fibers appear to

be unaffected by moisture), and/or degrade the strength of the fiber matrix interface. Since production risers will be immersed continuously for 10-20 years, they will certainly reach saturation levels of moisture absorption eventually. Thus, the effect of the absorbed moisture on long-term durability needs to be determined.

The purpose of this study has been to investigate effect of the absorbed moisture on the interfacial strength of several polymeric composite material systems and the low-cycle fatigue behavior. Direct observations of the initiation of damage in the systems investigated in this study indicate that the failure scenario begins with interfacial failure by debonding leading to transverse cracking, and subsequently, delamination. Absorbed moisture can perturb this failure scenario in four ways: reducing the chemical adhesion at the fiber/matrix interface; relaxing the residual compressive stresses at the fiber/matrix interface; reducing the ply level residual tensile stresses in the 90° plies; and plasticizing the polymeric matrix. Since these various effects of absorbed moisture can potentially postpone interfacial failure or cause it to occur prematurely, a more careful study has been undertaken to determine the effect of absorbed moisture on the interfacial strength and



Figure 1a. The test geometry for specimens loaded in fracture in the ESEM, indicating the stacking sequence for the hybrid composites (E-glass/epoxy 2 and carbon/epoxy 2).

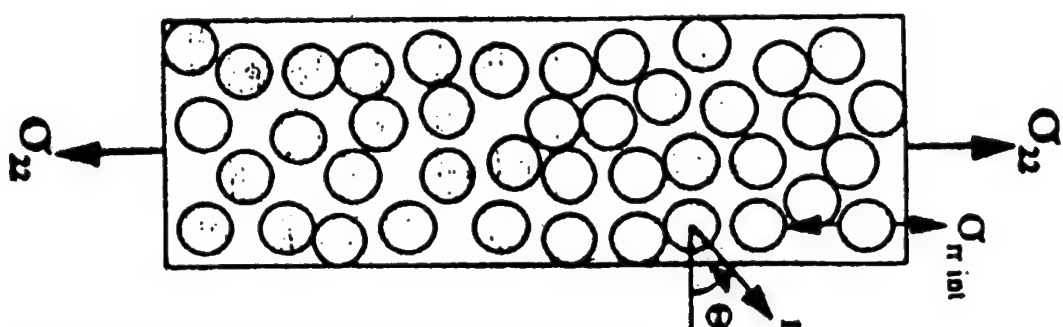


Figure 1b. Schematic of 90° ply in Fig. 1a, being tested, with axis labeled.

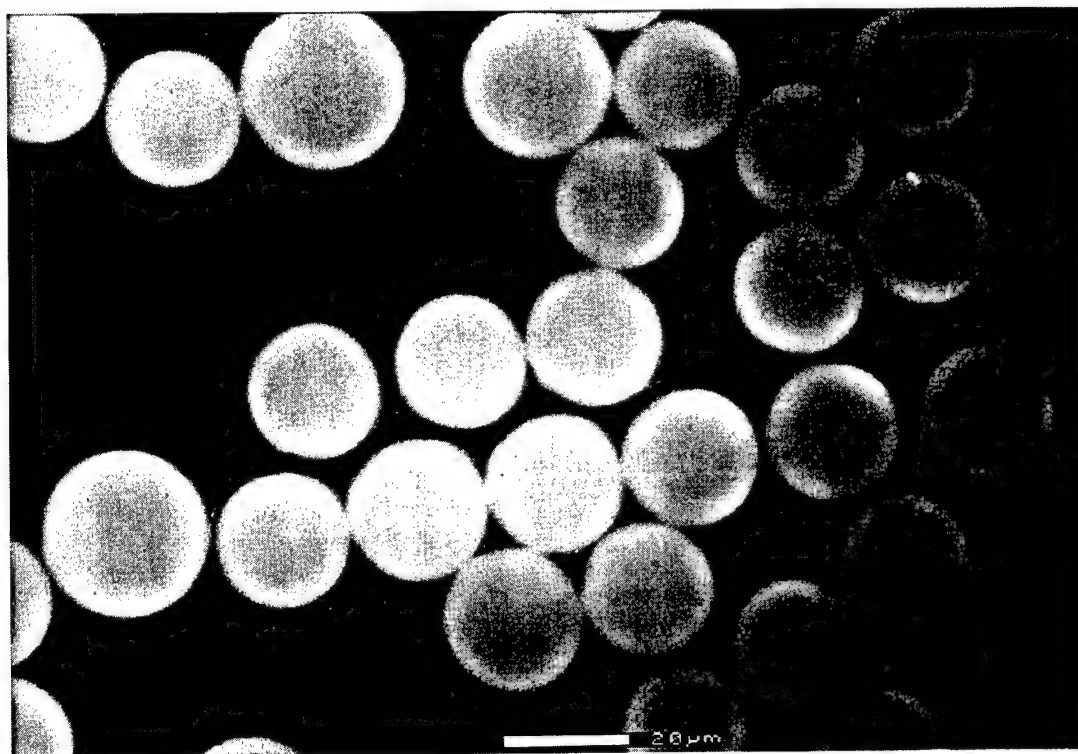


Figure 2. In-situ observation of local debonding in an E-glass/epoxy composite adjacent to a resin rich region.

on the ply level mechanical stress at which interfacial leading to transverse cracking occurs.

To determine the effect of absorbed moisture on the initiation of ply level damage in a multi-axial laminate, tensile tests in-situ in an environmental scanning electron microscope have been performed on laminate specimens as received and on specimens aged in seawater until a saturation level of moisture absorption has occurred. Filament wound tubes unaged and aged to saturation by soaking in simulated sea water have been tested to failure in a burst test and in a low-cycle fatigue test (not to failure) followed by a stress-rupture test to failure.

## 2 EXPERIMENTAL AND ANALYTICAL PROCEDURES

Two polymeric composite material systems have been studied in this investigation: (a) a Shell 828 epoxy (DGEBA), cured at 398K with meta-phenylene diamine (mPDA), reinforced with E-glass type 30-158B Owens Corning fibers and (b) BP719 which is a 5% rubber toughened epoxy, with a cure temperature of 422K, reinforced with E-glass fibers and AS4 graphite fibers (a hybrid composite). Hereafter, the 828 epoxy will be referred to as Epoxy 1 and the BP719 with 5% rubber additions will be referred to as Epoxy 2.

Epoxy 1/E-glass laminates were prepared from prepreg with a (+45/90)s layup. The fiber volume fraction was 0.65. The moisture content in the as-prepared laminate was 1.2% of the matrix weight, which was determined by drying a small sample in a vacuum oven. Epoxy 2 laminates were prepared by filament winding glass and graphite fibers with (0g/90c)s and (0c/90g)s layups. Filament wound tubes of E-glass with Epoxy 2 were prepared with a (+25/90)s with the ply thicknesses selected to give similar fiber stresses in the 25° and 90° plies. The moisture content in the as-prepared Epoxy 2 laminate was 1.0% of the matrix weight.

The tensile specimens cut from the laminates of Epoxy 1 and Epoxy 2 and the filament wound tubes from Epoxy 2 were aged by soaking at ambient temperature in simulated sea water prepared from Instant Ocean Mix (purchased at a pet store). All tensile specimens saturated after 3.5 months, with saturation moisture contents of 2.3%

of the matrix weight for Epoxy 1 based laminates and 2.2% of the matrix weight for Epoxy 2 based laminates. The filament wound tubes took 15 months to saturate due to their greater wall thickness, also with a saturation moisture content of 2.2% of the matrix weight, which is consistent with the saturation moisture content of the Epoxy 2 based laminate, as expected.

Tensile tests were performed in an environmental scanning electron microscope (ESEM) to allow direct observations of the failure scenario of 90° plies. Special tensile specimens were prepared by grinding and polishing the edges of rectangular specimens 38mm long by 6mm wide, as seen in Figure 1. The reduced specimen width at the midpoint of the specimen gauge length gives a maximum stress at this same location, causing the damage initiation to be sufficiently localized to allow it to be captured in the early stages by observations in the SEM. Getting a good metallographic polish on a curved surface required the development of some new polishing techniques. The aged specimens were tested in the ESEM with a 100% relative humidity to avoid dehydration during testing. Unaged specimens were tested at a much lower pressure and humidity in the ESEM. The specimens were loaded in displacement control, with both load and displacement monitored. The displacements were applied in step wise fashion, with careful surveying of the polished edge and photographic documentation of damage accumulation being done at each displacement step.

The laminate load measured at a given displacement was used to calculate the ply level stresses in the 90° plies at the initiation of debonding and at the first occurrence of transverse cracking using software based on classical laminate theory (Wood, 1996). The ply level residual stresses on cool down to room temperature were also calculated using the same laminate analysis (Wood, 1996). The residual stresses at the fiber/matrix interface were calculated using a micromechanics analysis based on linear elasticity called MICSTRAN (Naik, 1992; Crews, Naik and Lubowinski, 1993). MICSTRAN was also used to calculate the local stress concentration as a function of location around the circumference of the fiber/matrix interface as seen in Fig. 1b. The local residual stresses at the fiber matrix interface

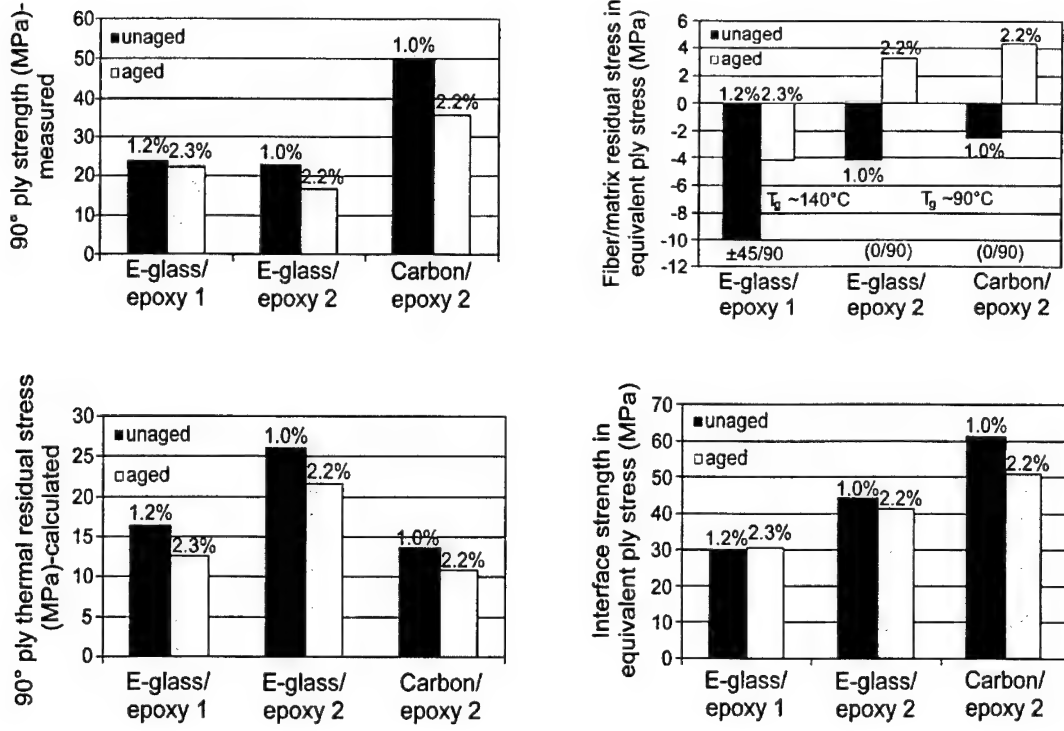


Figure 3. Ply stresses due to thermal residual stresses and due to mechanical loading at initiation of debonding of unaged and aged specimens (moisture content indicated) for the three systems studied; equivalent ply level stresses for fiber/matrix interfacial residual stresses and interfacial strength, calculated by dividing the local stress by the stress concentration SC.

due to ply level mechanical and residual thermal stresses can be calculated by multiplying the ply level nominal stress by the stress concentration factor calculated from MICSTRAN. Alternatively, the residual thermal stresses at the fiber/matrix interface or the interfacial strength for debonding due to normal stressing can be converted into an equivalent ply level residual or critical stress by dividing the local stress at the fiber matrix interface by the stress concentration factor at that location.

Burst tests and low-cycle fatigue tests (not to failure) followed by stress-rupture tests to failure were performed using a system capable of pressurizing the filament wound tubes and then releasing the pressure according to program instructions. The fixtures effectively capped the ends of the tubes, allowing axial and hoop stresses

to be developed. The tubes were fabricated with liners so that the higher pressures required for structural failures (and not just transverse cracking and weepage) could be achieved. The axial and hoop strains were monitored during testing using strain gages, and acoustic emission was used to determine damage development during the testing using the Locan-320 system from Physical Acoustics Corp.

Unaged and aged tubes were pressured monotonically until they experienced structural failures and rupture. In the low cycle fatigue tests, the specimens were cycled to ~25% of the burst pressure (6.9 MPa) for seven cycles, each cycle consisting of a pressurization and hold for six hours followed by a return to ambient pressure for 18 hours (one complete cycle per day). Cycles 8–14 were identical except that the hold pressure was

~50% of the burst pressure (13.8 MPa), as seen in Figure 4. After the 14 cycles, the tubes were pressured to ~75% of their burst pressure (20.0 MPa) and held until the tubes ruptured, monitoring, axial and hoop strain and acoustic emission hits as a function of time.

### 3 RESULTS AND DISCUSSION

#### 3.1 In-situ fracture observations

Direct observations of fracture in the ESEM are seen in Figure 2. In the E-glass/epoxy 1 system, interfacial failures usually occurred first adjacent to local heterogeneities such as voids whereas in the carbon and E-glass/epoxy 2 system it occurred adjacent to local resin rich regions. In neither composite was debonding found to be in a homogeneous region of the composite microstructure. Once debonding initiated in a local region, new debonds were found to occur adjacent to the original ones as the load is locally redistributed. A general observation of randomly arranged debonds which ultimately begin to coalesce when the local density reaches some critical level (like fiber failures) was never observed in any of the more than 50 tests run on a variety of composite materials. It seems clear that debonding leading to transverse cracking is controlled by local heterogeneities, and once initiated, tends to remain quite localized. Absorbed moisture was not found to affect the failure scenario, but only the load levels at which debonding began and transverse cracking ultimately was consummated.

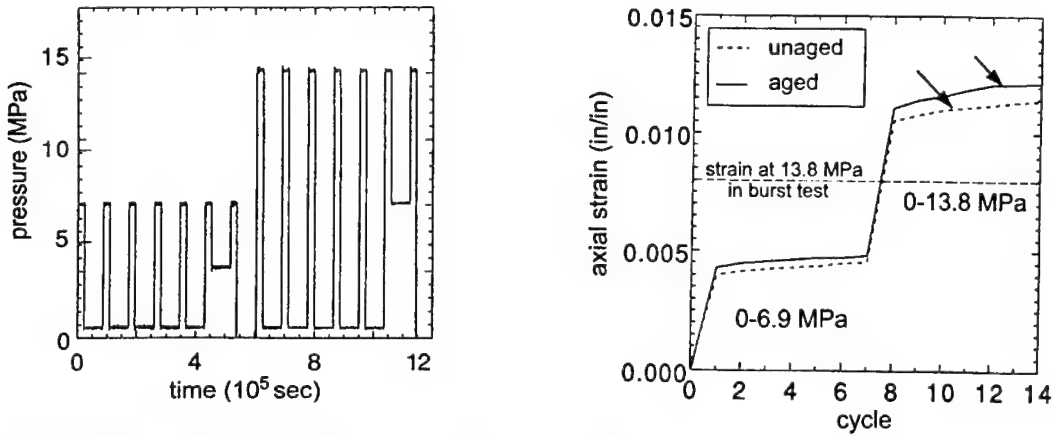
To analyze the interfacial stress at the fiber/matrix interface at which interfacial debonding occurs, the local stress at the fiber/matrix interface was calculated beginning with the local interfacial stress due to ply level stress as shown in Figure 1b with the value of the stress concentration factor used being determined from MICSTRAN. Since almost all debonds were observed at the top or bottom of the fibers (theta = 90°), the local stress due to ply level mechanical and residual thermal stresses was evaluated at this position. The local interfacial residual thermal stress in the radial direction was also determined using MICSTRAN. Finally, the interfacial strength was calculated as follows:

$$\sigma_{22 \text{ int}} = (\sigma_{22 \text{ mech ply}} + \sigma_{22 \text{ resid ply}}) \times SC(\theta = 90^\circ) + \sigma_{rr \text{ int th}} \quad (1)$$

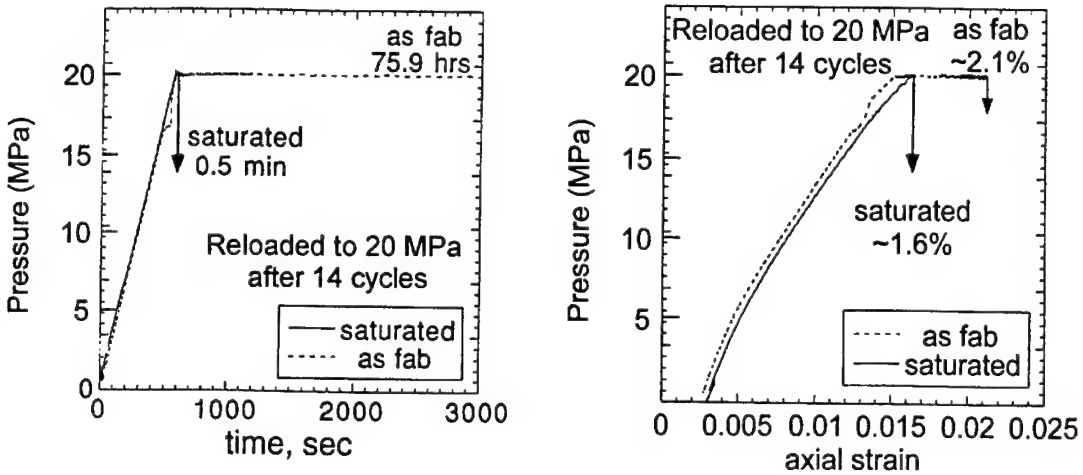
where  $\sigma_{22 \text{ mech ply}}$  and  $\sigma_{22 \text{ resid ply}}$  are the mechanical stress due to external loading and the residual thermal stress due to ply level differential thermal contraction during cool down (modified by moisture induced swelling) in the 90° ply, SC is the stress concentration factor relating local stress in the radial direction at  $\theta=90^\circ$  to ply level stress, and  $\sigma_{rr \text{ int th}}$  is the local residual thermal stresses due to differential thermal contraction between the fiber and the matrix. It is worth noting that the ply level residual thermal stress is tensile in the 90° plies whereas the local residual thermal stress is compressive. Thus, one is helpful in postponing debonding whereas the other makes debonding easier. Both the local level residual thermal stress and the interfacial strength can be converted to equivalent ply level stresses using the stress concentration factor (SC), which is 1.45 for carbon fiber/epoxy and 1.82 for E-glass/epoxy. When the debonding occurs next to a spherical void, an additional stress concentration factor of 2.18 (Timoshenko and Goodier, 1934) needs to be multiplied times the 1.82 to calculate the local interfacial stress from ply level stresses or to calculate equivalent ply level stresses from the local thermal residual stresses or interfacial strength. Equation 1 can be rearranged to express the ply level mechanical stress at which debonding and subsequent transverse cracking occurs, as follows:

$$\sigma_{22 \text{ mech ply}} = \frac{\sigma_{22 \text{ int}} - \sigma_{rr \text{ int th}}}{SC} - \sigma_{\text{resid ply}} \quad (2)$$

At transverse cracking,  $\sigma_{22 \text{ mech ply}}$  is the 90° ply strength and  $\sigma_{rr \text{ int}}$  is the interfacial strength for stresses applied normal to the fiber matrix interface. The results of this analysis are presented in Figure 3 for all three systems. From an engineering point of view, the effect of the absorbed moisture on the mechanical stress level at which debonding and subsequent transverse cracking initiates is most important, and is presented in Fig. 5. The remaining three graphs allow one to infer the reasons for the observed changes in the allowable mechanical stress level in a seawater saturated polymeric composite. The absorbed moisture decreases the residual thermal stresses in the radial direction at the fiber/matrix interfacial, causing them to go net positive in two of the systems. However, the ply level residual thermal stresses which are tensile are relaxed by the absorbed seawater, which would require a



Figures 4 and 5. Pressure loading history for cyclic testing of filament wound tubes of E-glass epoxy and resultant axial strain as a function of cycle number, with the strain at 13.8 MPa from the monotonic test indicated for comparison.



Figures 6 and 7. Time to failure and axial strain as a function of tube pressure for unaged and aged filament wound tubes, loaded after cyclic history indicated in Figure 4.

greater ply level mechanical stress to give debonding.

The reduction in interfacial strength and changes in ply level and fiber/matrix interfacial residual stresses resulted in a decrease in the ply strength ranging from 1.5 MPa in the Epoxy I system, which absorbed an additional 1.1% in seawater to 14 MPa, or 28% of the as prepared

strength in the carbon/epoxy-2 system, which absorbed 1.2% seawater. These results suggest that 70% of the overall decrease in the critical strain (or stress) at which damage begins in 90° plies is due to moisture reduced changes in interfacial strength with the remaining 30% due to changes in residual thermal stresses (at the ply and local level, combined).

The very low values of ply strength in the E-glass/epoxy-1 system were due to damage initiation always occurring at small, spherical voids in the microstructure which were introduced during processing. While the overall void content was less than 1%, these voids still dominated the failure process in the 90° plies. The low ply strength in the E-glass/epoxy-2 was due to the very high ply thermal stresses in the 90° plies due to the greater constraint resulting from very stiff 0° plies of carbon fiber. In the E-glass/epoxy-1 system, the plies adjacent to the 90s were +45s of glass. In the graphite/epoxy-2 system, adjacent 0° plies were E-glass.

Finally, the values presented in Figure 3 should be consider illustrative, but only semi-quantitative since the residual thermal stresses were not calculated with a viscoelastic analysis but just used the room temperature modulus of the matrix. The stress concentration and thermal residual stresses calculated with MICSTRAN are dependent on the local fiber arrangement, with only diamond and square arrangement permitted. The actual fiber arrangements in the microstructure were more complicated and were generally neither square nor diamond arrays, as seen in Figure 2.

### 3.2 Filament Wound Tube Tests

The burst tests gave tube failure at 26.9MPa of tube pressure and 1.9% axial strain in the unaged tube and 25.5MPa of tube pressure at an axial strain of 2.1% in the aged tube, for a 5% reduction. The pressure cycling history is presented in Fig. 4 with the measured axial strain presented in Fig. 5. The results of the subsequent creep rupture tests (pressurizing to 20MPa with a hold until failure occurred) is presented in Figs. 6 and 7. Acoustic emission results for both the burst tests and the cyclic tests are presented in Tables 1 and 2.

It is interesting to note that the axial strain to failure in all tests is approximately 2.0% except for cyclic testing of the aged specimen, which gave 1.6%. The cyclic tests achieved this magnitude of strain at a much lower pressure with a combination of cycling with hold times, which cumulatively were several days in duration, compared to the monotonic test which took less than one hour. Fig. 5 illustrates this behavior by comparing the axial strain for monotonic loading to 13.8 MPa to the cumulative strain for cyclic loading through the 14 cycles with peak cyclic pressure also at 13.8 MPa.

The number of hits in the cyclic test at 20MPa were similar to the monotonic test at 20 MPa as seen in Table 2, indicating that the pressure cycling does not appear to give more damage in the form of debonds, transverse cracking, or fiber breakage than does the monotonic loading to the same pressure. However, the hold times during cycling allowed for more viscoelastic deformation of the matrix, allowing the strain to failure to be achieved at a lower pressure. The effect of moisture appears to be to plasticize the matrix, giving more viscoelastic deformation. Finally, these tests suggest the possibility of a stress corrosion cracking effect of seawater on the glass fibers since the critical strain to failure decreased from 2.0% to 1.6% in the aged tubes with cyclic loading and hold times.

### 4 CONCLUSION

Absorbed seawater has been found to have a very small effect on the interfacial strength in glass/epoxy and graphite/epoxy composites. A similar small effect has been noted on the burst strength of filament wound tubes of glass/epoxy. The failure of filament wound tubes due to cyclic loading with hold times suggests the possibility of a critical strain failure criteria. The combination of seawater and static loading on glass/epoxy composites may reduce this critical strain value.

Table 1. Acoustic Emission “hits”- Burst Test

pressure (psi)	unaged	aged
1000	1000	2000
2000	8,000	10,000
2900	23,000	25,000
3700	48,000	36,000
3900	----	49,000

Table 2- Acoustic Emission “hits”  
Cyclic Loading

pressure (psi)	unaged	aged
0-1000 7 cycles	200	400
0-2000 7 cycles	2000	10,000
0-2900 hold	21,000	21,000

---

## REFERENCES

- Gibson, A.G., AComposite Structures in Offshore Applications,@ Composite Materials in Marine Structures, Chapter 3, 1993, R.A. Shenoi, Ed. Cambridge Ocean Technology Series.
- Tamarelle, P.J. C. and Sparks, C.P., Proceedings of Nineteenth Annual Offshore Technology Conference, Houston, TX, May 1987 (Richardson, TX: Offshore Technology Conference), p. 255.
- Wood, Catherine A., 1996. Determining The Effect of Seawater on the Interfacial Strength of an Interlayer E-Glass/Graphite/Epoxy Composite Using Observations of Transverse Cracking Made in-Situuation@, M.S. Thesis, Texas A&M University.
- Naik, R.A., 1992. AMicromechanical Combined Stress Analysis - MICSTRAN, A User Manual,@ NASA Contractor Report 189694, National Aeronautics and Space Administration, Langley Research Center, Hampton, VA.
- Crews, J.H., R.A. Naik, and S.J. Lubowinski, 1993. An Analysis of Fiber-Matrix Interface Failure Stresses for a Range of Ply Stress States,@ NASA Technical Memorandum 108999, National Aeronautics and Space Administration, Langley Research Center, Hampton, VA.
- Timoshenko, S.P. and Goodier, J.N., 1934. Theory of Elasticity, New York: McGraw-Hill Book Company.
- R.A. Schapery, personal communication.

## Characterizing the durability of PVDF and PPS for extended use in marine environments

D.Kranbuehl, W.Newby-Mahler, J.Garrett, A.Meyer, J.Warner, R.Gittleson, A.Ebersole,  
J.Rogozinski & D.Hood

*Chemistry Department, College of William and Mary, Williamsburg, Va., USA*

S.Case, K.Reifsnider & A.Loos

*Department of Engineering Science and Mechanics, Virginia Polytechnic Institute and State University,  
Blacksburg, Va., USA*

**ABSTRACT:** This report describes recent work on the use of FDEMS sensing to monitor aging in thermoplastics during use in the field, particularly those, Nylon 11, PVDF and PPS being used for flexible composite pipe to transport oil-gas in the offshore subsea environment. Current life monitoring work focuses on characterizing the chemical and physical processes occurring during aging, using FDEMS sensing to monitor the aging rate and state of the polymer, and integrating the sensor output with a model for predicting the remaining service life and state of the structure. The model is periodically updated through the insitu online sensing measurements. This report will also discuss work on developing a fundamental understanding of the relationship of the sensor measurement of the ionic and dipolar mobility to the macroscopic properties of polymeric materials.

### INTRODUCTION

The use of polymeric materials in extended use structures such as airplanes, bridges and pipelines where the expected lifetimes are 20 to 40 years and where failure can be catastrophic is rapidly expanding. As such there is a clear need to develop high quality processing and an insitu health monitoring sensor capability. This paper describes progress toward the development of a frequency dependent dielectric measurement sensor (FDEMS) which is capable of detecting the change in the physical and chemical state of a polymeric material insitu during processing-fabrication and insitu during use in the field environment.

Health monitoring involves monitoring the degradation of a polymeric materials performance properties. In one sense, health monitoring is the reversal of monitoring cure during which there is a buildup in properties.

Frequency dependent dielectric measurements (FDEMS) provide a sensitive, automated insitu sensing technique for intelligent processing and an insitu means for monitoring durability, that is degradation of polymers during use. FDEMS insitu sensing can be designed and calibrated to monitor changes in processing properties during fabrication and changes in mechanical service life properties of polymer materials during use in the field environment. With a proper understanding of the type of polymer and

the use environment, the sensor output can be related to changes such as viscosity, degree of cure and Tg during cure and modulus, maximum load and elongation at break during use. The FDEMS technique has advantages over other monitoring techniques, nondestructive; accuracy/reproduc-tivity; sensitivity; insitu capability; remote sensing; automated.

This report will discuss recent work on the use of FDEMS sensing to monitor aging in thermoplastics during use in the field, particularly those used in flexible composite pipe to transport oil-gas in the offshore subsea environment.

### BACKGROUND

Frequency dependent dielectric measurement, made over many decades of frequency, Hz-MHZ, are a sensitive, convenient automated means for characterizing the processing and performance properties of thermosets and thermoplastics.[Kranbuehl,Loos,Senturia] Using a planar wafer thin sensor, measurements can be made insitu in almost any environment. Through the frequency dependence of the impedance, this sensing technique is able to monitor changes in the molecular mobility of ions and dipoles. These changes in molecular mobility are then related to chemical and physical property changes which occur

during use or during processing. The FDEMS techniques have the advantage that measurements can be made both in the laboratory, insitu in the fabrication tool, and insitu during use. Few laboratory measurement techniques have the advantage of being able to make measurements in a processing tool and in the field in a composite, in an adhesive bond line, of a thin film or a coating. It can be used at temperatures exceeding 400°C and at pressures of 100 atm, with an accuracy of 0.1% and a range in magnitude of over 10 decades. It is difficult for most other in the field techniques to attain this level of sensitivity in harsh environments.

At the heart of dielectric sensing is the ability to measure the changes at the molecular level in the translational mobility of ions and changes in the rotational mobility of dipoles in the presence of a force created by an electric field. Mechanical properties reflect the response in displacement on a macroscopic level due to a mechanical force acting on the whole sample. The reason why dielectric sensing is quite sensitive is rooted in the fact that changes on the macroscopic level originate from changes in force displacement relationships on a molecular level. Indeed, it is these molecular changes in force-displacement relationships which dielectric sensing measures as the resin cures and ages. They are the origin of the resin's macroscopic changes in mechanical performance properties, during use and processing properties during procedure.

## INSTRUMENTATION

Frequency dependent complex dielectric measurements are made using an Impedance Analyzer controlled by a microcomputer.[Kranbuehl 1997] In the work discussed here, measurements at frequencies from Hz to MHz are taken continuously throughout the entire cure process at regular intervals and converted to the complex permittivity  $\epsilon^* = \epsilon' - i\epsilon''$ . The measurements are made with a geometry independent DekDyne micro sensor which has been patented and is now commercially available and a DekDyne automated dielectric measurement system. This system is used with either commercially available impedance bridges or specially built marine environmental bridges designed for use on offshore oil platforms. The system permits multiplexed measurement of several sensors. The sensor itself is planar, 2.5 cm x 1.25 cm area and 5 mm thick. This single sensor-bridge microcomputer assembly is able to make continuous uninterrupted measurements of

both  $\epsilon'$  and  $\epsilon''$  over decades in magnitude at all frequencies. The sensor is inert and has been used at temperatures exceeding 400°C and over 60 atm pressure.

## THEORY

Frequency dependent measurements of the materials' dielectric impedance as characterized by its equivalent capacitance,  $C$ , and conductance,  $G$ , are used to calculate the complex permittivity,  $\epsilon^* = \epsilon' - i\epsilon''$ , where  $\omega = 2\pi f$ ,  $f$  is the measurement frequency and  $C_o$  is the equivalent air replacement capacitance of the sensor.

$$\epsilon'(\omega) = \frac{C(\omega) \text{ material}}{C_o}$$

$$\epsilon''(\omega) = \frac{G(\omega) \text{ material}}{\omega C_o} \quad (1)$$

This calculation is possible when using the sensor whose geometry is invariant over all measurement conditions. Both the real and the imaginary parts of  $\epsilon^*$  can have dipolar and ionic-charge polarization components;

$$\epsilon' = \epsilon'_d + \epsilon'_i \quad \epsilon'' = \epsilon''_d + \epsilon''_i \quad (2)$$

Plots of the product of frequency ( $\omega$ ) multiplied by the imaginary component of the complex permittivity  $\epsilon''(\omega)$  make it relatively easy to visually determine when the low frequency magnitude of  $\epsilon''$  is dominated by the mobility of ions in the resin and when at higher frequencies the rotational mobility of bound charge dominates  $\epsilon''$ .

## LIFE MONITORING - EXPERIMENTAL

FDEMS life monitoring results are being conducted on three material systems; a polyamide nylon-11, polyvinylidene flouride (PVDF) and polyphenyl sulfide (PPS).[Kranbuehl, 1996] The first two materials are already in use in flexible subsea oil-gas transmission pipes on oil platforms throughout the world. The nylon-11 system is used as the oil-gas retention barrier in pipes with operating temperatures up to 80°C. The PVDF is a higher temperature polymer barrier used for oil-gas temperatures up to 130°C. The PPS material is being considered with graphite as an unidirectional tape for use as the axial wrap. It will replace steel bands and create a lighter, higher performance flexible pipe for extremely deep water and arctic environments. As the outer layer of the pipe, the PPS graphic tape is exposed to

seawater. The nylon-11 and PVDF, on the other hand, serve as the inner fluid gas barrier and are exposed to the acidic  $H_2S$ , water, oil mixture coming up from the ground.

FDEMS sensors were embedded in all three material systems by heating the polymer to its glass transition temperature, placing the sensor between 2 pieces of the polymer and encapsulating the sensor in the center with pressure. The resulting material sensor system is approximately 1 cm thick. The embedded sensor material system and mechanical test dog bones of ASTM D638 specifications were then placed in the following aging environments. Nylon-11: 95% oil, 5% water, pH 4.6, 70° and 105°C. PVDF: 95% oil, 5% water, pH 4.6 130°C. PPS: 100% simulated sea water 90° and 120°C. Periodically FDEMS sensor data was taken and pieces were removed for mechanical testing.

## LIFE MONITORING - RESULTS

For nylon-11, Figures 1-2, display the value of  $\epsilon''$  multiplied by the frequency at 100, 120, 10<sup>3</sup>, 10<sup>4</sup> and 10<sup>5</sup> Hz versus time in the 105° and 70° oil-water acidic aging environment.[4] The results are on a log scale. They show a rapid very large rise, 10<sup>4</sup>, during the initial days as water diffuses into the polymer. This process occurs over 30 days at 105°. It occurs over 150 days at 70°, although a large fraction of this change occurs in the initial 30 days. After water impregnation has occurred at 105° there is a gradual decline in  $\epsilon''$ . Other experimental work in our laboratory and recently reported by others has shown that the nylon's molecular weight is degrading due to hydrolysis.[4] This is accompanied by embrittlement, as shown in Figure 3. By making molecular weight measurements of the sensor at various times and of the mechanical tested dog

Nylon Sensor 2L in 105C 5%ASTM/95% H2O  
Log  $\epsilon''w$  vs Day

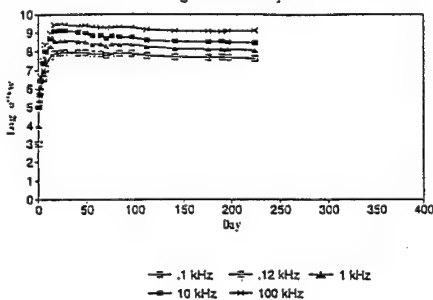


Figure 1 Log( $\epsilon''w$ ) versus day for nylon-11 at 105°C in oil water pH 4.68 frequencies from top to bottom 100, 10, 1, .12, .10 kHz.

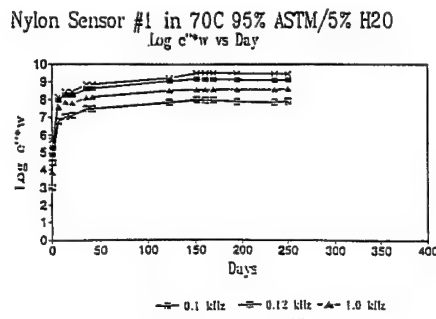


Figure 2 Log ( $\epsilon''w$ ) versus day 70°C.

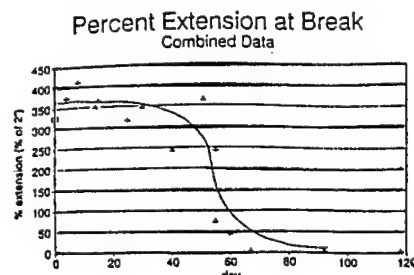


Figure 3 Percent elongation versus day at 105° oil-water pH 4.68.

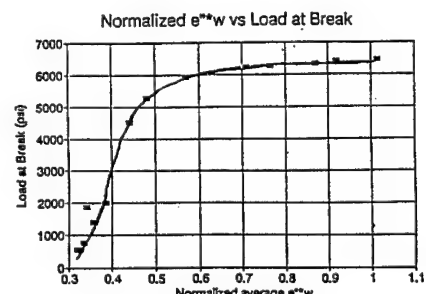


Figure 4 Normalized sensor output versus load at break.  
Normalized  $\epsilon''w$  vs %Extension at Break

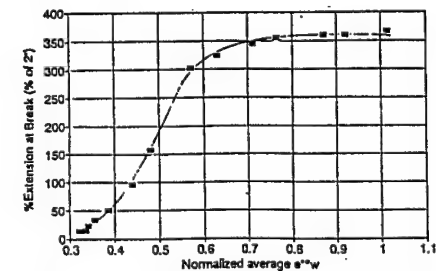


Figure 5 Normalized sensor output versus elongation at break.

bones, a calibration plot relating the normalized sensor output to the load and elongation at break was prepared. This is shown in Figures 4 and 5. The normalized value of  $\epsilon$  is defined as the absolute value of  $\epsilon$  at each time divided by the maximum value achieved around day 30 due to water impregnation.

Using the calibration, it is possible to monitor the mechanical properties of the critical polymer oil-gas barrier with time insitu in the field. This was done over a 400 day period on an oil platform in the British sector of the North sea in 1995-6. The sensor data suggested the pipe was in a failure state. The pipe did fail, was retrieved and the sensor data was verified by making molecular weight measurements on the retrieved pipe's polymer liner.

Similar work is being conducted on PVDF. Figure 6 shows the results of the sensor output over a 300 day period at 130°C. Figure 7 shows the change in mechanical properties. Again for this material system the sensor is able to monitor the gradual embrittlement of the polymer oil-gas barrier. The aging process in PVDF is not primarily molecular weight degradation as in nylon. Aging involves changes in polymer morphology in both the crystalline and amorphous regions and a resulting decrease in elongation at break as the polymer embrittles. This is observed in Fig. 7.

A long term aging experiment involving PPS carbon tape from 2 vendors, A and B was undertaken to establish the durability of these materials as the axial armour in flexible composite pipe. Also studies involving neat PPS have been initiated to establish the durability-stability of pure PPS were relative to the graphite tow. Comparing these two results makes it possible to determine whether aging is driven by the PPS or whether aging of the interface between the PPS and the graphite contributes to any long term change of performance properties.

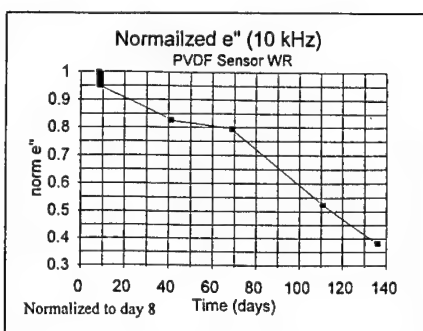


Figure 6 Output of sensor embedded in PVDF while at 130°C, oil-water pH 4.68.

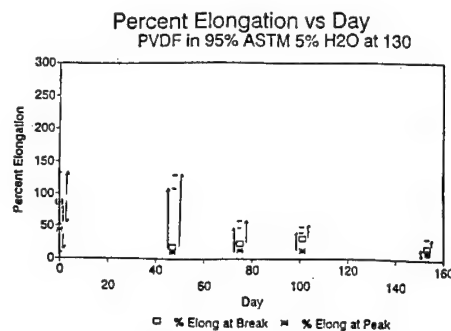


Figure 7 Displacement versus day.

Table I

DSC Data: PPS in 90C Air Oven

Day	dH (J/g)	Melt Temp (C)
0	30.5	279.8
1	22.8	279.2
4	22.0	279.3
5	21.3	280.1

DSC Data: PPS in 90C Seawater

Day	dH (J/g)	Melt Temp (C)
0	30.5	279.8
0	27.0	282.0 *
1	28.2	278.4
12	27.7	279.8
33	19.5	277.1
55	25.6	277.1 *
82	11.0	276.8
105	22.2	276.9 *
150	25.0	276.8 *

\* Mechanical Samples

Table II

DSC Data: PPS in 120C Seawater

Day	dH (J/g)	Melt Temp (C)
0	30.5	279.8
0	27.0	282.0 *
1	34.9	276.2
12	23.9	275.3
33	26.1	276.2
55	26.1	277.5 *
82	19.6	278.9
105	25.8	277.4 *
150	25.8	277.9 *

\* Mechanical Samples

DSC Data: PPS in 120C Air Oven

Day	dH (J/g)	Melt Temp (C)
0	30.5	279.8
1	28.7	278.8
4	25.8	279.0
5	23.7	279.6

First we examine the existing DSC data on PPS in an air oven and in seawater at both 90°C and 120°C. These results in Tables I and II suggest that the changes in  $\Delta H$  and the melt temperature are similar in their trend whether in the air oven or in seawater. There is a modest decrease in  $T_m$  and a

**Table III**

Environment	Day	Maximum Force (lbf)	dL (in)	At Break Force (lbf)	dL (in)
Fresh	0	206.4	0.0668	153.2	0.1991
90C Seawater	55	222.2	0.0628	169.5	0.1139
90C Seawater	105	231.9	0.0583	149.0	0.1444
90C Seawater	150	217.7	0.0551	133.6	0.1442
90C Seawater	203	220.3	0.0574	131.9	0.1297
120C Seawater	203	200.4	0.0631	136.9	0.2093

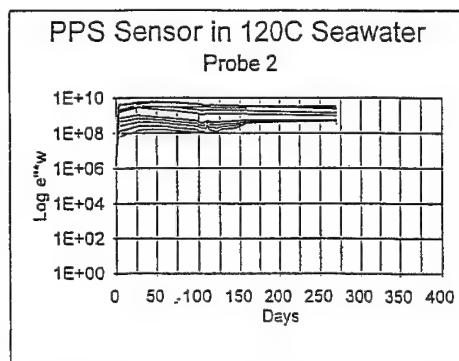
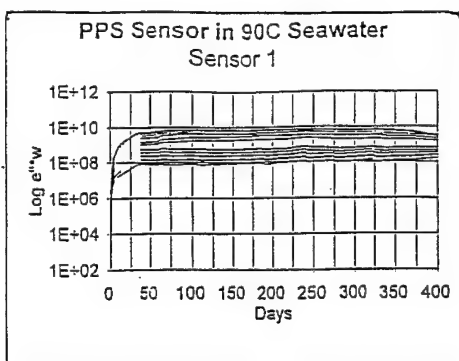


Figure 8 Output of sensor embedded in PPS while at 90° (a) and 120° (b).

rather large decrease in  $\Delta H$  for both the air oven and the seawater. Overall therefore the effect is a thermally stimulated decrease in the percent crystallinity ( $\Delta H$ ) and the crystal structure ( $T_m$ ).

The glass transition temperatures of amorphous PPS is about 88° and it is difficult to detect in the partially crystalline material, where it might be slightly higher. It is likely that this aging effect of a decrease in crystallinity is due to the known tendency of PPS to lightly cross-link with extended time at elevated temperatures. It is also likely the rate of this process drops significantly at temperatures below  $T_g$ .

Figures 8a and 8b report FDEMS sensor data over 400 days at 90° and 250 days at 120°. The FDEMS sensors at 90° show only a very slight drop in the stress-strain relationship of the dielectric loss, as seen by the movement of ions and dipolar groups in the presence of the electric field. At 120° this drop occurs sooner and is a little larger. Overall the drop in the mobility-displacement of these molecular entities suggests a slight stiffening of the polymer with time at 120° over 250 days and less stiffening after over a year, 400 days, at 90°C.

The results of mechanical tensile tests on the PPS tape from vendors A and B aged at 90° and 120° are shown in Figures 9a and 9b. Overall there is little difference in the displacement at break at this point in time. Similarly there is no detectable change in the load at peak, Vendor B's tape, which uses a different carbon fiber is slightly stronger but overall shows the same results, namely no change with age in tensile properties.

Torsion measurements, compared to tensile tests of the maximum value of  $G''$  and the temperature of this peak value are more revealing. Over 100 days, see Figures 10a,b, and 11a,b, there is a clear increase in  $G''$  and the peak temperatures. This increase is greater for vendor A's tape. Further the 100 day data suggests the rate of the increase may be decreasing. Vendor B uses a lower percentage of PPS with the graphite and a higher modulus graphite which would explain why the effect is less. Overall however the torsion results suggest some thermal cross linking leading to a higher modulus of the PPS is occurring.

Table III displays the force and displacement tensile tests on neat PPS dogbones aged at 90° and 120° over 200 days. The results show a modest increase in the strength of the PPS and a slight decrease in the displacement.

Overall, the FDEMS sensor data is encouraging in its ability to detect the slight increase in cross linking, strengthening of the PPS. Overall the DSC, torsion and tensile test data on Baycomps and PCI's PPS tape when aged at both 90° and 120° for about a year are all encouraging regarding the durability of this material in a marine environment. The modest change in stiffness of the PPS tape is explained by the change in the neat PPS resin itself suggesting there is no detectable interfacial aging of the PPS-fiber surface. In summary, with respect to age and temperature, PPS would appear to become slightly stronger and perhaps slightly stiffer with time.

**6" Graphite PPS in Simulated Seawater**  
**Load at Peak vs. Day**

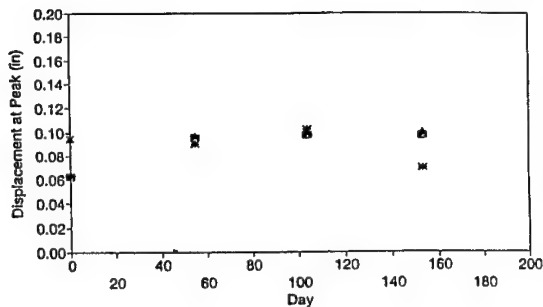


Figure 9a

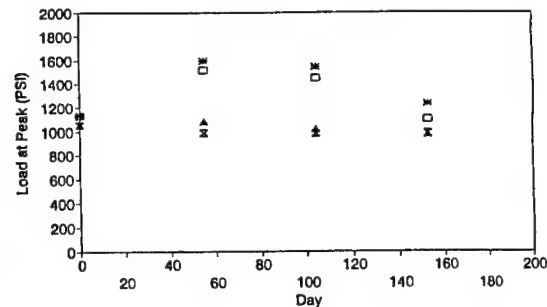


Figure 9b

\* A at 80C □ A at 120C ▲ B at 80C △ B at 120C

**Temperature at Maximum G" vs Day**  
**Graphite Fiber Composite PPS A**

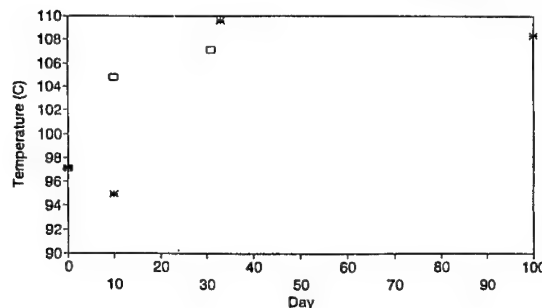


Figure 10a

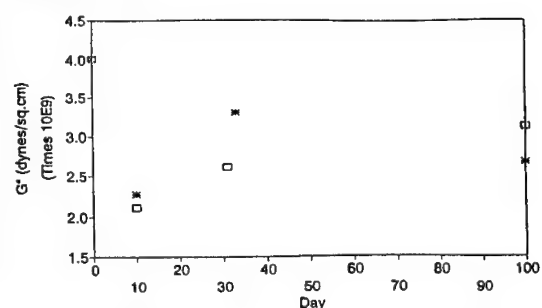


Figure 10b

\* 80C □ 120C

**Temperature at Maximum G" vs Day**  
**Graphite Fiber Composite PPS B**

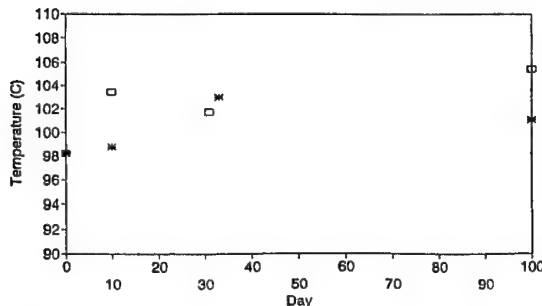
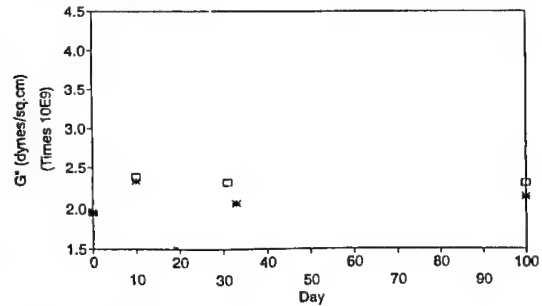


Figure 11a



\* 80C □ 120C

## CONCLUSIONS

FDEMS sensing is an attractive method for monitoring the changing state of a polymeric structure. FDEMS sensing can monitor aging during use in the field or to monitor the changing properties of a polymer during synthesis, and cure in virtually any environment. The polymer can be in the form of a film, coating, adhesive, composite, filler or neat. Through calibration in the laboratory, this electric field molecular displacement sensing technique can monitor continuously and insitu the changes in macroscopic structural properties during use such as load and elongation at break or processing properties such as viscosity, Tg and degree of cure.

- Loos, A.C., Kranbuehl, D. E. and Freeman, W. T., 1987, "Modeling and Measuring the Cure of a Composite", *Intelligent Processing of Materials and Advanced Sensors*, ed., H.N.G. Wadley, et al. The Metallurgical Society, Inc., Warrendale, PA, pp. 197-211.
- Senturia, S., Sheppard, S., 1986, *Applied Polymer Science*, **30** 1-48.

## ACKNOWLEDGMENT

David E. Kranbuehl appreciates partial support from the NSF Science and Technology Center at Virginia Polytechnic and State University under Contract #DMR91-2004; a NASA Langley grant NAGI-23; Exxon, Elf, Shell, BP, Amerada Hess, Statoil, Norsk Hydro and Robit, and a NIST ATP grant with Wellstream Corporation.

## REFERENCES

- Kranbuehl, D. Dielectric Spectroscopy of Polymeric Material, ed. J. Runt, Am. Chem. Soc., Washington, D.C., 1997, 303-328.
- Kranbuehl, D., 1989, "Dielectric Cure Monitoring", *Encyclopedia of Composites*, ed., Stuart M. Lee, VCH Publishers, New York, pp. 531-43.
- Kranbuehl, D., Hood, D., McCullough, L., Aandahl, H., Haralampus, N., Newby, W., Eriksen, M., 1996, "Frequency Dependant Electromagnetic Sensing for Life Monitoring of Polymers in Structural Composites During Use", Progress in Durability Analysis of Composite Systems, ed. A.H. Cordon, Balkema, Rotterdam, 53-62.
- Kranbuehl, D., Hood, D., Rogozinski, J., Barksdale, R., Loos, A., MacRae, D., 1995, "FDEMS Sensing for Automated Intelligent Processing of Polyimides", Proc. ASME International Mechanical Engineering Congress H1041A Vol 2 pp 1017-1030.
- Kranbuehl, D., Kingsley, P., Hart, S., Hasko, G., Dexter, B., Loos, A.C., 1994, "Control of Composite Cure, *Polymer Composites*, 15 (4), 297-305.

## Composites underwater

Peter Davies, Dominique Choqueuse, Florence Mazéas  
*Marine Materials Laboratory, IFREMER Centre de Brest, Plouzané, France*

**ABSTRACT:** This paper presents a summary of recent studies performed at IFREMER on the use of polymer matrix composites for underwater applications, with emphasis on the degradation in mechanical properties due to wet aging. Parameters used in laboratory aging tests such as temperature, hydrostatic pressure and the medium (sea water or distilled water) are discussed. Results from aging at sea are then presented and compared with laboratory aging results.

### 1. CURRENT STATUS

The use of polymeric composites in a marine environment is well established. Applications range from pleasure boats and military vessels to helidecks on offshore platforms, and one of the main reasons for using these materials is their good resistance to harsh environmental conditions. However, although much qualitative data and experience now exist, (reviewed recently by Weitsman<sup>1</sup>) the transfer of this « know-how » into quantified design rules is proving to be a long process. The multiplicity of resins, fibres, test conditions and environments makes generalisations very hazardous and the timescales necessary to validate predictions for particular systems are too long for most research projects. If the safety factors associated with aging uncertainties are to be reduced it is essential that existing data be pooled so that design tools can be developed more rapidly.

The use of composites in underwater applications is increasing, with recent examples in submarine structures<sup>2</sup>, wellhead protection structures for the offshore industry<sup>3</sup> and oceanographic equipment<sup>4</sup>. For these applications the influence of external pressure is an additional parameter which may be significant and must be studied. The importance of pressure on aging was recognized over 30 years ago by Fried<sup>5</sup>, but since then published results on pressure effects have often been rather contradictory.

This paper will present some results from wet aging studies performed at IFREMER in recent years. The aims are twofold : First, to indicate the results which exist, in order that they may be used elsewhere. Second, to discuss some specific examples of parameters which accelerate environmental degradation in underwater applications in order to evaluate accelerated test procedures. Given the limited space available emphasis will be given to the presentation of trends rather than the details of materials and aging conditions.

### 2. LABORATORY EVALUATION

The investigation of composite materials by tests at sea is expensive and generally too long to be of use to the designer, who needs an indication of the stability of different material options in an underwater environment. Accelerated tests are widely used and are generally designed to rank materials under « worst case » conditions. Unfortunately the test conditions are rarely validated even by short tests at sea. The validation will be considered later but first the influence of the main test parameters in laboratory tests will be considered separately.

#### - Temperature

Sea temperature decreases with increasing depth,

Table 1. Acceleration factors for initial diffusion rate,  $D_{66}$  (from modal analysis) and flexural strength when immersion temperature is increased from 5 to 60°C.

Property	Iso. polyester	Vinyl ester	Epoxy	Epoxy prepreg
Initial Diff <sup>n</sup> rate	12	6	5	5
Rigidity D <sub>66</sub>	12	63	5	5
$\sigma_f$	40	20	1.6	2.5

varying in the range from up to 30°C at the surface to 5°C at 1000 meters depth. The easiest parameter to modify in order to accelerate aging in the laboratory is the water temperature. A series of tests was performed recently in which 5 materials were immersed in distilled water at 5, 20, 40 and 60°C and weight gain and mechanical properties were followed over 2 years. The results are available<sup>6</sup> and show that over this range of temperatures both initial diffusion rate and loss in mechanical properties can be modelled by Arrhenius rate equations. However, the acceleration factors for diffusion and for the evolution of the different properties are very different, Table 1.

It is also very important to perform tests over sufficiently long times to validate modelling. An example of weight gains of E-glass/epoxy (LY556) panels immersed in distilled water for over 6 years is

shown in Figure 1. These materials were cured at 130°C and weight gains are well behaved initially but after some months degradation starts to occur and weight gain increases and then decreases. Such curves are frequently noted for polyesters, which evolve during accelerated aging and may undergo hydrolysis, but are more unusual for high T<sub>g</sub> (110°C) epoxies.

#### - Medium

Sea water parameters include salinity (varying from 27 g/l to 37 g/l and usually decreasing with depth), and pH, which varies from 7.5 to 8.5. Biological parameters may also play a role in aging processes, but few studies have addressed these<sup>7</sup>. It is generally accepted that distilled water diffuses into composites more quickly than sea water. A series of tests has been performed recently to examine this hypothesis for four resins and their glass composites (stitched 0/90°), and the initial diffusion rates measured by weight gain are shown in Table 2.

At first glance this indicates very small differences between sea water and distilled water, but in several cases while sea water subsequently reaches a saturation level and stable mass gain, the specimens in distilled water continue to increase in weight even after 18 months at 50°C, Figure 2. This continuous increase in weight in distilled water has been seen previously<sup>8</sup> and attributed to water entry along the fibre-matrix interface as the resin alone in distilled water reaches a plateau value. The salts in sea water may block this path and produce a plateau corresponding to that observed in the resin alone.

While weight gains are interesting, as they may provide information on the initiation of degradation processes, the important result for the

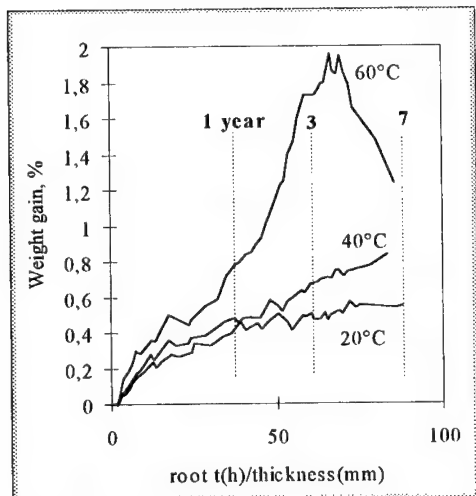


Figure 1. Weight gain of glass/epoxy panels in distilled water, 50000 hours. Each curve shows the mean of 5 panels.

Table 2. Initial diffusion rates (M% x thickness in mm/root time(hours)) for resins/composites in 50°C distilled water (DW) and natural sea water (SW) at 20°C and 50°C.

	Ortho. poly ester	Iso. poly ester	Vinyl ester	Epoxy
20°C Sea water	0.10	0.10	0.09	0.09
	0.09	0.15	0.07	0.12
50°C Sea water	0.25	0.34	0.21	0.30
	0.17	0.21	0.09	0.20
50°C DW	0.38	0.34	0.22	0.33
	0.21	0.22	0.08	0.23

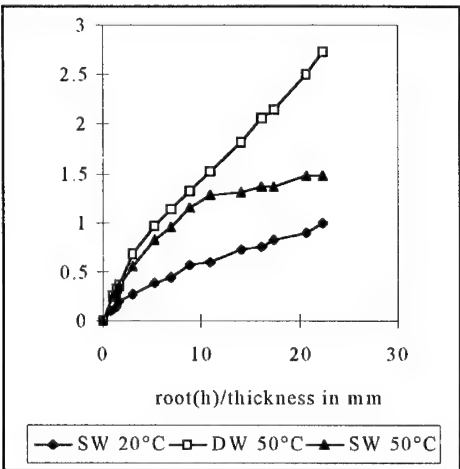


Figure 2. Weight gain (%) of glass/epoxy composite, 18 months' immersion, sea water (SW) and distilled water (DW).

user is whether or not the property degradation in laboratory distilled water tests can be related to that in sea water. Figure 3 shows some  $+/-45^\circ$  tensile test results for glass/epoxy. The shear properties of three composites are summarized in Table 3. It is apparent that the distilled water aging is consistently more severe than sea water.

Table 3. Change in Shear properties of composites after 18 months immersion.

Material	Condition	G, GPa	$\tau$ , MPa
Glass-Epoxy	20°C SW	-8%	-9%
	50°C SW	-18%	-23%
	50°C CDW	-28%	-26%
Glass-Iso polyester	20°C SW	-20%	-12%
	50°C SW	-43%	-32%
	50°C CDW	-46%	-34%
Glass-Vinyl ester	20°C SW	-12%	-10%
	50°C SW	-16%	-23%
	50°C CDW	-18%	-25%

#### - Pressure

Hydrostatic pressure is directly proportional to depth. While many applications are limited to a few hundred meters some oceanographic equipment must spend months or years at up to 6000 meters where a hydrostatic pressure of over 60 MPa is acting. Considerable work on the design, mechanical behaviour and NDE of both glass and carbon reinforced composite cylinders for such applications has been performed at IFREMER. In parallel with the mechanical tests some studies on aging under pressure have been carried out. Pressure effects on composites were discussed by Fried<sup>5</sup> and he noted the difference between low and high void

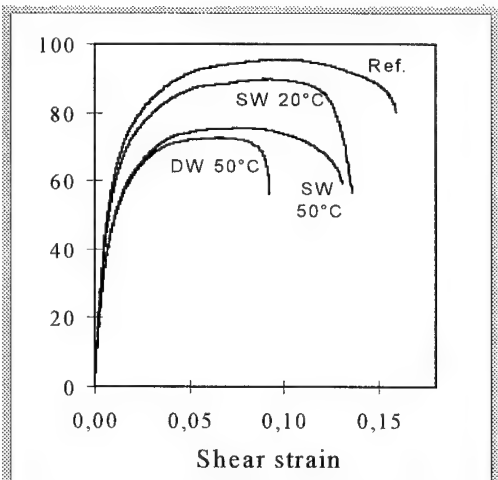


Figure 3. Shear stress (MPa)-shear strain plots from tensile tests on  $+/-45^\circ$  glass/epoxy.

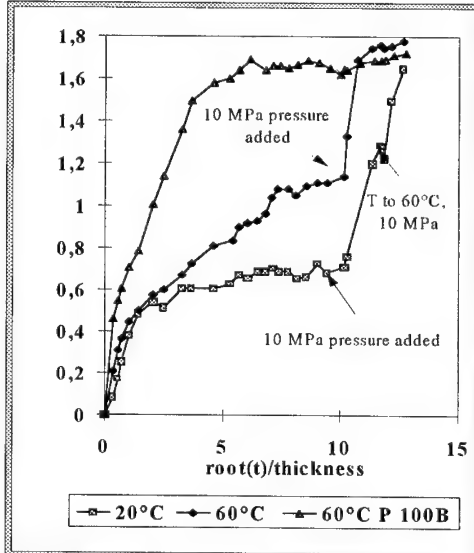


Figure 4. Influence of hydrostatic pressure on weight gain of carbon/epoxy  $+/-55^\circ$  samples immersed in distilled water for 3.5 years

Table 4. Percentage loss in ILSS after immersion in distilled water for 3.5 years (tube samples, with pressure loading as shown in Figure 4) and 4 years (plate samples)

Material	20°C	60°C	60°C+P
Tube +/-55°	-7%	-16%	-14%
Plate (+/-45°)	-1%	-11%	-10%

composites. In the study mentioned above<sup>6</sup> on flat composite panels the effect of 10 MPa pressure was also examined and found to be very small. Other authors have also noted rather small effects, both increases in moisture absorption<sup>9,10,11</sup> and no effect<sup>12</sup> or decreases in absorption<sup>13</sup> being reported. However, recent results at IFREMER for specimens taken from cylinders have shown strong pressure effects, Figure 4.

Filament wound composites are particularly susceptible to pressure effects as void contents tend to be quite high (several percent). Voids influence directly the moisture pick-up<sup>14</sup>. Nevertheless in spite of 3 to 4 years' aging at 60°C under pressure the interlaminar shear strength of these specimens, cut from +/-55° filament wound tubes and of others cut from 0/90° plates, decreased very little, Table 4.

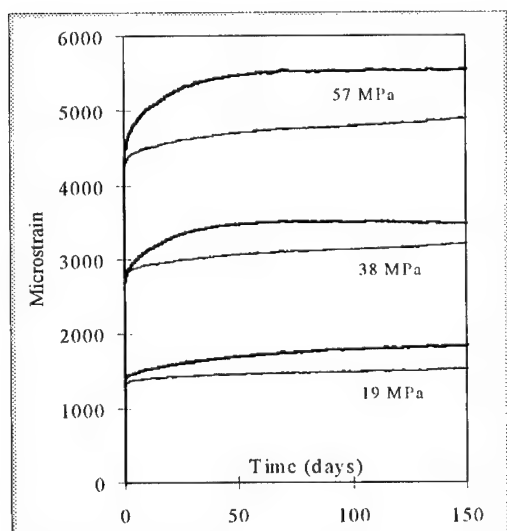


Figure 5. Tensile creep plots for glass rovimat/polyester, at three stress levels. Upper curve for each stress corresponds to test in sea water.

#### - Interaction mechanical loading/ water

Concern has been expressed in the past over the role damage induced by mechanical loading may play in the wet aging process. A series of glass/polyester specimens was loaded to different strain levels, up to 1%, and then immersed in water for 6 months. (This material shows permanent damage above about 0.4% strain). There was no significant influence of this damage on the rate of weight gain in distilled water at 60°C. The interaction of stress and water can be shown to produce increased creep however, as shown in Figure 5. These tests were performed in air and in natural sea water under different tensile loads.

On unloading these specimens almost all the applied strain was recovered after 3 months.

### 3. SEA AGING

In order to examine the correspondance between accelerated laboratory tests and sea conditions a series of tests was started in 1996. Panels (125 mm x 250 mm x 4 mm) of two glass reinforced composite materials (rovimat reinforced isophthalic polyester and stitched quadriaxial reinforced epoxy) were immersed at five meters depth in the Estuary at Brest, (temperature range 7 to 17°C over 12 months, pH 8, salinity 34 g/l) and panels from the same fabrication were placed in thermostatted distilled water baths at 20°C and 50°C in the laboratory. Some specimens were also immersed at 2500 m depth in the Mediterranean. Some of these tests are still underway, but results from 3, 6, 9 and 12 months sea immersion and 1, 2 and 3 months laboratory immersion at 50°C are available. Tensile, interlaminar shear and flexural tests were performed. Figures 6 and 7 show examples of the interlaminar shear strength (ILSS) and tensile moduli results obtained. It is interesting to note (Figure 7) that for the polyester composite the 3 month accelerated test at 50°C reduces the tensile modulus less than one year at sea, while for the epoxy composite the 3 month laboratory test is more severe.

A similar exercise to examine the correlation between accelerated and sea aging was performed for bonded composite/steel assemblies. Samples were placed in tidal zone and immersion sites for up to 12 months. The results will be presented elsewhere<sup>15</sup> but in this case it is interesting to note that corrosion effects on the steel make sea aging more severe than laboratory tests.

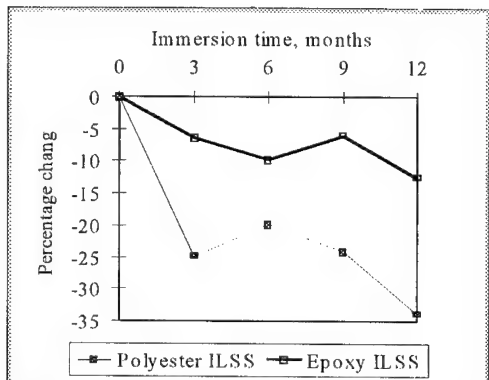


Figure 6. Reduction in ILSS values measured on composites after sea aging for different periods

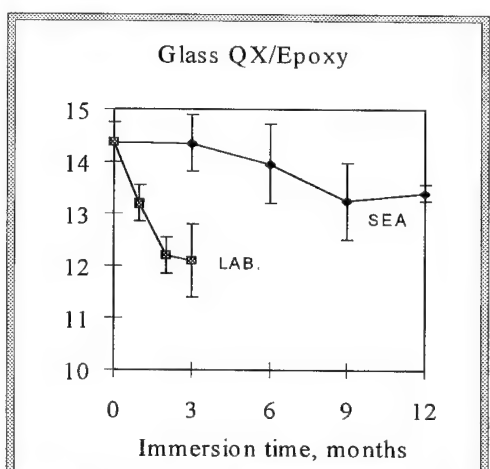
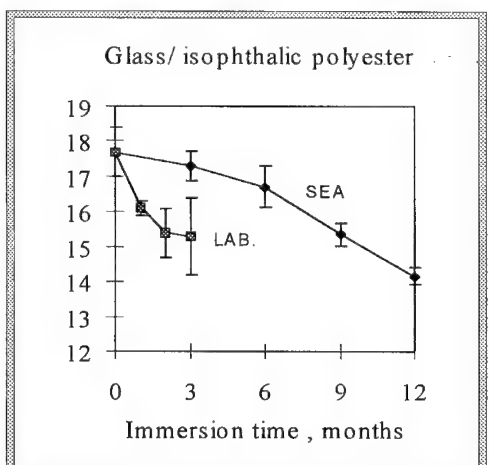


Figure 7. Tensile moduli (GPa) of glass/isophthalic polyester and glass/epoxy samples aged at sea and in laboratory (50°C DW)

#### 4. CONCLUSIONS

The logical extension of the many current composite underwater applications is towards manned deep sea submersibles and submarine primary hull structures. The feasibility of manufacturing small unmanned deep sea submersibles has been demonstrated already<sup>16,17</sup>. Degradation due to aging does not represent a major barrier to the development of such applications as the composites are very thick (tens of millimetres). For shallower water however, the optimization of wall thickness may require attention to be given to reducing current safety factors.

For future uses of composites in more critical underwater applications key issues are defect detection and damage tolerance of thick composites and work is underway to improve understanding of these aspects.

#### References

1. Weitsman Y. « Effect of fluids on polymeric composites- a review », Report MAES 95CM, July 1995, Univ. of Tennessee.
2. Lemière Y, « The evolution of composite materials in submarine structures », Proc 3rd IFREMER conf. on Nautical construction with composite materials, ed P. Davies, L. Lemoine, 1992, pp441-449.
3. Brevik AF, « Sandwich structures for subsea applications », Proc Sandwich Construction 3, Ed Allen, EMAS Publishers 1996 pp27-35.
4. Chauchot P, Guillermin O, « On the use of composite materials for 6000m containers », Proc 8th European SAMPE conf, 1987 pp312-28.
5. Fried N, « Degradation of composite materials », Proc 5th Symp on Naval Struct. Mech., May 1967, pp813-837.
6. Choqueuse D, Davies P, Mazéas F, Baizeau R, « Aging of composites in water », ASTM STP 1302, 1997 pp73-96.
7. Wagner P, Ray R, Hart K, Little B, Bradley W, Chiou P-L, « Microbial degradation of stressed fiber reinforced polymeric composites », Paper 200, Corrosion 95, NACE.
8. Davies P, Pomiès F, Carlsson LA, « Influence of water and accelerated aging on the Shear fracture properties of glass/epoxy composites », Appl. Comp. Mats., 3, 1996, pp71-87.
9. Tucker WC, Lee S-B, Rockett T, « The effects of pressure on water transport in polymers », J. Comp. Mats., 27, 8, 1993 pp756-763.

- 
10. Tucker WC, Brown R, « Moisture absorption of graphite/polymer composites under 2000 feet of seawater », J. Comp. Mats., 23, Aug. 1989, pp787-797.
11. Pollard A, Baggott R, Wostenholm GH, Yates B, George AP, « Influence of hydrostatic pressure on the moisture absorption of glass fibre reinforced polyester », J. Mat. Sci., 24, 1989, pp1665-1669.
12. Bradley WL, Chiou P-L, Grant TS, « The effect of seawater on plymeric composite materials », Offshore composites workshop, Houston 1993.
13. Avena A, Bunsell AR, « Effect of hydrostatic pressure on the water absorption of glass fibre reinforced epoxy resin », Composites, 19, 5, Sept. 1988, pp355-357.
14. Harper BD, Staab GH, Chen RS, « A note on the effects of voids on the hygral and mechanical properties of AS4/3502 graphite/epoxy », J. Comp. Mats., 21, March 1987, pp280-289.
15. Roy A, Gontcharova-Bénard E, Gacougnolle J-L, Davies P, « Hygrothermal effects on failure mechanisms of composite/steel bonded joints », to be presented at ASTM Symp. May 1998, Atlanta.
16. Stachiw JD, Frame B, « Graphite fiber reinforced plastic pressure hull Mod 2 for AUSS vehicle », NOSC Tech. report 1245, Aug. 1988.
17. Davies P, Choqueuse D, Riou L, Warnier P, Jegou P, Rolin JF, Bigourdan B, Chauchot P, « Composite materials for an underwater vehicle for 6000m depth », Proc. JNC 10, Paris 1996, pp 525-35 (in French).

## Fluids effects in polymeric composites – An overview

Y.J.Weitsman

*The University of Tennessee, Department of Mechanical and Aerospace Engineering and Engineering Science,  
Knoxville & Division of Engineering Technology, Oak Ridge National Laboratory, Tenn., USA*

**ABSTRACT:** This article provides a brief overview on several sorption processes of fluids in polymeric composites, and their effects on the mechanical response of those materials. Some emphasis is placed on recent studies regarding immersed fatigue.

### 1 INTRODUCTION

Polymeric composites are a large class of materials, consisting of many combinations of filler and matrix phases, with interfaces or interphases of various properties. In addition to mechanical loads and temperature excursions, these materials can be exposed to a large variety of fluids. These fluids diffuse into the polymeric matrix phase, but may also degrade the interface and attack fillers such as glass fibers. It follows that the effects of fluids on the mechanical response of polymeric composites fall within a wide range of qualitative and quantitative observations.

The main issues associated with the mechanical performance of composites upon the absorption of fluids concern their dimensional stability, strength, durability and fatigue response. On the other hand, many investigations regarding fluids in composites focused on sorption processes and weight-gain measurements alone. While fluid weight-gain magnitudes are not necessarily associated with the absence or presence of detrimental mechanical effects, the data exhibit certain characteristics that are indicative of irreversible processes within the composites. Such processes are related to various mechanisms of internal damage, including polymeric hydrolysis, micro-cracking at the fiber/matrix interfaces, or chemical etching of the fibers themselves. All the aforementioned mechanisms, which depend on the material system and the stress and temperature levels, as well as on the chemistry of the absorbed fluid, lead to degradations in mechanical properties of the composite material.

### 2 SORPTION PROCESSES

The above mentioned characteristic features of weight-gain data are sketched in Fig. 1. In that figure

LF denotes a "classical", linear Fickian diffusion process, while the curves A, B, C, D and S correspond to "anomalous", non-Fickian processes. Cases A and B, which are frequently encountered, correspond to observations where equilibrium levels are never reached and to the so-called "two stage diffusion", respectively. These circumstances typically represent "benign" departures from classical diffusion, which do not necessarily cause irreversible damage. On the other hand, weight-gain data along curve C is associated with severe damage while data along curve D corresponds to irreversible leaching out of material from the composite into the ambient fluid. Weight-gains along curves C and D suggest that the composite material at hand cannot accommodate the corresponding fluid (under the prescribed levels of stress and temperature). It is worth noting that weight-gains along curves A and B in Figure 1 can be explained by a coupled viscoelastic diffusion theory (Ref.1) while weight gains along curve D may be attributed to diffusion in the presence of a chemical reaction. Measurements along curve C are likely to correspond to increased microcracking.

Although the above suggestions seem to be supported by experimental evidence, other explanations are also possible.

Departures from classical diffusion (curve "LF" in Fig. 1) can be noted also during desorption tests. While classical diffusion predicts identical forms for weight-gain and weight-loss upon drying of saturated specimens, the most commonly observed behavior exhibits hysteresis-like loops as shown in Figure 2 for sorption and desorption under constant loads. (Ref. 2) Note that for comparison purposes weight-gains during exposure as well as weight losses during drying are drawn in the upward direction in Figure 2.

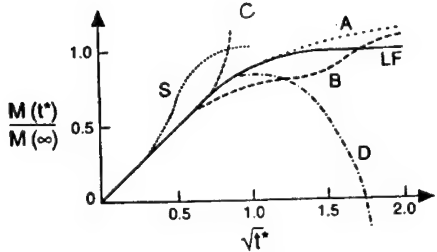


Fig. 1. Schematic curves of non-Fickian weight-gain sorption data in polymers and polymeric composites. The solid line corresponds to linear Fickian diffusion.

$M(t^*)/M(\infty)$  is relative weight gain,  $t^* = Dt/L^2$  is the nondimensional time;  $D$  is the diffusion coefficient,  $L$  is a length and  $t$  is the time variable.

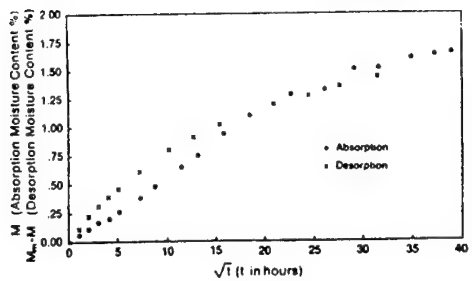


Fig. 2(a) Superimposed values of moisture content vs.  $\sqrt{t}$ . Unstressed, unidirectionally reinforced AS4/3502 coupons during absorption (at  $R_h = 97\%$ ) and desorption (at  $R_h = 0\%$ ) at  $T = 40^\circ\text{C}$ . (Ref. 2)

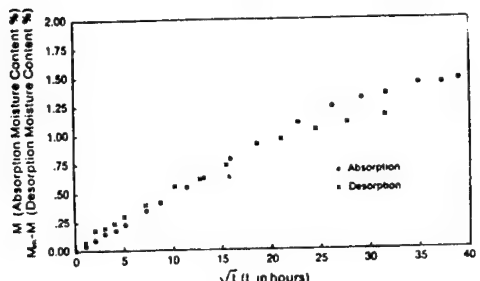


Fig. 2(b) Superimposed values of moisture content vs.  $\sqrt{t}$  in unidirectionally reinforced AS4/3502 composite coupons during absorption (at  $R_h = 97\%$ ) and desorption (at  $R_h = 0\%$ ) at  $T = 40^\circ\text{C}$ . Subiect to uniaxial tension of  $\sigma = 30\%\sigma_u$ . (Ref. 2)

### 3 MECHANISTIC EFFECTS

In many respects fluid effects on the mechanical response of polymeric composites resemble the influence of temperature. In analogy with temperature, fluid sorption is accompanied by expansional strains, which give rise to micro-level and ply level residual stresses. In typical fiber-reinforced epoxy resin composites the expansion due to a 1% relative weight-gain of water is approximately equivalent to the expansion under a temperature excursion of  $100^\circ\text{C}$ . Consequently, water absorption alleviates the level of residual stresses initiated during post-curing thermal cool-down. Fluids also accelerate time-dependent material response, such as creep and relaxation, of polymeric composites, as shown in Figure 3. (Ref. 3) This enhancement, caused by the mechanism of plasticization, may be accounted for by a time-moisture shift factor function  $a_T(m)$ , again in analogy with the temperature dependent  $a_T(T)$ . (Ref. 4)

In realistic circumstances the analogy with temperature could be rather misleading, because moisture diffusion occurs on a time scale that is four to five orders of magnitude slower than that of thermal diffusion. This disparity results in the coupling of moisture diffusion and mechanical creep as well as in long lasting transient, non-uniform, moisture profiles across the thickness of composite material layers, both in contrast with the case of temperature. Consequently, when performing viscoelastic stress analyses in the presence of moisture both spatial and temporal variations in the moisture content  $m$  must be considered. These variations affect the residual stress as well as the shift factor function  $a_T(m(x,t))$ , resulting in time varying inhomogeneity of the material response. Illustrative results concerning interfacial tractions in an adhesive layer of thickness  $a$  exposed to moisture at  $x=0$ , are

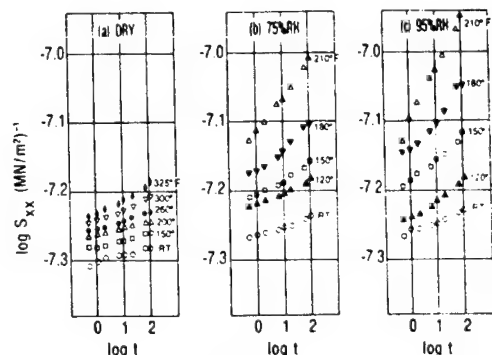


Fig. 3. The creep compliances  $S_{xx}$  as recorded at various temperatures and relative humidities, for  $[\pm 45]_2s$  AS/3502 composite specimens with (a)  $R_h = 0\%$ , (b)  $R_h = 75\%$  and (c)  $R_h = 95\%$ .

shown in Figures 4 and 5, where elastic predictions are provided for purpose of comparison. (Ref. 5)

Sorbed fluids were noted to degrade the strength of epoxies and the transverse strength of unidirectionally reinforced fibrous composites, with reductions of up to 80% in extreme cases. In some composites the reduction of strength increases with exposure time. The specific causes for these degradations vary with the material system. It was also noted that, in some circumstances, the critical energy release rates for transverse cracking and delamination can be reduced by about 30% due to the presence of moisture. (Ref. 6)

#### 4 EFFECTS ON FATIGUE LIFE

Fatigue life under immersed condition was observed to be shorter than that of the dry case by up to one order of magnitude, as demonstrated by the S-N curves for  $[0^\circ/90^\circ]_s$  AS4/3501-6 gr/ep coupons shown in Figure 6.

Immersed and dry fatigue also resulted in consistently distinct failure mechanisms. Specifically, failure under dry fatigue corresponded to a higher density of transverse cracks in the inner  $90^\circ$  ply group and a substantially reduced delaminations between the  $0^\circ$  and  $90^\circ$  plies, when compared to failure at immersed fatigue. Typical observations are shown in Figure 7.

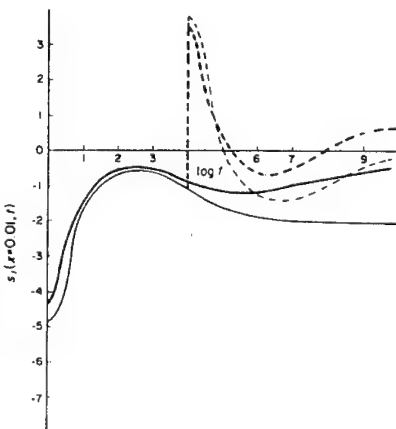


Fig. 4. Elastic and viscoelastic values of the non-dimensional tangential interlaminar traction  $s_t$  at  $x = X/a = 0.01$  vs.  $\log t$  (t in seconds). Heavy lines-viscoelastic, thin lines-elastic. Solid lines-exposure to a constant ambient R.H., dashed lines-exposure to fluctuating ambient R.H.

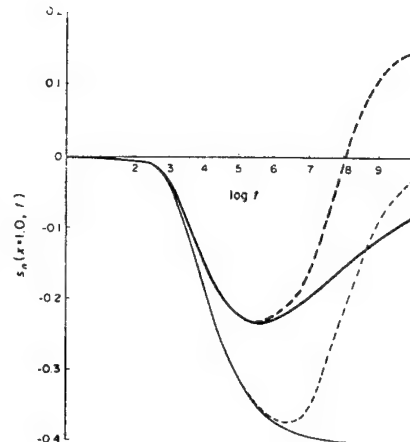


Fig. 5. Elastic and viscoelastic values of the non-dimensional normal interlaminar traction  $s_n$  at  $x = X/a = 1$  vs.  $\log t$  (t in seconds). Heavy lines-viscoelastic, thin lines-elastic. Solid lines-exposure to a constant ambient R.H., dashed lines-exposure to fluctuating ambient R.H.

The latter observations can be explained by the fact that under immersed circumstances the transverse cracks serve as channels that expose the composite to capillary action. Experiments have shown that in the coupons at hand the time for capillary motion, though 4 orders of magnitude shorter than moisture saturation

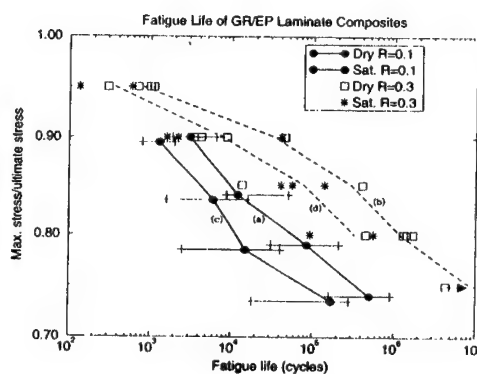
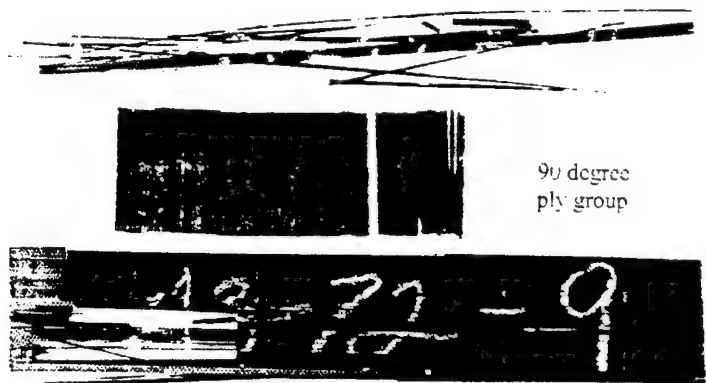
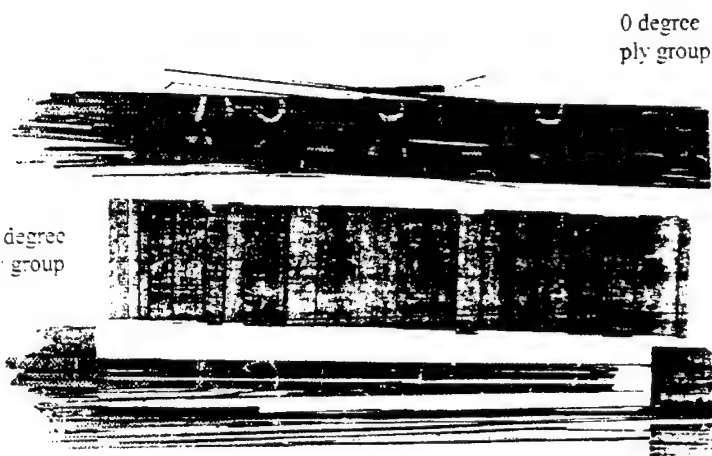


Fig. 6. A semi-Logarithmic Plot of  $\sigma_{\max}/\sigma_{ult}$  Vs. Number of Cycles to Failure  $N_f$  for  $[0^\circ/90^\circ]_s$  for AS4/3501-6 Graphite/Epoxy Coupons:  
(a) Saturated Immersed with  $R = 0.1$   
(b) Dry with  $R = 0.1$   
(c) Saturated Immersed with  $R = 0.3$   
(d) Dry with  $R = 0.3$ .



(a) Dry Fatigue, Specimen A3-72-9



(b) Saturated Immersed Fatigue, Specimen A3-34-3

Fig. 7. Typical Observations of Distinct Forms of Failure that occur in [0°/90°]s, AS4/3501-6 coupons under (a) Dry Fatigue and (b) Saturated Immersed Fatigue. Note the comparatively extensive amount of peeled-off 0° plies, indicating delamination, in the Immersed Case and the higher density of Transverse Cracks in the Dry Case.  
 $R=0.01, \sigma_{max}/\sigma_{ult}=0.8$ .

time, is still about 4 orders of magnitude longer than the fatigue cycling time. (Ref. 7) Consequently, once the transverse cracks are filled with water, which penetrates them by capillary action and through a random walk process, this water cannot escape during the down loading stages of the fatigue cycle and gets squeezed into the interlaminar regions. This explains the extensive delaminations observed in Figure 7(b) which are substantially smaller under fatigue in air.

A typical configuration of "H" shaped cracks, with delaminations emanating from the tips of a transverse crack is shown in Figure 8. Computations of comparative energy release rates for the competing mechanisms of transverse cracking and delaminations were performed employing finite element analysis. (Ref. 8) In the case of immersed fatigue the delamination fracture energy was evaluated at the minimal level of the applied stress, namely at the

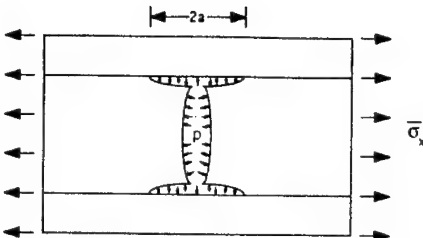


Fig. 8. Geometry of delaminated crack assumed in finite element model.

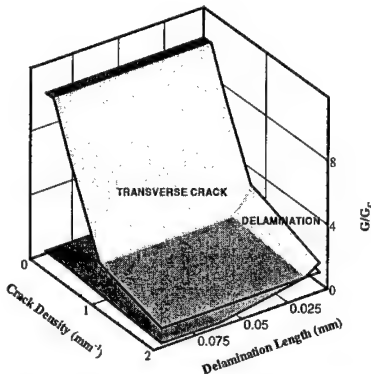


Fig. 9(a). Available Fracture Energies, scaled by the required levels, for Transverse Cracking and for Delamination at the maximal stress level ( $\sigma=450$  MPa) of Dry Fatigue, vs. Density of Transverse Cracks and Delamination Lengths in a  $[0^{\circ}/90^{\circ}]_s$  gr/ep coupon.

downloading stage, when water pressure within cracked regions is largest. Results are shown in Figures 9(a), (b), (c) for the  $[0^{\circ}/90^{\circ}]_s$  specimens at hand with  $\sigma_{\max}=450$  MPa and  $\sigma_{\min}=45$  MPa (i.e. an R ratio of 0.1). In this figure surfaces of  $G_{\text{available}}/G_{\text{required}}$  are drawn for transverse cracking and delamination. The amounts of  $G_{\text{required}}$  were adjusted to accommodate  $G/G_{II}$  ratios which increase with delamination length. (Ref. 9) For added clarity, the intersections of the pairs of surfaces in Figs. 9 are re-drawn in Fig. 10, exhibiting the switching from further transverse cracking to delamination. Note that the various curves in Fig. 10 emanate from disparate levels of transverse crack densities.

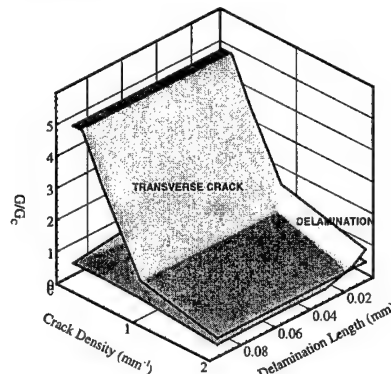


Fig. 9(b). Available Fracture Energies, scaled by the required levels, for Transverse Cracking and for Delamination at the maximal stress level (( $\sigma=450$  MPa) of saturated coupons fatigued in air, vs. Density of Transverse Cracks and Delamination Lengths in a  $[0^{\circ}/90^{\circ}]_s$  gr/ep coupon.

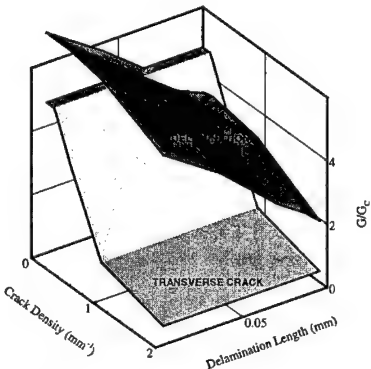


Fig. 9(c). Available Fracture Energies, scaled by required levels, for Transverse Cracking and for Delamination at the Downloading stage (( $\sigma=45$  MPa) Of Immersed Fatigue vs. Density of Transverse Cracks and Delamination Lengths in  $[0^{\circ}/90^{\circ}]_s$  gr/ep coupons.

## 5 CONCLUDING REMARKS

As noted earlier, it is important to realize that the effects of fluids on the response of composites vary most substantially with the specific circumstance at hand. Nevertheless, there exists an overall commonality in general trends that should be useful to investigators in this area.

This abbreviated review is based upon Report MAES 95-1.0CM "Effects of Fluids on Polymeric Composites - A Review", prepared under ONR Contract N00014-90-J-1556 (July 1995). An updated version of the review is expected to be published in Volume 2 of "Comprehensive Composites", Elsevier.

The results clearly demonstrate the preference for delamination in the immersed case.

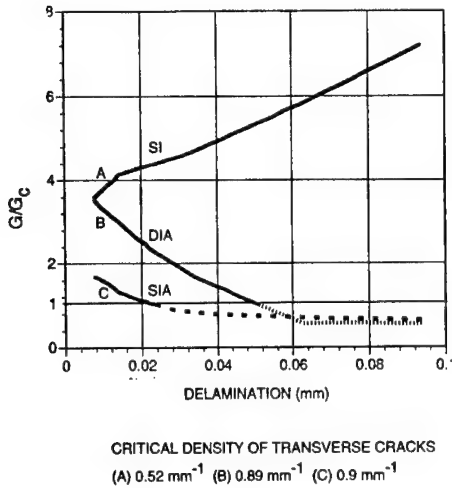


Fig. 10. The Intersection Curves of the surfaces shown in Figs.9(a),(b),(c), indicated by DIA ("Dry in Air"), SIA ("Saturated in Air"), and SI ("Saturated Immersed"), respectively. These Curves exhibit the trends towards increasing delaminations upon switching from failure by transverse cracking. Note that the above curves emanate from distinct values A,B,C of transverse crack density. Also, Delamination Arrest is predicted for the DIA and SIA cases when  $G/G_c \leq 1$ , while no arrest is predicted for the SI case.

## REFERENCES

- (1) Weitsman, Y., "A Continuum Diffusion Model for Viscoelastic Materials," *The Journal of Physical Chemistry*, Vol. 94, No. 2, pp. 961-968 (1990).
- (2) Henson, M.C. and Weitsman, Y., "Stress Effects on Moisture Transport in an Epoxy Resin and its Composite," *Proceedings of the Third Japan-U.S. Conference on Composite Materials*, Tokyo, Japan Society of Composite Materials, Tokyo, June 1986, pp. 775-783. (1986).
- (3) Kibler, K.F., "Time-Dependent Environmental Behavior of Graphite/Epoxy Composites," Final Report, General Dynamics Corporation, Fort Worth, TX, Contract F33 615-77-C-5109, Report AFWAL-TR-90-4052, (February 1980).
- (4) Harper, B.D. and Weitsman, Y., "On the Effects of Environmental Conditioning on Residual Stresses in Composite Laminates" *International Journal of Solids and Structures*, Vol. 21, No. 8, pp. 907-926 (1985).
- (5) Weitsman, Y., "Interfacial Stresses in Viscoelastic Adhesive Layers Due to Moisture Sorption." *International Journal of Solids and Structures*, Vol. 15, No. 9, pp. 701-714 (1979).
- (6) Norwood, L.S. and Marchant, A., "Recent Developments in Polyester Matrices and Reinforcements for Marine Applications, in Particular Polyester/Kevlar Composites," in *Composite Structures*, (Ed., Marshall, I. H.). Applied Science Publishers, pp. 158-181.(1981).
- (7) Smith, L. and Weitsman, Y. "The Immersed Fatigue Response of Polymer Composites," *International Journal of Fracture*, Vol. 82, pp. 31-42. (1996).
- (8) Selvarathinam, A. and Weitsman, Y., "Transverse Cracking and Delaminations in Cross-Ply Gr/Ep Composites under Dry, Saturated and Immersed Fatigue", Contract Technical Report No. MAES97-4.0CM, Department of Mechanical and Aerospace Engineering and Engineering Science, The University of Tennessee, Knoxville 37996-2030. (Nov. 1997).
- (9) O'Brien, T. Kevin, "Composite Interlaminar Shear Fracture Toughness,  $G_{IIc}$ : Shear Measurement or Sheer Myth?", NASA Technical Memorandum 110280, U.S. Army Research Laboratory Technical Report 1312. (1997).

## Effects of moisture and loading mode on transverse cracking of GFRP laminates

J.J.L. Morais

UTAD, Quinta dos Prados, Vila Real Codex, Portugal

A.T. Marques

INEGI/DEMEGI, FEUP, Porto Codex, Portugal

**ABSTRACT:** The results of an experimental program on the effects of moisture and loading mode (quasi-static and impact tensile loading) on the transverse cracking in crossply GFRP laminates are presented. It was found that the impact loading increases the first ply failure stress, the rate of transverse cracking growth and the crack density at the characteristic damage state. It was also observed that for the quasi-static loading the absorbed moisture reduces the first ply failure stress, leaving unchanged the rate of transverse cracking development and the final crack density. However, the extent of axial stiffness reduction depends on the moisture content. This moisture effects are only partially reversible. The Talreja's continuum damage theory was used to analyze the stiffness loss and a close agreement between predictions and measurements was found.

### 1 INTRODUCTION

Transverse matrix cracking in off-axis plies, removed from concentrated loads and free edges, is the initial damage mode that occurs in continuous fiber composite laminates under mechanical and hygrothermal loads. The matrix cracks does not lead necessarily to structural failure of a composite part. But its presence affects the laminate mechanical and physical properties, with severe implications for the durability of high performance applications. Although extensive experimental and theoretical work has been devoted to this damage mode, its growth law and its influence on the laminate properties are not completely understood.

Two important discoveries on the transverse matrix cracking process are the *in situ* transverse strength of a ply in a laminate (Parvizi et al. 1978, Crossman & Wang 1982, Flaggs & Kural 1982) and the characteristic damage state (CDS) (Reifsnider & Talug 1980, Masters & Reifsnider 1982). The stress or the strain at the onset of matrix cracking is not a ply property but is dependent on its thickness as well as on the constraining effect of the adjacent plies (Parvizi et al. 1978, Crossman & Wang 1982, Flaggs & Kural 1982, Xu 1995). As the loading continues the matrix cracking growth until eventually reaches a final regular crack pattern, called characteristic damage state (CDS). The CDS depends on the material properties and laminate construction, but it seems to be insensitive to the hygrothermomechanical loading history (Reifsnider & Talug 1980, Masters &

Reifsnider 1982, Kriz & Stinchcomb 1982, Rothschild et al. 1988, Reifsnider 1990, Xu 1995); however, the rate at which it is attained is related to the loading history.

Several models for transverse matrix cracking are now available, each of which has its own advantages and limitations. They can be grouped in two main categories: the models based on the analysis of stress and strain fields near the cracks and the models based on the continuum damage mechanics. To the first category belongs the different forms of shear-lag approximations (Highsmith & Reifsnider 1982, Fukunaga & Chou 1984, Lim & Hong 1989, Lee & Daniel 1990, Tsai & Daniel 1993, Xu 1995), the variational methods (Hashin 1986, Nairn & Hu 1992), the self-consistent scheme (Dvorak et al. 1985) and several other approximative analytical methods and finite element analysis (Nuismer & Tan 1988, Tan & Nuismer 1989, Gudmundson & Östlund 1992a,b, Guild et al. 1993, Shahid & Chang 1995). The continuum damage models, developed in the framework of thermodynamics with internal variables, ignore the details of the stress and strain fields in the vicinity of the cracks, modelling the representative volume element experimentally (Talreja 1987, Allen & Harris 1987a,b, Weitsman 1987, Talreja 1990).

In this paper we shall present the results of an experimental investigation on the effects of moisture and loading mode (quasi-static and impact tensile loading) in the onset and development of transverse cracks. The continuum damage theory developed by

Talreja (1987, 1990), will be used as a basis for analyzing the test data.

## 2 MATERIAL AND EXPERIMENTAL PROCEDURES

The material system used in this work was a quasi-unidirectional glass/epoxy composite, with 7% of the fibers in the transverse direction, supplied by PPG in a prepreg form, under the trade name PV245®. Laminate plates were fabricated in a hot press according to the manufacturer's cure schedule, with the following layups: [0/90<sub>3</sub>]<sub>s</sub>, [0<sub>2</sub>/90<sub>2</sub>]<sub>s</sub>, and [0/90]<sub>2s</sub>. The temperature drop between the maximum cure temperature and the ambient temperature was -105°C. The ply properties of the dry and wet material (0.792% and 1.777% equilibrium weight moisture content) are given in table 1 (Morais, in prep.).

Tensile coupons, 20mm wide and 220mm long, were cut from the plates using a diamond saw and the edges were prepared for microscopic examination, with 1µm diamond paste in the last polishing step. The ends of the specimens were reinforced with aluminum-alloy tabs, leaving a free length of 140mm.

In order to ensure an initially dry state, all specimens were desiccated at 75°C over silica gel, in an air circulating oven. The specimens were immediately placed in dessicated containers and maintained at room temperature until tested, except some [0/90<sub>3</sub>]<sub>s</sub> specimens which were exposed to moisture environments. The moisture conditioning was done at 75°C for two relative humidities (73% and 92%), until reaching an apparent equilibrium weight gain (0.792% and 1.777%, respectively). A number of specimens previously in equilibrium at 73% relative humidity and 75°C were subsequently dried at the same temperature, before testing.

The quasi-static tensile tests were conducted in an Instron Model 4208 universal testing machine at a crosshead displacement rate of 0.25 mm/min. Each specimen was initially loaded to an estimated value when transverse cracking may initiate, unloaded and reloaded to a higher preselected stress level (Figure 1). The procedure was repeated until the CDS was achieved. The axial strain was measured using an Instron clip-on type extensometer, with a 50 mm gauge length. The unaged [0/90<sub>3</sub>]<sub>s</sub> specimens were also instrumented with a CEA-13-250UW-350 strain gages, from Measurements Group, Inc.

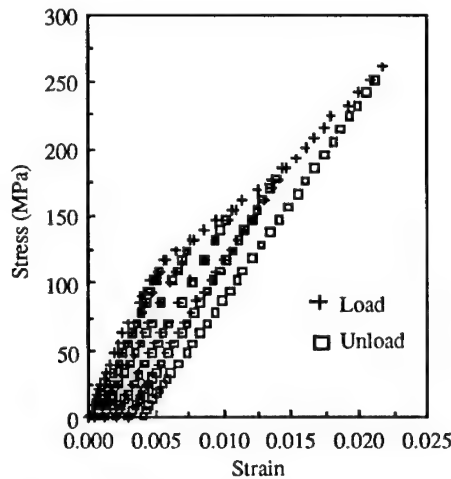


Figure 1. Repeated progressive loading of a [0/90<sub>3</sub>]<sub>s</sub> dry specimen.

Table 1. Ply properties.

Property	Value		
	Dry	Wet (0.792%)	Wet (1.777%)
Longitudinal modulus, E <sub>1</sub> (GPa)	40.83		
Transverse modulus, E <sub>2</sub> (GPa)	19.52	15.87	14.22
Poisson's ratio, ν <sub>12</sub>	0.24		
Longitudinal tensile strength, X <sub>+</sub> (MPa)	1063		
Transverse tensile strength, Y <sub>+</sub> (MPa)	103	62.0	48.5
Longitudinal thermal expansion coefficient, α <sub>1</sub> (K <sup>-1</sup> )	7.4x10 <sup>-6</sup>		
Transverse thermal expansion coefficient, α <sub>2</sub> (K <sup>-1</sup> )	23.3x10 <sup>-6</sup>		
Ply thickness, t (mm)	0.164		

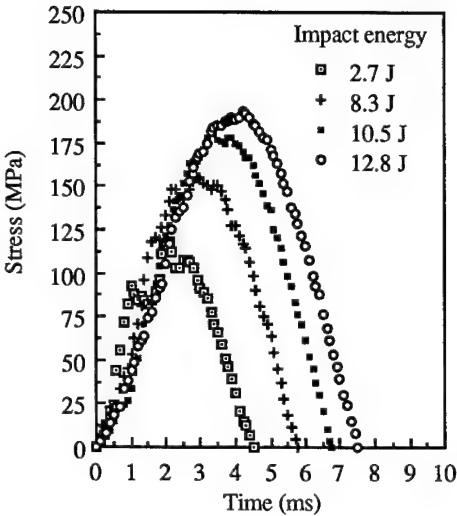


Figure 2. Recorded stress-time curves of a  $[0/90]_3s$  dry specimen repeatedly impacted under successive higher energies.

The transverse crack development during the repeated progressive quasi-static loading was recorded by edge replication. The edge replicas were obtained by pressing against specimen edges cellulose acetate tapes softened by acetone. The number of transverse cracks over a 60 mm gauge length, in both edges of the specimens, were counted using an optical microscope. The accuracy of this technique was evaluated by di-iodobutane enhanced X-ray radiography, performed on selected specimens of each laminate type by means of a SEIFERT point source X-ray chamber and an Agfa D4 type film. Acoustic emission technique was used to identify the onset of transverse cracking. The acoustic emission was monitored on a simple basis of event counting, with the aid of a LOCAN 320 (by Physical Acoustic Corp.) acquisition system and two piezoelectric transducers with 150 KHz central frequency.

Tensile impact tests were performed on unaged specimens, using a Rosand Type 5 instrumented falling-weight impact system. The specimens were successively impacted at higher energies, keeping unchanged the impact velocity. The basic experimental information arising from the impact tests was the stress-time curves (Figure 2). Before impact test and after each one, the quasi-static stress-strain response was determined, to a stress level which doesn't introduce additional damage. These quasi-static tests were run on an Instron Model 4208 testing

machine at a controlled displacement rate of 0.25 mm/min. The respective damage state was documented by edge replication.

### 3 CONTINUUM DAMAGE MODEL

A continuum damage model has been developed by Talreja (1987, 1990), wherein the transverse cracking and delamination damage modes in composite laminates are described by second-order tensor valued internal state variables. These damage variables are assumed as continuous fields throughout the cracked laminate, representing at each material point the average effect, on a macroscale level, of discontinuous damage inside the surrounding representative volume element (RVE). The actual mechanical response is determined by the internal state variables, along with the thermomechanical state variables, via constitutive relationships. We shall review the damage variables associated with transverse cracking, the inplane constitutive relationships for crossply laminates, and the methodology of model identification. Let us consider a RVE of a crossply laminate (Figure 3), of a volume  $V$  and containing a parallel array of  $k$  transverse cracks, with a uniforme crack space  $s$ . The tensor damage variable proposed by Talreja (1990), has the following general form, for non-interactive damage mode entities (cracks):

$$D_{ij} = \frac{1}{V} \sum_k \left( \int_S a_i n_j dS \right)_k \quad (1)$$

where  $S$  is the surface of each crack in the RVE and  $a_i$  is the activity vector at a point on  $S$  with a unit outward normal  $n_i$ . For transverse cracking in composite laminate of a brittle matrix it is assumed the vector  $a_i$  is given by (Talreja 1990):

$$a_i = \kappa t_c n_i, \quad (2)$$

where  $t_c$  is the thickness of the cracked plies and  $\kappa$  is a constant introduced to account for the constraining effect of the adjacent plies on the crack surface displacements. Thus, in the case of a crossply laminate, the damage tensor, referred to the coordinate axis of Figure 3, has only one non-zero component:

$$D_{11} = \frac{\kappa t_c^2}{st}, \quad (3)$$

where  $t$  is the laminate thickness.

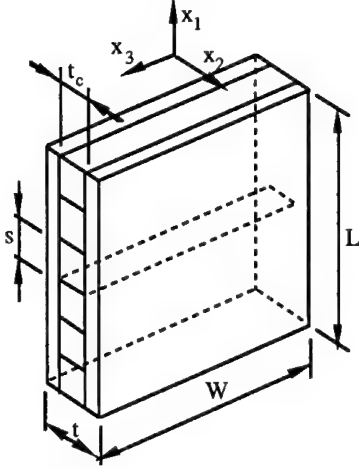


Figure 3. A representative volume element for transverse cracking of a crossply laminate.

Following the Coleman-Gurtin (1967) treatment of a thermodynamics with internal variables, Talreja (1990) derive the relationships between the damage tensor and the residual elastic properties of a composite laminate with transverse cracks, restricted to the isothermal loading and small damage. The inplane engineering elastic constants of a cracked crossply laminates are (Talreja 1987):

$$\begin{aligned} E_1 &= E_1^0 + 2 \frac{\kappa t_c^2}{ts} \left[ c_3 + c_8 (v_{12}^0)^2 - c_{16} v_{12}^0 \right] \\ E_2 &= E_2^0 + 2 \frac{\kappa t_c^2}{ts} \left[ c_8 + c_3 (v_{12}^0)^2 - c_{16} v_{12}^0 \right] \\ v_{12} &= v_{12}^0 + \frac{\kappa t_c^2}{ts} \left[ \frac{1 - v_{12}^0 v_{21}^0}{E_2^0} \right] (c_{16} - 2c_8 v_{12}^0) \\ G_{12} &= G_{12}^0 + \frac{\kappa t_c^2}{ts} c_{13}. \end{aligned} \quad (4)$$

The elastic response associated with a given damage state is thus determined by the initial undamaged elastic constants ( $E_1^0$ ,  $E_2^0$ ,  $v_{12}^0$ ,  $v_{21}^0$ , and  $G_{12}^0$ ) and by a new set of material constants:  $c_3$ ,  $c_8$ ,  $c_{13}$ , and  $c_{16}$ .

The identification methodology of material constants involves the use of equations (4) along with the experimental results on engineering constants reduction obtained by testing a particular crossply laminate (Talreja 1987, Talreja et al. 1992). Assuming the invariance of the transverse Young's modulus  $E_2$  with transverse cracking and excluding the shear modulus  $G_{12}$ , which is independent of the

other engineering constants, the material constants are given by (Talreja 1987, Talreja et al. 1992):

$$\begin{aligned} \kappa c_3 &= A_1 (2v_{12}^0 v_{21}^0 - 1) - 2A_3 E_2^0 v_{12}^0 \\ \kappa c_8 &= A_1 (v_{21}^0)^2 - 2A_3 E_2^0 v_{21}^0 \\ \kappa c_{16} &= 2A_1 v_{12}^0 (v_{21}^0)^2 - 2A_3 E_2^0 (1 + v_{12}^0 v_{21}^0) \end{aligned} \quad (5)$$

where

$$\begin{aligned} A_1 &= -\frac{t E_1^0}{2t_c^2 (1 - v_{12}^0 v_{21}^0)} \frac{1 - E_1 / E_1^0}{\eta} \\ A_3 &= -\frac{t v_{12}^0}{2t_c^2 (1 - v_{12}^0 v_{21}^0)} \frac{1 - v_{12} / v_{12}^0}{\eta} \end{aligned} \quad (6)$$

and  $\eta = 1/s$  is the transverse crack density.

## 4 TRANSVERSE CRACKING PROCESS

### 4.1 Unaged laminates

The results of crack density development in unaged laminates, under quasi-static and impact loading conditions, are shown in Figure 4 as a function of laminate axial stress. The matrix crack growth process revealed by the figures, namely for the quasi-static loading case, has the typical appearance reported widely in the literature (Highsmith & Reifsneider 1982, Masters & Reifsneider 1982, Talreja et al. 1992, Shahid & Chang 1995, Xu 1995): after the onset of transverse cracking, the cracks accumulate at a high rate which decreases gradually until a final CDS is achieved. It also can be seen that the loading mode affects all the specimen features of  $\eta-\sigma$  curves: the initiation, the accumulation and the CDS.

The laminate stress at the onset of transverse cracking,  $\sigma^F$ , can be obtained by fitting a polynomial through the  $\eta-\sigma$  test data, by polynomial regression analysis; the first ply failure (FPF) stress is then one of the roots of the resulting polynomial. The reliability of this procedure was examined by comparison with the stress at the knee-point in the stress-strain curves, identified as illustrated in Figure 5a, and at which is believed the matrix cracking initiates. Another comparison test is based on the cumulative acoustic emission counts versus stress curve (Roubini & Solomons 1995), as shown in Figure 5b:  $\sigma^F$  is the intersection with the  $\sigma$ -axis of a tangent line to the curve, where it is almost asymptotic to the vertical axis. The results of those identification methods of FPF stress are summarized in Table 2, where their consistency can be appreciated as well as the lamination construction

effect. Despite some objections about the physical situation corresponding to the FPF stress (Reifsneider & Talug 1980, Reifsneider 1990) it is an useful operational concept, widely used by the composite materials community.

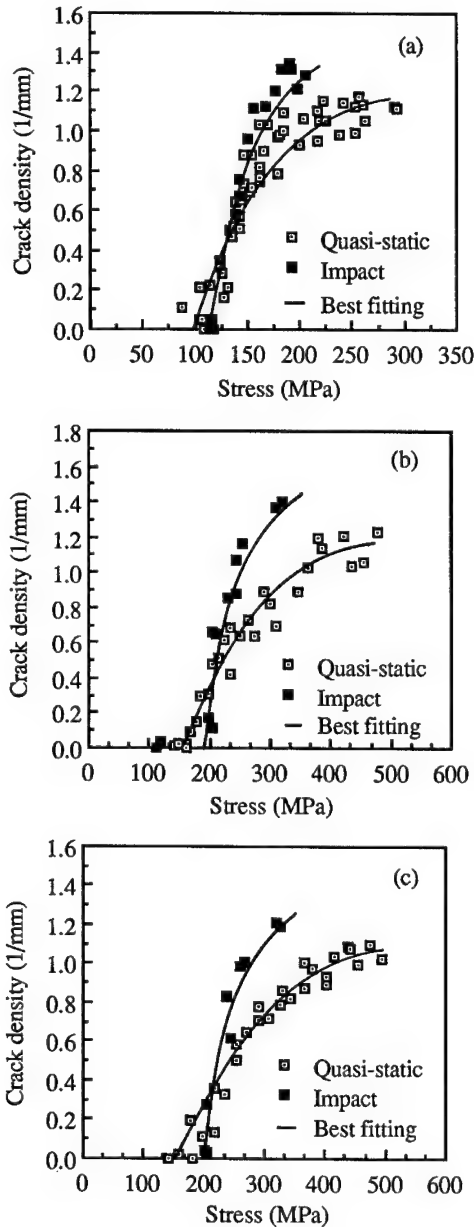


Figure 4. Transverse crack density plotted against laminate axial stress, under quasi-static and impact loading, for (a)  $[0/90]_3s$ , (b)  $[0_2/90]_2s$ , and (c)  $[0/90]_{2s}$ .

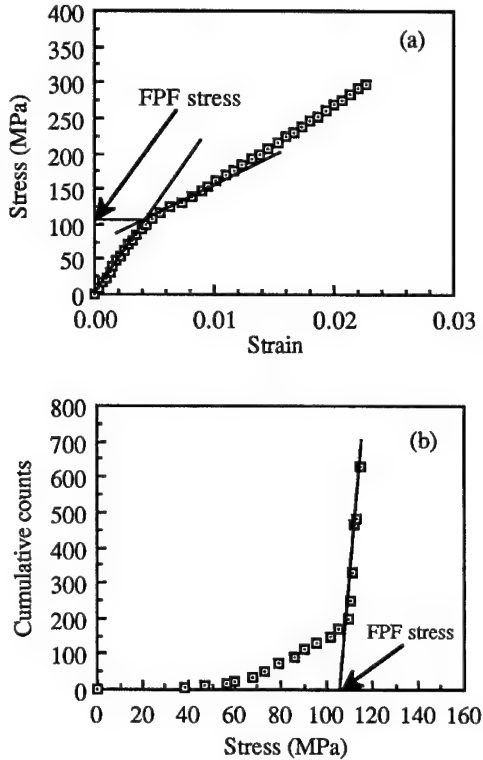


Figure 5. First ply failure stress identification of a  $[0/90]_3s$  laminate by (a) the stress-strain curve and (b) by the cumulative acoustic emission counts versus stress curve.

Table 2. First ply failure stress of unaged laminates,  $\sigma^F$  (MPa).

Laminate	$[0/90]_3s$	$[0_2/90]_2s$	$[0/90]_{2s}$
$\eta-\sigma$ curve	115.6	185.3	197.7
Impact loading			
$\eta-\epsilon$ curve	105.3	149.7	158.0
Static loading			
$\sigma-\epsilon$ curve	105.6	140.6	158.2
Acoustic emission	107.5	133.6	149.0

#### 4.2 Aged $[0/90]_3s$ laminates

The evolution of transverse crack density with the laminate axial stress for  $[0/90]_3s$  laminates aged under different environmental humidities, are presented in Figure 6 and compared with the unaged laminate. It can be seen that moisture shift the  $\eta-\sigma$  curves horizontally to the low stresses, as much as the

percent weight moisture content is high. Thus, the only effect of absorbed moisture is the reduction of  $\sigma^F$  (Table 3), whereas the rate of crack development and the CDS density remain unchanged. This hygrothermal effect is only partially reversible.

Careful examination of specimen edges after environmental conditioning doesn't reveal any induced moisture defects. The observed behavior is attributed to the changes in ply properties and in the laminate stress state due to the matrix plasticization and expansion promoted by absorbed moisture (Morais, in prep.).

Table 3. Moisture effect on the first ply failure stress of  $[0/90_3]_s$  laminates, determined by the  $\eta-\sigma$  and  $\sigma-\varepsilon$  curves.

Moisture content (%)	$\sigma^F$ (MPa)	
	$\eta-\sigma$ curve	$\sigma-\varepsilon$ curve
0	105.3	105.6
0.792	67.9	63.6
1.777	42.2	46.1
0.792-0	79.6	85.6

## 5 ANALYSIS OF STIFFNESS REDUCTION

We now turn our attention to the stiffness changes arising from the matrix cracking process. The methodology of data analysis developed by Talreja et al. (1992) will be followed.

### 5.1 Unaged laminates

First the material constants are derived using the experimental data for unaged  $[0/90_3]_s$  laminates. The initial undamaged moduli are given in Table 4. Figure 7 shows the quantities  $(1 - E_1 / E_1^0)$  and  $(1 - v_{12} / v_{12}^0)$  plotted against the crack density. By linear regression analysis straight lines are fitted through these test data, forcing them to contain the origin. The slopes of the straight lines and the initial moduli values are then entered in Equations 6 to calculate the material constants (Equations 5):

$$\begin{aligned} \kappa c_3 &= 5.157 \text{ GPa} \\ \kappa c_8 &= 0.304 \text{ GPa}, \\ \kappa c_{16} &= 2.895 \text{ GPa}. \end{aligned} \quad (7)$$

Table 4. Experimental values of initial undamaged moduli of unaged laminates.

Laminate	$[0/90_3]_s$	$[0_2/90_2]_s$	$[0/90]_{2s}$
$E_1^0$ (GPa)	24.83	30.67	30.49
$v_{12}^0$	0.143	----	----

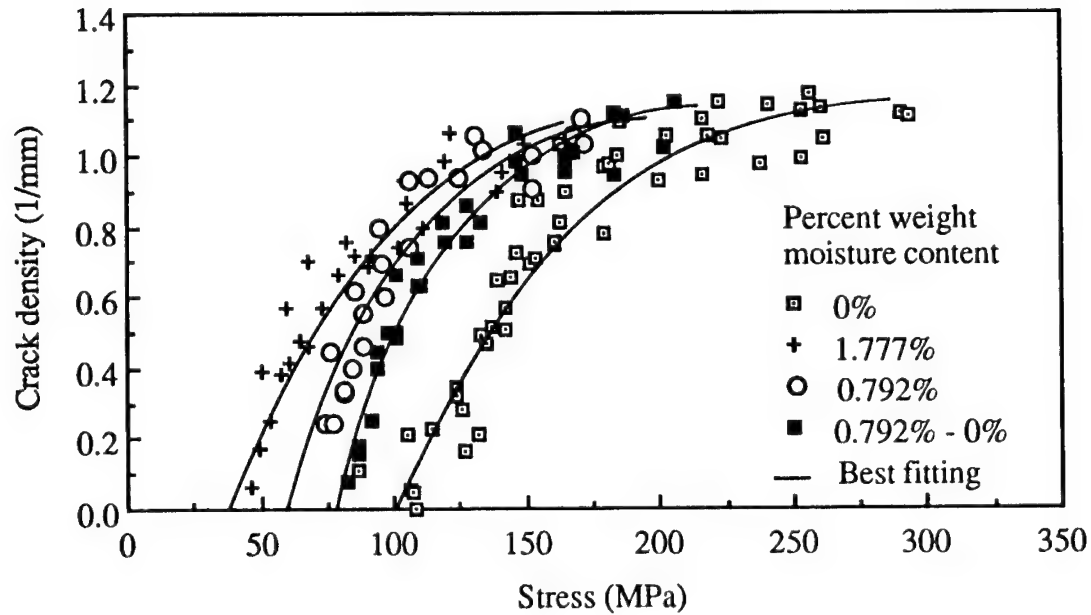


Figure 6. Transverse crack density plotted against axial stress for aged and unaged  $[0/90_3]_s$  laminates.

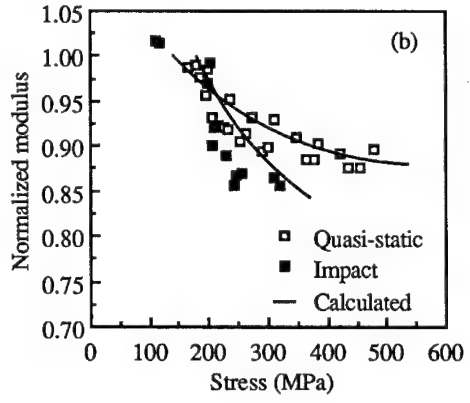
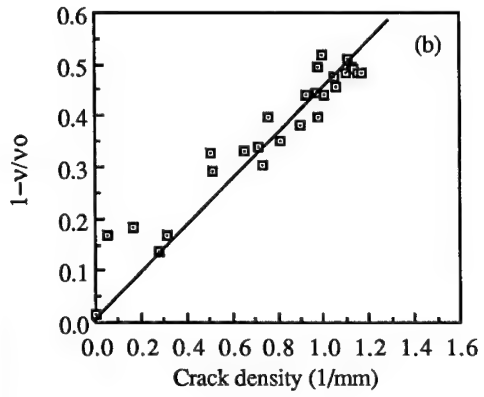
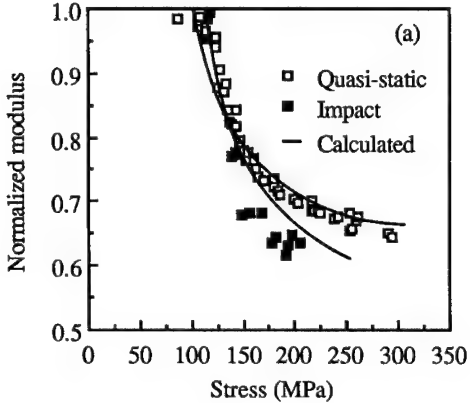
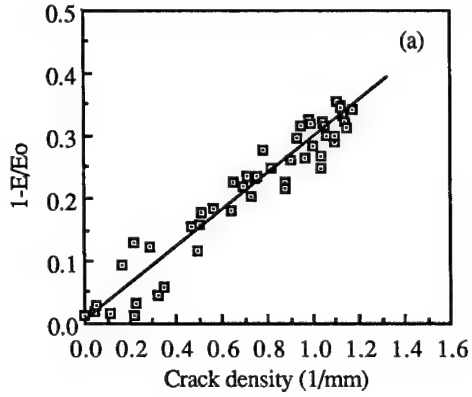


Figure 7. Changes in the axial Young's modulus (a) and Poisson's ratio (b) against the transverse crack density of unaged [0/90<sub>3</sub>]<sub>s</sub> laminates.

The material constants allow us to predict the reduction of axial modulus as a function of the laminate stress, for all laminates tested under quasi-static or impact loading conditions. To achieve this goal the  $\eta-\sigma$  polynomials of Figure 4 are substituted in the second of Equations 4, along with the initial moduli (Table 4), the material constants (Equations 7) and the ply thickness (Table 1). Figure 8 provides a comparison between the predictions of normalized modulus ( $E_1/E_1^0$ ) and the experimental data. It can be seen that the predictions overestimate the damaged modulus for high crack densities. However, the predictions and the measurements are fairly in good agreement over the entire experimental range.

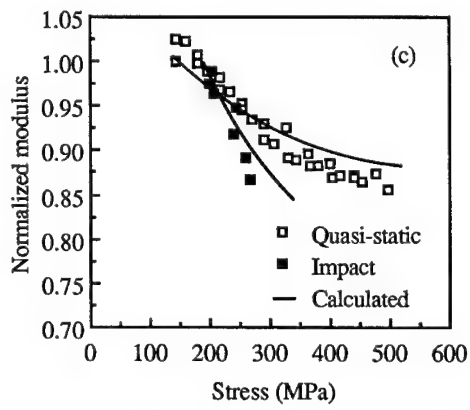


Figure 8. Measured and predicted normalized modulus reduction, under quasi-static and impact loading, for (a) [0/90<sub>3</sub>]<sub>s</sub>, (b) [0<sub>2</sub>/90<sub>2</sub>]<sub>s</sub>, and (c) [0/90]<sub>2s</sub>.

## 5.2 Aged [0/90<sub>3</sub>]<sub>s</sub> laminates

The undamaged axial moduli of aged [0/90<sub>3</sub>]<sub>s</sub> laminates are summarized in Table 5. With the multiplication of transverse cracks the axial modulus decreases as can be appreciated in Figure 9. In this Figure the experimental values of  $(1 - E_1 / E_1^0)$  are plotted versus the crack density and compared with the analytical representation of unaged laminates data (Figure 7a). Although the absorbed moisture reduces slightly the values of the modulus, its dimensionless variation  $(1 - E_1 / E_1^0)$  seems to obey the same law of the crack density as it does the non-aged laminates. So, the material constants obtained by testing the unaged laminates (Equations 7) are able to express the relationship between the aged modulus and the crack density.

Table 5. Moisture effect on the axial Young's modulus of aged [0/90<sub>3</sub>]<sub>s</sub> laminates.

Moisture content (%)	0	0.792	1.777	0.792-0
$E_1^0$ (GPa)	24.83	22.21	21.16	24.92

Proceeding in the same way as was done previously for the unaged laminates, the relationships between the normalized modulus and the applied laminate stress were predicted, based upon the material constants of Equations 7. Those predictions are plotted in Figure 10 together with the test data. For comparison purposes the results of the non-aged laminate are also shown in Figure 10. Again Figure 10 demonstrates a reasonably agreement between predictions and measurements, although the predictions underestimate the damaged modulus. Examination of the data also reveals a remarkable feature: the normalized modulus at the CDS increases with the absorbed

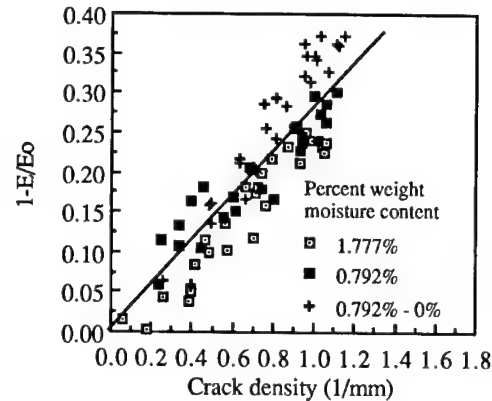


Figure 9. Changes in the axial Young's modulus of aged [0/90<sub>3</sub>]<sub>s</sub> laminates against the transverse crack density.

moisture, even though similar crack densities were observed at this limiting state.

## 6 CONCLUSIONS

1. Three different methods were used to identify the FPF stress, which give consistent results: the crack density versus stress curve, the stress versus strain curve, and the cumulative acoustic emission counts versus stress curve methods.
2. Compared to the quasi-static loading, the impact loading increases the stress at the onset of transverse cracking, the rate of crack development, and the crack density at the characteristic damage state of the unaged laminates.

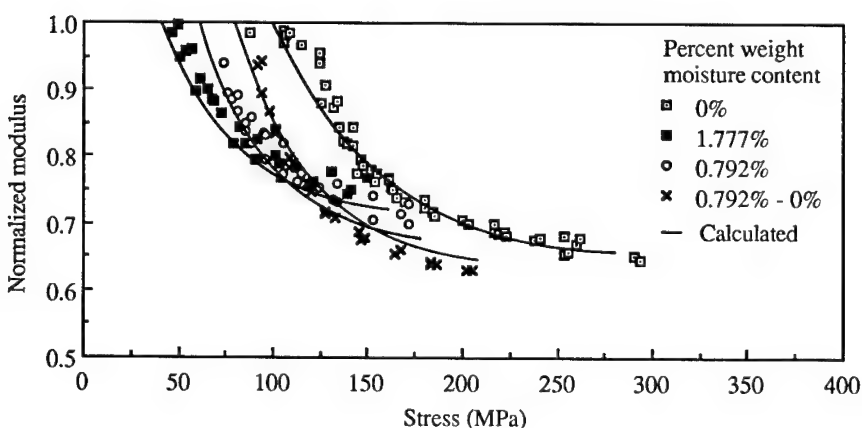


Figure 10. Measured and predicted normalized modulus reduction of the aged [0/90<sub>3</sub>]<sub>s</sub> laminates.

3. The absorption of moisture reduces the FPF stress under quasi-static loading, leaving unaffected the rate of transverse cracking progression and the crack density at the characteristic damage state.
4. The normalized Young's modulus ( $E_1/E_1^0$ ) at the characteristic damage state increases with the percent weight moisture content, even though the CDS density remains unchanged.
5. The moisture effects are only partially reversible probably due to the viscoelastic nature of polymeric matrix composites.
6. The continuum damage theory developed by Talreja has been demonstrated to be accurate in predicting the residual axial stiffness of several crossply laminates, after quasi-static and impact loading damage. This model is also adequate to model the damage stiffness of previously moisture equilibrated [0/90<sub>3</sub>]<sub>s</sub> laminates.
- ## REFERENCES
- Allen, D. H. & C. E. Harris 1987a. A thermomechanical constitutive theory for predicting damage - I. Theoretical development. *Int. J. Sol. Structures* 23(9): 1301-1318.
- Allen, D. H. & C. E. Harris 1987b. A thermomechanical constitutive theory for predicting damage - II. Application to matrix cracking in laminated composites. *Int. J. Sol. Structures* 23(9): 1319-1338.
- Coleman, B. D. & M. E. Gurtin 1967. Thermodynamics with internal state variables. *J. Chem. Phys.* 47: 597-613.
- Crossman, F. W. & A. S. D. Wang 1982. The dependence of transverse cracking and delamination on the ply thickness in graphite/epoxy laminates. In K. L. Reifsnider (ed.), ASTM STP 775, *Damage in composite materials*: 118-139.
- Dvorak, G. J., N. Laws & M. Haejazi 1985. Analysis of progressive matrix cracking in composite laminates I. Thermoelastic properties of a ply with cracks. *J. Comp. Mat.* 19: 216-234.
- Flaggs, D. L. & M. H. Kural 1982. Experimental determination of the in situ transverse lamina strength in graphite/epoxy laminates. *J. Comp. Mat.* 16: 103-116.
- Fukunaga, H., T.-W. Chou, P. W. M. Peters & K. Schulte 1984. Probabilistic failure strength analysis of graphite/epoxy cross-ply laminates. *J. Comp. Mat.* 18: 339-356.
- Gudmundson, P. & S. Östlund 1992a. First order analysis of stiffness reduction due to matrix cracking. *J. Comp. Mat.* 26(7): 1009-1029.
- Gudmundson, P. & S. Östlund 1992b. Numerical verification of a procedure for calculation of elastic constants in microcracking composite laminates. *J. Comp. Mat.* 26(17): 2480-2491.
- Guild, F. J., S. L. Ogin & P. A. Smith 1993. Modelling of 90° ply cracking in crossply laminates, including three-dimensional effects. *J. Comp. Mat.* 27(7): 646-667.
- Hashin, Z. 1986. Analysis of stiffness reduction of cracked cross-ply laminates. *Eng. Frac. Mech.* 25(5,6): 771-778.
- Hightsmith, A. L. & K. L. Reifsnider 1982. Stiffness-reduction mechanisms in composite laminates. In K. L. Reifsnider (ed.), ASTM STP 775, *Damage in composite laminates*: 103-117.
- Kriz, R. D. & W. W. Stinchcomb 1982. Effects of moisture, residual thermal curing stresses, and mechanical load on the damage development in quasi-isotropic laminates. In K. L. Reifsnider (ed.), ASTM STP 775, *Damage in composite laminates*: 63-80.
- Lee, J.-W. & I. M. Daniel 1990. Progressive transverse cracking of crossply composite laminates. *J. Comp. Mat.* 24: 1225-1243.
- Lim, S. G. & C. S. Hong 1989. Prediction of transverse cracking and stiffness reduction in cross-ply laminated composites. *J. Comp. Mat.* 23: 695-713.
- Masters, J. E. & K. L. Reifsnider 1982. An investigation of cumulative damage development in quasi-isotropic graphite/epoxy laminates. In K. L. Reifsnider (ed.), ASTM STP 775, *Damage in composite laminates*: 40-62.
- Morais, J. L. in prep. *Environmental influence on damage behavior of composite structures* (in portuguese). Ph. D. Dissertation, Vila Real: UTAD.
- Nairn, J. A. & S. Hu 1992. The formation and effect of outer-ply microcracks in cross-ply laminates: a variational approach. *Eng. Frac. Mech.* 41(2): 203-221.
- Nuismer, R. J. & S. C. Tan 1988. Constitutive relations of a cracked composite lamina. *J. Comp. Mat.* 22: 306-321.
- Parviz, A., K. W. Garret & J. E. Bailey 1978. Constrained cracking in glass fiber-reinforced epoxy cross-ply laminates. *J. Mat. Science* 13: 195-201.
- Reifsnider, K. L & A. Talug 1980. Analysis of fatigue damage in composite laminates. *Int. J. Fatigue*, January: 3-11.
- Reifsnider, K. L 1990. Damage and damage mechanics. In K. L. Reifsnider (ed.), *Fatigue of composite materials*: 11-77. Elsevier Science Publishers.
- Roubini, M & G. Solomons 1995. Composites strength determination via acoustic and thermal emission. *Technical note no. I.95.17*, ISEI IE/2860/95, Joint Research Center, European Commission.
- Rothschild, R. J., L. B. Illewicz, P. Nordin & S. H. Applegate 1988. The effect of hygrothermal

- 
- histories on matrix cracking in fiber reinforced laminates. *Trans. of the ASME* 110: 158-168.
- Shahid, I. & F.-K. Chang 1995. An accumulative damage model for tensile and shear failures of laminated composite plates. *J. Comp. Mat.* 29(7): 926-981.
- Talreja, R. 1987. Modelling of damage development in composites using internal variables concepts. In A. S. Wang & G. K. Haritos (eds.), *Damage mechanics in composites*: 11- 16. ASME.
- Talreja, R. 1990. Internal variable damage mechanics of composite materials. In J. P. Boehler (ed.), *Yielding, damage, and failure of anisotropic solids*: 509-533. Mech. Eng. Publications.
- Talreja, R., S. Yalvac, D. Yates & D. G. Wetters 1992. Transverse cracking and stiffness reduction in cross ply laminates of different matrix toughness. *J. Comp. Mat.* 26(11): 1644-1663.
- Tan, S. C. & R. J. Nuismier 1989. A theory for progressive matrix cracking in composite laminates. *J. Comp. Mat.* 23: 1029-1047.
- Tsai, C.-L. & I. M. Daniel 1993. The behavior of cracked crossply composite laminates under general in-plane loading. In G. Z. Voyatzis (ed.), *Damage in composite materials, Studies in applied mechanics* 34: 51-66. Elsevier Science Publishers.
- Xu, L.-Y. 1995. Influence of stacking sequence on the transverse matrix cracking in continuous fiber crossply laminates. *J. Comp. Mat.* 29(10): 1337-1358.
- Weitsman, Y. 1987. Coupled damage and moisture-transporte in fibre-reinforced, polymeric composites. *Int. J. Sol. Struct.* 23(7): 1003-1025.

## Flexible risers with composite armor for deep water oil and gas production

M.D. Kalman & J.R. Belcher  
Wellstream Inc., Panama City, Fla., USA

**ABSTRACT:** This paper discusses the development of a light weight high strength flexible pipe for the conveyance of oil and gas from deep water subsea wells to floating production vessels. Flexible pipe is a multilayer structure of helically wound metallic strips and tapes and extruded thermoplastics. The tensile armor layer in conventional pipe consists of high strength steel rectangular wires wound in opposing directions to provide torque balance. The light weight design incorporates carbon fiber/polymer thermoplastic composite strip to replace the steel armor. A weight reduction of 30% is expected for a pipe designed to meet the same performance requirements. The results of tests conducted to qualify the composite armor material and pipe structure and initial efforts to develop a composite armor layer service life model are presented herein.

### 1. INTRODUCTION

Non-bonded flexible pipe has been applied in the offshore oil and gas industry for about 20 years. It is used for dynamic risers connecting seabed flowlines to floating production facilities, and for static seabed flowlines where it is more cost effective to install than rigid pipe, such as in harsh environments, or it is desired to recover the flowline for reuse after a short field life. The basic pipe design (Figure 1) consists of a stainless steel internal carcass for collapse resistance, an extruded polymer fluid barrier, a carbon steel interlocked hoop strength layer, helically wound carbon steel tensile armor for axial strength, and an extruded watertight external sheath. For dynamic applications extruded polymer or tape polymer antiwear layers are applied between adjacent steel armor layers. For extremely high pressure applications, an additional layer of rectangular shaped helical reinforcement over the interlocked hoop strength layer, or a second set of tensile armor layers, may be applied.

Offshore exploration for production of oil & gas is currently expanding to deeper water environments, with some fields being developed in water depths in excess of 2000 meters. In a floating production application, the installation and operating vessel as well as the top section of the pipe itself, must support the hanging weight of the remainder of pipe with dynamic loading. It is desirable to reduce the weight of the pipe to minimize stress on the pipe and hangoff structure. It is also desirable to reduce the

vessel deck loads so that buoyancy requirements are reduced or payload capacity increased.

To reduce the weight of the flexible pipe, composite materials have been developed to replace the steel reinforcement layers. The initial application is to replace the rectangular tensile armor members since strength is only required in the wire direction. Figure 2 presents the pipe design and capabilities of the composite armor relative to the steel material currently being used. A pipe weight reduction of about 30% can be achieved by the steel to composite tensile armor substitution. In addition the composite armor offers the advantage of being essentially inert to corrosion, hydrogen induced cracking and sulfide stress cracking, all potential mechanisms for reducing the service life of a flexible pipe.

The main technical barriers to overcome in achieving the steel to composite material substitution are:

1. Composite armor material selection and verification
2. Termination of the composite armor in the flexible pipe end termination
3. Development and verification of the composite pipe structure
4. Development and verification of the service life model for the composite armor material

This paper describes the work which has been conducted to date by Wellstream to overcome these technical barriers. Much of this effort was funded by the U.S. Department of Commerce National Institute

of Standards Advanced Technology Program. Technical support was obtained through subcontracts with Virginia Polytechnic and State University and College of William & Mary.

There are numerous vendors and combinations of polymers and fibers which could be considered for the composite armor application. The material of choice must be sufficiently flexible, maintain the required mechanical properties over the service life under severe environmental and alternating stress loading, and be economical relative to competing technologies. A comprehensive screening of available materials was conducted against these criteria to determine the most suitable choices for consideration. This paper describes the material evaluation tests which were conducted to verify that the target allowable stress utilization factors of the material are met.

In flexible pipe, each layer must be terminated in a steel housing outfitted with a transition flange for termination to subsea or topside piping. The end fitting must maintain internal and external fluid containment and structural integrity over the service life. The tensile load transfer to the end fitting is obtained by adhesion and mechanical anchoring of the tensile armor layer in an epoxy wedge. In a

conventional flexible pipe with steel armor, the steel is plastically deformed into a hook or wave pattern to provide the mechanical portion of the anchoring. With composite armor, elongation after yield is negligible, and plastic deformation is not possible without destroying the material. The anchoring of the composite strip must be sufficient to prevent pullout from the end fitting over the service life. Tests which were conducted to verify the method selected for terminating the composite armor are presented in this paper.

A 4-inch ID prototype pipe complete with end fittings was designed and built. Burst test and failure tension tests were successfully completed with failure values within 5% of predicted values. The design of the pipe structure and results of the tests are presented.

Composite materials which may be suitable for this application were unproven at the start. Verification of the service life under the combined environmental and alternating stress loading requires long term testing to simulate the loading. The test methods which are being employed and their relevance in developing a service life model for the composite armored flexible pipe are presented.

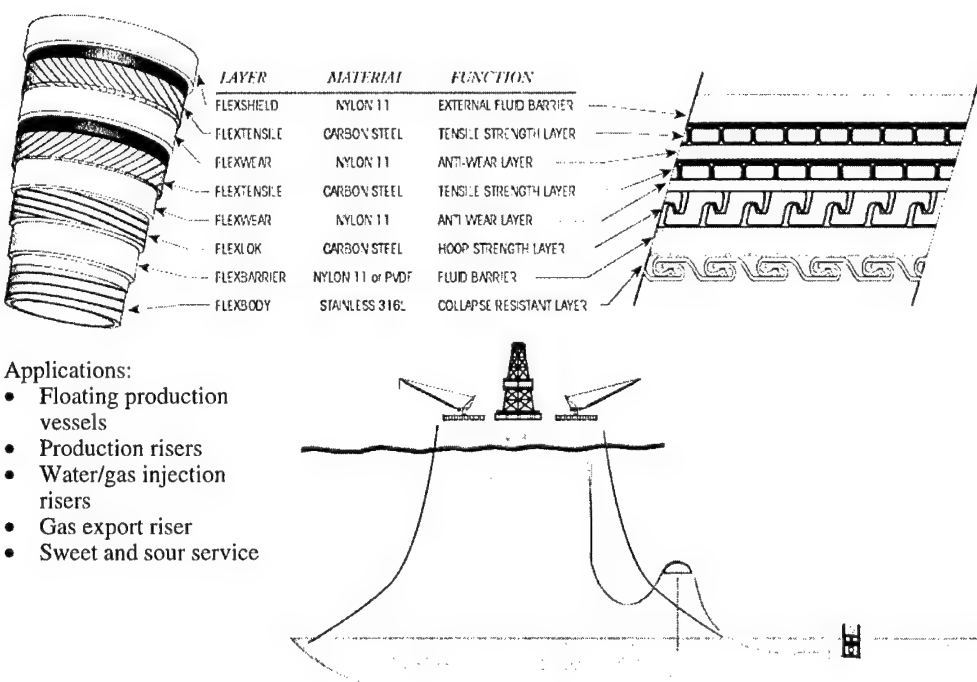
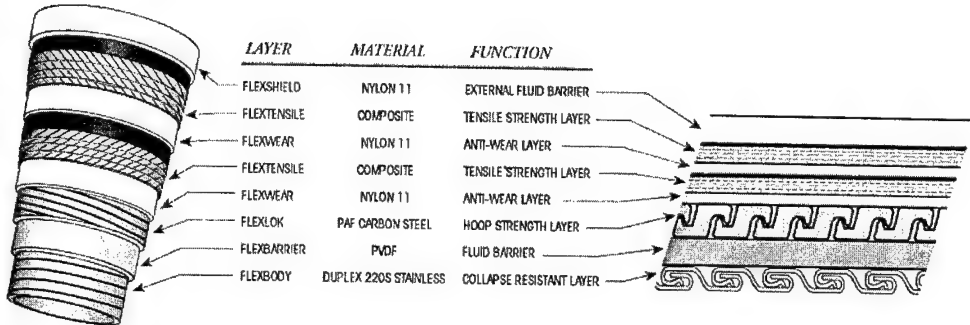


Figure 1. Conventional non-bonded flexible pipe construction for dynamic applications



	Steel	Carbon Fiber Composite
Configuration	Cold Rolled/Heat Treated Rectangular Cross Section 3-6 mm thick Mechanically Preformed to Helical Structure	Thermoplastic/Carbon Fiber Matrix Rectangular Cross Section 1 - 2 mm thick 2 - 4 layers Helically Wrapped
Strength	759 MPa	1,255 MPa
Modulus	207 GPa	80.7 GPa
Elongation	11% or higher	1.4%
Density	7.85 g/cc	1.48 g/cc
Relative Cost	1.0	2.5

Figure 2. Non-bonded flexible pipe structure employing composite materials

## 2. MATERIAL SELECTION AND VERIFICATION

There are numerous polymer/fiber material combinations which may be suitable for the flexible pipe tensile armor material application. In the initial screening, the following criteria were established:

Initial Strength	180 ksi
Flexibility	1 mm minimum thickness bent to a 152.4 mm bend radius with no damage
Allowable Utilization-Static	50% of UTS
Allowable Utilization - Dynamic	40% of UTS
Density	1.6 S.G.
Temperature Range (pipe annulus)	-40°C to 93°C
Environment	Seawater 5000 ppm H <sub>2</sub> S in pipe bore 5% CO <sub>2</sub> in pipe bore
Cost	Finished pipe cost no more than 25% greater than conventional pipe of same size/strength

The most severe of the requirements is the exposure to the high temperature water. It is known

that thermoplastic composite materials can suffer significant loss of strength due to disbondment of the polymer from the fiber. Disbondment can result from stress corrosion of the fibers themselves, aging of the polymer material, breakdown of the sizing between the polymer and fiber, and even differences in thermal expansion coefficient between the polymer and fiber. Disbondment results in non-uniform load application on the fibers. Since the elongation at break of the fibers is relatively low compared to the polymer, the unequal load sharing results in breakage of the fibers taking the highest portion of the load. Once these fibers break, the remaining fibers become overloaded resulting in ultimate failure of the composite strip. All of the standard fibers which are normally considered in polymer composite manufacture were evaluated: glass, aramid and carbon fiber.

The following polymer matrix materials were considered after an initial screening to rule out the most unlikely candidates. Materials were ruled out because it was known that they would be subject to degradation in the specified environment.

1. Polyurethane (PU)
2. Polyphenylene sulfide (PPS)
3. Polyvinylidene fluoride (PVDF)

Initial tests were conducted on an E-glass reinforced/ polyurethane matrix and a carbon fiber reinforced/polyurethane matrix. Samples were exposed to seawater at the design temperature of 93°C. The results of these tests verified that the

E-glass was not a suitable fiber and that the polyurethane was not a suitable polymer.

Aramid fiber was ruled out because it was only slightly more economically attractive relative to carbon fiber considering strength, and density of the finished product. In addition, the tensile modulus of carbon fiber composites is higher than that of aramid fibers. It is desirable to have a high axial stiffness so as to minimize the pipe elongation under combined internal pressure and tensile loading.

The initial strength and density target was achieved with a carbon fiber reinforced/polyurethane composite strip. The material strength was retained after 70 days. However after longer term exposure, significant loss of strength and disbondment between the polymer and fiber was noted. Subsequent investigation revealed that the polyurethane was suffering from loss of molecular weight in the 93°C test solution.

Based on the results of these tests and a review of the technical data which was available, it was determined that carbon fiber in a PPS or PVDF matrix were the most attractive materials for continued long term testing.

Through a screening process, three material vendors were identified who could provide the most suitable products. Two of the vendors preferred to employ PPS for the polymer because their processes were not set up for PVDF. One vendor preferred PVDF, but at the time of the development program was unable to supply samples within specification. Thus carbon fiber/PPS polymer thermoplastic composite strips from two vendors were evaluated in the material qualification test program.

Material performance for this application is evaluated in terms of resistance to loss of strength resulting from environmental degradation and fatigue. Environmental degradation results from exposure to permeated gases and seawater (if the flexible pipe outer sheath is damaged) at operating temperatures. Fatigue is a result of time dependent bending and tension loading in the flexible pipe in dynamic service.

The allowable utilization must be determined based on the residual static strength and the fatigue resistance of the material after long term environmental exposure. Full scale static and dynamic testing must be conducted on the pipe structure to verify the target material stress utilization.

### 3. MATERIAL TEST PROGRAM

The material test program was developed through consultation with NIST, Virginia Tech and College of William & Mary experts. The main objectives were to verify the performance of the material under environmental and mechanical loading conditions which would simulate performance in service and

Table 1. Tests conducted to evaluate the performance of thermoplastic composite strip

Environments	Temp	Samples
Simulated seawater saturated with CO <sub>2</sub> at 50 psi	90°C	10 Unstressed Polymer Strips each exposed 1, 10, 30, 100 days
Air		10 Unstressed Composite Strips each exposed 1, 10, 30, 100 days
Simulated seawater saturated with CO <sub>2</sub> at 50 psi	120°C	10 Unstressed Polymer Strips each exposed 1, 10, 30, 100 days
Air		10 Unstressed Composite Strips each exposed 1, 10, 30, 100 days
		40 Composite strips exposed 100 days to no failure with maximum bending stress

provide baseline data for development of a service life model.

The "100 days to no failure" bending stress was to be determined by short term aging tests at decreasing bend radii until the no failure condition was achieved at 100 days. (Failure defined as bending stress rupture.) Molecular weight measurement and SEM observations were made as necessary to identify the modes of failure. The number of days exposure vs. bend radius was recorded.

Torsional DMA testing was conducted on unstressed polymer strips and unstressed composite strips on unexposed samples and samples exposed for 1, 10, 30 and 100 days to each environment at each temperature.

Uniaxial Tensile Strength tests were conducted on unexposed and exposed samples to determine the strength as a function of temperature and exposure.

Uniaxial Fatigue Tests were conducted at room temperature and at 90°C on unexposed samples and samples exposed 100 days in seawater to no failure in bending @ 90°C. S/N curves were prepared for both the unexposed and exposed material.

Weight loss, thickness and crystallinity evaluation were conducted to certify the stability of the material during aging tests. Changes were quantified in terms of percent change relative to unaged PPS.

#### 4. MATERIAL TEST RESULTS

The results of tests conducted on only one of the vendor's materials is provided herein. The second vendor's material behaved similarly, and the data presented herein can be considered representative for carbon fiber/PPS polymer thermoplastic composite strips. Similar tests are recommended to qualify a strip manufacturing process for this application. These tests were conducted at Virginia Tech (Reifsnyder et al. 1997).

##### 4.1 Quasi-static tension tests

Table 2 provides a summary of the quasi-static tension tests conducted on unaged and aged samples in air.

Table 2. Results of quasi-static tension tests at temperature-aged and unaged samples

	Modulus Msi	Strength Ksi	Strain to Failure %
<b>Quasi-Static Tension Tests</b>			
23°C (10 replicates)	14.3 ± 0.13	186 ± 5.5	1.41 ± 0.033
90°C (5 replicates)	13.6 ± 0.26	188 ± 8.4	1.46 ± 0.061
120°C (5 replicates)	13.2 ± 0.36	174 ± 7.8	1.37 ± 0.081
<b>Quasi-Static Tension Test of Aged Specimens</b>			
1 Day @ 90°C (10 replicates)	14.3 ± 0.44	197 ± 14.4	1.41 ± 0.13
10 Day @ 90°C (10 replicates)	14.2 ± 0.33	199 ± 8.4	1.44 ± 0.054
30 Day @ 90°C (10 replicates)	14.2 ± 0.20	194 ± 6.7	1.46 ± 0.072
100 Day @ 90°C (4 replicates)	14.3 ± 0.70	194 ± 11.6	1.41 ± 0.061
1 Day @ 120°C (10 replicates)	14.3 ± 0.27	209 ± 6.3	1.55 ± 0.042
10 Day @ 120°C (10 replicates)	14.0 ± 0.48	199 ± 12.4	1.50 ± 0.062
30 Day @ 120°C (10 replicates)	14.4 ± 0.26	202 ± 5.4	1.47 ± 0.053
100 Day @ 120°C (10 replicates)	14.5 ± 0.66	194 ± 5.1	1.44 ± 0.096

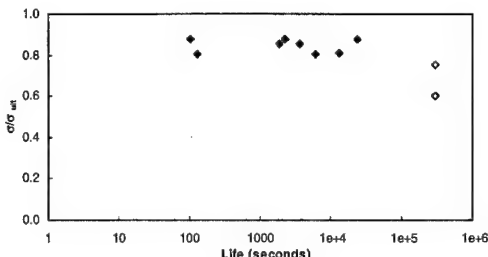


Figure 3. Normalized applied maximum stress vs. Fatigue Life at room temperature,  $R = 0.1$ ,  $f = 10$  Hz.

The results indicate little change in the behavior of the material as a function of temperature and resulting from aging in air. Results for tests conducted with exposure to seawater are similar (Kranbuehl et al. 1997).

##### 4.2 Fatigue resistance

Fatigue tests were conducted at both room temperature and at 90°C. The tests were conducted with a frequency of 10 Hz and a stress ratio of 0.1. The results of the fatigue tests are provided in Figures 3 and 4. Open symbols indicate runout, taken as 3 million cycles.

##### 4.3 Stress rupture

Stress rupture tests were conducted at elevated temperatures to evaluate the performance of the material under combined stress and environmental loading. After experimenting with several types of loading, a fixed-length bend-compression loading condition was chosen as the method of testing. This loading provides a condition where the matrix behavior contributes directly to the behavior of the composite system. The loading fixture is also uncomplicated and can accommodate large numbers of specimens in a wide variety of environments.

The test fixture design is presented in Figure 5. The outer fiber maximum tensile strain and inner fiber maximum compressive strain were determined

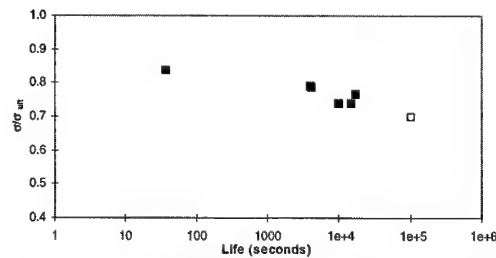


Figure 4. Normalized applied maximum stress vs. Fatigue Life at  $T = 90^\circ\text{C}$ ,  $R = 0.1$ ,  $f = 10$  Hz.

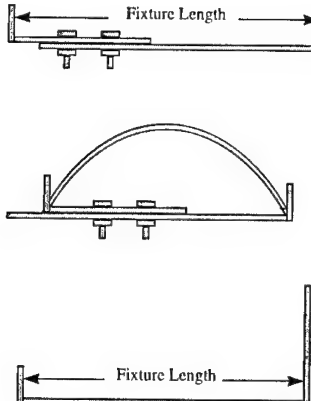


Figure 5. Compression-bend fixtures.

analytically using the solution for a pinned beam deflection with end loading. Validation of the analytical solution was conducted on material samples outfitted with strain gages at mid-span subject to bending in the fixture. Figure 6 provides a comparison of the analytical solution and measured strain for various end to end distances in the fixture.

The calculated values and measured data match quite well; the average error is about 6%. The calculated strains seem to provide an upper bound to the measured values. The error can largely be explained by the fact the strain gages averaged the strain around the point of maximum strain and do not report the actual maximum strain. Also contributing to the error, the previous equations assume a constant and uniform bending modulus. It is possible that the compressive and tensile bending moduli differ slightly so that the  $\epsilon=0$  at  $t/2$  assumption is no longer exact. From the behavior of the data and the small error compared to theoretical expectations it is obvious that these fixtures allow a good axial loading and reproducible data.

Figure 7 and 8 show representative results for the stress rupture data collected for the two materials, at 90 and 120°C, respectively. At 90°C, the time to rupture in bending, as a function of maximum

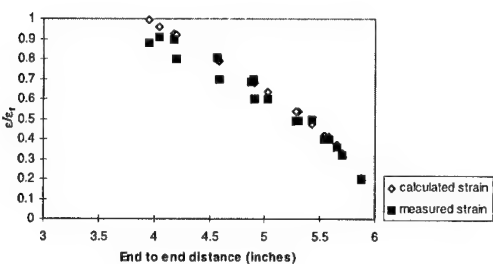


Figure 6. Normalized strain vs. fixture length.

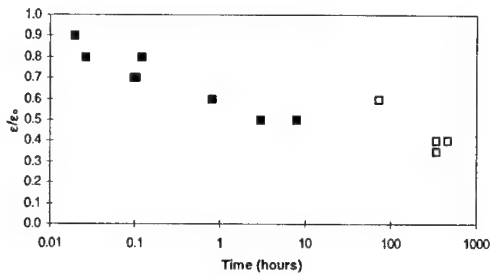


Figure 7. Applied maximum strain vs. observed time for rupture at 90°C

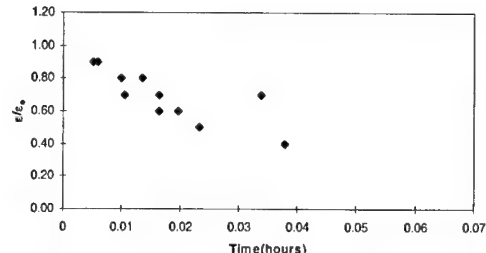


Figure 8. Applied maximum strain vs. observed time for rupture at 120°C.

applied strain level, becomes large below about 60 percent of the ultimate strain. For 120°C, the rupture times are all very short, as expected, since this is above the glass transition temperature of the matrix material.

#### 4.4 Long term stress aging in bending

One material sample was aged at 90°C in the end loaded bending condition with the maximum strain at 30% strain at failure at room temperature. No failure was observed in this sample for 100 days. Residual strength tensile tests were performed to determine the reduction in strength due to stress aging. Results from this sample along with data for comparison are presented in Table 3.

Table 3. Results of quasi-static tension tests of stress-aged Baycomp material.

Condition	Strength (ksi)	Modulus (Msi)
Aged in bending 30% $\epsilon_f$ at 90°C for 100 days	181.6	14.3
Aged unstressed at 90°C for 100 days	193.8	14.3
Unaged	186.6	14.2

#### 4.5 Tensile stress rupture vs. bending stress rupture

In the actual service condition, this material will be mainly subject to tensile loading, with small compressive loads due to curvature changes. A detailed examination of the bending stress rupture samples indicated that they had failed from microbuckling resulting from compressive stresses on the inside of the bend. A smaller number of tensile stress rupture tests were conducted to verify that the compressive loading indeed resulted in the premature failure. The resulting tests and detailed analyses were conducted to establish a tensile stress rupture design curve for a 90°C design temperature and the maximum allowable compression load in service.

#### 4.6 Initial service life curve

Based on the results of the tests conducted to date, an initial model has been developed by Virginia Tech for use in service life prediction (Figure 9). The service life curves will be encoded into a subroutine for integration into Wellstream's design codes for prediction of the service life of the composite armored flexible pipe.

### 5. PIPE STRUCTURE DESIGN AND MANUFACTURE

Two 4-inch ID, 6 m long prototype sections were manufactured by stripping down a conventional pipe to the Flexwear over Flexlok layer. The composite armor material was then laid on the pipe using a manual process. The armor material was taped to hold it in place. A heat shrink wrapping tape was used for the outer sheath, since the short lengths precluded the normal extrusion process for this layer.

The pipe designs were prepared using Wellstream's proprietary computer program PipeMaker™. The tensile armor mechanical

properties (strength, tensile modulus) were modified based on the minimum specified properties of the composite tensile armor material at 23°C. PipeMaker™ provides a prediction of the burst pressure, collapse pressure, failure tension, bending stiffness, weight per unit length, and other primary mechanical properties of the composite pipe structure.

### 6. END FITTING DESIGN

One of the main focuses of the design effort is the composite armor termination in the end fitting. Quoting API Specification 17J for unbonded flexible pipe:

"The end fittings shall be designed for reliable termination of all pipe layers, such that leakage, structural deformation, or pull-out of wires or extruded layers does not occur for the service life of the pipe."

The main area to address with composite armor, is prevention of tensile armor pullout over the life. It is not feasible to terminate the composite armor in the end fitting without some resulting stress concentration. With steel armored pipe, successful failure tension tests always results in breakage of the wire adjacent to the end fitting. As long as the resulting failure tension is above the predicted value, this is acceptable. With the composite armored pipe, the same result must be achieved. There can be no premature failure resulting from composite armor pullout or failure significantly below the material tensile strength. Otherwise the allowable utilization of the material is significantly impacted.

A typical end fitting design for composite armor is presented in Figure 10. The tensile strength of the end fitting results from the anchoring of the strip in the tapered section between the end fitting body and jacket. After assembly, the tapered section is filled with epoxy to anchor the tensile layer. A proprietary method for effectively tabbing the composite armor in high volume production has been established. The end tab results in an increase in cross sectional area at the strip end, which prevents pullout of the strip from the epoxy. The method was verified by conducting single strip pull tests. A termination method was considered acceptable if the strip broke at or near its known tensile strength before pulling out.

Special attention must also be paid to the transition of the composite armor into the end fitting. Tight bends and designs resulting in loading on the strip in directions other than along its length must be avoided to result in a successful design.

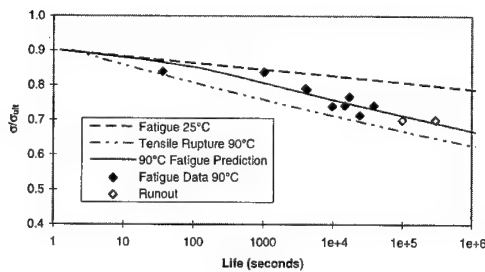


Figure 9. Applied maximum stress vs. Life at T = 90°C, R = 0.1, n = 10 Hz

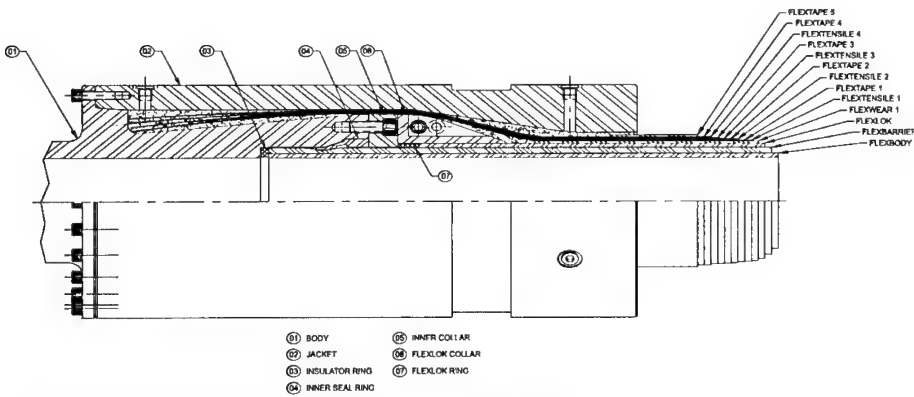


Figure 10. Typical end fitting design for composite armor

## 7. STATIC QUALIFICATION TEST PROGRAM AND RESULTS

One of the pipe samples was subject to a burst test and one was subject to a failure tension test. Prior to conducting the tests, each pipe sample was subject to a factory acceptance hydrostatic test to 310 barg (1.5 times the design pressure) with a 24 hour hold period. The results of the testing are summarized in Table 4.

Pressure elongation measurements were made on the burst test sample and tensile elongation measurements were made on the failure tension test sample. These results are being used for calibration of analytical models for pressure elongation and axial stiffness.

## 8. FUTURE WORK

The following work is in process or being planned to commercialize the composite armored composite flexible pipe.

Aging and stress rupture tests with up to 600 days exposure are being conducted to provide comprehensive data to finalize the material service life model.

The friction coefficient and wear resistance of the composite armor against the adjacent anti-wear tape layer is being measured.

The service life model will be updated based on the results of the long term tests and incorporated into Wellstream's computer programs.

A larger diameter, longer length full scale prototype pipe will be manufactured using an armoring

work center specifically designed for application of the composite armor on a production basis. Pipe samples will be subject to the burst and failure tension static qualification tests. In addition, a full scale dynamic test will be conducted to simulate the mean and alternating stress levels experienced by the composite armored pipe in service.

## 9. CONCLUSIONS

The feasibility of using thermoplastic composite strip for the tensile armor layer in unbonded flexible pipe has been established.

Material testing has verified that carbon fiber/PPS polymer thermoplastic strip is suitable for this application in high temperature and deep water service.

An initial service life model has been established based on the material qualification testing. The failure modes of stress rupture due to combined environmental and static loading and fatigue due to alternating stress loading have been incorporated into the model.

The pipe structure design and end termination design has been verified to be suitable based on a full scale burst test and failure tension test. The pipe design software predicts the failure values with acceptable accuracy.

## REFERENCES

- Reifsneider, K.L., Russell, B., Loverich, J., and Mahieux, C., "Characterization and Modeling of PMC Material for Flexible Piping," Blacksburg, Virginia, 1997.
- Kranbuchl, D.E., "Characterization of Chemical and Mechanical Aging of PPS Using FDEMS Sensing, Tensile Testing and Differential Scanning Calorimetry," Williamsburg, Virginia, 1997.

Table 4. Static Test Results

Test	Actual Value	Predicted Value	Actual/Predicted
Burst Test	711 bar	706 bar	1.01
Failure Tension Test	1583 kN	1528 kN	1.04

---

## 2 Physical and chemical aging processes in high temperature applications

## The effect of physical aging on the durability of carbon fiber reinforced PEI

A.D'Amore, G.Caprino & L.Nicolais

*University of Naples Federico II, Department of Materials and Production Engineering, Italy*

G.Marino

*Italian Aerospace Research Center, C.I.R.A., Capua (CE), Italy*

**ABSTRACT:** Glass forming materials, including thermoset and thermoplastic resins commonly used in polymer matrix composites for high performance applications, undergo structural relaxation when they are cooled through the glass transition region, due to the glassy non equilibrium state. The process towards the equilibrium follows complex paths deriving from its inherent nonlinear and nonexponential character. In this paper sub-T<sub>g</sub> annealing studies have been carried out with both neat PEI and its carbon fiber composites. The in-situ resin (i.e. the resin constrained into the fibers lattice) showed a marked decrease of the glass transition temperature. The comparison between the plain and the in situ matrix was done on the basis of the same degree of undercooling (i.e. the same distance from T<sub>g</sub>). It was found that the composite aged faster than the plain matrix.

The macroscopic effects of structural relaxation on PEI based composites were analyzed by fatigue tests in a four-point bending geometry at different level of stress ratio R (the ratio of the minimum to the maximum stress). The aged samples showed an higher characteristic strength which resulted in a correspondingly higher fatigue life compared to the as manufactured materials.

### 1 INTRODUCTION

An amorphous polymer (or the amorphous portion of a semicrystalline polymer) above its glass transition temperature is a viscoelastic rubber in thermodynamic equilibrium. When such a material is cooled below its glass transition, a nonequilibrium glass is obtained. This is a direct consequence of the considerably longer time scale of molecular relaxations within and below the glass transition region compared to the experimental time scale of the applied signal. In other words, even the slowest experimentally attainable cooling rate is much too fast for the polymer chains to relax to equilibrium while undergoing a rubber to glass transformation. The ensuing nonequilibrium structure first experience an abrupt contraction and then undergoes a time-dependent rearrangement toward the equilibrium state. The elastic (instantaneous) contraction results from the vibrational relaxations that originate in the response of the atomic bonds and whose characteristic relaxation times are extremely fast. The subsequent gradual

rearrangement of the nonequilibrium structure is much slower and is referred to as *structural relaxation*.

Experimentally, structural relaxation is followed by monitoring the variation in some structure sensitive property, such as enthalpy or volume. The most widely used experimental technique is differential scanning calorimetry (DSC), which measures the recovery of enthalpy during structural relaxation. Simultaneously, as the nonequilibrium structure spontaneously evolves towards equilibrium, mechanical properties of the glass also change and this has come to be known as *physical aging*.

The aging rate depends on the annealing temperature or, more precisely, on its distance from the glass transition temperature, T<sub>g0</sub>. Upon decreasing this distance molecular mobility will increase, accelerating the relaxation, while the driving force, defined as the entire path to cover (Fig.1), will reduce.

Over the years many authors have contributed to the understanding of structural relaxation and physical aging, as described in several book and key reviews (Kovacs 1958, Struik 1978, Ngai et al. 1985, Sherer

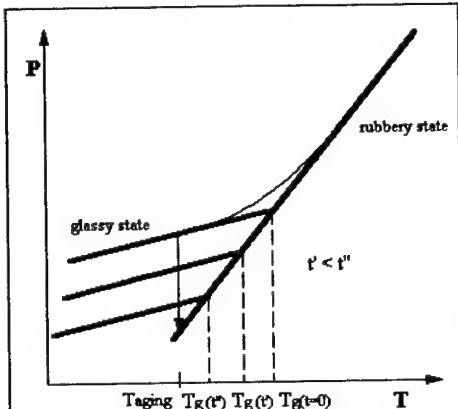


Fig. 1 Structure sensitive property as a function of temperature.

1988, Matsuoka 1992). The most complete account of enthalpy recovery during structural relaxation is given in the review by Hodge (Hodge 1994), which offers a comprehensive discourse on the theoretical and experimental aspects of the problem, presents an incisive analysis of its fundamental characteristics, and point out how the incorrect handling of nonlinearity (that has frequently appeared in the open literature) leads to the unreliable treatment of enthalpy recovery.

The two principal features of structural relaxation are nonexponentiality and nonlinearity. Nonexponentiality implies that structural relaxation is subdivided into a number of processes, each characterized by its own relaxation time. Thus a distribution of relaxation times must be known to fully describe the nonexponential character of structural relaxation. Nonlinearity, on the other hand, signifies a dependence of structural relaxation on the direction and magnitude of the applied perturbation (i.e. temperature jump). A major early contribution to the development of the theory of structural relaxation in the glassy state was the introduction of the concept of fictive temperature by Tool (Tool 1946), who recognized that a nonequilibrium glass could not be described by temperature and pressure only and suggested that the characteristic relaxation time must also be a function of the evolving structure, the latter being described by a parameter termed fictive temperature. Detailed discussion of nonexponentiality, nonlinearity and fictive temperature can be found in the above cited references.

The effect of physical aging on mechanical properties of neat polymers have been reported in a number papers dealing with several technique from

which it has been demonstrated that the modulus and the strength increases , while the fracture energy or toughness decreases with increasing aging time (Struick 1978, Yang et al. 1996). However, the effect of physical aging on polymer based composites has been rarely investigated. Indeed the mechanical properties of high performance composites are fiber dominated and even the in situ matrix undergoes physical aging subtle changes of mechanical properties are expected.(Dillard 1991). Further, it is to be recognized that during the manufacturing process of thermoplastic composites having a high fiber content, the fibers lattice function as a three-dimensional constraint to the matrix collapse subsequent to the cooling processes, and upon cooling through the glass transition region a latent state of stress will be frozen-in. The complex state of stress arising from the processing stage is dominated by either the overall geometry of the fibers ( i.e. the stacking sequence of laminates etc.) and by local inhomogeneity factors contributing to the formations of clusters of fibers as well as resin-rich areas (Asp 1996)

In such conditions the local stress state will vary between nearly shear dominated to nearly hydrostatic. Thus the same given matrix will be predisposed to different deformation and failure modes in different regions of the composite. In addition to this remarkable assumption it has to be mentioned that the state of stress of the in-situ resin is the source of the glass transition temperature variations. It is well known, in fact, that while the pressure increases the Tg (Ferry 1980) tensile and shear stress decrease it. Chow (Chow 1984) derived a theoretical expression for the Tg variation as a function of the stress state. Indeed a given decrease of Tg can be associated to either a shear or a tensile state of stress. The measure of the in-situ Tg is then an indirect measure of the overall stress state.

In this paper the multiparameter model based on the Narayanaswamy approach, which is able to correctly predict the nonexponential and nonlinear character of structural relaxation, is adopted. The model doesn't take into account the actual stress state particularly in the constitutive equation for the structural relaxation time. Qualitatively it can be argued that, upon annealing in the sub-Tg region a composite sample, two main effects occur simultaneously acting in opposite directions : a) the structural relaxation b) the stress relaxation. The structural relaxation would increase the stress state as the fiber lattice function as a three-dimensional constraint to the volume contraction while, on the other hand, the stress relaxation would decrease the

Tg depression originated during the cooling process. The manner the two phenomena interact is the subject under study in our laboratory. However, as a general rule, a correct constitutive equation for the structural relaxation times should include the effect of stress state when the presence of a superposed state of stress into the material is recognized. The anomalous results presented in the following concerning the calorimetric characterization of the in-situ resin are debited to the both unknown level of stress state and complex interaction between the two phenomena. The complex interaction of stress and structural relaxation occurring in the sub-Tg region influence the mechanical properties of the in-situ resin as well as those of the composite system. The composite under study is a quasi-isotropic laminate having a carbon fiber volume content of about 51% (58% by weight). Thus the in-plane moduli are completely fiber dominated and even the highest change of matrix modulus due to the physical aging results in a negligible effect on the composite elastic properties. The strength of a composite, on the contrary, is dominated by the statistical distribution of defects. For this reason a two parameters Weibull distribution is generally invoked for a correct description of such property. In this respect clusters of fibers as well as resin-rich areas (where the local stress state will vary between nearly shear dominated to nearly hydrostatic) act as the source of defects. The higher the level of stress (or strain) originated during cooling the lower the critical stress (or strain) to failure of the in-situ resin. Among the micromechanical events (fiber rupture, debonding, fiber buckling, matrix failure) determining the strength degradation in service life of a composite structure the role of the matrix aging can be observed by comparing the mechanical response of samples cut from the same composite tile and subjected to different sub-Tg annealing. In this paper mechanical as well as fatigue response of as manufactured and aged samples were compared. The aging time and temperature were selected, according to the calorimetric characterization, in order to test samples which experienced almost the overall relaxation process.

The durability of organic resin matrix composites (especially those used as component in many critical applications such as aerospace vehicles) is mostly related to both critical environments and extreme temperatures. In this conditions the fatigue life is highly affected by irreversible physical and chemical degradations. Instead, *physical aging* is a reversible phenomenon that can induce macroscopic change on mechanical properties of neat polymer

while its effect on composites is highly masked by fiber dominated properties.

In this work the property used to study structural relaxation is the enthalpy. This preference was established during the past decade, primarily as a result of the advancements in differential calorimetry (DSC) and subsequently of consolidated procedures for a correct measure of enthalpy relaxation (McKinney et al. 1967, Richardson 1972, Richardson & Savil 1975, Gilmour & Hay 1977, Kemmish & Hay 1985, Carfagna et al. 1986) by monitoring the continuous decrease of polymers' Tg (Richardson & Savil 1977). The Narayanaswamy-Moynham (NM) approach was utilized as the analytical tool for both the long term prediction for structural relaxation and the selection of a characteristic time at a given temperature needed to compare the mechanical behavior of aged and unaged sample.

## 2 EXPERIMENTAL

### 2.1 Materials

The composite used in this investigation was a continuous graphite fibers reinforced matrix of PEI. The prepreg utilized was a 5H satin 285g/m<sup>2</sup> having a nominal fiber content of 58% by weight (51% by volume).

The laminate composite tiles were manufactured in a mold with a hot-plates hydraulic press. The mold is made of two parts. The bottom one is a still plate onto which four ridges are bolted to form a square area measuring 20x20 cm., where the sheets of composite are set. The upper section of the mold is another steel plate that fits exactly over the square area. The mold surfaces in contact with the composite material are linked with a kapton film. The kapton film and the mold are preconditioned with a mold releasing agent. The previously cut-to-size sheets of composite are layered according to the required specifications and sandwiched with the kapton film in the mold. The mold-kapton film-composite sheet assembly is heated in the press to 608°F operating temperature. Once this temperature is reached a force of 12.4 Klbs is applied and maintained for the duration of the rest of the process, which consists of 10 min. at 608 °F and then cooling down to room temperature. At this point the mold is removed from the press and opened to extract the newly made composite tile. Eight-ply quasi-isotropic laminates were fabricated from prepgs.

## 2.2 Differential Scanning Calorimetry

Thermal analysis was carried out on both neat resin and composite samples cut from the laminate using a DSC 30 by Mettler: The measured Tg of the unaged materials were 214°C for PEI and 183°C for its composite.

Our study focused on three different aging temperatures: Tg-30, Tg-20 and Tg-10°C.

The experimental path for each calorimetric test carried on pure matrix was selected according to the following scheme: an isothermal annealing above Tg to erase all previous thermal histories, a quench to aging temperature holding the temperature constant for an assigned time. Then the sample was cooled to room temperature and finally reheated, at fixed rate (10°C/min.), up to a temperature well above Tg.

Composite samples were aged at Tg-20 and Tg-10°C after heating up from room temperature (at a heating rate of 10°C/min). This procedure avoid to erase the thermal history suffered during the manufacturing process.

The main effect of physical aging on calorimetric results is an endothermic peak in the glassy transition region. Petrie (Petrie 1972) drew the fundamentals for the study of enthalpy relaxation by differential scanning calorimetry. He considered the energy absorbed during heating be equivalent to the enthalpy relaxed during the previous annealing towards the equilibrium conditions (the lowest level of internal energy). However, it must be pointed out that calorimetric results are strictly dependent on the heating rate selected: two samples subjected to the same aging time and then heated at different rates give rise to two endothermic peaks characterized by different areas. This means that polymers restructure their internal configuration in accordance with the thermal path (Lagasse 1982)

These arguments confirm that even if the peak temperature is a quasi linear function of both aging temperature and log of annealing time, when the glass is not too close to equilibrium (Hodge 1983), it is not simple to correlate the peak area to the aging time.

In order to avoid estimation errors, the Cp-T curves will be transformed in the H-T curves following the procedure proposed by Richardson and Savil (Richardson & Savil 1977, Richardson & Savil 1979). Only this way a correct value of Tg can be determined (even during aging) as the intersection of the liquid and glassy asymptotes. The evaluation of Tg is not possible in the Cp-T diagram because the endothermic peak masks the glass transition region.

According to the “building block approach” scheme, the simplest thermal effect on selected material was considered. It consisted of an isothermal annealing that will be modeled within the frame of the *isothermal approach* described below. Then the experimental results obtained have been modeled by the Narayanaswamy-Mohynian theory which has come to be known as the *dynamic approach*. In both cases predictive models gave quite fair results.

## 2.3 Mechanical characterization

The specimens for static and fatigue tests were cut from rectangular plates, about 200 mm in length and width, and 2.2 mm in thickness, made of woven fabric carbon fiber reinforced Polyetheimide (PEI). The dimensions of the samples were 80 mm x 20 mm. The measured fibre content by volume was Vf = 51%. Both the static and fatigue tests were carried out in four-point bending at room temperature, adopting an outer span l = 66 mm, an inner span a = 22 mm. The testing machine was an Instron 8501 servo-hydraulic system in load control mode. A sinusoidal waveform was chosen. The frequencies used during the fatigue tests were in the range f = 2 - 5 Hz, to avoid significant heating of the material. The actual frequency was chosen so that the same initial stress rate could be applied on all the samples. Therefore, higher frequencies were used for lower maximum stress levels. The stress ratio was varied in the range R=0.1-0.7, and the criterion of complete failure was conventionally assumed to assess fatigue life. The load levels during fatigue were selected in the range 0.4 - 0.9 of the mean static failure load. The latter was measured in crosshead control, at a crosshead speed of 100 mm/min, to provide an initial stress rate similar to that attained in fatigue. In all, twenty-five static and twenty fatigue tests were performed.

## 3 RESULTS AND DISCUSSION

### 3.1 Enthalpy Relaxation

The study of enthalpy relaxation of in-situ resin cannot be approached separately from the effects involved in the manufacturing process. In fact, in Figure 2 are reported two Cp-T traces coming out from heating scans running from room temperature to well above Tg for the in-situ resin. The first scan of the as-manufactured composite shows a lower Tg (183°C) while the second one gives back the Tg of

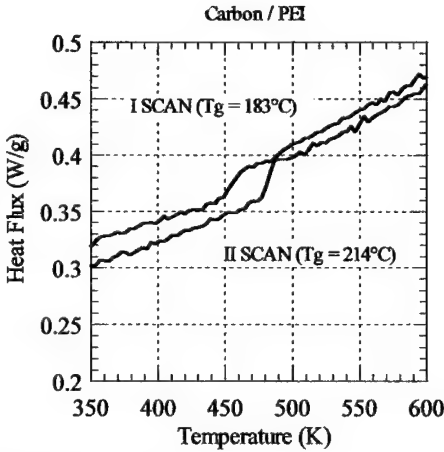


Fig. 2 DSC traces for the in-situ resin.

neat resin (214°C). Indeed upon passing through the glass transition region the previous thermal histories are fade away and an internal unstressed state is restored. The data in Figure 2 are a direct evidence of the influence of stress state on the calorimetric response of the in-situ resin. This is the reason why the thermal paths related to the neat and the in situ resin (described in the experimental section) are somewhat different.

In this work it has been assumed that the progress of structural relaxation of the in situ resin is only a little influenced (especially in the early stage of the process) by an up quench to the aging temperature.

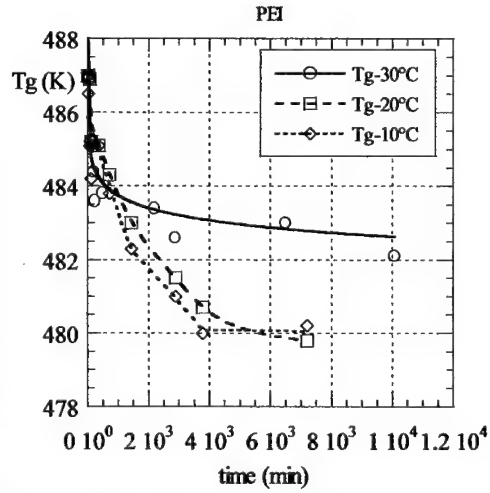


Fig. 3 The absolute progress of Tg (of  $T_f$ ) with time for neat PEI.

### 3.2 Isothermal Approach

The isothermal approach consists in monitoring Tg decrease towards the aging temperature and its scope is to identify the parameters of a simple model able to predict the progress of structural relaxation in isothermal conditions.

In Figure 3 Tg versus aging time at three different annealing temperatures is plotted for the neat resin. As mentioned above the values of the Tg were determined converting the Cp-T traces to the enthalpy-Temperature plot. Accordingly the progress of Tg was measured as the intersection of the liquid and glassy asymptotes. The analysis of these curves can be misleading due to the overlapping of the two competing factors that influence the relaxation: upon Ta approaches Tg the molecular mobility increases while correspondingly the driving force, defined as the entire path to cover (see Fig.1), is reduced.

A rational comparison of the relaxation process at different aging temperature Ta can be made by introducing a normalized relaxation function  $\phi(t)$  defined as follows:

$$\phi(t) = 1 - \frac{\Delta H(t)}{\Delta H_{\max}} = 1 - \frac{\Delta C_p(t)}{\Delta C_p} \frac{[T_{go} - T_g(t)]}{[T_{go} - T_a]} \quad (1)$$

where  $\Delta H(t)$  is the enthalpy relaxed at time t and  $\Delta H_{\max}$  represent maximum difference of enthalpy content between unaged and equilibrium state at a fixed aging temperature;  $T_{go}$  is the initial Tg and  $T_g(t)$  its variation during aging;  $\Delta C_p(t)$  and  $\Delta C_p$  are the differences between the asymptotic values of Cp in the rubbery and in the glassy state for aged and unaged material, respectively. It is generally assumed (Richardson & Savil 1979) that  $\Delta C_p$  doesn't change with aging (i.e.  $\Delta C_p(t)/\Delta C_p = 1$ ), then equation 1 can be simplified as follows:

$$\phi(t) = 1 - \frac{T_{go} - T_g(t)}{T_{go} - T_a} \quad (2)$$

Figure 4 shows the trends of the  $\phi(t)$  function concerning the three temperatures of interest. The experimental data were fitted through the Williams-Watts (Williams & Watts 1970, Williams et al. 1971) equation:

$$\phi(t) = \exp \left[ - \left( \frac{t}{\tau_o} \right)^{\beta} \right] \quad (3)$$

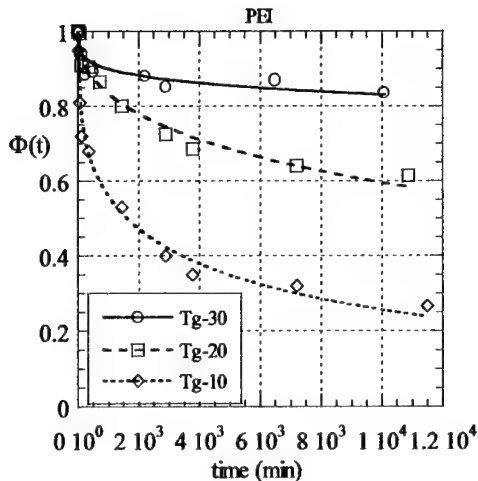


Fig. 4 The experimental and calculated  $\phi(t)$  function as obtained from the data of Figure 3.

where  $\tau_0$  is defined as the characteristic value of the relaxation times distribution and  $\beta$  as its width (a real number between 0 and 1). The parameters  $\tau_0$  and  $\beta$  were evaluated for the Tg-10°C curve. The resulting  $\beta$  was 0.37. This value was utilized to fit the data at Tg-30 and Tg-20°C.

The above procedure reflected both algebraic and physical needs:

a) the data at Tg-10°C correspond to an almost totally relaxed process (the function  $\phi(t)$  covers roughly 80% of its path). Only in such conditions realistic values of parameters of the stretched exponential can be obtained

b) It is postulated that the process in play is chemorheologically simple (i.e. its temperature dependence is such that the distribution of relaxation times suffers only a shift along the time axis without changing the shape)

From Figure 4 it can be seen that after about 10<sup>4</sup> min.  $\phi(t)$  reach the values of 0.9, 0.6, and 0.25 at Tg-30, Tg-20 and Tg-10°C, respectively.

### 3.3 Dynamic Approach

The material response to a complex thermal history involving stages of heating and cooling at constant rates can be modeled considering a series of successive steps in temperature, each one of fixed length ( $\Delta T$ ), with intermediate isothermal periods reproducing the rate of temperature change.

Linearization of equation 2 can be obtained

introducing the reduced time (Narayanaswamy 1971):

$$\xi = \int_{t_0}^t dt / \tau \quad (4)$$

allowing to apply the superposition principle to the response to different steps.

The already introduced thermal relaxation function  $\phi(t)$ , can be still expressed using the Williams-Watts equation referring to an instantaneous temperature change as follows:

$$\phi(t) = \frac{P - P_e}{P_o - P_e} = \exp \left[ - \left( \int_{t_0}^t dt' / \tau \right)^\beta \right] \quad (5)$$

where  $P_o$  is the value of property  $P$  at time  $t_1$  (time at which the change in temperature occurs) and  $P_e$  the equilibrium value of  $P$  at final temperature.

Several expressions for the structural relaxation time have been proposed, all exponential in form and containing temperature and fictive temperature as variables. In this study we select the Narayanaswamy-Moynihan (NM) expression:

$$\tau = A \exp \left[ x \frac{\Delta E}{RT} + (1-x) \frac{\Delta E}{RT_f} \right] \quad (6)$$

Here  $\tau$  is the characteristic relaxation time,  $A$  is a constant (pre-exponential factor),  $\Delta E$  is the characteristic activation energy. Parameter  $x$  ( $0 < x < 1$ ) partitions activation energy into two parts that characterize the relative effects of the temperature and structure, respectively, on the relaxation time (Narayanaswamy, 1971). The fictive temperature,  $T_f$ , is the temperature at which a nonequilibrium glass at temperature  $T$  would be in equilibrium. The choice of the empirical NM equation over the other more fundamental expressions will not be debated here; its use is a direct consequence of the excellent agreement with experimental results generated by our group and by other researchers. Numerically the glassy value of  $T_f$  provides a definition of Tg and corresponds to the temperature of intersection of the equilibrium He-T curve with a line drawn parallel to the glassy Hg-T curve and passing through the actual point (H-T). This definition is usually preferred over those given in terms of the heat capacity curve measured during heating either as the onset or the midpoint temperatures when the annealed glasses are considered. Mathematically,  $T_f$  is defined by:

$$\int_{T_f}^T \frac{\partial(P - P_g)}{\partial T} dT = \int_{T_f}^{T_r} \frac{\partial(P_e - P_g)}{\partial T} dT \quad (7)$$

where  $P_e$  is the equilibrium value of  $P$ ,  $P_g$  is the corresponding value in the glassy state,  $T_r$  a temperature in the equilibrium region and  $T$  the actual temperature.

Taking the derivative with respect to the temperature of both sides of equation (7) a new equation can be obtained in which the temperature derivatives ( $R$ ) of  $P$  appear:

$$\frac{dT_f}{dT} = \frac{R(T) - R_g(T)}{R_e(T_f) - R_g(T_f)} \quad (8)$$

When the investigated property is the enthalpy,  $R$  represents the specific heat and equation (8) can be rewritten as:

$$C_p^n(T) = \frac{C_p(T) - C_{pg}(T)}{C_{pl}(T) - C_{pg}(T)}. \quad (9)$$

The  $C_p(T)$  function is experimentally determined by DSC tests assuming for  $C_{pg}$  and  $C_{pl}$  the asymptotic experimental values. The normalized function  $C_p^n(T)$  gives by integration the  $T_f(T)$  function.

On the other side, thanks to the restored linearity (eq.4), the net response to a series of temperature jumps can be given by their superposition:

$$T_f = T_0 + \int_{T_0}^T \left[ 1 - \exp \left[ - \left( \frac{T_f(T)}{T_f(T_0)} \right)^\beta \right] \right] dT \quad (10)$$

with  $T_0$  being the initial temperature.

Equations (6) and (10) are coupled and can be solved by numerical methods (as the Marquardt algorithm) to find the optimum set of parameters ( $x$ ,  $\Delta E$ ,  $A$  and  $\beta$ ) that best describes the behavior of the  $C_p$  of the material in the glass transition region. The objective function for the optimization is:

$\sum (C_p^{N*} - C_p^N)^2$  where  $C_p^{N*}$  is the calculated value for the normalized specific heat in the transition region and  $C_p^N$  its experimental counterpart.

The iterative numerical method requires the input of starting values of the parameters. Their selection can be reasonably made in the following way:

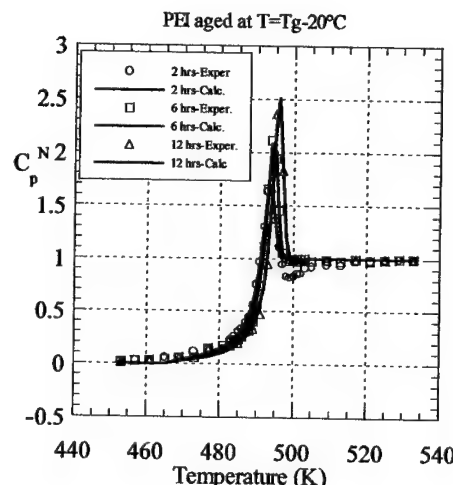


Fig. 5a Experimental and calculated (NM approach) normalized  $C_p$ .

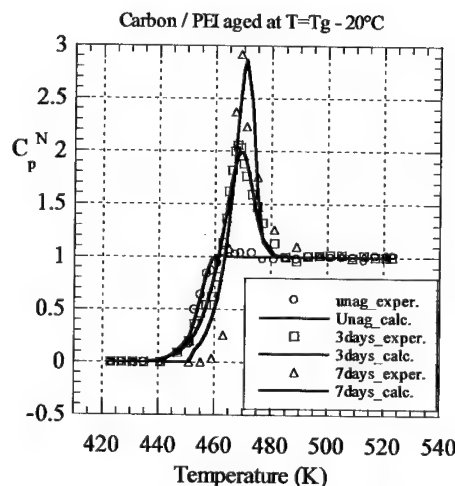


Fig. 5b Experimental and calculated (NM approach) normalized  $C_p$ .

- 1)  $\Delta E$  can be obtained experimentally from the dependence of  $T_f$  on the cooling rate,  $q$ : plotting  $\log(q)$  versus  $1/T_f$  a straight line will interpolate the experimental points and its slope gives the activation energy; in fact it is (Moynihan et al. 1976):

$$\frac{\Delta E}{R} = -\frac{d \ln(q)}{d(1/T_f)} \quad (11)$$

2)  $\ln A$  is determined from equation 6 by assuming that at  $T_g$ ,  $\tau$  is of order of unity and  $T = T_g = T_f$  then (Gomez Ribelles et al. 1990):

$$\ln A = -\frac{\Delta E}{RTg} \quad (12)$$

3) input values of  $x$  and  $\beta$  can be chosen according to literature data. Their field of variability is very limited.

Usually the computer calculation ends after about five or six iterations with the optimized parameters which define materials structure relaxation and allow to predict their behavior until very long times when subjected to any kind of previous thermal history.

In this work the dynamic approach was considered for neat and in-situ resin.

In Figure 5 a,b the experimental points and the calculated curves are reported. It can be observed that the model gives an excellent fitting in all cases. However the four parameters (assumed to be constant in the NM model) evaluated from each best fitting procedure change with aging time (see table I). Indeed, the variability of  $\Delta E/R$  and  $\ln A$  is very limited while  $x$  and  $\beta$  suffer more scatter.

Table I ( PEI aged at  $T = T_g - 20^\circ C$  )

	$x$	$\Delta E \cdot 10^{-6}$	$\ln A$ (min)	$\beta$
Unaged	.28	.225	-459	.489
2 hrs	.10	.227	-463	.363
6 hrs	.121	.242	-494	.356
12 hrs	.144	.288	-464	.358
24 hrs	.208	.208	-414	.419
48 hrs	.197	.213	-433	.374
63 hrs	.22	.219	-447	.416
120 hrs	.252	.222	-452	.512
Mean	.19	.223	-453	.411

Anyway, the fitting with averaged values still returns a good correlation. This result is not completely surprising. A number of authors (Plazek et al. 1984, McCrum 1984, Prest et al. 1980, Ngai 1979) found a variability of  $\beta$  and  $x$  with annealing time and temperature, in contrast to the theoretical prediction.

This probably because it should be used a model in which the relaxation time spectrum ( $\tau, \beta$ ) is considered to be an explicit function of both temperature and annealing time. Anyway, in order to minimize the possible errors, the mean values of each parameter were considered to define an unique set of variables to be used in the further model computations to predict  $C_p^N - T$  curves at longer aging times (until 6 months). The so obtained "virtual" plots (Figs. 6 a,b) were transformed in the  $T_f - T$  diagram and the corresponding  $T_f(t)$  estimation was done (Fig. 7).

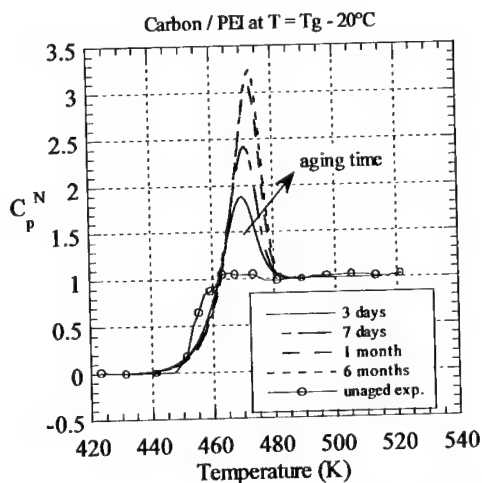


Fig. 6 Long time model prediction (NM approach) of normalized  $C_p$ .

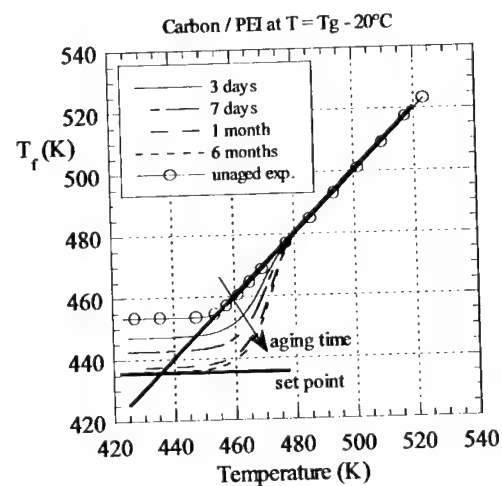


Fig. 7 Schematic plot of  $T_f$  versus  $T$ . The set point is the annealing temperature,  $T_a$ .

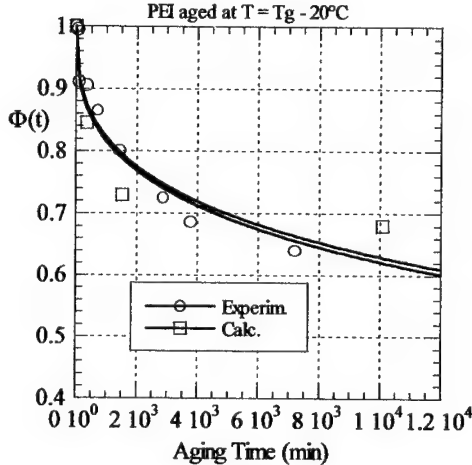


Fig. 8 Experimental and calculated isothermal behavior of neat PEI.

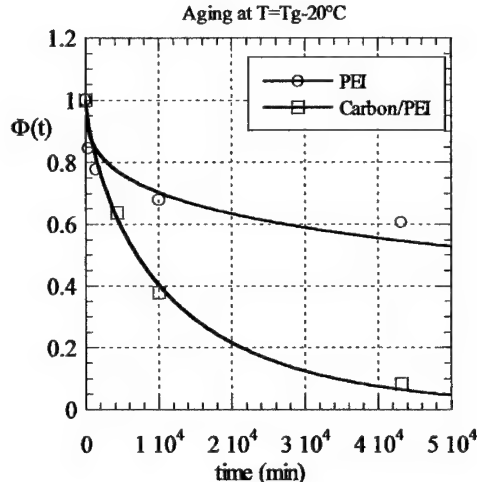


Fig. 9 Comparison of calculated isothermal behavior of neat and in-situ resin based on the same degree of undercooling,  $T_g - 20^\circ C$ .

From figure 8 it can be pointed out as the difference between estimated (by the model) and calculated (experimentally) interpolating curves adopting the WW equation, are very narrow, especially if we look at values reached at very long times.

A very interesting result came out from the comparison of the calculated and the already available (from the previous mentioned isothermal approach)  $\phi(t)$  function of the neat resin.

On the contrary a very visible difference was found in comparing neat resin and composite (Fig. 9) because the former seems much more resistant to the aging, approaching about the 60% of the relaxation after 6 months, while the latter, at the same time, is almost totally relaxed.

### 3.4 Mechanical Behavior

From the above calorimetric analysis it was concluded that composite samples annealed at  $T_g - 20^\circ C$  relaxes in a characteristic time,  $\tau_o$ , of  $10^4$  min. which roughly corresponds to one week aging.

#### 3.4.1 Strength Distribution

From the static flexural tests, the mean strength of the materials under concern was calculated through the well known strength of materials formulae, providing  $\sigma_o = 998$  MPa and  $\sigma_o = 1076$  MPa for unaged and aged samples, respectively.

Mechanical as well as fatigue tests were performed at room temperature.

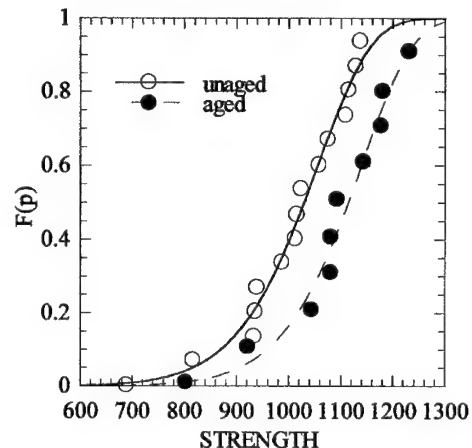


Fig. 10 Statistical distribution of measured static strength,  $\sigma_o$ , for both aged and unaged sample.

It is assumed that the scatter in the static material strength,  $\sigma_o$ , is well represented by a two-parameter Weibull distribution. Therefore, the probability to find a  $\sigma_o$  value  $\leq x$  is given by

$$F_{\sigma_o}(x) = P(\sigma_o \leq x) = 1 - \exp[-(x/\gamma)^{\delta}] \quad (13)$$

where  $\gamma$  is the characteristic strength and  $\delta$  the shape parameter.

The distributions of the static strength according to a two-parameter Weibull distribution are shown in Figure 10. The results of the static tests were used to evaluate, by the best fit method, the characteristic strength  $\gamma$  and the shape parameter  $\delta$ . The values of  $\gamma=1063$  Mpa,  $\delta=11.2$  and  $\gamma=1147$  Mpa,  $\delta=12.5$  were obtained for unaged and aged samples, respectively. From figure 10 it is clear that the sub T<sub>g</sub> aging treatments provoked a net shift of the distribution towards higher strength. The above results are somewhat in agreement with the hypotheses of a concurrent stress relaxation during the aging which in fact increases the critical stress to failure of the in-situ resin. It is to be underlined that both aged and unaged samples came from the same tile. In this respect the net shift of the distribution can be attributed solely to a change in the matrix behavior.

### 3.4.2. Fatigue model

In this section, the features of a model (D'Amore et al. 1996) relevant to the present work are recalled. The starting point for the model proposed was the hypothesis that, during cycle evolution, the material strength undergoes a continuous decay, following a power law:

$$\frac{d\sigma_n}{dn} = -a \cdot n^{-b} \quad (14)$$

where  $\sigma_n$  is the residual material strength after  $n$  cycles, and "b" is a positive definite constants, dependent on the material under concern, as well as on the loading modalities. The constant "a" was assumed to linearly increase with stress amplitude  $\Delta\sigma$ :

$$a = a_0 \cdot \Delta\sigma \quad (15)$$

where  $a_0$ , similarly to b, is a constant for given material and load conditions, and  $\Delta\sigma$  is defined as:

$$\Delta\sigma = \sigma_{max} - \sigma_{min} \quad (16)$$

In eq. (16),  $\sigma_{max}$ ,  $\sigma_{min}$  represent the maximum and minimum stress during fatigue cycling, respectively. Substituting eq. (15) in eq. (14), the latter was integrated, and the constant of integration was obtained by the boundary condition  $n=1 \rightarrow \sigma_n=\sigma_0$ , where  $\sigma_0$  is the static strength of virgin material. Introducing the stress ratio R, given by:

$$R = \frac{\sigma_{min}}{\sigma_{max}} \quad (17)$$

the following equation was obtained:

$$\sigma_0 - \sigma_n = \alpha \cdot \sigma_{max} \cdot (1 - R) \cdot (n^\beta - 1) \quad (18)$$

with

$$\alpha = \frac{a_0}{1 - b} \quad (19')$$

$$\beta = 1 - b \quad (19'')$$

Eq. (18) provided the evolution of strength degradation with fatigue cycling. Supposing that the fatigue failure happens when the residual material strength matches the maximum applied stress, the critical number of cycles to failure, N, was calculated putting  $\sigma_n = \sigma_{max}$  in eq. (18):

$$N = \left[ 1 + \frac{1}{\alpha \cdot (1 - R)} \cdot \left( \frac{\sigma_0}{\sigma_{max}} - 1 \right) \right]^{1/\beta} \quad (20)$$

Eq. (20) was rearranged in the following form:

$$\left( \frac{\sigma_0}{\sigma_{max}} - 1 \right) \cdot \frac{1}{1 - R} = \alpha \cdot (N^\beta - 1) \quad (21)$$

According to eq. (21), all the fatigue data should converge to a single master curve, irrespective of

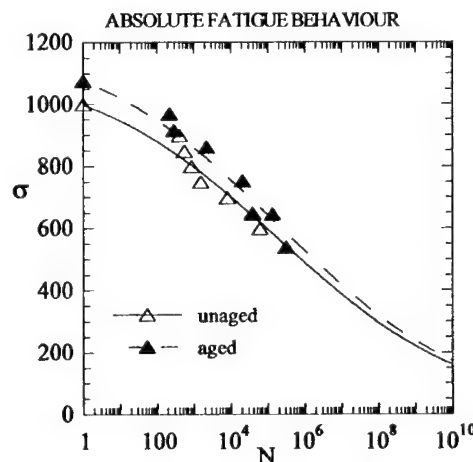


Fig. 11 - Semi-log plot of the maximum stress,  $\sigma_{max}$ , against number of cycles to failure, N. The stress ratio is  $R=0.1$ .

the stress ratio adopted, when the quantity on the left side of eq. (21) is reported against  $N$ . Moreover, reporting the term on the left side against  $(N^{\beta}-1)$  should result in a straight line passing through the origin, having slope  $\alpha$ . The latter observation was used to evaluate  $\alpha$  and  $\beta$  by suitably adjusting the  $\beta$  value until the best fit straight line fitting the experimental data actually passed through the origin.

### 3.4.3. Fatigue behavior

The fatigue data obtained selecting the loading ratio  $R=0.1$  were reported in figure 11 on a classical S-N plot on a semi-log scale. The net shift encountered in static test persists in the fatigue data. However, as depicted in figure 12, the data become indistinguishable when they are normalized to the mean strength,  $\sigma_0$ . The same behavior was observed on a different set of data (not shown here) concerning a loading ratio  $R=0.7$ . For these reasons the features of a two parameter model for the strength degradation with number of cycles accounting for the effect of stress ratio on the fatigue life was adopted.

To test the model eq.3.321 was utilized. According to it, all the fatigue data obtained for different  $R$  values should converge to a single curve, provided the term on the left side, indicated by the symbol  $K$  in the following, is reported against  $N$ . Indeed,

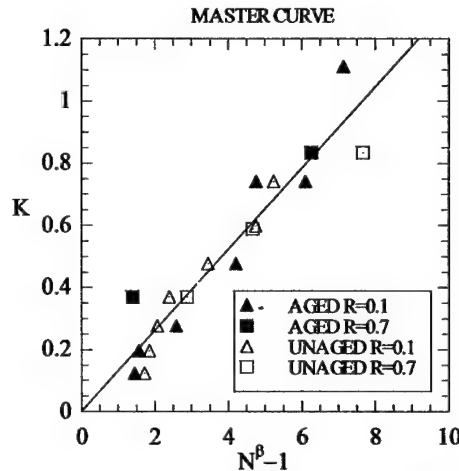


Fig. 13 - Plot for the evaluation of the constants  $\alpha$ ,  $\beta$  appearing in eq.21

according to eq. 21, plotting  $K$  against  $(N^{\beta}-1)$  should result in a straight line passing through the origin, provided the correct value is used for  $\beta$ . This observation was utilized to calculate both  $\beta$  and  $\alpha$ . The latter value should be given by the slope of the straight line. The previous procedure was followed also in this work, and the results reported in figure 13 were obtained, putting  $\beta= 0.16$ . In this figure, no distinction is visible between points referring to either different  $R$  values or aged and unaged materials. It can be seen that, although some scatter, all the points actually follow a linear trend. From the slope of the best fit straight line, the value  $\alpha=0.130$  was calculated. The continuous lines in figure 11 and 12 represent the fatigue predictions based on the above model, in which the specified constant  $\alpha$  and  $\beta$ , where adopted. The agreement with experimental data is satisfying.

### 4. Conclusions

The structural relaxation of PEI and its carbon fiber composites was investigated for the sake of studying the effect of physical aging on mechanical and fatigue behavior

The Narayanaswamy -Moynihan theory for enthalpy relaxation was utilized as the analytical tool capable to highlight the difference between the systems under concern. The different behavior between neat and in situ resin is debited to the level of frozen-in stresses originated during the processing stage of the composites. The effect of stress state on structural

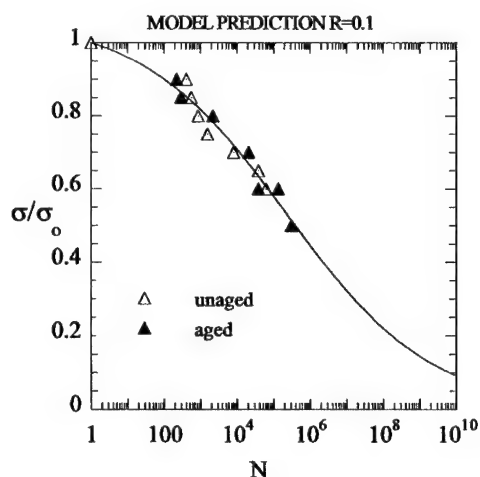


Fig. 12 - Semi-log plot of the normalized maximum stress,  $\sigma_{\max}/\sigma_0$ , against number of cycles to failure,  $N$ . The stress ratio is  $R=0.1$ .

relaxation is twofold: a depression of Tg and a concurrent stress relaxation which influence the progress of structural relaxation.

The in situ resin aged faster the plain resin. In this respect the comparison was done on the basis of the same degree of undercooling, i.e. the same distance from the proper Tg. The above approach represents a rational method for the accelerate evaluation of glassy state of polymer based system. The approach allowed the selection of a characteristic time for the study of the effect of physical aging on fatigue behavior of PEI based composite materials.

Aged materials showed a shift of the Weibull distribution function towards higher strength. Since the phenomenon is solely attributed to the resin relaxation it was argued that the in-situ resin undergoes stress relaxation, in fact increasing its critical stress or strain to failure. The absolute fatigue data suffered the same shift. However aged and unaged materials show a complete superposition of S-N curves when the maximum stress is normalized with respect to the corresponding static strength. A two-parameter model accounting for the effect of stress ratio was adopted for the description of fatigue data. A self consistent procedure was utilized for the estimation of model parameters.

## REFERENCES

- Asp L.E., Berglund L.A., Telreja R., Comp. Sci. Tech. Vol. 56, No 11 (1996).
- Carfagna C., Nicodemo L. and Nicolais L.; J. Therm. Analysis. 31, 597, (1986).
- Chow T.S., Polym. Eng. Sci, Mid-August, 1984, Vol.24, No 11.
- D'Amore A., Caprino G. Stipak P, Zhou J., Nicolais L., Sci. Engin. Comp. Mat. Vol.5, No 1, 1996 pp.1-6.
- De Bolt M.A., Easteal A.J., Macedo P.B. and Moynihan C.T.; J. Am. Ceram. Soc., 59, 16, (1976).
- Dillard D.A. in "Fatigue of Composite Materials" K.L. Reifsnider Ed. Vol. 4, Elsevier, Amsterdam 1991.
- Ferry J.F. "Viscoelastic Properties of Polymers", John Wiley & Sons, New York, 1980.
- Gilmour I.W. and Hay J.N.; Polymer, 18, 281, (1977).
- Gomez Ribelles J.L., Ribes Greus A. and Diaz Calleja R.; Polymer, 31, 223, (1990).
- Hodge I.M., J. Non-Cryst. Solids, 169, 211-266 (1994).
- Hodge I.M.; Macromol., 16, 898, (1983).
- Kemmish D.J. and Hay J.N.; Polymer, 26, 905, (1985).
- Kovacs A. J., J. Polym. Sci., 30, 131 (1958).
- Lagasse R.R.; J. Polym. Sci. Polym. Phys. Ed., 20, 279, (1982).
- Matsuoka S., "Relaxation Phenomena in Polymers", Hanser, Munich 1992.
- McCrum N.G.; Polym. Commun., 25, 2, (1984); Polymer 25, 309, (1984).
- McKenna G.B., in "Comprehensive Polymer Science", G. Allen and J.C. Bevington, Eds. Vol.2, Ch. 10, pp.311-362, 1988.
- McKinney P.V. and Foltz C.R.; J. Appl. Polym. Sci., vol II, 1189, (1967).
- Moynihan C.T., Easteal A.J., De Bolt M.A. and Tucker J.; J. Am. Ceram. Soc., 59, 12, (1976).
- Narayanaswamy O.S.; J. Am. Ceram. Soc., 54, 491, (1971).
- Ngai K.L. and G.B. Wright, Eds., "Relaxations in Complex Systems", U.S. Government Printing Office, Washington, D.C. 1985.
- Ngai K.L.; Comm. Sol. St. Phys., 9, 127, (1979); J. Phys. Colloq., c9 43, 607.
- Petrie S.E.B.; J. Polym. Sci., A-2, 10, 1255, (1972).
- Plazek D.J., Ngai K.L. and Rendel R.W.; Polym. Eng. Sci., 24, 1111, (1984).
- Prest W.M.Jr., Roberts F.J. Jr. and Hodge I.M.; Proc. 12th North Am. Therm..Anal. Soc. Conf. Williamsburg, VA, USA, 1980, pp 119-123.
- Richardson M.J and Savill N.G.; Polymer, 18, 413, (1977).
- Richardson M.J. and Savill N.G.; Brit. Polym. J., 11, 123, (1979).
- Richardson M.J. and Savill N.G.; Polymer, 16, 753, (1975).
- Richardson M.J.; J. Polym. Sci., part C, 38, 251, (1972).
- Sherer G., "Relaxation in Glass and Composites", Wiley, New York 1986.
- Struik L.C.E., "Physical Aging in Amorphous Polymers and Other Materials", Elsevier, Amsterdam 1978.
- Tool A.Q.; J. Am. Ceram. Soc., 29, 240, (1946).
- Williams G. and Watts D.C.; Trans. Faraday Soc., 66, 80, (1970).
- Williams G., Watts D.C., Dev S.B., North A.M.; Trans. Faraday Soc., 67, 1323, (1971).
- Yang Y., D'Amore A., Di Y., Nicolais L., Li B., J. Appl. Polym. Sci., Vol. 59, 1159-1166 (1966).
- D'Amore A., Caprino G., Stupak P., Khou L., Nicolais L., Sci. Engin. of Compos. Mater., Vol 4, No 1, 1995, pp.17-25.

## Mechanism-based modeling of long-term degradation

H.L. McManus

*Massachusetts Institute of Technology, Cambridge, Mass., USA*

B.J. Foch

*Space Systems/Loral, Palo Alto, Calif., USA*

R.A. Cunningham

*The Boeing Company, Seattle, Wash., USA*

**ABSTRACT:** The use of composites in high temperature, long lifetime applications requires a basic understanding of composite degradation mechanisms, advances in analytical capabilities, and accurate accelerated and scaled tests. To advance all of these goals, models are proposed based on a variety of fundamental material mechanisms. Thermal, oxygen, and moisture diffusion, chemical reactions, composite micromechanics, modified laminated plate theory, and fracture mechanics based damage models are used. All models attempt to stay as simple and fundamental as possible. All are coupled, so that interactions between various effects are modeled implicitly. Ongoing efforts at MIT are reviewed here, with some reference to other work, but no attempt is made to do a comprehensive review. Mechanism based models are yielding understanding of the mechanisms behind observed degradation phenomena, are helping to design accelerated tests, and are the first steps towards a predictive capability.

### 1 INTRODUCTION

The next generation of advanced aerospace vehicles will require composite primary structural components which meet strict performance requirements. Vehicles such as supersonic transport aircraft, supersonic cruise military aircraft, and reusable launch or hypervelocity vehicles are all exposed to severe, cyclic environments. Programs to develop these vehicles require assurance that composite structures can provide lifetime performance in severe environments.

Long term exposure to high temperatures, high stresses, moisture, oxidizing environments, corrosive substances, etc., are observed to degrade the performance of composite structures. These effects are magnified by cyclic loadings. Purely empirical approaches to these problems are difficult or impractical. The many material and configuration options available when designing composite structures makes testing all possible combinations impractical; conversely, locking in material and configuration choices before confirming durability is limiting at best, and potentially disastrous. The single worst problem is simply the *time* required. Waiting an aircraft lifetime to determine the suitability of a new material is not acceptable to most users.

Much of this complexity could be avoided if the degradation processes and their effects could be

modeled. There are a number of approaches available. Models which attempt to directly capture the relevant physical phenomena, and derive the resulting effects on the composite as a consequence of these phenomena, are referred to as mechanism-based. Based on gross experimental observations, a variety of simple mechanisms are assumed to be operating. Each of these can be described using fundamental engineering principles. Complex observed behavior is then predicted as a consequence of the operation and interaction of the simple mechanisms.

Ideally, mechanism-based models would be simple, well grounded on fundamental physical principles, and result in measures of direct interest to analysts and designers. In practice, compromises must be made; often the metrics easy to model or measure (e.g. weight loss) must be empirically or semi-empirically connected with metrics of interest (such as material mechanical properties).

This paper will cover mechanism-based models relevant to degradation of polymer matrix composites, and a proposed framework in which they can yield useful information on laminate behavior. The models will be explored by example more than by exhaustive review, with emphasis on, but not sole consideration of, MIT work. A running example will be presented. A thin skin for a supersonic aircraft will be used to illustrate each part of the model, with

the results building cumulatively until damage is (successfully) predicted based only on knowledge of the environment and material properties.

A frank discussion of the successes, failures, and difficulties of the models will be included. Finally, challenges to the community in the areas of improved models, integration, and the incorporation of mechanism-based models into practical analytical, test, and design methods will be presented.

## 2 APPROACH

Figure 1 schematically illustrates a composite in service. Heat from the environment conducts into the composite. The composite is observed to gain and lose weight in response to changes in the moisture environment; diffusion of moisture into the material is assumed to be the cause. Degradation is observed; it can be quantified in the form of changes in material properties, appearance, glass transition temperature, and weight, both in a visible surface layer, and throughout the composite. It is assumed that degradation is due to permanent chemical changes in the material, possibly aided by oxygen or other substances diffusing in from the environment. At any point in the composite, close examination will reveal changes in the properties of the individual constituents. It is assumed that these changes are consequences of their altered chemistry. The properties of the composite therefore change, and this change is presumed to be responsible for the observed changes in behavior at the laminate level, in particular the response of the laminate to mechanical loads. Observed damage such as cracking is assumed to be due to the combined effects of mechanical loads and environmental factors. Finally, damage affects the degradation process, presumably because the cracks allow freer ingress of the environment, affecting the diffusion and chemical degradation mechanisms.

Figure 2 shows the proposed mechanism-based modeling scheme, given these observed physics. Thermal conduction with appropriate boundary conditions models the heat transfer; coupled diffusion and chemical reaction processes model the invasion of degrading substances into the composite and the resulting chemical changes. The chemical state is presumed to change the properties of the composite, and hence its response to loads, and this may lead to damage. This in turn can affect the thermal, diffusion, and mechanical response of the composite, necessitating a coupled model. Note the figure illustrates the practical organization of the scheme developed here—for example, thermal and moisture diffusion processes are mathematically similar, but in practice operate at different time scales, and are handled by different codes.

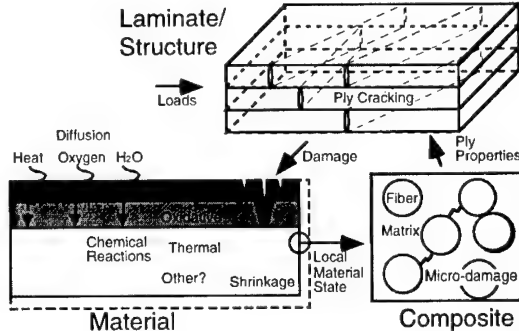


Figure 1. Schematic of events leading to degraded performance.

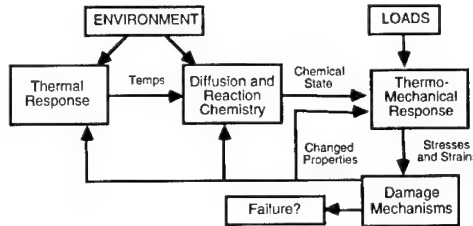


Figure 2. Modeling framework.

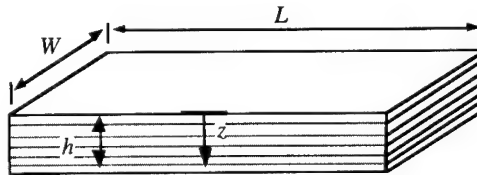


Figure 3. Geometry

## 3 MODELING

### 3.1 Geometry

Shown in Figure 3 is a long, wide, thin plate ( $L \times W \times h$ ) typical of composite structures. The plate consists of composite plies, each composed of fiber and matrix materials. An environment, uniform in space but time-varying, is applied to one or both sides. Temperature  $T_\infty$ , relative humidity  $\Phi_\infty$  and oxygen concentration  $C_{ox\infty}$  are specified at the surfaces, and loads  $N$  and moments  $M$  are specified at the edges, all as functions of time. The response is assumed to be a function only of the depth into the material  $z$  and time  $t$ .

### 3.2 Diffusion

Heat, moisture and oxygen diffuse into the plate. These phenomena are described by similar mathematics, but have very different time scales, and are handled quite differently in practice.

**3.2.1 Thermal response.** The thermal response is assumed to be controlled by conduction. Conductivity may be affected by degradation (charring) or damage (delamination) (McManus & Springer 1992a, b). The conductivity of composites is anisotropic; it may be fully anisotropic or orthotropic. Heat may also be consumed or liberated by chemical reactions. The general model for anisotropic conductivity with generation is

$$\frac{\partial T}{\partial t} = \frac{\partial}{\partial x_i} \left( D_{ij} \frac{\partial T}{\partial x_j} \right) - r_s \quad (1)$$

where  $D_{ij}$  is the thermal diffusivity ( $D_{ij} = K_{ij} / c_p \rho$ ) and  $r_s$  represents the effect of reactions. The composites considered have in-plane conductivity  $K_{xx}$ , and through thickness conductivity  $K_{zz}$ , with  $K_{xx}$  typically much greater than  $K_{zz}$ . Higher  $K_{xx}$  leads to increased heat flow to/from edges. For some problems, this may make the simplified geometry of Figure 2 inaccurate and require two- or three-dimensional analysis (Milke & Vizzini 1991). Parametric studies of transient thermal problems (Crews, in prep.) indicates that a one dimensional analysis will suffice if

$$h\sqrt{K_{xx}/K_{zz}} \ll L, W \quad (2)$$

This requirement becomes difficult to meet for typical composite thermal conductivities ( $K_{xx} < K_{zz}$ ). This requirement also applies to other transport properties such as moisture and oxygen diffusivities, which may be even more anisotropic.

For our example problem, a thin plate in typical aircraft service, thermal response is so much faster than other processes that it is convenient and acceptably accurate to assume that the temperature everywhere is simply equal to the environment temperature.

**3.2.2 Moisture.** Moisture ingress is modeled by Fickian diffusion. Equation 1 applies, with  $D_{ij}$  representing the moisture diffusivity, moisture concentration  $c_m$  replacing  $T$ , and  $r_s$  representing trapped or reacted water, if required. Saturation moisture content is assumed to be a simple function of environment relative humidity. The surface is assumed to always be in equilibrium with the environment. The diffusivity is exponentially temperature dependent; it may also depend on

degradation and damage. This model, and a very efficient method for implementing it to solve problems involving very large numbers of thermal and moisture cycles, is fully described in Foch (1997), and Foch & McManus (1997).

The model was applied to a typical high speed aircraft cyclic environment, shown in Figure 4. Hot dry supersonic flight conditions alternate with cold dry subsonic flight, and warm wet ground conditions. The results are shown schematically in Figure 5. Near the surface, each cycle causes large variations in the moisture content. In the interior, a quasi-equilibrium level is reached after a few hundred cycles. The simple model reveals the essential nature of the moisture absorption; it also coincidentally yields simple methods for estimating the depth of the moisture affected zone and the interior quasi-equilibrium level.

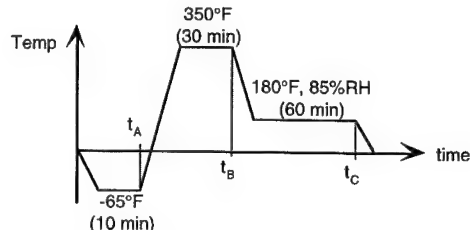


Figure 4. High speed aircraft environmental test profile.

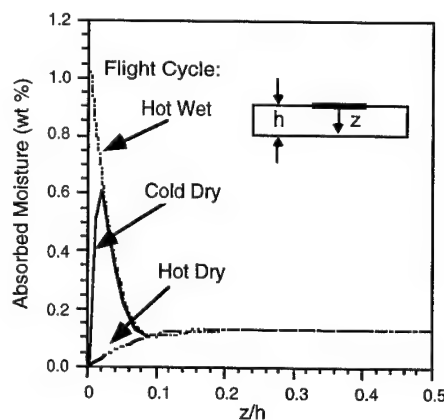


Figure 5. Moisture absorption in a cyclic environment.

**3.2.3 Oxygen and other substances.** Other substances are also assumed to enter the composite via anisotropic Fickian diffusion. Mathematically, this diffusion is modeled using Eq. 1, with the concentration  $c_s$  of diffusing substance  $s$  replacing  $T$  and consumption by reactions accounted for by the  $r_s$

term. Diffusion is assumed to be exponentially dependent on temperature, and can also be dependent on chemical degradation and damage.

### 3.3 Degradation

Temperature, time, and corrosive substances such as oxygen can chemically degrade the matrix. The actual chemistry of this degradation is very complex. Degradation can be modeled by tracking one or more degradation metrics  $\alpha_i$ . These metrics track processes such as postcuring, oxidative crosslinking, hydrolysis, or mass loss (charring) reactions. Virgin material has  $\alpha_i = 0$ , while  $\alpha_i = 1$  means that chemical reaction  $i$  has been completed. These metrics must be chosen with care; typically one selects metrics that correspond to measurable changes such as  $T_g$  changes (for post-curing reactions or physical aging), mass gain (for hydrolytic or oxidative crosslinking reactions), or mass loss (for polymer breakdown).

Typically, reaction rates are calculated from the local temperature  $T$ , concentration  $c_s$  of diffusing substance  $s$ , and previous progress of the reaction  $\alpha_i$ , using an Arrhenius reaction such as:

$$\frac{\partial \alpha_i}{\partial t} = k_i(1 - \alpha_i)^{n_i} c_s^{m_{si}} \exp\left(\frac{-E_i}{RT}\right) \quad (3)$$

Here, the rate  $k_i$ , activation energy  $E_i$ , and powers  $m_{si}$  and  $n_i$  are parameters of the reaction that must be determined experimentally. The concentration  $c_s$  must be calculated by diffusion modeling, and if the diffusing substance is consumed by the reaction, its concentration will be altered by the reaction. Thus the diffusion and reaction models are coupled.

This kind of modeling has been used extensively to model the charring and ablation of carbon-phenolic rocket motor liners (McManus 1992), the charring of graphite/epoxy composites in fires (Crews & McManus 1997), and to model the degradation of graphite/polyimide composites in engine applications (Cunningham & McManus 1996).

Use of these models requires accurate values for the degradation parameters. Unfortunately, it is often the case that an apparently simple degradation measurement will actually be a confounded mix of diffusion processes (e.g. diffusion of oxygen) and the results of several different degradation reactions. To untangle this, an analysis-driven test procedure has been established (Cunningham 1996, McManus & Cunningham 1997). First, the reactions are quantified using Thermogravimetric Analysis (TGA) tests performed on finely powdered specimens in both nitrogen and air. Powdered samples eliminate diffusion as a consideration. The nitrogen tests allow the parameters for the purely thermal reactions to be calculated; the air tests, plus the model developed for

the thermal reactions, allows the backing out of the parameters of the additional reactions due to the presence of oxygen. Finally, tests performed on macroscopic specimens of different geometries can be used to back out diffusion coefficients.

Figures 6 and 7 illustrate the use of a three-reaction model to match TGA results for the degradation of the matrix of a graphite/polyimide composite. Mass loss from a sample heated at a constant rate is shown. First, nitrogen TGA results are modeled using two reactions (Fig. 6); then oxidative reactions are captured using the thermal model along with a single additional reaction (Fig. 7). The resulting model captures the thermal and oxidative chemistry of the matrix.

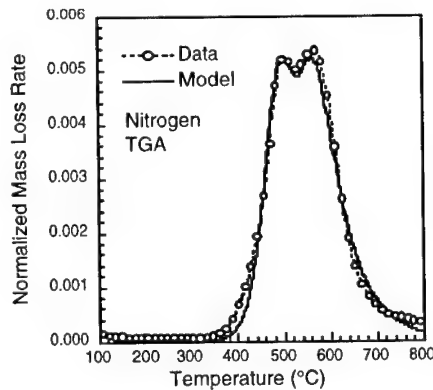


Figure 6. Two-part thermal reaction model fit to TGA mass loss data for powder specimens in nitrogen.

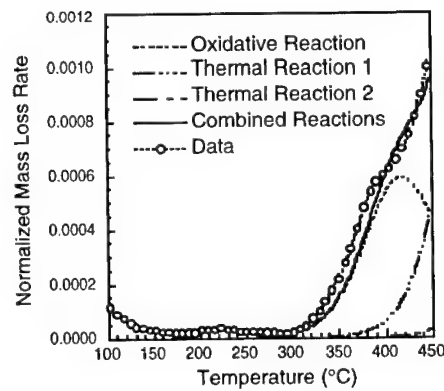


Figure 7. Two thermal and one oxidative reactions fit TGA mass loss data for powdered specimen in air.

Figure 8 shows sample results from a series of isothermal exposure tests carried out on macroscopic neat resin and composite specimens of varying dimensions. By measuring weight loss and the growth of a visibly degraded layer, diffusion constants can be determined, completing the model.

An important general result of the modeling and analysis-driven testing is that the degradation process is a multi-step process. It can be controlled by the diffusion or reaction rates. In the cases studied, the usual pattern was that the degradation was diffusion limited, with most mass loss occurring near the surface. The mass loss from macroscopic specimens was therefore a badly confounded metric, as it is an average of the mass loss from a badly degraded surface area and a relatively untouched interior.

The coupled diffusion-reaction model has been incorporated into the same code, CODSTRAN, used in the moisture analysis, and applied to similar flight cycles. The results are discussed in Foch & McManus (1997) and Foch (1997). Figure 9 shows a typical result. Severe degradation takes place near the surface, and proceeds slowly into the material from both exposed surfaces.

### 3.4 Mechanical properties of degraded material

Given an understanding of the chemical state, it is desirable to know mechanical properties as functions of the metrics of this state. This can be accomplished purely empirically, by testing the composite structure in the degraded state of interest, but this lacks generality. It is more desirable to measure properties at the most fundamental level (i.e. lamina or fiber-matrix), as functions of the metrics used to describe the degradation state (i.e. temperature and the metrics  $\alpha_i$ ). A truly mechanistic model would predict the mechanical properties from the chemistry of the degradation state, but this sort of capability is at best several decades in the future. A semi-empirical approach taken here is to measure the properties of the matrix or the composite as functions of the degradation metrics.

There are difficulties. Given a uniformly degraded test specimen, it is often difficult to isolate the effects of test temperature and the various degradation mechanisms. Worse, environmental exposure does not result in a uniformly degraded specimen. A popular method of measuring "material properties" of degraded specimens is shown in cartoon form in Figure 10. Bending induces a stress gradient; this gradient interacts with a severe material property gradient if, as is typical, the material degrades non-uniformly. What is measured is the response of a very complex structure to a moderately complex loading, NOT a material property.

However, analysis-driven test programs can be designed, exploiting the understanding gained by the

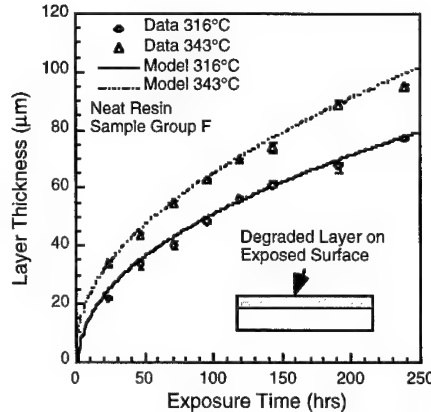


Figure 8. Diffusion/reaction model captures behavior of a macroscopic specimen.

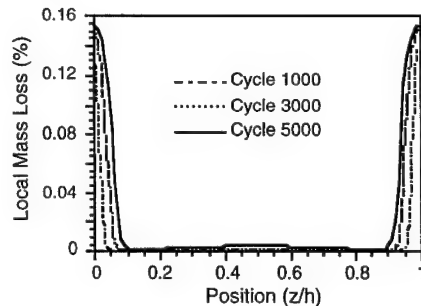


Figure 9. Combined model predicts surface degradation in cyclic use environment.

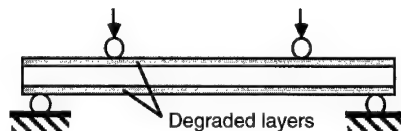


Figure 10. Bending test of a degraded specimen puts complex loading into a complex structure.

degradation models, to extract true material properties under many circumstances. In ongoing work (Tsuji, in prep.), mechanical and thermal bend tests with various specimen geometries are used to extract material properties from thin degraded layers. Another approach (Crews & McManus 1997) is to condition the specimens carefully to generate uniform desired degradation states.

### 3.5 Thermomechanical analyses

**3.5.1 Micromechanics.** Mechanical properties can be collected at the lamina level, obviating the need for micromechanical analysis. However, it is often more practical, and always more general, to collect degraded matrix properties, and attempt to predict the composite ply properties using micromechanics. Also, some degradation mechanics (e.g. matrix shrinkage) operate at the micromechanical level, and cannot be accurately characterized at the ply level. Here, a modified version of an existing set of micromechanical relations is used to predict the properties of composite plies as functions of the properties of the constituent materials, which are themselves functions of the degradation metrics. A link is thus made from the degradation state to the mechanical behavior of the composite.

A modified version of the micromechanics established by Chamis and his group are used (McManus 1994, McManus & Chamis 1996). The dependence of matrix properties on degradation states is handled by fitting a simple power law to data. For example, a property  $P$  at temperature  $T$  and in degradation state  $\alpha$  could be found from a relation such as

$$\frac{P}{P_0} = \sqrt{\frac{T_g - T}{T_g - T_0}} (1 + p\alpha^q) \quad (4)$$

Here,  $T_g$  is the glass transition temperature (which may itself be a degradation metric),  $T_0$  the reference temperature,  $P_0$  the undegraded property at the reference temperature, and  $p$  and  $q$  are parameters fit to data and provided as input to the code. Another complication is the fact that the matrix may shrink as it degrades. This is handled as a stress-free strain in the matrix, in a way similar to thermal expansion strains. In our example problem, Eq. 4 gives matrix properties as functions of material state, and the fibers are assumed to be stable.

**3.5.2 Composite analysis.** Once the properties and thermal and shrinkage strains at the ply level are calculated, all that is required is a Classical Laminated Plate Theory (CLPT) analysis that is slightly modified to handle shrinkage strains. Again, the treatment is similar to that for thermal expansion strains. Stresses and strains are predicted in the degrading composite, and any standard ply failure criteria can be applied.

The stress field in a typical degrading composite will be complex, with mechanical, thermal, hygral, and degradation-shrinkage-induced stresses all contributing. Figure 11 shows the stresses transverse to the plies of both unidirectional and quasi-isotropic laminates exposed to the environment

shown in Figure 4. These stresses are due to degradation (Fig. 9) and moisture (Fig. 5), and are in addition to stresses due to mechanical or thermal loading. The degradation state is also plotted on this figure to illustrate the severe stresses that build up in plies that are subject to degradation.

**3.5.3 Implementation.** The micromechanical and composite analyses have been implemented in a modified version of the ICAN code (McManus & Chamis 1996). The diffusion and degradation code CODSTRAN includes the option of writing ICAN input decks for automatic stress analyses at selected times during the degradation analysis.

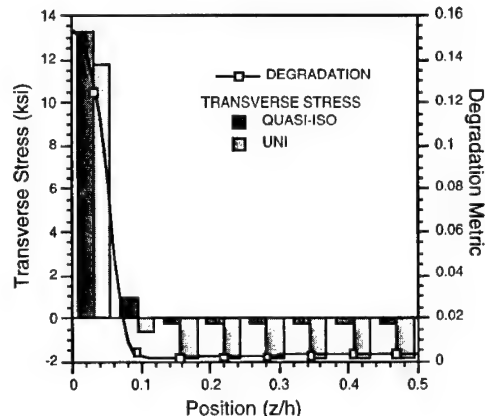


Figure 11. Stress due to degradation and moisture.

### 3.6 Microcracking

Microcracking is the most obvious form of damage seen in degraded composites. It can also arise from mechanical loads, or thermal residual stresses, and is accelerated by cycling of any of these causes. The prediction of microcracking based on shear-lag or other stress analyses and simple fracture mechanics principles is well established (McManus & Maddocks 1996), and modeling of fatigue is under development (Park & McManus 1996, Reynolds & McManus, in prep.). Microcracking due to degradation has been widely observed (e.g. Cunningham 1996); moisture and solvents also are observed to greatly accelerate microcracking (Dillard et al. 1997, Nairn, unpubl.). Given the degradation state, properties from previous analyses, and empirical knowledge of the effects of degradation on the in-situ toughness of the material, microcracking can be predicted using tools such as the CRACKOMATIC code (McManus & Maddocks 1996, Michii & McManus 1997). This interface is not yet automated, however.

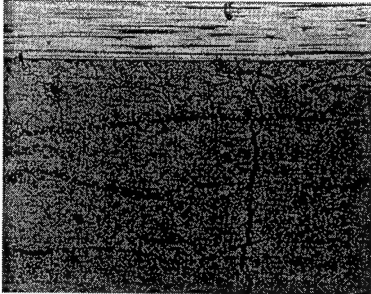


Figure 12. Cracks seen at exposed edge.

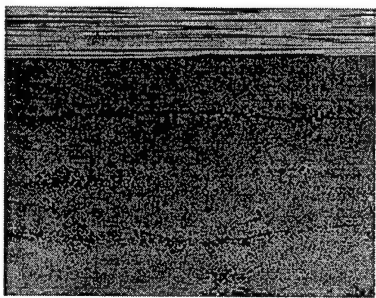


Figure 13. Uncracked material far from edges or surfaces.

Application of microcracking analyses to our example predicts severe microcracking in the material near exposed surfaces and edges due to both higher stresses and lower material toughness in these regions. No cracking is predicted in the interior of specimens, which are relatively unaffected by moisture and degradation, and not sufficiently stressed by the thermal cycling to crack. Figures 12 and 13 show rather dramatic, if qualitative, confirmation of the analysis- a polyimide composite shows extensive cracking at an exposed edge, but none more than a millimeter in from the edge.

#### 4 DISCUSSION

Primarily, mechanism-based models aid in the understanding of the actual mechanisms that are responsible for complex observed behavior—they help sort out what is really going on. In our example, complex moisture absorption behavior was revealed, with a surface layer subject to repeated severe cycles and a relatively dry core. Degradation was also restricted to a surface layer, although it continued to grow and could be a threat over very long times. The resulting stress state was complex, with moisture and degradation induced stresses interacting with thermal and mechanical stresses. Cracking was expected near

surfaces and edges, due to degraded material properties and added stresses, but the interior of most materials was predicted not to crack. The complex behaviors were predicted by combinations of very simple models.

In all of the above-mentioned cases, the models have helped to clarify the fundamental issues behind observed problems. They have been particularly important for designing tests. Typically, tests of degraded laminate properties (such as laminate strength) yield results that are dependent on specific test conditions, layups, etc. Such tests confound the effects of many mechanisms. The use of mechanism-based models allows the design of tests to measure discrete components of the degradation process (such as changes in matrix chemistry). Ideally, laminate behavior under specific environmental conditions can then be predicted from the models using such data.

This ideal picture is clouded by a number of difficulties. Models of individual phenomena are not fully mature. For example, recent work shows that full description of microcracking behavior requires statistical treatment of flaws and material properties (Michii & McManus 1997), and traditional models may not be sufficient to predict the effects of microcracking on strength. Models may also represent trade-offs between accuracy and usefulness. Full description of the reactions of degradation of polymers would require tracking a very complex set of reactions, for example. Models may not represent unique solutions—two very different sets of fundamental physical assumptions may lead to models that describe very similar behavior. Finally, existing models may simply be insufficient to describe the observed phenomena under some circumstances.

The models of individual phenomena are also not fully integrated. Both disciplinary and scale gaps stand in the way of integrating existing models. For example, reasonable success in determining the moisture and chemical degradation state in a complex, cyclical environment does not translate directly into the desired knowledge of reductions (if any) in laminate properties. Extensive data, which is difficult to collect, is required to translate changes in hydrochemical state into changes in matrix and interface properties. These changes must then be translated via micro and ply mechanics into changes in properties on the laminate scale.

Finally, truly mechanistic models can be unwieldy for design. Ideally, design methodologies will adapt to incorporate added modeling capability, but this does not happen overnight (Lagace et al. 1996). Mechanism-based models can be used to generate understanding, but must be reduced to simpler, more practical analysis, test, and design methods if they are to be immediately useful. In a similar fashion, the test programs designed using mechanism-based

models can get out of hand. A complete understanding of a material's long term behavior in complex environments is likely to require a great deal of fundamental testing. Such tests may be fairly simple, and their results applicable over wide ranges of conditions, but doing them all may not be the optimal strategy for collecting the information necessary to apply a given material to a given situation. In both analyses and tests, mechanism based understanding must be used to justify and understand the uses of (and limits of) simpler, perhaps semi-empirical methods.

## REFERENCES

- Crews, L. K. & H. L. McManus, 1997. Modeling the High-Temperature Degradation of Graphite/Epoxy. *American Society for Composites 12th Technical Conference on Composite Materials, Detroit MI, Oct. 1997*: 1123-1132.
- Cunningham, R., 1996. High Temperature Degradation Mechanisms in Polymer Matrix Composites. Master's Thesis, Massachusetts Institute of Technology, Cambridge MA.
- Cunningham, R. & H. L. McManus, 1996. Coupled Diffusion-Reaction Models for Predicting the Distribution of Degradation in Polymer Matrix Composites. *Symposium on Composite Materials, AMSE International Mechanical Engineering Congress and Exposition, Atlanta, GA, Nov. 1996*.
- Dillard, D. A., A. Furrow, H. Parvatareddy, T. St. Clair & J. Hinckley, 1997. Solvent Induced Environmental Stress Cracking in High Performance Composites and Adhesives. *DURACOSYS 97: Progress in Durability Analysis of Composite Systems, Blacksburg, VA, Sept. 1997*.
- Foch, B., 1997. Integrated Degradation Models for Polymer Matrix Composites. Master's Thesis, Massachusetts Institute of Technology, Cambridge MA.
- Foch, B. & H. L. McManus, 1997. Modeling of Environmentally-Induced Damage in Polymer Matrix Composites. *Proc. of the 11th Int. Conf. on Composite Materials, Gold Coast, Australia, July 1997*.
- Lagace, P. A., S. M. Spearing & H. L. McManus, 1996. A Proposed Methodology for the Failure and Durability of Composite Structures. *Proceedings of the 11th DoD/NASA/FAA Conference on Fibrous Composites in Structural Design, Fort Worth, Texas, August 1996*.
- McManus, H. L., 1992. Critical Factors in the Analysis of Decomposing Composites. In Salamon, N. J. & R. M. Sullivan (eds) *Computational Mechanics of Porous Materials and Their Thermal Decomposition, AMD-136, American Society of Mechanical Engineers, N. Y., NY, April 1992*: 113-119.
- McManus, H. L. & G. S. Springer, 1992. High Temperature Thermomechanical Behavior of Carbon-Phenolic and Carbon-Carbon Composites, I. Analysis. *J. of Composite Materials*, 26(2):206-229.
- McManus, H. L. & G. S. Springer, 1992. High Temperature Thermomechanical Behavior of Carbon-Phenolic and Carbon-Carbon Composites, II. Results. *J. of Composite Materials*, 26(2):230-255.
- McManus, H. L. 1994. Stress and Damage in Polymer Matrix Composite Materials Due to Material Degradation at High Temperatures. *35th AIAA/ASME/ASCE/AHS/ASC Structures, Structural Dynamics, and Materials Conference, CP942, Hilton Head, SC, April 1994*: 736-744.
- McManus, H. L., D. E. Bowles & S. S. Tompkins, 1996. Prediction of Thermal Cycling Induced Matrix Cracking. *J. of Reinforced Plastics and Composites* 15(2):124-140.
- McManus, H. L. & C. C. Chamis, 1996. Stress and Damage in Polymer Matrix Composite Materials Due to Material Degradation at High Temperatures. NASA Technical Memorandum 4682, January 1996.
- McManus, H. L. & J. R. Maddocks, 1996. On Microcracking in Composite Laminates under Thermal and Mechanical Loading. *Polymers and Polymer Composites* 4(5):304-314.
- McManus, H. L. & R. Cunningham, 1997. Coupled Materials and Mechanics Analyses of Durability Tests for High Temperature Polymer Matrix Composites", *ASTM STP 1302 High Temperature and Environmental Effects on Polymeric Composite*.
- Michii, Y. & H. L. McManus, 1997. Prediction of Microcracking Distributions in Composite Laminates using a Monte-Carlo Simulation Method. *J. of Reinforced Plastics and Composites* 16(13):1120-1130.
- Milke, J. A. & A. J. Vizzini, 1991. Thermal Response of Fire-Exposed Composites. *J. Composites Technology and Research*, 13(3):145-51.
- Park, C. H. & H. L. McManus, 1996. Thermally Induced Damage in Composite Laminates: Predictive Methodology and Experimental Investigation. *Composites Science and Technology* 56(10):1209-1219.

## Thermal and mechanical durability of graphite-fiber-reinforced PMR-15 composites

K.J. Bowles

*Polymers Branch, Materials Division, NASA Lewis Research Center, Cleveland, Ohio, USA*

**ABSTRACT:** Earlier work, which reported relationships between compression properties and elevated temperature aging times and weight losses, also pointed out the apparent influence of surface layer formation and growth on the retention of compression properties during extended aging times. Since that time, studies have been directed toward evaluating the growth of the surface layer. This layer was found to change in its composition and features as the aging temperature changed. Microcracks and small voids initiated and advanced inward at all temperatures. Visible oxidation at the surface occurred only at temperatures above 260 °C. Relationships between layer thickness and aging time and temperature were evaluated and empirically formulated. Then, the compression properties were graphically related to the surface layer thickness with excellent correlation. The surface layer was observed to influence the compression strength of thin samples only.

### 1 INTRODUCTION

Programs are under way at the NASA Lewis Research Center to develop advanced propulsion systems for 21st century aircraft. To do this, it is necessary to develop predictive models that describe the durability of polymer matrix composite structural propulsion components under extreme ambient conditions. This paper is aimed toward developing an engineering-based description of the thermal and mechanical durability of graphite-fabric-reinforced, polyimide, PMR-15 composites at temperatures ranging from 204 to 343 °C. Aging times reached 26,300 h for specimens aged at 204 °C. Particular attention was given to those chemically induced physical changes that have the most influence on the degradation of compression properties. Results were evaluated by the (1) thermal oxidative stability (TOS) of the composite, (2) composite compression properties, and (3) microstructural changes.

### 2 MATERIALS

The material that was studied was PMR-15 reinforced with T650-35, 24 by 23, 8 harness satin-weave graphite fiber fabric. The aged specimens measured about 11- by 9-cm in length and width and were either 4, 8, or 20 plies thick. These dimensions were chosen to provide nominal cut-edge to total-surface-area percent-

ages of 3, 5, and 12 percent, where the total surface area consisted of both cut and molded surfaces. The molded surfaces were those that were in contact with the metal mold or vacuum bag during the curing process. The materials were processed at GE Aircraft Engines, Inc., in Evendale, Ohio.

### 3 TESTING

The composite materials used were aged in air-circulating ovens at temperatures of 204, 260, 288, 316, and 343 °C, and an air flow maintained at 100 cm<sup>3</sup>/min. The laminates were removed periodically, allowed to cool in a desiccator, weighed, and either returned to the oven or permanently removed for testing. The aging time was considered to be complete when the weight loss exceeded 10 percent.

All specimens were conditioned at 125 °C for 16 h before compression tests were conducted. The compression tests were performed as specified in *Test Method for Compressive Properties of Rigid Plastics* (ASTM D-695M), with a cross-head speed of 1.2 mm/min, a temperature of 23.3 °C, and a relative humidity of 50 percent. No end tabs were used. Strain was measured with an extensometer, and moduli were measured using strains and loads at 500 and 1500 microstrain. Surface layer thicknesses were measured from photomicrographs of sectioned specimens.

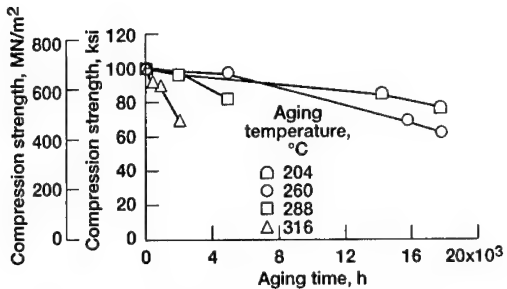


Figure 1. Compression strength of T650-35/PMR-15 composite specimens as a function of aging time at various temperatures. Number of plies, 20.

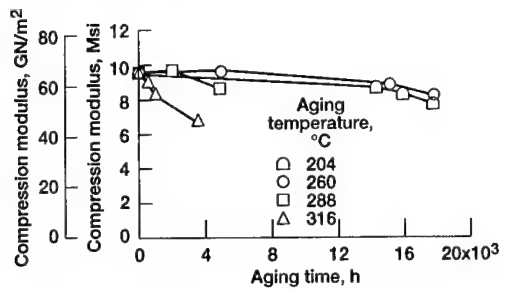


Figure 2. Compression modulus of T650-35/PMR-15 composite specimens as a function of aging time at various temperatures. Number of plies, 20.

#### 4 RESULTS

Selected specimens were removed from the aging ovens for compression testing at different times during the aging periods. Figures 1–2 (from Bowles et al. 1995) show strengths and moduli, respectively, of the 20-ply specimens plotted against aging time. When the ordinate variable is aging time, the relationships all appear to be separate linear curves with a different slope for each temperature. However, the data from the 204 and 260 °C tests appear to be identical. When percent weight loss is the independent variable, all the data except that of the specimens aged at 204 °C appear to collapse onto a single curve with the relationship  $\ln S_c = 4.614 - 10.259 \times 10^{-2} w$ , where  $S_c$  is the compression strength in MN/m<sup>2</sup> and  $w$  is the percent weight loss. Neither of these two relationships, percent weight loss or aging time, produce one weight loss curve that accommodates the data at all the temperatures that were studied. The data from Figure 1 indicate that the PMR-15 composite material will not retain its strength very long at temperatures over 260 °C. The initial moduli values appear to be retained for longer periods at the lower temperatures (Fig. 2).

As mentioned in the MATERIALS section, the fabric-reinforced composites had two types of surfaces. For these tests, the majority of surface area was composed of a resin-rich molded surface that was in

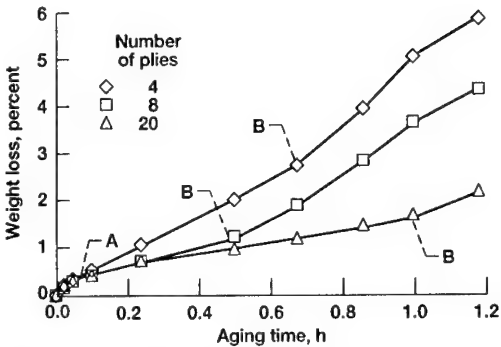


Figure 3. Weight loss of T650-35/PMR-15 composites as a function of aging time at 316 °C.

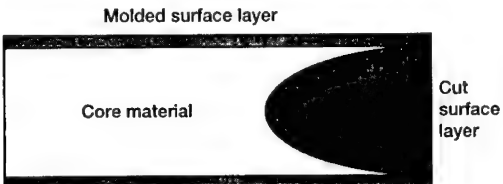


Figure 4. Microcrack and oxidation layer growth during isothermal aging

contact with the autoclave bagging material during the processing phase. The cut edges, which contained fiber ends and axial fiber surfaces, comprised the second type of surface. Previous studies showed that weight loss rates are different for these two types of surfaces (Bowles & Meyers 1986). This can be illustrated by the typical weight-loss versus aging-time plot (at 316 °C) shown in Figure 3. The plot can be broken into three distinct sections:

- (1) The origin to point A shows a rapid weight loss that is proportional to the specimen volume.
- (2) Point A to B shows a linear weight loss rate.
- (3) After point B, the weight loss rate is accelerated because of cracking and exposed fiber oxidation, mainly along cut surfaces.

Figure 4 shows a schematic of the surface damage growth during this period. The depth of cut surface damage increased with increasing specimen thickness. Because of this, weight loss data cannot be compared for specimens of different thicknesses. Also, weight losses from cut surfaces exceed those from molded surfaces (Bowles & Kamavouris 1995).

Two different types of surface degradation occur in these composites. Aging at the higher temperatures (288 to 316 °C) produces a light-colored surface layer that grows inward and causes voids and microcracks to initiate and grow within the layer, as in Figure 5a. The light color is attributed to the formation of solid oxidation products at the higher temperatures. At the lower temperatures (Fig. 5b), specimens show the same advance of voids and microcracks into the surface, but

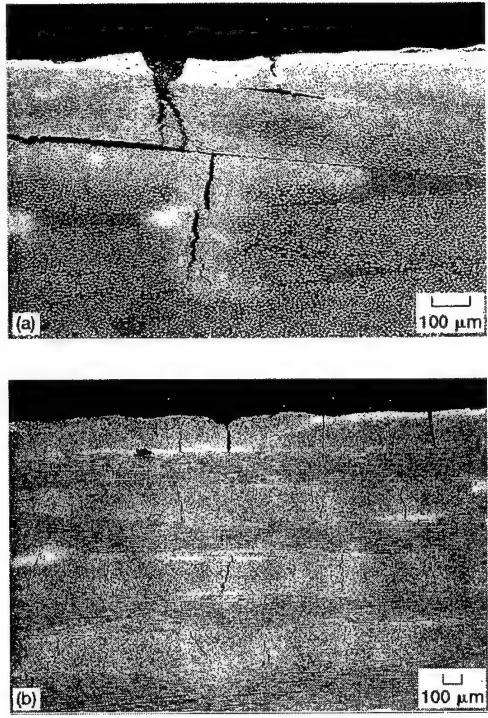


Figure 5. Surface oxidation of T650-35/PMR-15 composite specimens aged in air. (a) Aged 1000 h at 316 °C. (b) Aged 10,000 h at 204 °C.

the oxidized light band of matrix material is not visible. The two degradation mechanisms that are operating during isothermal aging are surface oxidation and bulk thermal degradation. Results of compression testing of composite layers that were machined parallel to the molded surface layer show that after aging was completed at 204 °C for 26,300 h the compression strength of the visibly damaged layer was one half that of the apparently less damaged central core material. This leads one to believe that the growth of the cracked surface layer contributes to the degradation of the mechanical properties of PMR-15 composite material.

Because the measured weight loss includes the cut-edge weight loss, it does not represent the material that was machined into the compression test specimens. Consequently, an estimate of the cut-edge weight loss was determined. Cut edges were trimmed off some of the aged 11- by 9-cm panels. These pieces were dried and weighed, and their dimensions were measured with calipers. The density of the central piece and each edge piece was calculated and compared with the calculated densities of the pristine laminate, and new (adjusted) percent weight loss values were calculated from the changes in densities. A sample of the results are shown in Figure 6. These data appear to lie

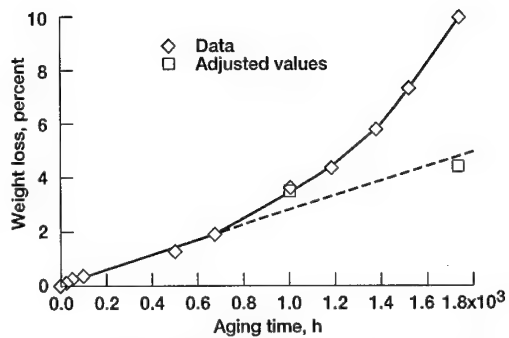


Figure 6. Adjusted weight loss of composites at 316 °C. Number of plies, 8.

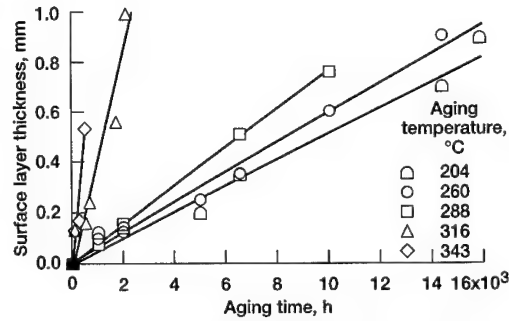


Figure 7. Surface layer thickness as a function of aging time at various temperatures.

on or near an extrapolated extension of the AB section of the weight loss curve, showing that the actual weight loss is much less than that measured during the isothermal oven tests. It is obvious that another means of evaluating composite damage should be investigated.

The thickness of the surface layer grows during the isothermal aging time. Figure 7 shows the relationship between the thickness of the resin-rich surface damage layer and the aging time at all temperatures. The relationships appear to be linear at all five temperatures, with slower growth rates at the lower temperatures. The data from the two lower temperature tests indicate what may be an initial fast rate of growth and then a slower steady rate after 1000 h of aging. This may be normal scatter, however. One item of interest is that these linear curves appear similar to the compression strength curves in Figure 1.

Figures 8–10 present compression strength, plotted as a function of the layer thickness of the composite at various temperatures. Each figure contains data for one specimen thickness: 1.50, 2.77, or 6.78 mm (4, 8, or 20 plies). All the data for the two thicker specimens (Figs 9–10) fall on one curve. The calculated, "best fit" set of data included in Figures 9–10 is consistently close to the measured values. For specimens machined parallel to the molded surfaces of large specimens, the

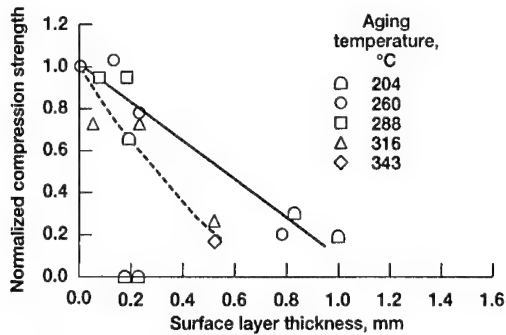


Figure 8. Composite compression strength as a function of surface layer thickness at various temperatures. Number of plies, 4.

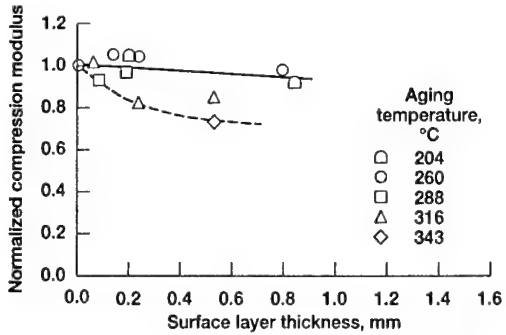


Figure 11. Compression modulus as a function of surface layer thickness at various temperatures. Number of plies, 4.

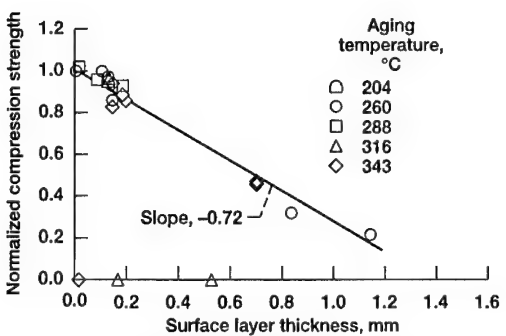


Figure 9. Composite compression strength as a function of surface layer thickness at various temperatures. Number of plies, 8.

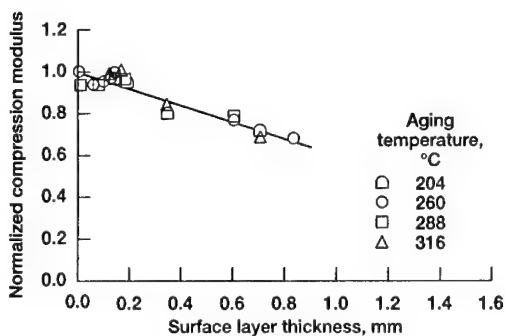


Figure 12. Compression modulus of composites as a function of surface layer thickness at various temperatures. Number of plies, 8.

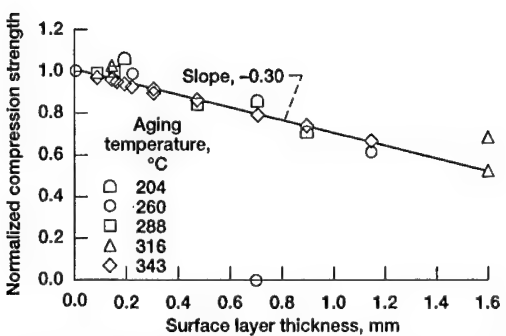


Figure 10. Composite compression strength as a function of surface layer thickness at various temperatures. Number of plies, 20.

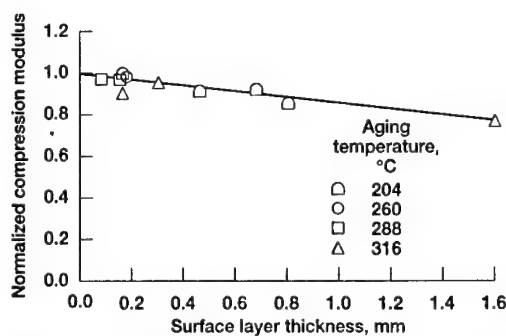


Figure 13. Composite compression modulus as a function of surface layer thickness at various temperatures. Number of plies, 20.

inner, crack-free material decreased in strength by a considerable amount (as much as 50 percent). The measured strength of the core material was close to that of an aged specimen with surface degradation and the same thickness. These data indicate that the formation and growth of the surface layer does not significantly reduce the compression properties of 8- and 12-ply fabric-reinforced composites. This was not so for the thinnest specimens. It is evident in Figure 8 that the 316 °C data fell below those of lower temperature compression strengths. This is due to the larger percentage of the weaker oxidation layers at the outer surfaces. Figures 11–13 show the moduli as a function of the layer thickness. In Figures 12–13, the modulus data collapsed onto one linear curve.

The relationship between specimen thickness and the retention of compression properties is evident in these figures. The 8- and 20-ply specimens retained their moduli considerably longer than the 4-ply composite. One other fact to acknowledge is that the moduli of the 8-ply composite material did not decrease by more than 30 percent over the time studied for aging at temperatures below 288 °C. Structures that are stiffness dependent should be useable for tens of thousands of hours.

## 5 SUMMARY AND CONCLUSIONS

The results of this study indicate that simple, linear relationships exist between the compression properties of graphite-fiber-fabric/PMR-15 composites and the depth of the surface layer that develops and grows during periods of aging at elevated temperatures. The buildup of the surface layer is indicative of the physical condition of the fabric-reinforced PMR-15 composites at all temperatures that were studied. However, although the surface layer is indicative of the decrease in strength, the central core volume is the main contributor.

Specimen thickness is a significant factor in the deterioration of compression properties during such periods of exposure. It is apparent from Figures 8–10 that the influence of the surface layer diminishes as the composite thickness increases. This is especially apparent in Figure 8. The strength data from the 4-ply specimens aged at 316 °C are below those measured at the other three temperatures. As noted earlier, the surface layer for a specimen aged at 316 °C had a compression strength about half that of the core material after aging at 204 °C for 26,300 h. Thus, for specimens that had a significant amount of oxidative attack in the surface layer, thinner specimens should show lower strengths than those aged at lower temperatures. That is what we see in Figure 8. Two deleterious mechanisms are observed within the specimens: surface oxidation and core reactions.

## REFERENCES

- Bowles, K.J., & J.E. Kamvouris 1995. Penetration of carbon-fabric-reinforced composites by edge cracks during thermal aging. *J. Advanced Materials* 26(2):2–11.
- Bowles, K.J. & A. Meyers 1986. Specimen geometry effects on graphite/PMR-15 composites during thermal oxidative aging. *32nd Int. SAMPE Symposium and Exhibition*, 1285.
- Bowles, K.J., G.D. Roberts & J.E. Kamvouris 1995. Long-term isothermal aging effects on carbon fabric-reinforced PMR-15 composites: compression strength. NASA TM-107129. (Also ASTM STP-1302, in press.)

## Environmental effects on the Mode I fracture and fatigue of bonded composites

L. M. Butkus & R. V. Valentin

*School of Mechanical Engineering, Georgia Institute of Technology, Atlanta, Ga., USA*

W.S. Johnson

*Schools of Materials Science and Engineering and Mechanical Engineering, Georgia Institute of Technology,  
Atlanta, Ga., USA*

**ABSTRACT:** Bonded composite materials are being specified for an increasing number of aircraft structures and also for repairs to damaged metallic components. Thus, ensuring the long-term operation of new airframes and extending the lives of today's aging aircraft depends, in part, on the durability of the adhesive bond line. The study described in this report used fracture mechanics concepts to assess the environmental durability of two bonded composite systems. Total strain energy release rates were determined using closed-form solutions and finite element analyses. Results showed that exposure to hot/dry or hot/wet conditions could cause significant reductions in fracture toughness and fatigue threshold. The fracture path depended upon the orientation of plies at the bond line interface. In both systems examined, threshold strain energy release rates were low compared to fracture toughness and crack growth rate sensitivities were extremely high. These results illustrate the importance of considering environmental effects in bonded composite design.

### 1 INTRODUCTION

Adhesive bonding is becoming more popular for applications involving the joining of aerospace composites. However, for this trend to continue, additional knowledge is required regarding the long term durability of bonded joints. This is especially the case for bonded composites which are being incorporated into the designs of aerospace vehicles intended to last far longer than their predecessors and into repairs of cracked, aging aircraft structures.

Stress-based approaches (Goland & Reissner 1944 and Hart-Smith & Thrall 1985) have traditionally been used for the analysis of adhesively bonded joints. However, fracture mechanics provides another method of analysis which accounts for bond line defects and for cyclic loading effects.

Fracture mechanics was adapted for use with bonded joints by Ripling et al. (1963). They proposed using the strain energy release rate,  $G$ , rather than the stress intensity,  $K$ , as a parameter to describe fracture. This proposal was based on the observation that full development of a plastic zone in the adhesive layer, required the use of  $K$ , was often impossible in the highly constrained bond line. Further studies by Shaw (1983) supported the choice of  $G$  rather than  $K$ . The strain energy release rate has since become the most often used parameter used for bonded joint analysis.

Many investigators have continued to add to the understanding of the fatigue and fracture of adhesively bonded composites. Fatigue aspects were investigated by Mall et al. (1982) who found that crack growth rates correlated well with applied strain energy release rate levels. This information led to the development of a fracture mechanics approach to the design of bonded joints (Johnson & Mall 1985). Fracture mechanics was also used by Johnson & Mangalgiri (1987) who examined the Mode I, Mode II, and mixed mode toughness of several adhesive and matrix materials, and proposed using  $G_{\text{Total}}$  ( $G_T$ ) as a design criteria.

This report describes a portion of a larger effort underway at Georgia Tech aimed at assessing the environmental durability of a number of adhesively bonded aerospace material systems using fracture mechanics. (Butkus et al., Johnson & Butkus, and Valentin et al., 1997) Two of the bonded composite systems which are directly related to current aerospace applications are the focus of this paper.

The first, a system consisting of boron-epoxy bonded to aluminum, represents bonded repairs being made to cracked metallic aircraft structures. In addition to not requiring that holes be drilled in the surrounding structure, as a riveted repair would require, the bonded patches have the added advantage of reducing the stress intensity factor at the tip of the crack in the underlying structure (Poole 1994). This system is currently used by the

US and Australian air forces as well as on a select number of commercial aircraft (Belason 1994).

The second system, consisting of bonded graphite-reinforced bismaleimide composite adherends, represents control surfaces on the US Air Force's new F-22 fighter. Again, the lack of a requirement to drill holes in the composite structure is an advantage of adhesive bonding for this application as is the potential weight savings.

Specimens consisting of these materials were subjected to a variety of environmental conditions prior to mechanical testing. These conditions were based upon the most severe temperature and humidity levels encountered by the specific bonded systems in their respective applications.

Investigations of these two systems employed the strain energy release rate, G, to compare and contrast the fracture and fatigue behavior of specimens exposed to various environments. Results showed that environmental effects can be significantly detrimental to the fracture toughness of bonded composites. Environmental exposure can also reduce the strain energy release rate necessary to cause threshold crack growth. In addition, the fracture path within these bonded systems was influenced by the direction of the composite plies located next to the bond line. These fatigue and fracture characteristics of bonded composite joints will be summarized in this paper and should be carefully considered in the design of adhesively bonded components.

## 2 MATERIALS AND SPECIMENS

To ensure this project was relevant to current bonded composite applications, bonded aerospace systems and their specific operating environments were examined. In addition, specimen fabrication was performed by an airframe manufacturer using current production methods surface preparations, materials, ply lay-ups, etc.

### 2.1 Bonded Material Systems and Fabrication

Two bonded material systems were investigated.

The first system (Al/FM®73M/B-Ep), representing bonded repairs to cracked aircraft structures, consisted of a boron-epoxy laminate bonded to a bare 7075-T651 aluminum adherend using a toughened aerospace adhesive. The composite laminate was manufactured from F4/5521 pre-preg using a lay-up of [0<sub>4</sub>/90/0<sub>3</sub>/90/0]<sub>s</sub> designed to withstand loads occurring during toughness testing. The laminate was pre-cured as a large panel in an autoclave. The composite surface

was prepared by abrasion followed by a methanol wipe. A 9.5 mm (0.375 in.) thick aluminum plate was prepared using an FPL sodium dichromate etch and BR-127 primer. The cured composite panel was bonded to the plate using CYTEC's FM®73M film which contained a non-woven polyester scrim cloth. The resulting bond line was approximately 200  $\mu\text{m}$  ( $7.9 \times 10^{-6}$  in.) thick. Individual specimens were cut from the bonded assembly.

The second system (Gr-BMI/AF-191M/Gr-BMI), representing materials in use on the F-22 fighter aircraft, consisted of two graphite fiber-reinforced bismaleimide adherends joined with a toughened epoxy adhesive. Two versions of this system were evaluated. One had primarily unidirectional [0<sub>4</sub>/90]<sub>s</sub> adherends, while the other used quasi-isotropic [ $\pm 45/0_2/\pm 45/90$ ]<sub>s</sub> adherends similar to the lay-up in actual components. The adherends were pre-cured as large panels in an autoclave using IM7/5250-4 pre-preg. The cured panels were abraded and wiped with methanol before being bonded together using 3M's AF-191M film which contained a non-woven nylon scrim cloth. The bond line was approximately 250  $\mu\text{m}$  ( $9.8 \times 10^{-6}$  in.) thick. Following bonding, individual specimens were cut from the adhesively joined assembly.

### 2.2 Specimen Geometry

Double cantilever beam (DCB) specimens used for this research were nominally 25 mm (1 in.) wide and 305 mm (12 in.) long. A Teflon™ release film was used to prevent bonding and create crack initiation sites at one end of each specimen. Loading was accomplished using hinges bonded to the end of each adherend.

The Al/FM®73M/B-Ep specimens were distinctly curved. This was caused by the dissimilar adherends in this system and the associated mismatch of thermal expansion coefficients ( $\alpha_{\text{AL}} = 22.1 \times 10^{-6}/^\circ\text{C}$  [ $12.3 \times 10^{-6}/^\circ\text{F}$ ],  $\alpha_{\text{B-Ep}} = 4.5 \times 10^{-6}/^\circ\text{C}$  [ $2.5 \times 10^{-6}/^\circ\text{F}$ ]).

## 3 EXPERIMENTAL PROCEDURES

Experiments were conducted in a way that permitted the behavior of as-received specimens to be compared with that of exposed specimens.

### 3.1 Environmental Exposure

Prior to mechanical testing, selected specimens were subjected to either isothermal or thermally cyclic exposure. Isothermal exposure was accomplished using an air circulating oven and, if

necessary, a humidity chamber inside the oven. Thermal cycling was performed using a specialized unit consisting of hot and cold chambers between which specimens were automatically shuttled. No humidity control was possible with the thermal cycling unit. No load was applied to the specimens during exposure.

Exposure conditions used were based upon those the material systems experience in service. "Hot/wet" conditions simulated runway operations in tropical environments. "Hot/dry" conditions simulated high performance operations. The low temperature of -54°C (-65°F) used in thermal cycling represented subsonic flight at high altitudes.

Selected Al/FM®73M/B-Ep specimens were exposed to one of the following three environments:

- 1) 100 thermal cycles between -54°C (-65°F) and 71°C (160°F) following 320 hours of preconditioning at 71°C (160°F), >90% relative humidity (rh) (Figure 1)
- 2) 5000 hours exposure to 71°C (160°F), >90% rh (hot/wet conditions)
- 3) 5000 hours exposure to 71°C (160°F), >90% rh (hot/wet conditions) followed by 5000 hours exposure to a desiccating environment of 22°C (72°F), 10% rh

Exposure to the desiccating environment was performed to determine whether the effects of the hot/wet exposure could be reversed.

Selected Gr-BMI/AF-191M/Gr-BMI were exposed to one of the following three environments:

- 1) 100 thermal cycles between -54°C (-65°F) and 104°C (220°F) following 320 hours of preconditioning at 71°C (160°F), >90% relative humidity (rh) (Figure 1)
- 2) 5000 hours exposure to 104°C (220°F), 0% rh (hot/dry conditions)
- 3) 10000 hours exposure to 104°C (220°F), 0% rh (hot/dry conditions)

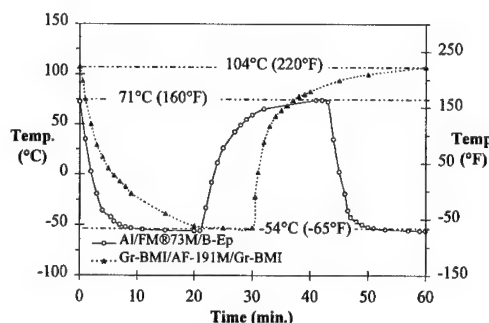


Figure 1. Thermal cycling profiles used for the Al/FM®73M/B-Ep and Gr-BMI/AF-191M/Gr-BMI bonded systems.

### 3.2 Testing Procedures

Prior to testing, specimen edges were sprayed with a thin coat of white paint and stamped with a scale having 0.5 mm (0.02 in.) increments. This facilitated the determination of crack length. During testing, the edges were monitored with a traveling microscope with a minimum 20X magnification.

Testing was conducted on either a servohydraulic or screw-driven test frame equipped with a computerized data acquisition and control system. Most testing was conducted under laboratory conditions (22±2°C, 50±5% rh). However, some as-received specimens were tested at their low and high service temperatures.

Monotonic tests were conducted under displacement control with a speed of 1 mm/min. (0.04 in./min.). ASTM D3433-75 and ASTM D5228-94a were used as guidelines. Crack growth in these specimens was not catastrophic, so the long bond line permitted repeated tests to be conducted on single specimens. This allowed several toughness values to be obtained from one specimen.

Fatigue tests at 1 Hz were also conducted under displacement control using a displacement R-ratio ( $\delta_{\min}/\delta_{\max}$ ) of 0.1. This resulted in load shedding and the facilitated the identification of G levels at threshold growth rates of  $da/dN = 10^{-6}$  mm/cycle ( $4 \times 10^{-8}$  in./cycle), a rate based on previous work (Marceau et al. 1978, and Mall et al. 1982).

## 4 ANALYSIS

Both closed form and finite element analyses were performed. The type of analysis depended upon the bonded system being examined.

### 4.1 Closed Form Solutions

Gr-BMI/AF-191M/Gr-BMI specimens were analyzed using a closed form solution (Hashemi et al. 1989, O'Brien et al. 1993).

Determination of the applied strain energy release rate,  $G_I$ , can be performed using Equation (1):

$$G_I = \frac{P^2}{2b} \frac{dC}{da} \quad (1)$$

where  $P$  = load;  $C$  = specimen compliance ( $\delta/P$ );  $b$  = specimen width;  $a$  = crack length; and  $\delta$  = crosshead or crack mouth opening displacement.

Using beam theory and modeling the DCB specimens as two cantilever beams with a built-in

support on the free end, (1) reduces to:

$$G_I = \frac{3P\delta}{2ba} \quad (2)$$

Equation (2) may be modified to account for the relationship between compliance and crack length:

$$G_I = \frac{3P\delta}{2b(a + |\Delta|)} \quad (3)$$

The value  $\Delta$  is the intercept of the  $a$ -axis by a line representing a linear relationship between  $C^{1/3}$  and  $a$ . It serves as a correction to account for the fact that the free end of the DCB specimen is not built-in.

To determine the fracture toughness ( $G_{Ic}$ ) of the Gr-BMI/AF-191M/Gr-BMI specimens, critical values for  $P$  and  $\delta$  were used in Equation (3). These values were obtained from the point at which crack growth began and corresponded to the point at which  $P$  vs.  $\delta$  data deviated from linearity.

Equation (3) was also used to determine the applied strain energy release rates for fatigue tests by substituting in minimum and maximum levels of applied load ( $P$ ) and displacement ( $\delta$ ).

#### 4.2 Finite Element Solutions

Due to the dissimilar adherends in the Al/FM<sup>®</sup>73M/B-Ep specimens, they exhibited pronounced curvature after curing. Thermal residual stresses caused this curvature and also produced a residual Mode II strain energy release rate ( $G_{II}$ ) at the crack tip.  $G_I$  and  $G_{II}$  levels could not be determined with a closed form solution. Thus, a numerical, finite element model was required to determine the amount of mode mixity and to fully understand the behavior of  $G_I$  and  $G_{II}$  during loading.

The ABAQUS finite element code was used to analyze a 2-D model of the DCB specimen. The adhesive layer was modeled using four rows of four-noded quadrilateral elements. The Al adherend was modeled with ten rows, and the B-Ep adherend was modeled with one row per ply. The model contained 4927 nodes and 4658 elements.

All materials were assumed to be linearly elastic due to a lack of tensile stress-strain curves for the adhesives needed to describe material nonlinearities. Because of the large ratio of specimen

width to bond line thickness, plane-strain was also assumed.

The analysis used experimental loads and crack lengths to provide crack tip nodal forces and displacements. The Mode I, Mode II, and total strain energy release rates ( $G_I$ ,  $G_{II}$ ,  $G_T$ ) were computed using a modified crack closure technique (Rybicki & Kanninen 1977).

Input of critical loads provided fracture toughness values for the monotonic tests while input of maximum and minimum applied loads yielded applied strain energy release rates experienced during fatigue testing.

## 5 RESULTS AND DISCUSSION

Testing revealed some distinct effects caused by environmental exposure.

### 5.1 Fracture Toughness of the Al/FM<sup>®</sup>73M/B-Ep System

The Al/FM<sup>®</sup>73M/B-Ep system exhibited an as-received fracture toughness ( $G_{TC}$ ) of approximately 815 J/m<sup>2</sup> (4.7 in.<sup>2</sup>/in.<sup>2</sup>).

The fracture path in this system tested appeared to be in the matrix of the boron-epoxy near the composite-adhesive interface. Little of the adhesive remained on the composite adherend following fracture. A few boron fibers were embedded in the FM<sup>®</sup>73M which remained on the aluminum adherend. The fracture paths of all Al/FM<sup>®</sup>73M/B-Ep specimens, regardless of pre-test exposure or test temperature, exhibited these characteristics.

Figure 2 shows the effect of pre-test environmental exposure on the fracture toughness of the Al/FM<sup>®</sup>73M/B-Ep system.

Thermal cycling reduced the fracture toughness by approximately 35%. It may be possible to attribute some of this loss to the 320 hours during which the specimens were exposed to hot/wet conditions prior to thermal cycling. However, the extent of this effect is unknown.

5000 hours of exposure to a hot/wet environment resulted in a 50% loss in toughness. These conditions can sometimes decrease fracture toughness by attacking insufficiently prepared metallic adherend surfaces and causing interfacial failure. However, the fracture surfaces of the specimens exposed to hot/wet conditions were similar to those of the as-received specimens. A logical hypothesis would be that the hot/wet environment adversely affected the adhesive and/or composite matrix material.

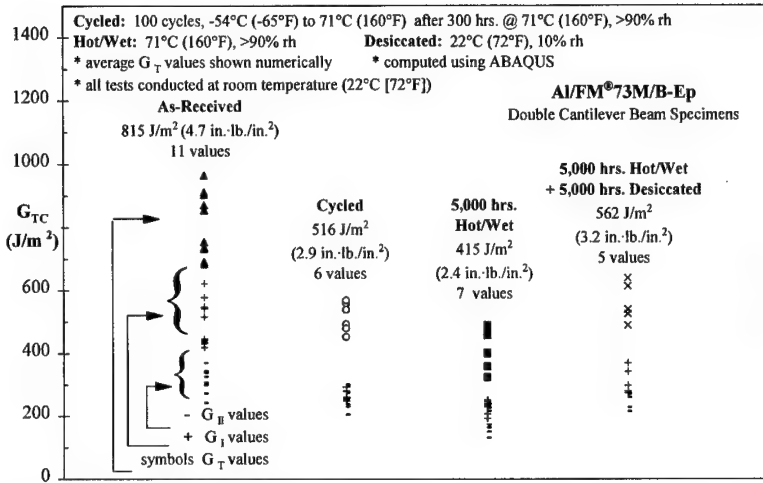


Figure 2. Effect of environmental exposure on the fracture toughness of the Al/FM®73M/B-Ep system.

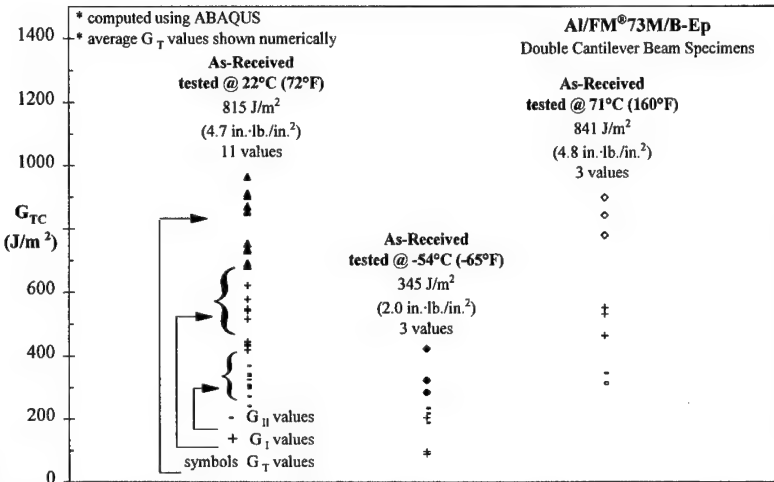


Figure 3. Effect of test temperature on the fracture toughness of the Al/FM®73M/B-Ep system.

Following initial testing, the same specimen used to determine hot/wet exposure values was placed in a desiccator at room temperature for 5000 hours. After desiccation, the toughness of this specimen appeared to have slightly recovered. However, the toughness of the desiccated specimen was still far below the as-received toughness.

Figure 3 shows the effect of test temperature on the fracture toughness of the Al/FM®73M/B-Ep system. Testing at -54°C (-65°F) reduced  $G_{Tc}$  by approximately 55%, while the toughness obtained from testing conducted at 71°C (160°F) did not differ appreciably from the as-received values. The difference in the thermal expansion coefficients of the adherends suggests that the thermally-induced strain energy release rate in the bond line was magnified at the lower test temperatures. This

magnification, combined with a probable decrease in the ductility of the adhesive at -54°C (-65°F), most likely caused the decreased fracture toughness.

### 5.2 Fatigue Behavior of the Al/FM®73M/B-Ep System

Fatigue test results are shown in Figure 4. Three characteristics of this data are significant.

The first is the extremely high degree of crack growth rate sensitivity shown by this bonded system. If the data can be represented by a Paris Law type relation of  $da/dN = C(\Delta G_T)^n$  (Roderick et al. 1974), the value of the exponent (n) representing the slope of the data and the crack growth rate sensitivity, is on the order of 10. This is far above

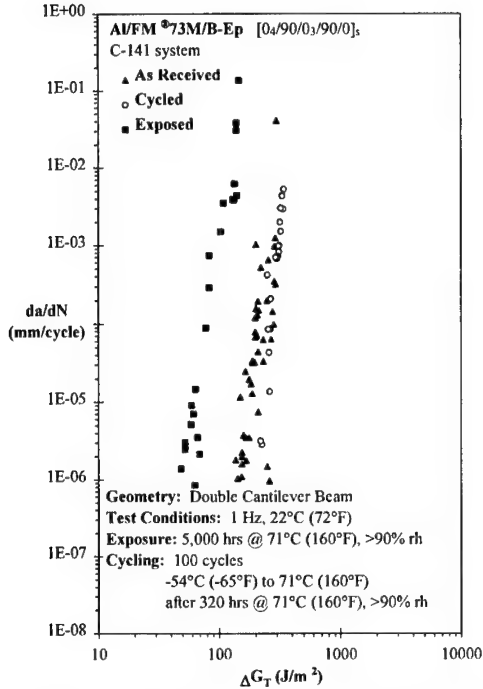


Figure 4. Fatigue behavior of the Al/FM®73M/B-Ep bonded system.

the growth rate sensitivity of metals which falls in the range of 2-3. (Skinn et al. 1994)

Second, the threshold strain energy release rate range ( $\Delta G_{I,th}$ ) at  $da/dN = 10^{-6}$  mm/cycle ( $4 \times 10^{-8}$  in./cycle) is approximately  $100 \text{ J/m}^2$  (0.6 in.<sup>-1</sup>lb/in.<sup>2</sup>), far below the fracture toughness. This trend was also observed by Johnson & Mall (1984).

Third, the detrimental effect of hot/wet exposure observed in the monotonic toughness testing was also reflected in a decrease in the threshold strain energy release rate. Hot/wet exposure, however, did not appear to affect the crack growth rate sensitivity.

The fracture path in the fatigue specimens was identical to that in the fracture toughness specimens.

### 5.3 Mode I Fracture Toughness of the Gr-BMI/AF-191M/Gr-BMI System

The Gr-BMI/AF-191M/Gr-BMI system exhibited an as-received fracture toughness ( $G_I$ ) of approximately  $1721 \text{ J/m}^2$  (9.8 in.<sup>-1</sup>lb/in.<sup>2</sup>). Because the specimens from this system had identical adherends, only Mode I was present and  $G_I = G_T$ .

Therefore, the fracture toughness of this system can be compared with that of the Al/FM®73M/B-Ep system which was expressed in terms of  $G_T$ .

The fracture path in the Gr-BMI/AF-191M/Gr-BMI system depended upon the nature of the adherends. Specimens with unidirectional adherends, having  $0^\circ$  plies next to the bond line, exhibited cohesive failure in the adhesive layer. However, the fracture path in the specimens with quasi-isotropic adherends repeatedly switched between the  $\pm 45^\circ$  plies on either side of the bond line. This resulted in extensive fiber bridging. The fracture paths of all Gr-BMI/AF-191M/Gr-BMI specimens, regardless of pre-test exposure or test temperature, exhibited these general characteristics.

Figure 5 shows the effect of pre-test environmental exposure on the Mode I toughness of the Gr-BMI/AF-191M/Gr-BMI system.

The most noticeable effect was caused by long-term isothermal exposure to a hot/dry condition. This reduced  $G_I$  of the unidirectional system by up to approximately 28%. In addition, the as-received toughness for the quasi-isotropic specimens was lower than the as-received toughness of the unidirectional specimens.

One possible explanation for the lower as-received  $G_I$  values exhibited by the specimens with quasi-isotropic adherends is the fracture path. Although the cracking in these specimens was more tortuous, much of the failure was in the composite laminates rather than in the bond line. Since the BMI matrix may be significantly less tough than the AF-191M adhesive, a fracture path away from the adhesive layer would be preferred. This would explain both the fracture location and relatively lower  $G_I$  values in the quasi-isotropic specimens.

Figure 6 shows the effect of test temperature on the fracture toughness of the Gr-BMI/AF-191M/Gr-BMI system. As in the Al/FM®73M/B-Ep system testing at  $-54^\circ\text{C}$  (-65°F) reduced the fracture toughness. This reduction may have been caused by a decrease in the ductility of the adhesive. However, testing conducted at  $104^\circ\text{C}$  (220°F) also appeared to result in lower toughness values, a trend for which no explanation can be offered at this time.

### 5.4 Fatigue Behavior of the Gr-BMI/AF-191M/Gr-BMI System

Figure 7 shows the results of fatigue tests carried out on the Gr-BMI/AF-191M/Gr-BMI system.

As with the Al/FM®73M/B-Ep system, the growth rate sensitivity is high (approximately 6 for Gr-BMI/AF-191M/Gr-BMI), and the threshold level,  $\Delta G_{I,th}$ , is near  $100 \text{ J/m}^2$  (0.6 in.<sup>-1</sup>lb/in.<sup>2</sup>).

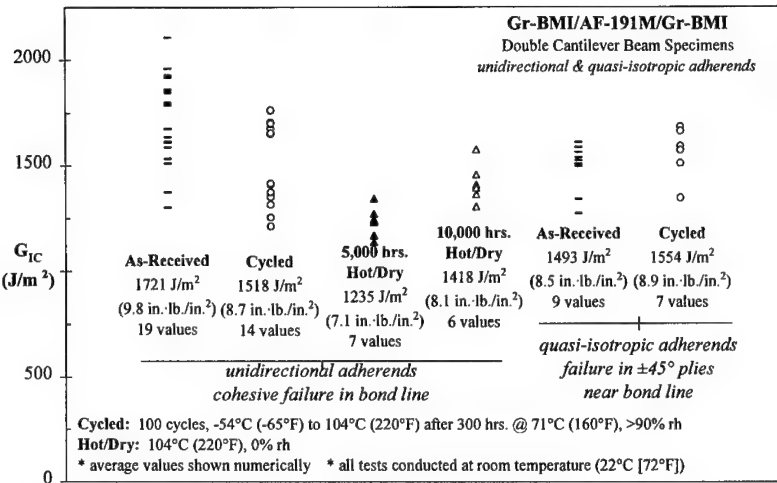


Figure 5. Effect of exposure on the Mode I fracture toughness of the Gr-BMI/AF-191M/Gr-BMI system.

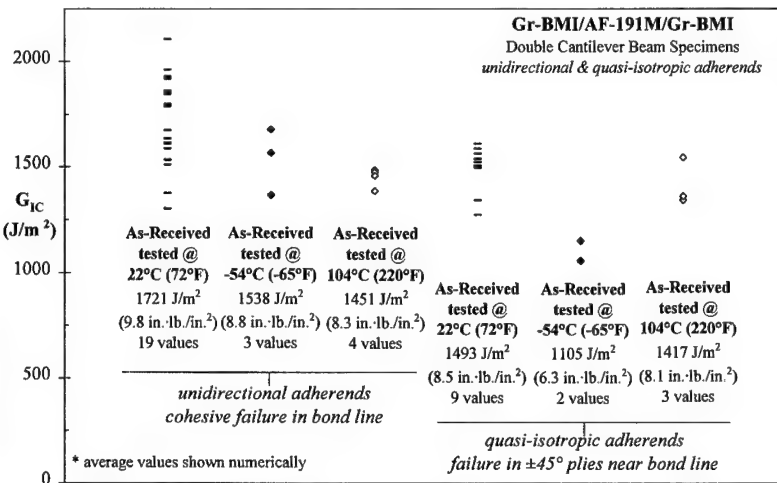


Figure 6. Effect of test temperature on the Mode I toughness of the Gr-BMI/AF-191M/Gr-BMI system.

Unlike the Al/FM®73M/B-Ep system, however, the fatigue behavior of the Gr-BMI/AF-191M/Gr-BMI system appeared insensitive to isothermal exposure to its most severe service condition.

The fracture path in the fatigue specimens was identical to that in the fracture toughness specimens.

## 6 CONCLUSIONS

Durability of bonded composite structures, as measured by resistance to fracture, to fatigue and to environmental degradation, is imperative for their economic and safe operation.

Studies conducted for this paper have shown that environmental exposure and operating temperatures

can have a significant effect on the performance of Al/FM®73M/B-Ep and Gr-BMI/AF-191M/Gr-BMI bonded systems. Fracture toughness was degraded by long term exposure to the most severe operating conditions expected for these systems. Testing at  $-54^\circ\text{C}$  (-65°F) also resulted in a loss of fracture toughness for both systems. In addition, long term exposure to a hot/wet environment reduced the fatigue threshold strain energy release rate of the Al/FM®73M/B-Ep system.

The fracture path appeared unaffected by the environments investigated. Fracture and fatigue crack growth in the Al/FM®73M/B-Ep system occurred in the composite matrix near the adhesive bond line. Crack growth in the Gr-BMI/AF-191M/Gr-BMI system was cohesive for specimens

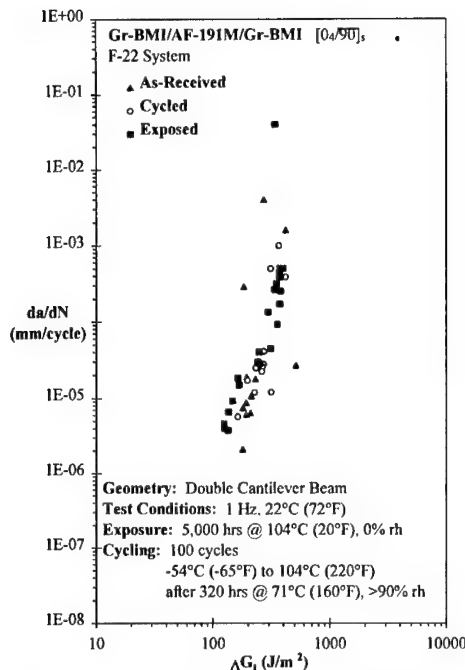


Figure 7. Fatigue behavior of the Gr-BMI/AF-191M/Gr-BMI bonded system

with unidirectional adherends and followed a path in the  $\pm 45^\circ$  plies near the bond line for specimens with quasi-isotropic adherends.

The crack growth rate sensitivity of the bonded specimens far exceeded that of metals. Though seemingly unaffected by long-term environmental exposure, these high sensitivities suggest that continued operation of bonded structures below the identified threshold (a safe life approach) is necessary to avoid unanticipated rapid Mode I crack growth.

Future research may show that environmental exposure produces different effects in the Mode II or mixed mode behavior of bonded composite joints. Nevertheless, the observed trends emphasize the need to carefully consider environmental conditions when specifying bonded composite materials for primary structures or for repairs.

#### ACKNOWLEDGMENTS

This research was conducted under an FAA Technical Center grant monitored by D. Oplinger. The authors also wish to thank Lockheed Martin for specimen fabrication, and the Technology & Engineering Sciences Division at Robins AFB, GA, for their assistance with thermal cycling.

#### REFERENCES

- Belason, E.B. 1994. Status of bonded boron/epoxy doublers for military and commercial aircraft structures. *Composite repair of military aircraft structures*. Seville: AGARD.
- Butkus, L.M., Mather, P.D., and Johnson, W.S. 1997. "Tensile properties and plane-stress fracture toughness of thin film aerospace adhesives," submitted: *J. of Adhesion*.
- Goland, M. & Reissner, E. 1944. The stresses In cemented *Journal of Applied Mechanics*. Vol. 11. March.
- Hart-Smith, L.J. & Thrall, E.W. 1985. Structural analysis of adhesive-bonded joints. In E.W. Thrall & R.W. Shannon (eds.), *Adhesive bonding of aluminum alloys*. New York: Marcel Dekker.
- Hashemi, S., Kinloch, A.J., & Williams, J.G. 1989. Corrections needed in double-cantilever beam tests for assessing the interlaminar failure of fibre-composites. *J. Materials Science Letters*. Vol. 8.
- Johnson, W.S. & Mall, S. 1984. Bonded joint strength: static versus fatigue. *Proc. V Int'l Cong. on Experimental Mechanics*. Montreal: Soc. for Exp. Stress Analysis.
- Johnson, W.S. & Mall, S. 1985. A fracture mechanics approach for designing adhesively bonded joints. In W.S. Johnson (ed.), *Delamination and debonding of materials*, STP 876. Philadelphia: ASTM.
- Johnson, W.S. & Mangalgiri, P.D. 1987. Influence of the resin on interlaminar mixed-mode fracture. In N.J. Johnston (ed.), *Toughened composites*, STP 937. ASTM.
- Johnson, W.S. & Butkus, L.M. 1997. "Considering environmental conditions in the design of bonded structures: a fracture mechanics approach," accepted: *Int'l. J. Fat. & Frac. Engr'g. Mat'l's. & Structs.*
- Mall, S., Johnson, W.S. and Everett, R.A., Jr. 1982. In K.L. Mittal (ed.), *Adhesive joints: formation, characteristics and testing*. Plenum Press: New York.
- Marceau, J.A., McMillan, J.C., & Scardino, W.M. 1978. Cyclic stress testing of adhesive bonds. *Adhesives Age*.
- O'Brien, T.K. & Martin, R.H. 1993. Round robin testing for mode I interlaminar fracture toughness of composite materials. *J. Composites Tech. & Research*. Vol. 15 (4).
- Poole, P., Young, A., & Ball, A.S. 1994. Adhesively bonded composite patch repair of cracked aluminum alloy structures." *Composite repair of military aircraft structures*. Seville: AGARD.
- Ripling, E.J., Mostovoy, S. & Patrick, R.L. 1963. Application of fracture mechanics to adhesive joints. *Adhesion*, STP 360. Philadelphia: ASTM.
- Roderick, G.L., Everett, R.A., & Crews, J.H. 1974. Cyclic debonding of unidirectional composites bonded to aluminum sheet for constant amplitude loading. *Fatigue of composites*, STP 569. Philadelphia: ASTM.
- Rybicki, E. F. & Kanninen, M. F. 1977. A finite element calculation of stress intensity factor by a modified crack closure integral. *Eng'g. Fracture Mechanics*. Vol. 9.
- Skinn, D.A., Gallagher, J.P., Berens, A.P., Huber, P.D., & Smith, J. 1994. *Damage tolerant design handbook*. West Lafayette: Purdue Research Foundation.
- Shaw, S.J. 1983. Adhesive joint failure - a fracture mechanics approach. In K.W. Allen (ed.), *Adhesion 7: Proc. 20th Conf. on Adhesion and Adhesives*. Elsevier: London.
- Valentin, R.V., Butkus, L.M., and Johnson, W.S. 1997. "A finite element and experimental evaluation of boron-epoxy doublers bonded to an aluminum substrate," submitted: *J. Composites Technology & Research*.

---

### 3 Applications of damage mechanics to durability

## Damage modeling of composite structures: Static and dynamic approach

Y.Chevalier, M.Louzar & M.Chafra

*Laboratoire d'Ingénierie des Structures Mécaniques et de Matériaux, Institut Supérieur des Matériaux et de la Construction Mécanique (ISMCM), Saint-Ouen, France*

G.A. Maugin

*Laboratoire de Modélisation en Mécanique, Université P.M. Curie, Paris, France*

**ABSTRACT :** This paper presents a series of investigations dealing with the damage of composite materials and composites structures, to predict damage when the features of loading are known, and to determine damage when the history of loading is unknown.

The first example deals with the tridimensional modeling of damage in composite materials. We propose a mechanism based mode which strongly depends on the structural anisotropy of the material and on the orientation of loading. In the second example we try to exhibit the relevant parameters of effective structures and we develop a simple case : gluing of two anisotropic materials with periodic array of slits with elastic slip situated at the interface between the two media. The effects are illustrated on woven composite materials.

### 1. INTRODUCTION

Many among the mechanical community have turned their attention to the problem of damage prediction and detection and finally health monitoring interest in the general topic of using modeling of material to predict damage and wave propagation to detect damage in composite structure and in structural components.

The modeling of composite structures is a **global** approach which can be compared to vibration measurement to detect damage. For example the vibration response of the actual structure can be compared with that of the healthy structure, if a small change occurs such as the appearance of voids or cracks, the structure's response produces substantial difference (vibration analysis enhances small differences).

Wave propagation is a **local** approach used to detect damage with more precision. An harmonic wave is defined by 10 parameters (Amplitude (3), frequency (1), complex wave number (6)) and can be suited to each kind of damage in composite structures: surface wave, for example, can be used to detect damage between two glued surfaces.

Damage in composite structures is defined as resulting from a large number of microstructural evolutions that give rise to irreversible processes and lead to destruction under mechanical or thermal loading. Damage is a phenomenon which happens first and before destruction, it softens the elastic stiffness and the damping of structures.

In composite materials the weakness of the mechanical properties is due to constituents. In structures the weakness is due to the connection of various transmission systems. Finally damage is

connected with the increase of defects at the meso-level which are the indicators of failure at the macro-level. In the field of composite materials formation of voids and micro-cracks in the matrix, plastic behavior of the matrix, voids at the fiber-matrix surface, delamination, slip or debonding of fibers, failure of fibers in tensile loading are to be taken into account in the damage process. In glued composite structures damage is generated by the existence of slip areas, elastic slips, slips with Coulomb friction, etc ...

Experts in composite structures are confronted by two problems :

- Is it possible to predict the material damage when the features of loading are known ?
- Is it possible to determine damage in composite structures or in composite materials when the history of loading is unknown ?

We will try to answer partially these questions and illustrate general concepts via the discussion of two examples.

### 2 - MODELING OF DAMAGE IN COMPOSITE MATERIALS

The first example deals with the tridimensional modeling of damage in composite materials. The often very marked anisotropy of such materials gives rise to some difficulties either in the description of reversible processes (elasticity) or in the irreversible processes (viscoelasticity, plasticity, damage, fracture). It is in the nature of composites to present a sensitivity with respect to loading mode and this effect is accounted for in this paper. We adopt isothermal and static loadings and study

elastic and damage properties of the composite in short time intervals on account of anisotropy and influence of loading orientation.

Experimental studies on composites are widely developed but often with preferential proportional loading applied on samples which are cut at various angles with respect to fibers orientations (Vinh 1981), (Fujii & al. 1981) (Baste 1991).

A variety of models which take into account anisotropy (Ladevèze 1993 a) are available. In some of them, sensitivity with respect to loading modes in tension and compression is examined (Ladevèze & al. 1993 b), it closely follows different material orientations in a composite. More sophisticated models take into account the length scales in damage process (Ladevèze 1992, Spearing & al. 1995), or the history of loading which is coupled with temperature and viscoelastic behavior (Park & Schapery 1997).

The purpose of the present study is to propose a modeling of the mechanical behavior of composite materials in a more general framework including a large range of geometrical variables used in industry.

## 2.1 The elastic behavior

### 2.1.1 Constitutive model

To take into consideration all main effects in a composite material, we introduce two 6-dimensional vectorial spaces.

(i) stress space spanned by elements of the basis of vectors  $\Sigma = \{\Sigma_\alpha\}$  defined by :

$$\{\Sigma_\alpha\} = \begin{cases} \Sigma_1 = \sigma_{11}, \Sigma_2 = \sigma_{22}, \Sigma_3 = \sqrt{2\sigma_{12}}, \\ \Sigma_4 = \sigma_{33}, \Sigma_5 = \sqrt{2\sigma_{13}}, \Sigma_6 = \sqrt{2\sigma_{23}} \end{cases}^T$$

( $\alpha = 1, 2, \dots, 6$ )

where  $\sigma_{ij}$  ( $i, j = 1, 2, 3$ ) are the components of the stress tensor

(ii) Strain space spanned by elements of the basis of vectors  $\varepsilon = \{\varepsilon_\alpha\}$  defined by :

$$\{\varepsilon_\alpha\} = \begin{cases} \varepsilon_1 = \epsilon_{11}, \varepsilon_2 = \epsilon_{22}, \varepsilon_3 = \sqrt{2\epsilon_{12}}, \\ \varepsilon_4 = \epsilon_{33}, \varepsilon_5 = \sqrt{2\epsilon_{13}}, \varepsilon_6 = \sqrt{2\epsilon_{23}} \end{cases}^T$$

( $\alpha = 1, 2, \dots, 6$ ).

Where  $\epsilon_{ij}$  ( $i, j = 1, 2, 3$ ) are the components of the strain tensor.

According to the definition of the two vectors  $\{\varepsilon_\alpha\}$  and  $\{\Sigma_\alpha\}$  the energy density of

proportional loading can be written in the following simple manner :

$$W = \frac{1}{2} \sigma_{ij} \varepsilon_{ij} = \frac{1}{2} \Sigma_\alpha \varepsilon_\alpha \quad (2.1)$$

We define two tensorial invariants, the stress intensity  $\Sigma_0 = \sqrt{\Sigma_\alpha \Sigma_\alpha}$  and the strain intensity  $\varepsilon_0 = \sqrt{\varepsilon_\alpha \varepsilon_\alpha}$ ; deduced from the second order strain (or stress) tensor.

To explain the unilateral effect we propose to characterize a loading in both direction and type :

- Loading direction : defined by a unit vector  $\sigma = \{\sigma_\alpha\}$  with  $\sqrt{\sigma_\alpha \sigma_\alpha} = 1$  and  $\Sigma_\alpha = \Sigma_0 \sigma_\alpha$ .

In the case of a proportional loading  $\{\sigma_\alpha\} = \text{const.}$

- Type of loading : defined as a function with various possibilities associated with the sign of the stress tensor, hence the stress space is decomposed into zones characterised by the sign attributed to each component of stresses.

To that purpose we define a parameter ( $\chi$ ) which corresponds to the number of lines of the matrix  $[I_{\chi\alpha}]$  and is equal to the line :

$$\{\text{sign}(\sigma_1), \text{sign}(\sigma_2), \dots, \text{sign}(\sigma_6)\}$$

$$\text{sign}(\sigma_\alpha) = \begin{cases} 1 & \text{if } \sigma_\alpha \geq 0 \\ -1 & \text{if } \sigma_\alpha < 0 \end{cases}$$

We consider all the combination of signs in the stress tensor, where the matrix  $[I_{\chi\alpha}]$  is composed of  $2^6$  rows : ( $\alpha = 1, 2, \dots, 6$ ;  $\chi = 1, 2, \dots, 2^6$ )

$$I_{\chi\alpha} = \begin{bmatrix} 1 & 1 & 1 & 1 & 1 & 1 \\ 1 & 1 & 1 & 1 & 1 & -1 \\ 1 & 1 & 1 & 1 & -1 & -1 \\ \cdots & \cdots & \cdots & \cdots & \cdots & \cdots \end{bmatrix}$$

In the one dimensional case, the parameter ( $\chi$ ) is equal to 1 or 2. We have two spaces with differences in behavior, and recognize the theory of Ladevèze (Ladevèze 1993 c). These differences in behavior are due to cases of closing (in compression) and opening (in traction) of micro-cracks.

When  $\alpha$ , ( $\alpha \leq 6$ ) is the dimension of the subspace of stresses ( $\chi = 1, 2, \dots, 2^\alpha$ ) we have

$2^\alpha$  zones of loading with different behaviors.

A sign convention is adopted according to the following rules : a positive sign is taken for the tensile stress and a negative sign for the compressive stress. For the shearing stress, we regard to the stress vector  $T$  belonging to the shear plane and corresponding to the surface element  $n$   $dS$  ( $T = [\sigma] n$ ).

sign (shear stress) = sign (  $N \cdot T \cdot \tan \varphi$  ) (2.2)  
where  $N$  is the projection of the normal vector  $n$  on the shear plane and  $\varphi$  the polar angle of  $N$  (see also (Chafra et al. 1996 b)).

During a proportional loading  $\{\sigma_\alpha\} = \text{const.}$ , we define a generalized modulus which relates a stress intensity to a strain intensity.

$$\Sigma_0 = E^{(x)} \varepsilon_0 \quad \text{or} \quad \varepsilon_0 = S^{(x)} \Sigma_0 \quad (2.3)$$

We associate to each type of loading (2.6), a hookean  $C$  operator and its inverse  $S$  such that

$$\Sigma_\alpha = C_{\alpha\beta}^{(x)} \varepsilon_\beta \quad \text{or} \quad \varepsilon_\alpha = S_{\alpha\beta}^{(x)} \Sigma_\beta \quad (2.4)$$

In the case of non-proportional loading, the constitutive law is defined as an incremental elastic linear law :

$$\Delta \Sigma_\alpha = C_{\alpha\beta}^{(x)} \Delta \varepsilon_\beta \quad \text{or} \quad \Delta \Sigma_\alpha = S_{\alpha\beta}^{(x)} \Delta \varepsilon_\beta \quad (2.5)$$

$$\phi_x^{(x)} \equiv R_{\alpha\beta}^{(x)} \Sigma_\alpha \Sigma_\beta - \varepsilon_0^2 = 0 \quad (2.6)$$

$\varepsilon_0 = \text{const.}$ , ( $\alpha, \beta = 1, \dots, 6$ )

$R_{\alpha\beta}^{(x)}$  is related to the components of the compliance matrix by

$$R_{\alpha\beta}^{(x)} = S_{\alpha\gamma}^{(x)} S_{\gamma\beta}^{(x)}$$

and is related to the generalized modulus  $E^{(x)}$  (2.3) by

$$E^{(x)} = \frac{1}{\sqrt{R_{\alpha\beta}^{(x)} \sigma_\alpha \sigma_\beta}} \quad (\{\sigma_\alpha\} = \text{const.}) \quad (2.7)$$

It can be shown (Chafra et al. 1996 a), (Chafra et al. 1996 b) that the matrix  $[R_{\alpha\beta}]$  is non negative and than the generalized modulus  $E^{(x)}$  exists.

### 2.1.2 Case of biaxial loading

In the case of plane stresses

$\Sigma = (\Sigma_1, \Sigma_2, \Sigma_3)$  the constitutive law is defined by 3 compliances  $S_{11}^{(x)}, S_{22}^{(x)}, S_{12}^{(x)}$ . The parameters  $R_{\alpha\beta}$  of the surface (2.6) depend on the generalized compliances (Chafra et al. 1996 b)  $S_{(\alpha)}^{(x)}$  in various directions  $\theta = 0^\circ$  ( $\alpha = 0^\circ$ ),  $\theta = 45^\circ$  ( $\alpha = 45^\circ$ ),  $\theta = 90^\circ$  ( $\alpha = 90^\circ$ ) ( $\tan \alpha = \tan \theta$ )

$$S_{(\alpha)}^{(x)} = \frac{\varepsilon_0}{\sqrt{\Sigma_1^2 + \Sigma_2^2}} \quad (2.8)$$

We often use an experimental method using samples out off axes for various directions. The results provided by a test are the longitudinal moduli, while the results used in the models are the generalized moduli.

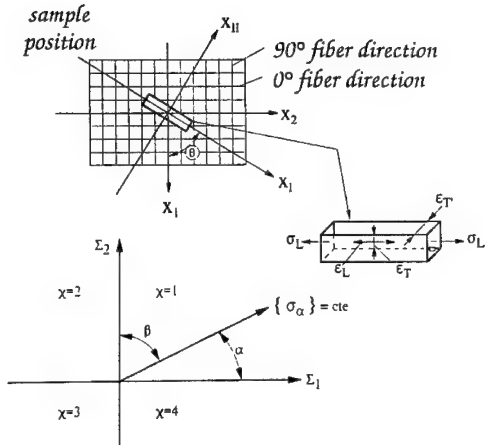


Figure 1 : Off axes tests and loading direction .

We present an application with woven carbon/epoxy composite materials as studied by Lené (Lené 1984).

Table 1 : Experimental characteristics of woven carbon/epoxy composite material (8 plies)  $E_L$  : longitudinal Young modulus ,  $v_{LT}$  : Poisson ratio.

Direction	Modulus	Numerical values
Warp	$E_1 = E_L(0^\circ)$	63.1 GPa
Weft	$E_2 = E_L(90^\circ)$	63.1 GPa
	$v_{12} = v_{LT}(0^\circ)$	0.053
main diagonal	$E_L(45^\circ)$	19.5 GPa
main diagonal	$v_{LT}(45^\circ)$	0.75
off axes	$E_L(15^\circ)$	46.8 GPa
off axes	$E_L(30^\circ)$	22.0 GPa

By mean of identification (rows 1, 2, 3, 4 of table 1) we obtain the parameters  $R_{\alpha\beta}$  of surface (2.6) and then we calculate  $\Sigma_0(\alpha)$  for  $\alpha = 0^\circ$  ( $\theta = 0^\circ$ ),  $\alpha = 4,2^\circ$  ( $\theta = 15^\circ$ ),  $\alpha = 18,5^\circ$  ( $\theta = 30^\circ$ ).

Experimental results, which are in agreement with the quadratic surface, permit us to describe the variation of elastic compliances in a linear domain with the type and the direction of a loading.

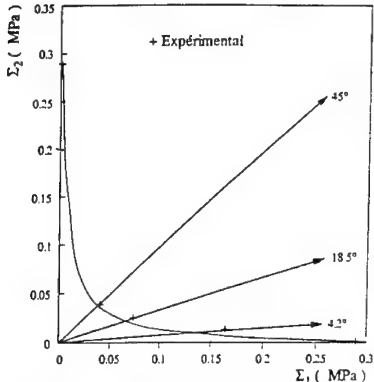


Figure 2 : Isostrain surface for 8 plies in a woven carbon/epoxy composite material ( $\varepsilon_0 = 0.5\%$ ) the characteristics of which are given in table 1 .

## 2.2 Damage modeling .

Damage is connected to the increase of defects at the meso level and leads to failure at the macro level. Before failure, mechanical properties of composite materials are strongly dependent on damage, reveal an anisotropic nature, and depend on the orientation of loading.

In the case of proportional loading  $\sigma = \{\sigma_\alpha\} = \text{const.}$ , we consider a loading process up to the strain level  $\varepsilon_0 = \sqrt{\varepsilon_\alpha \varepsilon_\alpha} = \varepsilon_{0M}$  beyond the limit of initial damage  $\Sigma_0 = \Sigma_0^d$ . This limit often meets exactly with the limit of plasticity  $\Sigma_0^P$  (see figure 3). When the loading decreases we find a residual strain  $\varepsilon_{0M}^P$  which provides an evaluation of the modification of mechanical properties of the composite. Damage produces a modification of the generalized initial Young's modulus  $E^{(x)}$  (2.3),

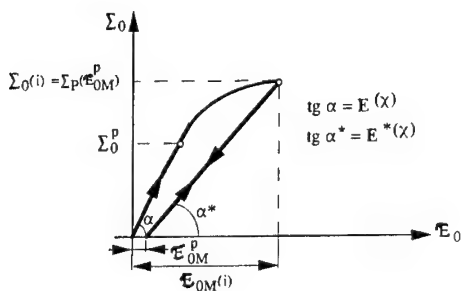


Figure 3 : Modification of elastic properties of composite material during a loading-unloading process .

$(\Sigma_0 = E^{(x)} \varepsilon_0)$  which becomes the modified Young's modulus  $E^{*(x)}$  depending on the residual strain level  $\varepsilon_{0M}^P$ .

Then we define a directional damage parameter  $D^{(\chi)}(\varepsilon_{0M}^P)$  which depends on the plastic residual strain :

$$D^{(\chi)}(\varepsilon_{0M}^P) = \frac{(E^{(x)} - E^{*(\varepsilon_{0M}^P)})}{E^{(x)}} \quad (2.9)$$

This parameter is connected to the damage defined par Lemaître-Chaboche (Lemaître et Chaboche 1985) and (Ladeveze 1996 b).

We define the strain  $\varepsilon'_0$

$$\varepsilon'_0 = \varepsilon_{0M} - \varepsilon_{0M}^P \quad (2.10)$$

The loading is divided into increments  $\Sigma_0(i)$

$i = 1, 2, \dots, M$  and we follow the history of the process. The model of the damaged material up to the level  $\Sigma_0(i) = \Sigma_{0M}(i)$  is a linear model (with damaged elastic moduli) with incremental nature and isostrain criteria.

$$\Delta \varepsilon_\alpha(i) = S^{*(\chi)}_{\alpha\beta}(\varepsilon_{0M}^P) \Delta \Sigma_\beta(i) \text{ or}$$

$$\Delta \Sigma_\alpha(i) = C^{*(\chi)}_{\alpha\beta}(\varepsilon_{0M}^P) \Delta \varepsilon_\beta(i) \quad (2.11)$$

$$(\alpha, \beta = 1, \dots, 6 ; i = 1, \dots, N ; \chi = 1, \dots, 2^6)$$

with  $[C^{*(\chi)}_{\alpha\beta}] = [S^{*(\chi)}_{\alpha\beta}]^{-1}$

The isostrain criteria are defined by a quadratic surface in the space of stresses

$$\Phi^{*(\chi)}_E \equiv R^{*(\chi)}_{\alpha\beta}(i) \sum_\alpha \sum_\beta -(\varepsilon'_0)^2 = 0 \quad (2.12)$$

$$\varepsilon'_0 = \sqrt{\varepsilon_\alpha \varepsilon_\alpha} = \text{const. and } \varepsilon_{0M}^P \text{ known}$$

$$(\varepsilon'_0 = \varepsilon_{0M} - \varepsilon_{0M}^P).$$

The parameters  $R^{*(\chi)}_{\alpha\beta}$  depend on the elastic moduli of the damaged material :

$$E^{*(\chi)} = \frac{1}{\sqrt{R^{*(\chi)}_{\alpha\beta} \sigma_\alpha \alpha_\beta}}$$

The parameter identification of the elastic law is described in sections II-1-2, see also (Chafra et al. 1996 a) and (Chafra et al. 1996 b).

Then we define the non symmetric damage matrix associated to the relative variation of the Hookean operator

$$D^{(\chi)}_{\alpha\beta}(\varepsilon_{0M}^P) = [C^{(\chi)}_{\alpha\beta} - C^{*(\chi)}_{\alpha\beta}(\varepsilon_{0M}^P)](C^{(\chi)}_{\alpha\beta})^{-1} \quad (13)$$

Here there is no summation over underlined subscripts.

Damage parameters  $D^{(\chi)}_{\alpha\beta}$  depend on the level of plastic strain  $\varepsilon_{0M}^P$  and on the area ( $\chi$ ). Then we can define an effective stress vector  $\tilde{\Sigma} = \{\tilde{\Sigma}_\alpha\}$

$$\tilde{\Sigma}_\alpha = [Z^{(\chi)}_{\alpha\beta}]^{-1} \Sigma_\beta \text{ or } \Sigma_\alpha = Z^{(\chi)}_{\alpha\beta} \tilde{\Sigma}_\beta \quad (2.14)$$

$$Z_{\alpha\beta}^{(\chi)} = \frac{C_{\alpha\beta}^{(\chi)}}{C_{\alpha\beta}^{(\chi)}} \quad (\alpha, \beta = 1, \dots, 6) \quad (2.15)$$

If we consider a thermodynamical approach of damage, the evolution equation of damage parameters are written as follows :

$$\Delta D_{\alpha\beta}^{(\chi)} = - M_{\alpha\beta}^{(\chi)} S_{\alpha\beta}^{(\chi)} \Delta E_{0M}^P \quad (2.16)$$

$$M_{\alpha\beta}^{(\chi)} (E_{0M}^P) = \frac{\partial C_{\alpha\beta}^{(\chi)} (E_{0M}^P)}{\partial E_{0M}^P} \quad (2.17)$$

( $\alpha, \beta = 1, \dots, 6$ )

The dual thermodynamical parameter of  $D_{\alpha\beta}^{(\chi)}$  is defined by :

$$Y_{\alpha\beta}^{(\chi)} = - \frac{\partial W_E^{*(\chi)}}{\partial D_{\alpha\beta}^{(\chi)}} \quad (2.18)$$

so that the dissipation energy  $Y_{\alpha\beta}^{(\chi)} \Delta D_{\alpha\beta}^{(\chi)}$  is positive.  $W_E^{*(\chi)}$  is the elastic energy of the damaged material.

### 2.3 Results

We present an application with a woven SiC/SiC composite material studied by Ladeveze [Ladeveze 1993] (in the case of plane stress). Parameters of the model are identified by off-axis tests in direction  $\theta$  described in section II-1-2

Table 2 : Experimental characteristic of SiC/SiC woven composite material in tensile test :  $\chi = 1$   
(see relation (9))

a)  $\alpha = \theta = 0^\circ$   $E^{(1)} = 2137 \text{ MPa}$

b)  $\alpha = \theta = 45^\circ$   $E^{(1)} = 1386 \text{ MPa}$

$E_{0M}^P$	$E^{*(1)}(0^\circ)$ (MPa)	$D^{(1)}(0^\circ)$
0.00	2137	0
0.0031	1706	0.202
0.0041	1291	0.396
0.0056	1082	0.494
0.0087	1022	0.522

a)

$E_{0M}^P$	$E^{*(1)}(45^\circ)$ (MPa)	$D^{(1)}(45^\circ)$
0	1386	0
0.0020	1060	0.235
0.0063	767	0.447
0.0145	619	0.553
0.0215	511	0.631

b)

The variation of damage parameters  $D_{11}^{(1)}$  and  $D_{22}^{(1)}$  in the loading area (1) (figure 4) versus the plastic deformation  $E_{0M}^P$  is similar to the results given by Baste 1991).

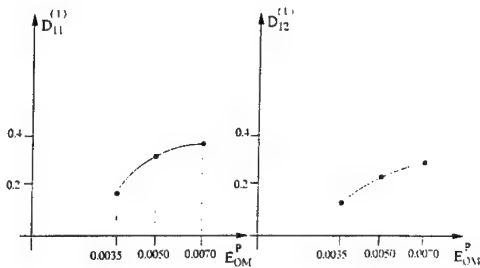
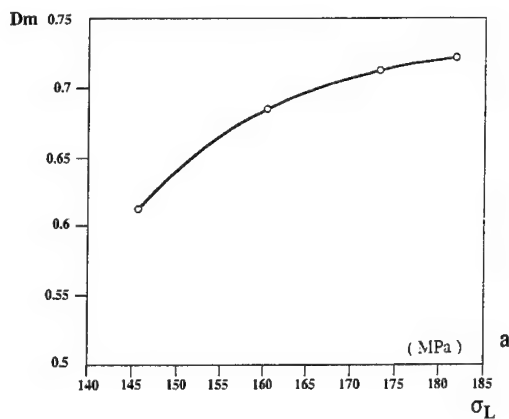
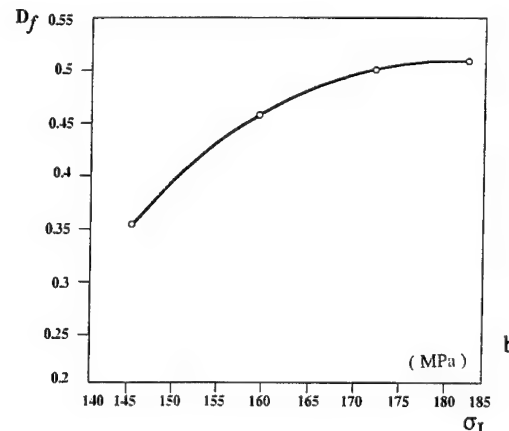


Figure 4 : Damage versus plastic deformation in woven SiC/SiC composite



a)



b)

Figure 5 : Variation of damage versus the tensile stress a)  
in the matrix b) in the fibers

Damage at the meso level

$$D_m = \frac{E_m - E_m^*}{E_m} \quad \text{for the matrix} \quad (2.19)$$

$$D_f = \frac{E_f - E_f^*}{E_f} \quad (2.20)$$

for the fibers (Thread of woven composite)

can be estimated from damage at the macro level

$$D_c = \frac{E_c - E_c^*}{E_c} \text{ by an iterative method coupled}$$

with a finite element computation. (figure 5). We assume that the mixture rule is satisfied :

$$E_c^* - E_m (1 - D_m) + E_f (1 - D_f) v_f \quad (2.21)$$

Subscripts c, f and m are related to the composite, fibers and matrix , respectively;  $v_f$  is the volume fraction of fibers.

### 3. DETERMINATION OF DAMAGE IN COMPOSITE STRUCTURES

Damage at the macro level can be evaluated by classical mechanical tests : tensile test, flexural or torsional vibration tests, wave propagation tests with large wave numbers in comparison with the length of inclusions.

In this section one tries to exhibit the relevant parameters which characterize damage of effective structures at the meso level. We assume that damage is mainly due to connection between various elements of the structure and can be evaluated by a wave propagation technique which is a promising approach. We developed the simplest case : gluing of two anisotropic materials with a periodic array of slits with elastic slips situated at the interface between two media.

#### 3.1 Formulation of the problem

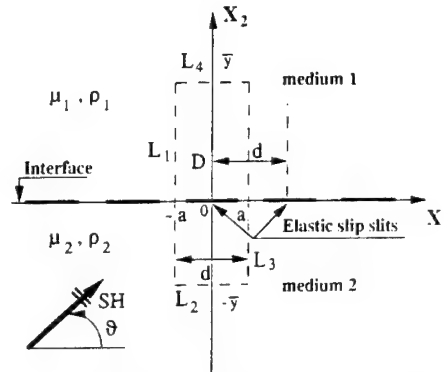
One considers a periodic array of slits along an interface between two isotropic media defined by the parameters  $a$  (width of the slit) and  $d$  (period of the slits along  $x_1$  direction), presenting elastic slip conditions (figure 6). Elastic slip corresponds to the absence of detachment, and the fact that the slip, of an elastic nature and related to the tangential displacement jump  $[U_T]$ , is characterized by a single positive coefficient  $b$  such as

$$\sigma_T^{(i)} = \sigma_T^{(2)} = b [U_T] \quad (3.1)$$

$\rho^{(i)}$  and  $\mu^{(i)}$  are respectively the mass density and the Coulomb modulus of the medium ( $i$ )  $i = 1, 2$ . The examination of the propagation of waves of any incidence, the reflection and transmission properties by the interface and the diffraction field far away from the interface is of interest for both practical and theoretical viewpoints. Without entering into the details of the computation, for which we refer the reader to the following references (Maugin 1996), (Chevalier et al. 1991), (Chevalier et al. 1995), we highlight the main

results in the case of elastic slip conditions (3.1) at the cracks (or slits).

The wave incident on the slit generates diffracted waves. Thus the total displacement and stress fields comprise contributions from the incident wave (in the absence of slits) and from diffracted waves. Using Fourier integrals one is finally led to an integral equation for the jump in the diffracted component at the interface (Louzar 1992). The solution is sought in the form of infinite expansion in Chebyshev polynomials from which these results an infinite inhomogeneous system (Maugin et al. 1994), (Chevalier et al. 1995).



$\bar{x}$  AND  $\bar{y}$  : LOCAL COORDINATES

Figure 6 : Incident SH wave on an interface with a periodic array of slits exhibiting elastic slip : notation.

#### 3.2 Results and application

In order to illustrate the dynamical behaviour of the interface, we display four graphs (figures 7 - 10) which emphasize the influence of the wave number, in the reduced form  $k_2 a$  ( $k_2$  is the wave number

in the medium 2), of the angle of incidence  $\theta$  and of the distribution of cracks  $d/a > 2$ , for the material pairing of glass and steel and for various reduced elastic stiffnesses  $ba$ . These four graphs highlight the following facts concerning the variations of the transmission and reflection coefficients.

In figures 7 and 8, which are drawn for spacings of  $d/a = 3$  and  $2.1$ , respectively, and a fixed incidence angle  $30^\circ$ , the full lines correspond to the case of cracks without slip.

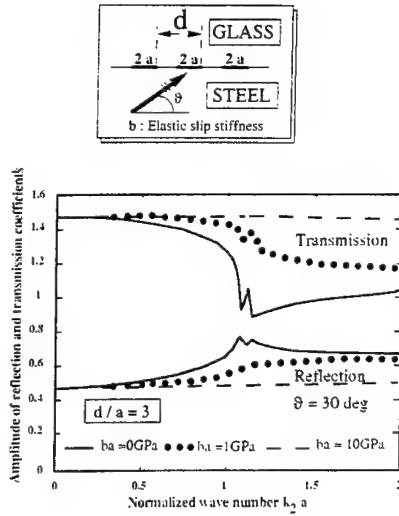


Figure 7 : Amplitude of reflection and transmission coefficients versus wave number for SH wave,  $\theta = 30^\circ$ , for various elastic-slip stiffnesses ( $d/a = 3$ )

It is noted that, with increasing  $ba$ , the interface behaves more and more as if it were not damaged as the transmission coefficient increases, tending towards that of the incident wave. Two extrema are in general present for low  $ba$ , each corresponding to a cut-off frequency. Beyond the first cut-off frequency the energy balance is no longer verified. This means that the zeroth-order mode is no longer the dominant one and there is need to account for

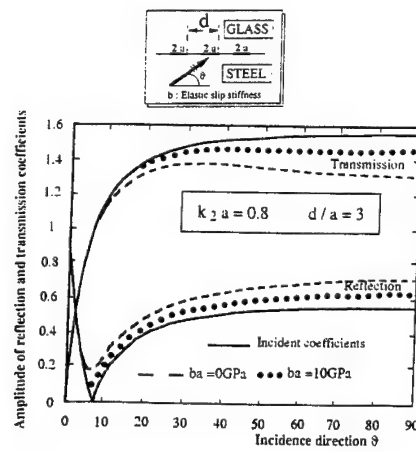


Figure 9 : Amplitude of reflection and transmission coefficients versus angle of incidence for  $k_2$   
 $a = 0.8$ ,  $d/a = 3$  and various elastic-slip stiffnesses.

higher order modes. But, for sufficiently large  $d/a$ , the first cut-off frequency becomes exceedingly small, and below those of the incident wave. For low frequencies the transmission coefficient becomes less sensitive to the spacing  $d/a$ . These two remarks lead us to conclude that, on the one hand, higher order modes must be taken into account when the slits are not too closely packed, while, on the other, it may be more rewarding from a practical viewpoint to measure the slit spacing on the transmission and reflection coefficients. They speak for themselves.

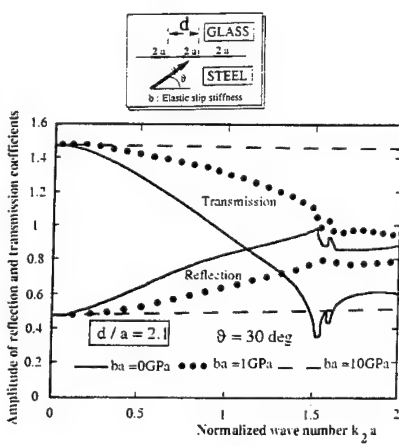


Figure 8 : Amplitude of reflection and transmission coefficients versus wave number for SH waves,  $\theta = 30^\circ$ , for various elastic-slip stiffnesses ( $d/a = 2.1$ )

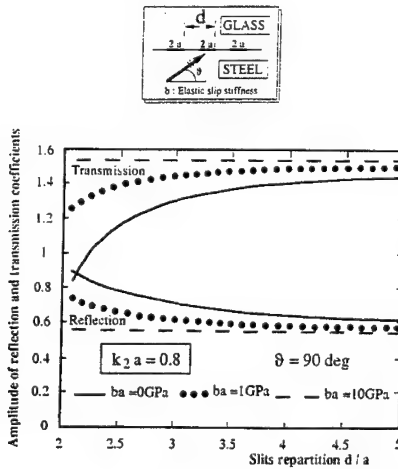


Figure 10 : Amplitude of reflection and transmission coefficients versus crack distribution ( $d/a > 2$ ), for SH waves for  $k_2 a = 0.8$ , and normal incidence, and various elastic-slip stiffnesses.

#### 4 . CONCLUSION

The model of mechanical behavior of material, based on isocrateria is used to describe the variation of the elastic compliance matrix in composite materials. This description which takes into account both the type and the direction of the loading can also be used in nonlinear behavior modeling: for plasticity and failure for example, we have introduced a condition of nonlinearity similar to the Hill criterion. It would be interesting to complete some tests with non-proportional loading in order to verify if the suggested model is always valid. This static approach is the first step which can be easily generalized to the dynamical modeling of damage.

To determine damage at the macro level in composite structures or in composite materials one can use classical static or dynamic tests. For damage at the meso level, the elastic slit approach is a naïve but first step description in the perfect contact of material at the interface. Transmission and reflection effects should be of evident interest in the control of the quality of interfaces by means of elastic waves. This point of view, which is called the inverse problem, is essentially an experimental approach which presents a lot of difficulties. This problem should be solved by the way of signal processing.

#### ACKNOWLEDGEMENTS

The authors would like to acknowledge the work of their colleagues A.BALTOV (Mechan.Inst.Bulgaria) and T.VINH (ISMCM) who contributed to the development of basic concepts which are presented here.

#### REFERENCES

- BASTE, S. 1991. Comportement non linéaire des composites à matrice fragile, théorie et mesure de leur endommagement. *Habilitation*. Univ. Bordeaux I, n°21.
- CHAFFRA, M. 1994 - Modélisation tridimensionnelle, endommagement et rupture. *Doctoral thesis in mechanics*. Conservatoire National des Arts et Métiers, Paris.
- CHAFFRA, M., BALTOV, A. & VINH T. 1995 . Tridimensional modeling of composite materials damage and failure. *Actes EUROMECH 334*. Lyon, 154-163.
- CHAFFRA, M., BALTOV, A. & VINH T. 1996 a . Modélisation tridimensionnel des matériaux composites - Endommagement et rupture . *Revue des composites et matériaux avancés* 56 (1) 549-72.
- CHAFFRA, M., VINH, T. & CHEVALIER, Y. 1996 b. Damage and failure of composite materials : Application to woven materials. *Progress in durability analysis of composite systems in A.Cardon, H.Fukuda, K.Reifsnider (ed)*. Rotterdam : Balkema.
- CHEVALIER, Y., LOUZAR, M. & MAUGIN, G.A. 1991. Surface wave characterization of the interface between two anisotropic media. *J. Acoust. Soc. Am.* 90 (6) : 3218-3227.
- CHEVALIER, Y., LOUZAR, M. & MAUGIN, G.A. 1995. Influence of interfacial slits with elastic slip on the propagation of SH waves. *J. Acoust. Soc. Am.* 98 (1) : 445-453.
- FUJU, T., AMUJIMA S. & FAN LIN . 1995. Study on strength and non linear stress - strain response of plan woven glass fiber laminates under brassical loading . *J. Comp. Mat.* 26 (17) : 2493-2510.
- LADEVEZE, P. 1992 . A damage computational method for composite structures. *Computer and Structures*. 44 (1,2) : 79-87.
- LADEVEZE, P. 1993 a. Damage in composites materials . *Studies in Appl.Mechanics* (34). Elsevier, London.
- LADEVEZE, P., ALLIX, O. & CLUZEL C. 1993 b. Damage modeling at the macro and meso-scales for 3D composites. *Damages in comp. Mat.* G.Z Voyiadis (ed) : 195-215.
- LADEVEZE P. 1993 c. Mécanique de l'endommagement des composites, une nouvelle approche des composites par la mécanique de l'endommagement - O. Allix, P.Ladeveze (ed) 97-127, Cachan.
- LEMAITRE, J. & CHABOCHE J.L. 1985 . Mécanique des matériaux solides. Dunod. Paris.
- LENE, F. 1984. Contribution à l'étude des matériaux et de leur endommagement (in French) *Doctoral thesis in Mechanics* Univ. P. M.Curie, Paris.
- LOUZAR, M. 1992. Contribution to the propagation of elastic waves at the interface of two solids (in French). *Doctoral thesis in Mechanics* . Univ. P. M. Curie, Paris.
- MAUGIN, G.A. 1990. Linear and nonlinear SH surface acoustic waves. in *SurfacesWaves in Solids and Layered Structures*. Borissov (ed) World Scientific, Singapore : 215-229.
- MAUGIN G.A., CHEVALIER Y. & LOUZAR M. 1994. Interfacial waves in the presence of areas of slip. *Geophys. J. Int.* 188 : 305-316.
- PARK, S.W. & SCHAPERY, R.A. 1997. A viscoelastic constitutive model for particulate composites with growing damage. *Int. J. Solids Structures* . 34 (8) : 931-947.
- SPEARING, P.A. , LAGACE, P.A. & MC MANUS. 1995; On the role of lengthscale in the prediction of failure of composite structures : Assessment and needs. *Proc. ICMM-10 whistler B.C. IV characterization and ceramic matrix composites*. Canada.
- VINH, T. 1981. Mesures ultrasonores des constantes élastiques des matériaux composites *Sci. et techniques de l'armement* . 54 : 265-189.

## Prediction of transverse cracking in CFRP laminates with interlaminar resin layers

S.Ogihara & A.Kobayashi

*Science University of Tokyo, Noda, Chiba, Japan*

N.Takeda

*Center for Collaborative Research (CCR), The University of Tokyo, Japan*

**ABSTRACT:** In recent years, interlaminar-toughened laminates are developed in which resin rich layers are placed in interlaminar regions in order to enhance the interlaminar fracture toughness of CFRP laminates. In the present study, tensile tests are conducted on CFRP cross-ply laminates with interlaminar resin layers at 0/90 interfaces. Young's modulus reduction due to transverse cracking is measured as a function of transverse crack density. Transverse crack density is measured as a function of the laminate strain. To investigate temperature effect, tests are conducted at room temperature and 80°C. Laminate configurations are cross-ply (0/90<sub>m</sub>/0)  $m=4, 8$  and  $12$ . The experimental results are compared with the theoretical prediction based on the two-dimensional analysis considering the interlaminar resin layers and thermal residual stresses.

### 1 INTRODUCTION

In many applications of fiber-reinforced plastics, fibers are aligned in more than one direction to provide high load-bearing capability. Among these composite laminates, cross-ply laminates have been extensively studied because this is a basic laminate configuration. The failure process of cross-ply laminates under static tensile loading is known to involve a sequential accumulation of damage in the form of matrix-dominated cracking. One type of damage consists of multiple transverse cracks running parallel to fibers in 90° plies. A second type of damage consists of delamination (Reifsnider 1982).

Transverse cracks occur at a stress which is much lower than the laminate strength. As the laminate stress increases, the number of transverse cracks increases. To establish damage tolerance design of this laminate, methodology to predict transverse crack behavior has to be introduced. That is, development of predictive method of transverse crack density as a function of the laminate stress is necessary. In this point of view, many investigations, which consist of experimental observation of onset and multiplication of transverse cracks and its modeling, have been conducted on cross-ply composite laminates.

Bailey et al. (1979) measured transverse crack spacing as a function of applied laminate stress and derived the relation between the transverse crack spacing and the laminate stress using the shear-lag analysis. They used the stress criterion which assumes that a transverse crack occurs when the maximum 90° ply stress reaches a critical value. They also showed experimentally that the transverse

crack onset strain (first cracking strain) increases with decreasing 90° ply thickness. This phenomenon was called the constraint effect and cannot be explained by the stress criterion. They explained the constraint effect by using the energy balance before and after transverse cracking. Though this concept does not consider the propagation in 90° ply, it can explain the dependence of first cracking strain on 90° ply thickness. This concept is called the energy criterion.

Predictions of the transverse crack density were also conducted by combining the shear-lag analysis and the energy criterion (Laws & Dvorak 1988, Han et al. 1988), by combining the shear-lag analysis and the stress criterion (Fukunaga et al. 1984, Lee & Daniel 1990), by combining the variational stress analysis and the energy criterion (Nairn 1989), and by considering the statistical character of 90° ply strength (Peters et al. 1989, Takeda & Ogihara 1994a,b, Ogihara & Takeda 1995).

In recent years, interlaminar-toughened laminates are developed in which resin rich layers are placed in interlaminar regions in order to enhance the interlaminar fracture toughness of CFRP laminates. Increase in interlaminar fracture toughness by introducing interlaminar resin layers is reported (Altus & Ishai 1990, Askoy & Carlsson 1992, Ozil & Carlsson 1992). However, transverse cracks will occur in interlaminar-toughened laminates in off-axis plies, because intralaminar fracture toughness is not improved.

The authors analyzed the stress and displacement fields in an interlaminar toughened CFRP cross-ply laminate with transverse cracks (Ogihara et al. in

press). In the present study, the thermomechanical properties of cracked laminates are derived based on the analysis. In addition, a prediction of transverse cracking is conducted by using both the stress and energy criteria. The experimental results of Young's modulus reduction due to transverse cracking and transverse crack density as a function of the laminate strain are compared with the theoretical prediction.

## 2 EXPERIMENTAL PROCEDURE

### 2.1 Materials

Two material systems were used. One was interleaved CFRP, T800H/3631-FM300 (0/90<sub>m</sub>/0) where  $m=4, 8$  and  $12$ , with epoxy resin (FM300) layers of thickness about  $100\mu\text{m}$  between the 0° and 90° plies. The other was toughness-improved CFRP, T800H/3900-2 (0/90<sub>m</sub>/0) where  $m=4, 8$  and  $12$ , with selectively toughened interlaminar layers of thickness about  $30\mu\text{m}$  at all ply interfaces. The interlaminar layers contain tough and fine polyamide particles dispersed in the epoxy.

T800H is a high strength carbon fiber. The 3631 is a modified epoxy system with improved toughness compared with conventional TGDDM/DDS epoxy resin. The average thickness of each ply was  $0.135\text{mm}$  for T800H/3631-FM300 and  $0.190\text{mm}$  for T800H/3900-2. The fiber volume fractions were 43-47% for T800H/3631-FM300 and 54-55% for T800H/3900-2. The low fiber volume fraction for T800H/3631-FM300 is due to the thick FM300 resin film.

### 2.2 Measurement of Young's modulus reduction and transverse crack density

Loading-unloading tests were performed to obtain the Young's modulus reduction as a function of the transverse crack density. The loading-unloading procedure cycles were repeated several times with the continuous recording of the stress-strain curves. To investigate the temperature effects, the tests were conducted at room temperature (R.T.) and at  $80^\circ\text{C}$ . The specimen edge was replicated at each perfectly-unloaded point. The Young's modulus reduction as a function of the transverse crack density were obtained based on the combination of the replica observation and the measurement of the stress-strain curves. The transverse crack density was defined as the number of transverse cracks per unit specimen length. Tensile tests where monotonously increasing loads were applied were also conducted to obtain the transverse crack density as a function of the laminate strain at R.T. and at  $80^\circ\text{C}$ .

## 3 ANALYSIS

The authors analyzed the stress and displacement fields in interlaminar toughened cross-ply laminates with transverse cracks as shown in Figure 1

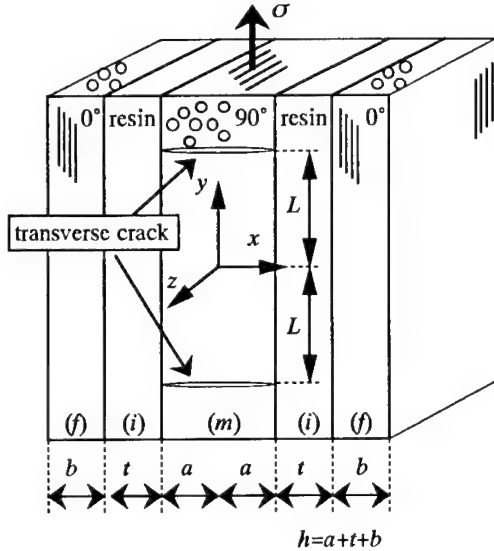


Figure 1. A model of interlaminar-toughened cross-ply laminate containing transverse cracks in 90° ply.

(Ogihara et al. in press). The analysis is based on two-dimensional elastic analysis for a cross-ply laminates without interlaminar resin layers conducted by McCartney (1992).

A set of rectangular Cartesian co-ordinates ( $x, y, z$ ) is selected as shown in Figure 1. The laminate is subjected to a tensile stress,  $\sigma$ , in  $y$ -direction. It is assumed that a parallel array of equally spaced (crack spacing is  $2L$ ) transverse cracks that run through the thickness and width of the 90° ply occurs. The transverse crack tips stop at the 90°/interlaminar resin layer interface. The thicknesses of outer 0° ply, interlaminar resin layer and inner 90° ply are  $b$ ,  $t$  and  $2a$ , respectively. The laminate thickness is denoted by  $2h$ , where  $h=b+t+a$ . Generalized plane strain condition is assumed and the stress and displacement fields are expressed as functions of  $x$  and  $y$ .

Using the results of the analysis, change in thermoelastic properties of laminates due to transverse cracking can be derived. The following stress-strain relation for the laminates with transverse cracks is obtained.

$$\varepsilon_c = \frac{\sigma}{E_c} + \alpha_c \Delta T \quad (1)$$

$$\frac{1}{E_c} = \frac{1}{E_A} \left[ 1 + \frac{a \Phi E_T^m}{L \xi} \right] \left\{ \frac{1}{E_A^f} \right\}$$

$$-\frac{\nu_A}{E_A} \left( \nu_A^m - \nu_A^f \frac{E_T^f}{E_A^f} \right) \left( 1 - \nu_A \nu_A^m \right) \quad (2)$$

$$\alpha_c = \alpha_A + \frac{a \Phi E_T^m}{L \xi} \left\{ \frac{1}{E_A^f} \right\}$$

$$-\frac{\nu_A}{E_A} \left( \nu_A^m - \nu_A^f \frac{E_T^f}{E_A^f} \right) \left( \alpha_A + \nu_A^m \alpha_T - \alpha^m \right) \quad (3)$$

where  $E_c$  and  $\alpha_c$  are longitudinal Young's modulus and longitudinal thermal expansion coefficient of the laminate with transverse cracks,  $E_A$  and  $\alpha_A$  are the axial Young's modulus and the axial thermal expansion coefficient of the damage-free laminate, respectively, and  $\Delta T = T - T_0$ , where  $T$  is the test temperature, and  $T_0$  is the stress-free temperature. The other parameters are shown in elsewhere (Ogihara et al. in press).

In the present study, a prediction of the transverse crack density as a function of the applied laminate stress (or strain) is conducted by using the results of the analysis. Both stress and energy criteria are considered.

In stress criterion, it is assumed that a transverse crack occurs when the normal stress in  $y$ -direction in  $90^\circ$  ply reaches a critical value. The normal stress in  $y$ -direction in  $90^\circ$  ply takes its maximum value at the midway between the transverse cracks, that is,  $y=0$ . When the transverse crack spacing is  $2L$ , the maximum normal stress in  $y$ -direction in  $90^\circ$  ply is

$$\sigma_{yy,\max}^m = -\frac{b}{a} P(\sigma, 2L) + \sigma_m \quad (4)$$

where  $\sigma_m$  is  $90^\circ$  ply normal stress in  $y$ -direction in the damage-free laminate and  $P$  the change in stress with transverse cracking. The parameter  $P$  is a

function of the laminate stress ( $\sigma$ ) and transverse crack spacing ( $2L$ ) and is also shown in elsewhere (Ogihara et al. in press). Assuming that the critical value is  $\sigma_B$ , transverse crack spacing will be  $L$  when the value of (4) reaches  $\sigma_B$ . Then, the relation between the transverse crack density (spacing) and the laminate stress is given by the following equation.

$$\sigma_B = -\frac{b}{a} P(\sigma, 2L) + \sigma_m \quad (5)$$

In energy criterion, it is assumed that a transverse crack occurs when the energy release rate associated with transverse cracking reaches a critical value. The energy release rate associated with transverse cracking can be derived as follows. Assuming that transverse cracks occur at a constant load, the energy release rate,  $G_t$ , associated with transverse crack formation at the midway between the transverse cracks whose spacing is  $2L$  is expressed as

$$G_t = \frac{1}{a} (\sigma - E_A \alpha_A \Delta T)^2 h L \left( \frac{1}{E_c(L)} - \frac{1}{E_c(2L)} \right) \quad (6)$$

where  $E_c(L)$  and  $E_c(2L)$  axial Young's modulus of the laminates with transverse cracks whose spacing is  $L$  and  $2L$ , respectively. Then, the laminate stress when the transverse crack spacing becomes  $L$  from  $2L$  is shown to be

$$\sigma = \sqrt{\frac{a G_{tc}}{h L} \left( \frac{1}{E_c(L)} - \frac{1}{E_c(2L)} \right)^{-1} + E_A \alpha_A \Delta T} \quad (7)$$

where  $G_{tc}$  is the critical energy release rate.

Table 1. Material properties used in the analysis.

Composite	T800H/3631	T800H/3900-2	Resin	FM300	Particle-dispersed layer
$E_A$ (GPa) (R.T)	152.2	130.4	$E^i$ (GPa) (R.T)	2.45	2.50
(80°C)	144.2	126.4	(80°C)	1.23	1.87
$E_T$ (GPa) (R.T)	9.57	7.96	$\mu^i$ (GPa) (R.T)	0.88	0.91
(80°C)	8.09	7.30	(80°C)	0.44	0.68
$\mu_A$ (GPa) (R.T)	4.50	4.50	$\nu^i$	0.38	0.38
(80°C)	4.26	3.80			
$\mu_T$ (GPa) (R.T)	3.21	2.67	$\alpha^i$ ( $\times 10^{-6}/^\circ C$ )	60.0	60.0
(80°C)	2.75	2.45			
$\nu_A$	0.349	0.349			
$\nu_T$	0.490	0.490			
$\alpha_A$ ( $\times 10^{-6}/^\circ C$ )	0.100	-1.73			
$\alpha_T$ ( $\times 10^{-6}/^\circ C$ )	35.5	34.7			
$\sigma_B$ (MPa) (R.T)	90	90			
(80°C)	100	90			
$G_{tc}$ (J/m <sup>2</sup> ) (R.T)	700	500			
(80°C)	1000	600			

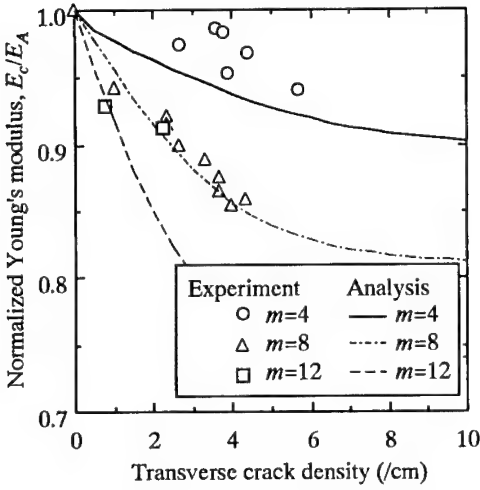
## 4 RESULTS AND DISCUSSION

### 4.1 Young's modulus reduction

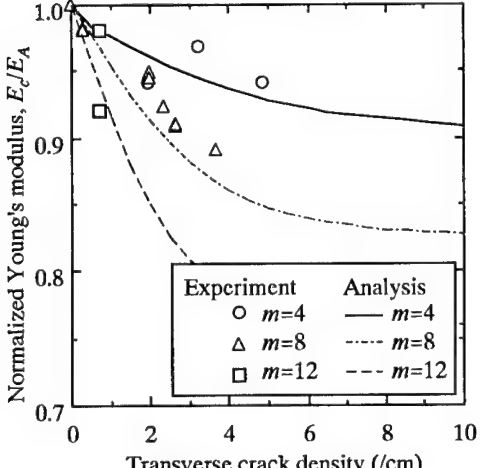
During the loading-unloading tests, transverse cracks whose surface is normal to the loading direction as modeled in Figure 1 were observed. Transverse cracks run through the thickness and width of the 90° ply. In T800H/3631-FM300, it may be reasonable to assume that the transverse crack tip stops at the 90°/FM300 interface. In T800H/3900-2, it is not easy to judge whether the assumption that the transverse crack tip stops at the

90°/interlaminar layer interface is reasonable or not, because the layer is thin. However, considering that the thickness and elastic moduli of the interlaminar layer are small, it may not affect analytical results much whether the transverse crack tip stops at the 90°/interlaminar layer or it penetrates into the interlaminar layer.

Figures 2 and 3 show the comparison of experimental data and analytical predictions of Young's modulus reduction as a function of the transverse crack density for T800H/3631-FM300 and T800H/3900-2, respectively. Eq.(2) is used to predict Young's modulus reduction. Young's

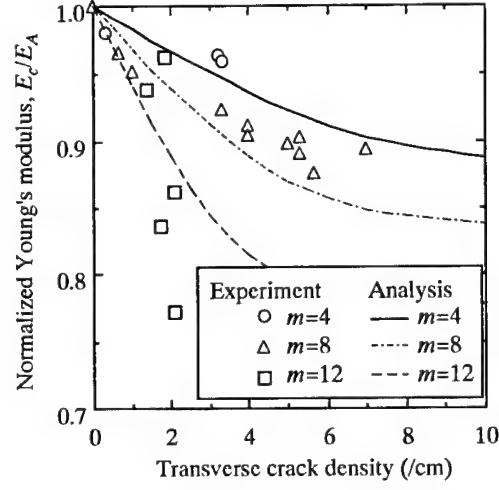


(a) R.T.

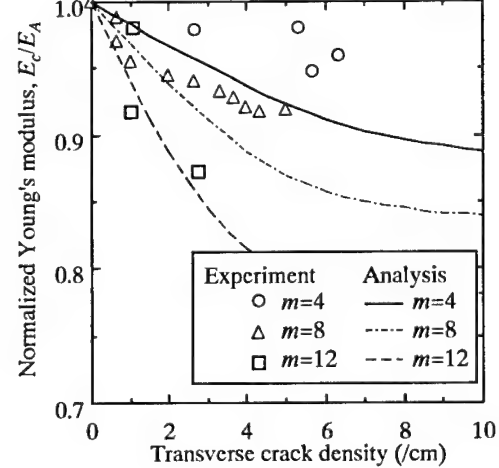


(b) 80°C

Figure 2. Normalized Young's modulus as a function of transverse crack density in T800H/3631-FM300 cross-ply laminates (0/90<sub>m</sub>/0). (a) R.T. (b)80°C.



(a) R.T.



(b) 80°C.

Figure 3. Normalized Young's modulus as a function of transverse crack density in T800H/3900-2 cross-ply laminates (0/90<sub>m</sub>/0). (a) R.T. (b)80°C.

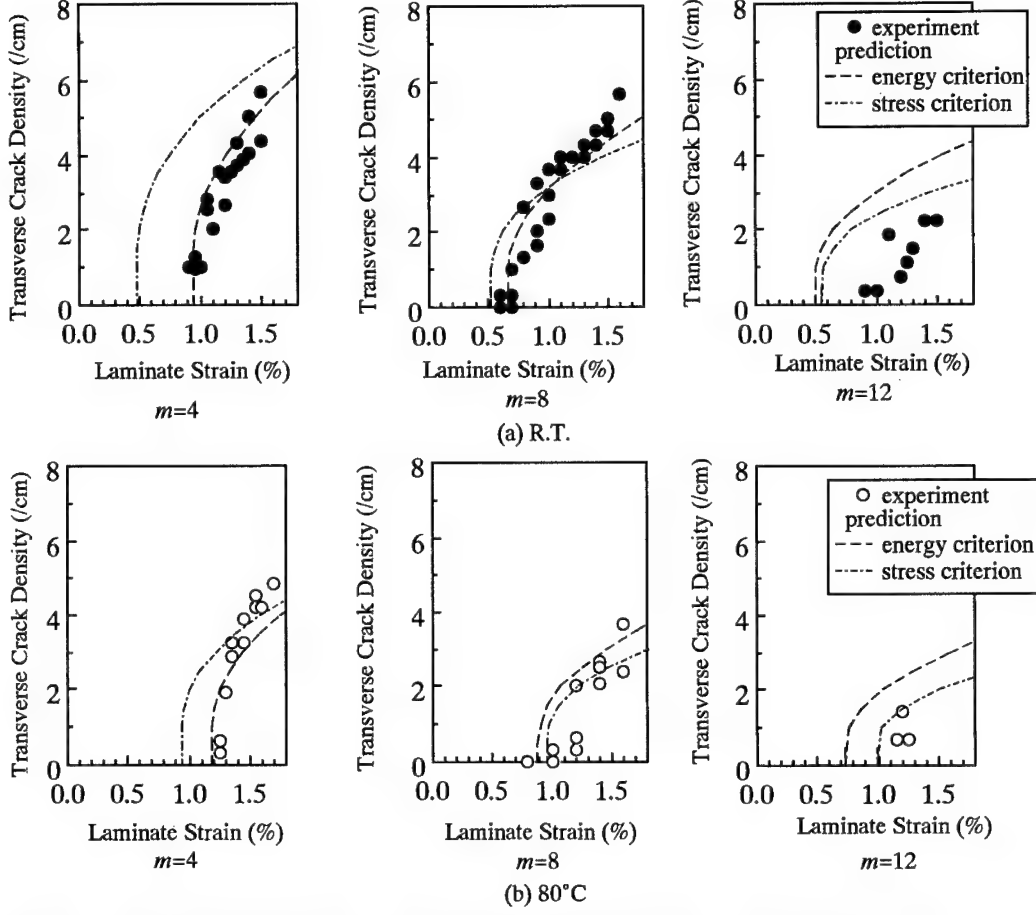


Figure 4. Transverse crack density as a function of applied laminate strain in T800H/3631-FM300 (0/90 <sub>$m$</sub> /0) . (a) R.T. (b) 80°C. Comparison of experimental results and analytical predictions.

modulus is normalized with the value of the damage-free laminate. The thermoelastic constants used in the analysis are listed in Table 1. The values for T800H/3631 and T800H/3900-2 are taken from References (Takeda & Ogihara 1994a, Ogihara et al. 1997) and those for FM300 at R.T. are taken from Reference (Askoy & Carlsson 1992). The values for FM300 at 80°C are assumed values. Poisson's ratios are assumed to be constant in this temperature range. The curing temperature of the laminates is 180°C for both material systems. A reasonable agreement is obtained for both material systems in this temperature range, which implies validity of this analysis.

#### 4.2 Transverse crack density

Figures 4 and 5 show experimental results for the transverse crack density as a function of the applied laminate strain in T800H/3631-FM300 and

T800H/3900-2, respectively. In both material systems, the first cracking strains for  $m=4$  and 12 are larger than that for  $m=8$  at the same temperature. The transverse crack density decreases with increasing  $m$  (90° ply thickness) in this temperature range. The first cracking strain is larger at 80°C than that at R.T. for the same  $m$ . This is because the tensile thermal residual stress in 90° ply decreases and the 90° ply failure strain increases as temperature increases.

In the first place, the applicability of the stress and energy criteria is discussed. Figure 6 shows plots of the predictions of transverse crack density as a function of the applied laminate strain by using the stress and energy criteria for T800H/3631-FM300 at R.T. Material properties used in this prediction is shown in Table 1. The critical values for the stress criterion,  $\sigma_B=90\text{ MPa}$  and for the energy criterion,  $G_{tc}=700\text{ J/m}^2$ .

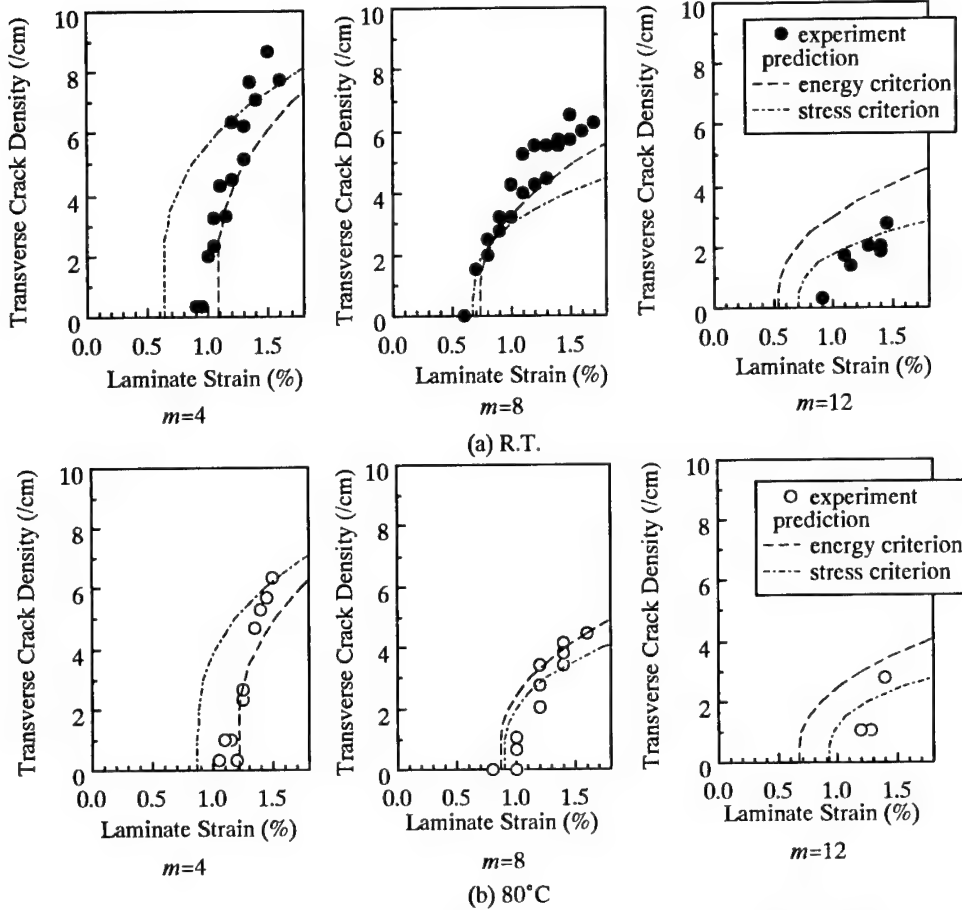


Figure 5. Transverse crack density as a function of applied laminate strain in T800H/3900-2 (0/90<sub>m</sub>/0). (a) R.T. (b) 80°C. Comparison of experimental results and analytical predictions.

All the predictions of the transverse crack density are increasing functions of the laminate strain and the derivative decreases as the strain increases. When the critical values are set larger, the predicted first cracking strain gets larger and smaller transverse crack density is predicted for the same laminate strain (this is not shown in the figure).

For a laminate configuration, two prediction curves exist. Transverse cracks can be considered to occur when both the stress and energy criteria are satisfied. If this is true, it should be reasonable to regard the prediction that gives smaller transverse crack density as the prediction of the present analysis.

As shown in Figure 6, first cracking strain increases as  $m$  increases in the stress criterion. This corresponds to the decreasing tensile thermal residual strain in 90° ply with increasing  $m$ . In the

energy criterion, the first cracking strain is smaller for larger  $m$ . This is due to the fact that the energy release rate is larger for larger  $m$ .

Considering the discussion above, comparison between the experimental results and the analytical predictions are conducted as shown in Figures 4 and 5 assuming the critical values. The critical values used are  $\sigma_B=90\text{ MPa}$  (R.T.),  $100\text{ MPa}$  ( $80^\circ\text{C}$ ),  $G_{tc}=700\text{ J/m}^2$  (R.T.),  $1000\text{ J/m}^2$  ( $80^\circ\text{C}$ ) for T800H/3631-FM300 and  $\sigma_B=90\text{ MPa}$  (R.T.),  $90\text{ MPa}$  ( $80^\circ\text{C}$ ),  $G_{tc}=500\text{ J/m}^2$  (R.T.),  $600\text{ J/m}^2$  ( $80^\circ\text{C}$ ) for T800H/3900-2. In this temperature range, the change in the critical value for the stress criterion is small. The critical value for the energy criterion increases as temperature increases due to the increase in toughness of the matrix material.

In Figures 4 and 5, a reasonable agreement between the experimental results and analytical prediction is obtained if the criterion which gives

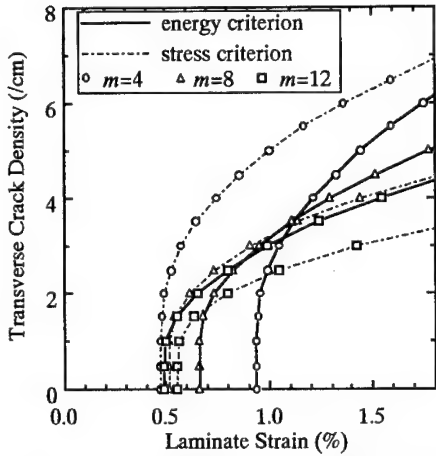


Figure 6. Predictions of transverse crack density as a function of laminate strain in T800 H/3631-FM300 (0/90<sub>m</sub>/0) cross-ply laminates. Comparison of the stress and energy criteria for various 90° ply thicknesses.

smaller transverse crack density is selected. Clearly, it cannot be explained that the first cracking strain is lower for  $m=8$  than that for  $m=4$  by only the stress criterion. It cannot be explained that the first cracking strain is higher for  $m=12$  than that for  $m=8$  by only the energy criterion. By using the both criteria, it will be possible to predict transverse cracking behavior in the laminates with more extensive range of laminate configuration.

## 5 CONCLUSION

Tensile tests were conducted on CFRP cross-ply laminates with interlaminar resin layer at 0/90 interfaces. Transverse crack density was measured as a function of the laminate strain. To investigate temperature effect, tests were conducted at room temperature and 80°C. The experimental results were compared with the theoretical prediction based on the two-dimensional analysis considering the interlaminar resin layers and thermal residual stresses. The validity of the energy criterion and strength criterion was discussed. It was found that the criterion which gave smaller transverse crack density should be selected. The analysis presented in the present paper will be a basis for the optimal design of this type of laminate.

## REFERENCES

- Altus, E. & O. Ishai 1990. The effect of soft interleaved layers on the combined transverse cracking/delamination mechanisms in composite laminates. *Comp. Sci. Tech.* 39: 13-27.
- Askoy, A. & L. A. Carlsson 1992. Interlaminar shear fracture of interleaved graphite/epoxy composites. *Comp. Sci. Tech.* 43: 55-69.
- Bailey, J. E., P. T. Curtis & A. Parviz 1979. On the transverse cracking and longitudinal splitting behavior of glass and carbon fiber reinforced epoxy cross ply laminates and the effect of Poisson and thermally generated strain. *Proc. R. Soc. Lond. A.* 366: 599-623.
- Fukunaga, H., T. -W. Chou, P. W. M. Peters & K. Schulte 1984. Probabilistic failure strength analyses of graphite/epoxy cross-ply laminate. *J. Comp. Mat.* 18: 339-356.
- Han, Y. M., H. T. Hahn & R. B. Croman 1988. A simplified analysis of transverse ply cracking in cross-ply laminates. *Comp. Sci. Tech.* 31: 165-177.
- Laws, N. & G. J. Dvorak 1988. Progressive transverse cracking in composite laminates. *J. Comp. Mat.* 22: 900-916.
- Lee, J. -W. & I. M. Daniel 1990. Progressive transverse cracking of crossply composite laminates. *J. Comp. Mat.* 24: 1225-1243.
- McCartney, L. N. 1992. Theory of stress transfer in a 0°-90°-0° cross-ply laminate containing a parallel array of transverse cracks. *J. Mech. Phys. Solids.* 40: 27-68.
- Nairn, J. A. 1989. The strain energy release rate of composite microcracking: a variational analysis. *J. Comp. Mat.* 23: 1106-1129.
- Ogihara, S. & N. Takeda 1995. Interaction between transverse cracks and delamination during damage progress in CFRP cross-ply laminates. *Comp. Sci. Tech.* 54: 395-404.
- Ogihara, S., N. Takeda & A. Kobayashi 1997. Experimental characterization of microscopic failure process under quasi-static tension in interleaved and toughness-improved CFRP cross-ply laminates. *Comp. Sci. Tech.* 57: 267-275.
- Ogihara, S., N. Takeda & A. Kobayashi (in press). Analysis of stress and displacement fields in interlaminar-toughened composite laminates with transverse cracks. *Adv. Comp. Mat.*
- Ozil, F. & L. A. Carlsson 1992. Plastic zone estimates in mode I interlaminar fracture of interleaved composites. *Engng. Fract. Mech.* 41: 645-658.
- Peters, P. W. M. 1989. The influence of fiber, matrix and interface on transverse cracking in carbon fiber reinforced plastic cross-ply laminates. *ASTM STP 1012*: 103-117.
- Reifsnider, K. L. 1982. *Damage in Composite Materials : Basic Mechanisms, Accumulation, Tolerance and Characterization*, ASTM STP 775. Philadelphia : ASTM.
- Takeda, N. & S. Ogihara 1994a. In-situ observation and probabilistic prediction of microscopic failure process in CFRP cross-ply laminates. *Comp. Sci. Tech.* 52: 189-195.
- Takeda, N. & S. Ogihara 1994b. Initiation and growth of delamination from the tips of transverse cracks in CFRP cross-ply laminates. *Comp. Sci. Tech.* 52: 309-318.

## Damage characterization of elastomeric composites using X-ray attenuation

C. Bathias, P. Houël & Y. N'Faly Bérété

*ITMA, Conservatoire National des Arts et Métiers, Paris, France*

K. Le Gorju

*Centre de Recherches, Hutchinson, Montargis, France*

**ABSTRACT:** X ray tomography is specially suitable to study damage of composites in 3D and with X ray attenuation. The first results from our laboratory were published in ASTM/STP 1128 on 1992 and in ASME Vol.43 on 1994. This new paper is devoted at elastomeric composites based on natural rubber reinforced with carbon black. Using X ray scanner it is shown that:

- the attenuation of X ray is correlated with the molecular structure, amorphous or crystallite phases. With an in situ tensile test, initiation of crystallization is detected.
- when a specimen in rubber is submitted at a compression fatigue loading the damage appears inside the specimen where the maximum shear located. The X ray tomography is able to detect the first damage and the crack growth inside the specimen. The damage crack is successfully compared with numerical simulation of the stress field in compression. Finally, the role of crystallization in shear before damage is shown by means of X ray attenuation.

All together, X ray tomography is shown to be an accurate tool to study molecular arrangement, reinforcement repartition, molecular transformation until damage and cracking in elastomeric matrix composite material, at mesoscopic scale.

### 1 INTRODUCTION

Elastomeric matrix composites are usually reinforced by mineral particles such as carbon black and sometime by long metallic or organic fibers. In this paper, only particle reinforced matrix is taken in consideration.

As soon as a rubber is cyclically loaded, the temperature increases inside the material. It results some modification of the chemical structure of the rubber before damage. In addition, small friction in compression is able to produce chemical instability from solid to liquid stage with an effect of ambient air. Finally, in service conditions, the fatigue damage of rubber is a combination of:

- mechanical damage
- chemical damage
- thermal damage

Experience shows that, in cyclic loading, rubbers are damaged to the point of formation of one or several

cracks which then propagate. As for metal it is recommended to study separately the initiation of cracks and then their propagation. But, we have to remember that cyclic damage of rubbers depends not only on the mechanical loading (including frequency and R ratio) also on temperature and on thermal dissipation and on environment. Rivlin and Thomas in 1953 (1), Lindley in 1972 (2), Lake in 1983 (3), Stevenson in 1973 (4) and Gent in 1992 (5) extended the application of Griffith's criterion, G, to the tearing of elastomers. In this case, the strain energy release rate G is substituted for the concept of tearing energy, T, with the same physical definition as G. The application of fracture mechanics to rubbers generates some difficulties because, of the important deformability of elastomers. In particular, elasticity of elastomers is not linear, and, more over, highly deformed cracks do not stay sharp as in the Griffith's model. Nevertheless there is no energy dissipation by plasticity.

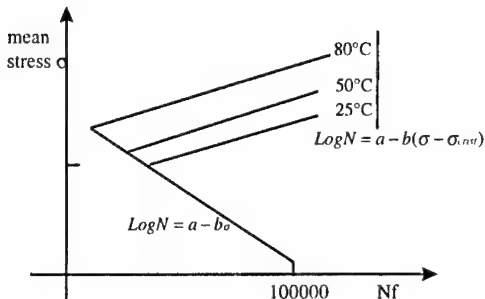


Figure 1.SN curves (NR)

The damage caused by fatigue and cracking in rubber or in elastomeric matrix composites seems considerably influenced by the transformation from an amorphous to a crystalline phase, when the crystalline phase exists. This hard-to-detect transformation is generally studied by X-ray diffraction, a method by which we cannot detect local transformation and damage. In contrast, X ray tomography allows for the observation of the crystalline transformation of rubber and its localization owing to the images generated by the scanner.

The attenuation of the intensity of the X-ray beam, similar to X-ray diffraction, reveals the existence of crystallites, but also detects local damage.

In this paper, the fatigue behavior of elastomers is sum up before an introduction of X ray tomography applied to study phase transformation and damage in tension, compression and shear loading.

## 2 FATIGUE LIFE OF RUBBER

Natural rubber reinforced by carbon black, is amorphous without loading and at room temperature. During elongation this rubber is supposed to be transformed from amorphous to crystallite phase. All the mechanical properties, including fatigue strength, are affected by the crystallization even if the transformation concerns a small amount of molecules.

To show this effect, some tests are carried out with axisymmetric hour-glass shape specimens, the diameter of which is 26 mm. In order to induce crystallization transformation, the mean stress varied since the alternative stress is constant. The results are presented at the figure 1 for a natural rubber tested at 25°, 50° and 80°. It is shown that the fatigue life increases when the mean stress of the cyclic loading is high enough to involve crystallization depending of the testing temperature. To confirm the effect of crystallization on fatigue strength the behavior of natural rubber (NR) is compared with SBR well known to stay amorphous and CR, a synthetic rubber with partial crystallite transformation. It has been found that, for high mean stress, the fatigue life of SBR is decreasing. The figure 2 shows, very well, three types of SN curve for NR, SBR and CR, depending of the crystallization effect. A sharp knee is observed on the SN curve for NR, when the minimum stress of the cycle load is in tension. This phenomena does not appear for SBR and is not so important for CR. Thus, the question is to know how the crystallization related with fatigue damage.

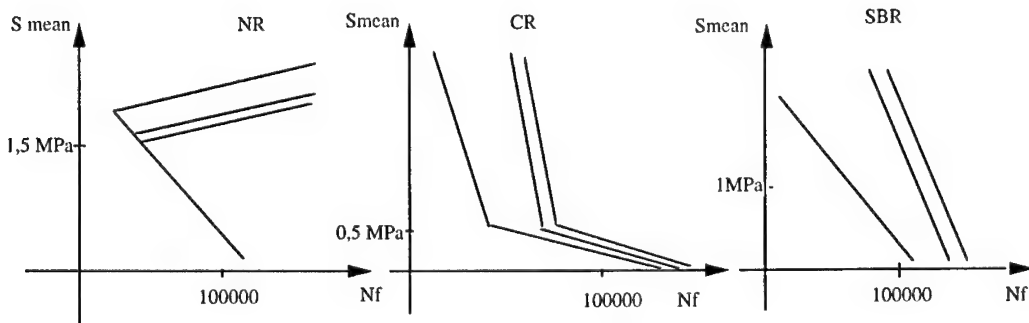


Figure 2.Comparison of SN curves (NR, CR, SBR)

### 3 FATIGUE CRACK PROPAGATION IN NATURAL RUBBER

In order to apply a tension compression loading it is recommended to use a thick specimen with two lateral grooves ( $W= 150 \text{ mm}$   $B= 25\text{mm}$ ) shown in the figure 3. For an elastic deformation, crack propagation is studied in terms of dissipating energy release rate, given by the relation:

$$T = \frac{1}{B} \frac{dU}{da}$$

Fatigue crack growth tests confirm that there is a sigmoidal relation between  $da/dN$  and  $\Delta T$ . Once, a relationship of the form:

$$\frac{da}{dN} = C \cdot \Delta T^n$$

is observed over only limited regions of behavior.

For low values of  $\Delta T$ , a threshold can be defined (figure 4). The threshold increases when  $R$  ratio increases, at contrary to what is observed for metals.

It was observed when  $R$  ratio is 0.5 cracks would not propagate in fatigue for the maximum loads used in this study. At the lower load ratio,  $R = -1$  a symmetrical tension-compression cycle, the threshold  $\Delta Ts$ , almost disappeared. Consequently, the fatigue crack propagated even for the lowest loading when  $R = -1$  (figure 5)

When the loading is in tension-compression, a chemical degradation of rubber is observed at the crack tip, where drops of black liquid are secreted from the crack surfaces. The cyclic damage in compression and the effect of crack surface friction probably lead to a chemical reaction of rubber oxidation.

For the high load ratio ( $R = 0.5$ ) the elongation or blunting of the crack tip causes local crystallization of the rubber which prevents crack propagation. This strain induced crystallization has been determined by X-ray crystallography and tomography. The effect of crystallization doesn't occur from  $R = -1$  because reversibility of the crystallization appears to occur during the compressive stage.

To summarize, the resistance to fatigue crack propagation in natural rubber is better under high static stress for tension-tension cyclic loading, but a minimum stress of the cycle in compression is very damaging.

### 4 X-RAY TOMOGRAPHY

The various applications of X-ray tomography permit the study of composite materials at any level, macroscopic, mesoscopic or microscopic. The X-ray scanner is well-adapted to reveal defects on a centimeter-scale, such as a interlaminar crack, but it is also capable of revealing the distribution of reinforcements on a millimeter-scale, and of detecting microcracking.

In addition, the attenuation of X-ray, which depends on the physical and chemical nature of the composite constituents, can be measured by X-ray scanner. Changes in the polymeric matrix due to aging, or even the transformation of amorphous polymers into crystallites, can be studied by X-ray tomography. This astonishing tool, long used by the medical field, is also well adapted to the study of composite materials, due to its ability to detect defects on a wide range of scales, as well as its ability of physical and chemical analysis by measuring X-ray attenuation.

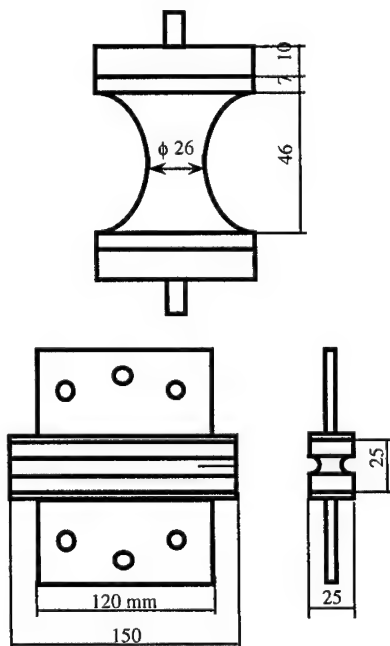
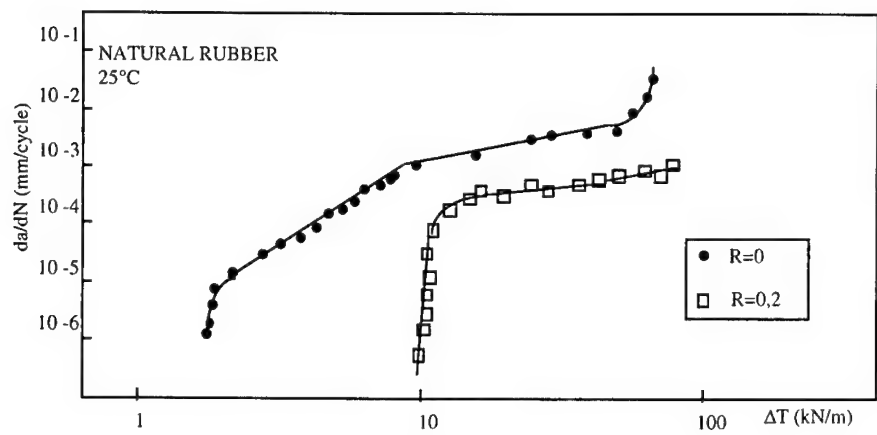
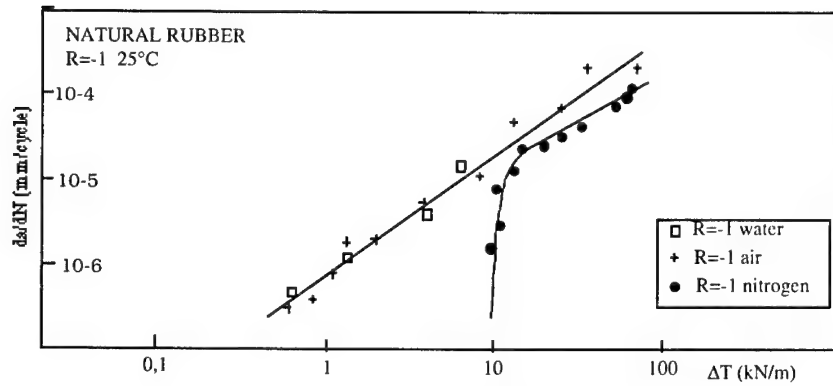


Figure 3. Fatigue specimen and crack growth specimen for rubber



Figures 4. Crack growth rate for  $R>0$  (NR)



Figures 5. Crack growth rate for  $R<0$  (NR)

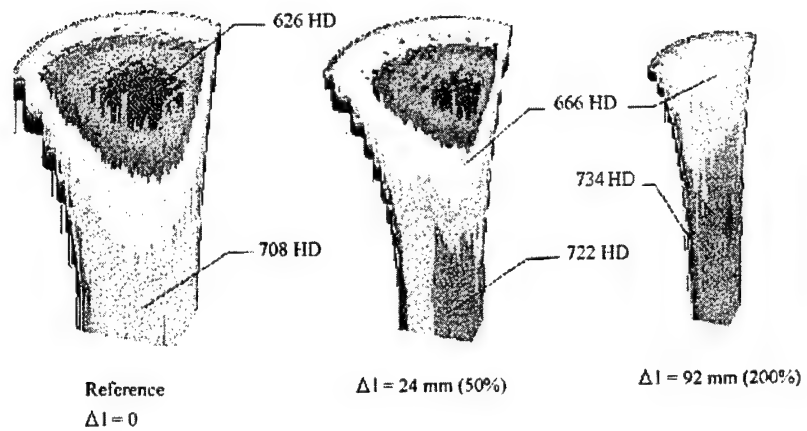


Figure 6. Evolution of X-ray attenuation during monotonic elongation in tension (NR)

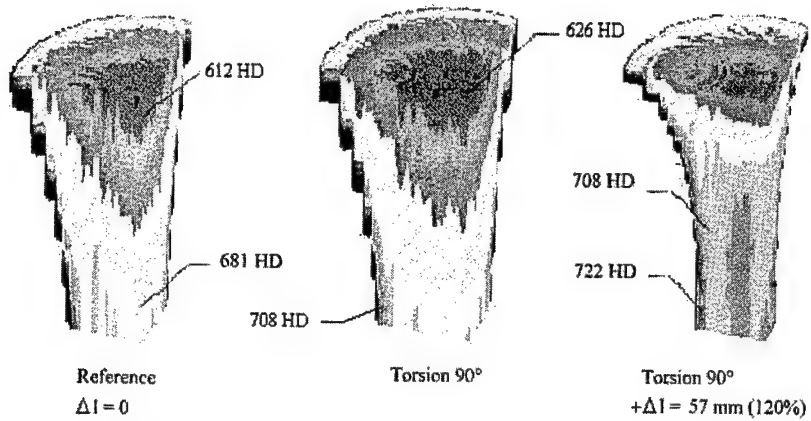


Figure 7. Evolution of X-ray attenuation during torsion and mixed-mode monotonic loading (NR).

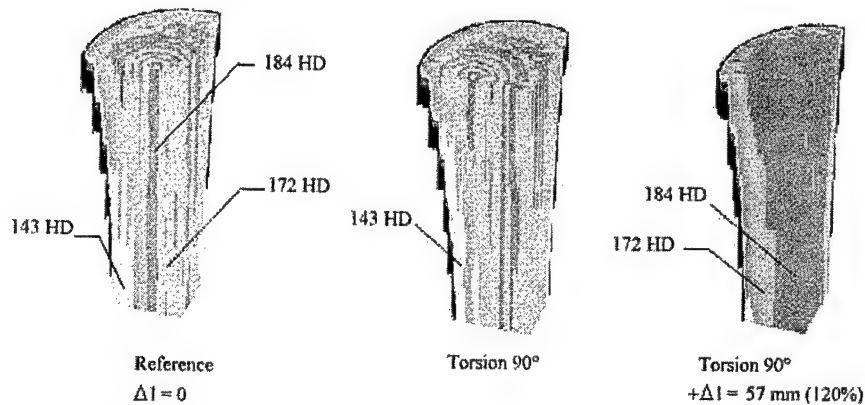


Figure 8. Stady-state X-ray attenuation in amorphous elastomer matrix SBR, during loading.

The medical scanner is able to measure the x-ray attenuation, or tomographic density, in Hounsfield units however, it cannot measure the local mass density. In order to obtain this density a calibration is necessary with the local mass density of water used as a reference. The tomographic density (TD) of a material is a relative measure of its attenuation coefficient ( $\mu$ ) with respect to that of water ( $\mu_w$ ).

It follows that:

$$TD = \frac{K}{\mu_w} \mu - K = \frac{\mu - \mu_w}{\mu_w} K$$

This calibration has been performed with several materials in order to obtain an empirical relationship

between the average TD of materials and their respective attenuation coefficients.

If  $I_0$  is defined as the photon intensity passing through a homogeneous absorber of thickness  $X$ , the emerging photon intensity  $I$  is given by:

$$I = I_0 \exp(-\mu(p, z, E)x)$$

where  $p$  is the physical density,  $z$  the atomic number, and  $E$  the photon energy.

A 10 000 GE medical scanner is used in these experiments. This scanner can accept samples with a maximum diameter of 600mm. The spatial resolution is better than  $250\mu$ . The Hounsfield density resolution is as low as 0,2%, which is,

useless for classical non-destructive testing. Our scanner has been equipped with a monotonic compression/tension machine capable of applying a load of up to 50KN. This permits observations of test pieces under mechanical loads.

For the reconstruction of images and the measurement of tomographic density, we use both commercial software and self-developed software called ULTISCAN VISA, which is used for image calculation and 3-D reconstruction.

## 5 APPLICATION OF X-RAY TOMOGRAPHY TO STUDY CRYSTALLIZATION

Crystallization has been studied before damage during elongation of hour-glass specimen. The results are given in figures 6 to 8. In natural rubber, an elongation of the specimen, inside the tensile machine, provokes an increase of the X-ray attenuation given in Hounsfield units. It is assumed that the high attenuation is related with crystallization. It is easy to observe that higher is the elongation, higher is the attenuation. In order to detect the location of crystallization inside the specimen a tension and a mixed mode loading have been applied. In torsion, high attenuation is located close to the surface since in mixed-mode the attenuation is more uniformed due to the tension (figure 7).

Finally, the figure 8 shows that aSBR specimen without loading, with torsion or torsion-tension does not exhibit any evolution of the X-ray attenuation, what is a good demonstration of the accuracy of X-ray attenuation to detect crystallization transformation in NR.

The last experiment has been done in compression with a NR specimen. A small decrease of the attenuation is observed after compression.

In tension, compression or shear, this phenomena is almost completely reversible when the deformed rubber is unstressed.

## 6 APPLICATION OF X-RAY TOMOGRAPHY TO STUDY FATIGUE DAMAGE

As it is mentioned in the paragraph 4, X-ray tomography is a power tool to detect phase transformation in elastomeric matrix. Obviously, defects such as inclusions, pores are also easy to detect. The problem now is to improve this technique to reveal fatigue damage after a number of cycles.

Firstly it appears, in natural rubber, that X-ray attenuation is not affected in the bulk of the materials but only locally, depending of the loading. To show this effect we have chosen two examples: one specimen loaded in cyclic-tension-compression fatigue and another one loaded in compression-compression fatigue.

In tensile fatigue, the first damage appears close to the surface of the specimen and generally grows from the exterior to inside the specimen. Using interrupted tests after an increasing number of cycles, we have followed the development of a crack in tension-compression fatigue. The figure 9 shows a 3D reconstruction of a fatigue specimen before failure with a small crack. At this stage of the fatigue damage, the difference of the Hounsfield density is less than 10%, compared with the initial attenuation, before damage.

At the contrary, in compression-compression fatigue the first damage appears inside the specimen which is a disc, 50 mm of diameter. It is shown by finite element calculation, the fatigue initiation is located at the maximum shear stress area. If  $N_f$  is the number of cycles for a visible damage, a specimen has been tested at  $\frac{N_f}{3}$  and observed by tomography before failure. Several damage zones have been detected inside the disc. A drastic low Hounsfield density is observed across a damage zone, surrounded with a higher density. To show the performances of the scanner several cross-section and 3D reconstruction are given in figures 10 to 1. This example of compression-compression fatigue damage is especially interesting because there is no other way to detect interior defect inside rubber.

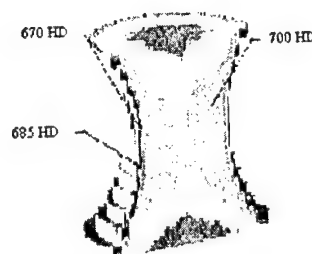


Figure 9. Evolution of X-ray attenuation after megacyclic fatigue tension-compression.

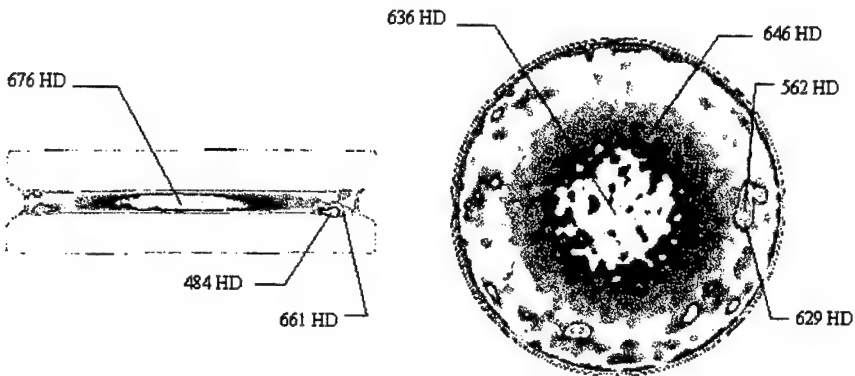


Figure 10 Evolution of X-ray attenuation after interrupted fatigue test at N/3.

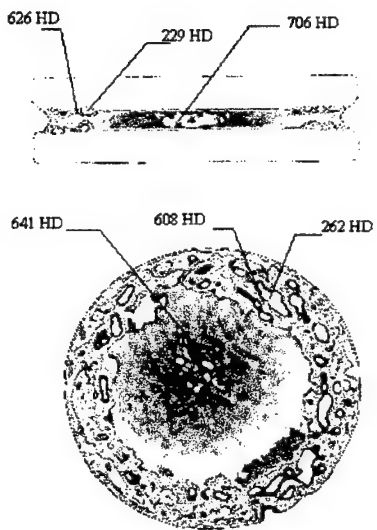


Figure 11. Evolution of X-ray attenuation after interrupted fatigue test at N.

## 7 CONCLUSION

In the first part of this paper, a method is proposed to study the mechanical behavior of elastomeric matrix, fatigue strength and cracking. The effect of crystallization is emphasized.

In the second part, it is shown that the application of medical scanner at rubber is an accurate tool to study molecular arrangement, reinforcement repartition, molecular transformation, until damage and cracking in elastomeric matrix composite materials, at mesoscopic scale.

## REFERENCES

- R.S Rivlin 1953. J.Polymer Sci., 291.
- P.B Lindley 1972. J.Strain Anal 7
- C.J Lake 1983. Prog. Rubber Technol 45
- A. Stevenson 1983. Int. J Fracture 23.
- A.N Gent 1992. *Engineering with rubber*. Hanser Publ.
- C. Bathias & A. Cagnasso 1992. STP/ASTM 1128 pp 33-54.
- C. Bathias , T.Wu & F. Potter 1994. ASME - Ad Vol 43 pp 37-65.

## Damage initiation and progression in notched unidirectional composites

C.L.Chow

*Department of Mechanical Engineering, University of Michigan-Dearborn, Mich., USA*

Fan Yang

*Petri Inc., Mich., USA*

**ABSTRACT:** This paper summarizes our recent research in a theoretical and experimental investigation of damage initiation and progression in unidirectional graphite/epoxy composites containing a central circular hole subjected to off-axis uniaxial tension. Theoretically, a newly developed damage constitutive equation model, together with a modified nonlinear finite element procedure, is applied to analyze the inelastic behavior of the composites with respect to material damage initiation and accumulation. A set of failure criteria is proposed and used to predict the threshold condition of failure and to identify different failure modes. Experimentally, to provide a validation analysis, the Moiré interferometry method with a computerized image processing system is employed to monitor deformation fields and failure characteristics of the composites. Results obtained from the tests are collated with those from analyses to gain a better understanding of the parameters affecting progressive damage in the composites.

### 1 INTRODUCTION

The wide use of fiber reinforced composite materials as secondary and primary engineering structures in industries has increased rapidly in recent years. While these materials continue to offer many desirable structural properties over conventional materials, they also generate many challenging problems in developing technologies to better understand and predict their performance and failure characteristics. A fundamental issue in analyzing the strength of composites is prediction of the initiation and propagation direction of macrocracks in composites with cutouts and notches under loading.

The behaviors of notched laminated composites under load have been studied extensively as these notches result in severe stress concentrations leading to significant strength reduction and material damage development. However, most of the previously performed investigations focused on determining the maximum design load that a composite structure can carry using linear elastic fracture mechanics or semi-empirical methods. Internal material damage in the forms of microcracks/voids generated due to the presence of notches was ignored (Chang & Lessard 1991). Experiments in the past (Reifsnider 1982) have revealed that these local damage events can initiate at an early stage of useful life of a composite and progress as the load increases until final rupture. The initiation and the evolution of these damage mechanisms significantly affect mechanical properties, ultimate strength, failure

modes of the constituent composite layers and subsequently, performance of composite structures. Accordingly, it is important to include the effects of these defects and their evolution on an accurate evaluation of composite durability and structural integrity. Since a unidirectional composite is the basic building block of a laminated composite, its damage behavior should be examined first in order to fully understand the failure characteristics of a composite laminate.

It has been well established that unidirectional fiber reinforced composites exhibit very complex damage modes under different loading conditions. Typical damage patterns in a unidirectional composite material include matrix cracking, matrix/fiber interface debonding, fiber breakage, and their interactions. The complexity of damage modes renders an exact analytical solution describing the fine details of a particular damage event untenable. Fortunately, as early stage internal damage in composites is noncatastrophic in many situations, it is rational to consider locally averaged effect of damage. To do this, the theory of damage mechanics provides an effective analytical tool. Based on the thermodynamics of irreversible process, damage accumulation due to matrix cracking, fiber-matrix interfacial debonding, or any combination of these events at the micromechanics level can be described macroscopically through an appropriately defined set of vector- or tensor-valued internal state variables. These internal state variables are used to formulate the damage-coupled constitutive relations for

composites. The damage evolution can be monitored to quantify progressive failure in composites from the initiation and propagation of damage to eventual failure. Damage mechanics is able not only to predict stiffness loss of the composites caused by the nucleation and the growth of distributed microscopic cavities and cracks, but also to provide a solid ground for an accurate macromechanics failure analysis for composite laminates.

The purpose of this paper is to examine the damage initiation and progression in unidirectional graphite/epoxy composites containing a central circular hole subjected to off-axis uniaxial tension. With the aid of a modified finite element procedure (Chow and Yang 1994), the anisotropic damage model proposed by Chow et al. (Chow et al. 1992) is extended to study the evolution of damage as applied load increases, the effect of fiber orientation on damage development, and crack initiation behaviors of the notched composites. The present analysis is justified through the comparison between the Moiré interferometry observations and the predicted finite element results.

## 2 FORMULATIONS

The geometry of a unidirectional fiber reinforced composite plate chosen for the investigation is shown in Figure 1. The plate with dimensions of  $L$ ,  $W$  contains a circular hole of radius  $R$  located at the center of the plate subjected to a uniform far-field uniaxial tensile stress  $p$  applied at both ends. Under the loading condition, the composite specimen is in a state of plane stress, and only three stress components,  $\sigma_i$  ( $i=1,2,6$ , the contracted notation is utilized), need to be considered. Two coordinate systems, global coordinates  $x-y$  and material principal system 1-2, are set at the center of the hole.  $\theta$  stands for the fiber orientation angle between the loading direction and the maximum principal material axis.

In an earlier work by the present authors (Chow et al. 1992), damage evolution in a brittle fiber reinforced unidirectional composite under static

loading can be theoretically described as an elastic-damaged process. The residual strain of the composite after unloading is negligible compared with its total deformation. The deviation of stiffness from the elastic response of the composite is attributed to irreversible energy dissipation processes caused by the nucleation of new damage entities and the growth of existing damage entities. A damage surface in stress space, a function of the stress state and the internal damage variable  $D$ , can be introduced to distinguish between the damage processes involving material degradation and the processes of elastic unloading or reloading without damage progression. It may be expressed as

$$F(\sigma_i, D) = \sigma_o - K(D) = 0 \quad (1)$$

where  $\sigma_o$  is an equivalent stress defined as

$$\sigma_o = (R_{mn} \sigma_m \sigma_n)^{1/2}. \quad (2)$$

The coefficients  $R_{ij}$  ( $R_{ij} = R_{ji}$  is assumed) depict the influence of each stress component on the material damage state and can be determined from experiments.  $K(D)$  in equation (1) is a state function which changes as  $D$  representing the energy dissipated during a damage process develops. The increment of  $D$  is represented by

$$dD = \frac{1}{2} \sigma_i d\epsilon^d \quad (3)$$

in which  $d\epsilon^d$  represents damage strain increments.

Therefore, the damage strain increment can be estimated from the normality rule or flow rule by using the damage function  $F$ ,

$$d\epsilon_i^d = d\lambda \frac{\partial F}{\partial \sigma_i} = d\lambda \frac{\partial \sigma_o}{\partial \sigma_i} \quad (4)$$

in which  $d\lambda$  is a scalar of proportionality,

$$d\lambda \begin{cases} > 0, & \text{if } F = 0 \text{ and } \frac{\partial F}{\partial \sigma_i} d\sigma_i > 0 \\ = 0, & \text{otherwise} \end{cases}$$

and it can be determined from the consistency condition  $dF=0$ .

The effective in-plane constitutive relations of a damaged unidirectional composite at a certain damage state can be written as

$$\epsilon_i = C_{ij} \sigma_j \quad \text{or} \quad \sigma_i = S_{ij} \epsilon_j \quad (5)$$

where  $C_{ij}=C_{ji}$  is the elastic compliance at the current state,  $S_{ij}=S_{ji}$  is the current material stiffness, and  $C_{ij}$

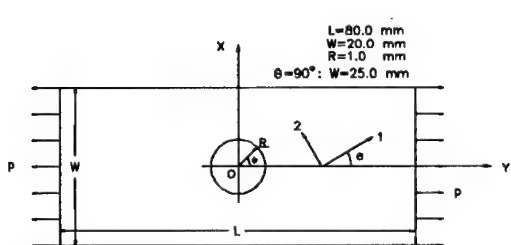


Figure 1. Unidirectional composite with a hole subjected to tension.

$= [S_{ij}]^{-1}$ . These material coefficients will change their values during a damage process. The total strain increment in a damage process is then

$$d\epsilon_i = C_{ij} d\sigma_j + dC_{ij} \sigma_j \quad (6)$$

which can be decomposed as:

$$d\epsilon_i^e = C_{ij} d\sigma_j \quad \text{and} \quad d\epsilon_i^d = dC_{ij} \sigma_j \quad (7)$$

where superscript  $e$  represents elastic components.

To establish the relationship between a damage surface and current material coefficients, it is convenient to introduce a quantity called equivalent damage strain  $\epsilon_o$  related to the energy dissipation increment  $dD$  as

$$dD = \frac{1}{2} \sigma_i d\epsilon_i^d = \frac{1}{2} \sigma_o d\epsilon_o. \quad (8)$$

The  $\sigma_o$ - $\epsilon_o$  relation is experimentally determined as

$$\epsilon_o = a \sigma_o^b - a \sigma_s^b \quad (9)$$

where  $a$  and  $b$  are material constants,  $\sigma_s$  is the equivalent stress level at the threshold of damage strain. The current compliance of a unidirectional composite during a damage process can be readily derived from equations (1), (4), (7), and (9), and expressed as (Chow et al. 1992)

$$C_{ij}(D) = C_{ij}(0) + \frac{ab}{(b-1)} \left[ \left( \frac{2(b+1)}{ab} D + \sigma_s^{b+1} \right)^{\frac{b-1}{b+1}} - \sigma_s^{b-1} \right] R_{ij} \quad (10)$$

where  $C_{ij}(0)$  denotes the virgin material compliance component, and

$$D = \frac{ab}{2(b+1)} (\sigma_o^{b+1} - \sigma_s^{b+1}) \quad (\text{for } d\sigma_o \geq 0). \quad (11)$$

These equations can be used to estimate the instantaneous values of  $C_{ij}$  and damage variable  $D$  during a damage process ( $\sigma_o \geq \sigma_s$ ). It can also be seen from equation (10) that the coefficients  $R_{ij}$  reflect the anisotropic behavior induced by material damage. For any loading processes inside the damage surface  $F$ , damage variable  $D$  and coefficients  $C_{ij}$  remain constants which are determined from the highest value of stress  $\sigma_o$  from the preceding applied load histories involving material damage progression.

From equations (6), (7), and (9), the constitutive relationship between the elastic-damaged stress increments and the total strain increments can be derived as

$$d\sigma_i = S_{ij}^{ed} d\epsilon_j \quad (12)$$

where  $S_{ij}^{ed}$  is the elastic-damaged instantaneous tangent modulus expressed as

$$S_{ij}^{ed} = S_{ij}(D) - \frac{ab\sigma_o^{b-3} S_{ip}(D) R_{pq} \sigma_q R_{uv} \sigma_v S_{uj}(D)}{1 + ab\sigma_o^{b-3} R_{st} \sigma_s S_{tl}(D) R_{lk} \sigma_k}$$

Usually,  $S_{ij}(D)$  in this equation also depends upon the previous damage histories as shown in equation (10).

Equations (5), (10), and (12) provide a constitutive description for the elastic-damaged behavior of a unidirectional composite material in the material principal system. The off-axis stress-strain relationship depending on the composite fiber orientation can be readily obtained through coordinate transformation rules.

### 3 FAILURE CRITERION

The development of an accurate failure analysis of composite materials requires not only a proper damage mechanics model characterizing material degradation due to damage as described above but also a set of failure criteria for the final failure mode. In-plane failure of a unidirectional composite can generally be classified into matrix dominant failure and fiber dominant failure. For the unidirectional fiber composites under static loading, experiments have found that the major portion of the load is carried by the fibers when loaded in the fiber direction, and the failure of the composite in the fiber direction is dominated by the ultimate strength of the fibers. Therefore, it is reasonable to assume that  $d\epsilon_i^d = 0$  along the fiber direction, which leads to  $R_{ij}=0$  ( $j=1, 2, 6$ ) in equation (2). For fiber failure, the failure criterion is thus postulated as

$$\epsilon_i = \epsilon_f \quad (13a)$$

where  $\epsilon_f$  is the fiber strain failure level.

On the other hand, when loaded in an off-axis direction, the matrix cracking and the fiber/matrix interface debonding become the dominant failure modes. Typically, the matrix cracking and fiber/matrix debonding occur in concert to produce transverse macrocracks aligned to the fiber direction. For resin matrix composites, this mode of failure is usually observed prior to other types of failure modes. Thus, final failure in the matrix or at the fiber/matrix interface occurs when the accumulated damage reaches a critical value, i.e.,

$$D = D_c \quad (13b)$$

where  $D_c$  is the critical damage at the threshold of a macrocrack initiation. The failure criterion is postulated in a way that the direct effect of the fiber reinforcement and thereby fiber failure has been decoupled from the type of failure that represents the matrix and fiber/matrix interaction, including the possible effect of the interface debonding.

#### 4 NUMERICAL ANALYSIS

To provide an analytical tool to examine the in-plane damage behaviors of various notched composite coupon specimens as shown in Figure 1 up to failure initiation, the proposed constitutive model and the corresponding numerical integration algorithms for the incremental load-deformation analysis have been discretized and implemented in a general-purpose nonlinear finite element program (Chow & Yang, 1994). The finite element procedure is developed based on the conventional displacement method. The unidirectional fiber reinforced composite is modeled as macroscopically continuous, homogeneous, and damage coupled orthotropic medium. Due to the inherent nonlinearity of the stress-strain relationship, the composite stiffness matrix is not constant but depends upon the previous loading histories, current stress state, and fiber orientation. The nonlinearities in the finite element equations are handled with the modified Newton-Raphson iteration procedure. All stress, strain, and damage quantities are monitored at each Gaussian integration point within each element. For each iteration at a given load increment, all the stresses at an integration point are formulated in a form of the damage function in equation (1) or the failure criterion in equation (13), in order to check the threshold condition of damage initiation or failure, respectively.

In the case of damage progression, a radial return algorithm with smaller strain increment is adopted for the integration of elastic-damaged constitutive equations. It is necessary to modify the stiffness matrix during the computation for a progressive damage process. For the entire loading process, this procedure is repeated until the failure criterion is fulfilled at certain integration points. Once failure is detected, fiber failure or matrix failure (which includes matrix/fiber interface debonding) can be separately identified. The computation is then terminated, and macrocracks are considered to initiate at these locations.

Theoretical calculations for the problem are performed with the two-dimensional finite element algorithm. The finite element analysis gives the stress-strain distribution of the entire composite plate. In particular, the stress concentrations around the hole play an important role in predicting damage development and crack initiation. In order to show the convergence of the numerical analysis results,

several finite element meshes having the same design but differing in element dimensions and number of elements are considered. The computing time varies significantly from one mesh design to another depending on the number of elements. Although a finer mesh leads to a more accurate prediction of the damage progression than a coarse mesh does, it suffers from a lengthy computing time. The increase in computing time may not justify the increase in accuracy after the number of elements reaches a certain value. Here, because of the non-symmetrical nature of the specimen, the whole off-axis unidirectional composite was modeled with 320 in-plane isoparametric elements totaling 1032 nodes after a careful study on the effects of the different mesh sizes. Around the hole area, the finite element mesh was refined as shown in Figure 2. Incremental loading step is carefully selected to be small enough to better predict the damage accumulations in a specimen and to capture the damage progression but large enough to avoid a lengthy and unnecessary computing time. The failure criterion described equation (13) is checked at all times to determine the onset of failure, i.e., a macrocrack formation.

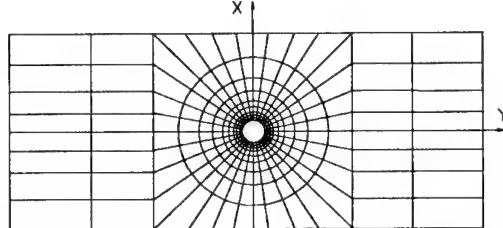


Figure 2. Finite element modeling.

#### 5 EXPERIMENTS

In order to check the validity and accuracy of the proposed damage behavior prediction procedure, comparison between experimental measurement and theoretical analysis on the response of composites is performed. The composite material chosen for the investigation was made of 648 epoxy matrix reinforced by 65 volume percent of T300 graphite fibers. The composite specimens were machined from the unidirectional composite panels with inclined angles to produce specimens of different fiber orientations. Thin aluminum plates were bonded to both ends of each composite specimen for reinforcement so that the specimen can sustain necessary gripping force.

To evaluate the material constants and the corresponding in-plane related damage coefficients required for the subsequent numerical analysis, a

series of uniaxial tests for standard tensile specimens with fibers oriented along  $\theta=0^\circ, 22.5^\circ, 45^\circ, 67.5^\circ$ , and  $90^\circ$  were performed first. All the off-axis test specimens were loaded quasi-statically. The axial strains were measured with strain gauge and extensometer, and the axial stresses were evaluated from the applied load divided by the current cross-section area of the specimen. The unloading tests confirmed that the residual deformation of the specimens was very small and could be considered negligible as compared with the total resulting strain. These tests also indicated that the composite specimen after damage initiation can be treated as an orthotropic medium in a principal axis system. Therefore, for the in-plane case, only  $R_{66}$  needs to be determined as  $R_{22}=1$  can be readily realized if the loading direction is perpendicular to the fibers. The measured  $\varepsilon_x-\sigma_x$  relationship of any two fiber angles was used to evaluate  $R_{66}$  and the function  $\varepsilon_o(\sigma_o)$ . Results from the tests at other fiber angles were recorded and served to check the accuracy of the evaluated  $R_{66}$ . The measured properties of the initial undamaged composite were determined at low load level and found to be

$$E_{11}(0) = 125.1 \text{ GPa}, \quad E_{22}(0) = 11.1 \text{ GPa}$$

$$v_{12}(0) = 0.338, \quad G_{12}(0) = 3.3 \text{ GPa}.$$

The corresponding material coefficients in equations (9), (10), and (13) are

$$a = 0.114 \times 10^{-4}, \quad b = 1.242, \quad \sigma_s = 9.0 \text{ MPa}$$

$$\varepsilon_f = 0.092, \quad D_c = 2.54 \times 10^3 \text{ Pa}$$

$$R_{11} = R_{12} = R_{16} = R_{26} = 0, \quad R_{22} = 1, \quad \text{and } R_{66} = 1.9.$$

These material coefficients describing the anisotropic damage characteristics of the composites are required as input for the finite element program.

The second set of the experiments was concerned with crack initiation and failure mechanisms in unidirectional graphite/epoxy composites containing a central circular hole subjected to off-axis uniaxial tension. To verify the accuracy of the damage formulation, the finite element predictions of the deformation and damage distributions in the specimens were compared with the results obtained from Moiré interferometry method. The design of a moiré interferometry device (Asundi & Yang, 1993) is shown in Figure 3. A video camera was zoomed in to observe the localized hole area and to examine the details of damage around the edge of a central hole while a photographic camera monitored the global response of the specimen. Moiré fringe patterns were captured periodically for subsequent image analysis. A computerized image processing system was employed to quantitatively evaluate the displacement field as well as strain distribution based on the moiré

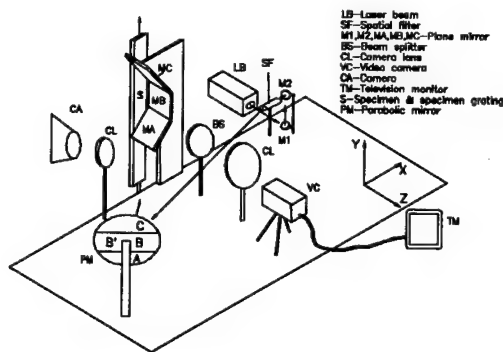


Figure 3. Moiré interferometry device.

patterns of the specimen at a certain load level. The system adopts a fast Fourier transform (FFT) technique which allows brightness function of a moiré image pattern to be Fourier-transformed and isolates the frequency components of the image containing displacement information.

## 6 RESULTS

Quantitative evaluation of the Moiré patterns taken from the experiment was performed by employing an image processing software. As an example, only one strain component distribution,  $\varepsilon_{yy}$ , along the x-axis for a  $90^\circ$  specimen is presented here. The same procedure can also be applied to obtain other strain components. In Figure 4, the predicted and measured results of the strain component,  $\varepsilon_{yy}$ , along the x-axis are compared for the  $90^\circ$  specimen under the load of 8.8 MPa. Under the

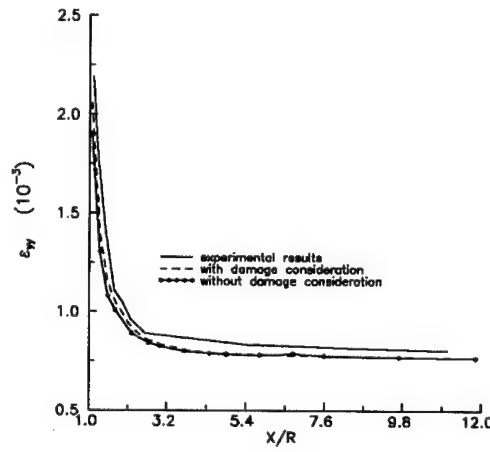
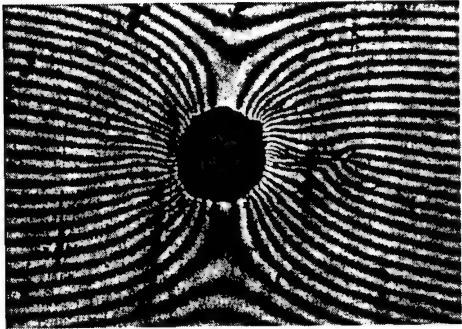
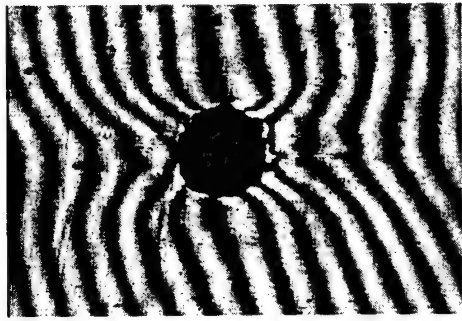


Figure 4. Strain  $\varepsilon_{yy}$  along x-axis for  $90^\circ$  specimen.



(a) V-field patterns

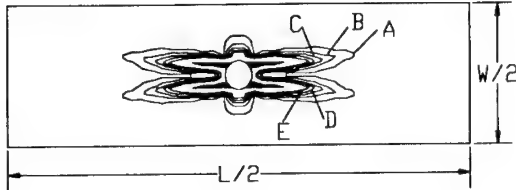


(b) U-field patterns

Figure 5. Fringe patterns for 90° specimen.

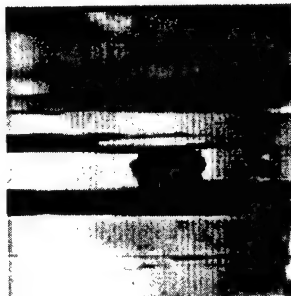
same external load, predictions from conventional linear elastic theory with the original undamaged material stiffness are also included. It can be observed that the damage theory produced a higher strain concentration effect due to material damage, and yielded more accurate prediction than that based on the conventional linear elastic theory without damage considerations. The discrepancy becomes more pronounced near the edge of the hole. The strain concentration effect is, as expected, enhanced due to damage. The difference in strain magnitude between linear elasticity and nonlinear damage theory becomes more significant with increased damage at higher applied loading.

Figures 5(a) and 5(b) depict the localized v and u moiré fringe patterns of the 90° specimens corresponding to, respectively, y and x directions at the load of 15.84 MPa. It can be observed from the figure that both v and u patterns show significantly dense fringes at the immediate vicinity of the hole, displaying a narrow zone of strain concentration. Examination of the moiré fringe patterns taken from



(a)

A: 0.1; B: 0.59; C: 1.08; D: 1.56; E: 2.05; (KPa)



(b)

Figure 6. Damage contours and a failed 0° specimen.

the experiments reveals that as the load increases, there is a corresponding increase in strain concentration near the hole area; however, the fringe pattern elsewhere remains uniform and smooth. At higher loads, the strain concentration zone continues to display a similar but enlarged narrow zone at the hole edge, expanding perpendicular to the loading direction. Similar observations can also be made for other specimens with different fiber orientations in terms of narrow band of strain concentration with increasing magnitude of applied load. Abrupt change in the moiré fringe pattern near the hole edge representing a macrocrack emergence can also be readily observed from the figure.

The damage model was extended to examine not only damage initiation and propagation, but also macro-crack initiation or failure in the composite specimens. For the sake of illustration, the damage contours of the 0° composite specimen at the load of 250 MPa are selected and shown in Figure 6(a). For this specimen, damage is first observed at the location of  $\phi=64.9^\circ$  (or  $115.1^\circ$ ,  $-64.9^\circ$ , and  $-115.1^\circ$ , due to the symmetry of the composite) on the hole edge where the calculated applied stress  $p$  is 35.95 MPa. Theoretical analysis indicates that the combination of normal and shear stress components at that location produces the highest equivalent damage stress within the specimen. Damage value of

this location increases with increase in applied load, and then expands to form a damage zone along the loading direction, the weakest region in the composite. The damage is always confined to an area at close proximity of the stress concentration. It is worth noting that the mechanical properties of the material elements within the damage zone change due to damage initiation and growth upon loading. The overall damage at a particular location can be calculated based on the damage evolution from the damage-coupled finite element analysis. When the overall damage reaches a critical value, which is a material constant, the material element is said to be ruptured to produce a macrocrack. From the damage zone pattern, it can be observed that a macrocrack appears at the damage initiation point and the angle of crack propagation is along the applied loading direction. Careful examination of the failure mode uncovers the fact that failure is initiated in matrix or fiber-matrix interface and the specimen finally fails due to the crack propagation along the fiber direction. The failure behavior can be readily observed from Figure 6(b). The observation also confirms the validity of the finite element analysis result.

The same analysis and test procedures were also applied to the composite specimens with different fiber orientations. Figure 7 illustrates the relationship between the failure initiation position and fiber orientations of the composite specimens with a central hole subjected to off-axis tension. The computer simulated results in Figure 7 are in close agreement with the experimental findings.

## 7 CONCLUSIONS

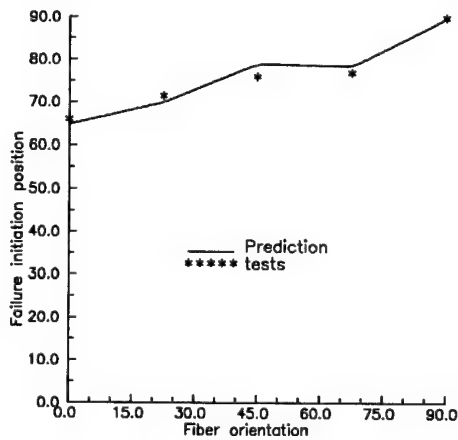
This paper presents an investigation in examining a progressive damage model with respect to crack

initiation and failure mechanisms in unidirectional graphite/epoxy composites containing a central circular hole subjected to off-axis uniaxial tension. Once damages occur in a material element, the stiffness degradation results. This phenomenon is fully characterized by the damage-coupled composite constitutive relations. The effective global stiffnesses are recalculated to include the effects of the material degradation, through which, the redistribution of stress can then be computed. The results of this model include the whole field stress-strain relationship, the composite stiffness degradations, and the extent of damages at any stress level. Two failure modes are distinguished: fiber failure dominant and matrix failure dominant including the fiber/matrix debonding. Both theoretical analysis and experimental observations have found that failure of the composite material near the hole area takes place within a damage zone. A macrocrack initiates at a material point at the hole boundary when the damage reaches its critical value and propagates along the direction of the extended damage zone in a matrix-dominated failure mode. The predicted results are in good agreement with those observed experimentally, thus verifying the validity and accuracy of the proposed damage model for damage and failure characterization in the notched unidirectional composite plates. The damage model is now being extended to characterize the damage mechanisms and failure behaviors of laminated composite structures and preliminary results have shown promise.

## REFERENCES

- Asundi, A. & Yang, F. 1993. Moiré Interferometry Strain Analysis Using FFT Technique for Fiber Reinforced Composite Laminates with Hole. *Composite Properties and Applications*, A. Miravete (ed.), *Proceedings of the 9th Int. Conf. on Composite Materials (ICCM/9)*, Madrid: 874-881.
- Chang, F.K. & Lessard, L. 1991. Damage Tolerance of Laminated Composites Containing an Open Hole and Subjected to Compressive Loading. *J. of Composite Materials*, 25: 2-13.
- Chow, C.L. & Yang, F. 1994. Inelastic Finite Element Analysis of Fiber Reinforced Composite Laminates with Damage. *Durability, and Damage Tolerance*, ASME AD. 34:111-136.
- Chow, C.L., Yang, F., and Asundi, A., 1992, "A Method of Nonlinear Damage Analysis for Anisotropic Materials and Its Application to Thin Composite Laminates", *Int. J. of Damage Mechanics*, Vol.1, pp.347-366.
- Reifsnider, K.L., Ed., 1982, "Damage in Composite Materials: Basic Mechanisms, Accumulation, Tolerance, and Characterization", ASTM STP 775.

Figure 7. Failure initiation position vs. fiber angle.



## Recent developments in damage mechanics of composite materials

R.Talreja

*School of Aerospace Engineering, Georgia Institute of Technology, Atlanta, Ga., USA*

**ABSTRACT:** This paper reviews some results of the efforts made by the author's research group and collaborators in applying damage mechanics to durability assessment of composite materials. The results are grouped in categories of damage initiation, stiffness-damage relationships, and damage evolution. Emphasis is placed on incorporating the actual damage mechanisms and real microstructures into continuum formulations of material response. The long term perspectives of this approach are then discussed.

### 1 INTRODUCTION

Increased applications of composite materials depend on their being made more cost-effective without compromising their safe and reliable performance. Since manufacturing related cost makes up the dominant part of life cycle cost of most composite structures, and since most composite structures are designed for long term performance, it appears that the way to achieving increased applications lies in connecting analysis of manufacturing processes with durability assessment. The field which can facilitate this connection is damage mechanics. However, damage mechanics in its conventional form must be modified to achieve this goal. The modification needed consists of providing an "opening" in the response function formulations through which details of the microstructure (phase and defect distributions) can be entered. This way connection with manufacturing processes, which result in the actual microstructure, can be made. Furthermore, when durability assessment with damage mechanics has been made, the result of that assessment can be taken as a feedback to improve the manufacturing processes.

At the DURACOSYS 95 conference this author presented a synergistic damage mechanics approach which enters selected micromechanics results through the "opening" in the response function formulation (Talreja 1996). The main advantage of the approach, as demonstrated in that paper, was that the burden of determining material coefficients in the stiffness-damage relationships was reduced. Further results, obtained since then, will be reviewed below. These results demonstrate that without the "opening" a continuum damage formulation risks becoming merely a formalistic structure for describing material response.

In view of the need to connect manufacturing process analysis with durability assessment mentioned above, some results of the approach being taken by the author's research group and collaborators to relate damage initiation in "real" microstructures (as against assumed ones) will also be described below. These results indicate that assuming uniform distributions or distributions of assumed random functions for microstructural entities may not suffice in determining initiation of damage under thermal or mechanical loading. The specific case of fiber/matrix debonding and radial matrix cracking resulting from transversely loaded unidirectional composites will be described.

Finally, evolution of damage which underlies changes in response of composites under thermal or mechanical loads will be discussed. The focus here is on effects of initial defect patterns on damage evolution. The ongoing activities in this area will be summarized and directions of further pursuit will be pointed out.

### 2 DAMAGE INITIATION

The cause of the first event of failure at the micro level (i.e. damage initiation) in composite laminates is often assumed to be debonding of fibers from matrix in an off-axis ply. However, our recent results (Asp, Berglund and Talreja, 1996a,b,c) indicate that this may not always be true. In these papers it is shown that in composites with a glassy polymer (e.g., epoxy) as matrix, the first event of failure may be cavitation induced brittle cracking rather than debonding. A criterion for cavitation induced brittle cracking is proposed to be the dilatation energy density reaching a critical value, and it is shown that this criterion can predict

transverse failure of unidirectional glass/epoxy composites. In a matrix material where cavitation is not likely, e.g., in a ceramic at room temperature, debonding and radial matrix cracking are the main mechanisms of damage initiation.

In the context of connecting processing and durability, it is important to deal with the nonuniformities of fiber distributions resulting from a given process with regards to their effects on damage initiation. One such effort was made by Sørensen and Talreja (1993). There, periodic clusters of fibers were considered and it was shown that significant changes in local residual stresses resulted from thermal cooldown of unidirectional ceramic matrix composites. Later, coatings and interphases in these materials were considered and their effects were clarified by a parametric study (Sørensen and Talreja 1994). In current studies concerning damage initiation actual fiber distributions resulting from a commercial type process for manufacturing ceramic fiber reinforced glass-ceramic are being incorporated (Bulsara, Talreja and Qu, submitted). In these studies local disorder in fiber distribution is described by a radial distribution function (also known as the pair distribution function) given by (Ripley 1977),

$$g(r) = \frac{A}{2\pi r N} \frac{dK(r)}{dr}, \quad (1)$$

where

$$K(r) = \frac{1}{N(r)} \sum_{k=1}^{N(r)} I_k(r) \quad (2)$$

and

$$dK(r) = K(r + dr) - K(r) \quad (3)$$

where  $K(r)$  is a descriptor of the fiber centroid distribution, called the second-order intensity function,  $I_k(r)$  is the number of fiber centroids within a circle of radius  $r$  (not counting the central fiber) and  $N(r)$  is the total number of fibers within the viewing area  $A$ .

The function  $g(r)$ , as determined by image analysis of cross-sections of a unidirectional SiC fiber reinforced glass-ceramic, is shown in Fig. 1 and the corresponding typical cross-section is shown in Fig. 2. This function provides information concerning the intensity of inter-distances of fibers. Thus, local maxima and minima in  $g(r)$  represent most frequent and least frequent occurrences, respectively, of these distances. If the fiber distribution results from a random Poisson process,  $g(r) = 1$  at all  $r$ . Whenever  $g(r) > 1$ , the fibers are more frequently present at

that  $r$ -value (i.e., within a circle of radius  $r$ ) than in the random Poisson process. In a statistically homogeneous pattern of fibers  $g(r)$  will approach unity at large  $r$ . Suppose the value of  $r$  at which this occurs is  $r_0$ , then the range of the local disorder is given by  $0 < r < r_0$ . For further discussion on this subject see Pyrz (1994).

We have used a scheme to generate realizations of microstructure (i.e., patterns of fiber distribution) that have equivalency to the actual microstructure in terms of the function  $g(r)$ , i.e. all realizations have the same  $g(r)$  as that of the actual microstructure. The scheme, described in Bulsara, et al. (submitted), generates realizations of the same  $g(r)$  with different  $\theta$ -distributions, where  $\theta$  measures the angle the line joining a fiber centroid and the central fiber centroid makes with a reference direction. Incorporation of several assumed  $\theta$ -distributions in the simulation scheme allows studying the influence of the orientation effects which are not captured in the function  $g(r)$ .

Unit cells containing the simulated fiber patterns are then investigated for their damage initiation characteristics by a finite element method. A unit cell is subjected to a uniaxial tensile load normal to the fiber axis or is allowed to contract under a uniform thermal cooldown. In both cases the local stress states are examined and failure criteria are applied to ascertain initiation of debonding and radial matrix cracking. Statistics are gathered in terms of the average number of fibers which debond or initiate radial cracks, and the fraction of this number with respect to the total number of fibers in a unit cell is then plotted against the assumed critical failure stress (strength). Figures 3 and 4 give two illustrative examples of the results of this analysis. Figure 3 relates to the case of thermal cooldown by 1000 °C and shows how the fraction of fibers with debonds increases with decreasing strength of the interface. (The x-axis in this plot is the assumed interfacial strength expressed as fraction of a reference value.) The various cases indicated in the legend are for the same  $g(r)$  with four different  $\theta$ -distributions, a uniform random distribution and a uniform distribution with periodic spacing of fibers. The differences in the damage initiation behavior are notable. For instance, the simulated cases of the actual fiber distribution produce earlier damage initiation than the random distribution case. The periodic fiber distribution causes no damage at the values shown; however, this occurs at higher values. Figure 4 shows the case of uniaxial tensile loading with the overall strain of 0.1 percent. Here the entire range of debonding is plotted in order to highlight the difference between the case of periodic fiber distribution and the other cases.

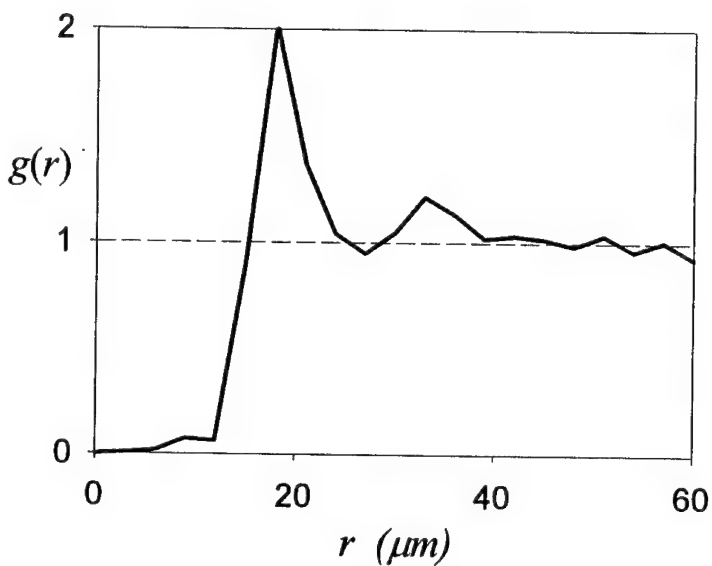


Fig. 1. The radial distribution function  $g(r)$  of a ceramic fiber reinforced glass-ceramic.

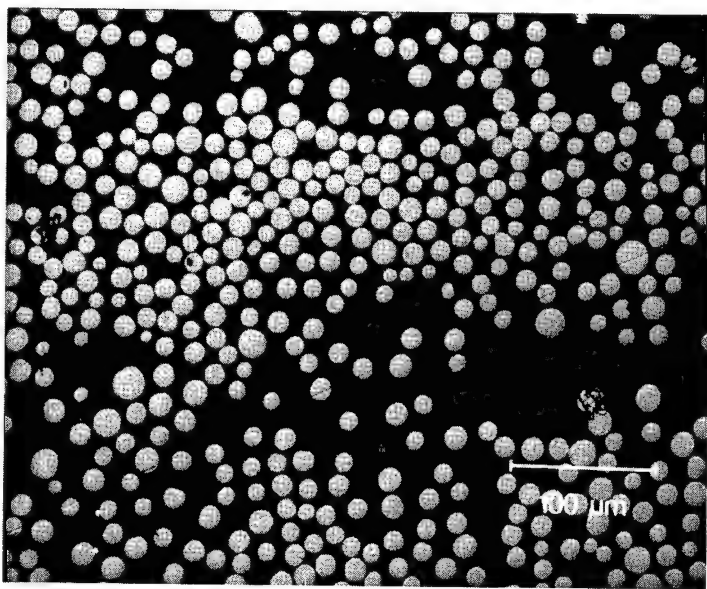


Fig. 2. Cross section of a ceramic fiber reinforced glass-ceramic corresponding to the radial distribution function in Fig. 1.

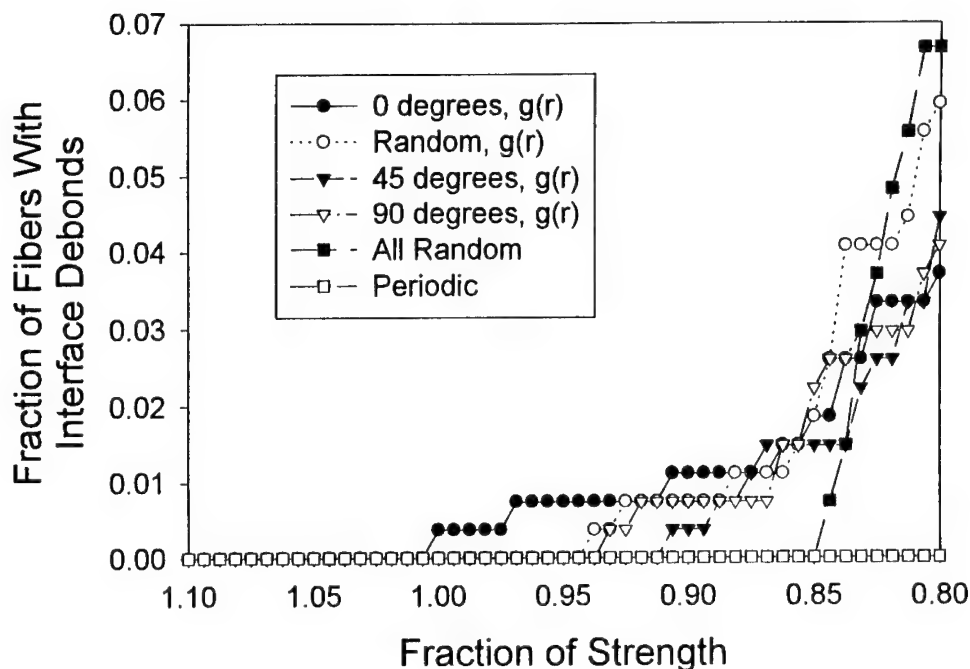


Fig. 3. Fraction of fibers with fiber/matrix debonds under a 1000 °C cooldown against decreasing interfacial bond strength for a ceramic fiber reinforced glass-ceramic.

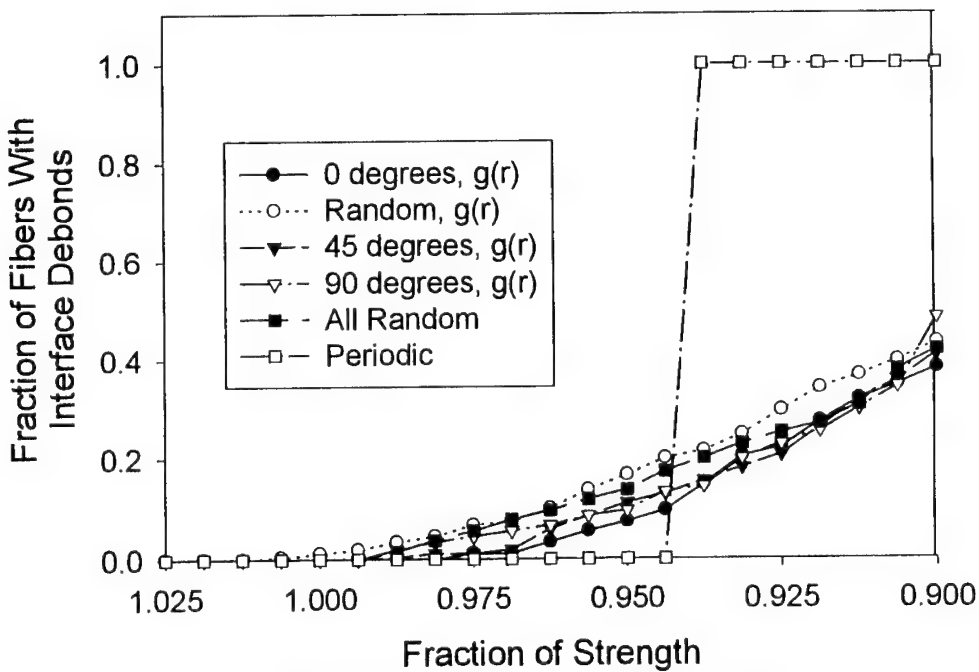


Fig. 4. Fraction of fibers with fiber/matrix debonds under an imposed mechanical strain of 1 percent against decreasing interfacial bond strength for a ceramic fiber reinforced glass-ceramic.

### 3 STIFFNESS-DAMAGE RELATIONSHIPS

In the previous DURACOSYS paper (Talreja 1996) a synergistic damage mechanics (SDM) approach was proposed which combines continuum damage mechanics (CDM) and micromechanics in a manner that retains the advantage of CDM while utilizing micromechanics to improve the implementation of CDM. The approach was demonstrated for  $(\pm\theta, 90_2)_s$  laminates where the opening displacement of transverse cracks calculated by a simple micromechanics analysis was utilized to reduce the necessity of determining several material constants. Later, the crack opening displacement was determined experimentally for the same laminates and its use in stiffness prediction was demonstrated (Varna, Akshantala and Talreja, submitted). In further studies conducted since that work it has been found that the SDM approach not only improves implementation of CDM but can also provide physical basis for generating proper CDM formulations. This will be explained further below by reviewing some results of these studies.

Consider laminates of lay-ups given by  $(0, +\theta_n, -\theta_n, 0_{1/2})_s$ . The  $\theta$ -plies in the sublamine  $(+\theta_n, -\theta_n)$  have equal deformational constraints from either side when the laminate is loaded along an axis of symmetry. Under an axial tension load, the  $\theta$ -plies experience in-plane stresses consisting of a shear stress and normal stresses parallel to and perpendicular to the fiber direction. The stress perpendicular to fibers may be tensile or compressive depending on the angle  $\theta$ . Thus, the  $\theta$ -plies may crack if this stress exceeds a threshold tensile stress, and remain uncracked for all angles  $\theta$  for which this stress is compressive. When the  $\theta$ -plies crack the deformational constraint from the neighboring plies will cause multiple cracking due to a process commonly described as shear-lag. The overall laminate moduli will change permanently as a result of the surface energy dissipated by formation of these cracks. When the normal stress perpendicular to the fibers is compressive, the shear-lag process and the consequent multiple ply cracking are not expected to come into effect. Therefore, the laminate unloading moduli would not be expected to change from the initial elastic moduli. However, experimental work conducted and to be reported elsewhere (Varna, Akshantala and Talreja, in preparation) showed laminate unloading moduli to change even for this case. The fact that no cracks formed in the  $\theta$ -plies was confirmed by direct observations under a microscope as well as by an edge replication technique.

It was thought that in the absence of ply cracks a most likely mechanism to cause changes in the laminate unloading moduli could be shear-induced degradation of the fiber/matrix interface. This

possibility was investigated by testing  $(+\theta_n, -\theta_n)_s$  laminates under axial tension for the  $\theta$ -angles which induce predominantly in-plane shear stresses. Assuring that no matrix cracks existed the laminate unloading moduli were measured at increasing strains. Significant changes in these moduli were found. The in-plane shear modulus degradation versus in-plane shear strain is shown in Fig. 5 as derived from testing a glass-epoxy  $(40_4, -40_4)_s$  laminate. Using these data as input the unloading moduli of a glass-epoxy  $(0, +25_4, -25_4, 0_{1/2})_s$  laminate are predicted and compared with experimental data in Figs. 6 and 7.

The results described above have profound repercussion concerning damage mechanics modeling. Firstly, the results demonstrate that prediction of moduli changes performed solely on phenomenological bases has limitations. For instance, CDM in its conventional form would be unsuccessful for the  $(0, +\theta_n, -\theta_n, 0_{1/2})_s$  laminates if the material constants are derived using  $\theta$  that falls in the range of multiple matrix cracking and prediction of moduli changes is made for  $\theta$  that falls outside this range. Also, unless specific physical mechanisms are associated with definition of damage variables, treatment of damage evolution and the resultant response changes by a CDM formulation would be in risk of diverging from the actual material behavior. This last remark is meant to sound caution directed to approaches that define damage variables in terms of stiffness changes.

The SDM approach proposed by this author (Talreja 1996) and discussed above is capable of avoiding the risks and limitations just discussed. This is because of the "window" provided in this approach to enter micromechanics results. The process of conducting the operation necessary to enter micromechanics results assures that the actual physical mechanisms are properly accounted for.

### 4 DAMAGE EVOLUTION

Stiffness-damage relationships discussed above relate altered stiffness properties to given states of damage. These relationships must be augmented by rate equations describing evolution of damage under imposed loading. There are several ways to accomplish this. In a CDM framework one can relate the thermodynamic forces conjugate to the internal variables (damage) to those variables. These "cause-effect" relationships can be obtained experimentally (e.g., Allix, Ladeveze, Le Dantec and Vittecoq, 1990). It should be noted that such relationships are not unique in the sense that if the damage variables are defined differently, then different relationships will result. In any damage evolution process, the rate of energy dissipation

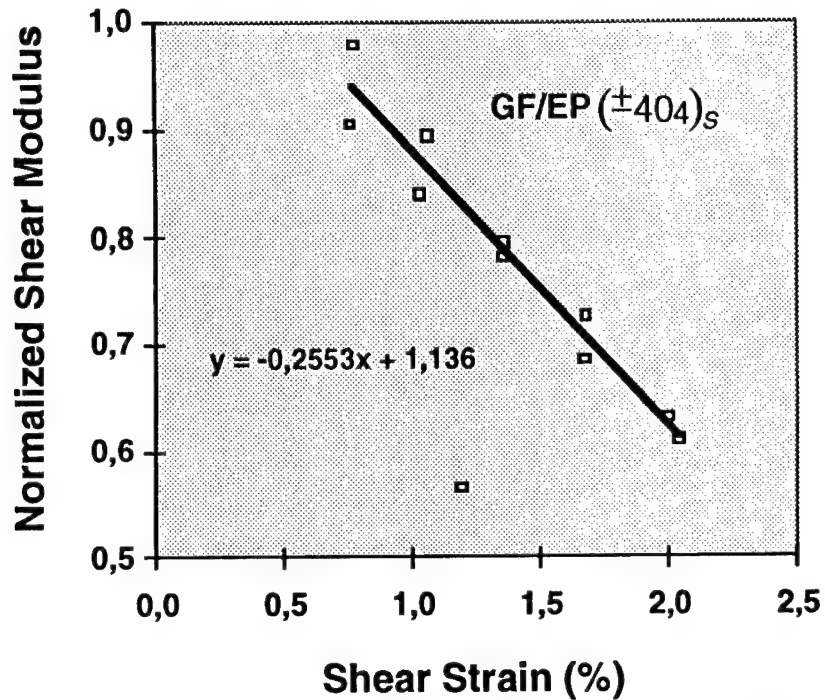


Fig. 5. The unloading ply shear modulus of glass-epoxy, normalized by its initial value, plotted against the in-plane shear strain, as derived from the measured unloading axial modulus of  $(\pm 404)_S$  laminate.

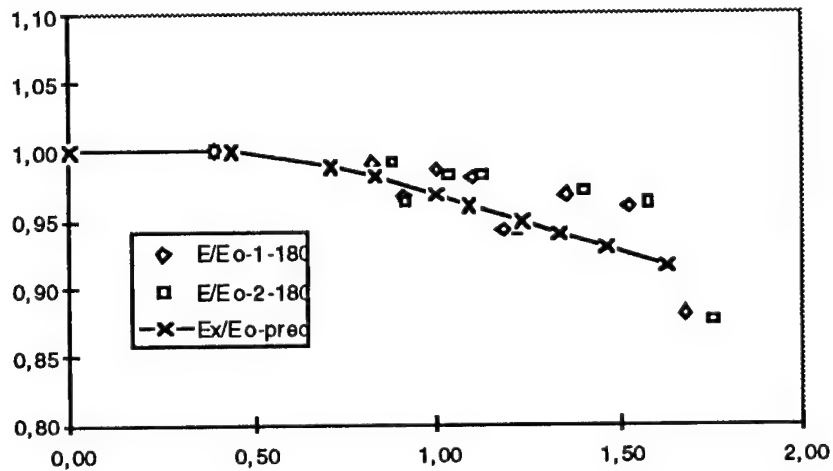


Fig. 6. Axial Young's modulus for  $(0, \pm 274, 0_{1/2})_S$  laminate normalized by its initial value, against the applied axial strain, predicted by accounting for the in-plane shear modulus degradation and compared to experimental results.

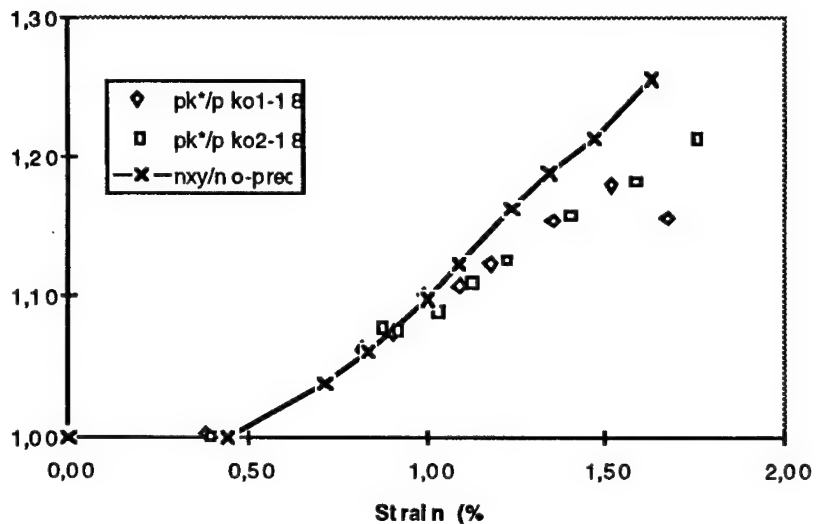


Fig. 7. Axial Poisson's ratio for  $(0, \pm 27.4, 0_{1/2})_8$  laminate normalized by its initial value, against the applied axial strain, predicted by accounting for the in-plane shear modulus degradation and compared to experimental results.

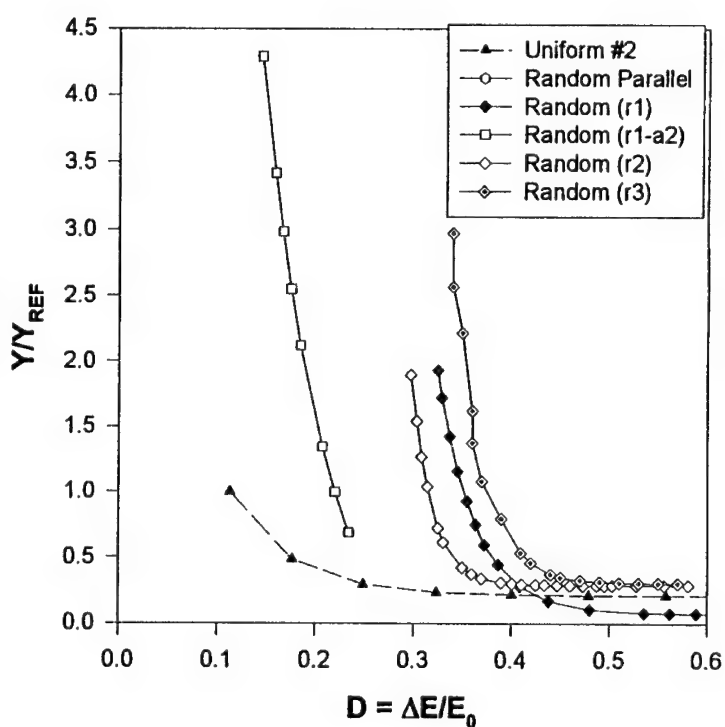


Fig. 8. The thermodynamic force Y conjugate to the damage variable D plotted against the damage variable D for evolution of different initial crack patterns.

must, however, comply with the internal dissipation inequality resulting from the second law of thermodynamics. (See Rice, 1971 for general cases and Talreja, 1990 for damage in composites.) Damage evolution relationships formulated only with this restriction do not necessarily provide information regarding the nature of the underlying mechanisms, except, perhaps, in simple cases such as transverse cracking in cross ply laminates. In particular if damage variables are defined in terms of stiffness changes, then the information concerning mechanisms of damage progression cannot always be derived from the evolution equations. The recent results on stiffness changes in  $(0, +\theta_n, -\theta_n, 0_{1/2})_s$  laminates, described above, illustrate this point clearly.

An alternative way to deal with damage evolution is to perform micromechanics, i.e., to analyze local stress states and apply appropriate failure criteria for evaluation of further damage. However, analytical determination of local stress states, even in approximate forms, is only possible for simple damage configurations such as transverse cracks in symmetrical cross ply laminates with or without associated delamination. It is safe to assume at this point that if micromechanics is to be a vehicle for describing damage evolution, a heavy reliance on numerical schemes is unavoidable. Although computational facilities available today do not set limitations in going this way, the efficiency and usefulness - in an engineering sense - of such an approach are questionable.

As discussed previously in the context of stiffness-damage relationships, a good case can be made for synergistic damage mechanics also for damage evolution. The CDM formulations are powerful integrators and carriers of micro level processes to descriptors of macro level response. The efficiency in achieving this can be at the cost of losing sight of the physics of damage progression if the damage variables and the associated rate formulations chosen do not permit incorporating specific micro level information. In particular, as pointed out above, if damage variables are taken as macro level stiffness changes, then if different configurations of micro level damage entities produce same stiffness changes, their rates of evolution cannot be distinguished from one another.

Recent and ongoing research, in which this author is involved, is aimed at generating CDM formulations which will be capable of reflecting the underlying damage evolution mechanisms. Realizing that density type measures of damage (e.g., crack number density and void volume fraction), and equivalently, the macro level stiffness changes, cannot distinguish between evolution characteristics of different patterns of damage, a systematic study was launched to clarify damage patterning effects on evolution. Some results of that study have been reported in two papers (Lacy, McDowell, Willice

and Talreja, 1997 and Lacy, Talreja and McDowell, 1997). One key result of that study is that the thermodynamic forces conjugate to crack density or stiffness based damage variables relate differently to these variables for different initial crack patterns during their evolution. This result is illustrated in Fig. 8 where the thermodynamic force  $Y$  is plotted against  $D$  defined as the normalized Young's modulus change for different crack patterns ranging from uniform parallel cracks to random parallel cracks to randomly oriented cracks of different sizes.

## 5 CONCLUSION

This paper has reviewed and discussed damage mechanics approaches aimed at durability assessment of composite materials. Key results of recent and ongoing studies have been presented in three related areas: damage initiation, stiffness-damage relationships and damage evolution. It has been argued that in order to meet the need of making composite structures cost-effective, damage mechanics approaches and formulations should have the capability to specifically and quantitatively account for processing induced defects and microstructures so that feedback rooted in long term performance assessment can be provided to processing techniques. A synergistic damage mechanics which is suited for component level durability analysis and, at the same time, has capability to incorporate micromechanics based analyses of damage initiation and evolution has been advocated for this purpose. Future work will report further progress in this direction.

## ACKNOWLEDGMENT

The work reported here has contributions from many individuals. It has benefitted from a long term collaboration with Lars Berglund and Janis Varna at Luleå University and with David McDowell and Jianmin Qu, both colleagues at Georgia Tech, and from persistent efforts of research associates N. Akshantala, L. Asp (Luleå), V. Bulsara, T. Lacy and P. Willice.

## REFERENCES

- Allix, O., Ladeveze, P., Le Dantec, E., and Vittecoq, E., 1990, "Damage Mechanics of Composite Laminates Under Complex Loading", In J. P. Boehler, (ed.), *Yielding, Damage and Failure of Anisotropic Solids*, 551-569. London: Mechanical Engineering Publications.
- Akshantala, N.V., and Talreja, R., "A Mechanistic Model for Fatigue Damage Evolution in Composite Laminates", submitted.

- Asp, L. E., Berglund, L. A. , and Talreja, R., 1996, "A Criterion for Crack Initiation in Glassy Polymers Subjected to a Composite-Like Stress State", *Composites Science and Technology*, 56: 1291-1301.
- Asp, L. E., Berglund, L.A., and Talreja, R., 1996, "Prediction of Matrix-Initiated Transverse Failure in Polymer Composites", *Composites Science and Technology*, 56:1089-1097.
- Asp, L. E., Berglund, L.A., and Talreja, R., 1996, "Effects of Fiber and Interphase on Matrix-Initiated Transverse Failure in Polymer Composites", *Composites Science and Technology*, 56: 657-665.
- Bulsara, V.N., Talreja, R., and Qu, J., "Damage Initiation Under Transverse Loading of Unidirectional Composites with Arbitrarily Distributed Fibers", submitted.
- Lacy, T.E., Willis, P.A., McDowell, D.L., and Talreja, R., "Crack Patterning Effects in Evolution of Damage", *Int J Damage Mechanics*, 6, 1997, p. 62.
- Lacy, T.E., Talreja, R., and McDowell, D.L., "Effects of Damage Distribution on Evolution", 1997, In D. L. McDowell, (ed.), *Applications of Continuum Damage Mechanics to Fatigue and Fracture*, ASTM STP 1315, in press.
- Pyrz, R., 1994, "Correlation of Microstructure variability and Local Stress Field in Two-Phase Materials", *Material Science and Engineering*, A177: 253-259.
- Rice, J., 1971, "Inelastic Constitutive Relations for Solids: An Internal Variable Theory and Its Application to Metal Plasticity", *Journal of the Mechanics and Physics of Solids*, 19: 433-455.
- Ripley, B. D., 1977, "Modeling Spatial Patterns", *Journal of the Royal Statistical Society*, B39: 172-212.
- Sørensen, B. F., and Talreja, R., 1993, "Effects of Nonuniformity of Fiber Distribution on Thermally-Induced Residual Stresses and Cracking in Ceramic Matrix Composites", *Mechanics of Materials*. 16: 351-363.
- Sørensen, B. F., and Talreja, R., 1994, "Effects of Interphase and Coating on Thermally-Induced Damage in Ceramic Matrix Composites", In R. Naslain, J. Lamont and D. Doumeingts, (eds.), *High Temperature Ceramic Matrix Composites*: 591-598. Cambridge: Woodhead.
- Talreja, R., 1990, "Internal Variable Damage Mechanics of Composite Materials", In J. P. Boehler , (ed.), *Yielding, Damage and Failure of Anisotropic Solids*, 509-533. London: Mechanical Engineering Publications.
- Talreja, R., "A Synergistic Damage Mechanics Approach to Durability of Composite Material Systems", 1996. In Cardon, Fukuda and Reifsneider, (eds.), *Progress in Durability Analysis of Composite Systems*: 117-129. Rotterdam: Balkema.
- Varna, J., Akshantala, N.V., and Talreja, R., "Crack Opening Displacement and the Associated Response of Laminates with Varying Constraints", submitted.
- Varna, J., Akshantala, N.V., and Talreja, R., "Effects of Intralaminar Cracking and Shear on Inelastic Response of Laminates", in preparation.

## The role of interphasial inhomogeneities on failure mechanism of fiber-reinforced composites

G.C. Papanicolaou, P.A. Kakavas & N.K. Anifantis

*Composite Materials Group, Mechanical and Aeronautical Engineering Department, University of Patras, Greece*

**ABSTRACT:** In the present work, a three-dimensional approach for the fiber-matrix load transfer mechanism in fibrous composites with interphasial inhomogeneities is developed. It is assumed that the interphase properties are variable in both the radial and the longitudinal direction. Imperfect adhesion is considered through introduction of appropriate discontinuities in interphasial properties in an averaged sense and assuming that the representative volume element is consisted from a definite number of homogeneous subdomains. The effect of both the degree of inhomogeneity and the quality of adhesion on the stress field developed in the composite is examined and discussed in conjunction to the failure mechanisms associated to fiber reinforced composites.

### 1 INTRODUCTION

The fiber-matrix interfacial load transferring mechanism plays a major role in determining the mechanical and physical behavior of fiber-reinforced composites (Miwa & Endo 1994). In a fiber-reinforced composite the fibers bear the major fraction of the load (Padgett et al. 1995). However, in fact the loads are transferred from the matrix to the fibers through an interfacial region, often called the "interphase" and which, to some extent, determines the nature and quality of the fiber-matrix adhesion (Kakavas et al. 1995). Accordingly, the interphase represents a third phase of finite volume developed in the area between the constituent phases of the composite and characterized by mechanical imperfections, physicochemical interactions and limited mobility of macromolecules due to their adsorption on the filler surface (Jayaraman et al. 1994). Thus, the interphase properties, depending on the fiber-matrix adhesion, are varied within this third phase in an unknown continuous/discontinuous way. Especially in the case of fiber reinforced composites, this interphasial region has the form of a shell type structure extending in the area between fiber and matrix. Furthermore, any interphasial degradation affects the overall properties of the composite material (Hashin 1979). From an engineering perspective, therefore, the interphase represents a potential means of influencing the macroscopic properties of composites. Among other factors, it has been shown that the presence of interphasial

inhomogeneities, even discontinuities simulating imperfect bonding conditions between fiber and matrix, play an important role in the load carrying capacity and failure mechanism of fiber reinforced composites. Three dimensional solutions to similar problems are not fully investigated (Shih & Ebert 1987, Nairn 1992) due to the mathematical difficulties involved (Zong & Folias 1992). Considering the fiber material alone, as the length to diameter ratio increases, a distribution in fiber properties along the fiber length may be present. Depending on the fibers manufacture treatment, these inhomogeneities may vary in a stochastic manner. This complicated structure permits the introduction of a model with interphasial properties varying in a continues/discontinues way in both the longitudinal and transverse directions.

### 2 MODELING MATERIAL INHOMOGENUITIES

The representative volume element (RVE) of the material under examination constitutes from the fiber, the interphase and the matrix, denoted by subscripts  $f$ ,  $i$ , and  $m$ , respectively. The fiber length is  $2\ell$  and the origin of the cylindrical coordinate system  $(r, \theta, z)$  is located at the center of the fiber thickness midway of the fiber length. The fiber ends were assumed as stress free. Axisymmetric type of material inhomogeneities are considered. Due to the axial symmetry only one half of the RVE needs to be examined, Figure 1.

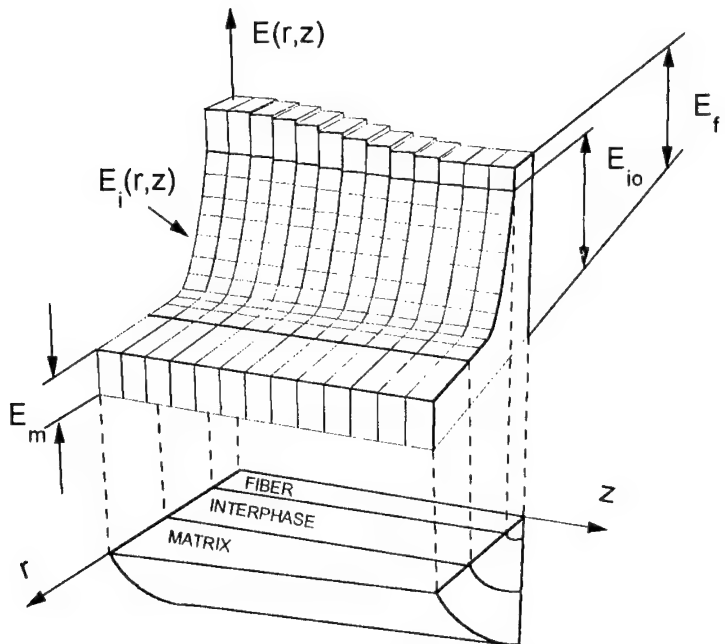


Figure 1. Assumed variation of modulus of elasticity inside the composite.

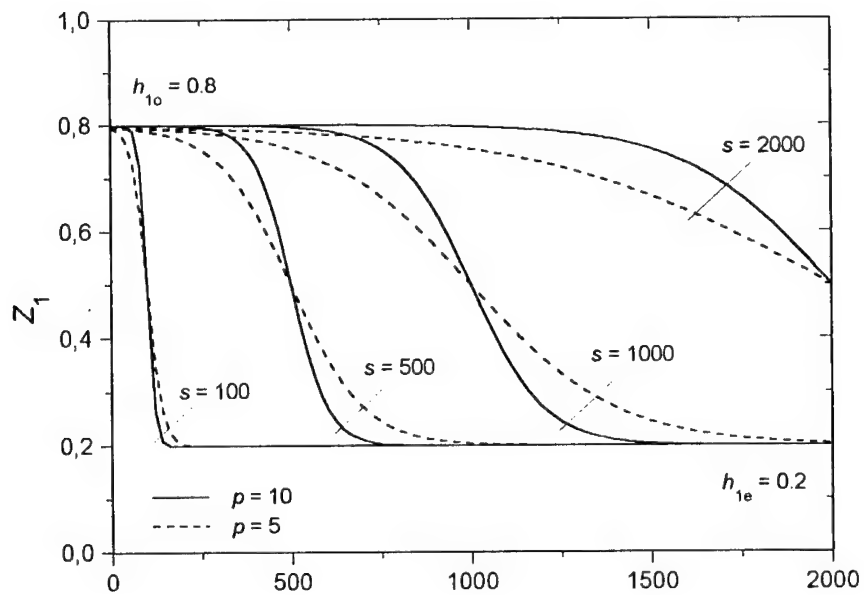


Figure 2. Assumed variation of longitudinal component determining Young modulus inhomogeneity.

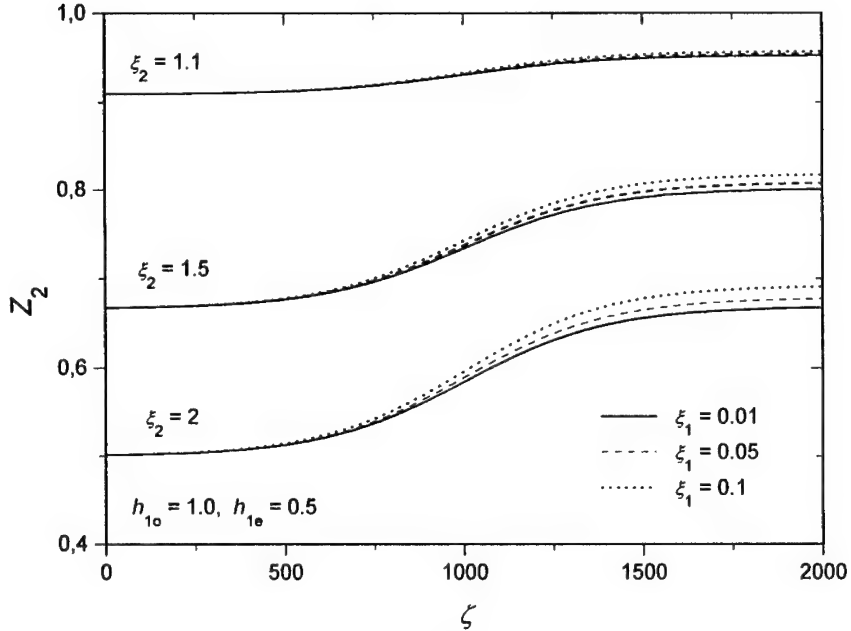


Figure 3. Assumed variation of longitudinal component determining Poisson's ratio inhomogeneity.

Defining a non-dimensional coordinate system  $(\rho, \zeta)$  in the form

$$R(\rho) = \frac{1 - \rho \exp(1 - \rho)}{1 - \rho_f \exp(1 - \rho_f)} \quad (6)$$

$$\rho = r/r_i, \quad \zeta = z/r_i \quad (1)$$

one can assume the following distribution of normalized property  $r_j, j = 1, 2$

$$P_j(\rho, \zeta) = \begin{cases} 1, & 0 \leq \rho \leq \rho_f, \quad 0 \leq \zeta \leq \ell \\ \xi_j + [Z_j(\zeta) - \xi_j]R(\rho), & \rho_f < \rho \leq 1, \quad 0 \leq \zeta \leq \ell \\ \xi_j, & 1 \leq \rho \leq \rho_m, \quad 0 \leq \zeta \leq \ell \end{cases} \quad (2)$$

Normalized parameters appearing in above equations are defined as

$$P_j(\rho, \zeta) = \begin{cases} E(\rho, \zeta) / E_f, & \text{when } j = 1 \\ v(\rho, \zeta) / v_f, & \text{when } j = 2 \end{cases} \quad (3)$$

$$\rho_f = r_f/r_i, \quad \rho_m = r_m/r_i \quad (4)$$

$$\xi_1 = E_m/E_f, \quad \xi_2 = v_m/v_f \quad (5)$$

In contrast, the function  $Z_j$  represents a sigmoidal type of distribution of properties in the axial direction,

$$Z_j(\zeta) = \frac{h_{j0} - h_{je}}{1 + \exp[p(\zeta/s - 1)]} + h_{je}, \quad j=1, 2 \quad (7)$$

where  $s = \ell/r_i$  is the slenderness parameter characterizing the fiber length, and the parameter  $p$  determines the extent of inhomogeneity in axial direction. In equation (7), imperfect adhesion between fiber and matrix is included also, by means of the coefficients  $h_{j0} \in [1, 0]$  and  $h_{je} \in [0, 1]$  which determine the degree of adhesion at the middle ( $\zeta=0$ ), and at the end ( $\zeta=\ell/r_i$ ) of the fiber, respectively. Imperfect adhesion coefficients corresponding to Poisson's ratio are assumed to depend on respective ones determining modulus of elasticity, in the following way

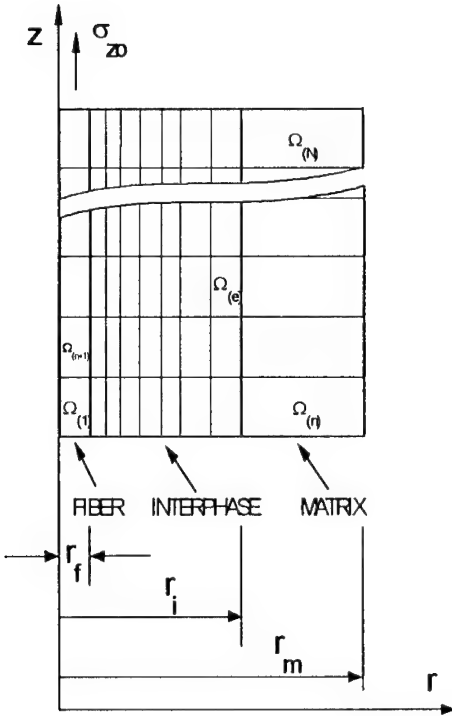


Figure 4. Subdomain idealization.

$$h_{20} = \frac{(1-\xi_1)\xi_2}{1-\xi_1\xi_2 + (\xi_2-1)h_{10}},$$

$$h_{2e} = \frac{(1-\xi_1)\xi_2}{1-\xi_1\xi_2 + (\xi_2-1)h_{1e}}. \quad (8)$$

Figures 2 and 3 illustrate the Young modulus and Poisson's ratio axial variation for various values of the factors representing different degrees of inhomogeneity.

### 3 PROBLEM FORMULATION

Figure 4 illustrates the domain of the problem in cylindrical coordinate system, that is a longitudinal cross section of the RVE. Due to the symmetry, only one half of the length is considered. One axial loading case,  $\sigma_{z0}$ , is examined. It is assumed that the domain of interest is discretized into  $N = n \times m$  subdomains as indicated in this Figure, where  $n, m$

are the numbers of subdivisions in  $r, z$  directions, respectively. Each subdomain  $\Omega_e$  has the form of a ring with cross section defined between the radii  $(r_j, r_{j+1})$  and the longitudinal positions  $(z_k, z_{k+1})$ , as shown in Figure 4. The relation between the indices  $j, k$  and  $e$  is

$$j = e - (k - 1)n,$$

$$k = \min \{1, 2, \dots, m\}, \quad e = 1, 2, \dots, N \quad (9)$$

where  $t, s$  assign adjacent subdomains and are given as

$$t = (k - 2)n + j, \quad s = kn + j \quad (10)$$

Each subdomain  $\Omega_e$  is assumed to be homogeneous one. This may be achieved by proper definition in averaged sense of its own properties. Then the modulus of elasticity and the Poisson's ratio that correspond to  $\Omega_e$  subdomain are defined by the relations

$$E_e = [E(r_j, z_k) + E(r_{j+1}, z_k) + E(r_j, z_{k+1}) + E(r_{j+1}, z_{k+1})] / 4 \quad (11.a)$$

$$v_e = [v(r_j, z_k) + v(r_{j+1}, z_k) + v(r_j, z_{k+1}) + v(r_{j+1}, z_{k+1})] / 4 \quad (11.b)$$

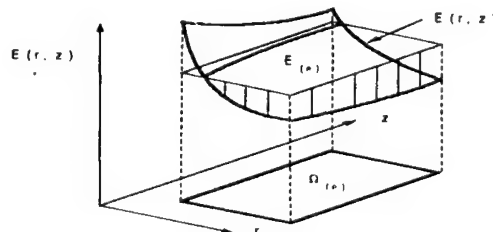


Figure 5. Definition of average Young modulus over a subdomain.

where the values of  $E(r_j, z_k)$ ,  $v(r_j, z_k)$  are determined by equation (2). This type of discretization allows for definition of a piecewise homogeneous problem that is an approximation of the given problem. This model includes the proposed variation of the properties as well as imperfections in adhesion between various material phases that constitute the composite. As the number of subdomains increases, the model converges to the exact one. A alternative technique the so-called method of cell was proposed by (Aboudi 1989). Substitution of the stress-strain relations and the strain-displacement relations into the equilibrium gives the governing equations in terms of displacements.

#### 4 METHOD OF SOLUTION

The solution of the governing equations in terms of displacements is obtained by using the Love's stress function, provided the stress function  $\Phi_e(r, z)$  satisfies the biharmonic equation (Timoshenko & Goodier 1951).

It can be shown that the following functions satisfy the biharmonic equation

$$\Phi_{1e}(r, z) = (A_e r^2 + B_e \ln r) + C_e z^3 \quad (12)$$

$$\begin{aligned} \Phi_{2e}(r, z) = & \sum_{p=1}^M \cos \mu_{pe} z [D_{1pe} I_0(\mu_{pe} r) \\ & + D_{3pe} \mu_{pe} r I_1(\mu_{pe} r)] \end{aligned} \quad (13)$$

where  $I_0$ ,  $I_1$  and  $K_0$ ,  $K_1$  are the modified Bessel Functions of the first and second kind, respectively, while  $A_e$ ,  $B_e$ ,  $C_e$ ,  $D_{1pe}$ , ...,  $D_{4pe}$  are constants to be determined by application of the boundary and interfacial conditions. The constant  $\mu_{pe}$  is selected so that

$$\mu_{pe} = \frac{(2j-1)\pi}{2(z_{k+1} - z_k)}, \quad j=1, 2, 3, \dots \quad (14)$$

The Love's stress function  $\Phi_e(r, z)$  is given as  $\Phi_e(r, z) = \Phi_{1e} + \Phi_{2e}$  from which displacements and stresses can be derived as (Sottos et al. 1994)

$$u_e = u_{1e} + u_{2e}, \quad w_e = w_{1e} + w_{2e} \quad (15.a)$$

$$\sigma_{\pi e} = \sigma_{\pi 1e} + \sigma_{\pi 2e}, \quad \sigma_{\theta\theta e} = \sigma_{\theta\theta 1e} + \sigma_{\theta\theta 2e} \quad (15.b)$$

$$\sigma_{zz e} = \sigma_{zz 1e} + \sigma_{zz 2e}, \quad \sigma_{rz e} = \sigma_{rz 1e} + \sigma_{rz 2e} \quad (15.c)$$

The boundary and the interfacial compatibility and equilibrium conditions on both solutions are the following

$$u_{1e}, u_{2e}, \sigma_{\pi 1e}, \sigma_{\pi 1e} \Big|_{\substack{r=0 \\ z_k \leq z \leq z_{k+1}}}$$

$$\text{for } e = (k-1)n + 1, k = 1, m, \text{ are bounded} \quad (16)$$

$$u_{1e-1} + u_{2e-1} = u_{1e} + u_{2e} \Big|_{\substack{r=r_j \\ z_k \leq z \leq z_{k+1}}}$$

$$\text{for } e = (k-1)n + j + 1, k = 1, m, j = 1, n-1 \quad (17)$$

$$\sigma_{\pi 1e-1} + \sigma_{\pi 2e-1} = \sigma_{\pi 1e} + \sigma_{\pi 2e} \Big|_{\substack{r=r_j \\ z_k \leq z \leq z_{k+1}}}$$

$$\text{for } e = (k-1)n + j + 1, k = 1, m, j = 1, n-1 \quad (18)$$

$$w_{1e} + w_{2e} = w_{1s} + w_{2s} \Big|_{\substack{r_j \leq r \leq r_{j+1} \\ z=z_{k+1}}}$$

$$\text{for } e = (k-1)n + j, s = k n + j, k = 1, m-1, j = 1, n \quad (19)$$

$$\int_{r_j}^{r_{j+1}} (\sigma_{zz 1e} + \sigma_{zz 2e}) dr = \int_{r_j}^{r_{j+1}} (\sigma_{zz 1s} + \sigma_{zz 2s}) dr \Big|_{\substack{r_j \leq r \leq r_{j+1} \\ z=z_{k+1}}}$$

$$\text{for } e = (k-1)n + j, s = k n + j, k = 1, m-1, j = 1, n$$

$$(20)$$

$$\int_{r_j}^{r_{j+1}} (\sigma_{zz1e} + \sigma_{zz2e} - \sigma_{zz0e}) dr = 0 \quad \left|_{\substack{r_j \leq r \leq r_{j+1} \\ z=\ell}} \right. \quad (21)$$

for  $e = (m-1)n + j, j = 1, n$

$$\int_{r_j}^{r_{j+1}} (\sigma_{rz1e} + \sigma_{rz2e}) dr = 0 \quad \left|_{\substack{r_j \leq r \leq r_{j+1} \\ z=\ell}} \right. \quad (22)$$

for  $e = (m-1)n + j, j = 1, n$

If equations (16) to (22) are sequentially applied on the whole range of the involved indices, then a linear algebraic system of equations with  $4mn(M+1)$  of unknowns results. Homogeneous boundary conditions at  $z=0$  are identically satisfied. Since the third of equations (15) is also identically satisfied, an additional condition of the form  $\sigma_{rr1e}(r_{n+1}, z) = 0$  is imposed, for  $e = nk, k = 1, m$ .

Numerical solution of the resulting system of equations yields the constants appearing in the general solution.

## 5 RESULTS AND DISCUSSION

The proposed numerical model was applied to an Epoxy/E-glass composite in order to evaluate the axial stress distribution in the fiber as well as the shear and radial stresses along the interface. The modulus of elasticity and the Poisson's ratio for the fiber and matrix, respectively are taken as  $E_f=70$  GPa,  $v_f=0.2$ ,  $E_m=3.45$  GPa  $v_m=0.35$ . The radius of the glass fibres was  $r_f=6$   $\mu\text{m}$ , the volume fraction of the fibres was taken 0.5 and the thickness of the interphase was taken 0.3  $\mu\text{m}$  (Kakavas et al. 1995). In addition, the ratio of the fiber length to the radius of the interphase region (i.e.  $s=l/r_f$ ) was taken equal to 10. The proposed model is based on the 3-D axisymmetric analysis already presented. A constant tensile axial load was applied to the composite.

For perfect fiber-interphase adhesion, the shear and radial stresses at the interphase are plotted in Figure 5. However, as is shown in the same Figure, a strong effect of imperfect adhesion on the above stress distribution is observed. The shear stress

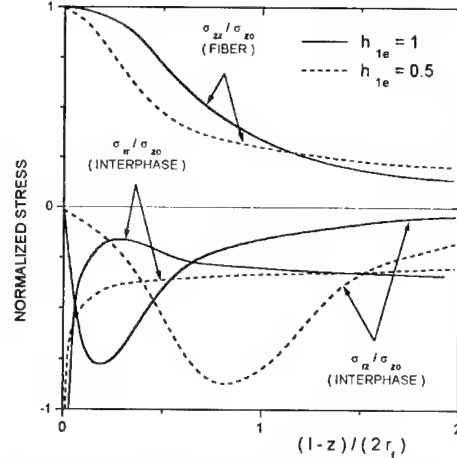


Figure 6. Computed stress components in the longitudinal direction

$\tau_{rz}$  becomes zero at  $z = 1$  and after two fiber diameters approaches zero. Also a maximum interphasial radial stress is observed close to the upper fiber end. The imperfect adhesion has a significant influence on the radial stress distribution too. The axial tensile stress developed at the fiber-interphase boundary is also shown on the same graph as a function of the axial distance from the upper fiber end ( $z = 1$ ). From this graph we may observe at  $z = 1$ ,  $\sigma_{zz}/\sigma_{zo} = 1$  while this stress ratio drops to zero after two fiber diameters. The imperfect adhesion has a significant influence on the stress axial distribution too. As a consequence, it becomes clear that the compressive radial stress concentration within the interphase should have a significant effect on the interfacial failure mechanism.

## 6 CONCLUSIONS

Both axial and radial non-homogenous dependence of interphasial properties was taken into account for the stress distribution numerical computation in a fiber-reinforced composite. The concept of imperfect adhesion was also introduced in the model and the numerical results showed that interphasial imperfections had a strong influence on the stress field developed within the interphase affecting the failure mechanism of the composite. Local interphasial stress concentrations at the fiber ends were found to be depended on both the degree of imperfection and inhomogeneity.

## ACKNOWLEDGMENTS

The authors wish to thank Greek State General Secretary of Research and Technology (GSRT) for financial support of the present study.

## REFERENCES

- Aboudi J. 1989. Micromechanical analysis of composites by the method of cells. *Applied Mechanics Reviews*. 42:193-221.
- Hashin, Z. 1979. Analysis of properties of fiber composites with anisotropic constituents, ASME *Journal of Applied Mechanics*. 46:543-550.
- Jayaraman, K., Z. Gao and K.L. Reifsneider 1994. The interphase in unidirectional fiber-reinforced composites: Effect on local stress fields. *Journal of Composites Technology and Research*, JCTRER. 16:21-31.
- Kakavas, P., N. Anifantis, K. Baxevanakis, D.Katsareas & G. Papanicolaou 1995. The Effect of interfacial imperfections on the micromechanical stress and strain distribution in fibre reinforced composites, *Journal of Material Science*. 30:4541-4548.
- Miwa, N. & I. Endo 1994. Critical fiber length and tensile strength for carbon fiber epoxy composites. *Journal of Material Science*. 29:1174.
- Nairn, J.A. 1992. Variational mechanics analysis of the stresses around breaks in embedded fibers. *Mechanics of Materials*. 13:131-154.
- Padgett, W. J., S. D. Durhan & A.M Mason 1995. Weibull analysis of the strength of carbon fibers using linear and power law models for the length effect. *Journal of Composite Materials*. 29:1873.
- Shih, G.C & L.J. Ebert 1987. Theoretical modelling of the effect of the interfacial shear strength of unidirectional composites. *Journal of Composite Materials*. 21:207.
- Sottos, N.R. , L. Li and G. Agrawal 1994. The effect of interphase properties on interfacial shear strength in polymer matrix composites. *Journal of Adhesion*. 45:105-124.
- Timoshenko S.& J.N. Goodier 1951. *Theory of Elasticity*. 2nd Edition, New York: Mc Graw Hill.
- Zong F.H. & E.S. Folias 1992. The 3D stress field of a fiber embedded into a matrix and subjected to an axial load. *Computational Mechanics*. 9:233-247.

## Influence of interfacial strength on micro- and macroscopic fatigue behavior of longitudinal glass fiber reinforced polypropylene

E.K.Gamstedt & L.A.Berglund

Luleå University of Technology, Sweden

T.Peij

Eindhoven University of Technology, Netherlands

**ABSTRACT:** In this study the thermoplastic polypropylene (PP) and maleic anhydride modified polypropylene (MA-PP) reinforced by continuous longitudinal glass fibers (GF) have been investigated. The most protruding effect of the modification with maleic anhydride in the composite is a stronger fiber/matrix interface. The effects of interfacial strength on fatigue performance and on the underlying micromechanisms were studied for these composite systems. Tension-tension fatigue tests ( $R = 0.1$ ) were carried out on  $0^\circ$  GF/PP and GF/MA-PP coupons. The macroscopic fatigue behavior was characterized in terms of stiffness reduction and fatigue life curves. The longitudinal Young modulus degraded more rapidly for GF/PP which was caused by a higher degree of damage growth and accumulation. The  $S-N$  curves show that the improvement in static strength is negligible, and the fatigue life is prolonged by about decade with the stronger interface by addition of maleic anhydride to the polypropylene matrix. The static strength is controlled by the strain to failure of the fibers, hence the superposition. The better fatigue resistance of GF/MA-PP is attributed to the greater interfacial strength and the resistance to debond propagation. During the course of the fatigue testing, the microscopic mechanisms were monitored intermittently using a surface replication technique. The observed differences in fatigue micromechanisms (debonding, fiber breakage, matrix cracking etc.) are presented and discussed in reference with the macroscopic fatigue behavior.

### 1 INTRODUCTION

#### 1.1 Fatigue of polymer matrix composites

Polymer matrix composites are finding increased use in structural applications, in particular for aerospace and automotive purposes. Mechanical fatigue is the most common type of failure of structures in service, both for homogeneous and composite materials. The relative importance of fatigue has yet to be reflected in design where static conditions still prevail. The fatigue behavior of composite materials is conventionally characterized by a Wöhler or  $S-N$  curve. For ease of interpretation, the fatigue life diagrams originally conceived by Talreja (1981) may be used. In this diagram the initial peak strain is plotted versus the number of cycles to failure, and different regions can be distinguished, each pertinent to a different set of damage mechanisms.

Unfortunately, for every new material, new lay-up, altered constituents or different processing procedure, a whole new set of fatigue life tests have to be repeated for such a characterization. If the active fatigue damage micromechanisms and the influence of the constituent properties and interface were known, it would be possible, at least qualitatively, to predict

the macroscopic fatigue behavior. More importantly, these mechanisms indicate the critical microstructural property responsible for the fatigue degradation, which is valuable information for materials development and improvement. In this context, the mechanisms of the longitudinal plies are the most important since these plies are the critical members and the last ones to fail in tensile fatigue of a multidirectional composite laminate (Talreja 1993). It is therefore desirable to establish a link from microscopic scale (properties and morphology of the matrix and the fibers, as well as their interface), over the mechanisms on a mesoscopic scale of a few fiber diameters, to the macroscopic fatigue behavior (e.g. fatigue life diagram) of unidirectional composites. This approach was aimed for in an investigation of carbon fiber reinforced plastics (Gamstedt & Talreja 1997), whereas this study is concerned with glass fiber reinforced polypropylene, and in particular the influence of interfacial adhesion.

#### 1.2 Glass fiber/polypropylene composites

In recent years, increased attention has been directed towards composite structures with thermoplastic matrices. In many cases, they offer advantages over

thermosets in handling, processing, damage tolerance, environmental resistance and recycling. In combination with glass fibers, thermoplastic composites may present a cost effective alternative to glass fiber/epoxy composites. Glass mat reinforced thermoplastic (GMT) materials are widely used in automotive applications, and the use of continuous fiber reinforcement for load carrying structures is steadily increasing. A strong contender in this market area is glass fiber reinforced polypropylene. The polymer may be modified with maleic anhydride for improved adhesion. In previous studies the macroscopic mechanical properties of these materials have been examined under static (Rijssdijk *et al.* 1993) and fatigue loading (van den Oever & Peijs 1997). The most protruding effect of the modification with maleic anhydride in the composite is a stronger fiber/matrix interface. For a weak interface debonds are likely to develop. Owen (1980) has pointed out the influence of fatigue on the incipient formation of debonds leading to larger scale resin cracks, and eventually to failure. In the present work, the effects of interfacial adhesion on fatigue performance in combination with the underlying micromechanisms for polypropylene composite systems are presented.

### 1.3 Maleic anhydride modification

Polypropylene is an apolar polymer, and has a limited affinity to fiber sizings. Maleic anhydride grafted onto the polymer results in polarity, and a more efficient interaction with the fiber sizing. The bond can be the result of chemical reaction (Xanthos 1988), or physisorption (see Figure 1) with interdiffusion of the polymer chains into the sizing and local dipole-dipole bonding (Mäder and Freitag 1990). Hydrogen bonding to the oxygen of the maleic anhydride endgroup is another likely bond type. A disadvantage is that the polarity of the matrix makes it hydrophilic, which facilitates water sorption at the interface. Water is known to degrade the glass fibers by stress corrosion.

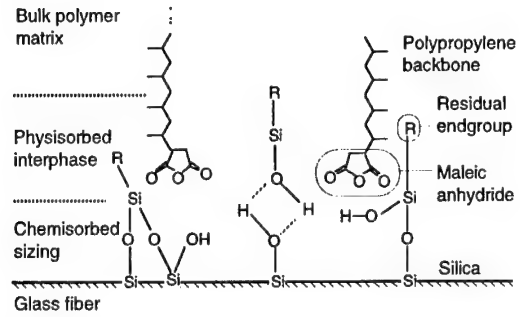


Figure 1. Physical bonding between MA-PP and glass fiber

## 2 EXPERIMENTAL DETAILS

### 2.1 Materials

In this study the thermoplastic polypropylene (PP) and maleic anhydride grafted polypropylene (MA-PP) reinforced by continuous longitudinal glass fibers (GF) have been investigated. The E-glass fiber type is identical for the two materials but the matrix has been modified to achieve a more efficient adhesion to the fibers. The fibers were PPG 854-1200 from PPG Industries Fibre Glass BV, and were treated with a PP compatible sizing. The MA-PP matrix was made by blending an isotactic PP homopolymer (VM 6100, Shell Chemicals) with a commercial maleic-anhydride grafted PP (Polybond 3002, BP Chemicals). The proportions of the blend was 90 w% homopolymer and 10 w% of the MA grafted PP, which has showed optimal static strength properties (Rijssdijk *et al.* 1993).

### 2.2 Processing

Unidirectional 0° laminates were manufactured by winding layers of glass fibers onto a steel mandrel with alternating sheets of the polymer film. After stacking, the mandrel was placed in a heated press at 25 bar and 200°C for one hour. The laminates were cooled in the press to minimize curvature. The specimens were cut and carefully polished into dimensions according to ASTM standard D3039. Tapered end tabs of glass fabric/epoxy were adhesively bonded to the specimens.

### 2.3 Testing

Tension-tension fatigue tests ( $R = 0.1$ ) were made on 0° GF/PP and GF/MA-PP coupons in a servo-hydraulic tensile machine. The underlying mechanisms that account for the observed resistance to fatigue of the GF/MA-PP composite were monitored by a surface replication technique. The replica films were made of cellulose acetate, and were rendered malleable by application of acetone. During the course of the fatigue testing, the surface replicas were intermittently pressed onto the specimen surface for both composite materials. The replicas were studied *a posteriori* in an optical microscope to determine the operative damage mechanisms. The fatigue tests for replications and stiffness measurements were performed at a stress amplitude of ~ 60% of the ultimate tensile strength (UTS).

Fracture surfaces were studied in a scanning electron microscope (SEM). The surfaces were coated with a thin gold layer in a Blazers SCD050 sputter coater. The SEM was a Cambridge CAMSCAN SH-80D operating at accelerating voltage of 20 kV.

### 3 RESULTS AND DISCUSSION

#### 3.1 Stiffness reduction

The macroscopic fatigue behavior has been characterized in terms of stiffness reduction and fatigue life diagrams. The longitudinal Young's modulus degraded more rapidly for GF/PP (see Figure 2) which indicates a higher degree of damage growth and accumulation. The GF/MA-PP exhibited a 'sudden-death' behavior, where the stiffness remained virtually constant until imminent failure. This implies localized small-scale damage, which can be explained by the more effective fiber-matrix bonding through maleic anhydride modification and the ensuing embrittlement.

#### 3.2 Fatigue life behavior

The fatigue life data show that the improvement in static strength is negligible, and the fatigue life is prolonged by as much as a decade with the stronger interface by modification of the PP matrix with maleic anhydride. A corresponding shift to longer fatigue lives as well as a retention of stiffness have been observed for a carbon fiber/epoxy system with improved interfacial properties (Subramanian *et al.* 1995). No distinct regions are indicated in Figure 3 since all data points seem to belong to the sloping scatter band associated with a progressive fatigue mechanism. The static strength is controlled by the strain to failure of the fibers, hence the overlapping for low cycles in the fatigue life curve.

The shorter fatigue lives of GF/PP for equal strain amplitudes suggest a more rapid growth of the critical damage site. The weaker interfacial bond presents itself as a possible reason for the enhanced propagation rate.

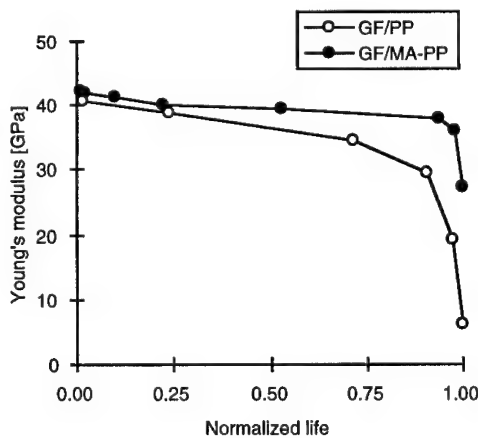


Figure 2. Stiffness degradation during fatigue at 60% of UTS

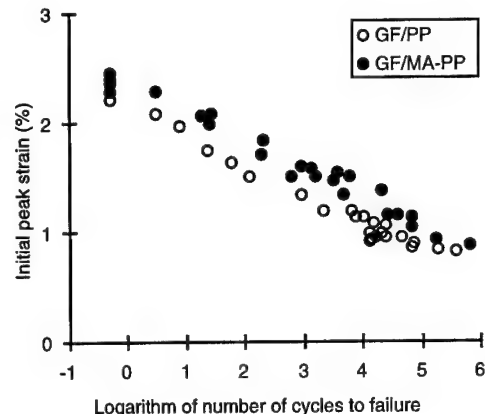


Figure 3. Fatigue life data of GF/MA-PP and GF/MA-PP

#### 3.3 Micromechanisms

A typical sequence of fatigue damage development in GF/PP is found in Figure 4. The fatigue damage in the GF/PP is characterized by large distributed debonds originating from flaws or fiber breaks, while the damage in GF/MA-PP is given by localized small cracks perpendicular to the load direction. The former grow in an accelerating-decelerating manner, and the debonds become more pronounced with thicker and darker appearance on the replicas during fatigue. This is due to attrition of the crack surface asperities as loading is mainly in mode II. The mismatch in elastic properties of the fiber and the surrounding matrix results in shear loading. When the effective frictional constraint has become low enough, the interfacial crack will propagate some further distance before being arrested by a microstructural obstacle. There is a large variability in interfacial properties on the micrometer size scale which will further enhance the erratic debond growth pattern. The debond mechanism is not critical *per se* since it does not directly result in ultimate failure, but as the debonds grow, the stress overload in the adjacent fibers redistributes. When the redistributed overload exceeds the local strength of a weak fiber segment, it

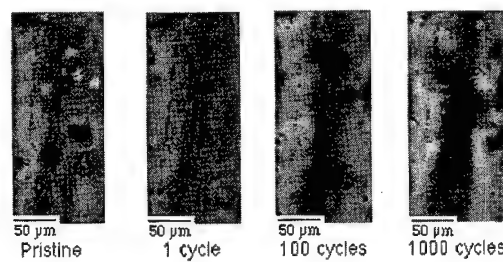


Figure 4. Fatigue damage growth in GF/PP

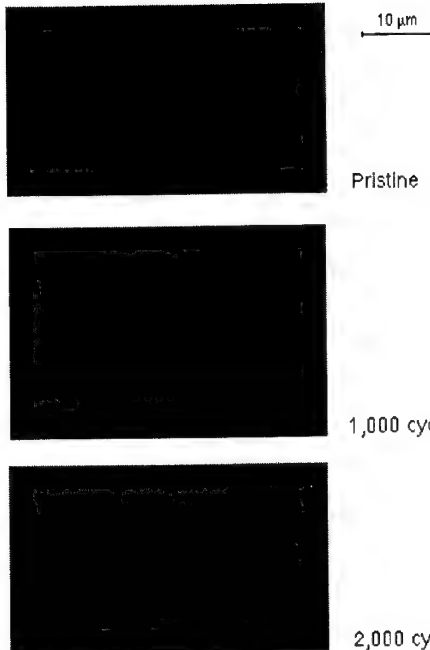


Figure 5. Fatigue crack growth in GF/MA-PP

will fail and serve as an initiation point for the growth of a new debond etc.

The fatigue damage in GF/MA-PP also initiate from fiber breaks or flaws, but takes a more tortuous crack path, and are arrested by the neighboring fibers. Replicas of fatigue crack growth in GF/MA-PP are found in Figures 5 and 6. The load and fiber directions are vertically oriented in all replicas. The difference in fatigue damage mechanisms observed on the replica pictures for GF/PP and GF/MA-PP is schematically depicted in Figure 7.

### 3.4 Fractography

Fractographic analysis indicate stronger interfacial bond for the GF/MA-PP material, since the fibers were covered with residual polymer matrix. The stronger interfacial bond is due to the affinity of the maleic anhydride groups to the fiber sizing. The GF/PP did not show any residual polymer on the fibers. The interfacial bond is here limited to compressive residual stresses, and interdiffusion of molecular segments into the sizing, with weak van der Waals bonds on the molecular level. Scanning electron micrographs of fibers at the fracture surfaces from failed specimens are shown in Figure 8. The failed GF/PP specimens were more bush-like and rougher in appearance with straggling fibers than those that failed under static loading. This

fractographic difference is another indication that debonding is a prevalent fatigue mechanism in GF/PP. There was no conspicuous difference in the fracture surfaces of GF/MA-PP subjected to fatigue and static tensile tests. Both of them were relatively even, which suggests localized small-scale damage, and is in concert with the replica observations. Comparing failures of the two composites, the GF/PP specimens showed notably more sprawling and uneven fractures both in static and fatigue loading.

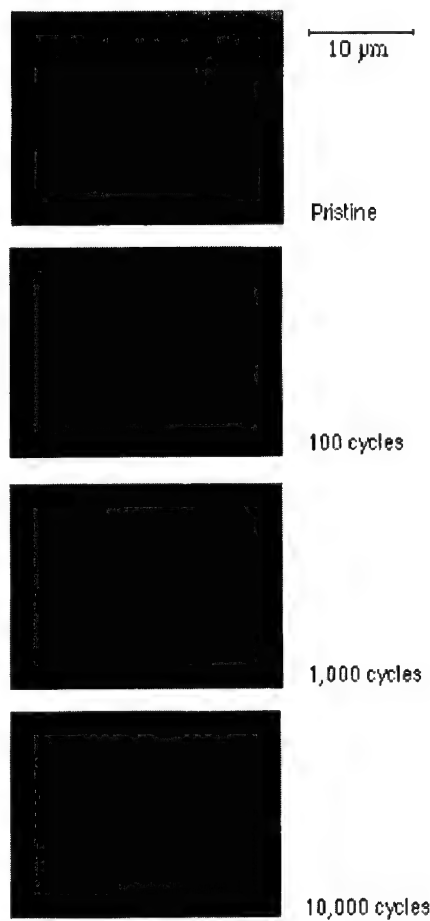


Figure 6. Fatigue crack growth in GF/MA-PP

### 3.5 Microstructure-property connection

On the molecular level, grafting MA groups to the PP results in a more efficient interfacial bond. This is illustrated by fractographic pictures with adhering polymer matrix caused by cohesive failure of GF/MA-PP. The stronger interface suppresses debond propagation during fatigue which has been observed by a replica technique throughout fatigue

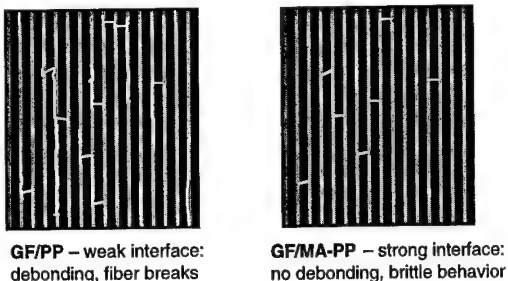


Figure 7. Illustration of difference in damage scenario

testing. In GF/PP, the widely distributed and progressively growing debonds with accompanying fiber breakage led to a more rapid stiffness reduction. This degradation indicates a higher rate of damage accumulation, and subsequently a shorter fatigue life. In this way, a qualitative link from chemical modification on the molecular level, over mesoscale damage mechanisms, to macroscopic fatigue life properties can be established.

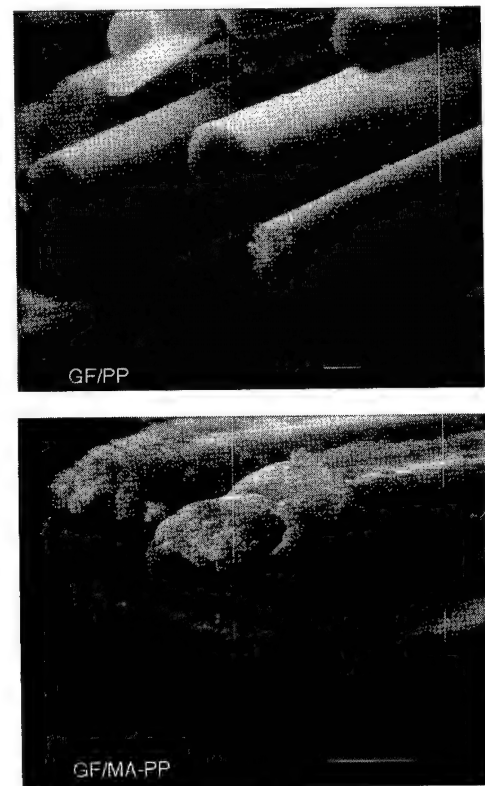


Figure 8. Fractographic scanning electron micrographs

Modeling endeavors must be focused in a way that reflects the operative damage mechanisms. A local load sharing model with debonds growing according to a phenomenological power law is amenable for GF/PP. The distribution of fiber strength result in distributed fiber breaks in the composite from which debonds may initiate. The following redistribution of stresses will cause further fiber breakage etc. This type of model has successfully been used for creep in unidirectional microcomposites (Otani *et al.* 1991). In GF/MA-PP, more localized damage development is present without apparent signs of debonding. Nevertheless, a similar modeling approach may be adopted were a growing longitudinal zone of irreversible deformation in the matrix occurs. The difference lies in the nature of this zone, which was not directly observable in this case. Cycle-dependent matrix yielding is a likely process for composites with strong interfacial adhesion. Its propagation rate should be low, since the damage was localized. The strong interface also results in a more effective load transfer between the fibers, which in turn means that the critical cluster size at catastrophic failure is small. Any model of the fatigue damage growth would not be adequate for design purposes at this point, but more useful for a parametric study where the influence of constituent properties can be investigated which would be valuable in materials engineering.

#### 4 CONCLUSIONS

The shorter fatigue lives and more rapid reduction of the Young's modulus of the GF/PP composite are explained by its relatively poor fiber-matrix adhesion, which leads to wide-spread debond growth from fiber breaks and flaws. The growing debonds result in overloads on the surviving adjacent fiber segments, which in turn lead to further fiber breakage with debonding etc. Conversely, the GF/MA-PP has a more brittle behavior with localized damage and non-propagating mechanisms, viz. small matrix cracks form from flaws and are generally arrested by adjacent fibers. This results in a more fatigue resistant behavior for the GF/MA-PP material. For this material combination, the propensity to debond propagation caused by a weaker interface has an adverse effect on the fatigue performance.

#### ACKNOWLEDGEMENTS

Gratitude is expressed to Stéphanie Baty, Greger Nilsson and Johnny Grahn for able help in the laboratory. Ramesh Talreja is acknowledged for constructive discussions. The Swedish Research Council for Engineering Sciences (TFR) has financially supported Kristofer Gamstedt.

---

## REFERENCES

- Gamstedt, E.K. & Talreja, R. 1997. Fatigue damage micromechanisms in unidirectional CFRPs. *Proceedings of the first international conference on fatigue of composites, Paris, 3-5 June 1997:* 221-227. Paris: SF2M.
- Mäder, E. & Freitag, K.-H. 1990. Interface properties and their influence on short fibre composites. *Composites.* 21:397-402.
- Otani, H., Phoenix, S.L. & Petrina, P. 1991. Matrix effects on lifetime statistics for carbon fibre-epoxy microcomposites in creep rupture. *Journal of Materials Science.* 26:1955-1970.
- Owen, M.J. 1980. Fatigue processes in fibre reinforced plastics. *Philosophical Transactions of the Royal Society.* A294:535-543.
- Rijssdijk, H.A., Contant, M. & Peijs, A.A.J.M. 1993. Continuous-glass-fibre-reinforced polypropylene composites: I. Influence of maleic-anhydride-modified polypropylene on mechanical properties. *Composites Science and Technology.* 48:161-172.
- Subramanian, S., Reifsnider, K.L. & Stinchcomb, W.W. 1995. A cumulative damage model to predict the fatigue life of composite laminates including the effect of a fibre-matrix interphase. *International Journal of Fatigue.* 17:343-351.
- Talreja, R. 1981. Fatigue of composite materials: Damage mechanics and fatigue life. *The Proceedings of the Royal Society.* A378:461-475.
- Talreja, R. 1993. Fatigue of fiber composites. In Chou, T.W. (ed), *Structure and properties of composites,* 13:538-607. Weinheim: VCH.
- van den Oever, M. & Peijs, T. 1997. Continuous-glass-fibre-reinforced polypropylene composites: II. Influence of maleic-anhydride-modified polypropylene on fatigue behaviour. *Advanced Composite Letters* (in press).
- Xanthos, M. 1988. Interfacial agents for multiphase polymer systems: Recent advances. *Polymer Engineering and Science.* 28:1392-1399.

## Creep-damage interaction in composites

V.Tamuzs, J.Andersons & K.Aniskevich

*Institute of Polymer Mechanics, Riga, Latvia*

J.Korsgaard

*LM Glasfiber, Denmark*

**ABSTRACT:** Experimental results and theoretical prediction of the response of glass-fiber reinforced polyester under quasi-static, creep, and fatigue loading are presented. Non-linear strain component at static loading and strain amplitude rate at cyclic off-axis loading for the orthotropic composite are shown to follow the associated flow rule with a single-parameter quadratic potential function. The influence of fatigue damage on deformation is essential by reducing the elastic modulus of the composite and apparently negligible by its effect on creep kernel parameters.

### 1 INTRODUCTION

A very well elaborated approach to predict the degradation of composite properties due damage is the ply discount model. Such approach can be applied for composites having well determined structure (i.e. angle ply laminates). The prediction of cyclic durability based on the damage accumulation in plies has been verified for complex stress state (Andersons et al 1989, 1990, 1991). Creep prediction models of angle ply laminate using as initial data the creep parameters of fibers and matrix or unidirectional ply have also been elaborated.

However, the application of ply analysis is inconvenient if the composite has a more complex structure. In this case, the approach of nonlinear stress strain behavior of anisotropic (usually orthotropic) body can be used (Sun & Chen 1989). Nevertheless, a commonly accepted model for time dependent behavior of orthotropic composites including the damage accumulation is not elaborated.

The essential problem of creep-damage interaction in composites consists in the way how the scattered fracture influences the parameters of creep equations: whether it changes irreversibly only the modulus or also the viscoelastic spectrum.

The paper comprises the experimental results of orthotropic composite behavior under constant and cyclic loading at different stress ratios  $R$  and loading directions, determined by angle  $\varphi$  to the principal

symmetry axis, and an attempt to describe the creep-damage behavior by minimum constants involved.

### 2 MATERIAL AND TESTS

The polyester-glassfiber composite studied contains layers of chopped stand mat, fabric reinforcement and 75% layers of unidirectionally oriented bundles of glass fibers (UD). Fiber mass fraction in composite is 0.6. The main axis 1 coincides with UD fiber direction. The structure of the composite is schematically shown in Figure 1.

Static strength, creep and fatigue tests were carried out on MTS test rig under stress control. The durability tests under cyclic and constant stress level were performed at different stress ratios and angles  $\varphi$  to axis 1. Cyclic loading frequency in the principal fiber direction was 2, 4 and 17 Hz, stress ratios  $R = 0.1, 0.3., 0.5, 0.8, 0.9$ . Although no systematic statistical study on the frequency effect on fatigue life was performed, test data obtained suggested that this effect, if any was rather negligible (Andersons & Korsgaard 1997). Off-axis tests were performed at 4 Hz frequency and stress ratio  $R= 0.1$ . The variation of minimum and maximum cyclic strain was monitored by means of a clip-on extensometer. The summary of the test program is shown in Figure 2.

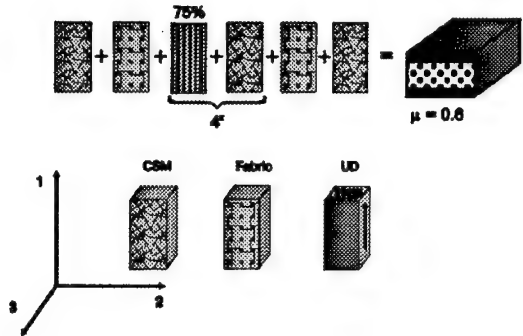


Figure 1. The structure of glass/polyester composite.

### 3 MODEL

#### 3.1 Strain components

Total composite strain  $\varepsilon$  is composed of four constituents: linear elastic  $\varepsilon_e$ , non-linear (elastic or plastic)  $\varepsilon_n$ , creep  $\varepsilon_c$  and damage  $\varepsilon_d$  (due to the reduction of stiffness):

$$\varepsilon = \varepsilon_e + \varepsilon_n + \varepsilon_c + \varepsilon_d$$

Under static loading it is assumed that

$$\varepsilon = \varepsilon_e + \varepsilon_n$$

Under creep at low stress level ( $\varphi \neq 0$ )

$$\varepsilon = \varepsilon_e + \varepsilon_n + \varepsilon_c$$

At cyclic loading in fiber direction the mean strain  $\varepsilon''$

$$\varepsilon'' = \varepsilon_e + \varepsilon_d + \varepsilon_c$$

and strain amplitude:

$$\varepsilon^a = \varepsilon_e + \varepsilon_d$$

Under cyclic loading at  $\varphi \neq 0$  all the constituents should be taken into account for mean strain  $\varepsilon''$ :

$$\varepsilon'' = \varepsilon_e'' + \varepsilon_n'' + \varepsilon_d'' + \varepsilon_c''$$

but strain amplitude is not influenced by creep

$$\varepsilon^a = \varepsilon_e^a + \varepsilon_n^a + \varepsilon_d^a$$

#### 3.2 Static loading

It is assumed that the nonlinear strain increment of fiber composite follows the associated flow rule with a quadratic stress yield function  $f(\sigma_{ij})$  (Sun & Chen 1989). The requirements of orthotropic symmetry and assumption that  $\varepsilon_{11n} = 0$  leads to simple potential function for plane stress state:

$$2f = \sigma_{22}^2 + 2a\sigma_{12}^2 = k \quad (1)$$

According to the associated flow rule the strain increments are determined by relation

$$\Delta\varepsilon_{ij} = \frac{\partial f}{\partial \sigma_{ij}} \Delta\lambda, \text{ i.e. } \begin{Bmatrix} \Delta\varepsilon_{11} \\ \Delta\varepsilon_{22} \\ \Delta\varepsilon_{12} \end{Bmatrix} = \begin{Bmatrix} 0 \\ \sigma_{22} \\ 2a\sigma_{12} \end{Bmatrix} \Delta\lambda$$

where proportionality factor  $\Delta\lambda$  is a nonlinear function of the applied stress. Usually it is expressed through plastic energy increment

$$2f\Delta\lambda = \sigma_{ij}\Delta\varepsilon_{ijn}$$

Applying the approach to off-axis tension test (stress  $\sigma_\varphi$  acts under angle  $\varphi$  to axis 1) we have

$$f = \sigma_\varphi^2 \cdot h^2(\varphi)$$

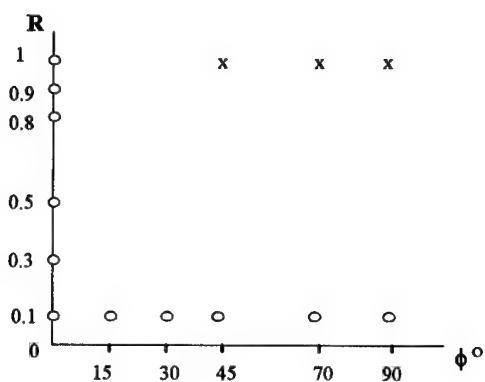


Figure 2. Summary of test program in terms of loading angle and stress ratio for tensile loading; o - denotes a full durability curve (or S-N curve); x - denotes only creep curve.

where

$$h^2 = \sin^4 \varphi + a \sin^2 \varphi \cos^2 \varphi$$

and

$$\Delta \varepsilon_{\varphi} = 2\sigma_{\varphi} \cdot h^2 \Delta \lambda$$

The equations comprise one unknown parameter  $a$ , which vanishes at tension in direction 2 ( $\varphi = 90^\circ$ ). Therefore it is convenient to determine  $\Delta \lambda$  by this test and consequently

$$\Delta \lambda = \frac{\Delta \varepsilon_{90}^p}{2\sigma_{90}^0}$$

Having only proportional loading, the function increments can be replaced by functions, and

$$\frac{\varepsilon_p^p}{\sigma_p h^2(\varphi)} = \frac{\varepsilon_{90}^p}{\sigma_{90}^0}$$

should be invariant function for all angles  $\varphi$ . The experimental results are displayed in Figure 3, as  $\bar{\sigma} = f(\bar{\varepsilon}_p)$  where the effective stress  $\bar{\sigma}$  and effective strain  $\bar{\varepsilon}_p$  is used following the designations of Sun & Chen (1989):

$$\bar{\sigma} = \sigma_{\varphi} h(\varphi) \quad \bar{\varepsilon}_p = \frac{\varepsilon_{\varphi}}{h(\varphi)}$$

and constant  $a$  used to fit all curves is  $a = 1.6$ .

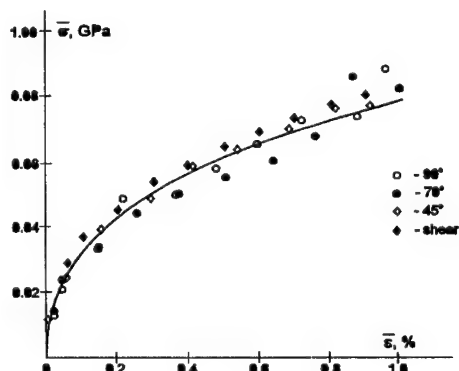


Figure 3. Effective stress vs. effective non-linear strain of composite in static tension and shear.

### 3.3 Creep

A series of short-term creep compliance curves  $I_{11}^p(t)$  for  $\varphi = 0^\circ, 45^\circ, 70^\circ, 90^\circ$  were obtained experimentally at stresses of 50% of the corresponding strength levels and temperatures 20, 30, 40 and 50°C, and were approximated by relation

$$I_{11}^p(t) = \frac{1}{E_{\varphi}} + \sum_{i=1}^k a_i \left( 1 - \exp\left(-\frac{t}{n_i}\right) \right)$$

The instantaneous compliance depends on the stress level, while the time-dependent part was found not to depend on stress. The relation results from integral equation:

$$\varepsilon^p = \frac{\sigma_{\varphi}}{E_{\varphi}} + \int_0^t \sigma_{\varphi}(\tau) K_{\varphi}(t-\tau) d\tau \quad (2)$$

with creep kernel in the form of exponent series

$$K_{\varphi}(t) = \sum_{i=1}^k \frac{a_i}{n_i} \exp\left(-\frac{t}{n_i}\right) \quad (3)$$

The number of exponents  $k$  depends on the time interval of the experiment.

The creep compliance at  $\varphi \neq 0$  is

$$I_{11}^p = I_1 \cos^4 \varphi + (2I_{12} + I_{44}) \sin^2 \varphi \cos^2 \varphi + I_2 \sin^4 \varphi$$

where  $I_{44}$  is a shear compliance in main axes,  $I_1$  and  $I_2$  - compliances in fiber direction and transverse direction. Having no shear creep test, the time-dependent value of  $2I_{12} + I_{44}$  was determined from  $45^\circ$  creep, and result verified for other angles  $\varphi$ . In Figure 4 the predicted and measured compliances at  $\varphi = 70^\circ$  are plotted for different temperatures. The agreement is rather good.

### 3.4 Damage effect at cyclic loading in fiber direction

Having viscoelastic relations (2), (3), where constants  $E, a_i, n_i$  are determined in static and creep tests, it is assumed that the influence of disperse damage on the deformation can be modelled by stiffness reduction (linear increasing of compliance) neglecting its effect, if any, on creep kernel parameters. The axial modulus is expressed as:

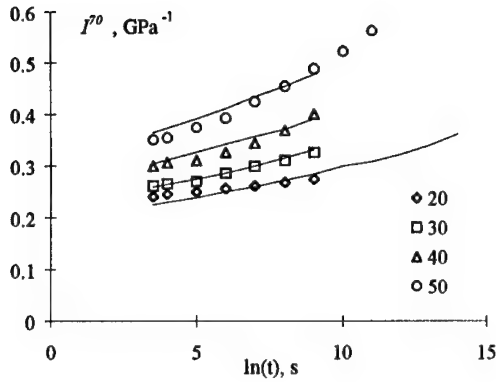


Figure 4. Creep compliance  $J^{70}$  under tensile loading at angle  $\varphi = 70^\circ$  at different temperatures. Lines - prediction based on  $J^{70}$  and  $J^5$  compliances.

$$\frac{1}{\bar{E}} = \frac{1 + cD}{E} \quad (4)$$

where  $D$  is the current relative life time

$$D(\sigma) = \frac{n}{N(\sigma)} \quad (5)$$

where  $n$  - current number of cycles,  $N(\sigma)$  - mean life time, determined from  $S-N$  curve,  $c$  - constant to be determined, which characterizes the reduction of modulus.

For sinusoidal load cycle

$$\sigma = \sigma_m + \sigma_a \cos \omega t \quad (6)$$

mean strain  $\varepsilon_m$  and strain amplitude  $\varepsilon_a$  variation is obtained by direct integration of (2), taking into account (3), (4) and (5):

$$\varepsilon_m = \sigma_m \left[ \frac{1 + cD}{E} + \sum a_i \left( 1 - \exp \left( \frac{-t}{n_i} \right) \right) \right] \quad (7)$$

$$\varepsilon_a \approx \sigma_a \frac{1 + cD}{E} \quad (8)$$

In Figure 5, peak strain, mean strain, and strain amplitude variation under two-stage cyclic loading of GRP with stress ratio  $R = 0.1$  is plotted. Cyclic loading was interrupted after about  $4 \cdot 10^4$  cycles, specimen unloaded for 12 hours, after which loading

was continued up to failure. It can be seen that strain amplitude grows almost linearly during cycling, and unloading does not affect it. Elastic modulus and parameter  $c$  were determined approximating test data by Eq. (8), and mean strain (Eq. 7) and peak strain variation calculated (shown by solid lines in Fig. 5). The model satisfactorily predicts cyclic strain variation both before and after unloading. The same response to interrupted cyclic loading is observed also at a much higher stress ratio loading, Figure 6.

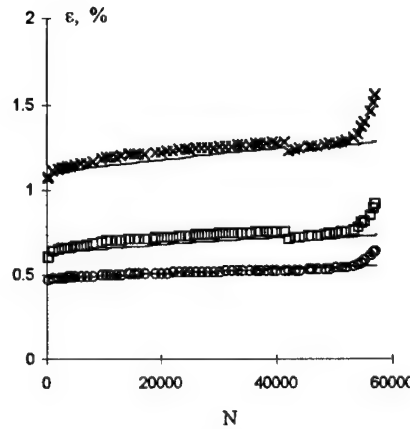


Figure 5. Strain variation during cyclic loading with  $R = 0.1$ ; (x) - peak strain, ( $\square$ ) - mean strain, ( $\circ$ ) - strain amplitude.

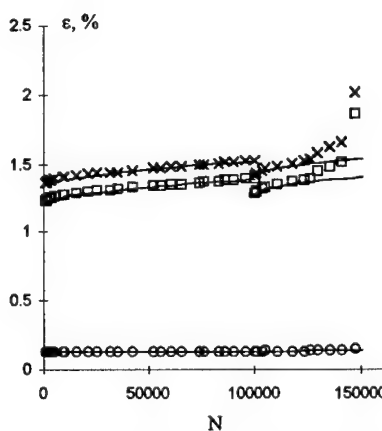


Figure 6. Strain variation during cyclic loading with  $R = 0.8$ ; (x) - peak strain, ( $\square$ ) - mean strain, ( $\circ$ ) - strain amplitude.

Comparison of the values of parameter  $c$  determined from the strain amplitude data obtained at different stress ratios (Fig. 7a) and cyclic stress levels (Fig. 7b) does not reveal any consistent trends, indicating that  $c$  can be considered a material parameter. The large scatter of  $c$  values reflects the experimentally observed variability of GRP response to fatigue loading which is probably caused by misalignments of plies due to manufacturing by hand lay-up.

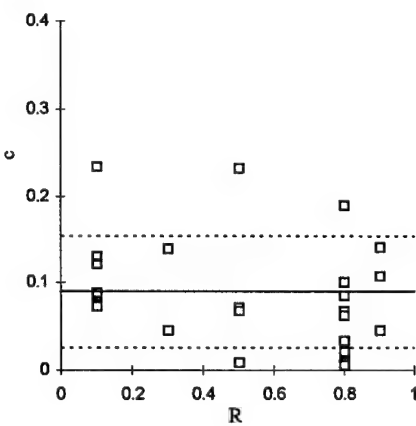


Figure 7a. Parameter  $c$  values for different stress ratios  $R$ ; lines - mean value  $\pm$  standard deviation.

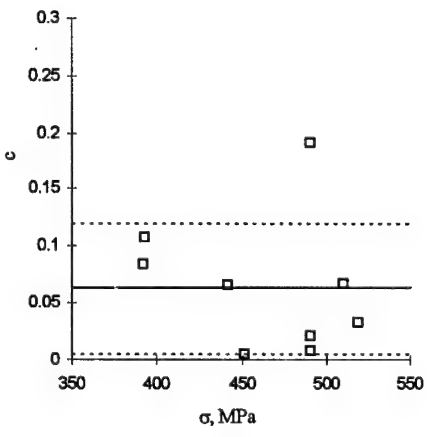


Figure 7b. Parameter  $c$  values for different peak stresses at  $R = 0.8$ , lines - mean value  $\pm$  standard deviation.

### 3.5 Damage strain in cyclic off-axis loading

In off-axis cyclic loading a significant strain increment is observed. The physical explanation of this phenomenon is rather complicated, and it is not obvious whether the accumulation of small defects influence mainly the stiffness or it causes a variation of viscoelastic spectrum also. In Figure 8 three creep curves in transverse direction ( $\varphi = 90^\circ$ ) are displayed obtained for virgin material, after 190 000 fatigue loading cycles at  $R = 0.1$ , and after 540 000 cycles. The results suggest that at least for the given composite and loading direction the cyclic fatigue results only in reduction of stiffness, retaining viscoelastic behavior without notable variation.

It is clear that the nonlinear deformation caused by damage should follow the orthotropic requirements. Besides, for sufficiently large angle  $\varphi \geq \varphi_0$  ( $\varphi_0 \approx 5^\circ \div 10^\circ$ ), the modulus reduction in fiber direction can be neglected. So we are coming to the analogical formalism as discussed above for nonlinear strain components. The damage strain potential turns to one parameter expression:

$$f_d = \sigma_{22}^2 + 2a_d \sigma_{12}^2$$

(the parameter  $a_d$  can be different from  $a$  in (1)).

The increment  $\Delta \varepsilon_{ijd}$  is supposed to be orthogonal to  $f_d$ :

$$\Delta \varepsilon_{ijd} = \frac{\partial f_d}{\partial \sigma_{ij}} \Delta \lambda_d$$

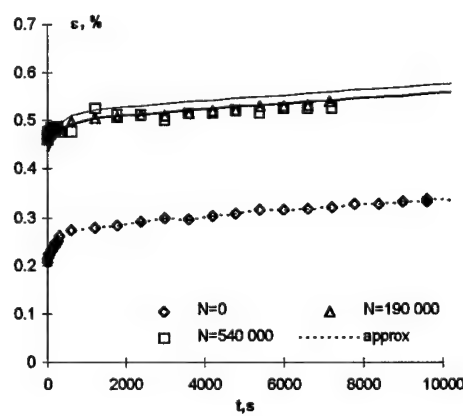


Figure 8. The effect of fatigue loading on creep in transverse direction.

where  $\Delta\lambda_d$  is a function of the damage potential

$$\Delta\lambda_d = \psi(f_d)\Delta n$$

For off-axis loading

$$f_d = \sigma_\varphi^2 (\sin^4 \varphi + 2\alpha_d \sin^2 \varphi \cos^2 \varphi) = \sigma_\varphi^2 h_d^2(\varphi)$$

$$\Delta\varepsilon_d^d = 2\sigma_\varphi h_d^2(\varphi) \Delta\lambda_d = \sigma_\varphi h_d^2(\varphi) \psi[\sigma_\varphi^2 h_d^2(\varphi)] \Delta n \quad (9)$$

Equation (9) becomes invariant to  $\varphi$  when new functions  $\tilde{\varepsilon}_\varphi^d$  and  $\tilde{\sigma}_\varphi$  are introduced:

$$\dot{\tilde{\varepsilon}}_\varphi^d = \frac{\dot{\varepsilon}_\varphi^d}{h_d(\varphi)} ; \quad \tilde{\sigma}_\varphi = \sigma_\varphi h_d(\varphi) \quad (10)$$

Equation (9) takes the form:

$$\dot{\tilde{\varepsilon}}_\varphi^d = \tilde{\sigma}_\varphi \cdot \psi(\tilde{\sigma}_\varphi^2) = \Psi(\tilde{\sigma}_\varphi^2) \quad (11)$$

$$\text{where } \dot{\tilde{\varepsilon}}_\varphi^d = \frac{\Delta\tilde{\varepsilon}_\varphi^d}{\Delta n}$$

In cyclic loading the mean strain is influenced by creep, but gradual stiffness reduction can be registered by monitoring the variation of cyclic strain amplitude  $\varepsilon_a$ . Typical strain variation in cyclic loading with stress ratio  $R = 0.1$  and  $\sigma_{max} = 34$  MPa is shown in Figure 9. The slope angle of curve  $\varepsilon_a$  in the main part is constant and characterizes the  $\dot{\varepsilon}_{35}^d$ . It is assumed that damage rate is determined by  $\sigma_{max}$  rather than  $\sigma_a$ . Therefore finally the formula to be verified is (10), (11) taking  $\dot{\varepsilon}_\varphi^d = \dot{\varepsilon}_{\varphi max}^d$  and  $\tilde{\sigma}_\varphi = \sigma_{\varphi max}$ .

In Figure 10a the  $\dot{\varepsilon}_\varphi^d$  versus  $\tilde{\sigma}_{\varphi max}$  data are summarized. In Figure 10b the same data are plotted in logarithmic coordinates. The value of constant  $a_d = 1.5$  is found, which is close to the value  $a = 1.6$  for nonlinear static strain.

Figure 9 shows that  $\varepsilon_a^d$  initially increases rapidly before linear growth sets in. Apparently such damage behavior can be described by using a damage equation similar to the viscoelastic relations. Such approach has been proposed by Iljushin (1967). As a simpler approach it can be assumed that the initial fast decrease of modulus is referred to the first loading cycle and the curve  $\varepsilon_a(n)$  is replaced by

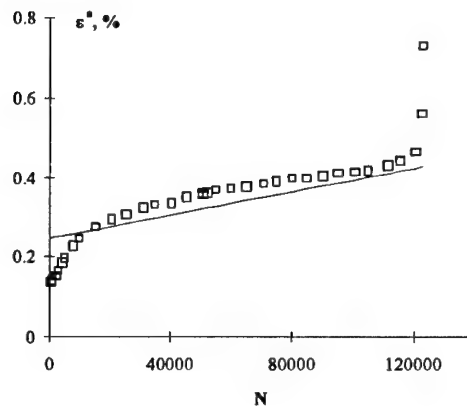


Figure 9. Strain amplitude variation for 45° off-axis specimen.

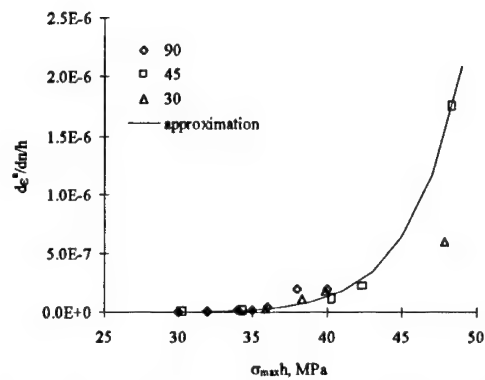


Figure 10a. Damage strain rate vs. effective peak stress for off-axis loading

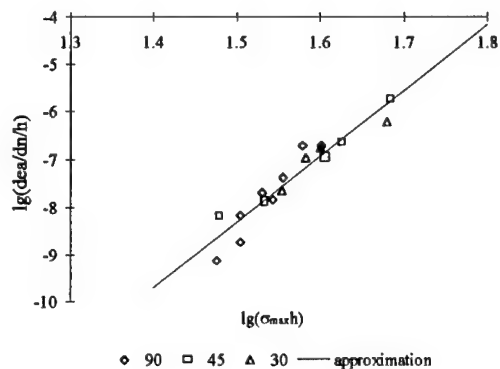


Figure 10b. Damage strain rate vs. effective peak stress for off-axis loading in logarithmic coordinates.

straight line. Taking the value of modulus for the first loading cycle equal to the secant modulus for  $\sigma_{\max}$  determined from the non-linear  $\sigma$ - $\varepsilon$  diagram (described in Section 3.2), good agreement between measured and predicted strain amplitude variation is observed (Fig. 9).

It should be noted nevertheless, that data scattering for damage strain velocity and the experimental point deviation from the master curve is rather significant, as it is seen in Figures 10a, b. It is the result of nonhomogeneity of the specimens and is a subject of further analysis.

#### 4. CONCLUSIONS

The model of creep and damage influence on cyclic deformation of orthotropic composite with complex structure is proposed and experimentally verified. The key features of model are as follows:

1. The damage affects composite strain value through its effect on modulus rather than on the parameters of viscoelastic spectrum of the material;
2. The strain in off-axis loading can be calculated separately from the strain at loading in the direction of unidirectional fibers;
3. The nonlinear static strain and the damage induced strain at off-axis loading are governed by single parameter quadratic potentials and the associated strain rate rule. The parameter values in the nonlinear and damage potential are rather close.

#### REFERENCES

- Andersons, J. & Korsgaard, J. 1997. The Effect of Stress Ratio on Durability and Damage Accumulation in GRP at Uniaxial Loading. In S. Degallaix, C. Bathias & R. Fougeres (eds), International Conference of Fatigue of Composites, Paris, 3-5 June 1997: 315-322.
- Andersons, J. A., Limonov, V. A. & Tamuzh, V. P. 1990. Failure during axial loading of a plastic reinforced at oblique angles with organic fibers. *Mechanics of Composite Materials* 26(2): 182-188.
- Andersons, J. A., Limonov, V. A. & Tamuzh, V. P. 1991. Effect of phase asynchronism on the fatigue resistance of laminated composites in a plane stress state. *Mechanics of Composite Materials* 27(5): 521-529.
- Andersons, J. A., Limonov, V. A., Tamuzh, V. P. & Perevozchikov, V. G. 1989. Fatigue of laminated composites with various reinforcement systems. 2. Plane stress state and calculation model. *Mechanics of Composite Materials* 25(4): 442-450.
- Iljushin, A. A. 1967. About a Theory of Durable Strength. *Mekhanika Tverdovo Tela* (2): 25-35.
- Sun, C. T. & Chen, J. L. 1989. A Simple Flow Rule for Characterizing Nonlinear Behavior of Fiber Composites. *Journal of Composite Materials* 23: 1009-1020.

---

## 4 Infrastructure applications

## Composite infrastructure applications: Concept, design and durability control and prediction

P.Hamelin

L2M, Université Lyon I, Villeurbanne, France

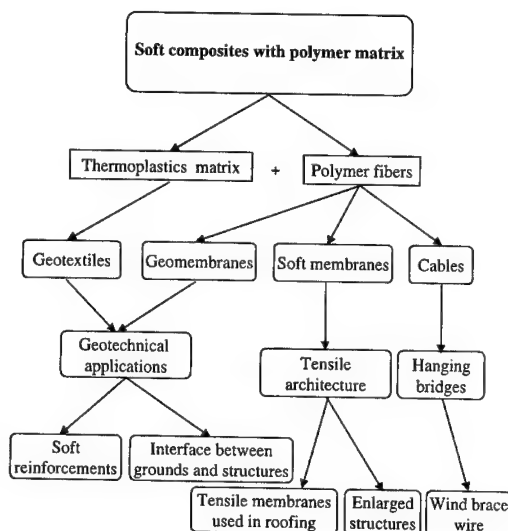
**ABSTRACT:** In the first part, we present the main applications of composites for infrastructures. Then, we develop the usual design method and we consider specific durability analysis illustrated by case studies examined on different scales.

### 1 INTRODUCTION

The composite materials associating fibers of different nature (glass, carbon, aramid, polyester, polyetylen...) with organic matrix (epoxy, polyester, polyurethane...) or with mineral matrix (portland cement, magnesian cement...) are certainly the XXIst century construction materials insofar as their specific properties (ratio between mechanical characteristics and density or natural weight), insofar as their moulding and forming capacities, insofar as their combined properties (multi-properties: mechanical - thermal - acoustic - corrosion...) allow to conceive and make more efficient and more durable structures than the ones with traditional materials (steel, concrete, reinforced concrete, wood...).

In the light of a lot of possible material formulations and combinations for the numerous structural applications, we propose the following classification.

Table 1: Soft composites



### 2 MAIN FAMILIES OF COMPOSITES AND CIVIL ENGINEERING APPLICATIONS

#### Part I

The main families of composites and their applications in the field of construction fall into the three following categories: soft composites and tensile architecture and suspension bridges (table 1), stiff composites and high performance structures (table 2), fibers-cement composites for the construction industry (table 3).

Independently of the usual characterization problems taking into account the anisotropic and orthotropic characteristics of these materials, their material non-linearity under uni-axial and multi-axial sollicitation, their thermo-rheological behavior and more particularly their creeping and relaxation functions are very important to design these structures. In particular, with respect to the failure initiation mechanisms in the vicinity of geometrical singularities and edge effects (figure 3).

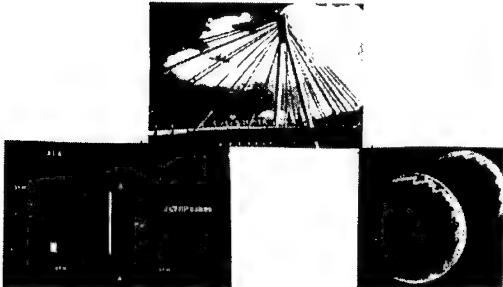


Figure 1: Cable stayed bridges (Ref. EMPA) [1]

One can find the same problem in the case of cables for suspension bridges or for reinforced concrete constructions with post-tensioning. The performance of these construction processes is directly dependent on the anchorage system where it is necessary to minimize the effects of stress concentration and the loss of tension loads due to environmental conditions. In the case of stiff composites (table 2) associating thermosets and glass, aramid or carbon fibers, the design problem is exactly the same as the one met for the aeronautical and automotive applications. Industrial applications use manufactured half-products such as pultruded profiles to create structures with a design similar to metallic ones. In this case, the critical problems essentially concern the joint and buckling stability.

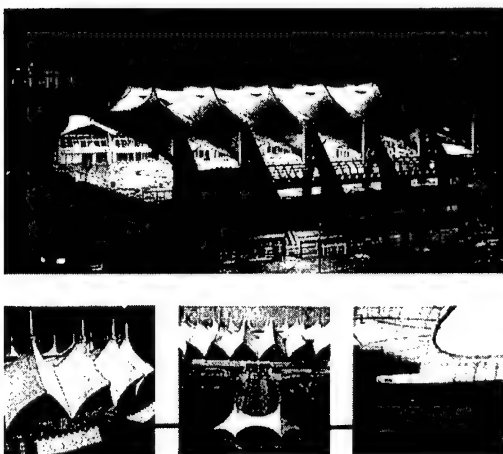
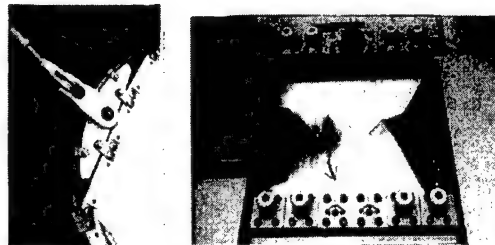


Figure 2: Tensile architecture [2]



Mechanical junction      Textile membrane holding to the crack

Figure 3: Local failure mode of tensile structure

Table 2: Stiff composite

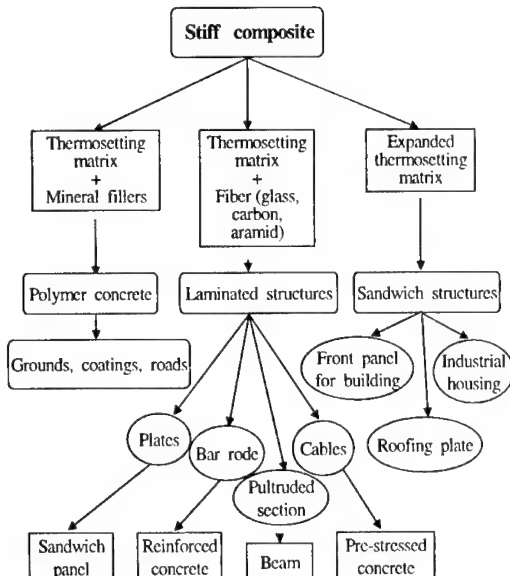
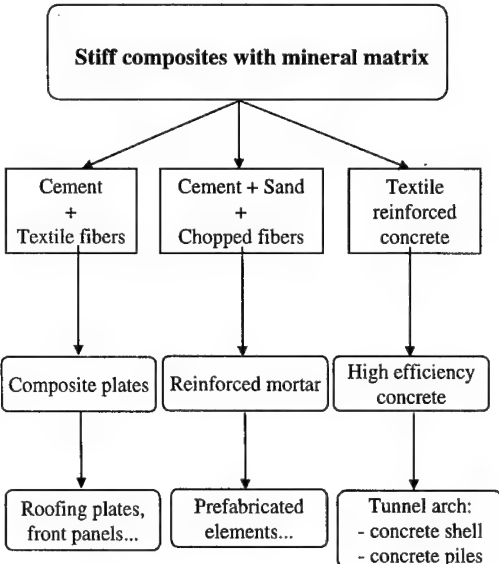


Figure 4: Pultruded composite structures

Table 3: Stiff composites with mineral matrix



In the case of fiber cement composites (table 3) associating different fiber natures with a mineral matrix, in order to obtain micro-concretes or mortars, the main problems concern the products formulation to achieve workability and in situ casting and, on the other hand, the identification of reinforcement characteristics by specific measurement methods such as toughness or strain energy density.

The design criteria for front (facade) panels (figure 5) and for protection elements in concrete and reinforced concrete are directly dependent on the durability of the fibers in a cementitious matrix.

Reinforcement of concrete  
Sewing effect of micro-crack  
Softening effect on the mechanical behaviour law

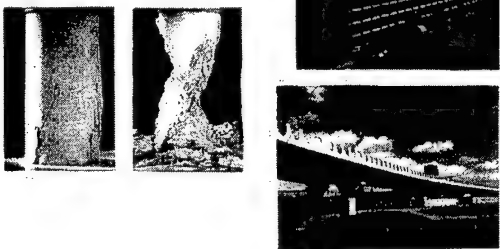


Figure 5: Cement based composite [3]

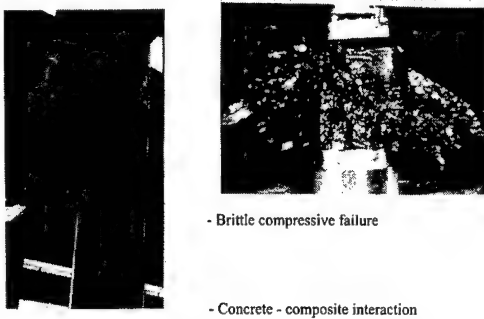


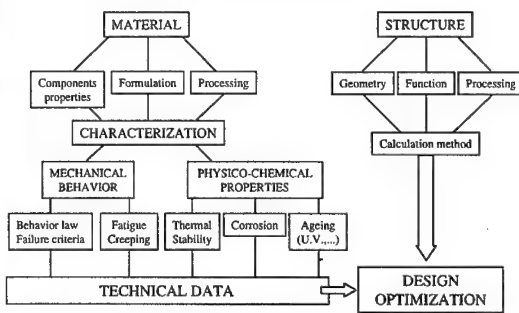
Figure 6: Design and durability control

Composite materials considerably developed during the last few years, to ensure repair, reinforcement and protection of existing civil engineering structures (reinforced concrete, prestressed concrete, metallic frames). The wrapping of bridge piles, the beam reinforcement (figure 6) towards traction or shear is particularly efficient in the case of carbon epoxy composite.

The design codes for traditional materials (ACI, Eurocode) might change, in order to take into account these new materials. However some difficulties concerning some realistic adhesion characteristics (figure 6) between concrete and composite and specific failure modes particularly catastrophic in the case of composites.

The dimensioning of works that include composite materials must take into account the interaction material - structure described in the table 4, where it is possible to understand that structure optimization can be made by new formulations selection (new matrix, new reinforcements, new stacking sequences, new

Table 4: Material-structure interaction



techniques of manufacturing) and not necessarily by the geometrical structure thickness modification that corresponds to the usual methods of dimensioning in the case of isotropic homogeneous structures.

As a consequence, it is necessary to know exactly how to define the load conditions of constructions (load conditions, environmental conditions, expected life time...).

### 3 GENERAL DATA FOR INFRASTRUCTURES DESIGN

The load conditions of structures are taking into account the own weight of the structure, the service loads, the extreme loads. The low density of composite materials is an asset in order to minimize the own weight of the construction. Moreover it is known that their use influence the design of tensile structures (tensile architecture, cable stayed bridges...). The service loads are generally standardized, hereby using values corresponding to the nature of the building or the bridge.

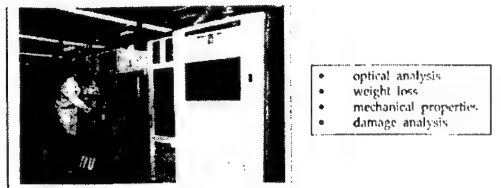
It is important to notice that the extreme sollicitations (impact sollicitation, seisms, explosions) are taken into account in the traditional design rules by a static loads redefinition. If this approach is not a significant problem, in the case of traditional materials, it is necessary to take into consideration multiplication coefficients that take include the sensitivity, the variation of materials behavior laws with respect to the loading conditions.

Likewise, in the case of extreme environmental sollicitations (temperature, hygrometry, corrosion...), it is imperative to take into account the variations of resistance, of ultime extensional modulus or damage variables specific for composite materials.

Consequently, for numerous applications, it is possible to transfer acquired knowledge on the ageing of polymers, composites used in the transportation field (aeronautic, automotive) to the civil engineering field. Nevertheless, we can notice that the accelerated aging methods, the prevision methods (time-temperature-dependence) are confronted to estimates of life time of 10 years, 20 years, 50 years...(figure 7)

So, the retrofitting and validation problems are more and more important when taking into consideration combined sollicitations (mechanical - thermal - hygrometric) and are more and more difficult to model.

In view of effects of composite materials heterogeneity analyzed at different scale levels: (fig.8)



- optical analysis
- weight loss
- mechanical properties
- damage analysis

COMBINED EFFECT OF TEMPERATURE  
ULTRAVIOLET LIGHT, HYGROMETRY PHYSICAL MEASUREMENT

Figure 7 : Accelerated ageing test

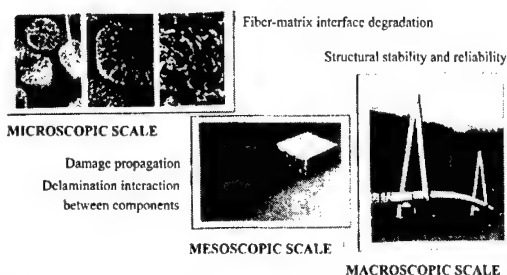


Figure 8 :Multiscale durability analysis

1. - microscopic scale: fiber - matrix - interface,
2. - mesoscopic scale: internal structure of stacking or weaving,
3. - macroscopic scale: multi-materials, mixed structures...

it is necessary to conceive analysis or design codes that integrate the physical phenomena which occur at each level.

### 4 SPECIFIC DURABILITY ANALYSIS AND CONTROL: CASE STUDY

#### 4.1. Durability analysis at microscopic scale

Alkali resistance of fibers in concrete

Performance and durability of fibre-cement composites depend on chemical resistance of the fiber in the cementitious matrix. Fig. 9 shows different ways to improve durability of these materials. First place, one can change the 'matrix' nature by adding mineral additives (eg. pouzzolanes,...), or organic polymers, in order to make it less aggressive. one can also use the new Portland cement formulations or use other hydraulic binders. In the case of glass-fiber, the addition of  $ZrO_2$ ,  $ThO_2$ ,  $SnO_2$  as fibre coatings, significantly modifies material aging. Of course, other fiber choices are possible (carbon, metallic,...).

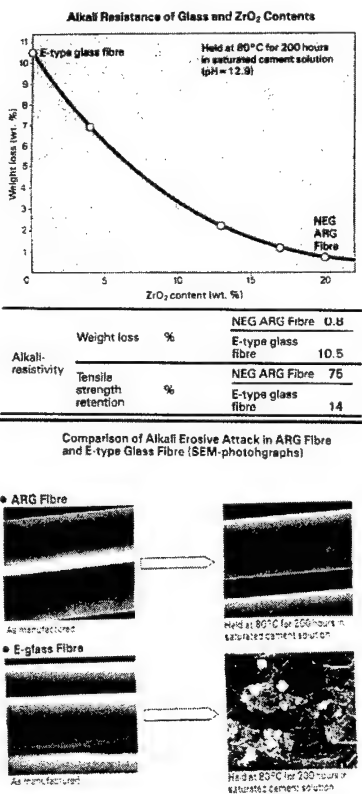
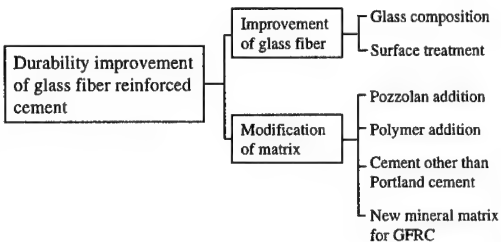


Figure 9 : Durability analysis in cement (doc. NEG)



From a scientific point of view, the following table show that accelerated aging conditions for alkaline resistance tests take different parameters into consideration, such als chemical composition, temperature, test duration...

The latter remark once again raises the issue of extrapolating accelerated test results (of aging) to real(istic) conditions. They allow for better material formulations, but not for life time prediction.

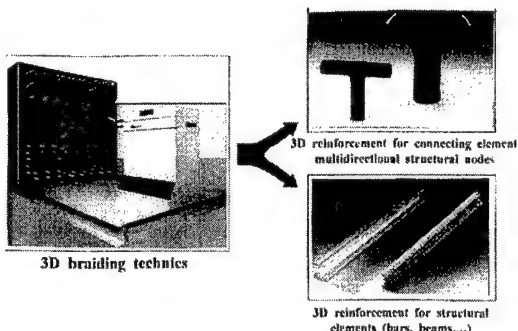


Figure 10 : Durability analysis in 3D composite structures [4] (doc. MURATA)

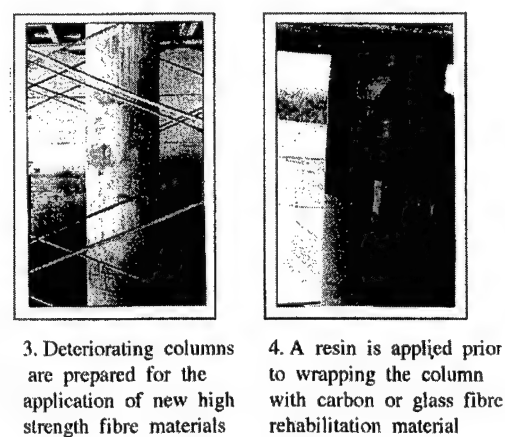
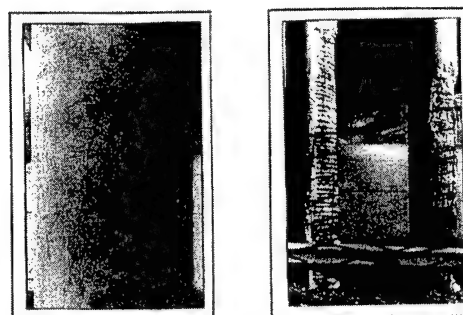


Figure 11 : Retrofitting of concrete structures by composites [5] (doc. ISIS)

#### **4.2. Mesoscopic scale analysis: 3D composite design for high performance applications.**

Laminated composite structures are particularly sensitive to failure mechanisms, due to interlaminar delamination, to bad transverse shear effects and to buckling. In order to improve the durability and reliability of these structures, it is possible to apply three-dimensional reinforcement techniques, such as 3D knitting and 3D braiding.

#### **4.3. Durability analysis at macroscopic scale: mixed composite structures in smart materials, able to assess their durability.**

Sensor integration (optical fibers, strain gauges,...) into repair sheets allows for the dimensional and general stability of the structure, on a real time basis. As an example, following figure illustrates this for a bridge pile, instrumented with optical fibers, in which damage evolution can be followed as a function of time.

### **5 CONCLUSIONS**

As a conclusion, the main problem that limits increased use of composite materials is the following:

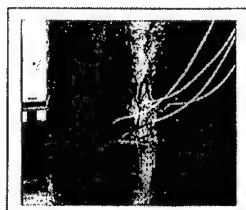
1. material aspects, related to the number of possible material formulations, the difficulty of a reliable material characterization, physical and chemical stability with cement or steel, defective stiffness and a difficult prediction of durability in variable environmental conditions.
2. structural aspects related to imperfections and weaknesses in the design methodology, as well as

poor predictability of environmental and load conditions.

We would like to recommend the development of correct data bases for the basic formulation, transfer of know-how between different industrial sectors (automotive, construction,...), encouragement in the development of prototypes of bridges, a reinforced engineering training in the direction of improved knowledge of composite materials and structures as well as their application fields.

### **REFERENCES**

1. Meier, U. & Betti, R. 1997. *Recent advances in Bridge engineering*. Proceeding of US-Canada-Europe Workshop on Bridge Engineering, Dubendorf & Zurich / Switzerland 11-16 July 1997, EMPA, Ueberlandstrasse 129, CH-8600 Dubendorf, Switzerland.
2. Hamelin, P. & Verchery, G. 1990. Proceeding of Textile Composites in Building Construction Symposium, Lyon France 16-18 July 1990, Ed. Pluralis, 24 rue Descartes 75005 Paris, ISBN 2-862-16-022-9.
3. Hamelin, P. & Verchery, G. 1992. Proceeding of Textile Composites in Building Construction Symposium, Part 1 & Part 2, Lyon France 23-25 June 1992 Ed. Pluralis, 24 rue Descartes 75005 Paris, ISBN 2-862-16-031-8.
4. *High performance fiber reinforced cement composite II*. 1995. Proceeding of The Second International RILEM Workshop, Ed. A.E. Naaman & H.W. Reinhardt, E. & F.N. Spon - Chapman & Hall.
5. *Advanced composite materials in bridge and structures*. 1996. Proceeding of The International Conference Montreal Canada, Ed. M. El Badry, ACMBS Network of Canada, ISBN 0-921-303-645.



Optic fibre strain sensors in a carbon sheet monitor how loads and temperature variations affect the structure

A view of columns repaired and strengthened with carbon and glass fibres, ready for painting

Figure 12 : Durability analysis on a macroscopic scale [5]

## Instantaneous damage kinetic of composite pipes and moisture effect

D.Perreux & C.Suri

*Laboratoire de Mécanique Appliquée R. Chaléat, UMR CNRS 6604, Besançon, France*

**ABSTRACT :** The damage kinetic of composite pipes and moisture effect is presented. At first, diffusion law and the influence of mechanical damage on absorption are presented. Secondly, the change in the kinetics of the damage is studied for various levels of water content. Mechanical tests, under tension and internal pressure with fixed ends, demonstrate an increase in the rate of damage as a function of water content. The damage rate acceleration is taken into account in a behaviour model. The effect of water content in the material is introduced into this model by using a damage-associated variable depending on the moisture level.

### 1 INTRODUCTION

Environmental and mechanical stresses cause degradation of the physical and chemical structure of glass/epoxy composite. This phenomenon has two different aspects : hygrothermal ageing and mechanical damage, each influencing the other. Composite material absorption may be accelerated by damage in the structure and, reciprocally, the aged material becomes damaged more quickly.

The influence of ageing on mechanical characteristics is very widely recognised for instance by: A. Naceri et al (1992), Y. Weitsman, (1991), A. Chateauminois (1991). This being necessarily related to the chemical nature of the matrix and the sizes that are used (A. Bunsell, 1994). Thus, variation of the glass transition temperature and the shear modulus are commonly observed. According to some authors (C.C Chamis 1978 ; H.T Hahn 1987), the loss of mechanical properties may be explained by the plasticization of the matrix and by the degradation of the fibre/matrix interface. The progress of water molecules into the molecular structure swells the matrix, generating internal stresses and inducing loss of resilience. This scenario, although qualitative, seems realistically to represent the influence of water in the damage kinetics.

The phenomena depend largely on the temperature. Thus, Bunsell (1994) suggested that for long-term applications with epoxy matrix, the temperature must be below 60°C, because the loss of mechanical properties is often observed above 70°C.

In the present paper the coupling between absorbed water and instantaneous mechanical damage kinetics of a glass/epoxy laminated tube will be analysed. The study of absorption in damaged composites is briefly presented. The present paper is devoted to a study of the kinetics of damage in aged materials. Finally, a method of coupling the two phenomena will be proposed.

### 2 ABSORPTION

The material adopted for this study is a composite, based on a Ciba Geigy LY 556 polyepoxy matrix with a HY 917 anhydride hardener and DY 30 accelerator, reinforced with 2400 tex E-glass fibres (long fibres). These pipes, manufactured by filament winding, are laminates of layup [+55°, -55°]3, having a diameter of 60 mm and a thickness of 2.5 mm.

An analysis (C Suri and D. Perreux, 1995) carried out on the through-thickness absorption in this material has enabled its absorption law to be

identified. It has been shown that both matrix and composite obey a Langmuir-type law :

$$\begin{aligned} \Delta \frac{\partial^2 C}{\partial x^2} &= \frac{\partial C}{\partial t} + \frac{\partial c}{\partial t} \\ \frac{\partial c}{\partial t} &= \gamma C - \beta c \\ \gamma C_\infty(H) &= \beta c_\infty(H) \end{aligned} \quad (1)$$

with initial and boundary conditions as follows :  
 $C(x,0) = 0$  and  $c(x,0) = 0$  for  $0 < x < h$  and  $t \leq 0$  ;  
 $C(x,t) = C_\infty$  and  $c(x,t) = c_\infty$  for  $x = 0$ ,  $x = h$  and  $t > 0$ .

Here,  $h$  is the thickness,  $\beta$  is the detrapping probability per unit of time (bound free),  $\gamma$  is the trapping probability per unit of time (free bound),  $c$  is the concentration of bound molecules,  $C$  is the concentration of mobile molecules,  $c_\infty$  is the concentration of bound molecules at saturation,  $C_\infty$  is the concentration of mobile molecules at saturation and  $H$  is the relative humidity.

The total absorbed mass of water is obtained by integrating the two phases over the volume :

$$M = \int_V (C + c) \rho dV \quad (2)$$

The absorption parameters are identified by using the method described by Carter and Kibler (1978). These laws are compared with experimental data in Fig. 1.

### 3 MODELLING THE ABSORPTION IN THE DAMAGED COMPOSITE

The damage considered in the present study is produced by mechanical loading. The defects are

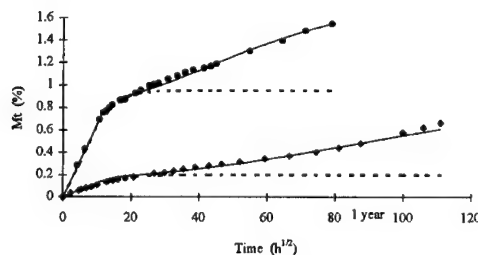


Fig. 1 : Matrix and composite absorption curves at 60°C.  $M_t(\%)$  = percentage of variation of the material mass ; • resin data ; ◆ composite data ; — Langmuir model ; --- Fick model.

mainly due to micro-cracking of the matrix. This type of damage can be assessed by one parameter, for instance the change in the axial modulus of the tubes :

$$D_{zz} = \frac{\Delta E_{zz}}{E_{zz}}$$

The model of absorption in damage composite is obtained by observing the changes in the physical structure of the composite as a consequence of microcracking. In this case, it is assumed that mechanical damage has no influence on the diffusion parameters, but it involves modifications of the absorption boundary conditions. In fact, this approach assumes that damage affects in the absorption rate, i.e. a damage material will absorb, at time  $t$ , the same mass of water as a virgin material at effective time  $\tilde{t}$ . The absorption in the damaged material may be derived from this in the virgin material by writing eqn (1) in terms of the variable  $\tilde{t}$  :

$$\begin{aligned} \Delta \frac{\partial^2 C}{\partial x^2} &= \frac{\partial C}{\partial \tilde{t}} + \frac{\partial c}{\partial \tilde{t}} \\ \frac{\partial c}{\partial \tilde{t}} &= \gamma C - \beta c \\ \gamma C_\infty(H) &= \beta c_\infty(H) \end{aligned} \quad (3)$$

The experimental identification of the relationship between  $\tilde{t}$  and  $t$  has been suggested to be as follows :

$$\tilde{t} = \frac{t}{(1-D_{zz})^{(1-D_{zz})}} \quad (4)$$

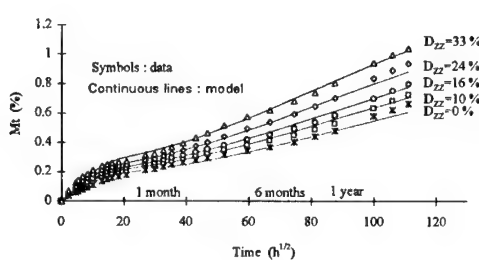


Fig. 2 : Experimental and modelling results of damaged material absorption.

However, the mass of water retained in the cracks cannot be separated from water absorbed by the material. The amount of water remaining in the cracks appears to increase  $M_\infty$  which cannot be interpreted by the equivalent-time description. In order to take damage into account in the Langmuir law, the following formula is proposed :

$$M_{\infty D} = \frac{M_\infty}{(1 - D_{zz})} \quad (5)$$

In Fig. 2, a comparison between the model and the experimental data is presented.

The concentration profile may be determined by means of a numerical calculation, by using the method of finite differences. For an undamaged material, this gives the results shown in Fig. 3. It may be seen that the concentration becomes uniform throughout the thickness after 400 h. Thus, we can assume that each aged layer of the laminated material has the same concentration of moisture after a short time of absorption, and, consequently, the change in mechanical properties due to moisture is independent of the layer position. This is a consequence of the particular nature of this type of material and results from the type of absorption law and the values of the absorption parameters. However, the uniform value of concentration of the material allows us to consider that the mechanical behaviour of the aged laminate can be described by the same model as the unaged material. The effect of moisture will be taken into account by the change in the parameter values. However, it has been observed that absorption from the inner surface of a tube is not similar to the absorption of the outer surface (Baizeau et al 1995 ; Suri 1995). This phenomenon is not yet completely understood, but, nevertheless, the concentration profile is almost unmodified by this characteristic.

#### 4 INFLUENCE OF AGEING ON THE MECHANICAL PROPERTIES

The variation in mechanical properties is greatly affected by the presence of moisture. This influence has been demonstrated through tensile fatigue tests and repeated progressive loading (RPL) tests under internal pressure with fixed ends.

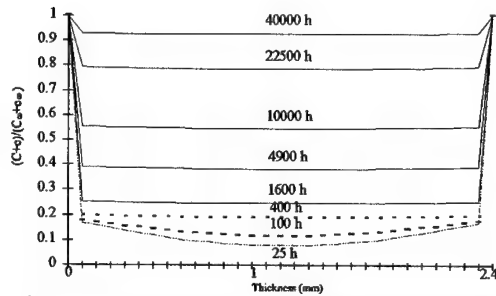


Fig. 3 : Concentration profile of a virgin composite.

#### 4.1 Experimental analysis

##### 4.1.1 Axial and hoop moduli

The influence of ageing has been characterised by experiments carried out on specimens subjected to various hydrothermal treatments at 60°C. In addition to the aged materials, oven-dried specimens and other specimens that were subjected to a complete absorption/desorption cycle were tested. The six states of the tested material are :

- unaged, oven-dried  $\rightarrow M_t \approx 0.0 \%$
- unaged  $\rightarrow M_t = 0.0 \%$  (reference state)
- aged at 336 h  $\rightarrow M_t = 0.2 \%$
- aged at 1500 h  $\rightarrow M_t = 0.3 \%$
- aged at 11 300 h  $\rightarrow M_t = 0.7 \%$
- aged at 11 300 h  $\rightarrow M_t = 0.7 \%$ , and then oven-dried  $\rightarrow M_t = 0.0 \%$ .

Identical test procedures and conditions were systematically applied in order to minimise the measurement error. Each test started with a measurement of Young's modulus. All tests were performed as follows. A tensile test is used to assess the axial modulus, and, still on the same specimen (aged or not), a pure internal pressure test allows us to obtain the hoop modulus. As may be seen in the Fig. 4, the rigidity of the composite remains constant during ageing.

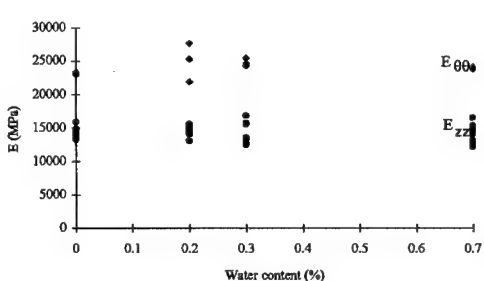


Fig. 4 : Variation of the elastic moduli of the composite as function of water content.

The scatter is mostly due to the manufacturing process which can involve a change in the fibre volume fraction and the difficulties to perform test with aged tubes.

#### 4.1.2 Tensile fatigue tests

This type of test consists of applying a tensile force to the material. It was carried out on a screw-type electromechanical tensile machine. The test starts with a measurement of the  $E_{zz}$  modulus, followed by cycling and a pause of 10 min. The purpose of the wait is to allow recovery of the retarded strains before the modulus measurement. This procedure is repeated until the material fails. The modulus measurement consists of a single rise and fall of load between 0 and 15 MPa, with a rate of loading of  $1 \text{ MPa s}^{-1}$ . As previously introduced, the damage parameter is  $D_{zz} = \Delta E_{zz}/E_{zz}$ . The cycling is composed of 50 or 100 triangular cycles between 0 and 55 MPa at a frequency of 0.05 Hz. By carrying out this process on aged and fresh specimens, the experimental damage data are obtained as shown in Fig. 5.

A very marked increase in the damage rate with water content may be observed. The number of cycles to failure also decreases significantly. This degradation in the properties is not irreversible - removing the water has a beneficial effect on the fatigue properties. Thus, a material aged for 18 months ( $M_t = 0.7\%$ ) and then oven-dried behaves like an unaged material. This tendency is logical. Indeed, the improvement of the behaviour between aged material and dried material could be expected, but the virtually complete recovery of the properties

is unexpected since a loss of material and change in the appearance of fibres, and therefore an hydrolysis, were observed during absorption. This seems to indicate that for the time of our experiment and even if irreversible chemical degradation occurs, its effect is insufficient to modify the mechanical properties significantly. Thus, the only element which has a wide influence on the mechanical properties is connected to the weight of absorbed water. This does not mean that chemical reaction is not present in the aged composite, but it means that, with regard to the change in mechanical properties only, the absorbed water mass must be considered as a variable. Therefore, for the time of our experiment, the influence of moisture on the mechanical properties must be described only by taking into account the amount of absorbed water mass. It is possible that for longer experiments incomplete recovery of the properties could be observed. In this case the mechanical behaviour laws should take into account explicitly the chemical changes. However, this problem is very difficult and should be solved by a group of researchers with competence in the mechanical and in physico-chemical field.

#### 4.1.3 Repeated progressive loading tests under internal pressure with fixed ends

A three-dimensional model cannot be developed without knowing the behaviour of the material in a complex stress state. In tubular specimens, internal pressure tests with hydrostatic end forces generate a state of plane stress. The pressure acts simultaneously on the clamping devices and on the walls of the tube, resulting in the stress state  $2\sigma_{zz} = \sigma_{yy}$ . The applied stresses as a function of time are shown in Fig. 6. An example of results of these experiments are given in Figs. 7.

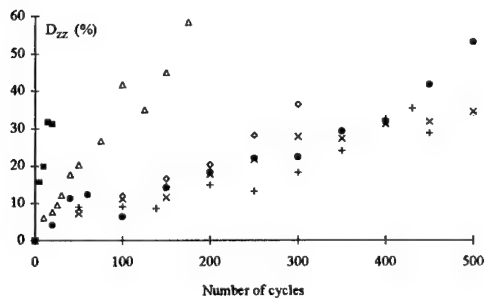


Fig. 5 : Influence of water content on the fatigue damage kinetics : +, oven dried ; X, unaged ; ◊, aged for 15 days ; V, aged for 2 months ; ■, aged for 18 months ; ●, aged for 18 months and oven-dried again.

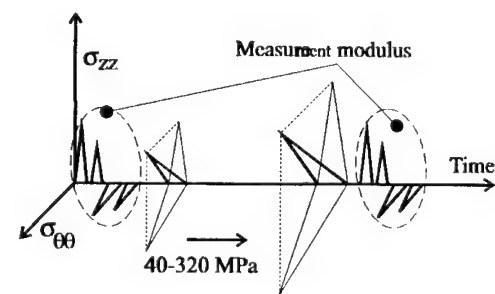


Fig. 6 : Stresses imposed in a biaxial RPL test

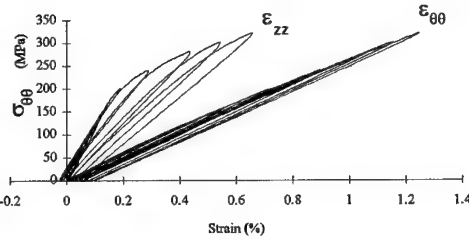


Fig. 7 : Stress/strain curves in a test under internal pressure with fixed ends on an aged material (18 months).

By measuring the elastic moduli  $E_{zz}$  and  $E_{\theta\theta}$  between each loading/unloading cycle with the previously described procedure, the damage variation during the tests can be obtained. If the same test is carried out on specimens having different water contents, the kinetics of the damage may be plotted as functions of the ageing parameters as shown in figure 8.

These results are in accordance with fatigue data. Indeed, the moisture increases the damage rate. Taking into account the reversibility of the effect of water on the composite material behaviour observed in the fatigue tests, mathematical modelling of the instantaneous damage of aged materials consists in determining the relationships linking the damage parameters of an unaged material to the water content, and then in introducing them into an existing behavioural model. This method is valid for the time period in which the reversibility of the water effect can be observed. If substantial hydrolysis were to occur, it would be necessary to modify the model presented later by introducing into the damage kinetics a term able to describe the damage due to the water. But in our case, the effect

of the water can be considered simply as a sort of "catalytic agent" of the damage which is produced by the mechanical loading.

## 5 MODEL OF MULTIAXIAL BEHAVIOUR

This model was developed to describe the instantaneous behaviour of composite pipes under multiaxial stresses. It is presented in detail in D Perreux and F. Thiebaud (1995). For overall behaviour including time dependant behaviour the present model have been improved (F. Thiebaud and D. Perreux 1996 ; D. Perreux and E. Joseph 1997). Only a restricted description of the part of the model accounting for the instantaneous damage in the material will be given here. By using a micromechanical model and the classical laminate theory, it has been shown that the stiffness tensor ( $\underline{\underline{C}}$ ) of the damaged material can be expressed as a function of  $D_{zz}$  :

$$\underline{\underline{\tilde{C}}} = \underline{\underline{C}} + D_{zz} \underline{\underline{C}}_1 + D_{zz}^2 \underline{\underline{C}}_2 \quad (6)$$

where  $\underline{\underline{C}}$  is the stiffness tensor of the undamaged materials and  $\underline{\underline{C}}_1$  and  $\underline{\underline{C}}_2$  are tensors obtained by the micromechanical modelling of the damage .

By similarity with the plastic theory, an internal variable,  $Y_{zz}$ , associated with the damage can be defined. This variable is the driving force for the damage :

$$Y_{zz} = \frac{\partial \psi_L}{\partial D_{zz}} \quad (7)$$

where  $\psi_L$  is the free energy density given by :

$$\psi_L = \frac{1}{2} \underline{\underline{\tilde{C}}} \underline{\epsilon}_e \cdot \underline{\epsilon}_e + \psi_L^* \quad (8)$$

$\psi_L^*$  is a function of the other internal variables and  $\underline{\epsilon}_e$  the elastic strain. Finally we obtain :

$$Y_{zz} = \frac{1}{2} (2\underline{\underline{C}}_2 D_{zz} + \underline{\underline{C}}_1) \cdot \underline{\epsilon}_e \cdot \underline{\epsilon}_e \quad (9)$$

A cumulative damage variable,  $\bar{D}_{zz}$ , is introduced in order to define an associated work-hardening variable,  $R_D$  :

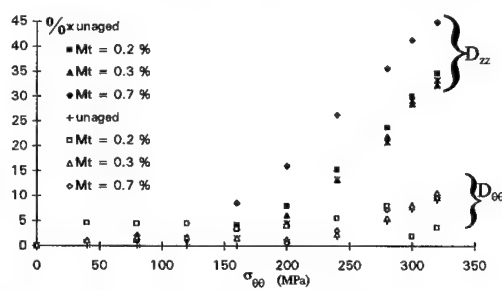


Fig. 8 : Variation in the damage versus the hoop stress in a RPL test under internal pressure with fixed ends for various aged material.

$$R_D = \frac{\partial \psi_L}{\partial D_{zz}} \quad (10)$$

The role of  $R_D$  is to store the maximum value of  $-Y_{zz}$ .  $\bar{D}_{zz}$  is a cumulative damage variable, which, according to the scalar description of the damage, may merge with the damage variable,  $D_{zz}$ , itself, but eqns (7) and (10) require the definition of both variables. To obtain the instantaneous damage kinetics we define a damage criterion,  $f_D$ , and by using the normality rule we can write :

$$\begin{aligned} D_{zz} &= -\lambda_D \frac{\partial f_D}{\partial Y_{zz}} \\ \bar{D}_{zz} &= -\lambda_D \frac{\partial f_D}{\partial R_D} \end{aligned} \quad (11)$$

where  $\lambda_D$  is the Lagrangian multiplier. For the damage criterion, the following form is proposed :

$$f_D = <-Y_{zz}> - R_D - Y_z^c \leq 0 \quad (12)$$

where  $Y_z^c = 0.075 \text{ MPa}^{-1}$  is a constant which represents the minimum value of the driving force  $Y_{zz}$  where damage can be observed.

The law connecting  $R_D$  to  $\bar{D}_{zz}$  is given by the relationship (Fig 9):

$$R_D = \alpha_D (\bar{D}_{zz})^{P_D} \quad (13)$$

## 6 MODELLING THE KINETICS OF THE DAMAGE OF AGED MATERIAL

This model is based on that given previously and on the assumption that the concentration of water is the same throughout the thickness. As we saw before, this assumption is satisfied by the material studied

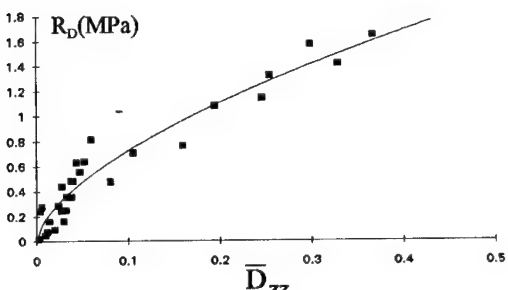


Fig. 9 : Relationship between  $R_D$  and  $\bar{D}_{zz}$ .

except for relatively short ageing times :

$$\begin{aligned} R_D &= -Y_{zz} - Y_z^c \\ &= \frac{1}{2}(C_1 + 2D_{zz}C_2)\tilde{C}^{-1}\cdot\sigma\cdot\tilde{C}^{-1}\cdot\sigma - Y_z^c \end{aligned} \quad (15)$$

The values of  $\alpha_D$  and  $P_D$  are determined from the experimental data by using the method of least squares.

According to this method, from using the data from the RPL tests under internal pressure with fixed ends, the values of the parameters  $\alpha_D$  and  $P_D$  are obtained for materials aged at different levels. Knowing the  $\alpha_D$  and  $P_D$  values as a function of the quantity of water absorbed, the laws describing how they vary may be determined. These relationships may be expressed in the form of two linear equations as functions of  $M_t$  :

$$\begin{aligned} P_D &= P_0 + qM_t \\ \alpha_D &= \alpha_0 + wM_t \end{aligned} \quad (16)$$

The graphical form of these laws is given Fig. 10. By incorporating these two laws of variation into the model, it is possible to model the change of the damage for instantaneous loading.

## 7 COUPLING

In use, the pipes are stressed simultaneously by the wet environment and by mechanical loads, due essentially to the pressure. In such a situation we are obliged to develop a model capable of taking into account the simultaneous changes in the damage and the water content. In fact, this model is a combination of both parts previously described :

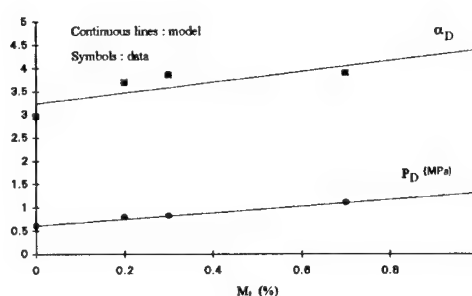


Fig. 10 : Variation in  $\alpha_D$  and  $P_D$  as functions of water content.

the absorption part of the damaged materials and the part connected with the damage kinetics of aged materials.

In what follows, the entire model will be validated through tests where there are successively some periods of damage and some periods of ageing. For instance, we consider that the first step to have a duration of 1500 h. During this time, we assume that there is a single loading/unloading cycle under internal pressure with fixed ends ( $\sigma_{00} = 250 \text{ MPa}$ ). By use of the damage model, the amount of damage in the material is calculated, and then, with the absorption model, it is possible to determine the water content of an initially damaged material aged for 1500 h. In this way, we obtain the water concentration profile and the level of damage acquired during the first step, which are the initial conditions for the second step.

The second step is considered to be of 700 h duration, containing loading/unloading cycle ( $\sigma_{00} = 300 \text{ MPa}$ ). By performing the above calculation, the moisture and damage levels at the end of 2200 h can be obtained, constituting the initial conditions for the third step. Continuing the calculation in this way, it is possible to model the quasi-simultaneous variations in the damage and the water concentration in the material.

To sum up, the material was exposed to the following stresses :

- 250 MPa loading/unloading, absorption for 1500 h
- 300 MPa loading/unloading, absorption for 700 h
- 350 MPa loading/unloading and absorption thereafter.

However, since the parameters  $\alpha_D$  and  $P_D$  depend on the moisture content, some of the formulae must be completed in the model of the mechanical behaviour. Indeed, for an aged material :

$$R_D = \alpha_D (M_t) (\bar{D}_{zz})^{P_D(M_t)} \quad (17)$$

and

$$dR = \frac{\partial R}{\partial M_t} dM_t + \frac{\partial R}{\partial \bar{D}_{zz}} d\bar{D}_{zz} \quad (18)$$

The latter equation indicates that during the absorption phase, changes in the value of  $R_D$  are due to variations of  $\alpha_D$  and  $P_D$  as a function of the absorbed mass. Moreover, this last relation suggests that desorption is able to damage the material.

Table 1 : Experimental and simulation results

Time (h)	0	1500	2200
Water content measured (%)	0	0.33	0.36
Water content calculated (%)	0	0.28	0.36
Load $\sigma_{00}$ (MPa)	250	300	350
Damaged measured (%)	9.6	36	47
Damaged calculated (%)	7.7	24	42

By introducing these modifications into the model, it is possible to obtain the results given in Table 1 and show in Fig. 11.

The rather good agreement between the simulation results and the experimental data show that the coupling between moisture absorption and instantaneous damage can be described by the proposed model. The main difficulty is to assess the material parameters required by the model application (tubes for fluid transportation). The model has been specially developed for an important type of application (laminated tubes ( $\pm \theta$ ) for fluid transportation). Then the identification is easy in this case if a biaxial test is used. In particular, it needs two steps. First of all the mechanical behaviour must be determined by using repeated biaxial loadings on tubes. Secondly the moisture absorption model must be identified.

## 8 CONCLUSION

The hydrothermal ageing of a  $[+55^\circ, -55^\circ]_3$  tubular laminated composite induces significant changes in the mechanical behaviour.

With the aid of two independent models, it has been demonstrated that the absorption of a damaged

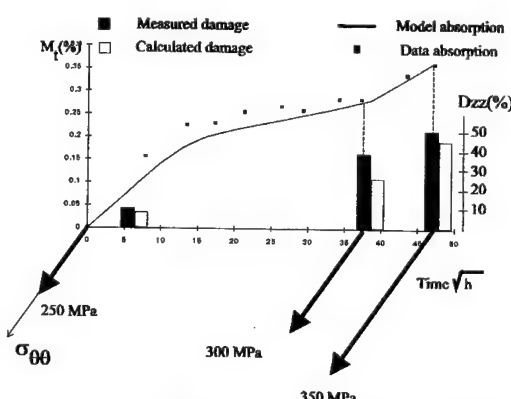


Fig. 11 : Model of the absorption/damage coupling.

material and the damage of an aged material are interrelated phenomena. The overall behaviour depends on the water content and on the level of damage.

The proposed model is well adapted to describe the instantaneous damage ; it is obvious that the time-dependent damage must be also modified by the mass of absorbed water. The identification of this effect will require very long and unusual tests for instance creep tests with water absorption and could be a perspective of this study.

#### ACKNOWLEDGEMENTS

The authors thanks EDF/DER/EMA, and most especially Mr. D. PARIS, for the support and interest in this work.

#### RÉFÉRENCES

- Baizeau, R. Davies, P. Choqueuse, D. & Le Bras, J 1996. *Evaluation of integrity of composite tubes, Progress in Durability Analysis of Composite Systems*, Ed by Cardon, A.H. Fukuda, H. & Reisnider K., Balkema Rotterdam , (1996) 225-232.
- Bunsell, A.R 1994. *Hygrothermal Ageing of Composite Materials, Proceeding of Composite Materials in the Petroleum Industry*, Les rencontres scientifiques de l'IFP, Rueil-Malmaison,
- Carter, H.G. & Kibler, K.G 1978. *Langmuir-Type Model for Anomalous Moisture Diffusion in Composite Resins*. J. Composite Materials, 12 , 118-131.
- Chamis, C.C. Lark, R. F. & Sinclair, J.H 1978. *Integrated Theory for predicting the hygrothermomechanical Response of Advanced Composite Structural Components*. ASTM STP 658, 160-192.
- Chateauminois, A 1991. *Comportement viscoélastique et tensile en fatigue statique de composites verre/époxy. Influence du vieillissement hygrothermique*. PhD thesis, Université Claude Bernard, Lyon.
- Hahn, H.T 1987. *Hygrothermal damage in graphite/epoxy laminates*. J. Engng Mater. Technol. 109, 3-11
- Naceri, A. Surrel, Y. & Vautrin, A 1992. *Influence de l'humidité sur le comportement en cisaillement de composites à matrice polymère*, Annales Des Composites 1992/1-2, Composites à matrice polymères et humidité, A Vautrin(eds), 5-14.
- Perreux, D. & Thiebaud, F 1995. *Damaged Elasto-Plastic Behaviour of  $[+φ,-φ]$  Fibre-Reinforced Composites Laminates in Biaxial Loading*. Composites Science and Technology 54, 275-285.
- Perreux, D. & Joseph, E. 1997. *The effect of the frequency on the fatigue performance of filament-wound pipes under biaxial loading : Experimental results and damage model*. Composites Science and Technology 57, 353-364.
- Suri, C 1995. *Etude du couplage des phénomènes d'absorption et d'endommagement dans un composite verre-époxy*. PhD thesis, Université de Franche-Comté, 446
- Suri, C. & Perreux, D 1995. *The Effect of Mechanical Damage in a Glass Fibre/Epoxy Composite on the Absorption Rate*. Composites Engineering, vol. 5, 4, 415-424.
- Thiebaud, F & Perreux, D 1996. *Overall mechanical behaviour modelling of composite laminate*. European J. mech, A/Solids, 15,n°3,423-445
- Weitsman, Y 1991. *Moisture and Composites : Sorption and Damage*. In *Fatigue of composite Materials*. K. Reifsneider (eds). Elsevier, Amsterdam. , (1991). 385-429

## Mechanical behavior of multiaxial reinforced composites sun light degraded

F.Segovia, C.Ferrer, V.Amigó & M.Salvador

Departamento de Ingeniería Mecánica y Materiales, E.T.S.I.I. Universidad Politécnica de Valencia, Spain

C.Bloem

Facultad de Ingeniería, Escuela de Ingeniería Mecánica, Universidad de los Andes, Mérida, Venezuela

**ABSTRACT:** We have studied the mechanical behavior of polyester composites reinforced with glass fiber cloth, taffeta, or multiaxial 2D which is degraded under sun light conditions. The elaboration procedure was the hand contact method, which is supposed to be the worst; so it could represent the most unfavorable conditions. Eight reinforced sheets were disposed asymmetrically. Laminates were exposed to a UV-visible IR light source, up to 7000 hr.

A mathematic correlation has been obtained on the mechanical properties. The degradation follows a damped exponential model. We studied the influence of kind of resin, reinforcement distribution, and cure conditions. Laminates done with resins with higher reactivity shows better behavior against fracture and higher plasticity. The cure heat treatment increases the mechanical properties.

### 1 INTRODUCTION

Day by day the glass fiber reinforced polyester GFRP are getting more usage, due to their relatively low weight, good mechanical behavior, microbiological durability, dissolvents stability (Blicblau et al. 1993), alkali and acid media (Somiya & Morishita 1993, Fujii et al. 1993).

The relatively low cost, the easy processing and elaboration techniques of GFRP are making wider the application in the aeronautical, naval and terrestrial industry (Castaing et al. 1993; Karama et al. 1993), furthermore, in some cases the GFRP mechanical properties are better than metal's ones.

The study of the toughness behavior and interlaminar crack growth in composites has been improved in the last ten years. Many of the researchers had been working on unidirectional reinforced PREPEG glass fiber-epoxy (Murri & Martin 1993), carbon-epoxy and carbon-PEEK (Hojo & Aoki 1993), graphite-bismaleimide (Sriram et al. 1993). Some authors (Iwamoto et al. 1993) had worked in the relation between fracture toughness (intra and interlaminar) and the toughness behavior in mode I and II.

It is commonly to find bibliography related to the harmful effect of sun light radiation. We found in the bibliographical review some works related to the behavior of carbon-epoxy (Pintado 1992) glass fiber-epoxy (Evans et al 1995) to the high energy radiation behavior. But no works were found in the effects of sun light effect upon the loss of mechanical

properties of multiaxial laminates. We try to study the accelerated effect on the mechanical properties of multiaxial reinforced polyester with UV-visible light emulating the sun light conditions. We also study the effects of kind of resins and cured temperature.

### 2 MATERIALS

Laminates were made of 8 asymmetrically sheets of equilibrated fabric with thickness of 3 mm for taffeta and 4.5 mm for multiaxial.

The matrix that we employed were an orthophthalic polyester with two different reactivity levels BASF PALATAL P5 and P6. We decide to use these resins due to their dissimilar mechanical properties and commonly industrial applicability. As could be seen on table 1.

Table 1 Resin physical properties.

	P5	P6
Tensile Strength	80 MPa	65 MPa
Elongation	2.3%	2.0%
Flexural Strength	110 MPa	115 MPa
E (flexural)	4 GPa	4.5 GPa
Toughness	14 kJ/m <sup>2</sup>	20 kJ/m <sup>2</sup>
Reactivity level.	Medium	High
HDT	70 °C	105 °C
T <sub>G</sub>	95 °C	121 °C

Table 2 Physical Properties.

Sample	Reinforce- ment	Density ( $\text{g/cm}^3$ )	Vf (%)	Va (%)
AT1	Taffeta (0-90°)	1.66	31.7 (A)	1.0 (A)
		1.62 (T)	32.0 (F) 32.2 (T)	2.5 (F) 5.0 (T)
AM2	Multiaxial (0-90°)	1.58	32.4 (A)	8.2 (A)
			32.9 (F) 33.6 (T)	8.9 (F) 9.6 (T)
BM3	Multiaxial (0-90°)	1.57	33.7 (A)	9.4 (A)
		1.61 (T)	32.8 (F) 32.2 (T)	6.8 (F) 4.1 (T)
BM3C	Multiaxial (0-90°)	1.58	33.4	8.7 (A)
			33.2 (T)	8.5 (F) 8.2 (T)

(A) Axial Samples    (F) Flexural Samples  
(T) Fracture Samples

The samples used on the fracture toughness test had an insert of Teflon sheet with thickness 45  $\mu\text{m}$  and length of  $22.5 \text{ mm} \pm 1.5 \text{ mm}$  placed between the 4th and 5th reinforced sheet. Laminates were cured at room temperature of 17° C with the exception of laminate BM3C which its controlled cured temperature was 40° C. We demolded all the laminates after 24 hours.

Laminates characteristics are summarized in the Table 2.

### 3 EXPERIMENTAL PROCEDURE

#### 3.1 Polymer Aging.

The aging essay has been done applying UV light to the prepared samples. Samples were positioned in a chamber equipped with one sun light radiation adjusted lamp 300 Watt OSRAM VITALUX. The chamber's temperature was of 50° C. Sample-lamp average distance were 50 cm which varies from 42 cm on center to 65 cm on lateral sides. Mechanical characterization were done after 500, 1000, 1500 hours of exposition, and in some cases up to 7000 h. These times are equivalent to an average sun light radiation of 300, 600, 900 and 4200 days (0.8, 1.6, 2.5 and 11.5 years).

#### 3.2 Mechanical characterization.

Tensile test were developed according to ASTM D3039-76 on an INSTRON 4202 Testing machine.

Sample length was of 207 mm, and length between marks of 127 mm. The essay was developed using an extensometer. The displacement speed was 1 mm/min.

The flexural test were developed according to ASTM D 790 M-86 with a three points bending tool on the INSTRON 4202. Sample length were of 150

mm, width 25 mm. The length thickness ratio were 25:1, with the exception on taffeta's laminates that was 30:1. Displacement speed was 5.1 mm/min.

The fracture toughness test were done on an INSTRON 4202, according to ASTM D 5528 for fracture mode I, but one difference were employed, that the sample never was completely discharged. Test were done in double cantilever beam (DCB). Sample length of 140 mm and width of 25 mm displacement speed 1 mm/min. Sample were positioned between the grips, hanged by a couple of two steel piano hinges, bonded to the sample with a heat cured epoxy (2 h, 85° C).

### 4 RESULTS

The Mechanical characteristics that we evaluated are: Plasticity A% (relative enlargement or deflection), Young Modulus E (axial or flexural rigidity), Maximum stress  $\sigma_m$ , on axial and flexural. See Tables 3a and 3b.

On the fracture test we evaluated the fracture toughness defined by the Strain Energy Release Rate  $G_I$  (SERR). Figure 1 shows one typical R curve, energy rate-crack length.

The G determination has been obtained fitted to the analytical method proposed by Kageyama & Hojo (1990) accordingly to the equations 1 and 2:

$$G = \frac{3 * (F * C^{1/3})}{2 * A_1 * B * h} \quad (1)$$

$$\frac{a}{h} = A_0 + A_1 * C^{1/3} \quad (2)$$

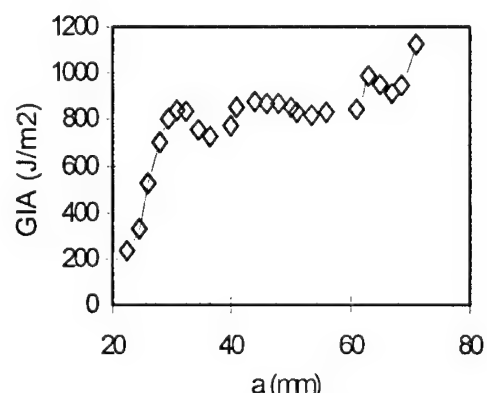


Figure 1. Energy rate versus crack length.

Table 3a. Mechanical Tensile Properties.

Laminate	Time (h)	A% Axial	E (GPa) Axial	$\sigma_m$ (MPa) Axial
AT1	0	3.6	17.5	293
	500	3.4	16.7	286
	1000	2.9	15.9	274
	1500	2.7	15.4	268
AM2	0	4.2	17.0	263
	500	3.9	16.4	252
	1000	3.6	15.7	234
	1500	3.4	15.2	230
BM3	0	4.5	15.6	247
	500	4.2	15.2	240
	1000	3.7	14.6	233
	1500	3.4	14.4	228
BM3C	0	5.0	16.0	267
	500	4.7	15.3	254
	1000	4.4	14.6	246
	1500	4.1	14.2	240

Table 3b. Mechanical Flexural and fracture toughness Properties.

Sample	A% Flex	E (GPa) Flex	$\sigma_m$ (MPa) Flexural	$G_{IA}$ (J/m <sup>2</sup> )	$G_{IB}$ (J/m <sup>2</sup> )
AT1	3.2	14.6	317	412	882
	3.1	14.2	305	392	832
	2.9	13.4	295	278	859
	2.8	13.0	286	294	788
AM2	4.0	12.5	369	393	1149
	3.8	11.9	356	237	1110
	3.6	11.4	338	278	1068
	3.5	11.2	333	234	1008
BM3	3.9	12.8	376	439	983
	3.7	12.4	358	427	902
	3.6	12.1	348	365	929
	3.4	11.7	341	322	904
BM3C	4.4	13.0	375	506	1015
	4.0	12.6	357	484	1004
	3.8	12.3	345	419	972
	3.7	11.8	336	407	958

Where  $a$  = crack length;  $h$  = half thickness;  $C$  = flexibility or compliance, relation between the crack opening  $d$  and the applied force  $F$ ;  $A_0$  and  $A_1$  = empirical values; and  $B$  = sample width.

The mechanical characteristics evaluated were  $G_{IA}$  critical energy rate after the crack tip is 2 mm beyond of precrack (just when it is clearly visible).  $G_{IB}$  is the energy rate where  $G$  becomes constant related to the crack length, in other words where the fiber bridging process is elevated (Marques et al 1996) as could be seen on figure 2.

Figure 2. Surface breakage with bridging process and intracrack deviation on laminate BM3C,  $\times 100$ .

#### 4.1 On materials degradation

A decreasing in the mechanical characteristics due to sun light exposition could be observed on all laminates. This decreasing should be observed on Figures 3, 4 where are represented the evolution of their characteristics respect of time of exposition.

Some experiences up to 7000 hours of exposition shows that the value obtained for this time is nearly the 90 % of the that obtained at 1500 hours. So as hypothesis we could accept that for long exposition time must exists an asymptotic value 10% less than that obtained at 1500 h. This asymptotic value is dependent of its own laminate characteristic. On Figure 4 we could appreciate the evolution of the differences between the characteristics evaluated at each time and their asymptotic value.

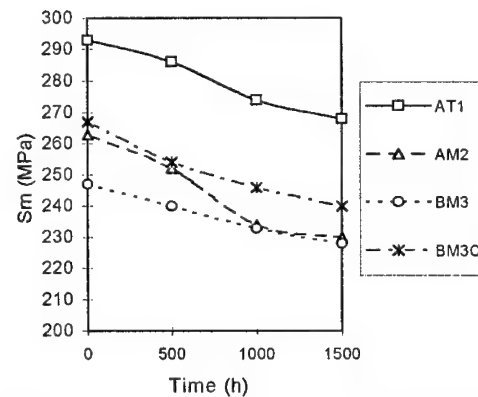


Figure 3. Decreasing on mechanical (axial) properties due to the sun light exposition time.

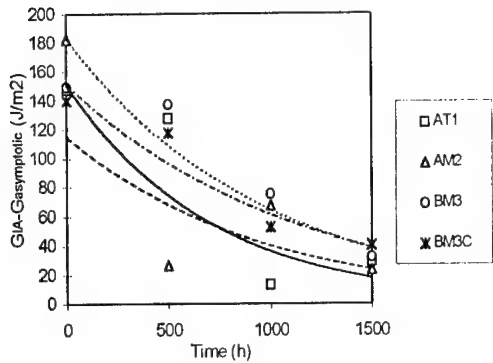


Figure 4. Critical SERR related to its asymptotic value versus time.

#### 4.2 Degradation model proposed

The general degradation model proposed is the damped exponential model as seen in equation 3:

$$Y = A + B e^{-Kt} \quad (3)$$

Where  $A$  = An asymptotic value;  $B$  = difference between the characteristic evaluated at time 0 and its own asymptotic value  $A$ ;  $K$  = extinction constant in hour<sup>-1</sup>; and  $t$  = time in hours. The values of the constants can be observed on Tables 4a, 4b.

We observed that the behavior in fracture is similarly and accordingly to the degradation of tensile and flexural mechanical properties.

We noted that there is a decreasing on the deformation energy nearly adjusted to our model proposed.

Table 4a. Degradation model's Parameter (tensile).

	A% Axial		E Axial		$\sigma_m$ Axial	
	B	$k 10^4$	B	$k 10^4$	B	$k 10^4$
AT1	1.40	9.7	3.7	6.0	54	4.6
AM2	1.20	8.7	3.5	5.5	57	6.4
BM3	1.60	10.0	2.6	4.4	42	4.1
BM3C	1.40	7.8	3.2	5.5	50	5.0

Table 4b. Degradation model's Parameter (flexural).

	A% Flexural.		E Flexural.		$\sigma_m$ Flexural	
	B	$k 10^4$	B	$k 10^4$	B	$k 10^4$
AT1	0.74	5.9	3.0	5.6	61	4.8
AM2	0.86	5.6	2.4	5.3	69	5.2
BM3	0.83	6.2	2.3	4.2	67	4.7
BM3C	1.04	6.8	2.6	4.7	72	5.1

#### 4.3 On matrix effect

Comparing the laminates AM2 and BM3 (multiaxial reinforced in two directions), which could be distinguished by the reactivity level of the resins. The results shows that there are a little better behavior on axial and fracture plasticity on resins of higher reactivity, it could be due to the higher reactivity of the resin, and it makes longer resin chains.

The differences in the porosity levels probably would shadowed the results in some cases, the porosity could be distinguished on figure 5.

#### 4.4 On temperature of cured

Contrasting the mechanical behavior of similar laminates BM3 and BM3C, could be perceived that the plasticity, tensile stress, modulus and G values are better those in BM3C, this phenomenon could be observed clearly on figure 6 and table 5b.

The higher temperature of cure plays an important role on the chemical process of polymerization and it is probably that the higher temperature improve the residual styrene polymerization, so its increases its mechanical properties. Either too is probably that the higher temperature of cured affects favorably on the adherence of fiber-matrix, as illustrated on figure 6.

The cure temperature affects favorably in all mechanical properties, except on the maximum flexural stress, reflected on BM3C laminate. That must be due to the higher porosity of the BM3C laminate.



Figure 5. Porosity on laminate AM2,  $\times 50$ . Tensile tested sample.

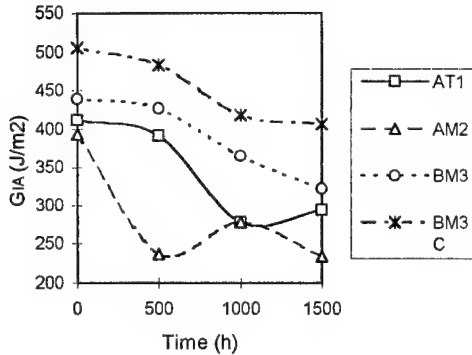


Figure 6. Critical SERR versus exposition time.

#### 4.5 On the relative loss of characteristics

The Intrinsic retention index I is the relation between the value of those characteristic at one time referred to time 0. The extrinsic retention index X is the relation between the characteristic of one laminate in relation to the taffeta's one at time 0. Table 4 shows those indexes. The extrinsic value are better because to its higher capability of discrimination.

Highlighting the better index of fracture toughness on multiaxial laminates even after 1500 hours. The multiaxial with P5 shows the worst behavior, probably due to its porosity distribution and the low reactivity level.

The typically taffeta waving did not represents an inconvenient on lost on interlaminar crack toughness as seen on figure 7.



Figure 7. Typical taffeta's break, on laminate AT1 x 50.

Table 5a. Intrinsic Retention Index.

	Intrinsic Parameter (I)							
	G <sub>IA</sub>				G <sub>IB</sub>			
	AT 1	AM 2	BM 3	BM 3C	AT 1	AM 2	BM 3	BM 3C
0	100	100	100	100	100	100	100	100
500	95	60	97	96	94	97	92	99
1000	67	71	83	83	97	93	95	96
1500	71	60	73	80	89	88	92	94

Table 5b. Extrinsic Retention Index.

	Extrinsic Parameter (X)							
	G <sub>IA</sub>				G <sub>IB</sub>			
	AT 1	AM 2	BM 3	BM 3C	AT 1	AM 2	BM 3	BM 3C
0	100	95	107	123	100	130	111	115
500	95	58	104	117	94	126	102	114
1000	67	67	89	102	97	121	105	110
1500	71	57	78	99	89	114	102	109

## 5 CONCLUSIONS

The Sun light exposition degrades the plastic and resistant mechanical properties in axial and flexural stress and the fracture toughness of the composites laminates made of glass fiber reinforced polyester.

The degradation follows a damped exponential model. The coefficients varies on dependence of the kind of reinforcement, resin and cure treatment. The losses will vary from 9 to 25 % in axial properties, from 9 to 21% in flexural and from 3 to 40% on fracture toughness.

The multiaxial configuration of the laminates shows as good or better capability to support strain and stress on axial and flexural stress than taffeta's ones and clearly better behavior against interlaminar cracking. Multiaxial configurations shows higher porosity.

The higher reactivity of the resin shows higher values on the plasticity in tensile mode and the behavior to the fracture toughness, but no relevant differences were observed in flexural behavior.

The heat treatment increases the general mechanical properties. In some cases the porosity would shadow the increment on the mechanical resistance.

The definition of the intrinsic and extrinsic values makes easier the comparison between the properties, and demonstrate that the multiaxial glass fiber reinforced polyester had better behavior than taffeta's one.

The rigidity is the most valuable property on taffeta reinforced polyester, while the plasticity and toughness are the best properties on multiaxial laminates.

---

## 6 REFERENCES

- Blicblau, A., L. Tran & P. Warden 1993. Environmental effects on carbon fiber/epoxy composites. *Proceedings of 9<sup>th</sup> International Conference on Composite Materials (ICCM)*, Madrid: 5, 660-664.
- Castaing, Ph., L. Lemoine & N. Tsouvalis. 1993. Experimental study of the variation in mechanical characteristics of orthotropic laminates immersed in water. *9<sup>th</sup> ICCM Proceedings*, Madrid: 5, 577-584.
- Evans, D., R. Reed & S. Hazeltone 1995. Fundamentals aspects of plastics materials at low temperatures. *Cryogenics*. 35 (11): 755-757.
- Fujii, Y., Z. Maekawa, T. Kubota, A. Murakami, & T. Yoshiki 1993. Evaluation of initial damage and stress corrosion of GFRP. *9<sup>th</sup> ICCM Proceedings*, Madrid: 5, 532-539.
- Hojo, M. & T. Aoki 1993. Thickness Effect of Double Cantilever Beam Specimen on Interlaminar Fracture Toughness of AS4/PEEK and T800/Epoxy laminates. *Composite Materials: Fatigue and Fracture*: (4), 281-298. Philadelphia: Stinchcomb Ashbaugh eds. ASTM.
- Iwamoto, M., S. Araki, K. Kurashiki & K. Saikto 1993. Comparison Between Mode I Interlaminar And Intralaminar Fracture Toughness of Thin Unidirectional Graphite (AS4)/Epoxy 1908 Laminates. *9<sup>th</sup> ICCM Proceedings*, Madrid: 5, 795-802.
- Kageyama, K. & M. Hojo 1990. Proposed Methods for Interlaminar Fracture Toughness Test of Composites Laminates. *Proceedings of the 5<sup>th</sup> US/Japan Conference on Composite Materials*, Tokyo: 227-234.
- Karama, M., M. Touratier & P. Pegoraro 1993. Test of accelerated aging composites material in shipbuilding. *9<sup>th</sup> ICCM proceedings*, Madrid: 5, 585-592.
- Marques, A., P. De Castro & A. De Moraes 1996. Fractura de materiais compósitos: una revisão de alguns resultados. *Anales de Mecánica de la fractura*. (13): 1-8.
- Murri, G. & R. Martin. 1993. Effect of Initial Delamination on Mode I and Mode II Fracture Toughness and Fatigue Fracture Threshold. *Composite materials Fatigue and Fracture*: (4), 239-256. Philadelphia: Stinchcomb Ashbaugh eds. ASTM.
- Pintado, J.M. 1992. Influencia en la radiación  $\Gamma$  sobre el comportamiento mecánico de compuestos de carbono epoxy. *11th Composite Plastics Conferences*, Barcelona: 1-18.
- Somiya, S. & T. Morishita 1993. Study on the Degradation Phenomena of SMC in Alkali condition. *9<sup>th</sup> ICCM proceeding*, Madrid: 5, 554-561.
- Sriram, P., Y. Khourchid & S. Hooper 1993. The effect of mixed mode loading on delamination fracture toughness. *Composite Materials Testing and design*: (11), 291-302. Philadelphia. Eugene T. Camponeschi, Jr de. ASTM.

## The effects of cyclic moisture aging on a glass/vinyl ester composite system

K.Garcia, M.D.Hayes, N.Vergheze & J.J.Lesko

*Department of Engineering Science and Mechanics, Virginia Polytechnic Institute and State University,  
Blacksburg, Va., USA*

**Abstract:** As composite materials find increasing use in infrastructure applications where the design lives are typically much longer than aerospace applications, the issue of durability becomes more critical for these materials. The tolerance of composites to damage by cyclic loading and moisture ingress is of utmost importance. This study addresses the change in quasi-static and  $R = 0.1$  (tension-tension) fatigue behavior of a commercial glass/vinyl ester system due to moisture. Quasi-static tensile strength is reduced by 24% at a moisture concentration of 0.95%, by weight. This reduction in strength is not recovered when the material is desorbed, suggesting that the exposure to moisture caused permanent damage in the material system. The fatigue performance of unaged, or "As Delivered", and saturated material is similar, but cyclical moisture ingress alters the fatigue performance of the composite system tested. This study highlights the effect of short term cyclic moisture aging and the effects on strength and fatigue performance of a glass/vinyl ester pultruded composite system.

### 1 INTRODUCTION

Fiber-reinforced polymer (FRP) composites are finding increasing use in construction and infrastructure applications where durability under harsh environmental conditions is required. The growing concern over the deterioration of the infrastructure has prompted civil engineers to consider alternatives for conventional materials. FRP's may offer superior resistance to fatigue and environmental effects as compared to metals, and they offer other advantages such as lower weight and ease of installation. However, while composites do not corrode via the same mechanisms as metals, they are prone to degradation. Moisture, caustic solutions, UV radiation, and freeze-thaw cycling may all significantly reduce the lives of composite structures. Moreover, damage caused by static and dynamic loading can be accelerated in the presence of these environmental factors.

The issue of moisture ingress into a composite is of utmost concern. While the time-scale of moisture diffusion is much slower than heat transfer, the effects can be more dramatic. Absorbed moisture can act as a plasticizer in the matrix, lowering the effective glass transition temperature of the resin [1,2,4]. This can cause pronounced changes in modulus, strength, strain to failure, and

fracture toughness [5,6]. While these effects may be reversible, the swelling stresses induced by moisture uptake can cause permanent damage such as matrix cracking, hydrolysis, and fiber-matrix debonding [2,4]. Moisture also corrodes glass fibers, especially under the presence of stress (i.e. stress corrosion or creep rupture) [1,2,3]. When the effects of moisture, temperature, and stress are combined, the damage mechanisms become even more complex and more difficult to predict. The implications of such changes on the design of structures are significant, especially in deflection-critical designs such as bridge superstructures.

The bulk of durability data currently available is mainly derived from the use of FRP's in the aerospace industries. However, this data is largely restricted to carbon fiber and epoxy matrix composites. Much less data is available for glass fibers and vinyl ester or polyester matrices – the current materials of choice for construction and infrastructure. The effects of moisture on glass composites have been investigated, but the focus of most experiments have been on the effects of a single cycle absorption process [7,8,9]. This study takes a different approach by repeating the aging process, multiple absorption-desorption cycles, to determine if cyclical aging introduces additional damage into the composite system. This study

addresses the effects of cyclic moisture aging on the material properties and fatigue performance of a glass/vinyl ester composite system.

## 2 MATERIAL SYSTEM

A standard off-the-shelf pultruded composite plate was selected for this study. The composite contains both unidirectional glass roving and random-fiber continuous strand mat (CSM) at a reported fiber volume fraction of 40%. The matrix is a standard vinyl ester resin containing a UV inhibitor and is 36% styrene content by weight. Coupons were cut with the long direction parallel to the unidirectional glass fibers. The edges of all of the coupons were sanded smooth using 180-grit sandpaper, and coated with a two-part epoxy and placed in an oven for two hours at 65°C to cure the epoxy.

## 3 EXPERIMENTAL PROCEDURE

### 3.1 Conditioning

Coupons were submerged in a 45°C circulating water bath. The material was immersed for a period

of approximately 30 days, until nearly saturated, removed, and then placed in a 45°C convection oven for 4 days to dry. The process was repeated as illustrated in Figure 1.

The moisture history was determined as a function of the percent change in weight with the initial weight being the measured weight of each specimen at the beginning of the study. Coupons were removed at various stages of conditioning process, denoted by the numbers 1 through 8 as shown in Figure 1, and were mechanically tested to identify and reductions in the material properties.

### 3.2 Quasi-Static Tension

Quasi-static or monotonic tensile tests were conducted to determine the modulus and ultimate tensile strength (UTS) of the material. Specimens were tested on an Instron 4505 screw driven testing machine at a stroke of 1.7 mm/min (0.05 in./min). A 2.5 cm (1 in.) extensometer was used to obtain strain data from the tests specimens.

### 3.3 Fatigue Testing

Fatigue S-N (stress-life) curves were constructed for specimens at points 1, 2, and 7 in Figure 1, by

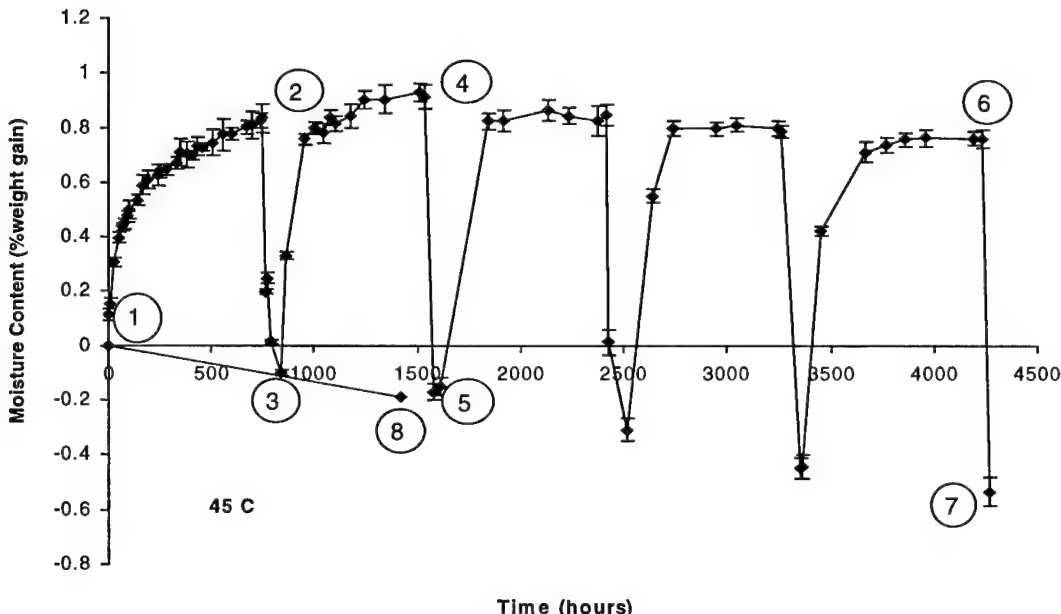


Figure 1: Moisture History

testing specimens at 45%, 55%, and 65% UTS. The fatigue tests were conducted on an MTS 810 servo-hydraulic testing machine at 10 Hz in tension-tension fatigue with a maximum to minimum load ratio of  $R = 0.1$ . A 2.5 cm (1 in.) extensometer was used to obtain a strain signal to observe stiffness reduction with cycles. The 1 cycle wet specimens were wrapped with moist towels during the testing to prevent moisture loss. Other work has indicated that this particular laminate heats up less than  $5^{\circ}\text{C}$  at 10 Hz [10], so moisture loss due to internal heating is likely to be minimal. In order to characterize the remaining strength of the material with fatigue cycles, new specimens were again fatigued at each load level, but interrupted at various increments of cycles prior to failure. These specimens were then tested in quasi-static tension to obtain the remaining strength of the material.

#### 4 RESULTS AND DISCUSSION

##### 4.1 Quasi-static Tension

Results from the quasi-static tensile tests indicate a mean Weibull modulus and strength of 15.5 GPa (2.25 Ms) and 212 MPa (30.8 ksi), respectively, for

the as delivered material. For the 1 cycle wet material, the modulus and strength dropped to 13.0 GPa (1.89 Ms) and 158 MPa (22.9 ksi), respectively. The results from the quasi-static testing are pictured in Figure 2, with the title numbers corresponding to the points in Figure 1.

The results indicate that the material properties are reduced significantly after the first conditioning cycle, but damage does not continue to accumulate with exposure time. Statistical analysis, consisting of a comparison of means test with a 95% significance interval, was conducted on the strength data for the material at different stages to determine if there are significant differences after cyclical moisture absorption. The analysis indicates that there is a significant reduction in strength from the first moisture cycle, similar to what was observed by Schultheisz et al [8] for glass/epoxy composites, and further cycling does not cause a significant alteration in the material properties. The second and fifth cycle properties are similar at the wet and the dry stages. This initial damage is not recovered when the material is allowed to return to its initial moisture content, suggesting that there is permanent damage to the matrix or fiber. There is significant difference between the wet and dry material states

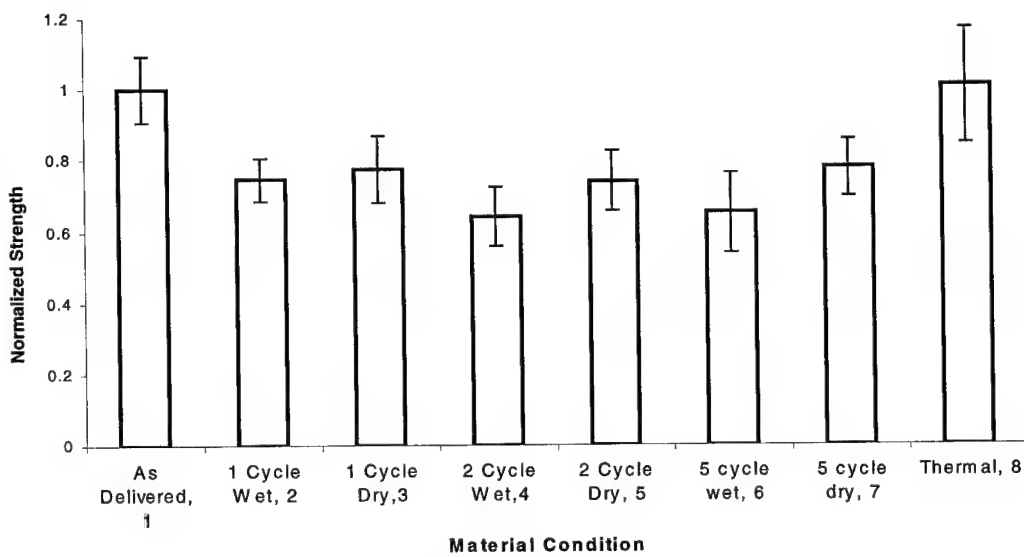


Figure 2: Material strength at different aging conditions

after the initial moisture cycle, but the changes in the strength are minimal and reversible, possibly indicating plasticization of the matrix material.

Specimens were aged in a 45°C oven and tested in quasi-static tension to determine if visco-elastic relaxation could have caused the reduction in strength. The aging history and material properties are denoted by stage 8 in Figures 1 and 2. Statistical analysis indicates that the material properties are similar to the initial properties, thus, the degradation cannot be attributed to thermal relaxation of residual stresses created in the manufacturing process. The question of the 25% drop off in strength remains. Preliminary examination of the failure surfaces indicate that the material interphase region is not affected by the moisture, so one explanation would be the degradation of the glass fiber. McKinnis reports that the strength of E-glass fiber is controlled by a stress corrosion mechanism induced by the adsorption of water on the surface of the fiber [3]. The reaction of the glass with the surfacesorbed water produces a microflaw (stress concentration) which is the precursor to fiber fracture. It is also recognized that the process is irreversible, except when extensive drying processes are employed, i.e. heating by irradiation [4]. This would explain the loss in strength of the material system after the initial exposure to moisture.

Data collected on the same material with a different moisture history (65°C for 17 days) but a

similar moisture content (0.1 weight %) indicate that the material has a strength of 146 MPa (21.2 ksi) [10]. Although the materials have different moisture histories, the strengths at 0.1 weight % appear similar. Moisture content appears to be the major variable in strength prediction for this material. The diffusion coefficient, moisture history, and a material strength profile at different moisture contents would yield all the necessary information to determine the minimum expected strength of the sample in a given environment. Further effort is being made looking at the failure mechanisms of the composite in this study, as well as cyclical moisture effects on different glass composite systems.

#### 4.2 Fatigue Testing

The S-N fatigue curves for the as delivered, 1-cycle wet, and 5-cycle dry samples are illustrated in Figure 3. Scatter in the fatigue data is typical of composites containing off-axis fibers; the variation being about one decade of life at each load level [2,12,13]. The curves have somewhat similar slopes with varying intercepts. The S-N curves are plotted again in Figure 4, with the curves normalized by their respective ultimate tensile strengths. The 95% confidence bands for the as delivered material were computed as per ASTM E 739-80 [11], and are also plotted in Figure 4.

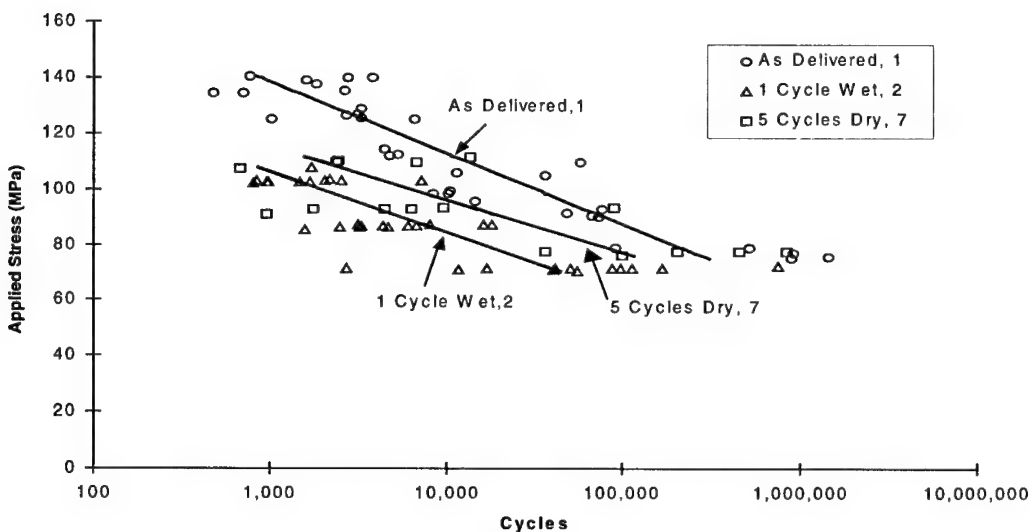


Figure 3: S-N curves for material at 3 different conditions

The S-N curves for the three samples are within the 95% confidence bands for the as delivered sample. Statistical analysis performed on the as delivered and 1-cycle wet that the two normalized S-N curves are the same. The 5-cycle wet material is within the 95% confidence bands of the dry material, but the curves are not similar compared with the as delivered and 1-cycle wet. The slope of the S-N curve decreases as does its intercept. Analyzing the remaining strength plots and dynamic modulus of the materials, it can be seen that there is a greater variation in the fatigue data for the 5-cycle dry. The remaining strength data indicates that the material strength remains constant for the 5-cycle dry material throughout the fatiguing process. The remaining strengths of the as delivered and 1-cycle wet specimens degrade gradually throughout the fatigue process, whereas the 5-cycle dry breaks, on average, near the single cycle strength. The damage mechanics for the moisture cycled material appear to be changing but there is a large amount of variation in the 5-cycle dry material data that may indicate degradation of the material.

Several other studies have dealt with the effects of moisture on the fatigue response of polymeric composites. Komai et al [14] examined the effects of water on unidirectional carbon-epoxy and aramid-epoxy under tension-tension fatigue and found that dry carbon-fiber specimens that were

fatigued in a water cell at 80°C had slightly longer fatigue lives than specimens that were tested in a dry environment. This was attributed to an increase in ductility of the resin and a decrease in the interfacial strength. However, specimens that were first pre-conditioned in 80°C deionized water for two months exhibited a considerable decrease in fatigue life (roughly 1 decade). "Degradation" of the matrix was thought to be the main cause of the drop, and the loss in life occurred for two different carbon fiber types – even though one (a heat-resistant type) actually showed an increase in tensile strength with moisture absorption. For the aramid-epoxy composites, water absorption did not affect the tensile strength, but the fatigue life was improved with moisture. The improvement was again attributed to increased matrix ductility [14].

In another study dealing with a glass-fiber chopped mat composite, Ellis and Found [15] demonstrated an increase in tensile strength in specimens that were first pre-conditioned in 51°C water. They also showed a significant increase in residual strength after fatigue cycling. This behavior was attributed to an increase in matrix ductility and internal stress redistribution after an initial stage of fiber-matrix debonding [15].

In a study utilizing the same glass/vinyl ester system that was used here (although slightly thicker), Liao et al [13] constructed fatigue curves

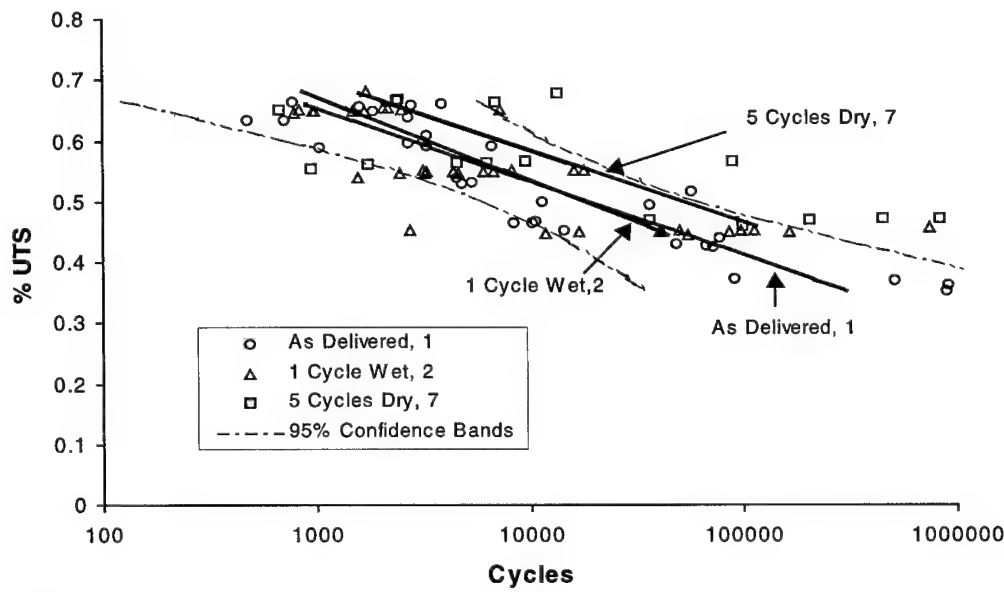


Figure 4: Normalized S-N curves

for four-point bending tests on bar-shaped specimens. They examined several different pre-conditioning schemes and found tensile failure in all specimens and conditions. Specimens that were soaked in water for 5 months at room temperature were slightly weaker in bending than the dry specimens. In fatigue, however, the conditioning did not seem to affect the fatigue life. There was little difference between specimens tested in air or water and between specimens pre-conditioned or unaged, although at 30% UTS the aged specimens did not survive as long as the dry material [13].

It is interesting to contrast the results of Liao et al and the current study, which were conducted on a nearly identical material system. The present study utilized a thinner laminate, which may contain a different ratio of glass roving to CSM. Of course, the damage mechanisms in bending may be different, but it is surprising that with the longer aging time (5 months compared to about 1 month), the effects of the moisture on fatigue life in that study were still minimal.

Mandell, et al. [16] produced results similar to those found in the wet and dry fatigue of the material system. Once again the material S-N curves shifted, and damage mechanisms throughout the fatigue process were similar, however no reference was made to the cause of the initial loss in fiber strength of the fiber upon short term exposure to moisture. The above process can possibly be described by work presented by McKinnis [3]. Thus, it appears that the stress concentration developed at the fiber surface does not change the mechanism of fatigue failure, but rather, only reduces the ultimate strength.

## 5 CONCLUSIONS

1. The properties of the material tested degrade at the maximum moisture content, but do not degrade any more if the material is cyclically aged to the same moisture content.
2. The strength of the material, based on stress-free hydrothermal aging, may be predicted knowing the maximum moisture content a sample has endured.
3. The S-N curves for the cyclically aged material system have similar slopes and intercepts, but the fatigue performance of the material appears to improve with increased moisture cycles.

## ACKNOWLEDGMENTS

The authors wish to thank the National Science Foundation Science and Technology Center for High Performance Polymeric Adhesives for their financial support, and Strongwell, Corp. for the

supply of EXTREN 625® material used in this study. Dr. Lesko would like to acknowledge the NSF Career Award Program for their support of his work.

## REFERENCES

1. L.C. Bank, T.R. Gentry, and A. Barkatt, "Accelerated Test Methods to Determine the Long-Term Behavior of FRP Composite Structures: Environmental Effects," *Journal of Reinforced Plastics and Composites*, 14, 1995, 559-587.
2. C.L. Shutte, "Environmental durability of glass-fiber composites," *Materials Science and Engineering*, R13, 1994, 265-324.
3. C.L. McKinnis, "Stress Corrosion Mechanisms in E-Glass Fiber," *Fracture Mechanics of Ceramics* #4, Crack Growth and Microstructure, 1977.
4. F.R. Jones, "The Role of Moisture Diffusion and Matrix Plasticization on the Environmental Stress Corrosion of GRP," *Journal of Strain Analysis*, 24 (4), 1989, 223-233.
5. C.H. Shen and G.S. Springer, "Moisture Absorption and Desorption of Composite Materials," *Journal of Composite Materials*, 10, 1976, 2-19.
6. G.S. Springer, B.A. Sanders, and R.W. Tung, "Environmental Effects on GFR Polyester and Vinyl Ester Composites," *Journal of Composite Materials*, 14, 1980, 213-223.
7. M. Watanabe, "Effect of Water Environment on the Fatigue Behavior of Fiberglass Reinforced Plastics," *Composite Materials: Testing and Design*, ASTM STP 674, S. W. Tsai, Ed., American Society for Testing and Materials, 1979, 345-367.
8. C.R. Schultheisz, W.G. McDonough, S. Kondagunta, C.L. Schutte, K.S. Macturk, M. McAuliffe, D.L. Hunston, "Effect of Moisture on E-Glass/Epoxy Interfacial and Fiber Strengths", American Society for Testing and Materials, 13th Symposium on Composite Materials: Testing and Design, 1996.
9. G.S. Springer, "Environmental Effects on Epoxy Matrix Composites," *Composite Materials: Testing and Design (Fifth Conference)*, ASTM STP 674, S.W. Tsai, editor, American Society for Testing and Materials, 1979, 291-312.
10. F. McBagonluri and J.J. Lesko, "The Effect of Fatigue Cycling and Applied Stress Level on Temperature Change in a Glass/Vinyl Ester Composite Coupon", Progress Report to the National Institute of Standards and Technology, May 1997.
11. Standard Practice for "Statistical Analysis of Linear or Linearized Stress-Life and Strain-Life

- Fatigue Data," ASTM E 739, American Society for Testing and Materials.
12. C.E. Demers, "E-Glass Fiber-Reinforced Polymeric Composites, Tension-Tension Axial Fatigue Life Diagram," The National Seminar on Advanced Composite Material Bridges, FHWA, May 1997.
13. K. Liao, R.L. Altkorn, S.M. Milkovich, J. Gomez, C.R. Schultheisz, L.C. Brinson, J.M. Fildes, and D.L. Hunston, "Long-Term Durability of Glass-Fiber Reinforced Composites in Infrastructure Applications," to appear in the Journal of Advanced Materials.
14. K. Komai, K. Minoshima, and S. Shiroshita, "Hygrothermal degradation and fracture process of advanced fibre-reinforced plastics," Materials Science and Engineering, A143, 1991, 155-166.
15. B. Ellis and M.S. Found, "The effects of water absorption on polyester/chopped strand mat laminate," Composites, 14 (3), 1983, 237-243.
16. J.Mandell, D. Huang, & F.J. McGarry, Proc. 35th Tech. Conf. on Reinforced Plastics/CI of SPI, 1980, paper 19-A.

## Polymer composites for infrastructure

A.Zureick

*Georgia Institute of Technology, Atlanta, Ga., USA*

**ABSTRACT:** This paper outlines some highlights of an investigation aimed toward the development of accelerated test methods for determining the long-term behavior of fiber-reinforced polymer composite structures. The work included the development of new destructive and non-destructive test methods for examining the engineering properties of civil engineering polymeric composite materials as well as the generation of short- and long-term design data for composites subjected to a variety of mechanical and environmental loading conditions.

### 1 INTRODUCTION

Nowadays, high-performance polymeric composite materials are gaining substantial popularity within the construction industry. This is due mainly to their superior properties, such as high strength-to-weight ratio, corrosion resistance, non-conductivity, and thermal resistance capability. Because of their light weight, lower transportation costs and quick erection time may lead to a notable cost reduction in the project. The corrosion resistant property makes the structure almost maintenance free, which in turn saves future costs.

In 1993, The Federal Highway Administration embarked on a research program aimed toward the development of accelerated test methods for determining the long-term behavior of fiber-reinforced polymer (FRP) composites for bridges. The purpose of the study was to provide future researchers with test methods acceptable to the highway bridge design community to examine the behavior of such materials and structures so that design criteria can be developed.

Because of the considerable interest in using polymeric composites for new construction, and also for the rehabilitation of existing structures, it was deemed necessary to devote the attention to:

1- Test methods for the mechanical loading of stand-alone FRP composite material structures; this included creep, fatigue and impact and non-destructive tests. The effects of temperature and moisture fluctuations that do not cause irreversible

material degradation were also considered.

2- Test methods for the mechanical characterization of FRP/concrete hybrid structural materials to examine the mechanism of interaction between FRP reinforcement and concrete for both prestressed and non-prestressed systems.

3- Test methods for the environmental loading of stand-alone FRP materials and FRP/concrete hybrid materials where the concern was with irreversible material degradation, damage and deterioration in the presence of adverse exposure and environmental conditions.

Brevity precludes a complete presentation of the results obtained from all the aforementioned tasks. Thus, only one task pertaining to the first of the above three categories will be presented in this paper.

### 2 TEST METHODS

#### 2.1 *Destructive Test Methods*

Destructive test methods were developed for the determination of the in-plane properties of composites. These test methods were based upon current ASTM Standards (ASTM D3039, ASTM D341, and ASTM D5379) that required many modifications to better represent the inhomogeneous materials at hand. These modifications varied in degree with most effort being devoted to the determination of the in-plane shear properties. The newly devel-

oped in-plane shear test adopts a specimen whose basic geometry and loading system are shown in Figure 1. The overall length of the specimen is 20.3 cm (8.0 in.) and the height is 3.81 cm (1.5 in.). The outside loads,  $P_e$ , are 15.2 cm (6.0 in.) and the inside loads,  $P_i$ , are 5.08 cm (2.0 in.) apart. Loading pads of 2.54 cm (1.0 in.) locally distribute the applied forces. This specimen and loading system are very similar to those devised by Iosipescu (1967) for producing a region of essentially pure shear in the central notch region.

This specimen and test configuration were used in a series of experiments (Zureick et al. 1997) to study the shear stresses in the various principal planes of pultruded plate material. Electrical resistance strain gages were used. The results showed very low extensional strains compared to shear strains, especially in the plane of the plate with the fibers horizontal in the specimen.

The loading system and the size of the specimen are different from those used in the ASTM shear test. The size in the specimen plane is twice as large as that of the ASTM specimen. The larger size is chosen to reduce the effect of the inherent heterogeneity of the material (Wang and Zureick 1995). This is evident in the roving spacing, which is somewhat variable, and which is of the order of 1.5 mm (0.06 in.). (The distance between the notches is 2.54 cm (1.0 in.), but is only about twice as much in the ASTM specimen. Furthermore, the test retains the specific load application locations used by Iosipescu (1967), compared to the flat platen used on the upper and lower specimen surfaces in the ASTM test. A typical shear stress-strain diagram resulting from this new test is shown in Figure 2.

## 2.2 Nondestructive Test Methods

Under this part of the experimental investigation, new nondestructive techniques were developed to estimate the engineering constants of pultruded specimens using ultrasonic methodologies (Littles, Jacobs, and Zureick 1995; Jacobs, Littles, and Zureick 1996a, 1996b). These ultrasonic methods have several advantages over mechanical tests: all of the engineering constants are measured for a single specimen; the measurements are made over a "local" volume of material, so it is possible to evaluate small specimens (i.e., the transverse dimension of a 101.6 mm by 101.6 mm angle). Due to the finite size of strain gages (approximately  $0.125 \text{ in}^2$ ), the actual strain values recorded in mechanical tests are

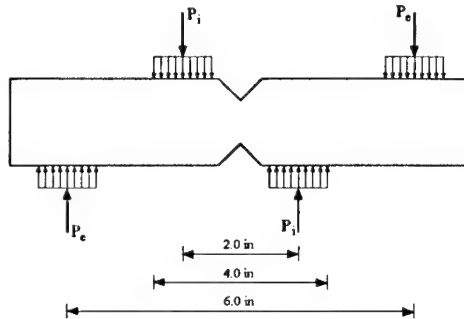


Figure 1: Time-reduction coefficient  $\phi_t$  vs. time

from a small area of the composite material. However, the strain experienced by this finite location is influenced by the surrounding material, (since the entire specimen is being loaded) resulting in more of an average value. The ultrasonic wave speeds are only influenced by the material through which the wave passes; these ultrasonic techniques provide much more of a local measurement. Another benefit of the local measurements is that spatial variations within a specimen can be observed. Further, these ultrasonic techniques do not destroy the specimen, so there is the potential for in-service monitoring of components or tracking time-dependent material properties in long term tests.

First, an ultrasonic immersion technique is applied to measure the phase velocities of ultrasonic waves that travel through the FRP specimens. These phase velocities are then used to calculate the components of the stiffness matrix. The engineering

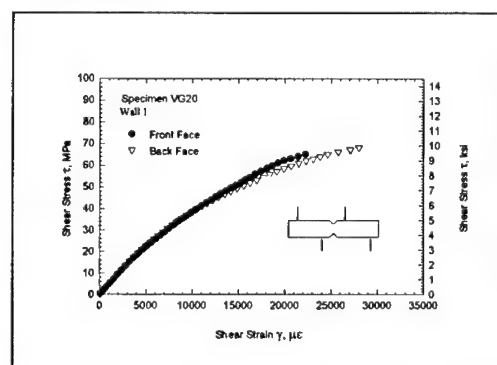


Figure 2: Typical In-Plane Shear Stress-Strain Response of FRP Materials

constants, which are the preferred material constants for structural design, are then calculated from the components of the stiffness matrix. The validity and accuracy of these values is determined through comparisons with the results from mechanical tests. The immersion technique is also used to ascertain the degree of spatial variation of this material; engineering constants are measured at several locations parallel to, and perpendicular to, the pultrusion (fiber) direction.

There are several limitations to ultrasonic immersion techniques; the most significant of which is that the specimen must be immersed in a water tank. As a result, it is impractical to use this immersion technique to monitor large components. Further, due to significant variation in one of the elastic constants obtained using the immersion technique, another relationship between this constant and an ultrasonic wave speed is sought. Therefore, a second ultrasonic technique is developed. This technique uses surface acoustic wave speeds for material characterization. These surface acoustic waves are generated and detected optically with a Q-switched, pulse laser and a heterodyne interferometer, respectively. A third technique, which also uses surface acoustic waves, is developed that measures all five of the independent elastic constants of a transversely isotropic material, when access to only one side of the specimen is available. Surface acoustic wave methods have great potential for applications where immersion is impractical; this research was a vital step toward the development of a technique for the "in-service" monitoring of polymeric composite structural components.

### 2.3 Long-Term Design Data

The long-term design data generated under this research program included the in-plane uniaxial strengths and moduli of pultruded composite materials under various mechanical and environmental loading conditions. Only the conclusion related to the compression creep test results will be presented in this paper.

The prediction of the long-term behavior of the longitudinal modulus was based on a series of compression coupon tests subjected to three different stress levels for time duration up to 10,000 hours. The three stress levels corresponded to approximately 20%, 40%, and 60% of the short-term compressive strength. All experiments were conducted in dead-weight lever-arm creep fixtures developed to apply compression loads to the coupons. The fixtures were constructed from structural steel with

pillow block roller bearings functioning as the fulcrum. The lever-arm was designed to magnify the load applied to the specimens by a factor of 10. Each fixture is capable of loading three coupons simultaneously at a desired constant load. A set of cages was constructed for each fixture to transfer the tensile load applied by the lever arm to each coupon as compression. Strain gages were attached to each coupon and data were recorded at specified time increments ranging from one minute to two weeks for the entire duration of the experiment.

Based upon the experimental results obtained from this creep experiment and from others (Holmes and Rahman 1980, Daniali 1991, Mosallam and Bank 1991, Bank and Mosallam 1992, Mottram, 1993, Scott, Lai, and Zureick 1995, McClure and Mohammadi 1995) the following practical power law creep model (Findley 1944, Findley and Khosla 1956) is proposed for the design of E-glass/vinylester pultruded structures:

$$E(t) = \phi_t E_0 \quad (1)$$

Where  $\phi_t$  is a time-dependent reduction factor given by:

$$\phi_t = \frac{1}{1 + \frac{\beta}{\beta} t^{0.25}} \quad (2)$$

In the above equations,  $t$  is the time in years and  $\beta = \frac{E_t}{E_0}$  is a time-dependent parameter that can be found in general for any polymeric composite material using Findley's power law from creep tests of only 1,000 hours in duration. For a class of composite materials for which the composition of the resin system is similar to that of the Derakane 411, values of  $\beta$  are generally less than 80. Figure 3 shows the reduction in the longitudinal modulus as a function of time for the case in which  $\beta = 60$ . For  $t = 10, 25, 50$ , and  $75$  years, the estimated reduction in the longitudinal modulus will approximately be 23%, 27%, 30%, and 33%, respectively.

### 3 ACKNOWLEDGEMENT

This work is supported by the Federal Highway Administration under Contract No. DTFH61-93-C-0012. Mr. Eric Munley serves as Program Director. The author would like to thank Drs. L. Jacobs, J. Littles Jr., D. Berghaus, and D. Scott for their continuous input to the development of this program.

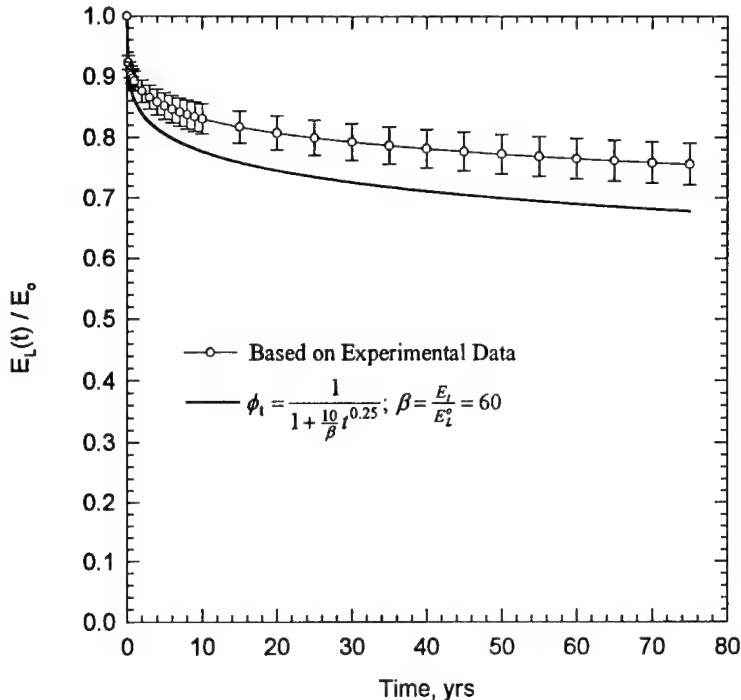


Figure 3

#### 4 REFERENCES

- Bank, L .C., and Mosallam, A. S. (1992), "Creep and Failure of a Full Size Fiber Reinforced Plastic Pultruded Frame," *Composites Engineering*, Vol. 2, No. 3, pp. 213-227.
- Daniali, S., "Short-Term and Long-Term Behavior of Two Types of Reinforced Plastic Beams," *46th Annual Conference, Composites Institute*, February 1991, pages. 13-A-1 through 5.
- Findley, W. N. (1944), "Creep Characteristics of Plastics," *1944 Symposium on Plastics*, ASTM.
- Findley, W. N., and Khosla, G. (1956), "An Equation for Tension Creep of Three Unfilled Thermoplastics," *SPE Journal*, December, pp. 20-25.
- Holmes, M., and Rahman, T. A. (1980), "Creep Behavior of Glass Reinforced Plastic Box Beams," *Composites*, No. 4, 1980, pages 797-802.
- McClure, G., and Mohammadi, Y. (1995), "Compression Creep of Pultruded E-Glass-Reinforced-Plastic Angles," *Journal of Materials in Civil Engineering*, Vol. 7, No. 4, pages 269-276.
- Mosallam, A. S., and Bank, L C. (1991), "Creep and Recovery of a Pultruded FRP Frame," *Advanced Composite Materials in Civil Engineering Structures*, ASCE, Edited by S. Iyer and R. Sen, pages 24-35.
- Mottram, J. T. (1993), "Short and long-term structural properties of pultruded beam assemblies fabricated using adhesive bonding," *Composite Structures*, March, pages 387-395.
- Scott, D., Lai, J., and Zureick, A. (1995), "Creep Behavior of Fiber-Reinforced Polymeric Composites: A Review of the Technical Literature," *Journal of Reinforced Plastics and Composites*, Vol. 14, June, pp. 588-617.
- Wang, Y., and Zureick, A.H. (1994) "Characterization of the Longitudinal Tensile Behavior of Pultruded I-Shape Structural Members Using Coupon Specimens," *Composite Structures*, No. 29, pp. 463-472.
- Zureick, A.H., Berghaus, D., Cho, B. and Javidinejad, A. (1997). "The In-plane Shear Properties of Pultruded Composite Materials," Georgia Institute of Technology.

## Applications of composite materials in the oil industry: Case studies

F.Dal Maso & P.Odru

*Institut Français du Pétrole, Rueil-Malmaison, France*

**ABSTRACT:** The oil and gas industry is faced to the challenge of exploration and production in deep water. In these conditions weight of the subsea equipment anchored to the platform or the vessel is one of the limitation; light materials are necessary. Composite materials are a good solution, due to their high specific properties. Two case studies are described in this paper: (1) high performance composite tubes used as risers, peripheral lines, or tendons and (2) composite tensile armors of Coflexip Stena Offshore flexible pipes.

### 1 INTRODUCTION

Up to now most engineering companies did not really consider organic matrix composites when designing offshore production platforms or drilling rigs, the main reason being that steel remained the cheapest and easy-to-design way. From now on, the oil industry, and especially offshore production and transport, is confronted with more and more severe conditions: deep water, high temperature, high pressure, corrosive crude or water, to say the least. This environment creates opportunities for innovative products and new materials to arise. Composite materials have high specific mechanical properties and therefore offer a good solution to the weight problem induced by deep water exploration and production. Moreover most composites behave well in hydrocarbons and water, as long as temperature remains reasonable (less than 100 °C).

Potential applications of composites offshore have been reviewed many times in the past. The conclusions from a study conducted by CLAROM (Club pour les Actions de Recherche sur les Ouvrages en Mer) (CLAROM 1992-1993) are summarized on figure 1. As shown, many parts can be designed with composites, topside as well as subsea. Among these parts, pipings are the most developed nowadays and found their applications in firewater systems. Secondary equipment made of composite is also common: gratings, ladders, railways, tanks. The most promising future applications are probably production and drilling risers, peripheral lines, and tethers. Composite flooring and sandwich panels could also emerge as

worthwhile options. In this paper the focus will be directed on high performance tubings, which have been extensively studied by the Institut Français du Pétrole (IFP) and Aerospatiale in the past (C. Sparks et al. 1986-1995) and have been lately subjected to renewed interest. Composite armors used in Coflexip Stena Offshore (CSO) flexible pipes (Dewimille & Martin 1989, Huvey 1989) will be a second case study examined hereafter.

### 2 FIRST CASE STUDY: TLP PRODUCTION RISERS

Many of the largest oil and gas fields and reservoirs are located offshore by deep water depths (for example, the Gulf of Guinea or the Gulf of Mexico) which could go as deep as 3000 m below sea level. In order to exploit these resources the oil industry is faced to technical challenges. The first step is to change from structures built on the seabed to floating structures, which is nowadays quite common. Several concepts have been developed and among these, Tension Leg Platforms (TLP) are most useful in deep water exploration and production conditions. TLPs are floating units anchored to the seabed by taut cables (tethers), the wellheads remaining subsea. With these structures, the problem of weight is coming soon. Indeed anything hanging on the platform increases the load on the deck and hence the dimension and cost of the floating unit. Reducing the weight of risers, tethers, pipes becomes therefore a necessity.

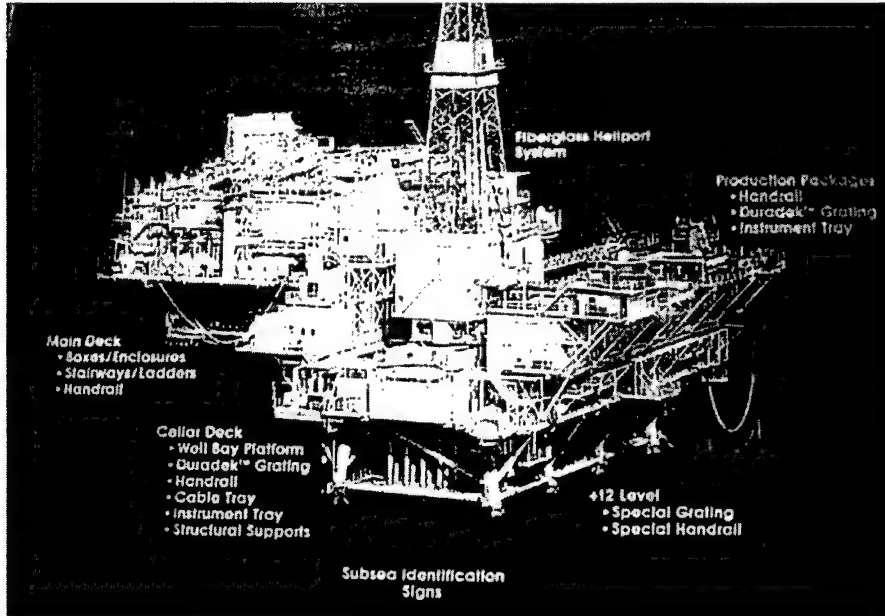


Figure 1. Potential applications of composite materials in the offshore industry.

IFP, in partnership with Aerospatiale, has looked into this problem and proposed designs of high performance composite tubes, including end fittings, able to fit several cases: production and drilling risers, kill and choke lines, tubular tendons (figure 2).

A riser is a tube of which function is to protect other tubes. In the production configuration, the inner tubes transport crude oil, water or fluids to control and enhance the production. In the drilling configuration risers protect the drilling rods and allows the drilling mud to circulate. Such tubes must withstand harsh environment conditions (sea water, hydrocarbons, heave, impacts...). The minimum lifetime in service is 20 years for the production risers and 5 years for the drilling risers.

To demonstrate the good behavior of composite risers, 9"5/8 OD production risers have been manufactured (figure 3) and tested during two JIPs supported by several oil companies (Agip, Chevron, Conoco, Elf Aquitaine, Shell IPM, Statoil). The risers were designed to accomodate a twin 3"1/2 steel tubing completion system, to resist a potential 35 MPa blow-out with a safety factor of 3, to reduce deck load and tensioning system complexity and to offer a fatigue resistance better than steel. Hybrid carbon fiber / glass fiber composite was used to manufacture the tube. Glass fibers were wound to resist blow-out pressure and carbon fibers wound to resist axial load (450 metric tons). Weight saving is

significant since the total weight of the riser is 60% less than its steel equivalent.



Figure 2. Example of drilling riser equipped with peripheral lines.

The JIP programs included tests to failure under pressure and in tension at 110°C, fatigue (figure 4), impact (figure 5), and evaluation of non destructive testing methods.

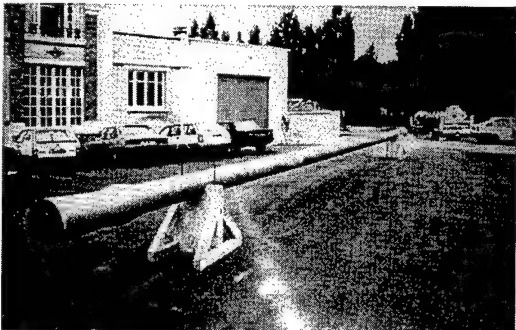


Figure 3. A 15-m long 9<sup>5</sup>/<sub>8</sub> OD tube, including end fitting.

A second fatigue test was conducted in conditions close to operational ones, that is a fatigue damage equivalent to 110 years in the North Sea. The tube was heated at 70°C. The loading program is given in table 1. Regularly during the fatigue test, the tube was submitted to internal pressure (35 MPa) and external pressure (10 MPa). No leaks were detected. While completed, a tensile test at 300 metric tons was conducted. The tube was still very good.

Composites offer other possibilities. Due to thermal or pressure changes, the length of a riser is modified and a 0.1% variation in length of a 1000 m riser equals 1 meter! To balance this effect,

The burst test at ambient temperature gave a final pressure of 111 MPa, which compared favorably to the specification of 105 MPa. Another tube was tested in tension at 100°C and failure occurred at 475 metric tons, again better than the specification. Several fatigue tests were carried out. One tube was subjected to 1 million cycles of +/- 75 metric tons about a mean tension of 100 metric tons, at ambient temperature. It is 3 times the number of cycles to fail a steel tube of equivalent strength. The test was stopped because a steel connection failed in fatigue after 984 000 cycles. The tube was still able to withstand a pressure test at 35 MPa.

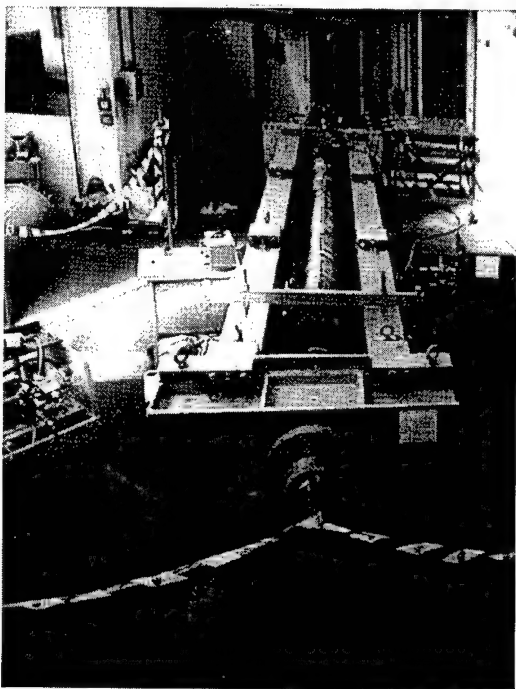


Figure 4. Fatigue testing of a 9<sup>5</sup>/<sub>8</sub> OD production riser.

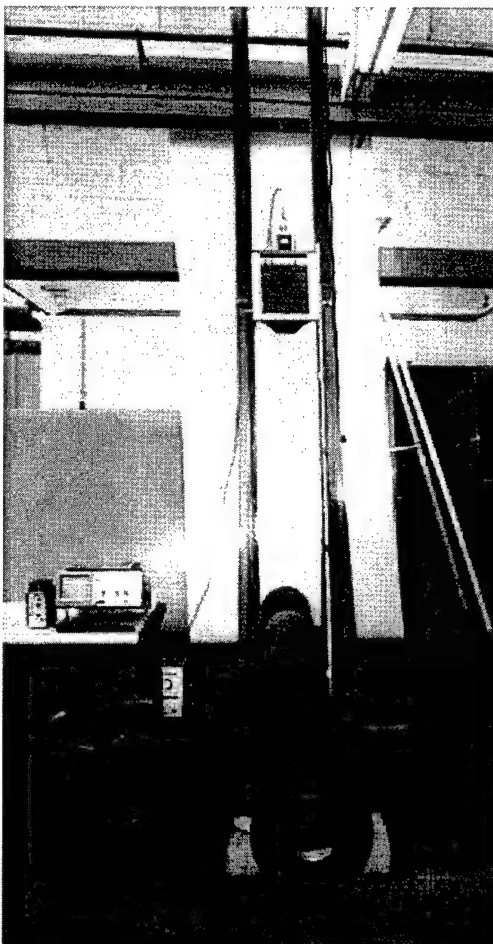


Figure 5. Impact testing of a 9<sup>5</sup>/<sub>8</sub> OD production riser.

tensioners are needed. With composite risers, an optimized design can be chosen so that the thermal expansion coefficient in the longitudinal direction is equal to zero and Poisson's ratio in the longitudinal / hoop direction is equal to 0.5. Such a tube has been manufactured and tested with success. Since tensioners are not needed anymore, a substantial cost saving is obtained.

Table 1. Loading program equivalent to fatigue damage in operational conditions in North Sea.

Sequence	Force (metric tons)	Number of cycles
1	100 +/- 6.2	0.13 10 <sup>6</sup>
2	100 +/- 12.8	0.08 10 <sup>6</sup>
3	100 +/- 27.8	0.34 10 <sup>6</sup>
4	100 +/- 16.6	7.60 10 <sup>6</sup>
5	100 +/- 11.8	32.4 10 <sup>6</sup>

Kill-and-choke lines are peripheral lines used in drilling operations to control the pressure and flow of muds and drilling fluids. These are very high pressure tubes, designed to withstand up to 180 MPa. In 1983 two of these lines were tested on field. The 4" tubes were made of hybrid composite (carbon fiber + glass fiber) by filament winding. There were fitted in parallel to the actual operating lines. Three campaigns of drilling were conducted and no specific procedures of handling or storage were taken for the composite lines. A pressure test was performed before installation, weekly during the campaigns and after the test. A final burst test completed this trial. The conclusion of the trial was that all the lines passed successfully the field evaluation. The design service pressure was 70 MPa and the remaining burst pressure was over 170 MPa. The lines could have been used for other operations. The weight of a drilling riser equipped with composite peripheral lines is significantly reduced. For example, in 3000 m of water, the weight is reduced by 26% compared to its steel equivalent (table 2).

Table 2. Mass of drilling riser for 3000 m water depth (in metric tons).

	Steel	Composite
Mass without buoyancy elements	1 325 T	1 055 T
Mass of buoyancy elements	880 T	570 T
Total mass	2 250 T	1 625 T

Not only this reduction of weight allows deeper drilling operations with the same rig or conversely allows the use of a smaller rig for the same depth of

water, but the dynamic behavior of the fully equipped riser is improved. This is due to the reduction of the resonant period of the line, resulting from its lower mass and the high specific mechanical properties of the composite.

### 3 SECOND CASE STUDY : TENSILE ARMORS OF FLEXIBLE PIPES

Flexible pipes are now commonly used in offshore operations, both as flowlines and as dynamic risers. A typical flexible pipe manufactured by CSO is depicted on figure 6.

This kind of pipe can withstand high levels of hoop and longitudinal stresses, while remaining flexible due to the possibility of displacement intra- and inter-layers and the high yield elongation of the plastic layers. In deepwater applications, or when laying long lengths of pipe, the weight is such that it creates important loads on the floating structure. Here again, weight saving is sought. In 1975, IFP started to work on this problem. Tensile armors were ideal cases for substitution (figure 7).

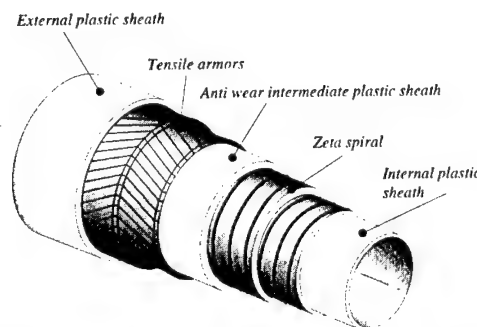


Figure 6. Example of a flexible pipe manufactured by Coflexip Stena Offshore (CSO).

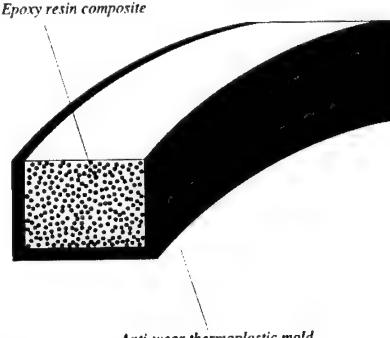


Figure 7 Preformed composite tensile armor.

A specific manufacturing process had to be conceived, since straight pultruded sections would develop high torsion and bending stresses when laid on the pipe. In table 3 performance of 8" ID flexible pipes with conventional steel armors and glass-epoxy armors are listed. Weight and laying tension are reduced by a factor of about 30%. Furthermore, the lower modulus of elasticity of the composite allows a better dynamic performance; indeed for a same curvature, stresses in the material are lower.

Table 3. Comparison of the performances of a flexible pipe with steel or composite tensile armors.

	Steel	Glass Fibers / Epoxy
Design pressure (MPa)	16.5	16.5
Weight in water full of water (daN/m)	84.7	58.6
Water depth to collapse (m)	1 430	1 430
Laying tension in 1000 m water depth (kN)	1067	738

Aging tests have been conducted, one of these being carried out according to method C of the TM0177-90 standard (National Association of Corrosion Engineers). First developed to test the resistance of metals to environmental cracking in H<sub>2</sub>S environment, it was interesting as way of demonstration to prove that composites could withstand such environments without problem.

C-shaped samples have been immersed at ambient temperature in a solution of water, salts, acid and H<sub>2</sub>S for 30 days, while being stressed at 500 MPa, which corresponds to 50% of their strength (figure 7). The test has been prolonged up to 3 months. The samples have been cut out of rings manufactured by filament winding, with the same parameters (resin and glass fibers, cure cycle) than those used to manufacture the armors.

After aging, the samples have been weighed and observed by optical microscopy. No visible degradations are noticed. The weight gain after 3 months is 0.6% for the samples, which means 1.6% for the neat resin. This value is typical of such resins. Interlaminar strength have been measured on a universal testing machine, with a 3-point bending feature and a short span (table 4). Surprisingly enough, the interlaminar strength increases after 3 months of ageing. It is attributed to relaxation of residual stresses (Plepy & Farris 1990, Kominar 1996).

Table 4 Interlaminar strength of samples vs. aging time.

Aging time (month)	0	1	3
Interlaminar strength (MPa)	71.7 ± 2.5%	71.9 ± 2.3%	78.3 ± 2.6%

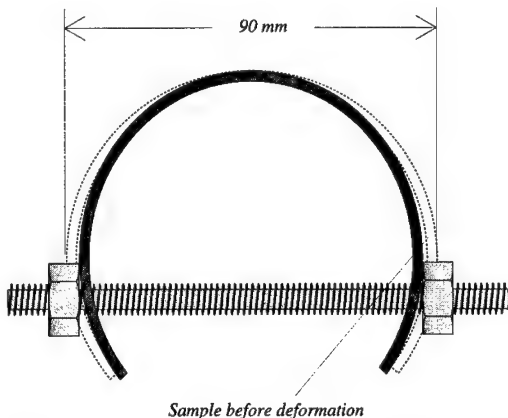


Figure 7 C-method of NACE TM0177-90 standard testing feature.

Viscoelastic properties have been obtained by mechanical spectroscopy. Storage modulus E' and loss tangent tan δ curves are shown on figure 8. The glass transition of the resin is not affected by ageing. The difference of E' is due to the volume fraction of fibers, not ageing.

This aging test shows that composite materials can be very well suited in conditions severe for steels. It has been confirmed shortly after by on-field tests in Lacq (France), for the production of very acid gases.

"Composite" flexible pipes are operational offshore nowadays. A first laying test was carried out in 1991 by 850 m water depth on the Marlim field in Brazil. A 11" ID pipe with composite armors has afterwards been manufactured and has been put in service in 1994 as a dynamic riser on the same field (910 m water depth). These pipes have been used without problem up to now. It confirms that composite tensile armors are a viable solution. More research is conducted to reduce the cost and broaden the application field of such armors.

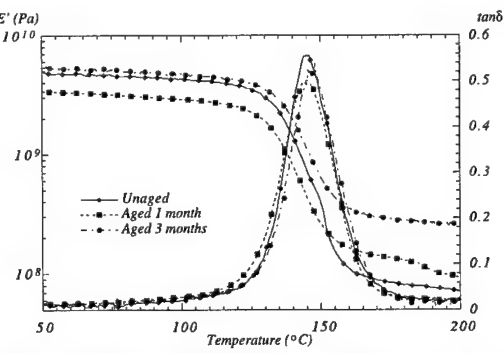


Figure 8 Storage modulus and tan δ of tensile armors, unaged and aged in NACE configuration.

---

## CONCLUSION

The oil and gas industry is facing technological challenges to exploit resources offshore by deep water depth. One of the most important parameters is weight, which is a barrier with conventional materials. Organic matrix composites have high specific mechanical physico-chemical properties and could be a solution to meet these challenges. It has been shown and proven through the two case studies presented in this paper, i.e. high performance composite risers and peripheral lines, and tensile armors of flexible pipes that composite materials are usable at an industrial scale in the offshore industry and could benefit their end-users. Other properties of composite materials have not been turned to account yet, like their low thermal conductivity for example and some applications could derive from these properties. Composite manufacturers should investigate all possible applications since large markets may open in a very next future if the right products are offered.

- Sparks, C.P., P. Odru, G. Métivaud & M. Auberon, 1992. Composite risers for deepwater applications. *Proc. 4th EC Symposium, Berlin.*
- Sparks, C.P., P. Odru & H. Bono 1994. High performance composite tubes: the challenge of the deep offshore. *Proc. Rencontres Scientifiques de l'IFP, Rueil-Malmaison, 2-4 november 1994*
- Tamarelle, P.J.C. & C.P. Sparks 1987. High performance composites tubes for offshore applications. *Proc. OTC Conference, Houston.*

## REFERENCES

- CLAROM internal reports, Bureau Veritas, IFP, Ifremer, Coflexip, Sofresid, 1992-93
- Dewimille, B. & J. Martin 1989. Bilan des campagnes 1987 et 1988 de fabrication industrielle d'armures composites pour flexibles allégés. *Internal report: Institut Français du Pétrole*
- Huvey, M. 1989. Dossier de qualification des Armures Préformées en Matériaux Composites pour Utilisation Dynamique. *Internal report: Institut Français du Pétrole*
- Kominar V. 1996. Thermo-mechanical regulation of residual stresses in polymers and polymer composites. *J. Comp. Mat.* 30(3): 406-415
- Odru, P., G. Metivaud & C.P. Sparks 1987. Lightening deepwater offshore structures by high performance composite tubes. *Proc. DOT Conference, Monte Carlo.*
- Odru, P. 1992. Structures tubulaires et ancrages composites pour utilisation pétrolière en mer. *Internal report: Institut Français du Pétrole.*
- Odru, P. & C.P. Sparks 1995. Advanced composite materials for the deep offshore. Challenges; first applications. *Proc. DOT Conference, Rio de Janeiro.*
- Plepys, A.R & R.J. Farris 1990. Evolution of residual stresses in three-dimensionally constrained epoxy resins. *Polymer* 31: 1932-1936.
- Sparks, C.P. 1986. Lightweight composite production risers for a deep water TLP. *Proc. 5th International OMAE Symposium, Tokyo.*

---

## **5 Manufacturing, processing and durability**

## Aging analyses of polymer composites through time-temperature equivalence

James C. Seferis

*Polymeric Composites Laboratory, Department of Chemical Engineering, University of Washington, Seattle,  
Wash., USA*

**ABSTRACT:** A fundamental problem of advanced airplane composite systems is the lack of understanding of the aging process and how it affects the material properties associated with degradation. The concept of Equivalent Property Time (EPT) was established and can be used to understand degradation of polymers and composites in a uniform manner, both for isothermal and dynamic elevated temperature exposures. In this work, bismaleimide neat resin and composite degradation was analyzed with isothermal and dynamic thermogravimetric analysis adapting a descriptive time-temperature concept originally developed for the curing of thermosets. The concept, defined as EPT, described the experimental data accurately for the experimental conditions tested. Thus, this methodology was demonstrated to be a useful tool in designing aging experiments and assessing lifetime of composite systems. An extension of this concept was developed to include Equivalent Cycle Time (ECT) which involves the effects of cycling - heating, cooling, holding, which can be used to understand degradation aging phenomena from repeated exposure. Analyses of degradation in relation to mechanical properties for composite laminates were performed to verify the concept. Collectively, this work focused on providing an understanding of cycling phenomena for polymers and composites as they relate to environmental influences and their accelerated aging behavior.

### 1 INTRODUCTION

Polymeric composites have become an integral part of aerospace structure due to their high strength-to-weight ratio. The most common matrix materials currently used in aircraft composite structures are epoxies because of their wide range of properties and ease of processing. As supersonic commercial aircraft and aerospace vehicles are being considered, high temperature polymeric composites with matrices such as bismaleimides are under consideration. A fundamental problem that remains, however, is that the long-term properties of composites are not well understood in comparison to metals such as aluminum. Accordingly, in the aerospace industry there is a tremendous need for reliable prediction of the maximum lifetime for polymeric composites which have been exposed to extreme environmental conditions such as hygrothermal cycling, load cycling, ultraviolet radiation, jet fuel, hydraulic fluid, and paint strippers that may be used during vehicle service (1). When the matrix candidates are selected for a specific application, evaluation and

validation processes should be performed to predict long-term properties with respect to temperature and moisture since they can have detrimental effects on polymeric composites (2,3). Therefore, the concept of Equivalent Property Time (EPT) was developed to provide a means to calculate the time required to reach a specific degree of cure at some temperature when the time to this degree of cure was known at some reference temperature. In addition, by extending the concept of EPT to include temperature variation (4-6), Equivalent Cycle Time (ECT) was suggested as an effective method not only to understand the long-term properties of composites, but also to enable the technology to be implemented in a faster manner using controlled experimental conditions. Collectively, in this study, the concepts of EPT and ECT are reviewed and applied to degradation of polymers and composites.

### 2 BACKGROUND / THEORY

Since the relaxation time of polymers can be significantly long, it may be a time consuming

process to investigate the long-term properties of viscoelastic materials. However, it can be more readily measured if a variety of temperatures with a fixed time scale are used (time-temperature superposition). A descriptive approach based on an Arrhenius expression for degradation phenomena was introduced by Prime (4) and first applied to the degree of cure for reacting thermoset systems (5-6). This approach was also applied to dynamic, non-isothermal conditions and viscosity change during cure for poly(amide imide) systems (7). Conversion may be defined as the ratio of actual weight loss to total weight loss corresponding to a given stage of the degradation process

$$\alpha = \frac{(M_0 - M)}{(M_0 - M_f)} \quad [1]$$

where  $M$ ,  $M_0$ ,  $M_f$  are the current, initial, and final weights of specimen, respectively.

## 2.1 EPT

### 2.1.1 EPT in Isothermal Conditions

The rate of conversion commonly used in reaction kinetics is expressed as,

$$\frac{d\alpha}{dt} = kf(\alpha) \quad [2]$$

where the rate constant  $k$  is assumed to depend only on temperature and  $f(\alpha)$  is some function of conversion. In an ideal case,  $f(\alpha)$  is known and  $k$  is assumed to follow an Arrhenius-type expression. Often simple forms of  $f(\alpha)$  do not fit the data, and thus a more complicated mechanism must be assumed (8-10). However, if the concept of EPT is used, the effect of  $f(\alpha)$  can be eliminated. At constant temperature, Equation [2] can be integrated over time and conversion,

$$\int_{\alpha_i}^{\alpha_j} \frac{d\alpha}{f(\alpha)} = \int_0^t k dt \quad [3]$$

or

$$F(\alpha) = \int_0^t k dt \quad [4]$$

where  $F(\alpha)$  is the integral of  $f(\alpha)$ . To eliminate  $F(\alpha)$  at a fixed conversion ( $\alpha = \text{constant}$ ), Equation [4] at any temperature  $T$  can be divided by the corresponding equation at some reference temperature  $T_{ref}$ . Since  $F(\alpha)$  is independent of temperature,

$$\frac{t}{t_{ref}} = \frac{k_{ref}}{k} \quad [5]$$

The rate constant may be assumed to follow an Arrhenius type expression:

$$k = A \exp\left(-\frac{E}{RT}\right) \quad [6]$$

where  $A$ ,  $E$ ,  $R$  are the pre-exponential factor, activation energy, and gas constant, respectively.

Assuming  $E$  and  $A$  are constant and independent of temperature, Equations [5] and [6] can be combined as

$$\frac{t}{t_{ref}} = \exp\left[\frac{E}{R}\left(\frac{1}{T} - \frac{1}{T_{ref}}\right)\right] \quad [7]$$

where the activation energy can be determined from the slope of  $\ln t$  vs.  $1/T$ . When activation energy and time to a certain conversion at reference temperature  $T_{ref}$  are known, the time to the same conversion (EPT) at other temperatures can be obtained from

$$t = EPT = t_{ref} \exp\left[\frac{E}{R}\left(\frac{1}{T} - \frac{1}{T_{ref}}\right)\right] \quad [8]$$

### 2.1.2 EPT in Dynamic Conditions

Equation [2] can be written for dynamic conditions as:

$$\frac{d\alpha}{dt} = \frac{A}{q} f(\alpha) = \frac{A}{q} \exp\left(-\frac{E}{RT}\right) f(\alpha) \quad [9]$$

where  $q$  is heating rate. Integrating over conversion and temperature,

$$\int_0^\alpha \frac{d\alpha}{f(\alpha)} = \frac{A}{q} \exp\left(-\frac{E}{RT}\right) f(\alpha) dT \quad [10]$$

The integral on the right side of Equation [10] cannot be solved analytically. It can be integrated numerically (11) or by using Doyle's approximation (12) as first proposed by Flynn and Wall (11). Equation [10] can be written as:

$$F(\alpha) = \frac{AE}{qR} p(x) \quad [11]$$

where  $p(x) = -\int_x^\infty \frac{\exp(-x)}{x^2} dx$  and  $x = -E/RT$

Doyle's approximation can be used to estimate the values of  $\log p(x)$  as a function of temperature by taking the logarithm of Equation [11], in which the following expression is obtained:

$$\begin{aligned}\log F(\alpha) &= \log\left(\frac{AE}{R}\right) - \log q - 2.315 \\ &\quad - 0.457\left(\frac{E}{RT}\right)\end{aligned}\quad [12]$$

Activation energy can be determined from the slope of  $\log q$  vs.  $1/T$  at constant conversion. To eliminate  $F(\alpha)$ , Equation [12] at any heating rate  $q$  can be divided by the corresponding equation at some reference heating rate  $q_{ref}$ . At constant conversion, and assuming that  $E$  and  $A$  are independent of temperature, Equation [12] can be defined as:

$$\log \frac{q}{q_{ref}} = 0.457 \frac{E}{R} \left( \frac{1}{T_{ref}} - \frac{1}{T} \right)\quad [13]$$

The activation energy can be determined from the slope of  $\log q$  vs.  $1/T$  at constant conversion as in the Flynn and Wall method (11). Solving for  $T$  in [13] allows for description of data at any heating rate:

$$T = \left( \frac{1}{T_{ref}} - \frac{R}{0.457} \log \frac{q_{ref}}{q} \right)^{-1}\quad [14]$$

Thus, when activation energy and temperature at a certain conversion and heating rate are known, the temperature at which the same conversion level is reached at other heating rates can be determined from Equation [13]. If a time to certain conversion is desired rather than temperature, it can be calculated from:

$$t = EPT = \frac{T - T_0}{q}\quad [15]$$

where  $T_0$  is the initial temperature of the sample before heating.

### 2.1.3 EPT in Mixed Conditions

In real service conditions, composites are exposed to both isothermal and dynamic temperature profiles. If the temperature profile consists of a ramp followed by an isothermal hold, the EPT concept can be applied separately to both parts and combined as in the following expression.

$$EPT = (EPT)_{dynamic} + (EPT)_{isothermal}\quad [16]$$

Combining Equations [8], [13], and [15], Equation [16] can be written as

$$\begin{aligned}EPT &= \left[ \left( \frac{1}{T_{ref}} + \frac{R}{0.457E} \log \frac{q_{ref}}{q} \right)^{-1} - T_0 \right] \\ &\quad + t_{ref,iso} \exp \left[ \frac{E}{R} \left( \frac{1}{T} - \frac{1}{T_{ref,iso}} \right) \right]\end{aligned}\quad [17]$$

Use of Equation [17] requires both dynamic and isothermal reference data, since experimental data ( $T_{ref,dyn}$ ) generated at reference heating rate  $q_{ref}$  are required for  $(EPT)_{dynamic}$ , and experimental data at  $T_{ref,iso}$  are needed for  $(EPT)_{isothermal}$ . If both dynamic and isothermal data are easily generated, then Equation [17] provides a simpler solution.

## 2.2 ECT

ECT by definition is the characteristic time which equates properties of an isothermally aged material to that subjected to temperature cycles. Figure 1 shows a diagram of a thermal cycle and how it may be divided into four segments, i.e., isothermal holding ( $T_i$ ), heating ( $T_i \rightarrow T_j$ ) with a heating rate  $q_{ij}$ , isothermal holding ( $T_j$ ), and cooling ( $T_j \rightarrow T_i$ ) with a cooling rate  $q_{ji}$ . These four segments repeat as a function of time. It would be reasonable to assume that most environmental thermal cycles can be approximated by this type of trapezoidal shape except for distinctive sinusoidal variables. Similar to Equation [17], the ECT that has been derived for isothermal holding in Equation [8] and dynamic heating in Equation [13] and [15] can be applied to each segment of the cycle with the reference temperature,  $T_{ref}$ . It should be noted that the reference temperature may be any temperature of interest. For the temperatures and times, the ECT at  $T_{ref}$  can be derived as:

$$\begin{aligned}ECT &= \sum_k^N [EPT_{iso}(T_i) + EPT_{dyn}(T_{ij}) + EPT_{iso}(T_j) \\ &\quad + EPT_{dyn}(T_{ji})]_k\end{aligned}\quad [18]$$

where  $N$  is the total number of cycles. ECT at  $T_{ref}$  provides the isothermal time required for the same extent of reaction to be obtained through  $N$  cycles of thermal history. Only one parameter, the activation energy, is required in addition to experimental data. The activation energy can be evaluated from the isothermal or dynamic data for the degradation of the specimen.

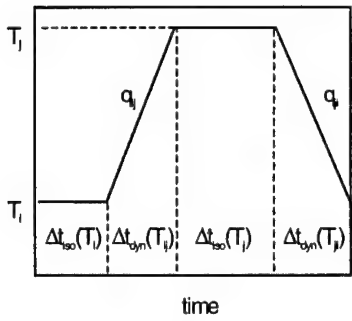


Figure 1 Schematic diagram of a thermal cycle orientation effect

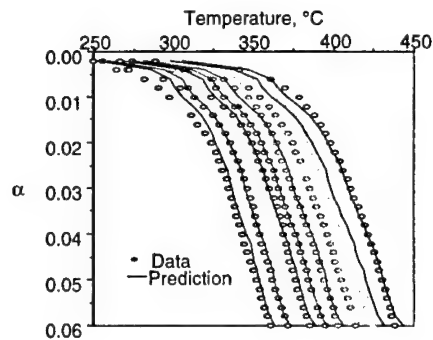


Figure 4 Data and prediction for BMI laminate in air (Heating Rates: 0.05, 0.1, 0.3, 0.5, 1, 2, 5, 10 °C/min from left to right)

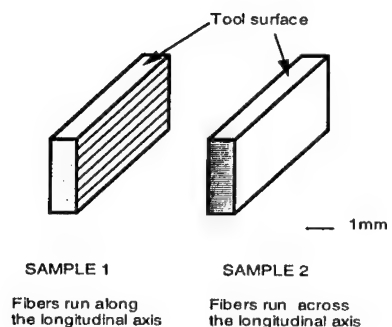


Figure 2 Samples used to illustrate fiber

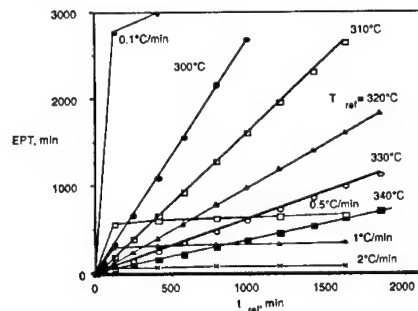


Figure 5 EPT-plot for BMI laminate in air (with isothermal reference data)

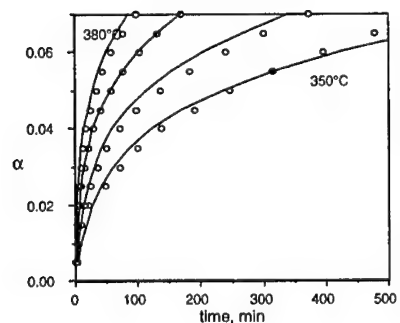


Figure 3 Data and prediction for BMI laminate in air at 350°C - 380°C

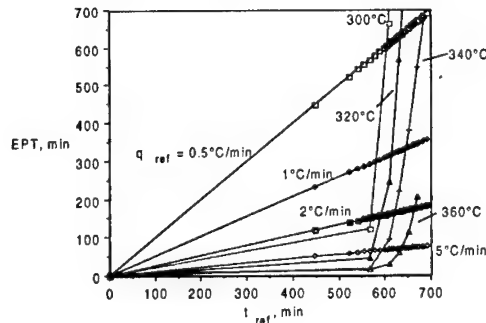


Figure 6 EPT-plot for BMI laminate in air (with dynamic reference data)

### 2.3 The Effect of Sample Anisotropy

The effect of sample anisotropy, i.e. fiber orientation, in carbon fiber reinforced composite weight loss data from larger scale isothermal oven aging experiments has been reported for PMR-15 (13-14) and BMI materials (15-18). Nam and Seferis (17-18) quantitatively analyzed this phenomenon for a layer toughened unidirectional carbon fiber reinforced bismaleimide, and details of the theory were discussed. It is thus very important when discussing degradation of fiber reinforced polymeric composites not to lose sight of the importance of anisotropy. Although EPT and ECT concepts are currently being extended to include anisotropy, in this study we will use existing data to demonstrate such influences in a simplified manner.

### 3 EXPERIMENTAL

The carbon fiber reinforced material investigated here included a toughened BMI obtained from BASF and a high temperature epoxy from Hexcel. Samples were cured and post-cured according to the manufacturer's recommendations. Weight loss for the bismaleimide was examined using a TA Instruments Thermogravimetric Analyzer TGA 951. A flow rate of gas of nitrogen/air was fixed at 50 cm<sup>3</sup>/min, and sample size was 20±0.1mg. Samples were cut from laminates and subsequently dried in an oven at 120°C for 2 days. All samples were stored in a dessicator to prevent moisture absorption. Both isothermal and dynamic experiments were performed. Isothermal experiments were performed between 300°C and 380°C at 10°C increments whereas heating rates in dynamic experiments were 0.05, 0.1, 0.3, 0.5, 1, 2, 5, and 10°C/min.

To investigate ECT, carbon fabric/epoxy prepreg (F584) from Hexcel was used to make specimens. Prepreg was cured at 177°C (350°F) for two hours using 550 Kpa (80 Psi) autoclave pressure. Final specimen sizes were approximately 5 cm x 5 cm. A group of specimens was put into an oven and thermally cycled from room temperature (25°C) to 177°C to evaluate the thermal degradation behavior. A separate group was placed in an oven that was set to 170, 177, and 185°C to evaluate the kinetic constants for degradation. The specimens were weighed periodically within 0.0001g accuracy, and specimen morphology was observed using optical microscopy. In experiments to determine the effect of anisotropy, samples were

carefully cut to constant weight (20 mg). Weight loss for bismaleimide was examined using TA Instruments Thermogravimetric Analyzer TGA 951. Sample sketches and dimensions are shown in Figure 2, and the sample sizes were kept at approximately 1.8 mm by 1.8 mm by 3.8 mm (thickness).

## 4 RESULTS AND DISCUSSION

Weight loss data describing degradation phenomena using bismaleimide and epoxy laminates have been generated. Activation energies for bismaleimide were determined from isothermal data by plotting  $\ln t$  vs.  $1/T$  at constant conversion and were found to be 143 kJ/mol in the temperature range 300-340°C and 240 kJ/mol in 350-380°C, respectively. Since derivation of equation [16] assumes constant activation energy, these two temperature regions must be treated separately. Thus, two activation energies obtained from the data as described above were used to predict isothermal data in air. In principle, only one reference temperature could be used if the reaction mechanism ( $f(\alpha)$ ) was independent of temperature. However, this approach was unsuccessful, implying that not only the activation energy, but also the conversion dependent function,  $f(\alpha)$ , was different in these two temperature regions. Therefore, two activation energies determined from the data as well as two reference temperatures were used to predict isothermal data. Figure 3 shows the comparison of data and predictions using EPT (EPT) for BMI laminates at temperatures higher than 350°C ( $T_{ref}=300°C$ ). It was found from the figure that the prediction matched well with experimental data. Activation energies from isothermal data were used to predict dynamic data at various heating rates. As with isothermal conditions, derivation of Equation [12] assumes constant activation energy. Therefore, prediction of data by two activation energies must also be done in two parts, and these parts combine to give one continuous weight loss curve. A reference heating rate of 0.5°C/min was used for the model. Data and predictions are shown in Figure 4. As shown in the figure, the concept of EPT described the data quite well.

### 4.1 Application of EPT

When considering polymeric materials for long term applications, the ultimate question is how to estimate their lifetime. Since EPT can describe both isothermal and dynamic data, it could be used

as a tool in designing tests for candidate materials. In these experiments, data can be presented as time (EPT) and as a function of reference time chosen. To convert dynamic data (temperatures) to a corresponding time, the initial temperature must be specified. Here,  $T_0 = 50^\circ\text{C}$  was chosen. Figure 5 shows an example of a BMI laminate exposed to air at selected temperatures and heating rates. In this figure, isothermal data at  $320^\circ\text{C}$  are used as the reference, and both isothermal and dynamic data are then plotted as a function of this reference. In Figure 6, dynamic data at  $0.5^\circ\text{C}/\text{min}$  was used as the reference, and selected isothermal and dynamic data are plotted as a function of reference time. When the reference is isothermal, data at other temperatures should be linear when plotted as a function of reference time if activation energy is constant with respect to conversion. Similarly, when the reference is dynamic, dynamic data should be linear. This observation was found to be true for the data examined, validating the constant activation energy assumption.

#### 4.2 Application of ECT

As mentioned earlier, ECT (ECT) was suggested as an effective method not only to understand the long-term properties of composites, but also to enable the technology to be implemented in a faster manner using controlled experimental conditions. Figure 7 shows the weight loss of the epoxy specimens as a function of number of thermal cycles. As expected, the weight loss increased as the thermal cycles proceeded. The rate of weight loss was found to be 3.17% at 650 cycles. As shown in the figure, the weight loss of the specimen was dramatically accelerated after 500 cycles. Figure 8 shows a cross-section of a specimen generated using optical microscopy. Microcracks were initially observed after 150 cycles and propagated from the surface to the center of the specimen as the cycles proceeded. At 500 cycles, the number and length of cracks in the specimen dramatically increased as shown in Figure 8.

These results indicated that the volume contraction due to weight loss initiated and propagated the microcracks in the matrix so that the effective surface area for the degradation reaction with oxygen increased, thereby accelerating the weight loss. Therefore, it is concluded that evaluation of weight loss represents not only the reaction kinetics of degradation, but also the degradation that results in the microcrack formation in the matrix. The microcracks cause decrease of strength which

affects the stiffness of composites. Accordingly, weight loss measurements may be regarded as an important method to evaluate the material property changes due to thermal degradation.

Figure 9 shows the ECT of the specimens through 650 cycles in comparison to the isothermal data. A fourth order reaction equation for  $f(\alpha)$  was selected to evaluate the activation energy since it showed a linear relationship when the data were applied by using Eq.5 as shown in Figure 6. From the slope of the Arrhenius plot using the isothermal data at  $170^\circ\text{C}$ ,  $177^\circ\text{C}$ ,  $185^\circ\text{C}$ , the activation energy was found to be 233 kJ/mol for the degradation of the specimen. It was found that the weight loss of ECT was lower than that of the isothermal experiments over the entire time range in this work. One possible reason for this behavior is that thermal degradation requires an induction period before reaction initiation. This induction period is related to the time lag caused by molecular relaxation as well as heterogeneity and anisotropy resulting in retardation of diffusion of oxygen and anisotropic intrinsic characteristics of the reaction kinetics of the composite material (10). In this experiment, the isothermal holding time, 2 hours, at  $177^\circ\text{C}$  may not have been long enough to overcome the induction period of the degradation reaction.

#### 4.3 Effect of Sample Anisotropy

Experiments have been made to understand the effect of sample anisotropy, i.e. fiber orientation, on carbon reinforced composite weight loss. Sample 1 (fibers along the longitudinal axis) in Figure 2 lost approximately 6% of its weight whereas Sample 2 (fibers across the width) lost about 15% during 5700 minutes. This is in agreement with previous studies which found that weight loss was accelerated in the fiber direction (13-18). Based on this and previous results, the fiber orientation must be taken into account when planning aging or TGA experiments, and applying EPT analysis. It can be assumed that the effect of the fibers is more pronounced in the high temperature region than in the low temperature region, as higher temperatures may promote fiber degradation and/or microcracking. Although direct comparison of the matrix and composite degradation may not be possible for this complex system, a simple qualitative comparison was shown here.

The weight loss of a material from TGA experiments is always obtained on a weight percent basis. Earlier work found that for laminates in air,

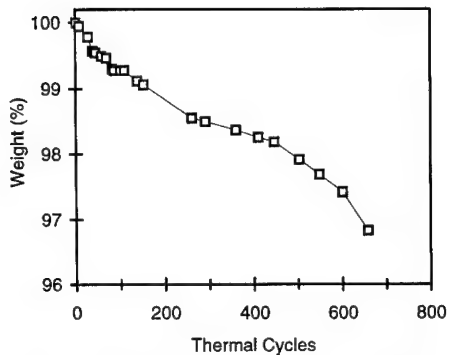


Figure 7 Weight loss as a function of thermal Cycles for epoxy/CF laminate



Figure 8 Cross-section of Epoxy CF fabric laminate at 500 cycles

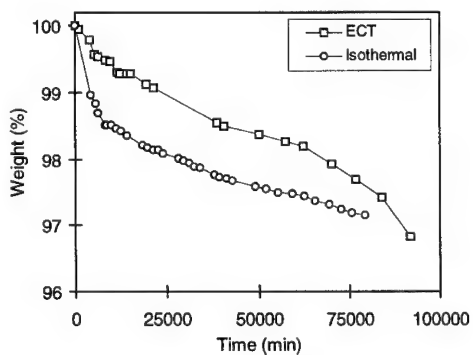


Figure 9 ECT with isothermal data at 177°C for epoxy CF fabric laminate

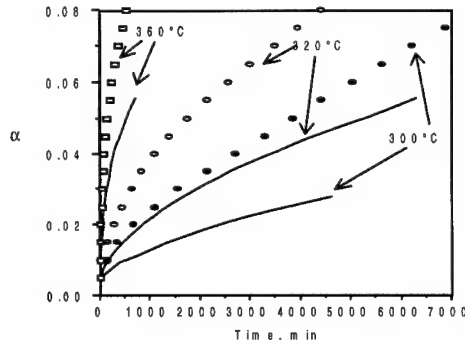


Figure 10 Comparison of BMI neat resin and composite weight losses in air assuming uniform degradation

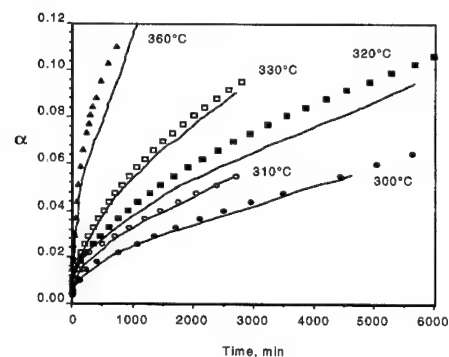


Figure 11 Comparison of BMI neat resin and composite weight losses in air assuming surface area dependent degradation

the weight loss can be expressed as a surface flux (13-18). Consequently, the conversions of the resin and the resin in the composite could be compared on a surface area basis. Another logical way to compare the conversions is to assume that the resin degrades uniformly, and therefore, the weight loss is not dependent of the surface area. This assumption, of course, is contradictory to surface area dependent degradation, but is used here for comparative purposes only. The latter assumption leads to the following connection between the neat resin and laminate conversion,

$$\alpha_c = w_r \alpha_n \quad [19]$$

where  $w_r$  is the resin weight fraction in the laminate. The conversions  $\alpha_c$  and  $\alpha_n$  refer to the measured total conversions for the composite and

neat resin as defined in Equation 1-2. Since the resin weight fraction was 0.37, it follows that total composite conversion should be about 0.37 times that of the neat resin. If degradation is assumed to be a surface area dependent phenomena, the comparison can be performed based on the resin surface area in the neat resin and composite. The composite samples had three different types of surfaces: the manufactured surface fully covered by resin, and two cut surfaces where fibers were exposed. The fiber angle in these surfaces was either 0° or 90°. Here, the macroscopic resin surface area was taken as

$$A = A_m + v_r (A_{0^\circ} + A_{90^\circ}) \quad [20]$$

where  $v_r$  is the resin surface area fraction, which is equal to the resin volume fraction.  $A_m$ ,  $A_{0^\circ}$ , and  $A_{90^\circ}$  refer to the areas of the resin covered surface, the 0°-surface (fibers perpendicular to the surface), and the 90°-surface (fibers parallel to the surface), respectively. Naturally, Equation [20] is not valid after the resin covering the manufactured surfaces has decomposed. Since this work concentrated on the initial degradation up to 6% weight loss, Equation [20] was assumed applicable. The sample size was kept at approximately 1.8mm by 1.8mm by 3.8mm (thickness). Using these dimensions, and assuming that the neat resin and composite samples had the same total surface area, the neat resin and composite conversion was simply related by,

$$\frac{\alpha_c}{\alpha_n} = \frac{A}{A_n} \quad [21]$$

which gives the composite conversion as approximately 0.74 times that of the neat resin.

Figures 10 and 11 show comparisons of the measured conversion for the laminate at selected temperatures and the conversion obtained from Equation [19] and Equation [20] and [21] in air. Solid lines represented the weight loss data of neat resin, and weight loss data of the laminate in the figures were normalized with respect to resin surface area. Clearly, assuming uniform degradation, Equation [19] underestimated the composite conversion whereas assuming a purely surface area dependent degradation overpredicted the conversion. The uniform surface area assumption seemed to successfully estimate the laminate degradation at 300-310°C, but at higher temperatures the laminate degraded faster than predicted. It was determined that the observed conversion was much closer to that estimated based

on the surface dependent degradation than the uniform degradation assumption. This is in agreement with the hypothesis behind the anisotropic degradation phenomenon, i. e. that degradation in air proceeds from the sample surfaces towards the interior.

## 5 CONCLUSIONS

The EPT concept was used to describe TGA weight loss of BMI and epoxy composites. Both isothermal and dynamic experiments as well as thermal cycling were performed in air. Activation energies were determined from isothermal data, and then used to describe weight loss under both isothermal and dynamic conditions. The model successfully described up to 6 weight % loss for the laminate. To enhance the effect of the thermal cycling, thermal cycle conditions at high temperatures were devised which proved to be an efficient method to evaluate the long-term properties of the composite. It was found that the specimen lost weight as a function of the number of thermal cycles utilized. Microcracks were initially observed in the matrix after 150 cycles and they gradually increased as a function of thermal cycles. A methodology was used to convert thermal cycle time to ECT at a reference isothermal temperature, and it was demonstrated as an effective technique for the evaluation of long-term thermal degradation behavior by thermal cycling. Collectively, the EPT and ECT methodologies were shown to have the potential for correlating a variety of data relating to the time and temperature equivalence of properties that continuously change.

## ACKNOWLEDGEMENT

The author expresses his appreciation to both past and present graduate students of the Polymeric Composites Laboratory for helpful discussions in developing these concepts. Financial assistance for this work is provided by the U.S. Air Force Office of Scientific Research.

## REFERENCES

- Starke, E.A., Ed., "Accelerated Aging of Materials and Structures". Publication NMAB-479, National Research Council (1996)
- Apicella, A., L. Nicolais, G. Astarita, and E. Drioli, *Polymer*, **20**, 1143-1148 (1979)
- Keenan, J.D., J.C. Seferis, and J.T. Quinlivan, J.

- Appl. Polym. Sci., **24**, 2375-2387 (1979)
- Prime, R.B., Proc.14th NATAS Conference, 137-144 (1985)
- Salin, I.M., J.C. Seferis, C.L. Loechelt, and R. Rothschilds, SAMPE Qtr., **24**, 54-63 (1992)
- Salin, I.M., J. C. Seferis, C. L. Loechelt, and R. Rothschilds, Proc.37th Int.SAMPE Symp. Exh, **37**, 1365 (1992).
- Copeland, S.D., J.C. Seferis, and M. Carrega, J. Appl. Polym. Sci., **44**, 41-53 (1992)
- Nam, J. D., Doctoral Dissertation, University of Washington, Seattle, Washington (1991)
- Nam, J. D. and J. C. Seferis, *J. Polym. Sci. Polym. Phys. Ed.*, **29**, 601 (1991).
- Nam, J. D. and J. C. Seferis, *J. Polym. Sci. Polym. Phys. Ed.*, **30**, 455 (1992).
- Flynn, J. H. and L. A. Wall, *Polym. Lett.*, **4**, 323 (1966).
- Doyle, C. D., *J. Appl. Polym. Sci.*, **5**, 285 (1961).
- Bowles, K.J., *SAMPE Quarterly*, **6**, (1990).
- Bowles, K.J. and G. Nowak, *J. Comp. Mat.*, **22**, 966 (1988).
- Magendie, F.J., Master's Thesis, University of Washington, Seattle, WA (1990).
- Copeland, S.D., J. C. Seferis, and M. Carrega, *J. Appl. Polym. Sci.*, **44**, 41 (1992).
- Seferis, J.C. and J. D. Nam, *Proc. of National Academy of Athens*, Greece-Mtg. February 1992 (1992).
- Nam, J. D., and J. C. Seferis, *SAMPE Quarterly* **24** (1), 54 (1992).

## Influence of matrix ductility and fibre architecture on the repeated impact response of glass-fibre-reinforced composites

B.A.G. Schrauwen & T. Peijs

*Centre for Polymers and Composites, Eindhoven University of Technology, Netherlands*

**ABSTRACT:** This paper describes the results of falling weight impact tests on glass-fibre-reinforced laminates. The test program consisted of (i) falling weight impact tests for the determination of the penetration energy and the influence of laminate construction on damage development and (ii) repeated falling weight impact tests for the determination of the impact fatigue life-time and damage development under repeated impact conditions at sub-penetration energy levels. The objective of this work is to compare the impact behaviour of cross-ply laminates based on a standard isophthalic unsaturated polyester and a rubber toughened vinyl ester resin and two types of glass reinforcement, i.e. a woven roving and a multiaxial fabric. The penetration energy of the various composite laminates appeared to be mainly influenced by the type of reinforcement, whereas damage development during (repeated) impact is strongly influenced by both fibre architecture and resin. No significant effect of the different material parameters investigated on the number of impacts to penetration (impact fatigue life-time) is observed. Especially when the repeated impact energy is normalized with respect to the penetration energy, all laminates showed similar behaviour.

### 1 INTRODUCTION

Upon impact loadings transverse cracking, delaminations, fibre/matrix debonding and fibre fracture are the potential failure modes in laminated composites. It has been demonstrated that damage due to impact substantially reduces the residual strength after impact of a composite structure, even when damage cannot be visually observed (Starnes et al. 1979). For these reasons, impact damage is generally recognized as the most severe threat to composite structures (Greszczuk 1975). The impact resistance of a composite material can be optimized with respect to different end-use requirements. Important criteria are:

- Energy absorption
- Damage resistance (or tolerance)

These two types of approaches are to some extent conflicting. The first approach often involves *energy absorption* processes such as fibre breakage, delaminations, debonding, pull-out, etc. The latter, however, is controlled by *energy storage* processes other than damage. Several attempts were made to improve the impact behaviour of laminated composites. However, many of the concepts were in most cases applied to relatively brittle aerospace grade carbon-fibre-reinforced plastics (CFRP)

(Hunston et al. 1987, Peijs et al. 1990, Evans & Masters 1987). Less studies were directed towards glass-fibre-reinforced plastics (GRPs) (Van Eijk & Peijs 1995). Previous studies showed that, in addition to matrix based toughening concepts, the impact behaviour of laminated composites is also influenced by the architecture of the 2D reinforcement (Curtis & Bishop 1984, Winkel & Adams 1985).

The present research had two objectives. First, the determination of the penetration resistance and the damage development during penetration of a number of thin section GRP laminates (energy absorption) and secondly, the repeated falling weight impact behaviour or impact fatigue behaviour of the same set of laminates at sub-penetration energy levels, including impact fatigue life and damage development during repeated impact (damage resistance/damage tolerance).

Impact tests were performed on a number of GRP laminates. Material parameters that have been studied are:

- (i) Influence of *fibre architecture*: composite laminates were manufactured based on either E-glass woven rovings or biaxial stitched fabrics.
- (ii) Influence of *matrix ductility*: composite laminates were manufactured based on two types of resins, i.e. a 'brittle' unsaturated

polyester resin and a more 'ductile' rubber toughened vinyl ester resin with failure strains of 3% and 12%, respectively.

Previous studies on the influence of reinforcement architecture have been mainly focused on single hit impact tests. Again most investigations focused on aerospace type of CFRP and less studies were directed towards GRP.

Curtis & Bishop (1984) compared the damage tolerance under non-penetrating impact conditions of woven CFRP with those of cross-ply composites based on unidirectional (UD) prepgs. Results showed that impact damage (read: delaminated area) as a result of non-penetration falling weight impact tests (FWIT) was, significantly lower for the woven material. Delaminated areas in woven composites showed a more circular damage area, whereas in the case of UD's extensive splitting along the fibre direction at the back surface ply resulted in a highly non-circular damage area. Another study by Winkel & Adams (1985) on carbon-, aramid- and E-glass/epoxy focused on full-penetration FWIT and reported the highest energy absorption in the case of cross-ply laminates based on UD's for all laminate configurations investigated. The optimal type of fibre reinforcement for maximum *penetration energy* as reported by Winkel & Adams (1985), i.e. cross-plies based on UD's, and the optimal reinforcement for *damage tolerance* as reported by Curtis & Bishop (1984), i.e. woven fabric, showed ones more that materials should be optimized either for energy absorption or damage tolerance and that both types of approaches can, to some extent, be conflicting.

Studies on the influence of matrix effects on impact performance of composite materials focused mainly on damage tolerance. Generally, toughened matrix systems with a higher strain to failure yield a reduction in the extend of the damage area and consequently improved residual strength after impact (Tobukuro et al. 1988). Although the ductility of the matrix material significantly affects the damage tolerance of the resulting composites under non-penetrating FWIT, matrix effects are less predominant with respect to energy absorption during penetration. In the case of full-penetration most of the energy absorption is the result of fibre breakage (Peijs et al. 1994). Even in the case of tough thermoplastics such as PEEK in the case of APC-2®, only a relatively small increase in total impact energy (-20%) was obtained compared to a brittle epoxy based CFRP system (Davies et al. 1985).

In certain practical situations, a composite can be subjected to repeated impacts. However, relatively few studies have been directed towards the problem of repeated impact or impact fatigue of laminated composites and the corresponding damage mechanism. Again also here most studies reported in

literature are related to CFRP (Wyrick & Adams 1988, Rotem 1988, Jang et al. 1992). A recent investigation by Boukhili et al. (1994) deals with the fatigue impact behaviour of quasi-isotropic carbon/epoxy laminates. Damage growth during the test was monitored by ultrasonic C-scan imaging. The damage area plotted as a function of the number of impacts displayed a multi-stage pattern behaviour, with stage 1 corresponding to matrix cracking in the region of the impactor, stage 2 to a rapid delamination propagation.

## 2 EXPERIMENTAL

### 2.1 Materials

The composite laminates used in this investigation were manufactured by DSM-BASF Structural Resins (Zwolle, The Netherlands). From these laminates different test samples were cut with the dimensions 100x100 mm.

Table 1 shows the resins and reinforcements of the four materials used in this investigation.

Table 1. Material codes

Material code	Reinforcement	Resin
WF/UP	woven roving	unsaturated polyester
WF/VE	woven roving	rubber mod. vinyl ester
MA/UP	multiaxial fabric	unsaturated polyester
MA/VE	multiaxial fabric	rubber mod. vinyl ester

Two resins were used for the fabrication of the laminates: a standard isophthalic acid based unsaturated polyester resin and a rubber modified vinyl ester resin. Laminates consisting of 4 plies of glass reinforcement were manufactured using a hand lay-up method.

The woven roving is a E-glass fabric with a coarse (2x2) structure, with a yarn width of about 6 mm. The amount of warp and weft fibres is the same.

The multiaxial stitched fabric had a relatively fine structure. In these fabrics the E-glass yarns are fully stretched in multiple directions. In this study, biaxial stitched fabrics with the fibres oriented in the 0° and 90° directions are used. Since the fibres lie straight and flat, layer by layer, stress concentrations as seen in woven fabrics will not occur in these multiaxial reinforcements.

Both the woven fabric and multiaxial reinforcements had an areal density of about 800 g/m<sup>2</sup>, giving for each layer of reinforcement an average thickness of

0.31 mm. The achieved average fibre volume fraction of the tested thin section laminates was in all cases about 35%.

## 2.2 Impact testing

**Penetration energy:** Full penetration falling weight impact tests (FWIT) were performed using the home build instrumented falling weight impact tester of the Eindhoven University of Technology. Tests were performed on laminates of the dimensions 100x100 mm using a hemispherical dart with a diameter of 10 mm. The laminates were clamped between two plates with a circular opening of 80 mm. Both force versus time and impact velocity just before impact are recorded and transferred to a data-acquisition board in a PC computer. Force was measured using a piezoelectric force transducer. Throughout the testing, the mass (2.85 kg) and the drop heights (2 m) remained constant. Impact velocity just before impact is measured to eliminate (relatively small) effects of cross-head friction. Impact velocities were about 6 m/s, yielding impact energies in the order of 50 J, which is high enough to give full penetration for all laminate configurations. Post-processing of data results in the complete energy history during impact and gives a listing of impact velocity, maximum force, total energy, absorbed energy and maximum deflection.

At least four specimens of a total of four laminate configurations (four different reinforcement/resin combinations) were impacted. After penetration the specimens were C-scanned and visually examined to determine the size and geometry of the (largest) delamination.

**Repeated impact:** Non-penetrating FWIT's were conducted with the instrumented falling weight impact tester using the same set-up as mentioned above. All four laminate configurations were tested in repeated impact. Impact energies were generated by dropping a hemispherical impactor loaded with a mass of 1.39 kg from different heights varying between 0.6 and 1.5 m.

The energy levels at which the repeated impacts were performed were set at 25, 30, 40 and 50% of the penetration energy. At these fixed energy levels the different laminate configurations were repeatedly impacted until full penetration. Typical incident impact energies varied between 8 and 20 J. The complete energy history, similar to the listing given above for the single hit full-penetrating impacts, was intermittently recorded at different numbers of impacts. The evolution of damage area as a function of the number of impacts was determined from visual observation.

## 3 RESULTS AND DISCUSSION

### 3.1 Full-penetrating falling-weight impact tests

**Penetration energy:** FWIT were performed to determine the penetration energy of the various laminate configuration. Figure 1 shows a typical force-time curve of a falling weight penetration test. In this case the force-time curve for a MA/VE specimen is shown. After an impact time of about 2 ms the force remains constant, indicating that the penetration process is completed and a remaining frictional force (~ 500 N) between dart and laminate is measured. For the calculation of the penetration energy, therefore, only the first part of the force-time curve is used. Typically, the force-time curves show linear behaviour up to a certain force. All laminate configurations tested showed a deviation from linear behaviour at a load around 3000-4000 N. Around this load level delamination is initiated and the laminate responds in a more compliant way with an almost linear secondary modulus up to the maximum load. The energy stored in the laminates up to this point of initiation of delamination, i.e. the threshold incident impact energy, is in the order of 3 J. An overview of the absolute penetration energies of all laminate configurations is shown in Figure 2. Absolute impact energies varied between 34 J for the WF/UP laminate system up to 40 J for the MA/UP laminate. The lowest impact performance was reported for the systems based on woven fabric. Replacement of the woven fabric with multiaxial reinforcements showed an increase in penetration energy, presumably due to the higher strength of the multiaxial material (see Table 2 for strength data of laminates based on unsaturated polyester). The influence of the ductility of the resin on the penetration energy is less clear, i.e. the penetration energy of the 'brittle matrix' MA/UP system is even

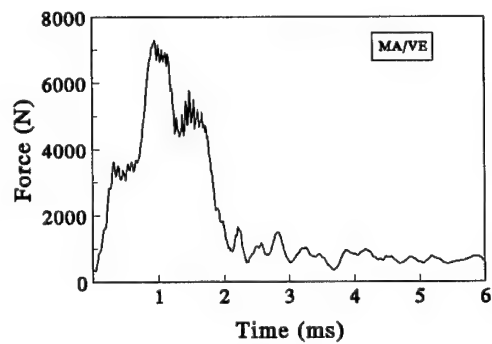


Figure 1. Typical force-time curve during penetration for a MA/VE laminate using the FWIT set-up.

somewhat higher than that of its 'ductile matrix' counterpart (MA/VE).

In short, the following conclusion can be drawn from these full-penetration impact experiments. In general, the impact strength of the specimens with multiaxial reinforcement is up to 17% higher than that of specimens with woven fabrics. Similar effects were found in a previous study for the tensile strength of these materials, indicating some correlation between tensile strength and impact energy (Dorey 1987). These results are also consistent with previous studies on CFRP which showed an enhanced impact performance for cross-ply laminates compared to woven fabric composites due to the higher tensile strength of the non-woven materials (Winkel & Adams 1985). No clear effect of the influence of matrix ductility on penetration energy was observed, which is again in good agreement with previous studies, which showed that under similar impact conditions energy absorption is mainly controlled by fibre breakage with only a small contribution from matrix dominated failure modes such as matrix cracking and delaminations (Peijs et al. 1994, Davies et al. 1985).

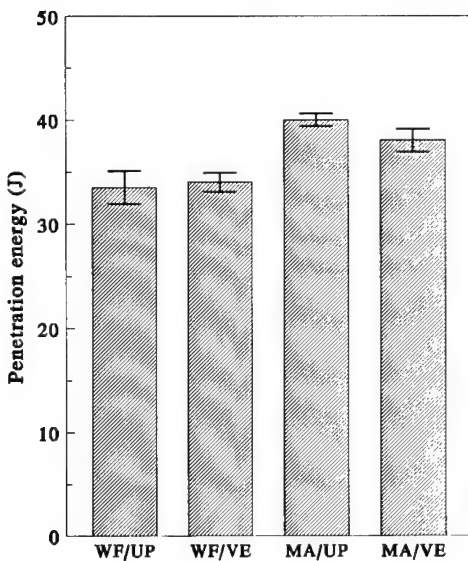


Figure 2. Penetration energy for the different laminate configurations as measured using FWIT.

Table 2. Influence of type of fibre reinforcement on mechanical properties of unsaturated polyester based GRP laminates (Loete & Marissen 1996).

	WF/UP	MA/UP
Tensile strength [MPa]	224 (8)	272 (4)
Young's modulus [GPa]	20.6 (0.5)	19.0 (0.3)

*Damage development:* Figure 3 shows the size of the (largest) delamination after penetration of the different laminates as obtained from visual observations. In spite of the similarities in penetration energy, significant differences in damage area are observed between the various laminate configurations. Obviously, the contribution of delaminations to the total energy absorption is relatively small and differences in delaminated area do not significantly affect the energy absorption, indicating once more that the penetration energy is mainly controlled by fibre dominated fracture rather than matrix dominated failure modes.

Significant differences in shape and size of the delaminations are observed between laminates based on woven fabric and laminates based on multiaxial reinforcements. The largest delaminated areas are observed in the laminates based on the multiaxial tapes. Compare for example the delaminated areas of MA/UP with WF/UP. Delaminated areas in woven composites showed a more circular damage area, whereas in the case of multiaxials extensive splitting along the fibre direction at the back surface ply and/or plies resulted in a highly non-circular damage area. Generally, the use of woven fabric restricts the

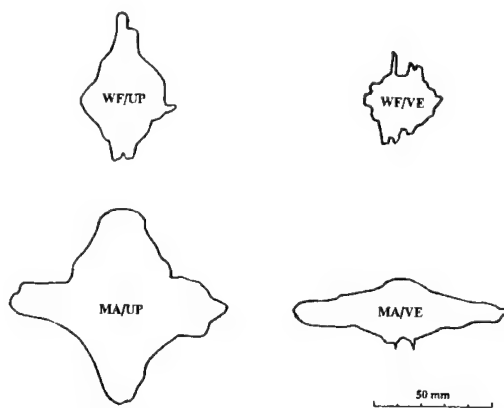


Figure 3. Size and shape of glass delaminated area after penetration for the different laminate configurations.

extend of the delamination, with the coarse fibre bundles acting as crackstopper. Particularly the splitting along the fibre direction at the back surface layer(s) that occurred in the case of multiaxial reinforcements (see MA/UP and MA/VE) is significantly reduced. Again, these results are in good agreement with previous impact studies on cross-ply UD's and woven fabric CFRP (Curtis & Bishop 1984).

Besides a significant influence of the type of glass fibre reinforcement, also a large effect of matrix ductility on damage area was observed. In the case of the woven fabric composites, the (circular) shape of the delamination remains the same but is simply reduced in the more ductile resin system (compare the delaminated area of 'brittle matrix' specimen WF/UP with 'ductile matrix' specimen WF/VE). In the case of the multiaxial reinforcements both the size and shape of the delaminated area are affected (compare MA/UP with MA/VE). It should be noted, however, that the length of the largest delamination crack is not significantly affected by the type of resin. In both cases the length of this crack is somewhat larger than the circular opening of 80 mm in the base plate, meaning that in this case the extend of the delamination is influenced by the test geometry. Although the resin did not have any (measurable) effect on the extend of the largest split length along the fibres in the outer ply, the use of a more ductile resin did significantly reduce the delamination in the second outer ply. In the case of specimen MA/UP a symmetric damage area is observed with equal crack lengths in the 0° and 90° direction, indicating not only extensive splitting along the fibres in the outer ply but a similar failure process in the second outer ply. In the case of vinyl ester resin (specimen MA/VE) extensive splitting occurred only in the outer ply, whereas no extensive delamination and splitting occurred in the other plies.

### 3.2 Repeated impact tests

The main objective of this part of the investigation was to obtain some data on the response of GRP laminates to repeated impact or impact fatigue.

**Response to first impact:** Prior to the repeated impact tests, the load-time curves obtained for the different specimen in response to the first impact was recorded along with the numerical data of the maximum load and the absorbed energy. If the incident energy of the first impact exceeds a certain threshold energy level, the laminate will be damaged. All samples were impacted at four different energy levels, i.e. 25, 30, 40 and 50% of the penetration energy of each laminate configuration. Full penetration FWIT data indicated already that the energy necessary to initiate damage (read: delamination) is approximately 3 J. Typically, the

incident impact energies in the repeated impact tests were varied between 8 and 20 J, which is sufficiently high to initiate delamination at the first impact. Upon non-penetrating impact the total impact energy can be divided into two parts:

- The elastically stored energy in the composite plate which is released after maximum deflection by rebounding of the laminate. This rebounding energy is successively transferred back to the impactor.
- The energy absorbed in the composite laminate which is available for damage and consequently controls the extent of damage.

In Figure 4 the absorbed energy (= impact energy minus elastic energy) is plotted against the impact energy for all laminate configurations. All the investigated material parameters, i.e. glass reinforcement and resin type, do not result in a change in energy absorption mode. Surprisingly, for all specimens the absorbed energy is similar, meaning that for all composites the same amount of energy is available for damage. Based on these observations no significant differences in damage tolerance between the different specimens should be anticipated. It is interesting to note that extrapolation of the data to zero absorbed energy yields an impact energy of 4 J, which is close to the threshold energy for delamination as determined from the full penetration tests (~ 3 J). This means that all energy is elastically stored in the laminate and transferred back to the impactor at impact levels below this threshold energy.

Following the impact tests the laminates were examined visually for the extend of damage. It can be expected that higher levels of absorbed energy results in more damage. Figure 5 shows the glass delaminated area after the first impact as a function of the impact energy. Clearly, large differences are

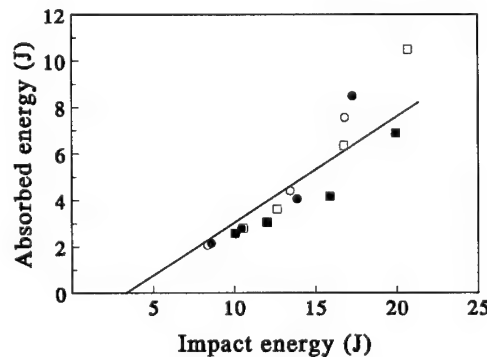


Figure 4. Absorbed energy versus impact energy for first impact event: ○ WF/UP, ● WF/VE, □ MA/UP and ■ MA/VE.

observed in initial damage area. The overall level of damage in all the laminates increased proportional with increasing impact energy. Similar to full-penetrating impacts, also at relatively low energy non-penetrating impacts the delaminated area is the highest for composites based on the rather brittle polyester resin system in combination with the multiaxial reinforcement (MA/UP). The smallest delaminated areas are obtained in the case of systems based on vinyl ester resin. At sub-penetration impact levels the effect of the type of reinforcement on the extend of the damage is less profound as in the case of full penetrating impacts (see Fig. 3). Again, linear extrapolation of the data to zero delaminated area yields an impact energy, which is in the order of the threshold energy for delamination.

**Impact fatigue life-time:** All laminate configurations were repeatedly impacted at the same energy level as the first strike until penetration. Figure 6 shows the impact life-time curve for a MA/VE laminate. Typically, all laminates showed a similar exponentially shaped life-time curve with only a few impacts to penetration at relatively high energy levels (e.g. 50% of the penetration energy) and a large number of impacts to penetration at relatively low impact energy levels (e.g. 25% of the penetration energy). Moreover, the shape of the life-time curves suggests that there is a kind of fatigue limit below which no penetration will occur. It is not clear if this fatigue limit correlates with the threshold value for delamination. However, based on the data obtained so far there is an indication that, at least for most practical applications, this fatigue limit ( $\sim 9$  J) is higher than the threshold value for the initiation of delamination ( $\sim 3$  J).

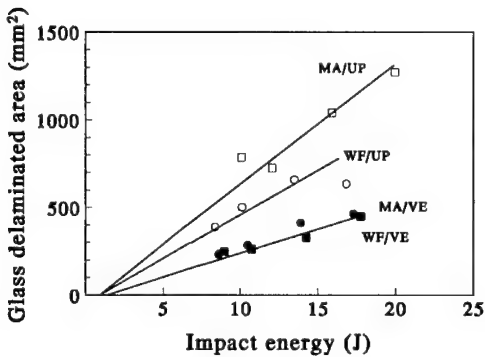


Figure 5. Glass delaminated area after first impact event as a function of impact energy:  $\circ$  WF/UP,  $\bullet$  WF/VE,  $\square$  MA/UP and  $\blacksquare$  MA/VE. (Extrapolation of the data to zero delaminated area yields the threshold impact energy).

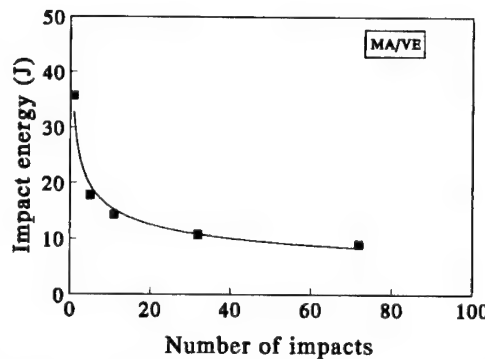


Figure 6. Impact fatigue life-time curve for a MA/VE laminate.

For most laminate configurations no significant differences in the number of impact to penetration are observed. The similarity in relative resistance against impact fatigue for all specimens tested is clearly visualized in Figure 7, when the number of impacts to penetration is plotted as a function of the normalized impact energy. Especially when the (repeated) impact energy is normalized with respect to the penetration energy, all composites show the same behaviour, resulting in a sort of 'Master-Curve' for impact fatigue life-time.

**Damage development during repeated impact:** Damage development of a large number of fibre composites subjected to impact fatigue has been examined. For a given material, there usually exists a critical impact energy, above which a significant delamination crack will initiate in response to a single impact. In our experiments delamination was

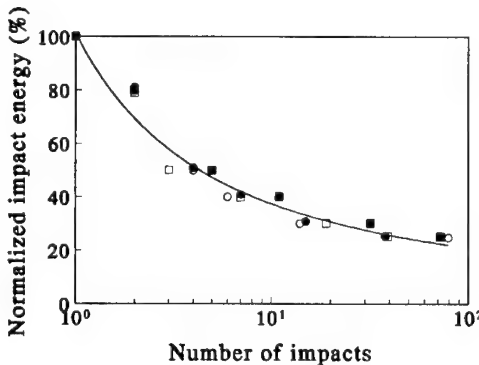


Figure 7. Impact fatigue life-time curve normalized by its penetration energy:  $\circ$  WF/UP,  $\bullet$  WF/VE,  $\square$  MA/UP and  $\blacksquare$  MA/VE.

observed in all specimens after the initial impact. When impacts are repeated this delaminated area will grow. These observations are shown in Figure 8 for all laminate configurations. In this graph the glass delaminated area with increasing number of impacts is plotted for a low energy repeated impact test (25% of the penetration energy). For most woven fabric specimens the glass delaminated area increased gradually with the number of impacts. Only in laminates based on multiaxial reinforcements a clear two stage damage growth process is active. The damage area remains constant at low impact numbers and increases rapidly at high ( $n > 10$ ) impact numbers. Similar multi-stage delamination pattern behaviour has also been reported by Boukhili et al (1994), where stage 1 corresponds to matrix cracking in the region of the impactor and stage 2 to rapid delamination propagation. It is also shown in Figure 8 that for systems based on vinyl ester resin deviations between the laminates based on woven fabric and multiaxials only occur at high impact numbers, whereas at low impact numbers the delaminated areas in both laminates are the same. This is in good agreement with the similarities in delaminated area at sub-penetration impact levels as shown in Figure 5 and the differences in delaminated areas at full penetration impact levels as shown in Figure 3.

Figure 9 shows that these delaminations grow at the same rate for both low and high energy impacts, as visualized by the slopes of the stage 2 delamination growth curves for a MA/VE laminated composite, which was repeatedly impacted at different percentages of the penetration energy.

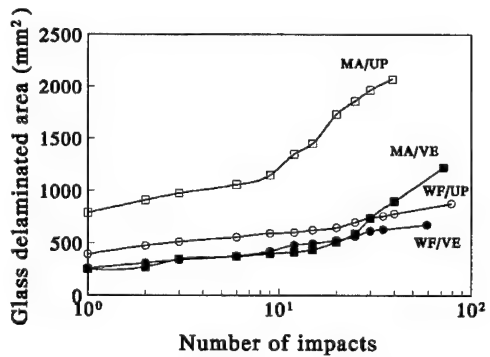


Figure 8. Delamination growth as a function of number of repeated impacts for low energy repeated impacts (25% of the penetration energy):  $\circ$  WF/UP,  $\bullet$  WF/VE,  $\square$  MA/UP and  $\blacksquare$  MA/VE.

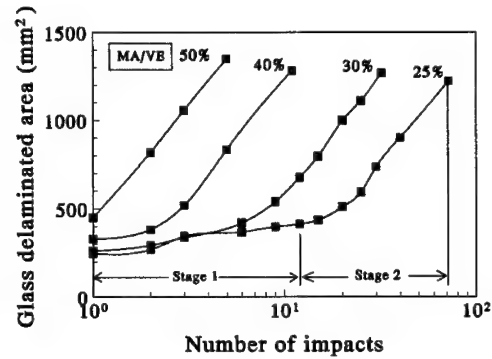


Figure 9. Damage growth in MA/VE laminates as a function of number of repeated impacts at different energy levels (25, 30, 40 and 50% of the penetration energy), showing slow damage grow due to matrix cracking in the vicinity of the impactor (stage 1) and similar stage 2 delamination growth rates at different impact energy levels.

Figure 10 shows the absorbed energy as a function of the number of impacts for MA/VE laminate. Typically, at low energy levels (25% of penetration energy) the absorbed energy remains relatively constant up to approximately 20% of its life-time (stage 1). Next, the absorbed energy starts to increase as a result of extensive delamination growth (stage 2a), whereas at relatively high impact numbers (above 70% life-time) a dramatic increase in absorbed energy is observed as a result an additional fibre breakage process in the vicinity of the impactor (stage 2b). This sudden change in absorbed energy, due to extensive fibre breakage in the vicinity of the impact, at approximately 70% life-time was observed for all the other laminate configurations.

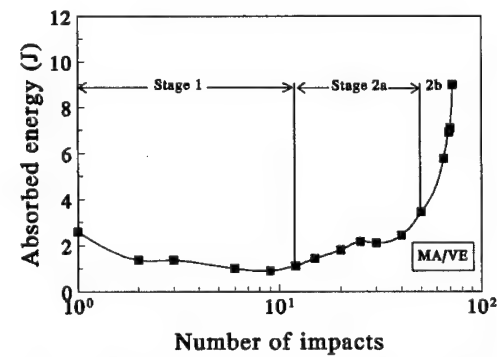


Figure 10. Absorbed energy force as a function of number of low energy (25% penetration energy) repeated impacts for a MA/VE laminate. Rapid delamination (stage 2a) and fibre breakage (stage 2b).

#### 4 CONCLUSIONS

- The optimal type of fibre architecture for energy absorption (penetration resistance) is a multiaxial fabric, whereas the optimal fibre architecture for damage resistance is a woven fabric. These results once more indicate that approaches towards improved energy absorption and damage resistance can be to some extent conflicting.
- No clear optimal resin system could be identified for energy absorption, where the optimal resin system for damage resistance is the more ductile rubber toughened vinyl ester system.
- For most laminate configurations no significant differences in the number of impact to penetration (impact fatigue life-time) are observed for the different laminate configurations. When the (repeated) impact energy is normalized with respect to the penetration energy, all composites show the same behaviour, resulting in a sort of 'Master-Curve' for impact fatigue.
- For most specimens the glass delaminated area increased gradually with the number of impacts. Only in laminates based on multiaxial tapes a two stage damage growth process is active, where stage 1 corresponds to matrix cracking in the region of the impactor and stage 2 to a rapid delamination propagation.
- When the impacts are repeated the absorbed energy increases. Typically, at low repeated impact energy levels (25% of the penetration energy) the absorbed energy levels started to increase dramatically at 70% life-time, indicating that only in the last part of the impact fatigue-life extensive fibre breakage occurs in the vicinity of the impact.

#### ACKNOWLEDGEMENT

This work was part of the EUCLID RTP3.8 project. The project was lead by: Det Norske Veritas (Norway-lead company), Direction des Construction Navales (France), Defence and Evaluation Research Agency (UK), Fincantieri (Italy), TNO (The Netherlands). The support of the Ministries of Defence of the five participating nations is gratefully acknowledged. Furthermore, the authors would like to thank B. Drog of DSM-BASF Structural Resins (Zwolle, the Netherlands) and M. Jacobs of DSM High Performance Fibres (Heerlen, the Netherlands) for providing the GRP laminates and stimulating discussions.

#### REFERENCES

- Boukhili, R., Bojji, C. and Gauvin, R., *J. Reinforced Plast. Comp.*, 13(10) (1994) 856.
- Curtis, P.T. and Bishop, S.M., *Composites*, 15(4) (1984) 259.
- Davies, C.K.L., Turner, S. and Williamson, K.H., *Composites*, 16(4) (1985) 279.
- Dorey, G. in: *Proc. ICCM*, London (1987) 3.1
- Evans, R.E. and Masters, J.E. in: *Toughened Composites*, ASTM STP937, ed .N.J. Johnston (1987) 413.
- Greszczuk, L.G., *ASTM STP 568, American Society for Testing and Materials* (1975).
- Hunston, D.L. et al. in: *Toughened Composites*, *ASTM STP 937*, ed. N.J. Johnston (1987) 74.
- Jang, B.P., Knowbel, W. and Jang, B.Z., *Comp. Sci. & Techn.*, 44 (1992) 107.
- Loete, J. and Marissen, R., Quasi-static mechanical tests of thin section laminates, Technical Report Naval Application Technology EUCLID RTP3.8 TD-1131-9601 (1996).
- Peijs, A.A.J.M., Venderbosch, R.W. and Lemstra, P.J., *Composites*, 21(6) (1990) 522.
- Peijs, T., Smets, E.A.M. and Govaert, L.E., *Applied Composite Materials*, 1 (1994) 35.
- Rotem, A., *J. Comp. Technn. & Research*, 10(2) (1988) 74.
- Starnes, J.H., Rhodes, M.D. and Williams, J.G., *Nondestructive Evaluation and Flaw Criticality for Composite Materials*, *ASTM STP 696*, Philadelphia (1979) 145.
- Tobukuro, K., Odagiri, N., Ito, Y. and Nishimura, T. in: *New generation materials and processes*, ed. F. Saporiti et al., Proc. 9th Int. Conference of Sampe European Chapter, Milano, (1988) 293.
- Van Eijk, R. and Peijs, T. in: *Proc. of ICCM/10*, ed. A. Poursartip & K. Street, Whistler, BC, Canada (Woodhead Publ. Ltd., 1995) Vol. V, 599.
- Winkel, J.D. and Adams, D.F., *Composites*, 16(4) (1985) 268.
- Wyrick, D.A. and Adams, D.F., *Composites*, 19(1) (1988) 19.

## Reliability methods for structural composite applications in vehicle suspensions

Patrick T. MacLellan & Johnny R. Gentry  
*Delphi Chassis Systems, Dayton, Ohio, USA*

**ABSTRACT:** Delphi Chassis efforts in the area of advanced composites have focused on developing highly reliable suspension modules and components at a low cost and reduced mass. Delphi Chassis has developed two processes for use in automotive suspension applications. The first is a fiberglass filament winding process used to manufacture Liteflex™ composite leaf springs. A more recent process, used to manufacture Litecast™ suspension links, consists of die casting a metal (aluminum) end fitting directly onto a pultruded polymeric composite rod (fiberglass, graphite). High reliability and confidence targets are met through lab and field validation testing that duplicates customer usage. Accelerated lab testing is utilized to reduce test times and cost by identifying what types of inputs are damaging to specific component. An accelerated, multi-environment, overstressed forced failure approach is utilized to predict reliability based on customer usage. Delphi is utilizing this forced failure reliability test approach to thoroughly understand and optimize their components before reaching the customers hands.

### INTRODUCTION

Delphi Chassis efforts in the area of advanced composites have focused on developing highly reliable suspension components, and more recently systems, at a low cost and reduced mass. Delphi Chassis has developed two processes for use in automotive suspension applications. The first is a fiberglass filament winding process used to manufacture LITEFLEX™ composite leaf springs. Vehicle applications utilizing this process have been in the field for over 15 years. A more recent process, used to manufacture Litecast™ suspension links, consists of die casting a metal (aluminum) end fitting onto a pultruded polymeric composite rod (fiberglass, graphite). Delphi's LITECAST™ technology offers a unique solution for attachment problems with structural composites. A photo of LITEFLEX™ composite leaf springs and LITECAST™ suspension components are shown in Figure 1.

### DEVELOPMENT OF TESTING FOR LITEFLEX™ SPRINGS

#### *Liteflex™ composite leaf springs*

Liteflex™ composite leaf springs are manufactured

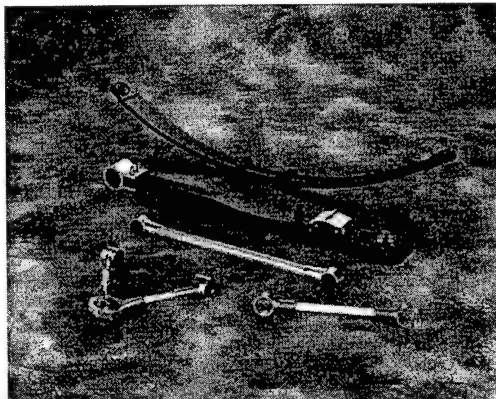


Figure 1. Photo of LITEFLEX™ Composite Leaf Springs & Litecast™ Composite Suspension Links and Control Arm Components

by Delphi Chassis Systems, a division of General Motors. The composite springs are composed of 72% by weight unidirectional fiberglass reinforcing an epoxy matrix. The manufacturing process consists of a filament winding/compression mold process to shape and cure the final component. The specific strength of these composite materials is significantly greater than steel. Aluminum castings and/or forgings are typical end attachments, attached

by fasteners to the composite. LITEFLEX<sup>TM</sup> springs have been in production since 1981 on a variety of passenger vehicles and more recently on heavy-duty tractor/trailer trucks. More information on applications of LITEFLEX<sup>TM</sup> can be found in the literature as detailed by Mutzner and Richard<sup>1</sup>.

LITEFLEX<sup>TM</sup> leaf springs offer many advantages in comparison to steel leaf springs such as durability, weight savings, and unique design capabilities that can be translated into ride and handling advantages. For example, a composite spring is installed as a single leaf spring instead of multiple steel leafs, thus eliminating a large majority of the hysteresis in the suspension which translates into improved ride. Another ride and handling benefit is the ability to change the geometric cross-sectional area of the spring along its length, which can be utilized for optimization of a vertical to roll rate ratio (i.e. soft ride rate and high roll rate) in transverse suspension applications. Typical weight savings for tractor-trailer Class 8 applications, if all steel springs are replaced with composite springs can be on the order of 171 to 278 kg (377 to 613 lbs). One of the most advantageous benefits that a composite spring offers is a 'soft' damage mode. Instead of a large stress concentration which leads to catastrophic failure in a steel product, LITEFLEX<sup>TM</sup> leaf springs typically exhibit compressive, tensile, and shear damage modes which result in a slightly lower spring rate only. In this manner, the spring still retains its ability to operate and carry a load, with some indication to the operator of the vehicle.

In addition, on some applications, a cost savings can be realized due to the extended durability of the

composite. For comparison, a load vs cycle fatigue curve is shown in Figure 2 for a LITEFLEX<sup>TM</sup> spring, an OEM steel spring and an aftermarket steel spring. Composite springs typically outlast a steel spring by 1 to 4 years. More information on this topic can be found in the literature as outlined by Knouff and Hurtubise<sup>2</sup> or Sliemers and Knouff<sup>3</sup>.

In the late '70s and early 80's time frame, LITEFLEX<sup>TM</sup> spring test methodologies were being developed to produce a spring that would be more durable than its steel counterpart. Typically, steel leaf spring suppliers were performing routine room temperature fatigue tests only. A good rule of thumb for testing back then was 100,000 cycles from design position to rebound position to full jounce position and back to design position without failure on a given number of springs (sample size is determined by reliability requirements). This was considered to be approximately equal to one life in a vehicle. Jounce and rebound position for a vehicle are typically defined as metal-to-metal limit of travel (or shock absorber limit of travel) in the upward and downward direction respectively. Design position is defined as the position of the suspension members when the vehicle is on level ground and at trim height. A typical application for a LITEFLEX<sup>TM</sup> spring in a suspension is shown in Figure 3. In most cases, failure of a spring is considered to be a loss in load and/or rate by more than 5 or 10%, depending on the application and/or test, not complete separation. Material selection is performed on springs to determine detrimental effects from chemical and environmental effects previous to a spring design.

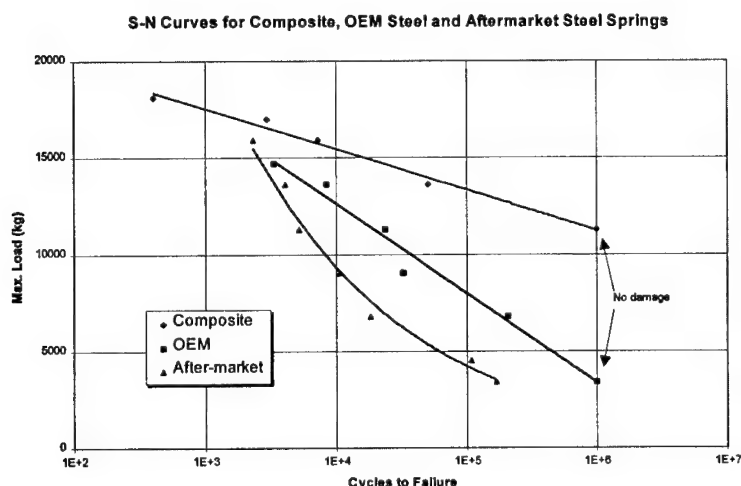


Figure 2. S-N curves for truck trailer composite, OEM steel, and aftermarket steel springs fatigued in flexure.

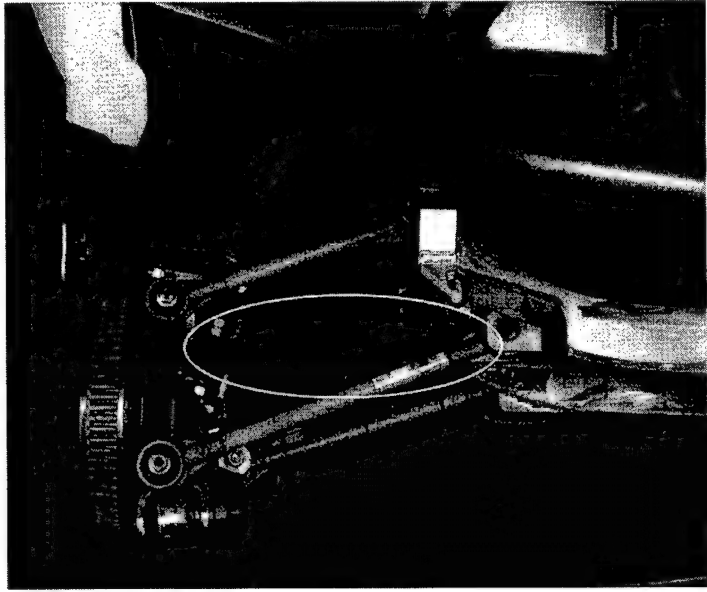


Figure 3. Application of Liteflex™ Composite Transverse Leaf Spring in Rear Suspension of Passenger Vehicle.

Delphi Chassis recognized that a composite spring would have to meet more stringent and extensive durability requirements, due to both the more complex nature of the material and the manufacturing process, in addition to bringing a new product to market. Delphi stepped up to these needs initially by doubling the number of cycles to 200,000 cycles (2 lives) and performing extensive vehicle durability. Testing to multiple lives for a component using a standard 'representative' block cycle test is known as 'bogey' testing. In many cases, 'bogey' tests are more severe than they need to be, to ensure little possibility of failure in the field. Our customers were satisfied with this response, however Delphi felt that more extensive testing would be necessary.

The next step was to refine our test methods by incorporating hot/cold temperatures during fatigue, time at temperature while under load (CREEP/Stress relaxation) and humidity. High temperature fatigue testing is performed in a chamber for 200,000 cycles and similarly for cold temperature fatigue testing. Temperatures are based on customer/vehicle data from the field. Stress relaxation resistance testing is also performed on a given number of springs. Typically, a spring is compressed to full jounce or design position in a fixture and then placed in a heat chamber at high temperature for a predetermined number of hours. Springs are also tested for stress relaxation resistance under heat and high humidity.

Again, temperature, time at temperature and humidity requirements are driven by customer extremes seen in the field. Almost all of these test specifications were refined over the years to reflect customer usage and information from a proving grounds.

Based on Delphi's historical data, it has been well established that if a spring can pass these types of tests, failure of a spring will not occur from normal customer usage during the specified 'life' of the vehicle (as defined by the customer). One of the problems with this type of testing philosophy is that large sample sizes must be tested (and/or long test times) to meet high reliability and confidence targets. One of the reasons for large sample sizes is because we are not testing the component to failure. Typically, for a composite spring, as long as the stress level in the part remains below the design (threshold) stress the spring will see a run out condition (i.e.: spring will never fail). Hence, testing multiple springs to multiple lives yields long test times with little confidence in the reliability. Based on this type of a testing philosophy, it would take a very long time to meet customer reliability and confidence levels for any new product and/or design change. In an effort to meet increased reliability and confidence in our products faster, Delphi Chassis has developed new test methodologies for new products that has allowed us to understand our components in a way that was previously unrealized.

---

## RELIABILITY TEST METHODOLOGY--'A New Approach'

### *Litecast™ link(s)*

Delphi Chassis has developed another structural composite application that is not only economical, but offers many advantages to design and function in a suspension system. This product, called LITECAST™ LINK(S), involves die casting attachment fittings directly onto a polymeric composite which yields a high strength structure. In this process, a molding alloy with a low temperature melt point (i.e.: aluminum) is brought into contact with a highly filled polymer matrix composite utilizing a rapid casting technique. Prior to die casting the composite rod is notched to provide a mechanical interlock between the rod and casting to increase load transfer efficiency. More information on LITECAST™ LINK(S) can be found in the literature by Gentry & Graham<sup>4</sup>. A current application for this product in a rear suspension (upper & lower fore/aft links) is shown in Figure 4.

Due to the structural nature of the application, the environment, and the performance criteria for these products, the requirement for high reliability in the field is essential. The purpose of reliability testing is

to ensure that the components strength distribution is sufficient to withstand the distribution of all the customer stresses during a vehicle's lifetime. The Delphi Chassis test philosophy that was utilized to validate the LITECAST™ LINK will be outlined in this paper.

#### *Test preparation*

The first step in developing a test plan is to determine the possible Design Failure Modes and Effects Analysis (DFMEA) for the component and its interfaces. A DFMEA expands on the thought process engineers go through when evaluating their designs. The intent is to identify potential failure modes and their causes and then prioritize the type and quantity of testing necessary to eliminate the potential failures identified at a component, system and/or interface level.

The next step is to determine test specifications based on the 'customer profile'. The customer profile can be defined as the loads and environments accumulated by the product over the life of a vehicle. There are many test aspects that are critical for the optimization of the product design. The first is understanding the combined stress (i.e.: damage) during the life of the product. This includes not only

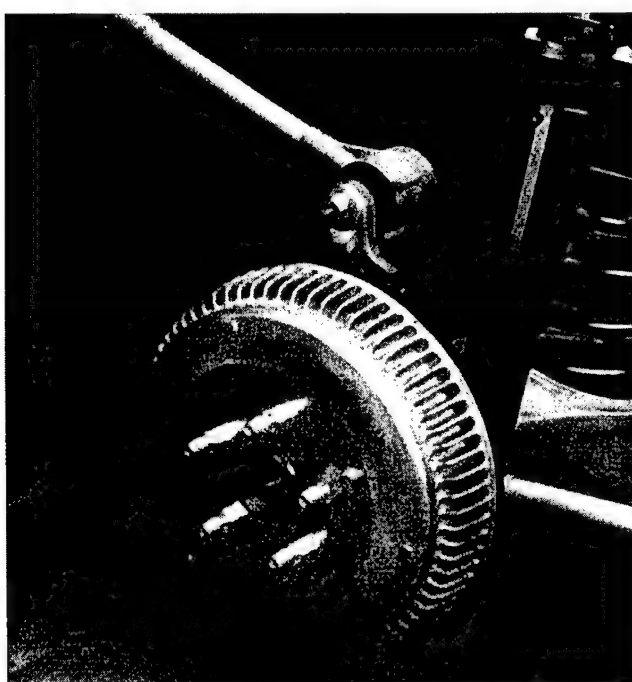


Figure 4. Photo of current Litecast™ Composite Suspension Links Installed in Rear Suspension of Passenger Vehicle.

load & displacements on component, but also the environment, such as chemicals, temperatures and humidity. Typically, this information is gathered at a proving grounds with instrumented vehicles (i.e.: road data). The second is a measure of the customer severity. Obviously, we would not want to design all of our components to withstand stresses outside a particular design window that a typical customer operates in. For most of Delphi's products, the typical customer severity level for suspension components is 97.5%. Customer usage is also necessary in determining test requirements. Typical customer usage levels for passenger vehicles range from 100,000 -150,000 miles. Finally, the reliability and confidence levels for a test must be determined. Delphi's goals for the LITECAST™ LINK product were 99% reliability with 90% confidence. All of these specifications determine the customer profile or the 'operating rectangle'.

After determining the test specifications, much emphasis is placed on gathering representative customer/road data. This includes instrumenting individual components for loads, displacements, accelerations, temperatures and humidity levels. After data collection, it should be determined whether a durability test needs to encompass a multi-axis loading condition, or if a single-axis is sufficient. Multi-axis test rigs can become quite complex and expensive but are sometimes necessary for proper testing. The instrumented parts on the vehicle should be utilized in the lab to verify all stresses, temperatures, etc... To simulate the stresses in the lab on the component, hydraulic actuators and temperature/humidity chambers are utilized. To simulate environments such as harmful chemicals, per the DFMEA, preconditioning is sometimes necessary and/or immersion of the component in a fluid during fatigue. Delphi's current testing strategies include an overstress test technique that forces failure in a component to predict reliability and the distribution of failures. This technique is designed to detect the representative manufacturing variation in our parts relative to customer usage.

#### *Reliability overstress testing*

Overstress testing is designed to reveal any overlap of the operating load distribution and the part strength distribution. In general, overstress testing consists of gradually increasing the loads on a component until failure occurs. The robustness of the design is then measured by the difference between the tails of the distribution of the fracture strength and the design loads. This technique will then reveal the systems/components weakest failure mode.

The first step is to come up with a list of all the possible environments and loading conditions for the component. In addition, the first 'foolish failure' of the component *for each environment* should be determined. In the simplest case, this might be an ultimate tension/compression test. This failure mode does not have to be similar in nature to typical field failures. It is an estimate utilized in the overstress step-size calculation. The overstress step-size for each environment should then be calculated. This is performed by determining the highest and lowest load/environment conditions in the operating rectangle. The overstress step-size percent is then:

$$[(\text{Foolish} - \text{Highest}) / (\text{Highest} - \text{Lowest})] / 10 \quad (1)$$

where the lowest calculated step-size for all 'stresses' is utilized in the test.

Before utilizing the overstress portion of testing, it is necessary to condition (test) the part through the normal operating portion of its design life. After conditioning, the stresses are increased by the overstress step-size calculated above. Be aware that the corresponding number of cycles is decreased by the above percentage also. In this manner the stresses are continually increased after each phase until failure occurs. Keep in mind that this includes all stresses, such as temperatures, environmental effects and chemicals too. A good rule of thumb is to desire a minimum of ten total overstress steps after conditioning until failure (See figure 5). This allows enough resolution in the data for analysis purposes.

Data analysis is performed by plotting the percent overstress at which failure occurred on Weibull paper using a median ranks approach. The weibull function is utilized because of its flexibility to represent many types of failures. One very important point, when utilizing this method is to analyze only similar failure modes on the same plot. The typical sample size ranges from 10 to 12 components/systems. For final design validation, these parts must encompass the expected range of variation in the manufacturing process. A typical weibull plot with components tested using the overstress method is shown in figure 6. A design is considered to have passed when the confidence band on the data is to the right of the operating rectangle at the a-priori specified reliability (99%). In this way, we are making a reliability prediction based on the operating range of the part. Therefore, it is extremely important to understand the customer stresses in the operating range. Care should be taken when performing a bogey test and then utilizing the

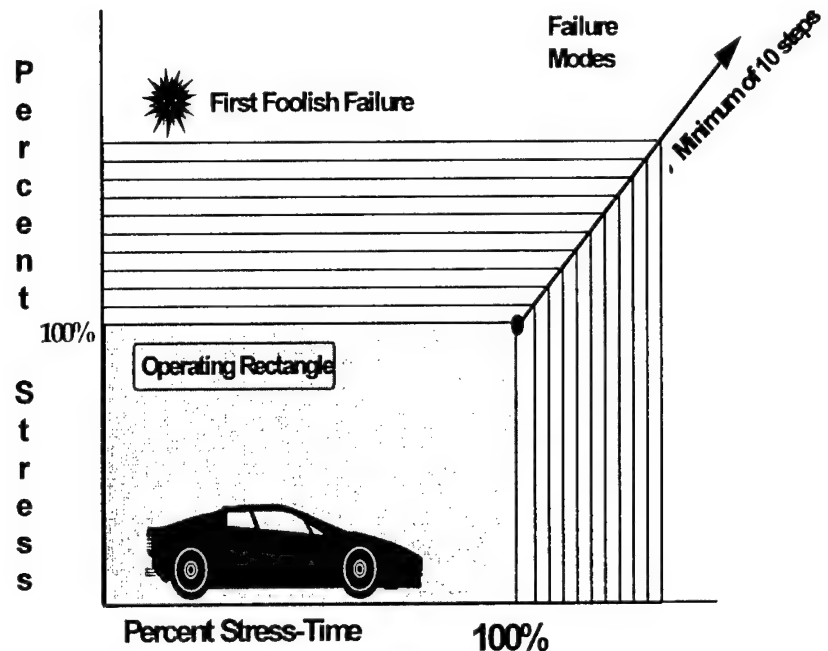


Figure 5. Schematic of Overstress Reliability Test Process.

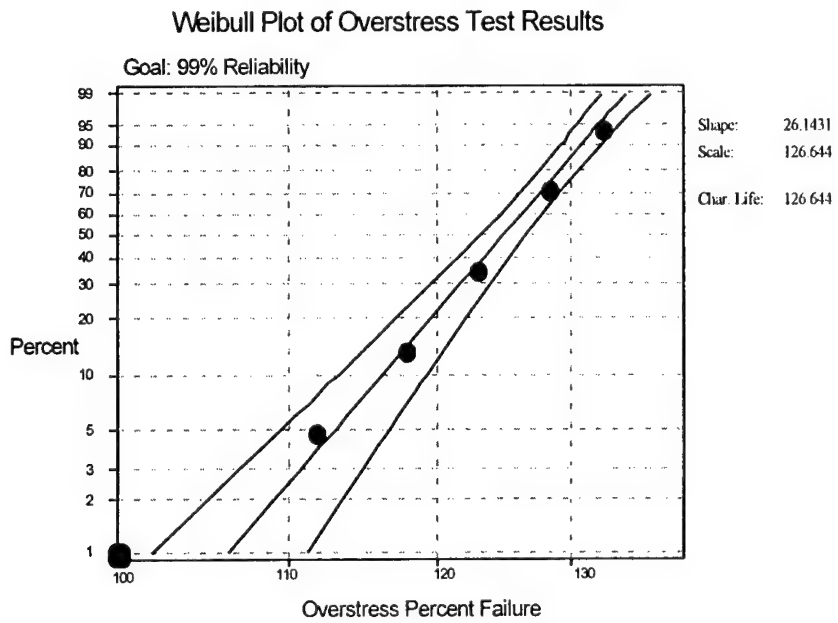


Figure 6. Weibull Plot of Overstress Test Results.

overstress technique. Many times, bogey tests are conservative and may in fact represent more than one operating life. In that case, you will predict reliability to something non-representative of the customer and over-design the system which will cost you time and money. The importance of this technique is not necessarily the number of steps it takes to fail the component but to understand the weakest link in the system and propose remedies. This process allows a thorough understanding of the types and number of failure modes in the system. Thus, it also allows the prediction of high reliability *with* high confidence using relatively small sample sizes in comparison to multiple life testing. More information on overstress reliability testing can be found in the literature by Carter<sup>3</sup>.

#### *Accelerated testing--using fatigue damage approach*

Accelerated testing is typically utilized when the life of the product is extremely long and information is needed quickly about failure distributions, reliability, etc... The approach that Delphi Chassis utilizes involves a calculation of the *fatigue* damage due to the loading conditions on the part and then eliminating the non-damaging portions. This process allows a thorough understanding of the stresses and their effects on the part thus giving way

to a reliable and optimal product design. This technique has allowed test time reductions (1 test) of greater than 90% for the LITECAST™ LINK product.

The first step in this process is to ensure that a damage model exists for the type of failure exhibited during testing. In this case, a uniaxial fatigue damage model was utilized, due to the nature of the loading on the component and failures seen in long term durability testing of the LITECAST™ LINK. Failures typically occurred due to low cycle fatigue at high stress levels *beyond* the operating rectangle stresses in the diecast aluminum attachments and not in the composite. The next step is to develop a Stress vs Cycles (S-N) curve for the product. The recommended sample size will vary with the product, however the knee in the curve should be well defined. This information can then be utilized to calculate a stress concentration factor ( $k_c$ ) which defines the load to stress relationship for the component. Next, the customer profile data (i.e. road surfaces, time histories, etc...) is utilized to calculate the 'damage' using a cumulative fatigue damage model (eg: Miner). The road data encompasses many different types of road surfaces and is typically very lengthy. For this purpose, the data is reduced into a 'rainflow with mean' format

## LITECAST™ LINK OSP DAMAGE ANALYSIS

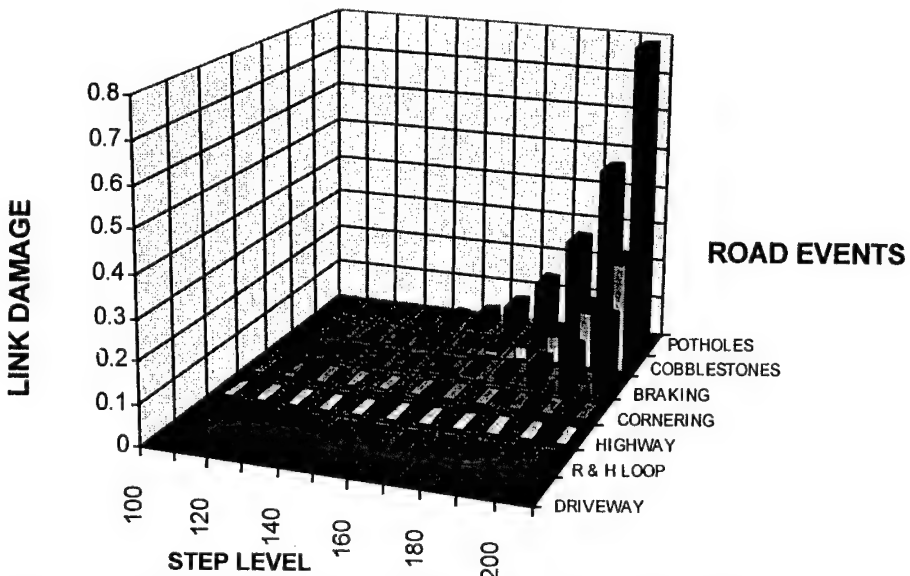


Figure 7. Fatigue Damage Analysis of Link Damage for Various Road Events Utilized for Accelerated Testing

and fed into the model using the  $k_i$  calculated from the S-N data. The output from the model will be a damage value where the summation of the damage from each event (along with the corresponding cycles for each event) are summed. A damage value equal to 1.0 would indicate failure. However, the damage summation for the operating rectangle stresses should be less than 1.0 if the product is to survive at least one 'life'. The next step in this process is to incorporate the overstress portion of the test data into the fatigue model. In many cases, events that were considered to be non-damaging before can be significant when utilizing overstress techniques. An example plot of damage vs overstress step vs road input type is shown in Figure 7. Notice that only certain events are damaging to the component and not until 150% overstress and above. In this particular case, the part was not overdesigned but had other requirements to meet besides durability (i.e. stiffness).

#### CONCLUSIONS

Development of reliable, customer correlated, 'damage-only' accelerated testing in the lab is necessary to ensure competitiveness in today's market. Delphi is utilizing this forced-failure reliability approach to thoroughly understand and optimize their components before reaching the customers hands. Currently, Delphi is starting to test suspension corner modules as a whole and utilize multi-axis, multi-environment overstress testing techniques to understand the component interface issues with our own and other customers components. Current low mass suspension systems developed with composites at Delphi show up to 33% mass savings in the system.

#### REFERENCES

- <sup>1</sup> J.E. Mutzner and D.S. Richard, "Development and Testing of Composite Truck Trailer Springs", *SAE Technical Paper Series, International Congress and Exposition*, Detroit, MI, (Feb. 27-Mar. 3, 1989):105-110.
- <sup>2</sup> B. Knouff and D. Hurtubise, "Advantages of Structural Composites in Class 8 Truck Suspensions", *Proceedings of 1996 SAE Truck and Bus Show*, Detroit, MI, USA, October 16, 1996.
- <sup>3</sup> J. Sliemers and B. Knouff, "Fatigue Characterization Of The Liteflex<sup>TM</sup> Composite Truck Trailer Spring", *Proceedings of the 11th Annual ESD Advanced Composites Conference & Exposition*, Dearborn, MI, November 6-9, 1995, pp. 37-58.
- <sup>4</sup> J. R. Gentry and B.P. Graham, "LITECAST<sup>TM</sup>: A Novel Solution for Attachment Problems with

Structural Composites", *Proceedings of the 10th Annual ASM/ESD Advanced Composites Conference*, Dearborn, MI, USA, September 7-10, 1994.

<sup>5</sup> A.D.S. Carter, "Mechanical Reliability", Halstead Press, Copyright 1986, 310-319.

## Durability in the life cycle of polymer composites

Y.Leterrier, Y.Wyser & J.-A.E. Måson

*Laboratoire de Technologie des Composites et Polymères, Ecole Polytechnique Fédérale de Lausanne,  
Switzerland*

**ABSTRACT:** The effect of interface structure and stress state on the long-term strength of polymer composites is investigated and related to the adhesion between the polymer and the second phase. The approach specifically accounts for the previous life-cycle steps of the material, through the evolution of the size of the reinforcement phase and of the interfacial internal stress state. PET/SiO<sub>x</sub> multilayer films are used and found appropriate to tailor the interface interactions and introduce controlled compressive stresses in the interface region. Adhesion is characterized by means of micromechanical and thermodynamic complementary approaches. The long-term strength of PET multilayer composites aged below the glass transition temperature of the polymer is predicted from the failure mechanism of the interface. It is shown that reliable predictions require the knowledge of the evolution of the interface shear strength, interface internal stress and particle size through the whole life-cycle of the composite.

### 1 INTRODUCTION

Durability prediction of polymer composites becomes a central activity in structural design, as reflected by the increasing body of literature on the topic (Ishida 1990, Cardon et al. 1996). It is also a considerable challenge since these materials exhibit a strong life cycle memory. Each life cycle step, including initial manufacture, recycling, and related service lives, changes both material structure and stress state, and therefore influences the subsequent steps, which ultimately impacts the durability of the material (Reifsnider 1987, Wyser et al. 1997).

It is well established that the reliability of composite materials depends directly upon the adhesion between the different constituents. The long-term evolution of the interface characteristics determines to a large extent the durability of the composite. The mechanisms of adhesion between a polymer and another material have been extensively studied, although only partially elucidated. Among the reasons for this lies the variety of polymer structures and material combinations, and of bonding procedures, resulting in a multiplicity of interface structures and stress states. As a consequence, a large amount of adhesion theories and adhesion measurement methods have emerged since the early 30's, and reviewed by several authors (cf. Mittal

1987). According to Mittal (1987), the most appropriate adhesion measurement method is the one that simulates stress conditions achieved during service. This principle is at the base of the development of several quantitative methods developed together with a mechanical description of the interface stress transfer, to model the test results (Steinmann & Hintermann 1989, Pitkethly et al. 1993).

However, the practical dimensions and geometry of the manufactured product together with the often very complex arrangement of the various material phases, like in fiber reinforced composite parts, prohibit a direct and comprehensive characterization of interfacial adhesion. Nevertheless, most of the recent techniques have proven to be useful to determine the effect of specific treatments on adhesion performance, although the manufacture of the specimens inevitably generates inhomogeneous interfacial structures and internal stresses, resulting from polymer flow and thermal and pressure gradients.

The influence of such factors on adhesion, and thereafter on the durability of the composite is *a priori* unknown, although it is recognized that it can be considerable (Pitkethly et al. 1993, Andrews et al. 1996), following for instance analyses of Huang & Young (1994).

Another challenging problem is to predict the structural evolution of polymers below their glass transition temperature, in the presence of a second phase, as discussed by Brinson & Gates (1995). In particular, it is of central importance to clarify the role of stresses on this evolution (McKenna et al., 1991).

To overcome these issues, the first objective of the study was to tailor the interface structure and independently control the interface stress state to elucidate their specific role on adhesion, with attention paid on long-term evolution. To this end, polyethylene terephthalate films coated with silicon oxide coatings of thickness of the order of 100 nm (PET/SiO<sub>x</sub>) were used. These materials are of considerable interest as oxygen-barrier for food and pharmaceutical packaging applications (Felts 1993). The films were processed and aged according to several procedures yielding precise, unique and homogeneous interface structures or stress states. The second objective was to scale the above understanding to simulate recycling and predict the long-term strength of multilayer PET/SiO<sub>x</sub> composites, with attention paid to the effect of the size of the reinforcement phase. Since the recovery of multiphase polymer based materials has become a central issue, the conclusions drawn from this work should thus be of a broad significance.

## 2 THEORETICAL APPROACHES TO ADHESION

The deposition processes of thin films on polymers are known to promote intimate contact between the two substances, resulting in a high density of short distance intermolecular interactions. It is therefore natural to characterize the basic adhesion between PET and SiO<sub>x</sub> from the wetting theory developed by Sharpe and Shornhorn (1963), and calculate the work of adhesion, defined as the reversible work done to create a unit area of interface between the two substances. Moreover, when limited delamination occurs at the interface, even at high applied strains, stress transfer models are likely to be best applied to derive basic adhesion (Leterrier et al. 1994). These two independent approaches -- thermodynamics and micromechanics -- are briefly described in the following.

### 2.1 Thermodynamic approach to adhesion

The work of adhesion  $W_a$  between PET and SiO<sub>x</sub> was calculated according to the model of Fowkes (1987):

$$W_a = 2\sqrt{\gamma_{SiO_x}^d \gamma_{PET}^d} + 2\sqrt{\gamma_{SiO_x}^{nd} \gamma_{PET}^{nd}} \quad (1)$$

The model is based on the wetting theory indicated above (Owens & Wendt 1969), and accounts for the dispersive components  $\gamma_{SiO_x}^d$  and  $\gamma_{PET}^d$  (London interactions) and the non-dispersive components  $\gamma_{SiO_x}^{nd}$  and  $\gamma_{PET}^{nd}$  (polar interactions, including acid-base interactions such as hydrogen bonds) whose respective sums constitute the surface energies of the oxide coating and the polymer. The various components were derived from contact angles measurements of water and apolar  $\alpha$ -bromonaphthalene of known surface energy characteristics (Fourche 1995, Leterrier et al. 1997c).

### 2.2 Micromechanical approach to the adhesion

The interface shear strength,  $\tau$ , was derived from the classical Kelly-Tyson (1965) model of stress transfer, accounting for the internal stress  $\sigma_i$  (Wyser 1997):

$$\tau = 1.337 \cdot h \frac{(\sigma_{max}(l_c) - 2/3 \sigma_i)}{l_{sat}} \quad (2)$$

where  $h$  is the coating thickness,  $\sigma_{max}$  is the coating strength at critical length  $l_c$  and  $l_{sat}$  is the average fragment length at saturation, directly measured from micrographs of fragmented coatings on substrates strained above the saturation onset strain (Leterrier et al. 1994). The critical length  $l_c$  was calculated to be very close to  $3/2 \cdot l_{sat}$ . The dependence of the oxide strength  $\sigma_{max}$  with fragment length was calculated from a linear extrapolation of the initial part of the curve  $\ln(CD)$  versus  $\ln(\epsilon)$ , where CD is the crack density, inverse of the average fragment length, and  $\epsilon$  is the nominal strain, assuming a two-parameter Weibull distribution (Weibull 1951, Andersons et al. 1995). The coating strength was found to be equal to 1500 MPa at critical length, and to be independent of the various treatments described later, within experimental uncertainty.

### 2.3 The role and nature of the interfacial interactions

The work of adhesion was related to the interface strength according to the approach developed by Nardin and Schultz (1996) based on elastic stress transfer, through the interaction distance  $\delta$  typical of physical interactions:

$$\delta = W_a / (E_{SiO_x} / E_{PET})^{1/2} \cdot \tau \quad (3)$$

The distance  $\delta$  was found to be of the order of 5 Å in a number of composite systems (Nardin &

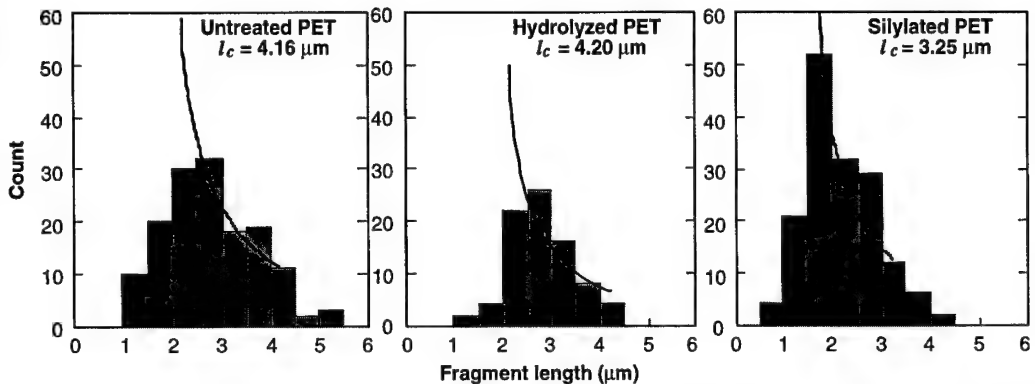


Figure 1. Effect of PET surface treatment on experimental (bars) and theoretical (lines)  $\text{SiO}_x$  fragment length distributions at saturation; critical fragment lengths are also indicated.

Schultz 1996),  $E_{\text{PET}}$  and  $E_{\text{SiO}_x}$  are the elastic moduli of the polymer and the oxide coating.

An independent determination of the interaction distance  $\delta$  would require a comprehensive description of the interface microstructure. Alternatively,  $\delta$  was calculated from Equation 3 from the experimental values of the moduli,  $W_a$  and  $\tau$ . The calculation of  $\delta$  enables a detailed examination of the nature of the interfacial interactions, in particular the respective role of the dispersive and polar forces acting at the interface.

### 3 THE ROLE OF INTERFACE STRUCTURE AND STRESS STATE ON ADHESION

#### 3.1 Effect of hydrolysis and silylation on interfacial interactions

Different interface structures were prepared by means of hydrolysis or silylation of the PET surface prior to the deposition of 120 nm thick coatings. The polymer substrates were injection molded plaques of thickness 1 mm. Their Young modulus equal to 2500 MPa was found to be unaffected by the surface treatments. Hydrolysis was done in a concentrated sodium hydroxide solution during 20 min at 60 °C. Silylation was performed in  $\gamma$ -aminopropyltriethoxysilane ( $\gamma$ -APS, OSI Specialties A1100) during 10 min at 60 °C.

The experimental and theoretical distributions of fragment lengths at saturation resulting from straining the substrate are shown in Figure 1 for the untreated and treated PET/ $\text{SiO}_x$  materials. The critical lengths of untreated and hydrolyzed materials, reported in the histograms, can be considered to be equal, the difference being less than 1 %, which is well below the typical uncertainty of the order of

10 % related to such measurement (Leterrier et al. 1997a). Conversely, the fragment length distribution of the silylated material is shifted to smaller lengths, its theoretical fit is better, and the corresponding critical length is much lower than that of the two other materials.

The interface strength of the untreated material was found equal to 86 MPa and the work of adhesion to 190 mJ/m<sup>2</sup>, corresponding to an interaction distance close to 0.4 nm. These values were almost identical in the case of the hydrolyzed material.

By contrast, the interface strength of the silylated material was found equal to 112 MPa, the work adhesion to 203 mJ/m<sup>2</sup>, and the interaction distance to 0.3 nm. This 25 % decrease compared to the untreated material indicates an increased interface interaction density, and a detailed analysis of the various components of the surface energies (Leterrier et al. 1997c) reveals that acid-base interactions such as hydrogen bonds control to a large extent the interface structure.

#### 3.2 Tailoring of interface stress and effect on long-term adhesion

Axial compressive strains up to 1.3 % were introduced by bonding with an elastomeric glue biaxially stretched PET films of thickness 12  $\mu\text{m}$ , coated by physical vapor deposition with a 100 nm thin oxide layer, to a 90  $\mu\text{m}$  thick polypropylene (PP) substrate. The PP was subsequently shrunk by means of an appropriate thermal treatment, resulting in the introduction of the desired compression in the coated PET (Wyser et al. 1997).

The fragmentation process of the coating during straining the polymer is shown in Figure 2 at different levels of interface compression, by plotting

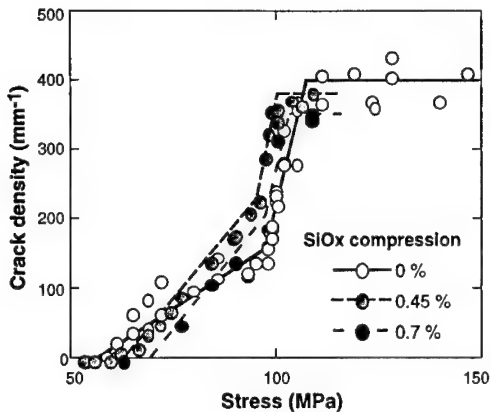


Figure 2. Increase of the crack density CD of the oxide vs. applied stress at different levels of interface compression.

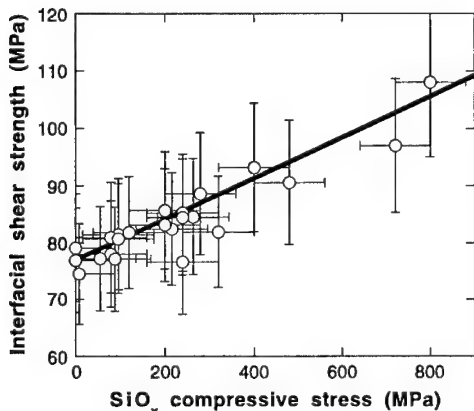


Figure 3. Experimental (dots) and theoretical (line) interface shear strength vs. internal stress.

the crack density increase versus the applied tensile stress (Leterrier et al., 1997a). It is evident that compressive internal stresses increase the crack onset stress while it does not significantly affect the crack density at fragmentation saturation. Coated PET films were also aged at several temperatures below the glass transition temperature of the polymer up to 250 days. It was observed that the structural recovery process of the polymer which takes place during aging could be described in terms of the progressive development of interface internal stress (Wyser 1997).

The experimental findings were compared to the prediction (Equation 2), which was found to reproduce remarkably the linear increase shown in Figure 3. This agreement provides clues of the relation between interface stress transfer and internal stress.

#### 4 SCALING INTERFACE STRUCTURE AND STRESS STATE FROM FILMS TO MULTILAYER COMPOSITES

Scaling to three-dimensional composite structures was performed with multilayer PET/SiO<sub>x</sub> composites, in which the oxide particles have the shape of platelets of different aspect ratios. Platelets offer a cost-effective alternative to fibers for reinforced composites with moderate drop in strength and toughness. The structures depicted in Figure 4 were compression molded from stacks of 100 films. One multilayer type was plain PET for reference, a second type was characterized by oxide platelets all larger than several 100 μm ("non-fragmented PET/SiO<sub>x</sub>"), a third type was characterized by oxide platelets all smaller than the stress transfer critical length, close to 4 μm ("fragmented PET/SiO<sub>x</sub>"). Similarly to the films, the composites were thermally aged at various temperatures below the glass transition T<sub>g</sub> of the polymer to study specifically physical aging effects (Hutchinson 1995). In order to prevent the occurrence of other time-dependent mechanisms during the aging process, the multilayer materials were initially annealed above the T<sub>g</sub> of the polymer to attain the maximum crystallinity and the aging temperatures were low enough so it was verified that recrystallization and oxidative degradation did not take place within the duration of the experiment.

##### 4.1 Analysis of the structural recovery process in multilayer composites

The enthalpy recovery peaks of the aged materials resulting from the aging process (Struik 1978) were analyzed by means of differential scanning calorimetry in the vicinity of the glass transition temperature. While the plain and fragmented materials were found to exhibit almost identical recovery processes, a clear shift of the enthalpy recovery peak to higher temperatures was systematically observed at all times and temperatures for the non-fragmented material. A linear relationship was further observed between the peak temperature and the logarithm of the aging time, as reported by Hutchinson (1995). The slope of this linear relationship, which measures the structural recovery rate of the material, was found to be independent of the aging temperature, in agreement with the work of Hodge (1994). It was observed that the aging rates for the plain and fragmented materials were equal within experimental error. Conversely, the aging rate of the non-fragmented material was significantly higher by almost 40 %.

Moreover, the activation energies of the enthalpy recovery process were found to be equal for all

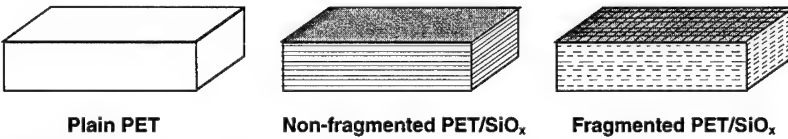


Figure 4. Multilayer composite structures compression molded from stacks of 100 films.

material types, indicating that it is not a change in the recovery mechanism which affects the enthalpy recovery peak position, but indeed a change in the enthalpy relaxation kinetics. It is therefore clear that a factor, other than the presence of the  $\text{SiO}_x$  phase and the crystallinity of the PET (which is equal for all specimens and remains constant during the whole aging procedure), affects the aging kinetics of the PET. To elucidate this, plain specimens were aged one month at 55 °C under constant tensile strains of 0.4 or 0.6 %, in order to simulate internal stresses. A clear shift of the enthalpy recovery peak towards higher temperatures is evident in Figure 5, indicating that it is indeed the internal stresses induced by the presence of the  $\text{SiO}_x$  phase that increases the aging rate. Tool (1946) has introduced the concept of a fictive temperature, which controls the aging kinetics, defined as the temperature at which the polymer would be at equilibrium, considering its volume. A tensile strain, whether applied or induced by the presence of a second phase, increases the volume of the polymer affected by this strain, which, in turn increases the fictive temperature and, therefore the aging rate. This is confirmed by the fact that, as already observed by McKenna et al. (1991), the application of stresses during the aging procedure does not affect the time taken by a glass to reach

equilibrium. Starting from a higher volume, a strained (or stressed) polymer, has therefore to age faster in order to reach equilibrium in the same time.

#### 4.2 Prediction of the long-term interfacial failure

The scaling from the film to the composite structure, i.e., from one life-cycle step to another, which simulates recycling, considers two factors. First is the interfacial adhesion and stress state, characterized on individual  $\text{PET}/\text{SiO}_x$  films, where the latter could be precisely related to the aging process. Second is the particle size, accurately controlled from the fragmentation process described previously. A model was developed to predict interfacial crack propagation in multilayer composites, from the long-term evolution of interface stress. The model is based on the stress transfer equations developed by Hsueh (1994) for the platelet geometry. A criteria for interface failure versus particle failure was written, where the stress field at the interface vicinity resulting from an applied stress on the composite is balanced with the interface shear strength and oxide tensile strength (Wyser 1997). A critical toughening particle size  $\xi$  is derived from the criteria. Particles smaller than  $\xi$  toughen the composite as these induce interface delamination. By contrast, particles larger than  $\xi$  fail before the interface, and therefore the strength of composites containing such particles is expected to mimic that of the plain polymer throughout the aging process. It was observed that  $\xi$  decreases from ca 20  $\mu\text{m}$  to below 6  $\mu\text{m}$  during aging as the internal interface stress increases. This evolution clearly defines a ductile-to-brittle transition: particles initially smaller than  $\xi$  may well become larger than  $\xi$  upon aging, which therefore embrittles the composite, as  $\xi$  decreases with aging time.

Predictions of long-term mechanical endurance are compared in Figure 6 with experimental data for both non-fragmented and fragmented multilayer composites tested in three-point bending. As predicted by the analysis reported above, the non-fragmented material was found to behave similarly to the plain PET reference, with a rapid drop in strength resulting from embrittlement due to physical aging. By contrast, it is evident that the small  $\text{SiO}_x$  flakes toughen the polymer. Such a difference in

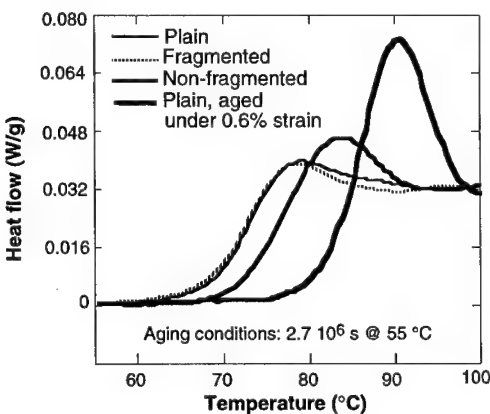


Figure 5. Enthalpy relaxation peaks of PET multilayer composites and PET aged under tensile strain.

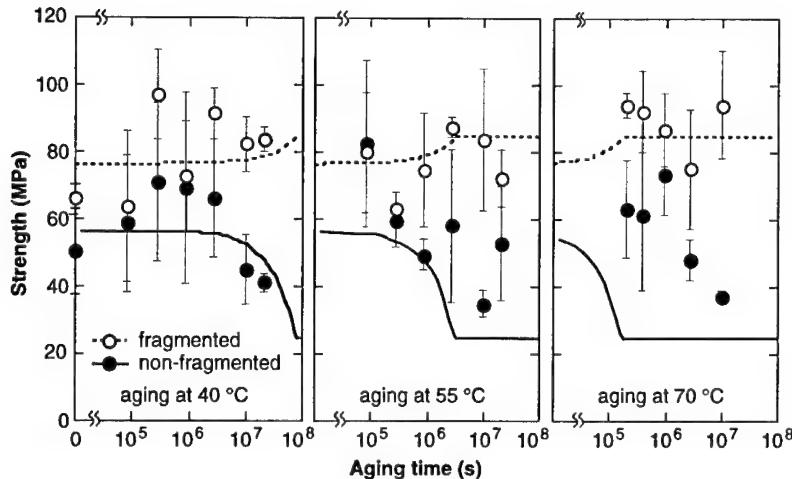


Figure 6. Comparison between experimental data (dots) and predictions (lines) of the long-term strength of fragmented and non-fragmented multilayer composites aged at different temperatures below the  $T_g$  of the polymer.

behavior between composite materials with strictly the same composition, but different particle size and stress state, is worthwhile to point out. The present agreement obtained in the case of model composite structures indicates that accounting for previous life cycle steps enables reliable long-term predictions.

The implications of this approach should be of a broad importance as life extension of polymer based materials, including recycling, are central concerns in technological developments.

## 5 CONCLUSIONS

Polymer composites are known to present a strong life-cycle memory. To study specifically this issue on the durability of the material, the effect of interface structure and stress state on the long-term strength of PET multilayer composites was investigated. It was related to the adhesion between the polymer and the second phase, and to the previous life-cycle steps of the material.

PET films coated with thin oxide coatings developed for packaging applications were used and subjected to several treatments to tailor the interface structure and introduce controlled levels of internal stress. The films were also aged below the glass transition temperature of the polymer. Fragmentation tests and wetting measurements were carried out to derive the interface shear strength and the work of adhesion, and gain insight into the interfacial interactions. The films were further processed into multilayer composites whose mechanical strength was measured after long-term aging, during which any crystallization and chemical degradation

processes was avoided. The analysis of the experimental results leads to several conclusions.

- 1  $\text{SiO}_x$  coated PET films are appropriate to tailor the interfacial structure and independently control the stress state, and explore their specific role on adhesion by combining micromechanical and thermodynamic approaches.
- 2 Polar interactions such as hydrogen bonding control to a large extent the adhesion between PET and  $\text{SiO}_x$ .
- 3 The interface shear strength between PET and  $\text{SiO}_x$  increases linearly with the interface internal compression.
- 4 The strength of multilayer PET/ $\text{SiO}_x$  composites is controlled by a critical toughening  $\text{SiO}_x$  platelet size.
  - Platelets smaller than the critical size toughen the PET, whereas larger platelets embrittle the polymer.
  - The critical size decreases with aging time as a result of increased internal stresses.

## ACKNOWLEDGMENTS

The authors are gratefully indebted to the Swiss Priority Program for Materials Research and to the Swiss National Science Foundation for funding this work.

## REFERENCES

- Andersons J., Joffe R., Sandmark R., Mech. Compos. Mater., **31**, 35 (1995).
- Andrews M.C., Bannister D.J., Young R.J., J. Mater. Sci., **31**, 3893 (1996).
- Brinson L.C., Gates T.S., Int. J. Solids Struct., **32**, 827 (1995).
- Cardon A.H., Fukuda H., Reifsnider K., Eds., "Progress in Durability Analysis of Composite Systems", A.A. Balkema Publishers, Rotterdam (1996).
- Drzal L.T., Madhukar M., J. Mater. Sci., **28**, 569 (1990).
- Felts J.T., J. Plastic Film & Sheeting, **9**, 201 (1993).
- Fourche G., Polym. Eng. Sci., **35**, 957 (1995).
- Fowkes F.M., J. Adhesion Sci. Technol., **1**, 7 (1987).
- Fraser A.A., Anker F.H., DiBenedetto A.T., Proc. 30th Conf. SPI Reinforced Plastics Division, Section 22-A, p.1. (1975).
- Hodge I.M., J. Non-Cryst. Sol., **169**, 211 (1994).
- Hsueh C.-H., Compos. Eng., **4**, 1033 (1994).
- Huang Y., Young R.J., Compos. Sci. Technol., **52**, 505 (1994).
- Hutchinson J.M., Prog. Polym. Sci., **20**, 703 (1995).
- Ishida H., Ed., "Controlled Interphases in Composite Materials", Elsevier, New-York (1990).
- Kelly A., Tyson W.R., J. Mech. Phys. Sol., **13**, 329 (1965).
- Leterrier Y., Wyser Y., Hilborn J., Månsen J.-A. E., J. Adhesion, **44**, 213 (1994).
- Leterrier Y., Boogh L., Andersons J., Månsen J.-A. E., J. Polym. Sci. B: Polym. Phys., **35**, 1449 (1997a).
- Leterrier Y., Andersons J., Pitton Y., Månsen J.-A. E., J. Polym. Sci. B: Polym. Phys., **35**, 1463 (1997b).
- Leterrier Y., Sutter P., Månsen J.-A. E., to be submitted to J. Adhesion (1997c).
- McKenna G.B., Santore M.M., Lee A., Duran R.S., J. Non-Cryst. Sol., **131-133**, 497 (1991).
- Mittal K.L., J. Adhesion Sci. Technol., **1**, 247 (1987).
- Nardin M., Schultz J., Langmuir, **12**, 4238 (1996).
- Pitkethly M.J., Favre J.P., Gaur U., Jakubowski J., Mudrich S.F., Caldwell D.L., Drzal L.T., Nardin M., Wagner H.D., Dilandro L., Hampe A., Armistead J.P., Desaeger M., Verpoest I., Compos. Sci. Technol., **48**, 205 (1993).
- Owens D.K., Wendt R.C., J. Appl. Polym. Sci., **13**, 1741 (1969).
- Reisnider K.L., Proc. ICCM/ECCM, p. 4.1 (1987).
- Sharpe L.H., Schonhorn H., Chem. Eng. News, **15**, 67 (1963).
- Steinmann P.A., Hintermann H.E., J. Vac. Sci. Technol., **A7**, 2267 (1989).
- Tool Q., J. Amer. Ceram. Soc., **29**, 240 (1946).
- Weibull W., J. Appl. Mech., **18**, 293 (1951).
- Wyser Y., Leterrier Y., Maspero F., Månsen J.-A. E, in Proc. R'97, Eds. Barrage A. and Edelmann X., EMPA, Dübendorf, p. II-149 (1997).
- Wyser Y., Ph. D. Thesis, EPFL, in preparation (1997).

## Environmental stress cracking in polyimide composites and adhesives

David A. Dillard, A. Paige Clifton Furrow & Hari Parvatareddy

*Engineering Science and Mechanics Department, Virginia Polytechnic Institute and State University, Blacksburg, Va., USA*

Terry L. St.Clair & Jeffrey Hinkley

*Composites and Polymers Branch, NASA-Langley Research Center, Hampton, Va., USA*

**ABSTRACT:** High residual stresses and minimal crosslinking in some modern high performance composites and adhesives may enhance susceptibility to environmental stress cracking in the presence of organic solvents. Cross-ply laminates of several polyimide-based composite materials are subjected to various solvents and liquids which might be encountered during aircraft service conditions. Extensive matrix microcracking is observed for several composite / liquid combinations. Unidirectional composite specimens subjected to such liquids for various exposure conditions also show strength reductions for certain combinations. Solvent resistance of a modern high performance polyimide adhesive is also determined. The most recent versions of the polyimide show improved resistance to environmental stress cracking.

### 1. INTRODUCTION

For several decades, certain polymers have been known to be susceptible to environmental stress cracking (ESC) or crazing in the presence of certain liquids or gases (Lustinger, A 1986). Common thermoplastics such as polyethylene and polycarbonate have been shown to crack or craze in liquids such as detergent solutions or simple organic solvents. This paper will review the susceptibility of several high performance polyimides to environmental stress cracking in the presence of organic solvents and other liquids which may be routinely used in fabricating and maintaining modern composite or adhesively bonded structures. A previous paper addressed the ESC susceptibility of several other composite systems (Parvatareddy et al. 1996).

Environmental stress cracking involves a synergism between an applied stress state and the presence of certain materials which lower the resistance of the polymer to cracking or crazing. The applied stresses can result from mechanical loading or can occur due to residual stresses which are present within a material due to the fabrication

process. For the case of composites and adhesive bonds, both of which involve bi-material systems, the residual stresses can be quite large. This is especially true for some of the modern high performance thermoplastic systems which have very high processing temperatures and glass transition temperatures. At the service temperature, the residual stress states can be very significant, and will be shown to be sufficient to cause considerable environmental stress cracking in the presence of certain liquids for some of the polymers considered.

Several mechanisms have been used to explain environmental stress cracking. Suggestions that the presence of a liquid may decrease the surface energy of the polymer, allowing the crack to grow more easily, seem to have given way to the idea that the solvent may locally diffuse into the highly stressed region at a defect or crack tip. The triaxial tensile stress field seems to facilitate this diffusion which then results in significant plasticization of the polymer. Molecular mobility is significantly increased, and the molecular chains are able to reptate free from their surrounding

material. The rapid cracking commonly observed suggests that these processes can occur quite quickly. Amorphous thermoplastics are especially susceptible to ESC because of the lack of crosslinks which could reduce the molecular pullout, and the lack of crystalline regions which serve as physical crosslinks. In some systems, the solubility parameter has proven to be a useful parameter in estimating the susceptibility of a polymer to a given liquid.

## 2. EXPERIMENTAL METHODS

### 2.1 Materials

The emphasis of the paper will be on a family of polyimide materials which have been developed in the Composite and Polymers Branch (CPB) at NASA Langley Research Center for use as matrix material for composites as well as adhesives for bonding metal and composite structural components. The material systems studied were IM7/LaRC™-IAX, IM7/LaRC™-IAX2, IM7/LaRC™-8515 (5.5%), and IM7/LaRC™-PETI-5. The LaRC™-IAX, LaRC™-IAX2, LaRC™-8515 (5.5%) and LaRC™-PETI-5 resins were provided by IMITEC of Schenectady, New York. The fibers were 12k unsized IM7 carbon fibers supplied by Hercules. Further details on these materials and test results reported herein may be found in (Clifton, 1996).

LaRC™-IAX and LaRC™-IAX2 are matrix resins based on their predecessor LaRC™-IA (Hou et al. 1995). Alterations in the LaRC™-IA polymers produced stiffer backbones, better mechanical properties and higher glass transition temperatures. LaRC™-8515 (5.5%) is prepared from 3,3',4,4'-biphenyltetracarboxylic dianhydride (BPDA) and a ratio of 85:15 of 3,4'-oxydianiline (3,4'-ODA) and 1,3-bis(3-aminophenoxy)benzene (APB) (Hou et al. 1995a). LaRC™-PETI-5 is based on BPDA and a 85/15 mole percent ratio of 3,4'-ODA/APB and has phenylethynyl endcappers (Jensen et al 1995). The phenylethynyl endcappers provide the material with more chemical and thermal stability. LaRC™-IAX, LaRC™-IAX2 and LaRC™-8515 are

thermoplastic polyimides; LaRC™-PETI-5 is a lightly-crosslinked thermoset polyimide. Laminates of each material system were prepared at NASA-Langley using cure procedures appropriate for each respective resin.

Exposure liquids chosen for the study included runway deicer, aircraft deicer, JP5 (jet fuel), diglyme (sometimes used as an adhesion promoter), MEK (a common paint stripper), acetone (a degreaser), and Hyjet IV (hydraulic fluid). In addition to these liquids which might be encountered during usage or maintenance of an aircraft, two laboratory solvents were also used: toluene and TCE 1,1,1.

The ESC resistance of an adhesive designated FM-5 has also been characterized. FM-5 is produced and supplied by Cytec Engineered Materials, Inc., Havre de Grace, Maryland. This adhesive is based on the LaRC PETI-5 material described above.

### 2.2 Cross-ply Coupons

Small coupons of cross-ply laminates were fabricated to be submerged in solvents or exposed to solvent vapors for small periods of time. In many cases, extensive matrix cracking was seen within the layers. Special [0°/90°/0°/90°/0°/90°] laminates were selected because they provided 1, 2, and 4-ply groupings of 90° plies. Although the residual stresses were nominally the same within each of these ply groupings, the available strain energy release rate for matrix cracking is linearly proportional to the thickness of the 90° group (Nairn 1989), thus providing a range of available energy release rates within a small coupon. No mechanical loads were applied to these specimens; the effects of the residual stresses were found to be sufficient to cause cracking in many of these polymer/liquid combinations.

The specimens were immersed in the solvents for a total of 96 hours. During the 96 hours, the specimens were removed from the solvents at specific time intervals and were allowed to dry briefly at room temperature and humidity. Upon drying, the polished edges of the specimens were examined for solvent induced

microcracking under an optical microscope. The crack densities were recorded for each of the three different transverse ply groups at each time interval. After recording the crack densities, the specimens were placed back into the solvents. Figure 1 illustrates the matrix cracking which can typically result from brief exposure to a solvent.

[0<sub>2</sub>/90<sub>6</sub>] panels were also fabricated to measure thermal expansion properties. Changes in curvature of these unsymmetric laminates were monitored as the panels were heated in order to determine the stress-free temperature and coefficient of thermal expansion for each material system. The properties were used in conjunction with classical lamination theory to estimate the magnitude of the residual stresses. Predicted residual stresses in the transverse direction at room temperature ranged from +33 to +50 MPa, depending on the resin system.

In attempting to characterize the damage states which resulted in these composite coupons, standard dye penetrant solutions were employed. X-radiographs of dye penetrant conditioned specimens exhibited extensive damage which appeared to be greater than the damage seen in specimens which had not been exposed to the dye penetrant. Subsequent testing showed that the dye penetrant alone is sufficient to cause extensive matrix cracking in some of the composite systems studied. Figure 2 illustrates "through-the-width" cracks seen in a typical x-radiograph. Details of this work may be found in (Furrow et al., in press)

### 2.3 Transverse Flex of Unidirectional Specimens

Transverse flexure tests were conducted on unidirectional [90°] specimens using three-point bending in the presence of solvents. Five solvent exposures were investigated: Solvent Drop, where 2-4 drops of solvent were applied to the center of the specimen just prior to loading to failure; Solvent Vapor, whereby specimens were tested directly above a reservoir of solvent; Submerged Solvent, in which specimens were submerged in solvent and quickly tested while submerged; Solvent Soak - Wet, where specimens were removed from a 14 day soak in solvent and tested quickly; and Solvent Soak - Dry, where specimens

were soaked in solvent for 14 days, allowed to dry under ambient conditions for 14 days, and then tested. The specimens were supported at a distance of 40 mm and tested at a rate of 1 mm / min.

### 2.4 Adhesive Bond Wedge Tests

In addition to the studies on the polyimide-based composites, the effects of several organic solvents on adhesive bonds have also been studied. Ti-6Al-4V adherends having a thickness of 3.18 mm were prepared using a chromic acid anodization (CAA) surface pretreatment. Glass cloth scrim-supported films of FM-5 adhesive were used to bond the titanium adherends during a sequenced processing procedure. 2 mm thick wedges were inserted into the bonded samples using a vice. Groups of specimens were then exposed to several liquids at room temperature (including water), and to boiling water. Debond lengths were periodically measured, and rates of debonding were estimated. Using a simple relationship for determining the available strain energy release rate for the geometry and adherend stiffness, debond rates as a function of available strain energy release rates could be determined.

$$G = \frac{9\Delta^2 EI}{4ba^4}$$

where  $\Delta$  is the wedge thickness, E is the Young's modulus of the adherends, I is the second moment of area of the adherend, b is the specimen width, and a is the debond length.

## 3. RESULTS AND DISCUSSION

### 3.1 ESC of Cross-ply Laminates

Monitoring crack density within the single, double, and quadruple ply groupings proved to be tedious and somewhat subjective. In many cases, optical microscopy of the polished edge revealed cracks which spanned the entire group of 90° plies. These cracks opened noticeably, and were assumed to extend throughout the width of the coupon. Attempts to verify that these cracks

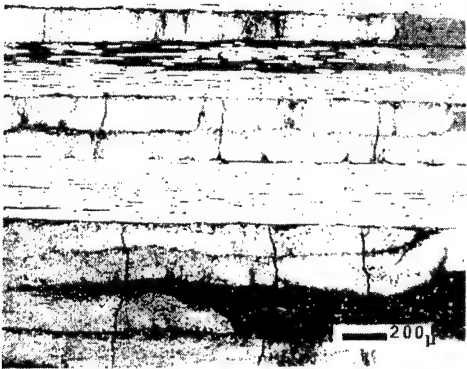


Figure 1. Typical environmental stress cracking patterns in a LaRC™-IAX2 laminate showing single, double, and quadruple 90° ply groupings.

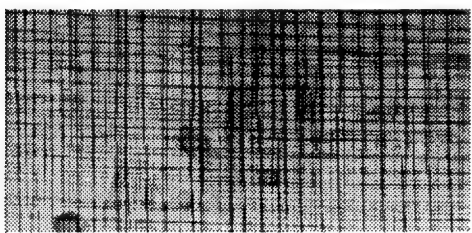


Figure 2. Extensive matrix cracking in [0°/90°/0°/90°/0°/90°]s, LaRC™-IAX coupon following 18 hours in dye penetrant.

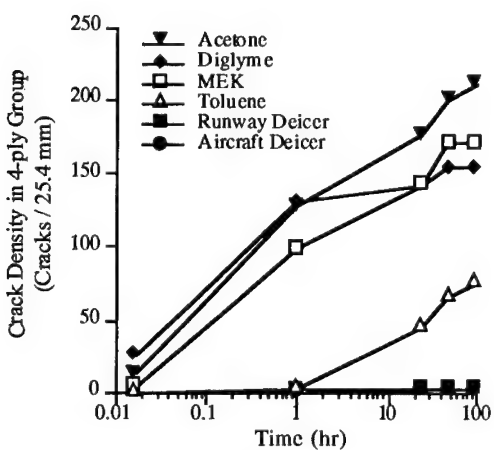


Figure 3. Time dependent development of matrix cracking in 4-ply grouping in LaRC-IAX specimens exposed to solvent soak.

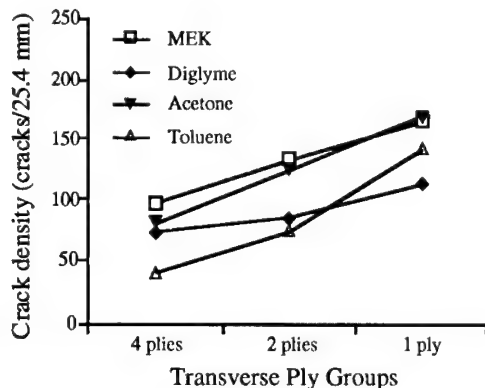


Figure 4. Crack density in LaRC-8515 laminate following a 96 hour immersion period.

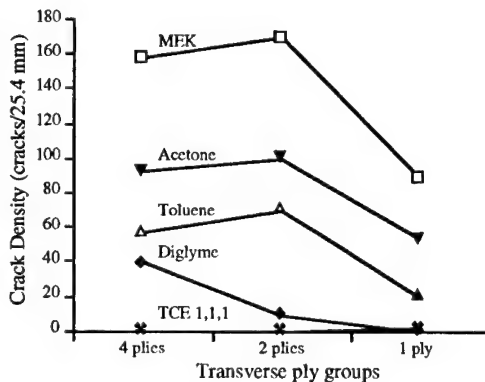


Figure 5. Crack density in LaRC-PETI-5 laminate following a 96 hour immersion period.

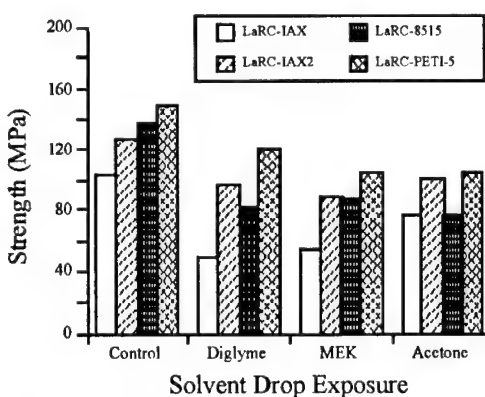


Figure 6. Strength retention of transverse flex specimens subjected to solvent drop exposure: diglyme, MEK, and acetone.

extended across the width using dye penetrant and x-radiography were unsuccessful for reasons cited earlier. In some cases, the cracks did not span the entire ply group, and the crack did not open significantly. These flaws may have been limited to the surface of the specimen. In many cases, flaws appeared to initiate from observable defects on the surface. In spite of difficulties in monitoring these solvent-induced cracks, some useful insights were gained into the susceptibility of matrix / liquid combinations. Because the residual stresses present are similar to any practical laminate, the microcracking observed is indicative of how an actual laminate might respond to these liquids.

The matrix cracks such as those shown in Figure 1 may develop in a time-dependent fashion as illustrated in Figure 3. The saturation spacing of the matrix cracks is predicted to be proportional to the thickness of the ply grouping. As seen in Figure 4 the LaRC-8515 showed a substantial increase in crack density for the smaller ply groupings for several solvents, consistent with expectations for saturation cracking. Figure 5 illustrates that the saturation spacing is not reached on the smaller ply groupings in LaRC-PETI-5, suggesting that the available strain energy release rate is not sufficient to cause the saturation damage state. Based on the degree of cracking in the various groupings, one may estimate the critical strain energy release rate in the presence of these liquids. Further results on this can be found in (Clifton, 1996, Dillard et al., in prep).

### 3.2 Flexure Strength Reduction

Significant reductions in the transverse strength were seen for some of the polymer / liquid / exposure method combinations. For MEK, acetone, and toluene solvent drop exposure, Figure 6 illustrates that all four of the composite materials exhibit a reduced strength. Strength reductions are not as pronounced when exposed to solvent vapor as shown in Figure 7. As might be expected, solvent soak produces the greatest reductions (see Figure 8). Even though the exposure to solvent is brief, the simultaneous presence of solvent and stress leads to failures at lower loads. Following a

14 day soak in the respective solvents, no significant strength reduction is observed in Figure 9 except for the diglyme exposure. Diglyme has a very low volatility compared to the other solvents studied, and does not evaporate as quickly as the other solvents. Figure 10 illustrates that strength retention is excellent even for the diglyme exposed specimens if allowed to dry 14 days prior to testing. None of the solvents appear to cause any lasting damage provided they have evaporated prior to the introduction of significant stresses.

### 3.3 Debond Kinetics of Wedge Specimens

Debond growth as a function of the applied strain energy release rate is plotted in Figure 11 for the titanium / FM-5 wedge specimens. Data points represent an average of five specimens. Failures for samples appeared to be occurring near the glass scrim interface as opposed to the titanium interface. It is interesting to note that for this adhesive, the presence of solvents resulted in debond rates which were intermediate between the rates of debonding seen in room temperature and boiling water, suggesting a fairly weak sensitivity to solvents for this system. Again, the FM-5 is based in part on the LaRC PETI-5 polyimide, which also showed the best ESC resistance in the composite tests. Further details on this work can be found in (Parvatareddy, 1997, & Parvatareddy, in press).

### 3.4 Expected Significance

In spite of the rather extensive matrix cracking seen in some of the cross-ply laminates, it is not clear how significantly the structural properties would be affected by such damage states. Matrix cracking is often encountered in polymer matrix composites, and is not believed to substantially alter static strengths. On the other hand, such matrix cracks can serve as initiation sites from which delamination and other more detrimental damage patterns can develop. Further studies should be done to examine how residual strength and life of practical laminates are affected by solvent-induced matrix cracks. Ultimately, the polymer synthesists should be aware of the

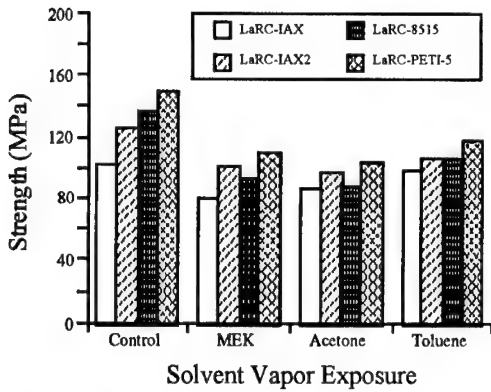


Figure 7. Strength retention of transverse flex specimens subjected to solvent vapor exposure: MEK, acetone, and toluene.

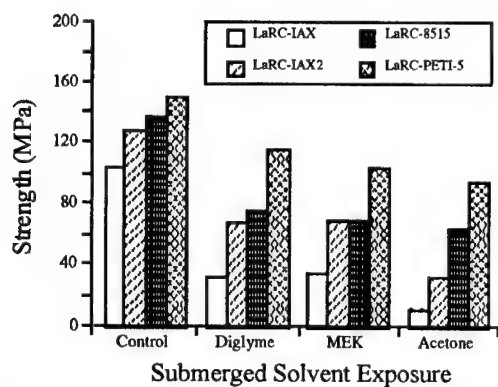


Figure 8. Strength retention of transverse flex specimens subjected to submerged solvent exposure: diglyme, MEK, and acetone.

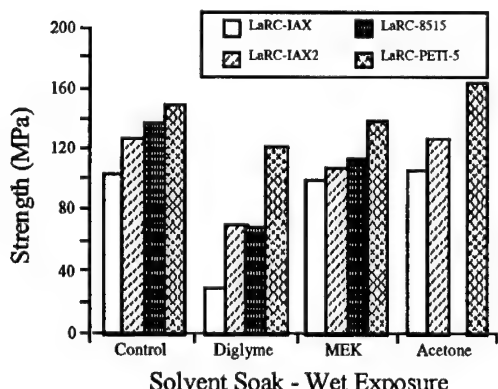


Figure 9. Strength retention of transverse flex specimens subjected to solvent soak - wet exposure: diglyme, MEK, and acetone.

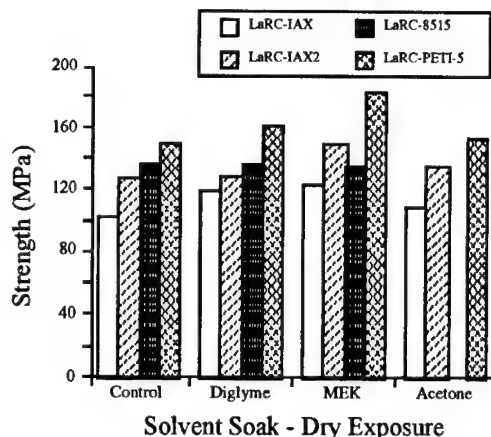


Figure 10. Strength retention of transverse flex specimens subjected to solvent soak - dry exposure: diglyme, MEK, and acetone.

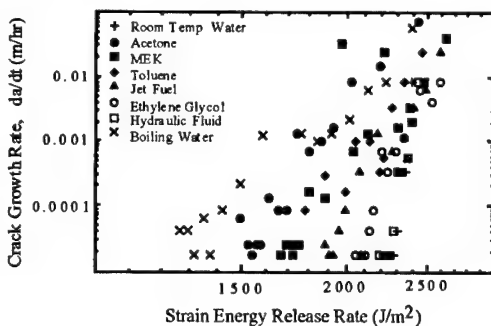


Figure 11. Debond propagation rates in wedge specimens subjected to various liquid environments.

potential for such damage, and minimize its likelihood. As can be seen from the material series considered, the PETI-5 system appears to represent an improvement over some of the prior systems in resistance to ESC.

The flexure tests clearly reveal that some polymer / solvent combinations have significant strength losses when solvent (or vapor) comes in contact with stressed material. Although all of the LaRC-IAX showed susceptibility to matrix cracking in the presence of runway deicer and Hyjet IV, both 8515 and PETI-5 showed good resistance to runway deicer, aircraft deicer, JP-5, and Hyjet IV at stress levels induced by residual stresses alone. It is encouraging that these latter polymers are resistant to fluids commonly used under aircraft service conditions. Organic liquids

used in aircraft maintenance, however, produced matrix cracking and noticeable strength reductions.

#### 4. SUMMARY AND CONCLUSIONS

Concerns are raised over the resistance of some high performance polymeric composites and adhesives to even brief exposure to a variety of liquids which may be commonly used around high performance structures. Thermoplastic systems appear to be particularly susceptible because of the high residual stress states present and the lack of crosslinking. Of the materials tested, the PETI-5 system with light crosslinking appears to be more resistant to environmental stress cracking than the related thermoplastic systems. Industries making use of these materials should be aware of the possible damage states which can develop within these material systems. Even a common dye penetrant was found to produce extensive matrix cracking in some of the materials, raising cautions about its use and interpretation.

A 20-ply cross-ply laminate containing 1, 2, and 4-ply groupings of 90° plies was introduced for evaluating ESC resistance in composite materials. The residual stresses induced are similar to those encountered in practical laminates, and afford a self-loading specimen which can be easily subjected to various environments. Observations of matrix cracks, evident along the edge of the specimen, permit qualitative and even quantitative estimates of ESC susceptibility.

Unidirectional specimens tested under three-point bend conditions showed reduced transverse flexure strength for some polymer / liquid combinations. For most susceptible systems, testing specimens submerged in solvent produced the greatest strength decrease. A two week soak in solvents showed no significant effect provided the solvent was allowed to evaporate prior to testing. Clearly ESC of these material systems requires the simultaneous application of stress and solvent. In real composite laminates and bonded joints, however, ever-present residual stresses may be sufficient to induce ESC upon even brief exposure to liquids used in servicing aircraft, etc. in susceptible systems.

#### ACKNOWLEDGMENTS

The VT authors are grateful to NASA-Langley, Boeing Commercial Airplane Group, and the National Science Foundation Science and Technology Center: High Performance Polymeric Adhesives and Composites, contract DMR 9120004 for financial support of this work. We would also like to acknowledge helpful discussions with Dr. Richard Mayhew of Cytec Engineered Materials, Inc., Paul Hergenrother of NASA-Langley, and Professors John Dillard and Ronald Kander of Virginia Tech.

#### REFERENCES

- Clifton, A. P. 1996, "Solvent Induced Microcracking in High Performance Polymeric Composites", M. S. thesis, Virginia Tech, Blacksburg, Virginia.
- Dillard, D. A., A. P. Clifton Furrow, T. L. St. Clair, J. A. Hinkley, "Environmental Stress Cracking in Polyimide Composites", *J. Composites*, (in prep.)
- Furrow, A. P. C., D. A. Dillard, T. L. St. Clair, J. A. Hinkley, "Dye Penetrant Induced Microcracking in High Performance Thermoplastic Polyimide Composites", *J. Composites*, (in press).
- Hou, T H, Johnson, N J, and St. Clair, T L 1995, "IM7/LaRC-IA Polyimide Composites", *High Performance Polymers*, 7, , 105-124.
- Hou, T. H., Wilkinson, S. P., and Jensen, B. J. 1995a, "Processing and Properties of IM7/LaRC™-8515 Composites," *Polyimides: Synthesis, Characterization, and Applications*, edited by C. Feger, Plenum Press, New York.
- Jensen, B J, Bryant, R G, Smith, J G, Hergenrother, P M 1995, "Adhesive Properties of Phenylethynyl-Terminate Imide Oligomers", *J Adhesion*, 54, 1-10.
- Lustinger, A 1986, "Environmental Stress Cracking: the Phenomenon and its Utility", in *Failure of Plastics*, W. Brostow and R D Cornliussen, Eds., Hanser Publishers, Munich
- Nairn, J A 1989, "The Strain Energy Release Rate of Composite Microcracking: A Variational Approach", *J. Composite Materials*, 23, 1106-1129.

- 
- Parvatareddy, H., C. Heithoff, A. P. Clifton, D. A. Dillard, and R. G. Kander 1996, "Environmental Stress Cracking and Solvent Effects in High Performance Polymeric Composites", *Composite Materials: Testing and Design (Twelve Volume)*, ASTM STP 1274, R. B. Deo & C. R. Saff (Eds.), American Society for Testing and Materials, 56-68.
- Parvatareddy, H. 1997, "Durability of Polyimide Adhesives and Their Bonded Joints for High Temperature Applications", PhD dissertation, Virginia Tech, Blacksburg, VA.
- Parvatareddy, H., J. G. Dillard, D. A. Dillard, in press, "Environmental Aging of Ti-6Al-4V / FM-5 Adhesive Bonded System: Implications of Physical and Chemical Aging on Durability", *J. Adhesion Sci. and Technol.*

## Affordable processing of composite structures for the civilian infrastructure

J.L.Kardos, B.Khomami, P.Ramachandran, B.Yang & R.Shepard

*Department of Chemical Engineering and Materials Research Laboratory, Washington University, St. Louis, Mo., USA*

**ABSTRACT:** The success of transferring high performance composite materials technology from defense-related to civilian applications depends primarily on making material and manufacturing costs affordable. Carbon fibers are highly desirable for their mechanical properties and corrosion resistance, but their per-pound cost is currently too high. Structural laminates in aerospace use are amazingly strong, stiff, and fatigue resistant, but their manufacturing cost, even with state-of-the art automation of layup and autoclave processing, is too high for civilian structural applications, even when total life-cycle cost is considered. This presentation will discuss important factors in reducing carbon fiber production costs, as well as a new injected pultrusion process for continuously producing structural shapes at much reduced costs.

### 1 INTRODUCTION

The success of transferring high performance composite materials technology from defense-related to civilian applications depends primarily on lowering material and manufacturing costs. Carbon fibers are highly desirable for their mechanical properties, lightweight, and corrosion resistance, but their per-pound cost is currently too high. Structural laminates utilizing carbon fibers are amazingly light, strong, stiff, and fatigue resistant, but their manufacturing cost, even with state-of-the-art automation lay-up and autoclave processing, is too high for civilian structural applications, even when total life-cycle cost is considered. In what follows we describe full simulation models for the oxidation reactors in a continuous carbon fiber process and for a new injected pultrusion process pioneered by the Hexcel, Inc. These models involve the process equipment geometry and operating parameters as boundary conditions for solving the differential equation sets describing the basic materials physics. They can indeed be used for process design, optimization, and eventually for model-based, on-line control strategies.

### 2 CARBON FIBER PROCESS

The manufacture of carbon fibers from polyacrylonitrile-based (PAN) precursor involves several steps and chemical reactions (Fig. 1). The first reaction is thermooxidative stabilization of the PAN fibers, after which the fibers can be carbonized without melting. This complex reaction is one of the most expensive and time-consuming steps in the manufacture of carbon fibers. Because the stabilization reactions are exothermic, control of the temperature within the tow is critical to the stabilization process. Currently, process conditions are developed through trial and error for each specific precursor. Thus, optimization of the stabilization process requires a significant amount of testing that must be repeated if the precursor is changed. This increases the cost of the process and limits the ability to take advantage quickly of new, and possibly less expensive, precursor fibers.

A new simulation model has been developed for the oxidation process. Based on the shrinking core model for gas-solid reactions in porous catalyst reactors (1), the model can predict temperature and its

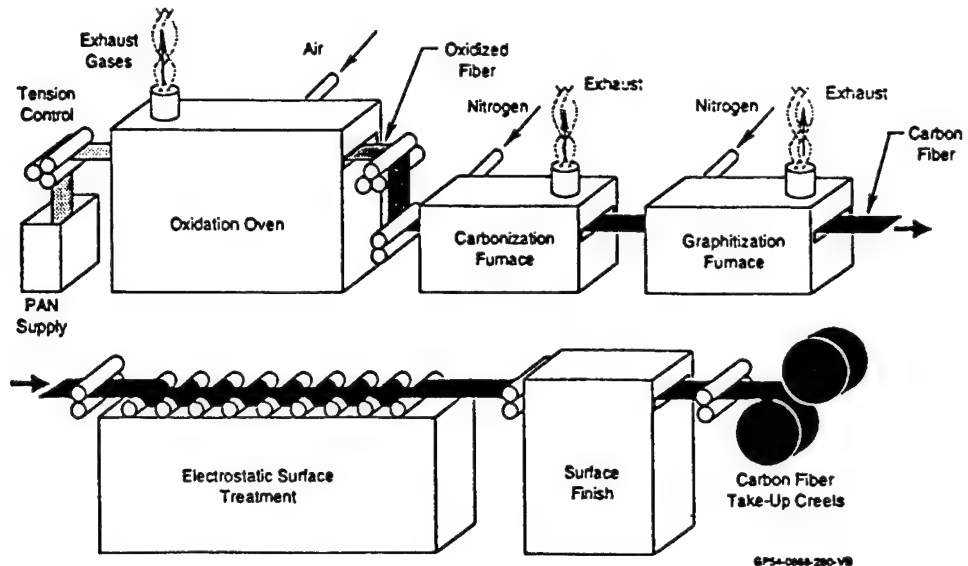


**Figure 1 - Schematic of Commercial Continuous Carbonization Line**

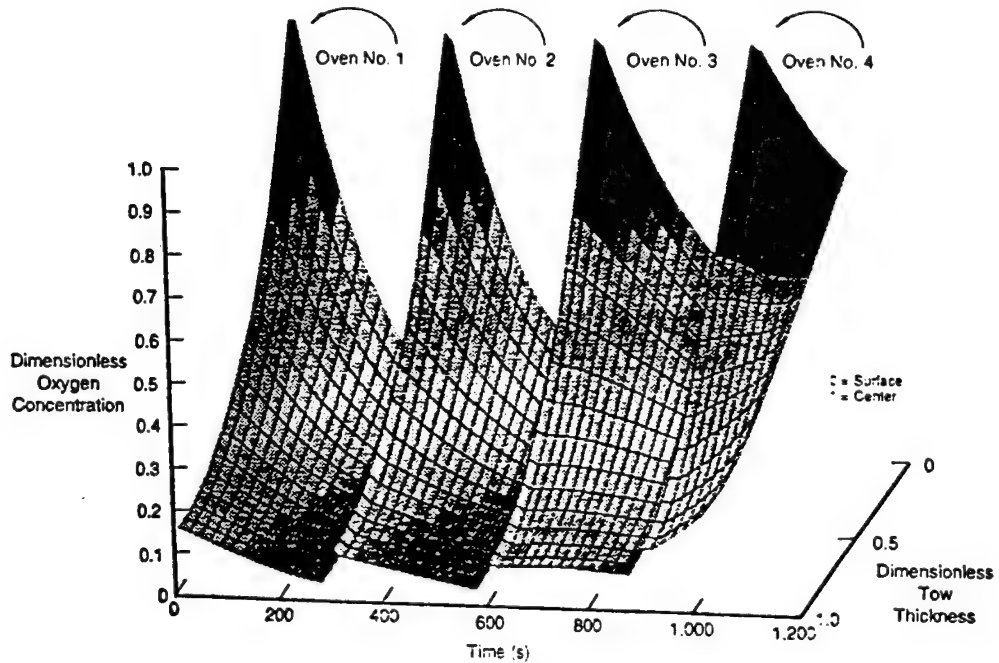


**Figure 2 - Predicted Oxygen Concentration Within Tow as a Function of Time Within Four Oxidation Reactors in Series**

gradient, oxygen concentration and its gradient, the fraction of fiber radius reacted, and the fiber density, all as a function of location in the tow, air flow rate, tow tension, residence time in the reactor, reactor size, tow thickness and geometry, physical properties of the tow, and the reaction kinetics of the PAN precursor.

Figure 2 shows the oxygen concentration at a low air flow rate as a function of location in the tow thickness and residence time (or location) in each of the four oxidation reactors in a typical commercial carbon fiber process. The oxygen concentration is lowest at the center of the tow due to a high Thiele modulus (ratio of kinetic to diffusion parameters) and at the reactor exits after the reaction has depleted the oxygen supply. Oxygen is replenished at each reactor entrance. The model can predict the air rate at which oxygen starvation takes place.

The PAN precursor reaction kinetics were measured using both isothermal and constant heating rates on a differential scanning calorimeter (DSC). From the reaction rate and conversion data, the reaction rate constant and activation energy were both determined as a function of temperature. From the conversion data for single fibers and an isothermal mass balance, the effective oxygen diffusivity was also calculated. Table 1 (top) shows the effect of fiber tension on the kinetic parameters of a typical PAN precursor used by industry. The fibers were held under tension in a Rheometrics Mechanical Spectrometer and reacted using the temperature profiles found in commercial reactors. The effect of tension is significant.

Table 1 also shows the predicted and actual conversions for reactions run under commercial reactor temperature profiles with and without commercial tension values. The agreement is within that necessary to assure high quality fiber during commercial production.

It also turns out that the DSC-RMS analysis can detect "bad" lots of PAN precursor. When heated in the RMS under proper tension, the tow "fuzzes" and destabilizes much like it does in the commercial line. The rate constant and activation energy also differ considerably when measured in the DSC.

The simulation model can be used with currently operating lines to specify the proper values of process parameters needed to produce an oxidized stabilized fiber with 50-60% conversion for optimal mechanical properties. It can also be used to optimize the reactor design of new continuous fiber lines.

### 3 INJECTED PULTRUSION PROCESS

Continuous Resin Transfer Molding (CRTM™) is a manufacturing process which consists of an injection chamber where the resin impregnates the fiber preform as it is fed through a pultrusion-like die. The CRTM™ process is non-isothermal and the analytical modeling of such processes is precluded by the temperature dependent viscosity, rate of cure, energy convection, and arbitrary shape of the cavity, along with non-Newtonian behavior of the fluid. Although finite difference and boundary element methods can be adopted to simulate such flow, the finite element/control volume method offers the most flexibility and computational efficiency in terms of dealing with arbitrary cavity shapes as well as variable physical properties.

The current version of the code has the flexibility of generating an arbitrary computational domain using triangular and quadrilateral elements that may be open (i.e., partly filled) or closed (i.e. filled) to the flow. The current flow model is two-dimensional and is based on Darcy's law with the capability of handling variable permeability and thickness for arbitrary alignment of the fibers. It can also couple the energy calculation with temperature-dependent viscosity and the rate of cure under specified temperature and/or convective boundary conditions. Two or more different conducting materials may enclose the mold that is subjected to the inlet flow boundary conditions of a specified pressure and/or a specified flow rate. If required, the energy calculation allows heat conduction to occur in the third dimension (mold thickness direction). The computational efficiency of this model allows its use in complex geometries frequently encountered in industrial operations.

The actual process die consists of an approximately isothermal entry region where the resin is injected, followed by a longer non-isothermal region where the viscosity, degree of cure, and temperature are all changing with position and time.

A schematic of the die geometry and finite element mesh is shown in Figure 3. The non-isothermal section is shown in three dimensions. The solution is made 3-dimensional by solving the energy balance and flow equations for a 2-dimensional slab in the y-x plane and then marching this solution in the z direction for the same instant in time. The actual isothermal entry region is not rectangular, but we will illustrate the model capability by assuming a rectangular cross section. The actual geometry is

**TABLE 1: Predicted and Actual Conversion of Rheometer-Reacted PAN**

No Tensile Force $D_{eA} = 3.5e - 12 \text{ m}^2/\text{s}$ $k_o = 3.76e4$ $E = 9.99e4$	Tensile Force (3.45 MPa) $D_{eA} = 3.5e - 12 \text{ m}^2/\text{s}$ $k_o = 1.20e8$ $E = 1.34e5$	
Experimental Run	Actual Conversion	Predicted Conversion
657.5 sec@206.6°C	51.4	45.7
657.5 sec@211.6°C		
657.5 sec@216.5°C		
657.5 sec@221.6°C		
Tensile Force (3.45 MPa)		
Ramp 0.5°C/min 212.2°C to 222.2°C	31.2	28.3
Tensile Force (3.45 MPa)		
Ramp 0.5°C/min 206.6°C to 216.6°C	24.9	20.6
Tensile Force (3.45 MPa)		

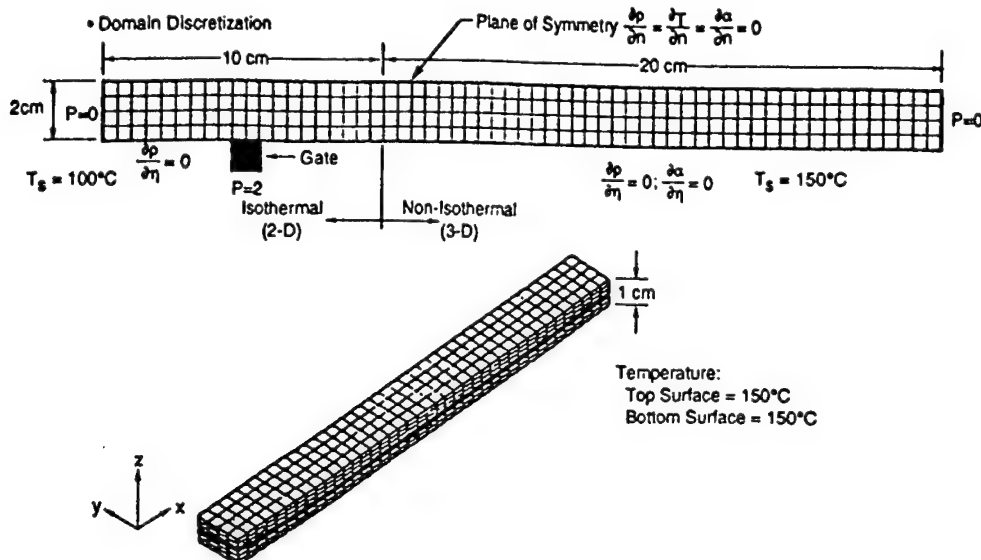


**Figure 3 - 3-D Finite Element Model for CRTM™ Process Showing Boundary Conditions**

currently a proprietary design variable which is a geometric boundary condition accounted for in the finite element meshing procedure. For the results shown here, the temperature of the isothermal region was held at 100°C. Resin is fed at 2 bars gage pressure through two gates at the center of the xz walls of the isothermal section of the die. The top portion of Figure 3 shows only half of the xy plane of the die; the boundary conditions at the plane of symmetry are

indicated. In the non-isothermal section, the top and bottom (xy) walls of the die are kept at 150°C, while the side walls (xz) are insulated. For the boundary conditions shown,  $n$  is the unit normal to the flow direction.

For the 3-dimensional calculation illustration, we have chosen the following input parameter values:

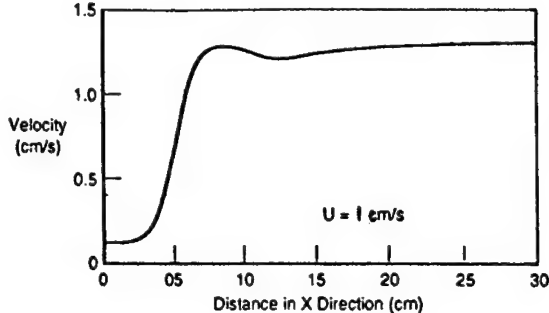


**Figure 4 - Resin Velocity Profile on Symmetric Plane of Figure 3**

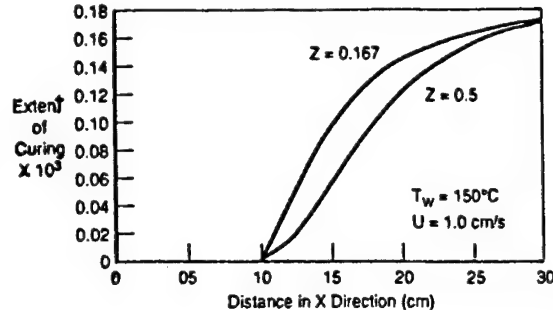


**Figure 5 - Profile of the Extent of Cure on the Symmetric Plane of Figure 3**

$$\text{Thermal Diffusivity: } \frac{k}{pC_p} = 1.9 \times 10^{-1} \text{ cm}^2/\text{s}$$

$$\text{Heat of Reaction: } \Delta H_R = 473.6 \text{ J/g}$$

$$\text{Permeabilities: } k_{xx} = k_{yy} = 1.0 \times 10^{-6} \text{ cm}^2$$

$$k_{xy} = 0$$

$$\text{Fiber Volume Fraction: } V_f = 0.5$$

The viscosity and cure kinetics data are for Hercules 3501-6 resin.

The velocity profile on the same symmetric plane as the above figure is shown in Figure 4 for a fiber pull of one cm./sec. Note that for the input parameters employed, the model shows a finite resin velocity at both the die entrance and exit, meaning that the resin has not yet gelled and is squirting out both ends. This of course is an unallowable condition in practice, and illustrates the utility of the model in defining improper die designs and operating conditions.

Figure 5 shows the extent of cure in the x direction on the plane of symmetry as a function of distance along the thickness direction. In agreement with the prior figure, the extent of cure is lower in the cooler regions. The very low extent of cure is the reason why the resin has a finite velocity at the exit and entrance and the resin is squirting out both ends of the die, a condition of course to be avoided.

We are in the process of upgrading the model to full 3-D capability. It will then be verified against the full-scale commercial process at Hexcel. We hope to eventually link the model to a non-linear, neural

network-based control algorithm to provide a model-based, on-line control strategy.

#### 4 REFERENCES

1. J. Szekely, J.W. Evans, and H.Y. Sohn, Gas-Solid Reactions, Academic Press, (1976)

#### 5 ACKNOWLEDGEMENT

This paper is based on work supported by the Advanced Research Projects Agency under ARPA order No. 9284, Affordable Polymeric Composite Materials Synthesis and Processing Program.

## Improved adhesive performance through surface treatment

M.A.Gaynes, J.M.Spalik & H.Shaukatullah

*Microelectronics Division, IBM Corporation, Endicott, N.Y., USA*

**ABSTRACT:** A surface mount tape ball grid array package uses flexible polyimide film that has been circuitized on both sides. To facilitate processing and handling, a picture frame metal stiffener is bonded to the film. The opening in the stiffener defines the location wherein an integrated chip is placed and interconnected to the flexible circuit with thermo-compression bonds or flip-chip solder balls. With the chip backside exposed, heat transfer is enhanced by adhesively bonding a metal heat spreader. This heat spreader is also bonded to the stiffener and appears as a cover plate on the package. The adhesive bond to the cover plate, above the chip, degraded during the high heat exposure of solder reflow and temperature stress testing. Adhesion was improved significantly by oxidizing and hydrating the nickel plated surface of the cover plate. A silane coupler was also applied to the cover plate and further improved adhesion reliability.

### 1 INTRODUCTION

Three major challenges in microelectronic packaging are increased function density, improved electrical performance and increased heat dissipation. Polymer materials must interface and join materials that have a mismatch in coefficients of thermal expansion as much as 20 ppm/ $^{\circ}$ C in the case of silicon to aluminum (Gaynes & Shaukatullah 1993).

In addition, these materials must maintain reliable performance through a life of extreme and varied environmental conditions.

A new semiconductor chip package, Tape Ball Grid Array (TBGA), provides advances in all three areas. The TBGA package (Figure 1) consists of a flexible polyimide tape with copper circuitry on both sides. The flex circuit is attached to a nickel plated copper stiffener using an electrically

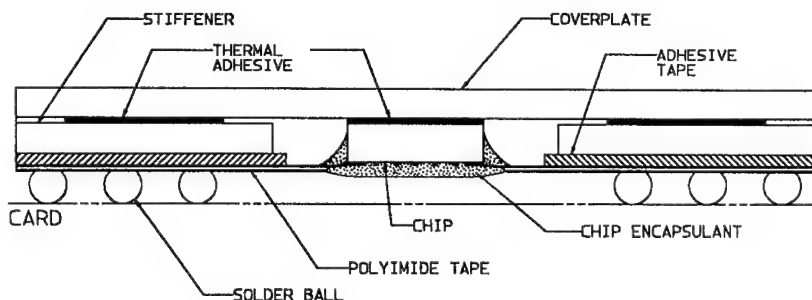


Figure 1. Cross-section schematic of the Tape Ball Grid Array (TBGA) package.

insulating adhesive. An integrated circuit chip is bonded to one side of the tape using thermo-compression bonding or flip-chip solder balls, both of which provide improved electrical performance compared to wire bond interconnection. The other side of the tape has an array of solder balls for soldering the package to the card. Due to the metal stiffener and exposed back side of the chip, the TBGA package lends itself well to thermal enhancement. A metal cover plate can be bonded directly to the back side of the chip and stiffener to improve the thermal performance. For further thermal enhancement, heat sinks can be attached with thermally conductive adhesive to the cover plate.

A flexible thermally conductive epoxy adhesive was selected to bond the cover plate to the chip and the stiffener. The low Young's modulus of 69 MPa (10,000 psi) accommodated the thermal mismatch between copper and silicon during thermal cycling. As part of new package evaluation, the TBGA package was tested to establish thermal performance. Details of the thermal test hardware and procedure have been published (Shaukatullah et al. 1996). Initial testing was done using six 25 mm TBGA packages with 240 I/O connections and 9.6 mm nominal size test chip. During thermal tests, the internal thermal resistance,  $R_{int}$  (chip-to-cover plate thermal resistance), defined as

$$R_{int} = \frac{T_{chip} - T_{case}}{P} \quad (1)$$

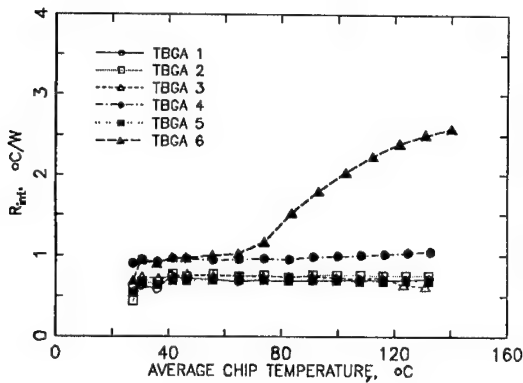


Figure 2. Chip-to-case thermal resistance of 25 mm, 240 I/O TBGA packages with 9.6 mm nominal size chip as a function of chip temperature in natural convection.

Here,  $T_{chip}$  is the average temperature of the chip,  $T_{case}$  is temperature of the cover plate and  $P$  is the power dissipation in the chip. The  $R_{int}$  is an indicator of the thermal resistance of the adhesive bond between the chip and the cover plate. During testing, it was observed that the  $R_{int}$  of one of the packages (#6) increased as the package temperature (power) was increased. This is shown in Figure 2. The other five packages did not show this behavior and their thermal resistance remained almost constant with temperature.

To understand the increase in thermal resistance and check for adhesive coverage on the chip, the packages were scanned using C-mode scanning acoustic microscopy (C-SAM). The C-SAM image of package #6 whose  $R_{int}$  increased with temperature is shown in Figure 3. The dark area in the center shows complete delamination between the adhesive and the cover plate over the chip. The light colored areas indicate good adhesion between the cover plate and adhesive. The delamination observed in the C-SAM image was verified by peeling off the cover plate in one of the packages. Areas where the adhesive peeled away cleanly from the cover plate matched the delaminated areas that were observed in the C-SAM image. The other five TBGA packages also showed varying amount of delamination between the cover plate and the adhesive, but not as complete as in package #6. Difficulty in bonding resulted because of the low surface energy of the nickel plating on the copper in conjunction with thermal degradation of the adhesive. Adhesive

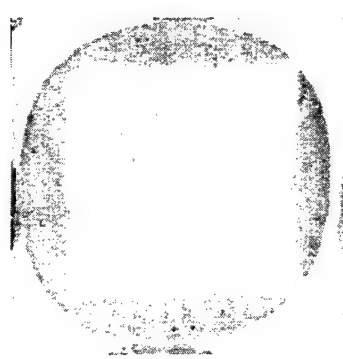


Figure 3. C-SAM image of TBGA package #6 showing delamination between the cover plate and adhesive.

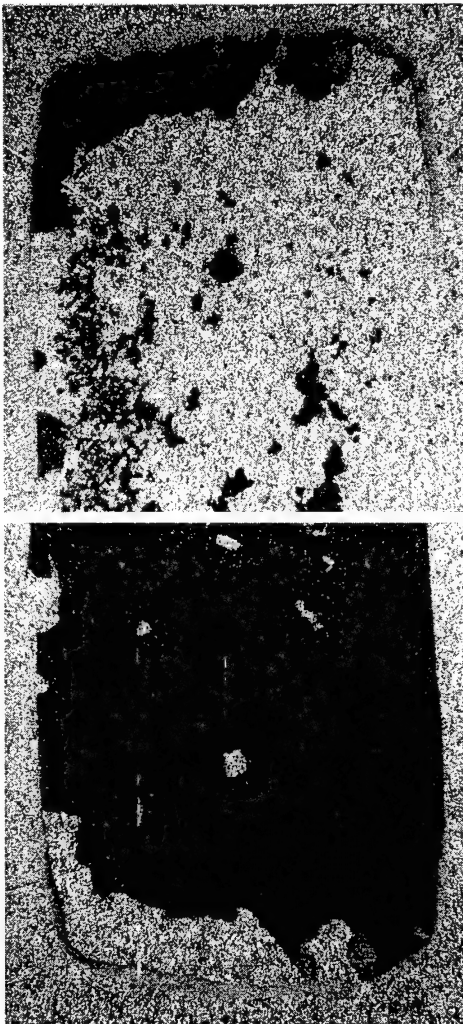


Figure 4. Adhesive fracture mode in peel of two bonded cover plates reveals poor adhesion.

fracture modes were observed at the nickel surface of a test coupon (Figure 4). This weak interface provided a fast diffusion path for oxygen ingress at high temperature. The adhesive was found to oxidize when exposed to solder reflow (220 °C) or 150 °C environmental stress. Process enhancements were used to improve the epoxy adhesion. These included controlled oxidation of the nickel surface and application of a silane coupler. The treatments

did not completely eliminate adhesive degradation, but did significantly improve adhesion durability.

## 2 ADHESION PROCESS IMPROVEMENT

Nickel and nickel coating are highly desirable because of their appearance, resistance to corrosion and absence of particle release. Because of these properties, they are well suited to many applications in the computer industry regarding chip carriers and heat sinks, especially where particle release may be extremely detrimental. The TBGA package is one such application where the stiffener and cover plate are nickel plated. In such applications, it is usually necessary to utilize a thermally conductive adhesive that will perform without bond degradation during the mechanical and thermal stresses through which the package is subjected during assembly and subsequent usage. Because of serious adhesion problems in attempting to bond chips to electroless nickel or electrolytic nickel platings with brighteners, it became necessary to find a way to effect a good bond without visually altering the surface or adding ionic contamination (Arndt et al. 1996). It had been noted that increased water wettability correlated with better bonding, and cleaning methods giving better wettability generally showed some improvement, but were not consistently adequate. Several cleaning procedures were investigated, including 10%-100% isopropyl and various detergents, but none of these could consistently give a completely wettable surface. Some attempts at chemical etching using HNO<sub>3</sub> and other acid solutions appeared to be inappropriate because of significant visual alteration, difficulty in controlling the remaining nickel thickness and increased potential for particle release.

Knowing that a highly wettable surface probably consisted of a clean, hydrated oxide surface an approach to achieving good wettability seemed to consist of a way of simultaneously cleaning, oxidizing and hydrating the nickel without otherwise substantially altering the surface. To this effect an ideal treatment would utilize only H<sub>2</sub>O<sub>2</sub>, preferably 30%, since no extraneous salts would be formed, as in acid etching, which might be an additional corrosion concern. However, at ambient temperature without the addition of an acid or base, 30% H<sub>2</sub>O<sub>2</sub> reacts very slowly on nickel and no improvement would be observed.

One very useful method of determining the potential for improved nickel-epoxy adhesive bonding is by observing the water wettability of the nickel surface. Wetting angles are typically used, but a water break test according to ASTM B-322-68 can be used for a real-time evaluation of the effectiveness of treatment. Parts are immersed in deionized water and withdrawn. Wettability or water break is assessed by observing the uniformity of wetting and whether beading exists. Observation of the water break on the nickel surface quickly showed that at elevated temperatures, 30% H<sub>2</sub>O<sub>2</sub> became very effective at increasing the surface wettability to 100%. No water beading was observed and water did not pull away from the edges. Above 40 °C, the auto catalytic decomposition of H<sub>2</sub>O<sub>2</sub> to H<sub>2</sub>O and O<sub>2</sub> begins to provide increased wettability with the resultant improved epoxy adhesive bond.

### 3 RESULTS AND DISCUSSION

Typically, adhesion improvement is assessed by measuring the fracture strength of the bonded members. An alternative is to observe fracture modes and changes in fracture modes. Table 1 describes the fracture mode differences for four cover plate conditions. The adhesion test was done by bonding two coverplates face to face. The bond area was the width of the 25 mm square cover plate and about 13 mm deep. This 13 mm band was off-centered so that two adhesive free bands about eight and four mm respectively bordered the bond area on either side. The bond line thickness was 0.08 mm. These samples could be peeled apart by prying to reveal fracture mode. A more controlled alternative was to bond fixture blocks on either side of the bonded cover plates to yield a test specimen that resembled a compact-tension mode I fracture toughness sample. The sample as pulled in tension to provide fracture mode information as reported in Tables 1 and 2.

Table 1

Comparison of Adhesion at Time Zero

Treatment	Cohesive Fraction
As-received	0%
O <sub>2</sub> -plasma	15%
H <sub>2</sub> O <sub>2</sub>	90%
H <sub>2</sub> O <sub>2</sub> + coupler	80-95%

Table 2  
Comparison of Adhesion Treatments Through Thermal Stress

Treatment	Cohesive Fraction
Untreated controls	0%-10%
H <sub>2</sub> O <sub>2</sub>	20%-80%
H <sub>2</sub> O <sub>2</sub> + coupling agent	75%-100%

Adhesion was very poor for no treatment and the adhesive would separate cleanly away from the cover plate. Oxygen plasma treatment yielded encouraging

results as mild cohesive fracturing appeared in the adhesive. Controlled oxidation and hydration of the nickel surface resulted in a very significant improvement in cohesive fracture mode. The use of a coupling agent, 3-glycidoxypolypropyltrimethoxysilane, did not provide any noticeable improvement. Table 2 shows the results for three cover plate conditions after three passes of solder reflow with a peak temperature of 220 °C. Bond degradation was observed for the controlled oxidation condition, although this cell is still better than no treatment. Even though time zero observations showed that H<sub>2</sub>O<sub>2</sub> treatment alone was equivalent to H<sub>2</sub>O<sub>2</sub> + coupling agent, subsequent thermal stress caused a faster degradation without the coupling agent.

The optimized treatment process began with an ultrasonic preclean with heated 70% isopropyl alcohol to remove organic and ionic contaminants. Next, hot H<sub>2</sub>O<sub>2</sub> further oxidized the nickel and hydrated the oxide at the surface. The final step was to apply the chemical coupler. Silane reacts with the hydrated nickel oxide to form SiO bonds. The glycidoxyl group reacts with the curing epoxy. In this manner, the interface between the nickel and epoxy adhesive is chemically linked and the fast diffusion path for oxygen ingress is reduced significantly. Figure 5 shows a cohesive fracture mode in peel of a test coupon with this treatment. Figure 6 shows the C-SAM image of a TBGA package whose cover plate and stiffener were treated, indicating no delamination after reflow. Dark areas represent adhesive coverage.

### DISCUSSION

The water break test showed that the treated nickel surface would wet with water readily. Water contact angle measurements made with a goniometer showed wetting angles less than 10°. Adhesion tests showed a shift in fracture mode from adhesive to cohesive. C-SAM imaging showed that delamination from

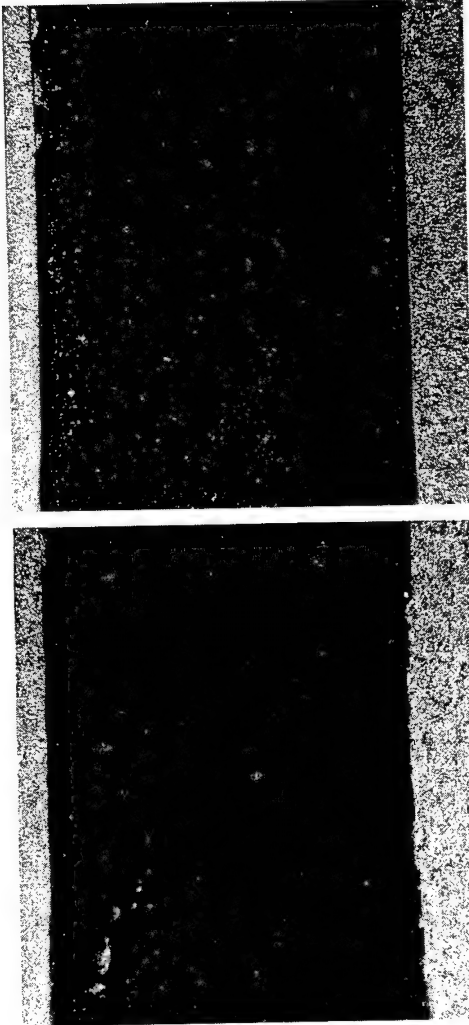


Figure 5. Cohesive fracture after bonding with cover plate that was treated with  $H_2O_2$  and silane coupler.

exposure to solder reflow temperatures was eliminated. In an effort to understand how the nickel surface was altered, chemical analysis was performed using scanning electron microscopy (SEM) and electron spectroscopy for chemical analysis (ESCA). SEM images of untreated and treated nickel surfaces revealed no morphological changes. ESCA depth profiles of untreated and treated coverplates reveal that the nickel oxide layer increases from about 0.1 nm to about 0.8 nm.

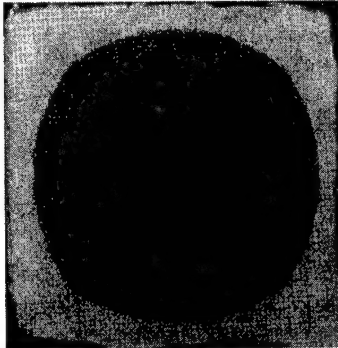


Figure 6. C-SAM image of TBGA package showing no delamination between the treated cover plate and adhesive after solder reflow.

## CONCLUSION

Epoxy adhesives were found to bond poorly to nickel plated surfaces. Cleaning in isopropyl alcohol removed organic and ionic surface contaminants. Hot  $H_2O_2$  treatment deepens the oxide layer by a factor of eight and most likely hydrates it. The result is improved adhesion as evidenced by a change in fracture mode from adhesive to cohesive. This treatment still resulted in some delamination occurring during exposure to temperature aging at 125 °C and to solder reflow at 220 °C. A chemical coupling agent was used to provide long term reliability to the adhesive-nickel interface under high temperature conditions.

While TBGA packages could be made successfully with the flexible epoxy and treated cover plate, a more robust adhesive was found that could survive the arduous stress tests without mechanical or to achieve a cohesive fracture mode. Silicone adhesives are very flexible and can withstand both extreme thermal cycling as well as long term high temperature storage. C-SAM imaging of a TBGA that was bonded with a thermally conductive silicone adhesive and aged at 175 °C for 1000 hours showed no evidence of delamination. Shear test specimen showed no degradation in strength after environmental stress testing.

## ACKNOWLEDGMENTS

Luis Matienzo for chemical surface analysis.

---

## REFERENCES

- Gaynes, M. A. & Shaukatullah, H. 1993. Evaluation of Thermally Conductive Adhesives for Bonding Heat Sinks to Electronic Packages, *Proceedings of 43rd Electronics Components and Technology Conference, Orlando, Florida, June 1993*: 765-771.
- Shaukatullah, H. et al. 1996. Thermal Characterization of Tape Ball Grid Array Packages, *Proceedings of the 1996 International Electronics Packaging Conference, Austin, Texas, September 29-October 1, 1996*: 377-395.
- Arndt, S. F. et al. 1996. Method for Improving Adhesion of Polymeric Adhesives to Nickel Surfaces, United States Patent Number 5,532,024, July 2, 1996.

---

## **6 Emerging technologies and case studies**

## Characterization and prediction of nonlinear VE-VP behaviour of CRP under cyclic loading by using a neuro-fuzzy model

Y.Qin & A.H.Cardon

*Composite System and Adhesion Research Group, Free University of Brussels, Belgium*

R.Guedes

*Department of Mechanical Engineering, University of Porto, Portugal*

**ABSTRACT:** This paper presents a neuro-fuzzy approach in characterizing and predicting the nonlinear viscoelastic-viscoplastic behaviour of a carbon fibre reinforced polymer under cyclic loading. The data collected from the first loading-unloading cycle was used to train the Neuro-Fuzzy model. Then this model was used to predict the creep and creep-recovery strain under cyclic loading. The predicted results were compared with the experimental data.

### 1. INTRODUCTION

The structural applications of composites with specified reliability require the quantitative characterization of the composites time-dependent behaviour and time-dependent damage evolution. For the prediction of the long term behaviour, it is necessary not only to consider the simple loading modes, but also the accelerating effects on the damage development resulting from the interaction between different loading modes (Cardon *EMAMP* 1995). It is important to identify *accelerators* of the material properties in order to be able to extrapolate long term behaviour under *normal* conditions of the *accelerators* from the short term results obtained under hight level of those *accelerators* (Cardon *ICCM-10* 1995).

This paper presents a neuro-fuzzy approach for characterizing and predicting the nonlinear viscoelastic-viscoplastic behaviour of a carbon fibre reinforced polymer under cyclic loading. With the neuro-fuzzy inference system, a material designer may simply connect the processing units with the fundamental theory such as Schapery's viscoelastic theory; collect all information and experimental data from the concerned material; use them all as model input and run the program on a computer. The parameters of the material constitutive relation and/or the predicted properties will be obtained as model output.

The experimental data collected by Edward M. Wu (Wu 1969) on carbon fiber reinforced polymer laminate under cyclic loading are used here. The data collected from the first loading-unloading cycle was used to train the Neuro-Fuzzy model, the other data

are used to compare with the predictions obtained from the trained model.

### 2. MATERIAL CONSTITUTIVE MODEL

The irrecoverable strain was found from experimental data as shown in Figure 1. Based on this observation, a modified *Schapery* (Schapery 1969) nonlinear viscoelastic-viscoplastic constitutive model was chosen for the characterization and prediction.

For the case of uniaxial loading at a constant temperature, and applying the stress history of a creep/creep-recovery testing cycle, the Schapery theory is reduced to the expressions:

$$\epsilon_c = g_0 S_0 \sigma + g_1 g_2 \frac{S_\infty - S_0}{1 + (\frac{\tau_{max}}{t})^n} \sigma, \quad (1)$$

for creep and

$$\epsilon_r = g_2 \left[ \frac{(S_\infty - S_0)}{1 + (\frac{\tau_0}{a_\sigma})^n} - \frac{(S_\infty - S_0)}{1 + (\frac{\tau_1}{t-t_1})^n} \right] \sigma, \quad (2)$$

for creep-recovery with

$$\psi = \frac{t_1}{a_\sigma} + t - t_1; \quad \psi' = \frac{t_1}{a_\sigma}$$

where, for a constant temperature and humidity, both  $\tau_0$  and  $n$  are constants,  $S_0$  and  $S_\infty$  are the initial and the infinite compliance respectively.  $g_0$ ,  $g_1$ ,  $g_2$  and  $a_\sigma$  are stress and temperature dependent nonlinearizing material parameters.

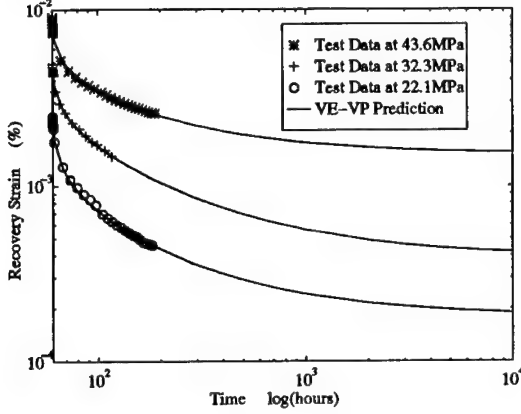


Figure 1: Irrecoverable strain found in experimental data

The viscoplastic response was modeled by the functional introduced by Zapas and Crissman (Zapas 1984) in their study of ultra-high molecular weight polyethylene. According to their approach the viscoplastic component of the transverse strain,  $\epsilon_{vp}$ , induced by an arbitrary stress history  $\sigma(t)$  is given by:

$$\epsilon_{vp} = \phi \left\{ \int_0^t g_3[\sigma^*(\psi)] d\psi \right\} \quad (1)$$

where  $\phi \{ \}$  is a stress history dependent functional and  $\sigma^*(\psi) = (\sigma(\psi)/\sigma)$  is a dimensionless stress. We found that the viscoplastic response of the T300/5208 composite can well be modeled by using a form as:

$$\epsilon_{vp} = g_3(\sigma) \frac{A}{1 + \left( \frac{\tau_{vp}}{t} \right)^m}; \quad (2)$$

$$\text{with } g_3(\sigma) = \frac{C}{1 + \left( \frac{\sigma}{\sigma_0} \right)^n}.$$

A rheological schematic diagram for this modified Schapery viscoelastic-viscoplastic model is shown in Figure 2.

### 3. NEURO-FUZZY INFERENCE SYSTEM

#### 3.1 Neural Networks

A neural network is a processing device, either an algorithm, or actual hardware, whose design was motivated by the design and functioning of the human brain and components. It is a network of many very simple processors (*units*), each possibly having a (small

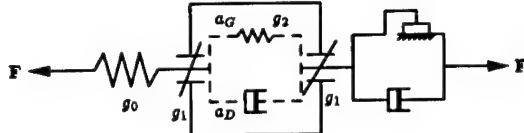


Figure 2: Schematic diagram of modified Schapery's VE-VP model

amount of) local memory. The units are connected by unidirectional communication channels (*connections*), which carry numeric (as opposed to symbolic) data. The units operate only on their local data and on the inputs they receive via the connections.

The neural network, as shown in Figure 3, is a multi-layer feedforward network. Each layer consists of nodes which receive their input from nodes in a layer directly below and send their output to nodes in a layer directly above. In a feedforward network each node performs a particular function (*node function*) on incoming signals as well as a set of parameters pertaining to this node. The nature of the node function may vary from node to node.

In order to achieve a desired input-output mapping, the parameters of the neural networks are updated according to given training data and a gradient-based learning procedure. This procedure is generally referred to as the **back-propagation learning rule** because the gradient vector is calculated in the direction opposite to the flow of the output of each node.

#### 3.2 Fuzzy Inference System

The **fuzzy inference system** is a computing framework based on the concepts of fuzzy set theory, fuzzy if-then rules, and fuzzy reasoning. Figure 4 illustrates the block diagram of a fuzzy inference system.

The **rule base** contains a number of fuzzy "if-then" rules; the **data base** defines the membership functions of the fuzzy set; the **decision-making unit** performs the inference operations; the **fuzzification interface**

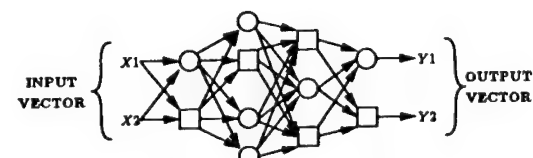


Figure 3: A feedforward neural network

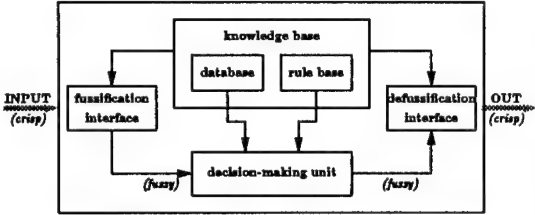


Figure 4: Diagram of a Fuzzy inference system

transforms the crisp input into degrees of match with linguistic values; the **defuzzification interface** transforms the fuzzy rules of the inference into a crisp output.

### 3.3 Neuro-Fuzzy Inference System

The combination of neural networks and fuzzy inference system offer the possibility to integrate prior knowledge to simplify the learning process and/or to extract knowledge in form of rules from the trained networks.

Figure 5 shows a neuro-fuzzy model based on Schapery's thermodynamic constitutive theory. The model has two inputs, time  $t$  and stress  $\sigma$  ( $t_1$ , the load removing time, is a point on  $t$ ), one output, the strain  $\epsilon$  and five layers (considering the inputs as Layer 0).

## 4. RESULTS AND DISCUSSION

The test data were collected by Edward M. Wu (Wu 1984) on four ply  $\pm 45^\circ$  T300/5208 symmetric laminates. The test coupons were submitted to 8 loading-unloading creep/creep-recovery cycles at 6 stress levels from 22.15 MPa to 48.95 MPa. The data col-

lected from first cycle were used to characterize the behaviour of the material and the other data were used to compare with the predicted results.

### 4.1 Training Results

After model training with experimental data collected from the first creep/creep-recovery cycle at all test stress levels, the result of the output of the proposed neuro-fuzzy inference system (NNFIS) are compared with the test data in Figure 6. The experimental data (marked as "o") are fitted by model output (marked as "+") very well.

The nonlinear parameters in Schapery's model are obtained directly in the closed-form expression after model training as shown in Figure 7.

From this Figure, it can be seen that the nonlinearity does not appear at the same stress level for these four parameters.

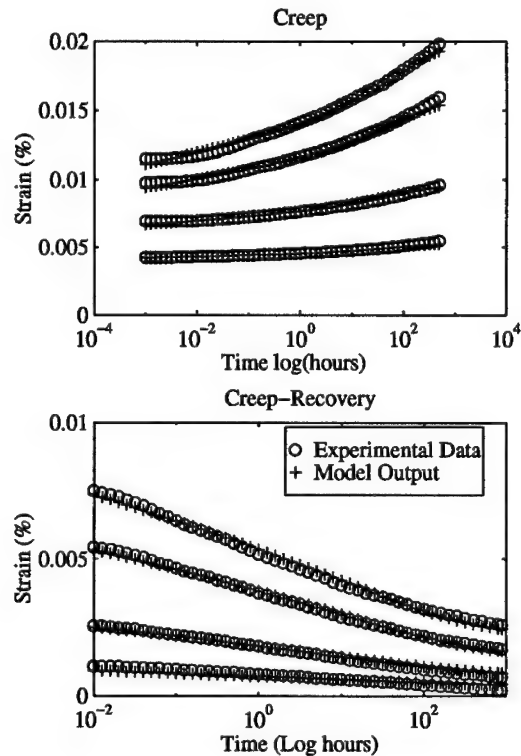


Figure 6: Neuro-Fuzzy Inference System training result

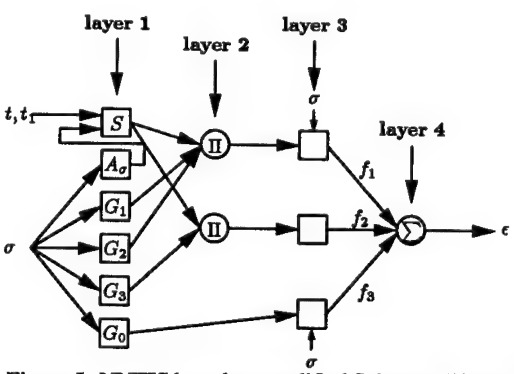


Figure 5: NNFIS based on modified Schapery Theory

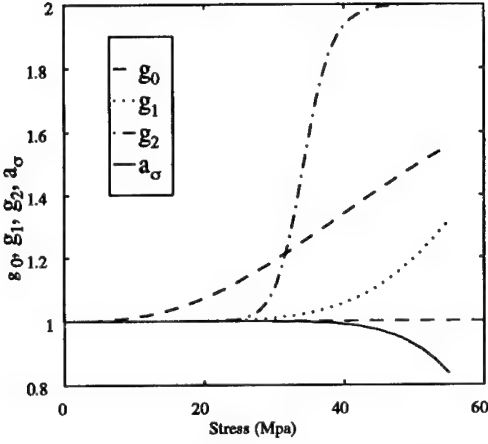


Figure 7: Nonlinear parameters as the output of the NNFIS model

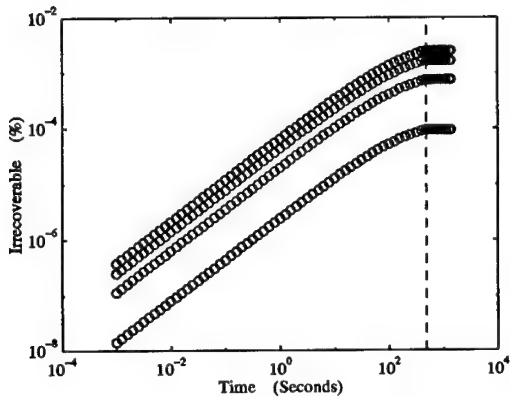


Figure 8: Irrecoverable strain obtained after system straining

Figure 8 shows the irrecoverable strain obtained from the trained model. The dotted line indicates the loading release time  $t_1$ .

#### 4.2 Prediction

The expression for a multi-step loading creep test introduced by Schapery (Schapery 1969) is used together with the trained neuro-fuzzy model to make the prediction on creep behaviour under the loading-unloading cycles. The experimental data were used to check the prediction.

By using identical mathematical procedures, as used by Mark Tuttle (Tuttle 1984), the recursive relationship can be obtained. It gives the summation of viscoelastic and viscoplastic strains  $\epsilon_j$  at time  $t > t_j$ , following j-steps in stress:

$$\begin{aligned} \epsilon_j = & \left\{ g_0^j S_0 \sigma_j \right\} + \left\{ g_1^j [g_1^1 \Delta S(\psi) \sigma_1 \right. \\ & +(g_2^2 \sigma_2 - g_2^1 \sigma_1) \Delta S(\psi - \frac{t_1}{a_\sigma}) \\ & +(g_2^3 \sigma_3 - g_2^2 \sigma_2) \Delta S(\psi - (\frac{t_2-t_1}{a_\sigma} + \frac{t_1}{a_\sigma})) \\ & + \vdots \\ & +(g_2^j \sigma_j - g_2^{j-1} \sigma_{j-1}) \Delta S(\psi - \psi')] \left. \right\} + \quad (3) \\ & \left\{ g_3^1 S_{vp}(t_1) + g_3^2 S_{vp}(u - t_1) \right. \\ & + g_3^3 S_{vp}(u - (t - t_1 + t_1)) \\ & + \vdots \\ & \left. + g_3^j S_{vp}(u - u') \right\} \end{aligned}$$

where

$$\psi = \sum_{k=1}^j \frac{t - t_{k-1}}{a_\sigma^k} \quad \psi' = \sum_{k=1}^{j-1} \frac{t - t_{k-1}}{a_\sigma^k} \quad t > t_{k-1}$$

$$u = \sum_{k=1}^j t - t_{k-1} \quad u' = \sum_{k=1}^{j-1} t - t_{k-1} \quad t > t_{k-1}$$

In Equation (3) the superscripts associated with each of the non-linear parameters denote the stress level at which these parameters are to be evaluated. ( $g_0^j$  indicates that  $g_0$  is to be evaluated at stress  $\sigma_j$ ).

Equation (3) constitutes the closed-form solution for the non-linear response to j-step in stress based upon the modified Schapery non-linear viscoelastic-viscoplastic model. By setting the time step smaller and smaller, Equation (3) can be used to obtain an approximate solution to any complex uniaxial stress history. In this case, Equation (3) becomes, essentially, a numerical integration of the original Schapery single-integral constitutive equation plus a viscoplastic term.

The prediction made by the Neuro-Fuzzy model is compared with experimental data in Figure 9, the dotted line being the experimental data and the solid line is the model output. It can be seen from Figure 9 that after two loading-unloading cycles, the creep-recovery strain in the experimental data is larger than the predicted one. This may be caused by aging (physical and/or chemical), micro- and/or macro-damage induced during the loading from zero to the test stress level.

## 5. CONCLUSION

We have described the architecture of a neural network based fuzzy inference system (NNFIS) for the characterization and the prediction of long term viscoelastic behavior of fiber reinforced polymer composites under cyclic loading. The NNFIS refines the fuzzy logic obtained from human experts to describe the input-output behavior of the system and approximate a desired data set.

By treating the data collected at all test stress levels together, the Neuro-Fuzzy inference system characterizes the transient compliance for the material not only from those data collected in the linear domain, but also from those collected in the nonlinear domain. In other words, by using this new approach, the transient compliance can be represented in a much better way than by characterizing it using only linear creep data. Moreover, with this Neuro-Fuzzy inference system, the nonlinear parameters in the Schapery model are obtained directly in a closed-form. No further curve fitting is required. As consequence, the predicting accuracy of the prediction is improved.

To obtain a good prediction on long term behaviour of polymer based composite materials, the interaction between the loading modes, aging and micro-/macro-damage evolution should be taken in to account.

## REFERENCE

- Cardon, A. H., Bruggeman, M., Qin, Y., Zaoutsos, S., Mitropoulos, Y. and Guedes, R. "Specific Aspect of Time Dependent Behaviour of Polymeric Matrix Composites", *Proceedings of The 4th European Conference on Advanced Materials and Processes*, "369-373", 1995.
- Cardon, A. H. and Bruggeman, M. "Iteration Procedure for the Prediction of Residual Properties of Polymer Based Structural Composites", *Proceedings of ICCM-10*, IV, "391-397", 1995.
- Wu, E. M., Sanches, R. J., Nguyen N. Q., "Matrix-Dominated Time-Dependent Deformation and Damage of Graphite/Epoxy Composite Experimental Data Under Creep and Recovery" AFWAL-TR-83-3066 Report. Lawrence Livermore National Lab. 1083.
- Schapery, R. A., "On the Characterization of Nonlinear Viscoelastic Materials", in *Polymer Eng. and Sci.*, 9, 1969.
- Zapas, L. J. and Crissman, J. M. "Creep and Recovery Behaviour of ultra-high molecular weight polyethylene in the region of small uniaxial deformations.", in *Polymer*, 25:57-62, 1984.
- Tuttle, M. and Brinson, H. F. "Accelerated viscoelastic characterization of T300/5208 graphite/epoxy laminates" in VPI-E-84-9, Virginia Polytechnic Institute and State University, Blacksburg, 1984.

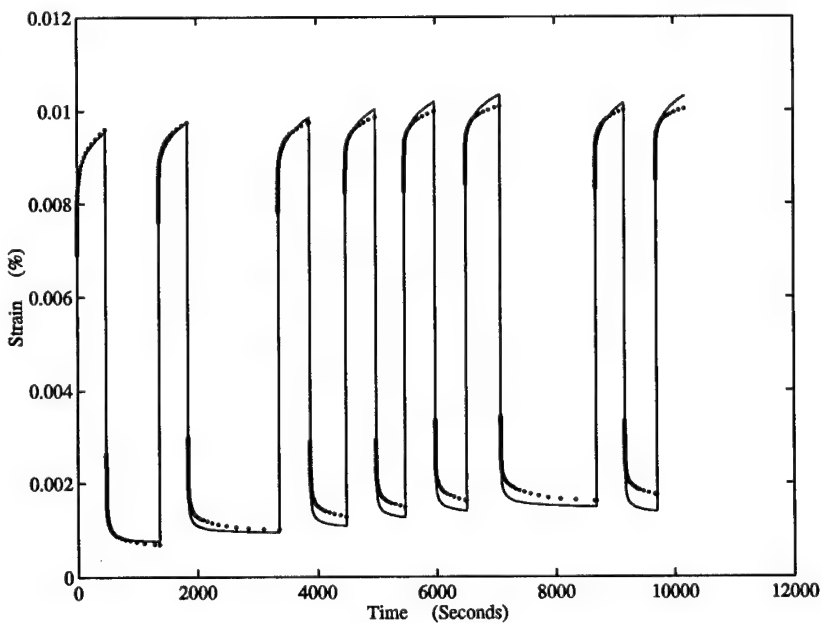


Figure 9: Prediction made by Neuro-Fuzzy Model

## In-situ SEM/micro-line methods for microscopic deformation and damage evolution analysis of composites

N.Takeda

*Center for Collaborative Research (CCR), The University of Tokyo, Japan*

S.Ogihara

*Science University of Tokyo, Noda, Chiba, Japan*

**ABSTRACT:** A novel experimental method based on temperature-controlled in-situ SEM (scanning electron microscope) combined with micro-lines printed on specimens was proposed to measure quantitatively the microscopic interlaminar deformation and damage evolution in composite laminates. Microscopic interlaminar deformation and damage near the transverse crack tip was clearly visualized under tensile loading for CFRP cross-ply laminates with and without the interlaminar resin-rich region. Temperature dependence of interlaminar shear deformation near transverse crack tips and the axial COD (crack opening displacement) was measured to demonstrate the effect of thermal residual stress, and then successfully compared with the modified two-dimensional (2D) approximate elastic analysis.

### 1 INTRODUCTION

In many applications of fiber-reinforced plastics, they are mainly used in the form of multi-directional laminates. Among these composites, cross-ply laminates have been extensively investigated through both theoretical and experimental studies because this is a basic laminate configuration (for example, Garrett & Bailey 1977). The failure process of cross-ply laminates is known to involve an accumulation of transverse cracks and delamination (Reifsnider 1982).

Most previous studies of the failure process in cross-ply laminates have been focused on the experimental measurement of transverse crack density as a function of applied load or the theoretical prediction of the onset of transverse cracking and its multiplication. In conjunction with the theoretical prediction of mechanical behavior and damage progress of cracked laminates, micro-mechanical stress analyses of damaged cross-ply laminates have been conducted. *In-situ* observation of microscopic failure process in CFRP cross-ply laminates at R.T. and at 80°C was conducted, and probabilistic prediction was made for progressive damage parameters, the transverse crack density and delamination ratio (Takeda & Ogihara 1994a, b, Ogihara & Takeda 1995). It was pointed out that the thermal residual stress had significant effect on the failure process. Variational 2D stress analysis for cracked cross-ply laminates under tension was found effective to predict the stiffness reduction due to transverse cracking, where the principle of minimum

complementary energy (Hashin 1985) and the principle of minimum potential energy (Lee et al. 1989) were used. Hashin's analysis was extended to consider the thermal residual stresses and the energy release rate associated with transverse crack formation was derived (Nairn 1989). The energy release rate was used to predict transverse crack density as a function of laminate stress. Another accurate approximate 2D solution was obtained by satisfying the stress-strain-temperature relations either exactly or in an average sense (McCartney 1992).

In recent years, interleaved laminates have been developed in which resin-rich layers are placed in interlaminar regions to enhance the interlaminar fracture toughness of CFRP laminates and to restrict delamination onset (Takeda et al. 1997a, Ogihara et al. 1997). The corresponding 2D elastic solutions (Ogihara et al. in press) should provide a basis for material optimization of the thickness and stiffness of the interleaf.

In spite of the above progress in the theoretical model, few micro-mechanical experiments have been conducted to quantify the microscopic deformation and damage evolution especially in the interlaminar region. A novel experimental method based on temperature-controlled in-situ SEM combined with micro-lines printed on specimens has been proposed by the authors (Takeda et al. 1997b, c) for quantitative measurement of the microscopic interlaminar deformation and damage evolution for comparison with the theoretical results of cross-ply laminates.

In this paper, our recent studies are summarized for microscopic interlaminar deformation and damage

near the transverse crack tip of some representative CFRP cross-ply laminates with and without the interlaminar resin-rich region. Temperature dependence of interlaminar shear deformation near transverse crack tips and the axial COD was measured to demonstrate the effect of thermal residual stress, and then successfully compared with the modified two-dimensional (2D) approximate elastic analysis.

## 2 EXPERIMENTAL PROCEDURE

### 2.1 Materials

Three material systems were used and all of them were supplied by Toray Inc. The laminate configuration was cross-ply  $[0/90_2]_S$ . The first one was toughened CFRP, T800H/3631. T800H is a high strength carbon fiber. The 3631 is a modified epoxy system with improved toughness compared with a conventional TGDDM/DDS epoxy system. The second one was interleaved CFRP, T800H/3631-FM300, with toughened epoxy resin film layers (FM300) about 100  $\mu\text{m}$  thick between 0° and 90° plies. The third one was also interleaved CFRP, T800H/3900-2, with selectively toughened interlaminar layers about 30  $\mu\text{m}$  thick at all the ply interfaces. The interlaminar layers contain tough and fine thermoplastic resin particles dispersed in the base epoxy resin (Odagiri et al. 1988). The average thickness of each ply excluding the interleaf region was 0.135 mm. The fiber volume fraction was about 60% for T800H/3631, 45% for T800H/3631-FM300 and 55% for T800H/3900-2. All the specimens were cut into 60 mm long and 3 mm wide, and stored in a desiccator to conduct tests in a dry condition with the water content less than 1 wt%. Some typical mechanical properties are listed in Table 1, and will be used later for quantitative theoretical prediction.

### 2.2 Preparation of micro-lines

The micro-lines (or micro-grids) were made using the photolithography technique on specimen edge surfaces, as schematically shown in Figure 1 (Takeda et al. 1997b). First, the edge surface of the specimen was polished using an automatic polishing machine and 1  $\mu\text{m}$  diamond paste, then coated by the photo-resist, or photo-chemical reactive resin. The specimen was, then, heated to cure the resist, and the surface was exposed to the light through the photo-mask, or the glass plate with micro-lines or grids. After that, the exposed part of the resist was removed in the developer, and vacuum-evaporated metal was deposited on the surface. Finally, the remaining resist was removed in the solvent to prepare the micro-lines or grids on the specimen surface. The minimum reproducible line width and spacing is 1  $\mu\text{m}$  at present.

Table 1. Properties of unidirectional laminates and interleaf materials used in the analysis.

	T800H/3631	FM300
$E_A$ (GPa)	169 -0.111 $\times T$	$E^i$ (GPa) 2.65 -0.010 $\times T$
$E_T$ (GPa)	9.62 -0.010 $\times T$	$\nu^i$ 0.38
$G_A$ (GPa)	4.50	$\alpha^i$ ( $^\circ\text{C}$ ) $60.6 \times 10^{-6}$
$\nu_A$	0.349	
$\nu_T$	0.490	
$\alpha_A$ ( $^\circ\text{C}$ )	$0.10 \times 10^{-6}$	
$\alpha_T$ ( $^\circ\text{C}$ )	$35.5 \times 10^{-6}$	

	T800H/3900-2	
Base Composite	Thermoplastic Particle -Dispersed Layer	
$E_A$ (GPa)	132 -0.090 $\times T$	$E^i$ (GPa) 2.71 -0.0105 $\times T$
$E_T$ (GPa)	8.17 -0.007 $\times T$	$\nu^i$ 0.38
$G_A$ (GPa)	4.50	$\alpha^i$ ( $^\circ\text{C}$ ) $60.6 \times 10^{-6}$
$\nu_A$	0.349	
$\nu_T$	0.490	
$\alpha_A$ ( $^\circ\text{C}$ )	$-1.73 \times 10^{-6}$	
$\alpha_T$ ( $^\circ\text{C}$ )	$34.7 \times 10^{-6}$	

$T$ : degrees centigrade ( $^\circ\text{C}$ ). Subscripts  $A$  and  $T$  denote axial and transverse directions, respectively,

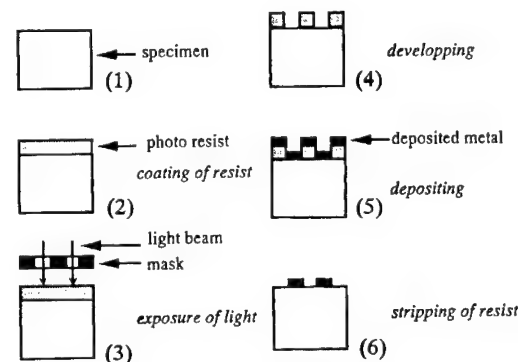


Figure 1. Procedure to print micro-lines/grids by photolithography technique.

### 2.3 Tensile test and measurement of microscopic deformation

Tensile tests of CFRP symmetric cross-ply laminates were carried out in a SEM with a servo-hydraulic loading machine and a specimen heating unit, as shown in Figure 2. The specimen was loaded at 20°C until the transverse crack intervals became uniform, and the images of local area near the crack tip and a whole view of the crack were photographed. Then the temperature was raised to 80°C and the crack was

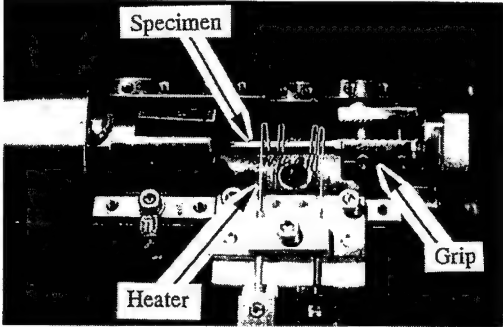


Figure 2. Experimental setup for in-situ SEM tests.

photographed again. This procedure was repeated at 120°C and 160°C. The COD of the transverse cracks and the interlaminar shear strain,  $\gamma_{xy}$  ( $= \partial v/\partial x + \partial u/\partial y$ ) near the transverse crack tip were measured from these photos, where  $u$  and  $v$  are displacements in  $x$  and  $y$  directions, respectively. Since the  $\partial u/\partial y$  component is considered small, the shear strain was replaced by  $\partial v/\partial x$  in the following.

### 3 ANALYSIS

In the present study, 2D stress and displacement fields in CFRP cross-ply laminates with transverse cracks proposed by Lee et al. (1989) and McCartney (1992), were modified for comparison with the present experimental results. The analysis by Lee et al. (1989) was extended and used for cross-ply laminates without interleaves. The thermal residual stress was considered, which was not included in the original analysis, and the details can be found in our recent paper (Takeda et al. 1997b).

The analysis by McCartney (1992) was extended and used for cross-ply laminates with interleaves at 0°/90° interfaces. The analysis is based on the approximated two dimensional elastic model which assumes that generalized plane strain conditions prevail. Account is taken of thermal residual stresses arising from a mismatch in thermal expansion coefficients of 0° and 90° plies as well as the interleaf layer (Ogihara et al. in press) as in the following.

Consider a cross-ply laminate subjected to mechanical and thermal loading as shown in Figure 3 in which interleaf layers are of thickness  $t$ . In the present study, two cases are considered; (a) the transverse crack tip stops at 90°/interleaf interface, and (b) the transverse crack penetrates into the interleaf and stops at 0°/interleaf interface. The displacements in  $y$ -direction in interleaf,  $v_i$ , and that in 90° ply,  $v_m$ , are expressed as equations (1) and (2), respectively.

$$v_i = \left( \frac{1}{\mu} - \frac{\nu_T^m}{E_T^m} \right) b(x-a) C(y) - C''(y) \left[ \frac{b}{E'} \left\{ -\frac{1}{6}(x^3 - a^3) + \frac{1}{2}a^2(x-a) \right. \right. \\ \left. \left. + \left( a+t + \frac{b}{2} \right) \left\{ \frac{1}{2}(x^2 - a^2) - a(x-a) \right\} \right\} \right] - \frac{ab}{6E_T^m} \{a - 3(h+t)\}(x-a) + A_2(y) \quad (1)$$

$$v_m = \frac{b}{2a} \left( \frac{1}{\mu_T^m} - \frac{\nu_T^m}{E_T^m} \right) (x^2 - a^2) C(y) + \frac{b}{6aE_T^m} C''(y) \\ \left\{ \frac{1}{4}(x^4 - a^4) - \frac{3}{2}a(h+t)(x^2 - a^2) \right\} + A_2(y) \quad (2)$$

where  $2a$  and  $2b$  are thicknesses of 90° and 0° plies, respectively,  $C(y)$  is a function found for each case, and  $A_2(y)$  is an arbitrary function arising from integration.  $E$ ,  $\mu$ , and  $\nu$  are constants determined from the mechanical properties of the plies and the interleaf material. Here, the shear strain and crack opening displacement are compared with experimental results.

### 4 RESULTS AND DISCUSSION

#### 4.1 Cross-ply laminates without interleaves

Figure 4 shows a transverse crack in a T800H/3631 laminate (lamine stress  $\sigma = 260$  MPa, crack interval  $2L = 1.4$  mm). It is observed that COD decreases at higher temperature although the applied stress is the same, due to the reduction in thermal residual stress in 90° ply. Figure 5 shows the temperature dependence of COD as a function of normalized thickness, where

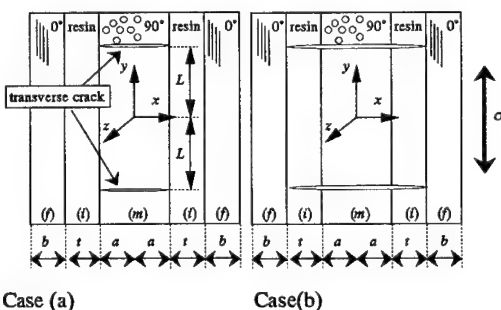


Figure 3. Models of interleaved cross-ply laminates containing transverse cracks in 90° ply.  
Case (a): Transverse crack tips stop at 90°/interleaf interface, Case (b): Transverse cracks penetrate into the interleaf and stop at interleaf/0° interface.

0 and 1 correspond to the center of the 90° ply and 0/90 interface, respectively. The experimental results are well predicted by the modified theoretical analysis considering the thermal residual stress.

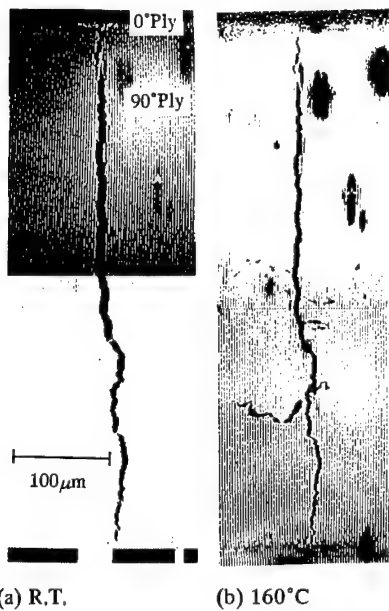


Figure 4. A transverse crack in a T800H/3631 [0/90]<sub>s</sub> cross-ply laminate ( $\sigma = 260$  MPa,  $2L = 1.4$  mm).

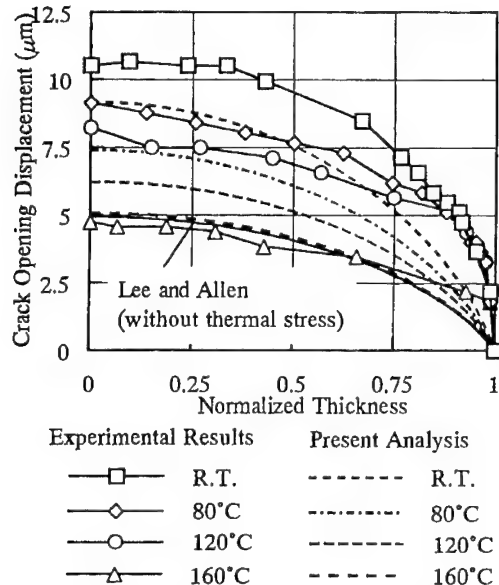


Figure 5. Temperature Dependence of COD in a T800H/3631 [0/90]<sub>s</sub> Cross-ply Laminate ( $\sigma = 260$  MPa,  $2L = 1.4$  mm).

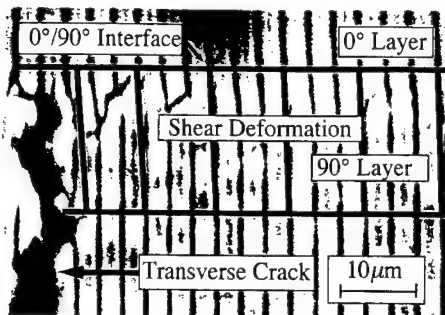


Figure 6. Shear deformation near the transverse crack tip in a T800H/3631 [0/90]<sub>s</sub> Cross-ply Laminate ( $\sigma = 160$  MPa,  $2L = 2.1$  mm).

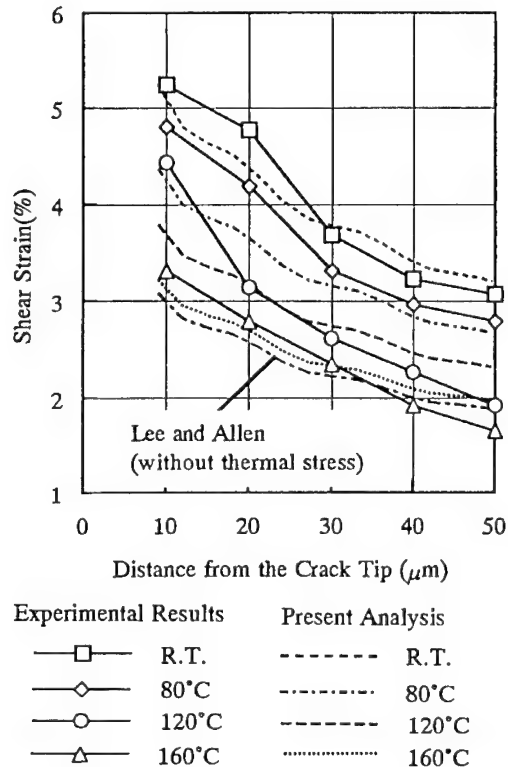
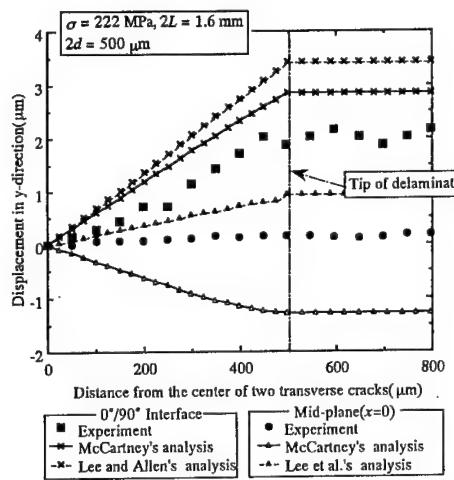


Figure 7. Distribution of interlaminar shear strain at 0/90 interface in a T800H/3631 [0/90]<sub>s</sub> cross-ply laminate ( $\sigma = 160$  MPa,  $2L = 2.1$  mm).

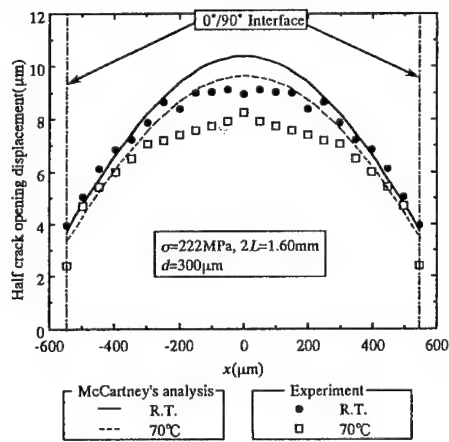
Figure 6 shows a local deformed area near a transverse crack tip in a T800H/3631 laminate ( $\sigma = 160$  MPa,  $2L = 2.1$  mm, R.T.). An interlaminar shear region can be observed, as assumed in the so-called shear lag analysis. The shear strain is found to become very large near the crack tip. Figure 7 shows

the temperature dependence of the shear strain (averaged in the thickness direction) distribution as a function of distance from the crack tip. The shear strain reduces as the temperature rises, which is also considered due to the reduction in the thermal residual stress. This tendency was also well predicted by the present modified analysis.

Figure 8 shows other experimental results of (a) the displacements in the tensile ( $y$ ) direction at  $0^\circ/90^\circ$  interface and the mid-plane, and (b) half COD of the laminates with delamination ( $\sigma = 222$  MPa,  $2L = 1.6$  mm)

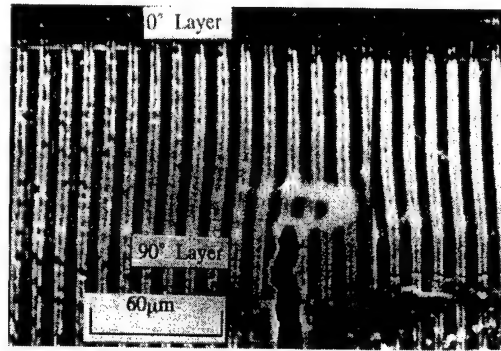


(a) Displacement in the tensile direction at  $0^\circ/90^\circ$  interface and at mid-plane.

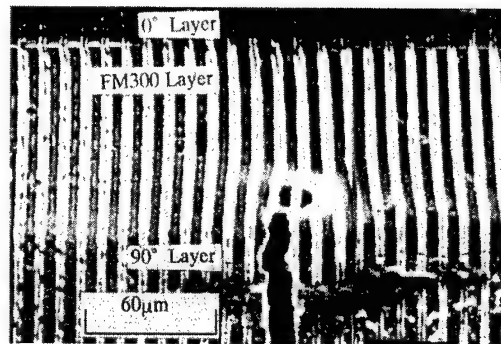


(b) Half crack opening displacement.

Figure 8. Temperature dependence of displacements in a T800H/3631  $[0/90_2]_s$  cross-ply laminate with delamination ( $\sigma = 222$  MPa,  $2L = 1.6$  mm,  $2d = 500$   $\mu\text{m}$ ).



(a) R.T.



(b) 100°C

Figure 9. A transverse Crack in T800H/3631-FM300  $[0/90_2]_s$  cross-ply laminate ( $\sigma = 296$  MPa).

mm, delamination length  $2d = 500 \mu\text{m}$ ), which also shows reasonable agreement with the theoretical predictions considering delamination initiating at transverse crack tips (Takeda et al. 1997c).

#### 4.2 Cross-ply laminates with interleaves

Figure 9 shows a transverse crack in a T800H/3631-FM300 cross-ply laminate ( $\sigma = 296$  MPa). By printing micro-lines, we can much clearly observe shear deformation in the FM300 layer. By inserting the FM300 layer, delamination initiating from the tips of the transverse cracks is restricted, which is due to the enhancement of interlaminar fracture toughness. The transverse crack tip propagates into the FM300 layer at some depth and crack tip blunting can be observed.

Figure 10 shows the temperature dependence of the shear strain for T800H/3631-FM300 as a function of distance from the crack tip. The shear strain at  $160^\circ\text{C}$  is much larger than that at other temperatures, which is considered due to the drastic reduction in the shear

modulus of FM300 at 160°C. The average shear strain in the interleaf layer is larger than that at 90°/interleaf interface. In Figure 10, the analytical predictions are also shown only for Case (b), because it seems more realistic than Case (a).

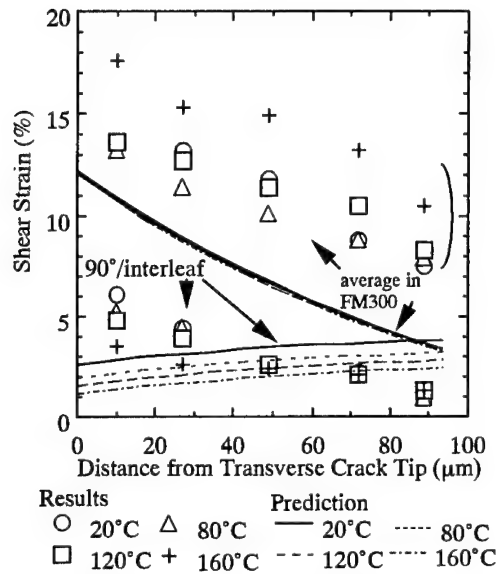


Figure 10. Shear strain as a function of distance from the transverse crack tip in T800H/3631-FM300 [0/90]<sub>s</sub> cross-ply laminate ( $\sigma = 216$  MPa).

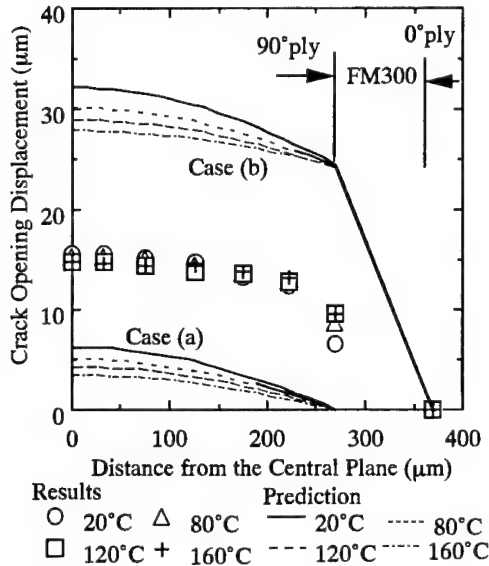


Figure 11. COD as a function of distance from the central plane in T800H/3631-FM300 [0/90]<sub>s</sub> cross-ply laminate ( $\sigma = 216$  MPa).

Figure 11 shows the temperature dependence of COD as a function of the position in the thickness direction. The experimental results show that temperature dependence of COD is small. This is due to the combined effect of the decrease in the thermal residual stress and the decrease in shear modulus of the interleaf and 90° ply at higher temperature. The analytical predictions are also shown in Figure 11 for both Cases (a) and (b). Cases (a) and (b) are considered lower and upper bounds for COD, respectively. For more quantitative estimation of COD, a model in which a transverse crack penetrates into the interleaf at arbitrary depth is necessary.

Figure 12 shows a transverse crack in a T800H/3900-2 cross-ply laminate ( $\sigma = 160$  MPa). As the temperature rises, the COD in the interlaminar layer increases, while that at the center of the 90° layer changes little.

Figure 13 shows the temperature dependence of COD as a function of the position in the thickness direction for T800H/3900-2. Similar to T800H/3631-FM300, temperature dependence of COD is small. This is considered to be due to the reduction in the thermal residual stress and the decrease in the load transmission capability of the softened interlaminar layer. In Figure 13, the analytical predictions are also

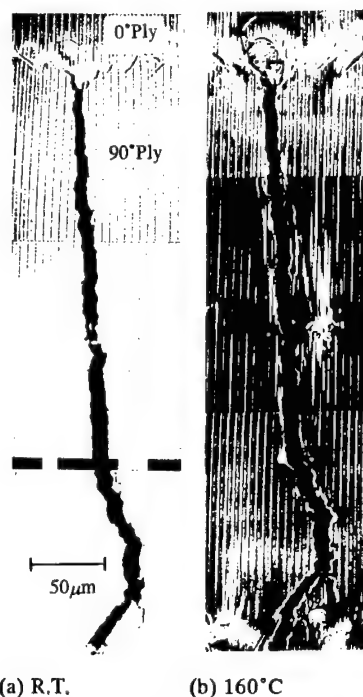


Figure 12. A transverse Crack in T800H/3900-2 [0/90]<sub>s</sub> cross-ply laminate ( $\sigma = 160$  MPa).

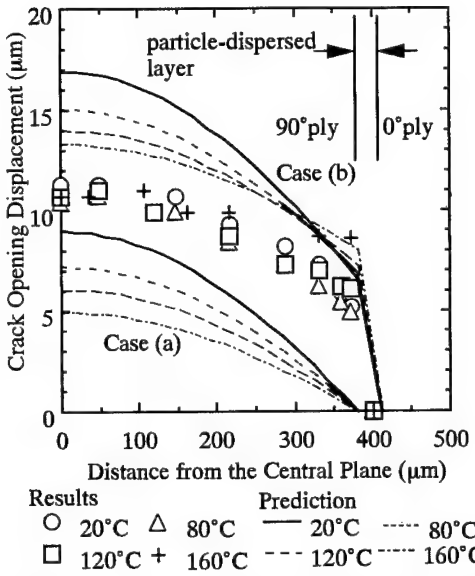


Figure 13. COD as a function of distance from the central plane in T800H/3900-2 [0/90]<sub>s</sub> cross-ply laminate ( $\sigma = 160$  MPa).

shown for both Cases (a) and (b). The difference in lower and upper bounds for COD is smaller than for T800H/3631-FM300, because the interleaf thickness is small. Case (b) seems to be a good approximation to this material system.

Figure 14 shows the local highly-deformed area near a transverse crack tip in a T800H/3900-2 cross-ply laminate ( $\sigma = 160$  MPa). It is observed that at 160°C the shear strain in the interlaminar layer becomes rather large. The shear strain in 90° ply, on the contrary, slightly decreases.

Figure 15 shows the temperature dependence of the shear strain for T800H/3900-2 as a function of distance from the crack tip. Larger shear strain is observed in the interlaminar layer at higher temperature, which is considered due to the softening of the interlaminar layer. This corresponds well with the experimental results where the COD in the interlaminar layer magnifies at higher temperature. In Figure 15, the analytical predictions are also shown for Case (b). A reasonable agreement is obtained between the experimental and analytical results except for 160°C. With more proper selection of mechanical properties of interleaf material as a function of temperature, the deformation will be predicted more precisely.

## 5 CONCLUSIONS

Tensile tests of CFRP cross-ply laminates without and with interleaves were carried out in a SEM, and microscopic interlaminar deformation and damage around the transverse crack was observed at different temperatures by means of micro-lines printed on the specimen edge surface. Temperature dependence of

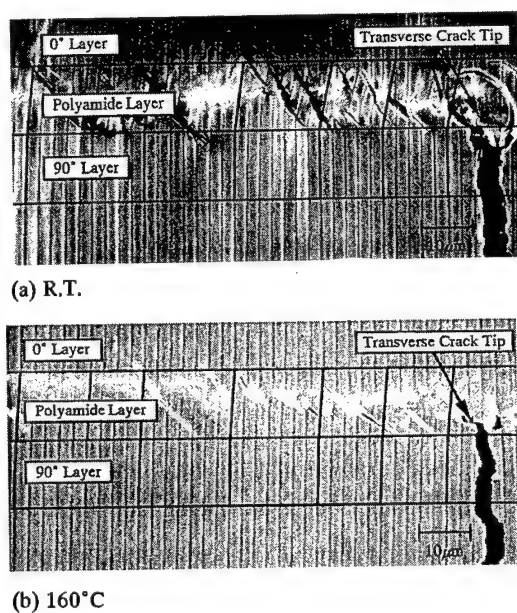


Figure 14. Shear deformation near the transverse crack tip in a T800H/900-2 [0/90]<sub>s</sub> Cross-ply Laminate ( $\sigma = 160$  MPa).

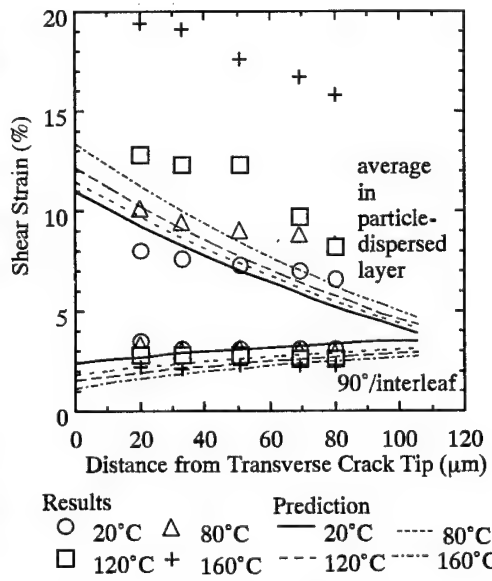


Figure 15. Shear strain as a function of distance from the transverse crack tip in T800H/3900-2 [0/90]<sub>s</sub> cross-ply laminate ( $\sigma = 160$  MPa).

the experimentally-obtained interlaminar shear strain and crack opening displacement were successively compared with the approximate two dimensional elastic analysis.

The present in-situ SEM/micro-line method can also be applied generally to any kinds of fiber reinforced composites. The authors have recently extended it for use in short glass fiber reinforced thermoplastic composites (Takeda et al., in press) as well as SiC fiber reinforced glass matrix composites (Takeda & Kiriyama, in press) to demonstrate the validity of this method for precise micro-mechanical experimental characterization.

#### ACKNOWLEDGEMENTS

The authors appreciate Monbusho (the Ministry of Education, Science, Sports and Culture, Japan) for support of the entire work through the Grant-in-Aid for Scientific Research from 1992 to present. They also thank The Mitsubishi Foundation which partially supported the research through the grant to one of the authors (N. T.). They also appreciate the continuous encouragement of Prof. A. Kobayashi, Science University of Tokyo.

Continuous efforts in time-consuming experiments by Mr. H. Niizuma, Mr. S. Suzuki, Mr. N. Suzuki, Mr. K. Koizumi and Ms. M. Kiriyama are appreciated. Specimens have been supplied by Toray Inc. and its support is highly appreciated.

#### REFERENCES

- Garrett, K. W. & J. E. Bailey 1977. Multiple transverse fracture in 90° cross-ply laminate of a glass fiber-reinforced polyester. *J. Mater. Sci.* 12: 157-168.
- Hashin, Z. 1985. Analysis of cracked laminates: a variational approach. *Mech. Mater.* 4: 121-136.
- Lee, J. W., D. H. Allen & C. E. Harris 1989. Internal state variable approach for predicting stiffness reductions in fibrous laminated composites with matrix cracks. *J. Comp. Mater.* 23: 1273-1291.
- McCartney, L. N. 1992. Theory of stress transfer in a 0°-90°-0° cross-ply laminate containing a parallel array of transverse cracks. *J. Mech. Phys. Solids*, 40: 27-68.
- Nairn, J. A. 1989. The strain energy release rate of composite microcracking: a variational approach. *J. Comp. Mat.* 23: 1106-1129.
- Odagiri, N., T. Muraki & K. Tobokura 1988. Toughness improved high performance Torayca prepreg T800H/3900-2 series. *Proceedings of 33rd Int. SAMPE Symp.*: 272-283. Covina, SAMPE.
- Ogihara, S. & N. Takeda 1995. Interaction between transverse cracks and delamination during damage progress in CFRP cross-ply laminates. *Compos. Sci. Tech.* 54: 395-404.
- Ogihara, S., N. Takeda & A. Kobayashi 1997. Experimental characterization of microscopic failure process under quasi-static tension in interleaved and toughness-improved CFRP cross-ply laminates. *Compos. Sci. Tech.* 57: 267-275.
- Ogihara, S., N. Takeda & A. Kobayashi (in press). Analysis of stress and displacement fields in interlaminar-toughened composite laminates with transverse cracks. *Adv. Compos. Mater.*
- Reifsnider, K. L. 1982. *Damage in Composite Materials: Basic Mechanisms, Accumulation, Tolerance, and Characterization*, ASTM STP 775, Philadelphia: ASTM.
- Takeda, N. & M. Kiriyama (in press). Damage growth sequence of SiC fiber reinforced glass matrix cross-ply laminates. *Proceedings of Am. Soc. Comp. 12th Annual Conf.*, Dearborn, 6-8 Oct. 1997: Lancaster: Technomic.
- Takeda, N. & S. Ogihara 1994a. In-situ observation and probabilistic prediction of microscopic failure processes in CFRP cross-ply laminates. *Compos. Sci. Tech.* 52: 183-195.
- Takeda, N. & S. Ogihara 1994b. Initiation and growth of delamination from the tips of transverse cracks in CFRP cross-ply laminates. *Compos. Sci. Tech.* 52: 309-318.
- Takeda, N., S. Ogihara, A. Kobayashi & D. Y. Song 1997a. Microscopic fatigue failure process in interleaved and toughness-improved CFRP cross-ply laminates. *Adv. Compos. Mater.* 6(4): 309-326.
- Takeda, N., H. Niizuma, S. Ogihara & A. Kobayashi 1997b. Application of micro-line/grid methods to temperature-dependent microscopic deformation and damage in CFRP laminates. *Exper. Mech.* 37(2): 182-187.
- Takeda, N., S. Ogihara, S. Suzuki & A. Kobayashi 1997c. Evaluation of microscopic deformation in CFRP laminates with delamination by micro-grid methods. *J. Compos. Mater.* 15: (in printing).
- Takeda, N., S. Ogihara, N. Nakata & A. Kobayashi (in press). Characterization of microscopic failure process and deformation in glass/nylon 6 composites by micro-grid methods. *Compos. Inter.*

## Micromechanically based constitutive models for damage evolution in composite laminates

P.Gudmundson

*Department of Solid Mechanics, Royal Institute of Technology (KTH), Stockholm, Sweden*

**ABSTRACT:** The structure of micromechanically based constitutive models for composite laminates developing transverse matrix cracks, local delaminations, fibre/matrix debonding and fibre fractures is discussed. Nondimensional damage variables describing these four damage modes are introduced and the principal form of a damage dependent constitutive law is formulated. As a special case transverse matrix cracking is investigated in further detail. A previously developed model for stiffness changes resulting from transverse matrix cracking is presented and criteria for initiation and growth of transverse cracks are discussed. In particular, limitations of the linear elastic fracture mechanics approach are investigated and a cohesive zone model capturing crack bridging effects is suggested.

### 1 INTRODUCTION

Composite laminates generally develop various kinds of damage prior to final failure. The damage often initiate at relatively low loads and then progressively evolves with increased loading. A common scenario is that transverse matrix cracks first initiate and grow. At some higher load, local delaminations and/or fibre fractures may form, sometimes triggered by the presence of matrix cracks. The above mentioned damage modes influence the thermomechanical properties and hence lead to load redistribution in a composite component. In order to capture these phenomena in finite element calculations, damage dependent constitutive models must be applied. Basically two approaches have emerged for the development of such models, a phenomenological (continuum damage mechanics) and a micromechanically based approach. The differences between the two methods are in fact not so large. In the extreme case, a phenomenologically based constitutive model is purely based on macroscopic measurements of the mechanical behaviour at various damage states whereas a micromechanically based model is entirely based on micromechanical models. Models which have been presented in the literature are generally either phenomenologically based with some micromechanical submodels or micromechanically based with phenomenological submodels. For an overview on continuum damage mechanics, confer to Talreja (1994). In this paper, the micromechanical approach will shortly be described and for the case of matrix

cracking as the sole damage mechanism, more detailed results and a thorough discussion on initiation and growth criteria will be presented.

### 2 DAMAGE DEPENDENT CONSTITUTIVE LAW

Four damage modes will be discussed, namely transverse matrix cracking, local delaminations, fibre fractures and fibre/matrix debonding. First of all, damage parameters must be defined which describe the extent of damage for the individual modes. All four damage modes have in common that they represent the formation of new crack surface areas. A convenient measure would then simply be the crack surface area per unit area of the laminate. Since the damage generally vary from ply to ply and from ply interface to ply interface, damage parameters for each ply and ply interface have to be defined. For matrix cracking (*MC*), fibre fracture (*FF*) and fibre/matrix debonding (*FM*), the damage parameter for each ply is here defined as the corresponding crack surface area in the ply per unit area of the laminate. For local delaminations (*DE*) the damage parameter for each ply interface is defined as the delaminated area in the ply interface per unit area of the laminate.

A laminate with  $N$  plies is considered. According to the definition above, nondimensional damage variables for each damage mode can be defined as:

$$\omega_i^K = \frac{A_i}{A_0} \quad (1)$$

where  $A_i$  denotes the crack surface area in ply ( $i$ ) or, in the case of local delaminations, interface ( $i$ ) of damage mode  $K$  ( $K = MC, FF, FM, DE$ ) within the representative laminate area  $A_0$ . All the damage variables ( $\omega_i^{MC}, \omega_i^{FF}, \omega_i^{FM}$ ) for  $i = 1, 2, \dots, N$  and  $\omega_i^{DE}$  for  $i = 1, 2, \dots, N-1$  may be collected into a single damage vector  $\omega_i$ ,  $i = 1, 2, \dots, 4N-1$ .

If for simplicity only linear elastic material behaviour without effects of residual stresses is considered, the laminate is described by a damage dependent laminate stiffness matrix  $C(\omega_i)$  or equivalently a damage dependent compliance matrix  $S(\omega_i)$  which define the relationship between the six-dimensional vector of in-plane strains and curvatures  $\xi$  and membrane forces and bending moments per unit length  $\sigma$ .

$$\begin{aligned}\sigma &= C(\omega_i)\xi \\ \xi &= S(\omega_i)\sigma\end{aligned}\quad (2)$$

Using the micromechanical approach, it is evident that a micromechanical model including all damage variables must be developed. A general model of this type does not exist today, but for particular cases accurate models have been developed.

Incremental changes in stresses, strains and damage may be investigated by taking the time derivative of eq. (2).

$$\dot{\sigma} = C\dot{\xi} + \sum_{i=1}^{4N-1} \frac{\partial C}{\partial \omega_i} \dot{\omega}_i \xi \quad (3)$$

It is evident from eq. (3) that the constitutive relationship (2) must be complemented by damage evolution laws for  $\dot{\omega}_i$  in order to model the stress-strain behaviour. A criterion for initiation and growth of damage variable ( $i$ ) may be expressed in terms of a damage and load dependent variable, say  $\psi_i$ , and the corresponding critical value of that variable, say  $\psi_{ic}$ . In case of an energy release rate criterion,  $\psi_i$  should be interpreted as the applied energy release rate, which depends on laminate geometry and loading, and  $\psi_{ic}$  as the critical energy release rate. The complete constitutive law for a laminate with evolving damage can then be expressed in incremental form as eqs. (3-5):

$$\dot{\omega}_i = 0 \text{ if } \psi_i < \psi_{ic} \text{ or if } \psi_i = \psi_{ic} \text{ and } \psi_i \leq 0 \quad (4)$$

or

$$\psi_i = \psi_{ic} \text{ if } \psi_i = \psi_{ic} \text{ and } \psi_i > 0 \quad (5)$$

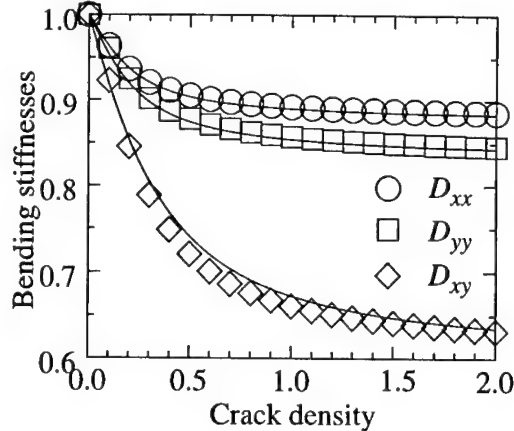


Figure 1. Normalized bending stiffnesses for a [90,-55,0,-55,90,55,0] CFRP laminate (Adolfsson & Gudmundson 1997). The solid lines denote analytical predictions and the symbols FE-results.

Many authors have suggested that the energy release rate may be a proper parameter for control of damage initiation and growth, see for example Aveston & Kelly (1973), Parviz et al. (1978), Wang & Crossman (1980), Nairn (1989), Xia et al. (1993), Hashin (1996). With the definition of damage variables according to eq. (1), it may be shown that the energy release rate ( $G_i$ ), defined as the change in potential energy resulting from an increase in crack surface area, simply can be expressed as:

$$G_i = -\frac{1}{2} \xi^T \frac{\partial C}{\partial \omega_i} \xi \quad (6)$$

or in terms of the compliance matrix as:

$$G_i = \frac{1}{2} \sigma^T \frac{\partial S}{\partial \omega_i} \sigma \quad (7)$$

Thus, if a micromechanical model for the damage dependent stiffnesses has been derived, the energy release rate may easily be determined from eq.(6) or eq.(7).

If a micromechanical model has been developed for determination of laminate stiffness, it is generally possible also to derive expressions for alternative initiation and growth parameters  $\psi_i$ . In the case of energy release rate as the controlling parameter, explicit expressions are given in eqs. (6, 7). A more difficult task is to determine which loading parameter that actually controls damage initiation and growth. To be generally applicable, the damage evo-

lution law should only depend on the material and not on geometry such as ply thickness, laminate layup, etc. In the case of matrix cracking it seems that an energy release rate approach is relevant for moderately small ply thicknesses, but for larger ply thicknesses a stress or strain criterion is better suited.

### 3 TRANSVERSE MATRIX CRACKING

As an example of a micromechanically based damage dependent constitutive model, the case of transverse matrix cracking without fibre fractures, fibre/matrix debonding and local delaminations is considered. Adolfsson & Gudmundson (1997) have recently developed an analytic model that can predict the laminate stiffness matrix to a good accuracy for arbitrary layup configurations and matrix crack distributions. In Figure 1, predictions of bending stiffnesses are compared to unit cell finite element calculations for a [90,-55,0<sub>2</sub>,-55<sub>2</sub>,90,55<sub>2</sub>,0] carbon fibre reinforced composite laminate containing cracks in all plies. A range of laminate layup configurations and transverse crack densities were considered by Adolfsson & Gudmundson (1997) and it was found that the analytic model to a good accuracy could predict the thermoelastic properties of laminates containing transverse cracks. The principal structure of a periodic unit cell used in the finite ele-

ment calculations is shown in Figure 2.

If it is assumed that the energy release rate controls the initiation and growth of matrix cracking, it can simply be estimated from eqs. (6) or (7) and the constitutive model is defined in eqs. (3-5) with  $\psi_i$  interpreted as  $G_i$  and  $\psi_{ic}$  as the critical energy release rate  $G_c$ .

In order to verify the analytic model for stiffness prediction in tension and bending for various laminate layups and to investigate relevant matrix crack initiation and growth criteria an experimental program on glass fibre reinforced epoxy laminates was conducted by Adolfsson (1996). For the particular composite material investigated, it turned out that the energy release rate was not a proper criterion, since it did not give consistent results at varying ply thicknesses. More consistent values were obtained if the laminate strain normal to the matrix cracks was used as a criterion, see Figure 3. A criterion based on laminate strain fits into the general description in eqs. (3-5). Simulations of the stress-strain behaviour using eqs. (3-5) based on a strain criterion according to the curve fit in Figure 3 are compared to experimental data in Figure 4.

In the literature, several investigations have shown that the strain necessary to initiate matrix cracking generally is dependent on the ply thickness, see for example Parviz et al. (1978), Bailey et al. (1978). For ply thicknesses larger than a material dependent transition thickness, the critical strain is almost con-

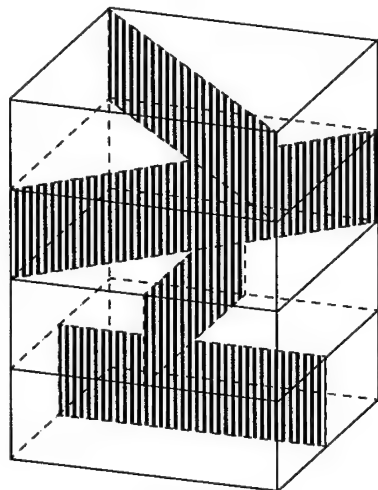


Figure 2. Example of a periodic unit cell used in the finite element calculations (Adolfsson & Gudmundson 1997). The shaded parts denote transverse matrix cracks.

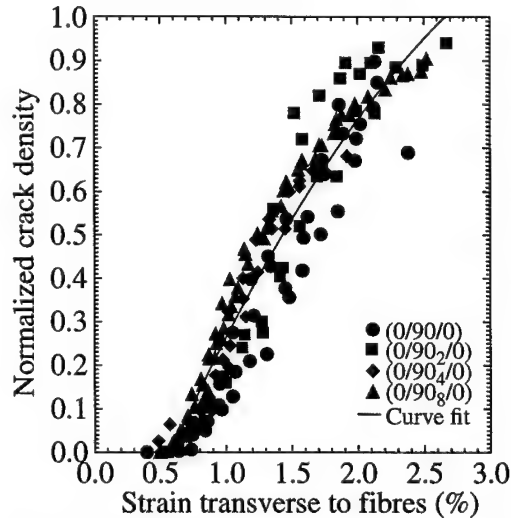


Figure 3. Normalized crack density versus laminate strain transverse to the fibres for GFRP cross ply laminates of varying ply thicknesses (Adolfsson 1996).

stant but for smaller ply thicknesses the critical strain increases with decreasing ply thickness. An interpretation of the results by Adolfsson (1996) would then be that the investigated ply thicknesses were larger than the transition thickness. The transition between large and small ply thicknesses may be explained by the concept of initial flaws, see for example Wang & Crossman (1980). If the critical flaw size is smaller than the ply thickness, then the critical strain will be independent on ply thickness. In case the critical flaw size is larger than the ply thickness, the flaw is prevented to grow due to the small ply thickness and the stress necessary to initiate unstable growth of the crack will be larger. Arguments based on linear elastic fracture mechanics will then predict a critical strain which is inversely proportional to the square root of the ply thickness.

#### 4 DISCUSSION

The energy release rate criterion discussed above for transverse matrix cracking is based on concepts of linear elastic fracture mechanics. Hence, it is implicitly assumed that the fracture process zone is much smaller than other geometrical dimensions such as the ply thickness and that linear elastic conditions prevail outside this process zone. In reality one can expect that a zone of crack bridging is active in front of a growing transverse matrix crack. Several investigations have shown that a transverse crack is developed from microscopic fibre/matrix debonds or matrix cracks which under increased loading grow, coalesce and finally form a crack without bridging.

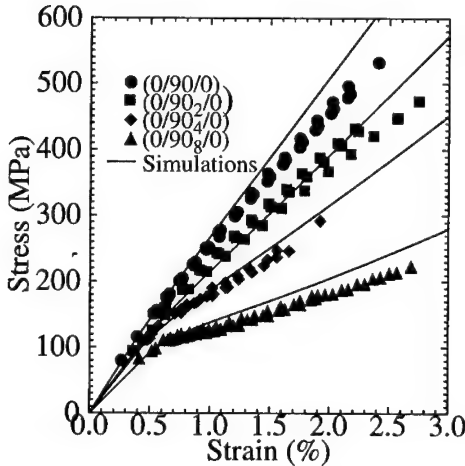


Figure 4. Predicted stress-strain behaviour for cross-ply laminates  $[0/90_n/0]$  ( $n = 1, 2, 3, 4$ ) and comparisons to experimental data (Adolfsson 1996).

When the crack has fully developed, its opening is generally of the order of fractions of the fibre diameter, say  $1-5 \mu\text{m}$ . This opening may be compared to the crack opening which can be predicted from linear elastic calculations. It may be shown that the average transverse crack opening  $u$  for a ply of thickness  $t$  under a macroscopic strain  $\epsilon$  is of the order

$$u \approx \epsilon t \quad (8)$$

For a strain of 1% and a ply thickness of  $125 \mu\text{m}$ , a crack opening of  $1-2 \mu\text{m}$  is predicted. It is observed that this opening is of the same order as that estimated for crack bridging. If also fibre bridging is considered, even larger crack openings are required to effectively release the bridging stresses.

Generally, there will be a minimum ply thickness which enables the crack to grow without bridging. An energy release rate criterion results in a critical strain which is inversely proportional to the square root of the ply thickness  $t$ . The resulting crack opening at the critical condition will then according to eq. (8) be proportional to  $\sqrt{t}$ , and for a sufficient small  $t$ , the opening will be less than that required to release crack bridging. A transverse crack initiation and growth criterion based on linear elastic energy release rate will hence not work for arbitrary small ply thicknesses.

It is here suggested that a model for transverse crack growth may be based on a cohesive zone description, which in a natural way gives a connection to linear elastic fracture mechanics. It is assumed that the stress  $\sigma_b$  necessary to open the crack can be

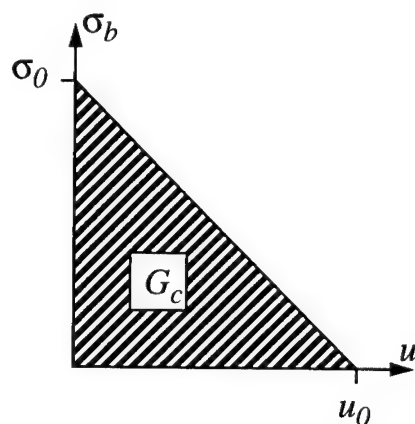


Figure 5. Simplified model of a bridging stresses in a cohesive zone.

determined as a function of crack opening  $u$ , say  $\sigma_b = \sigma_b(u)$ . Just as an example, a simplified relation as in Figure 5 can be considered. The crack opening  $u_0$  denotes the opening necessary to release the bridging stresses and the area under the curve can be interpreted as the critical energy release rate  $G_c$ ,

$$G_c = \frac{1}{2} u_0 \sigma_0 \quad (9)$$

A laminate with a transverse crack that has grown a distance  $L$  is now considered. If the energy balance for an assumed increase in crack length  $\Delta L$  is considered, it is possible to judge whether the crack growth is possible or not. Without going into details, it may be shown that the relation between the transverse stress  $\sigma_T$  far away from the crack and the crack opening displacement  $u$  may be written as:

$$\sigma_T = \frac{\alpha E_T}{t} u + \sigma_b(u) \quad (10)$$

where  $E_T$  denotes the transverse modulus,  $\sigma_b$  the bridging stress and  $\alpha$  a nondimensional constant of the order of one. The energy criterion for crack growth may then be formulated as:

$$\sigma_T(u) \cdot u \geq \int_0^u \sigma_T(u) du \quad (11)$$

Depending on the shape of  $\sigma_b(u)$ , different scenarios can be expected. If  $\sigma_b(u)$  is in the form of a Dirac delta function at  $u = 0$ , then the linear elastic fracture mechanics result is recovered for all ply thicknesses  $t$ . If  $\sigma_b(u)$  vanishes for  $u > u_0$ , then if

$$t \geq t_0 = \frac{\alpha E_T}{2 G_c} u_0^2 \quad (12)$$

the linear elastic result is again obtained. For  $t < t_0$  eq.(11) has to be further investigated. Considering the simplified cohesive law according to Figure 5, the criterion (12) is translated into  $\sigma_T = \sigma_0$ , which corresponds to a laminate strain of about  $\varepsilon = \sigma_0/E_T$ . Thus for thicknesses larger than  $t_0$  according to (12) the critical strain is inversely proportional to  $\sqrt{t}$  and for ply thicknesses smaller than  $t_0$  bridged cracks are expected over the whole specimen width at a strain of  $\varepsilon = \sigma_0/E_T$ . These observations can be summarized in Figure 6. Considering now the initial flaw concept which define another characteristic ply thickness and strain level, it can be expected that for certain materials there may be a very limited range in which the linear elastic fracture mechanics result is valid.

The concept of cohesive zones may also be applied to the simulation of growth of local delaminations, which develop in a similar way as transverse matrix cracks. This would open possibilities for a unified treatment of these two damage modes. Much remains however to be done in this area.

## 5 CONCLUSIONS

The structure of micromechanically based constitutive equations that govern damage evolution in composite laminates has been formulated. The large number of damage variables which may be active in a composite laminate makes the micromechanical approach difficult to apply in a general case. To be able to model more complex damage states, probably a combination of a continuum damage mechanics and a micromechanically based approach is the most fruitful way to go.

In case there are only a few damage modes active, the micromechanical approach is more feasible. The example of transverse matrix cracking discussed above shows that micromechanical models well can capture the stiffness changes due to transverse cracks. A more difficult task is however to determine a reliable criterion for initiation and growth of transverse cracks. As was shown in the discussion above, one can expect that methods based on linear fracture mechanics concepts will fail in certain cases. Methods based on nonlinear fracture mechanics has to be

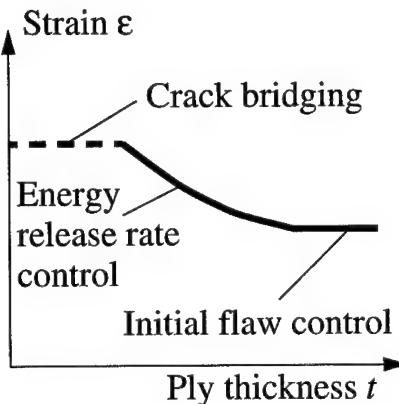


Figure 6. Critical strain as a function of ply thickness for initiation transverse cracking.

---

applied in these cases. A simplified approach based on a cohesive zone model was introduced in the discussion. This model includes as a special case linear fracture mechanics and it can capture effects of crack bridging. A cohesive zone model would also be suitable for the modelling of local delaminations, which basically develop in a similar way as transverse matrix cracks.

#### REFERENCES

- Aveston, J. & A. Kelly 1973. Theory of multiple fracture of fibrous composites. *J. Mater. Science* 8: 352-362.
- Adolfsson, E. & P. Gudmundson 1997. Thermoelastic properties in combined bending and extension of thin composite laminates with matrix cracks. *Int. J. Solids Structures* 34: 2035- 2060.
- Adolfsson, E. 1996. Matrix cracking in composite laminates. *Doctoral Dissertation*, Department of Solid Mechanics, Royal Institute of Technology, Stockholm, Sweden.
- Bailey, J.E., P.T. Curtis & A. Parvizi 1979. On the transverse cracking and longitudinal splitting behaviour of glass and carbon fibre reinforced epoxy cross ply laminates and the effect of Poisson and thermally generated strain. *Proc. R. Soc. Lond.* A366: 599-623.
- Hashin, Z. 1996. Finite thermoelastic fracture criterion with application to laminate cracking analysis. *J. Mech. Phys. Solids* 44: 1129-1145.
- Nairn, J.A. 1989. The strain energy release rate of composite microcracking: A variational approach. *J. Composite Materials* 23: 1106-1129.
- Parvizi, A., K.W. Garrett & J.E. Bailey 1978. Constrained cracking in glass fibre-reinforced epoxy cross-ply laminates. *J. Mater. Science* 13: 195-201.
- Talreja, R. 1994. Damage characterization by internal variables. In R. Talreja (ed.), *Damage Mechanics of Composite Materials*: 53-78. Netherlands: Elsevier Science.
- Wang, A.S.D. & F.W. Crossman 1980. Initiation and growth of transverse cracks and delamination in composite laminates. Part 1. An energy method. *J. Composite Materials Supplement* 14: 71-87.
- Xia, Z.C., R.R. Carr & J.W. Hutchinson 1993. Transverse cracking in fiber-reinforced brittle matrix, cross-ply laminates. *Acta Metall. Mater.* 41: 2365-2376.

---

Technical posters

## A predictive method for the nonlinear viscoelastic characterization of carbon/epoxy fibre composites

G.C. Papanicolaou & S.P. Zaoutsos

*Composite Materials Group, Mechanical and Aeronautical Engineering Department, University of Patras, Greece*

**ABSTRACT:** In the present work, a method for the characterization of the nonlinear viscoelastic response of a UD/90° carbon/epoxy composite is presented. Based on the characteristic creep-recovery response of the material, both analytical and numerical expressions for the nonlinear parameters included in the Schapery's constitutive thermodynamic equation were developed. The viscoplastic response developed during creep is also taken into account. For the full viscoelastic characterization of the material under consideration, creep-recovery tests at different applied stress levels were conducted. A generic function for the prediction of the variation of all the four parameters with the applied stress was developed. A minimum number of experimental data for the prediction of the nonlinear parameters is needed.

### 1 INTRODUCTION

Fiber reinforced composites have received much attention during the last decades as their use as structural parts increases rapidly in a wide spectrum of engineering applications. Although their excellent mechanical properties are advantageous in comparison to conventional materials, these properties are strongly time dependent and their evolution as design tools has to be taken into account. The long-term mechanical degradation of these materials is affected by the above-mentioned time-dependent behavior they exhibit under mechanical and/or environmental conditions and which is due to the viscoelastic nature of the polymer matrix. This behavior becomes more complex due to the nonlinearity that occurs under high loading conditions. Thus, although the linear viscoelastic principles are quite useful for preliminary design purposes, the nonlinear effect has to be taken into consideration too. Efforts for modeling this behavior have led to a certain number of representations most of them based on multiple (Green & Rivlin 1957, Pipkin & Rogers 1968) or single integral approaches where the nonlinearity is expressed by functionals or nonlinear factors.

Due to its simplicity in application and accuracy of results in a wide range of composite systems special attention has been given in Schapery's single integral formulation (Schapery 1966, 1968, 1969) by a number of researchers (Mohan & Adams 1985, Howard & Hollaway 1987, Walrath 1991). In

comparison (Smart & Williams 1972) to other formulations as those of Leederman (1943) or BKZ theory (Bernstein et al. 1963), Schapery's single integral formulation gives in many cases more accurate results while it can be used satisfactory to complex stress histories (Tuttle et al. 1993).

In the current investigation, the nonlinear viscoelastic behavior of a unidirectional carbon fibre-reinforced polymer composite is studied. Schapery's nonlinear formulation is used for the description of the nonlinearity occurring in the viscoelastic response of a unidirectional carbon/epoxy composite. Based on a modified Schapery's constitutive relation a new data reduction method for the determination of the nonlinear parameters has been developed. The method takes into account the viscoplastic response of the material through an additional term introduced in the model formulation. According to this method, the viscoelastic parameters  $g_0$ ,  $g_1$ ,  $g_2$  were analytically estimated while a numerical procedure has been applied for the determination of the shift factor  $a_s$ .

Apart from the method, a generic function for the prediction of all the four parameters is also presented. For the experimental evaluation of both the proposed method and the generic function predictions, creep-recovery tests under different stress levels were performed. Useful conclusions for the applicability of the method and the long term viscoelastic characterization of the material have been extracted.

## 2 THEORETICAL BACKGROUND

Boltzmann, based on the linear stress-strain behavior, suggested a single integral formulation, for the linear viscoelastic strain response:

$$\varepsilon(t) = D_0 \sigma_0 + \int_0^t \Delta D(t-\tau) \frac{d\sigma}{d\tau} d\tau \quad (1)$$

where  $D_0$  and  $\Delta D(t)$  is the instantaneous and transient compliance value respectively.

The nonlinear viscoelastic response can be described by means of the Schapery's nonlinear principle, which under constant stress and temperature conditions can be expressed as :

$$\varepsilon(t) = g_0 D_0 \sigma_0 + g_1 \int_0^t \Delta D(\psi - \psi') \frac{d(g_2 \sigma_0)}{d\tau} d\tau \quad (2)$$

where  $D_0$  and  $\Delta D(\psi)$  are the instantaneous and transient creep compliance components respectively, while  $\psi$  and  $\psi'$  are the so-called "reduced" times defined as:

$$\psi = \int_0^t \frac{dt'}{\alpha_\sigma} \quad \text{and} \quad \psi' = \psi(\tau) = \int_0^\tau \frac{dt'}{\alpha_\sigma}$$

and  $g_0, g_1, g_2, \alpha_\sigma$  are time independent, but stress dependent nonlinear parameters.

For the description of the viscoplastic creep strain component, a viscoplastic term,  $\varepsilon_{vp}$ , can also be introduced into the above constitutive equation, so that:

$$\varepsilon(t) = g_0 D_0 \sigma_0 + g_1 \int_0^t \Delta D(\psi - \psi') \frac{d(g_2 \sigma_0)}{d\tau} d\tau + \varepsilon_{vp}(t) \quad (3)$$

By applying a unit step stress history to the above formulation, we obtain for the creep and the creep-recovery response respectively:

$$\varepsilon_c(t) = g_0 D_0 \sigma_0 + g_1 g_2 \Delta D \left( \frac{t}{a_\sigma} \right) \sigma_0 + \varepsilon_{vp}(t), \text{ for } 0 < t < t_a \quad (4)$$

$$\varepsilon_r(t) = \left[ \Delta D \left( \frac{t_a}{a_\sigma} + t - t_a \right) - \Delta D(t - t_a) \right] g_2 \sigma_0 + \varepsilon_{vp}(t_a^+), \text{ for } t > t_a \quad (5)$$

Next, if we assume that the compliance of the material follows a power law of time i.e.  $\Delta D(t) = C * t^n$  then eq. (5) can also be rewritten as :

$$\varepsilon_r(t) = \frac{\Delta \varepsilon_c}{g_1} \left[ (1 + a_\sigma \lambda)^n - (a_\sigma \lambda)^n \right] + \varepsilon_{vp}(t_a^+) \quad \text{for } t > t_a \quad (6)$$

where  $\lambda = \frac{t - t_a}{t_a}$ , is the nondimensional time and

$\Delta \varepsilon_c$  is the amount of transient strain accumulated during creep :

$$\Delta \varepsilon_c = g_1 g_2 C \left( \frac{t_a}{a_\sigma} \right)^n \sigma_0 + \varepsilon_{vp}(t_a) \quad (7)$$

In the linear viscoelastic case, where  $g_0=g_1=g_2=a_\sigma=1$ , equation (6) takes the form :

$$\varepsilon_r(t) = \Delta \varepsilon_c \left[ (1 + \lambda)^n - (\lambda)^n \right] \quad (8)$$

## 3 THE PROPOSED DATA REDUCTION METHOD

At  $t = t_a^-$  (Fig. 1), which is the time just before the unloading in the creep-recovery test, the pure viscoelastic part of  $\Delta \varepsilon_c$  can be given from Eq. (5) as :

$$\Delta \varepsilon_c(t_a^-) - \varepsilon_{vp}(t_a^-) = g_1 g_2 \Delta D \left( \frac{t_a^-}{a_\sigma} \right) \sigma_0 \quad (9)$$

Similarly, the recovery response at  $t = t_a^+$ , i.e. just after unloading, can be given by Eq. (6) as :

$$\varepsilon_r(t_a^+) = g_2 \Delta D \left( \frac{t_a^+}{a_\sigma} \right) \sigma_0 + \varepsilon_{vp}(t_a^+) \quad (10)$$

It is worth to notice that, for perfect linear viscoelastic behavior, the instantaneous strain response at  $t=0^+$  is equal to the instantaneous strain jump at  $t = t_a^+$  (Fig. 1). However, in the nonlinear case these two responses are not equal. This is a significant point which enables us to study in a more detail manner the sudden material responses at the moments of instantaneous loading and unloading respectively.

Thus, if  $\Delta \varepsilon_0$  is the difference between the two responses corresponding to the time of the instantaneous unloading ( $t = t_a^+$ ) and the time of the instantaneous loading ( $t = 0^+$ ) respectively, then we obtain :

$$\Delta \varepsilon_0 = \varepsilon_{0r} - \varepsilon_{0c} \quad (11)$$

where  $\varepsilon_{0r}$  and  $\varepsilon_{0c}$  can be given by Eqs. (10) and (4) respectively, as :

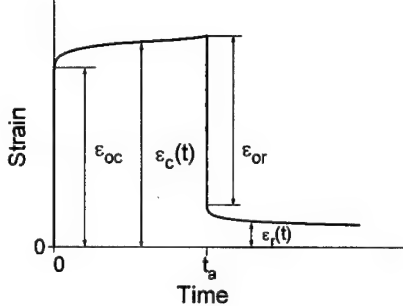


Figure 1. A typical creep - recovery curve.

$$\varepsilon_{0r} = \varepsilon_c(t_a^-) - \varepsilon_r(t_a^+) = \varepsilon_c(t_a^-) - g_2 \Delta D \left( \frac{t_a^+}{a_\sigma} \right) \sigma_0 - \varepsilon_{vp}(t_a^+) \quad (12)$$

$$\varepsilon_{0c} = g_0 D_0 \sigma_0 = \varepsilon_c(t_a^-) - g_1 g_2 \Delta D \left( \frac{t_a^-}{a_\sigma} \right) \sigma_0 - \varepsilon_{vp}(t_a^-) \quad (13)$$

Substitution of Eq. (12) and (13) into Eq. (11) and taking into consideration that  $\varepsilon_{vp}(t_a^+) = \varepsilon_{vp}(t_a^-) = \varepsilon_{vp}(t_a)$ , yields to :

$$\Delta \varepsilon_0 = g_2(g_1 - 1) \Delta D \left( \frac{t_a}{a_\sigma} \right) \sigma_0 \quad (14)$$

Then partial division of Eq. (9) and (14) results in:

$$g_1 = \frac{\Delta \varepsilon_c - \varepsilon_{vp}}{\Delta \varepsilon_c - \Delta \varepsilon_0 - \varepsilon_{vp}} \quad (15)$$

The obvious significance of Eq. (15) comes from the fact that the nonlinear parameter  $g_1$  can be easily calculated, as the values of  $\Delta \varepsilon_0$ ,  $\Delta \varepsilon_c$  and  $\varepsilon_{vp}$  can be experimentally measured from the creep/recovery test.

It is also obvious that the parameter  $g_0$ , which indicates the nonlinear elastic response  $\varepsilon(0^+)$  due to the instantaneous application of the given load at  $t=0^+$ , can be determined from the initial experimental values of the strain response of the material. In other words, the ratio of the value of the instantaneous compliance of the system in the linear viscoelastic case (i.e. at very low applied stress level) over the value of the instantaneous compliance in the nonlinear case (i.e. at high stress level) provides the value of  $g_0$ .

Having analytically determined the values of  $g_0$  and  $g_1$ , while  $\Delta \varepsilon_c$  and  $\varepsilon_{vp}$  can also be experimentally

measured, the value of  $a_\sigma$  can be found by means of a numerical fitting of Eq. (6) to the experimentally found  $\varepsilon_r(t)$  values.

Next, assuming that the transient compliance  $\Delta D(t)$  is expressed as  $\Delta D(t) = C * t^n$ , then the analytical expression given by Eq.(14), can be written as :

$$\Delta \varepsilon_{0(nl)} = g_2(g_1 - 1) C \left( \frac{t_a}{a_\sigma} \right)^n \sigma_{0(nl)} \quad (16)$$

It is also obvious that the pure viscoelastic response can be written as:

$$\Delta \varepsilon_{c(l)} = C t_a^n \sigma_{0(l)} \quad (17)$$

where indices 1 and nl, stand for the linear and nonlinear viscoelastic response, respectively.

Dividing Eq. (16) and (17), and then solving for  $g_2$ , we obtain:

$$g_2 = \frac{\Delta \varepsilon_{0(nl)}}{\Delta \varepsilon_{c(l)}} \frac{a_\sigma^n}{(g_1 - 1)} \frac{\sigma_{0(l)}}{\sigma_{0(nl)}} \quad (18)$$

Since the values of  $\Delta \varepsilon_{0(nl)}$  and  $\Delta \varepsilon_{c(l)}$  can experimentally be measured from two creep-recovery tests, one at high stress level (nonlinear viscoelastic behaviour) and the other at low stress level (linear viscoelastic behaviour) respectively, then knowing the applied stresses  $\sigma_{0(l)}$ ,  $\sigma_{0(nl)}$ , while the values of  $a_\sigma$  and  $g_1$  have already been determined using the techniques presented in the previous section, the value of  $g_2$  can be easily determined.

In summary, in order to estimate the four nonlinear parameters, the following steps can be followed:

- I. The ratio of the value of the instantaneous compliance of the system in the linear viscoelastic case (i.e. at very low applied stress level) over the value of the instantaneous compliance in the nonlinear case (i.e. at high stress level) provides the value of  $g_0$ .
- II. Using experimental data in combination with Eq. (15) the analytical estimation of  $g_1$  can be performed.
- III. Eq. (8), is numerically curve fitted to the linear recovery data and the value of the n exponent is determined.
- IV. Eq. (6) is numerically curve fitted to the recovery test data and the value of  $a_\sigma$  is determined.

V. Knowing the values of  $a_G$  and  $g_1$ , the value of  $g_2$  is analytically estimated using Eq. (18).

#### 4 MODELLING THE STRESS VARIATION OF THE NONLINEAR PARAMETERS

A generic function for the prediction under isothermal conditions of all the four nonlinear parameters is developed.

It is clear that for the linear viscoelastic response, the values of the non-linear parameters are equal to unity.

For the application of the generic function, the critical value,  $\sigma_{cr}$  (stress threshold), of the stress at which the material response passes from the linear to the non-linear one, is of great importance. In the present study, and for constant temperature conditions, it is assumed that any of the four nonlinear parameters, denoted as  $G$ , can be expressed as a function of the applied stress  $\sigma$ , the tensile strength,  $\sigma_u$ , and the critical stress value,  $\sigma_{cr}$ . Then,

$$G = F\{\sigma, \sigma_u, \sigma_{cr}\} \quad (19)$$

It is evident that for applied stresses higher than  $\sigma_{cr}$ ,  $G$  must be a monotonically increasing or decreasing function of the applied stress. Then, the following two limiting conditions can be considered :

$$G = 1 \quad \text{for} \quad \sigma_{min} = \sigma_{cr}$$

and

$$\lim_{\sigma \rightarrow \sigma_u} G = K_G \quad \text{for} \quad \sigma_{max} = \sigma_u$$

From the creep curve it is evident that the nonlinearity developed depends on the applied stress following an exponential mode of variation. A similar type of behaviour has also been observed by Leaderman (1943).

The deviation of  $g_0$  and  $g_2$  values from unity with increasing applied stress represent a physical transition state of the material i.e. material softening or hardening with stress. Also, experimental results showed a nonlinear increase of  $g_1$  with applied stress.

Based on the above-mentioned observations, the following generic function for the prediction of any of the four nonlinear parameters has been introduced:

$$G = \begin{cases} 1 & \text{for } \sigma \leq \sigma_{cr} \\ \frac{1 - K_G}{1 + \frac{x - \lambda}{1 - x} e^{\left(\frac{x - \lambda}{1 - x}\right)}} + K_G & \text{for } \sigma \geq \sigma_{cr} \end{cases} \quad (20)$$

where  $x = \frac{\sigma}{\sigma_u}$ ,  $\lambda = \frac{\sigma_{cr}}{\sigma_u}$ ,  $\sigma_u$  is the ultimate tensile strength measured at high strain rate,  $\sigma_{cr}$  is the critical stress threshold for the linear - nonlinear viscoelastic transition and  $K_G$  is the  $G$  limiting value when  $\sigma$  tends to  $\sigma_u$ .

#### 5 EXPERIMENTAL PROCEDURE AND LOADING PROGRAM

All the experiments in the present investigation as well as the manufacturing of the specimens were conducted by the first author in the Department of Mechanics of Materials and Structures of the Free University of Brussels (VUB) within the frame of a scientific co-operation.

Creep-recovery data were obtained on a 90 degrees Carbon-Epoxy composite. Standard prepreg types FIBREDUX-920C-TS-5-42 with nominal weight 0.231 (Kg/m<sup>2</sup>) were used. 12 layers carbon-epoxy unidirectional composite plates were fabricated using the hand lay-up technique. All plates were cured in a SCHOLTZ autoclave following the standard curing cycle proposed by CIBA-GEIGY consisted of a 300 kN/m<sup>2</sup> pressure and a curing temperature of 125 °C for 120 minutes applied to the plates in the autoclave.

Laminate specimens were postcured in an air oven at about 120°C for 3h and then slowly cooled in the oven.

Transverse straight-sided specimens were cut from the unidirectional plates, using a diamond wheel saw. The nominal size of each specimen was 300mm long, 17mm wide, and 1.75mm thick. All specimens were tabbed using LEXAN tabbing material. The nominal size of each end tab was 50mm long, 17mm wide and 2 mm thick.

Two Micromeasurement EA-13-240LZ-120 and CEA-13-240UZ-120 strain gauges were mounted back to back on the center of each specimen along the loading direction by using M-Bond 610 adhesive. Specimens were wired and set in the creep frame at least for 12 hours prior loading. All tests were conducted at 20°C using a four-station dead load creep frame. The loading mode consisted of 168 h of tensile creep at constant stress level,  $\sigma_0$ , followed by 168 h of recovery. Six levels of load below tensile failure strength, namely 30%, 40%, 50%, 55%, 60% and 70% of the tensile failure stress,  $\sigma_{cr}$ , were

applied and the variation of strain was recorded versus time. In all cases the load was applied and removed gradually over a very short time span of the order of 3s, which was quite short compared with the whole creep testing period of 168 h. To achieve this, an oil pump was used to apply and remove the load. Both short-term tensile elastic modulus and ultimate tensile strength tests were performed for five specimens using an Instron tensile testing machine. Strains were measured with electrical resistance foil gauges bonded to the specimens. A displacement rate of 1mm/s was used for all tests. The fibre volume fraction was established from loss of ignition tests.

## 6 RESULTS AND DISCUSSION

The creep and the recovery response of the carbon/epoxy system for different stress levels is illustrated in Figures 2 and 3 respectively.

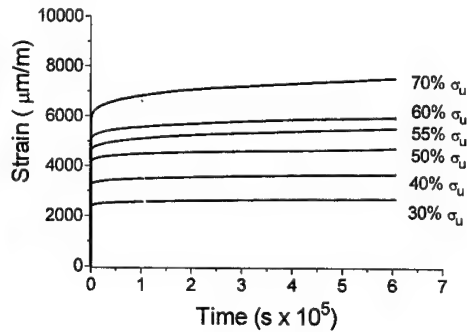


Figure 2. The creep response of the carbon-epoxy composite at different applied stress levels.

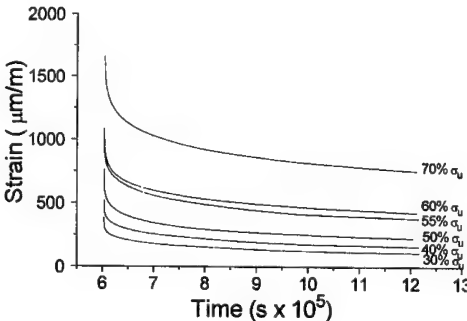


Figure 3. The recovery response of the carbon epoxy for different stress levels.

As it can be seen from Figure 4, a nonlinear viscoelastic behavior is observed for stress values higher than 30% of the ultimate tensile strength,  $\sigma_u$ . The same observation can also be derived from the isochronous curves shown in Figure 5.

As the main target of the present investigation is the determination of the nonlinear parameters included in Schapery's model, the viscoplastic response was taken into account through the viscoplastic strain term introduced in Eqs. (3), (4) and (5). The value of this term was experimentally recorded in order to be taken into account.

Next, following the steps already described, the separate estimation of each of the nonlinear parameters  $g_0$ ,  $g_1$ ,  $a_g$  and  $g_2$  was performed.

Experimentally obtained and fitted recovery curves for three different applied creep stress levels are shown in Figure 6.

Prior to this step, as shown in Figure 7, the value of the  $n$  exponent was determined by means of a

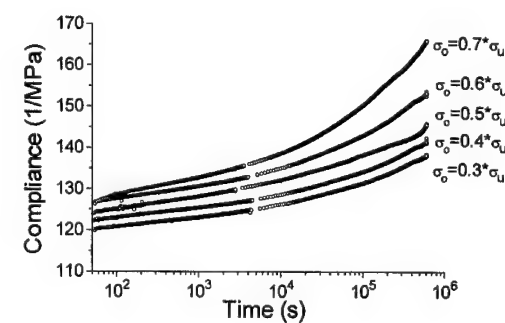


Figure 4. Compliance versus time for different applied stress levels

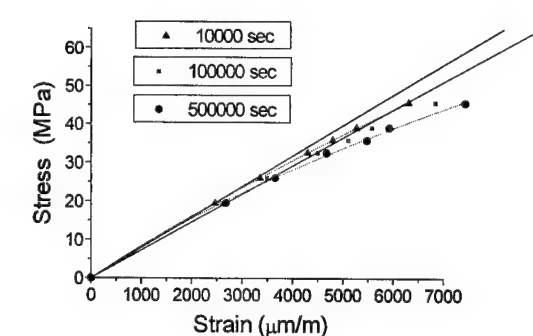


Figure 5. Isochronous curves for the carbon/epoxy system under consideration.

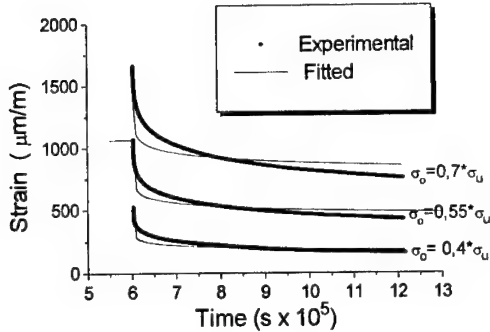


Figure 6. Experimentally obtained 168h recovery response and respective fitted curves for the carbon/epoxy system and for three different applied creep stress levels.

curve fitting procedure applied to experimentally obtained recovery data.

Although earlier investigations (Hiel 1983) have shown that  $n$ , being sensitive on creep duration, is the most sensitive factor in introducing errors in the predicted values of viscoelastic response, in the present investigation the value of  $n$  as calculated from both Eq.(8) and after successive curve fitting procedures applied to different recovery time intervals, as shown in Figure 8, was found in all cases constant having a value of 0.091143. Thus, no sensitivity from the recovery duration was found.

The estimated values of each of the nonlinear parameters at the respective applied stress level, are given in Table I.

Next, concerning the proposed generic function used to model the nonlinear parameters as a function of stress, all terms included in it have a clear physical meaning, while the values predicted by the function

Table-I. The values of the nonlinear factors  $g_0$ ,  $g_1$ ,  $g_2$  and  $\alpha_\sigma$ , for different applied stress levels.

Applied Stress (MPa)	(%) of rupture Stress	$g_0$	$g_1$	$\alpha_\sigma$	$g_2$
19.50	30	1.000	1.000	1.000	1.000
26.00	40	0.972	1.389	0.927	1.040
32.50	50	0.954	1.504	0.816	1.228
35.75	55	0.923	1.834	0.570	1.279
39.00	60	0.904	1.970	0.424	1.269
45.50	70	0.870	2.280	0.389	1.378

are in good agreement with the respective ones as they have estimated by means of the method proposed and already presented.

Both the ultimate tensile strength,  $\sigma_u$ , and the critical nonlinear viscoelastic stress threshold  $\sigma_{cr}$ , are known physical stress variables, easy to identify, the former through short term tensile tests and the latter from simple creep tensile tests.

Plots for each of the four nonlinear parameters against applied stress, as they have been derived from both the proposed method and the generic function, are shown in Figure 9. As one can see, a fair agreement between calculated and predicted values is observed.

## 7 CONCLUSIONS

In the present investigation a method for the full nonlinear viscoelastic characterization of a  $90^0$  carbon/epoxy composite system is presented. The method, using a minimum number of experiments, is able to determine the nonlinear parameters included in the well known Schapery's formulation.

Next, a generic function, with a clear physical meaning, for the prediction of the stress dependence of the nonlinear parameters is proposed. A fair agreement between calculated by the method and predicted from the generic function values of the nonlinear parameters was found.

## ACKNOWLEDGEMENTS

The scientific and technical help of COSARGUB of the Free University of Brussels is gratefully acknowledged. Special thanks are also given to Professor Albert H. Cardon for his assistance and useful advises.

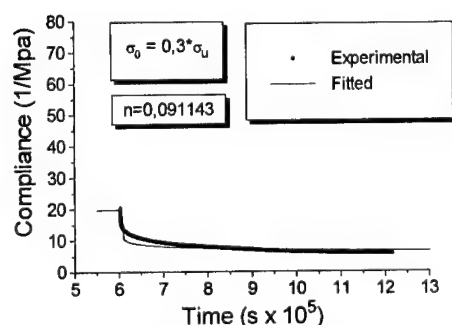


Figure 7. Derivation of the  $n$ -value by means of a curve fitting procedure.

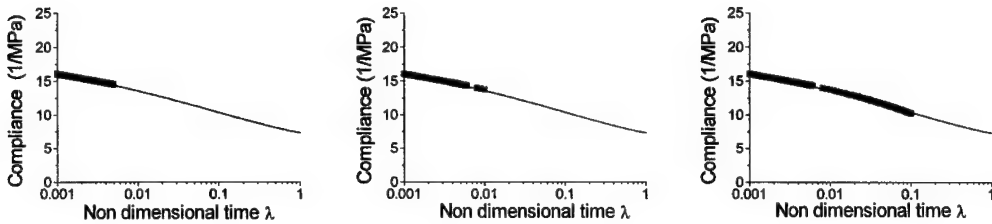


Figure 8. Successive curve fitting procedures applied to different recovery time intervals for the evaluation of the exponent, n.

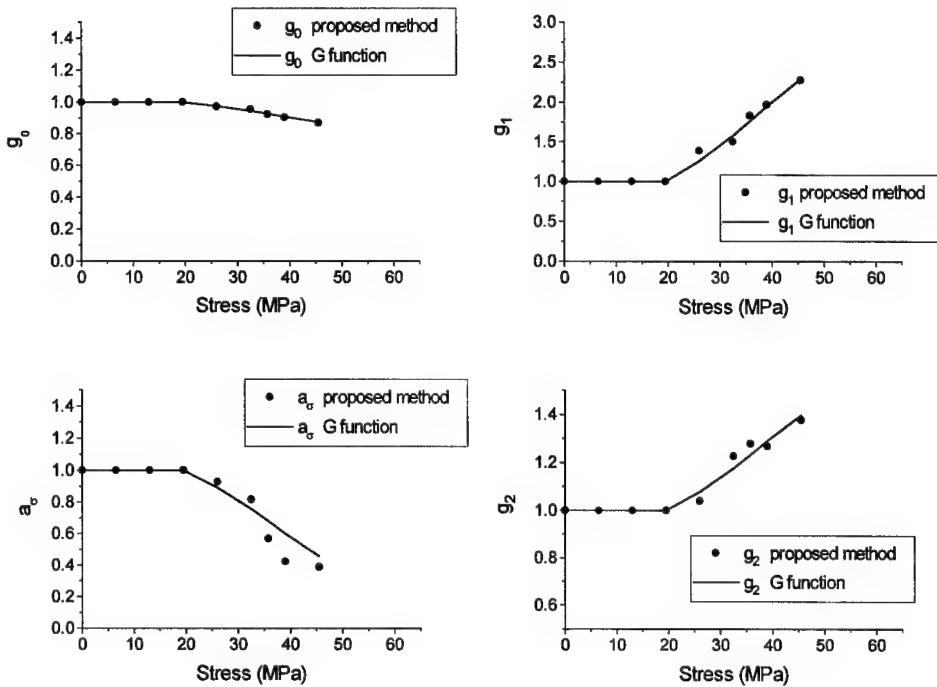


Figure 9. Plots for each of the four nonlinear parameters against applied stress, as they have been derived from both the proposed method and the generic function

## REFERENCES

- Bernstein, B., E.A. Kearsley & L.J. Zapas 1963. A Study of Stress Relaxation with Finite strain. *Trans. Soc. Rheol.* 7:391.
- Green, A.E. & R.S. Rivlin 1957. The Mechanics of Nonlinear Materials with Memory. *Arch. Ration. Mech. Anal.* 1(1):1-21.
- Hiel, C.C. 1983. *The Nonlinear Viscoelastic Response of Resin Matrix Composites*. Ph.D.Thesis, Vrije Universiteit Brussel, Brussel, Belgium.
- Howard, M. & L. Hollaway 1987. The characterization of the nonlinear viscoelastic properties of a randomly orientated fibre/matrix composite. *Composites*. 18(4):317-323.
- Leaderman, H. 1943. *Elastic and Creep Properties of Filamentous Materials and Other High Polymers*. Textile Foundation, Washington, D.C.
- Mohan, R. & D.F. Adams 1985. "Nonlinear Creep-Recovery Response of a Polymer Matrix and its Composites", *Experimental Mechanics*. 25(3):262-271.

- 
- Pipkin,A.C. & T.G. Rogers 1968. A Nonlinear Integral Representation for Viscoelastic Behavior. *J. Mech. Phys. Solids.* 16: 59-72.
- Schapery, R.A. 1966. A Theory of Nonlinear Thermo-viscoelasticity Based on Irreversible Thermodynamics. *Proc. 5th. U.S. Nat. Cong. Appl. Mech.* New York: ASME, 511-530.
- Schapery, R.A. 1968. On a Thermodynamic Constitutive Theory and It's Application to Various Nonlinear Materials. *Proc. UITAM symp. on Thermoelasticity*, New York: 259-284.
- Schapery, R.A. 1969. On the Characterization of Nonlinear Viscoelastic Materials. *Polymer Eng. Sci.* 9:295-310.
- Smart, J. & J.G. Williams 1972. A comparison of Single Integral Nonlinear Viscoelasticity Theories. *J. Mech. Phys. Solids.* 20:313-324.
- Tuttle, M.E., A. Pasricha & A.F. Emery 1993. Time Dependent Behaviour of IM7/5260 Composites Subjected to Cyclic Loads and Temperatures. *ASME Mechanics of Composite Materials : Nonlinear Effects.* 159:343-357.
- Walrath, E. 1991. Viscoelastic Response of a Unidirectional Composite Containing Two Viscoelastic Constituents. *Experimental Mechanics.* 31(2):111-117.

## Time-dependent behaviour of T300/5208 under creep, relaxation and ramp loading

Rui Miranda Guedes & António Torres Marques

*Faculty of Engineering (FEUP), University of Porto (UP), Portugal*

Albert Cardon

*Faculty of Engineering (TW), Free University of Brussels (VUB), Belgium*

**ABSTRACT:** An investigation of the effect of time-dependent behaviour for various stress and strain histories was done for the T300/5208 composite. It is shown that Schapery's non-linear theory integrated with a viscoplastic model allows to predict for long-term cyclic mechanical loading, ramp loading with constant strain rate and multiple-step relaxation. Material constants associated with constitutive models were determined. The results were combined with a recursive numerical procedure to handle the hereditary effects and to predict the time-dependent behaviour of the composite.

### 1 INTRODUCTION

Edward Wu (1982, 1983a, 1983b) published experimental data for the T300/5208 composite under creep/creep-recovery and ramp loading, so it became accessible to the technical community. The aim of that program was to provide a data base that could be used to characterise overall matrix-dominated time-dependent deformation and time-dependent strength. The specimens were ±45° laminates tested in tension.

The nonlinear viscoelastic model developed by Schapery was selected to study the time dependent behaviour of composite. The material properties were obtained through the creep/creep-recovery data at four different shear stress levels of 22.15, 32.30, 43.60 and 48.95 MPa. Along with the viscoelastic behaviour, we observed a viscoplastic behaviour well modelled by the viscoplastic functional employed by Zapas and Crissman (1984) and later by Tuttle (1995). The linear viscoelastic compliance was modelled by an exponential Prony series expansion. The calculation of the unrecoverable strain, i.e. viscoplastic strain, was accomplished by extrapolation of the series expansion.

Comparisons for the multi-step loading with the predictions from the previous model were made.

Findley (1989) described the relation between creep and stress relaxation for uniaxial nonlinear viscoelasticity, discussing the principles and a method for the interconversion. From those principles a method for the interconversion was developed and applied to the Schapery constitutive relations. Comparisons were made with the direct measured relaxation data.

For the ramp loading tests, where the shear strain rate was imposed, comparisons with predictions were made for the shear stress,  $\tau_{12}$ , and shear plastic

strain,  $\gamma_{12}^{\text{plastic}}$ . The shear plastic strain was calculated as

$$\gamma_{12}^{\text{plastic}} = \gamma_{12} - \tau_{12} \cdot G \quad (1)$$

where  $G$  represents the initial modulus in the elastic region and  $\gamma_{12}$  the shear strain.

### 2 CONSTITUTIVE MODEL

The total strain associated with the matrix-dominated compliance  $S_{66}$  was modelled using the modified Schapery theory that includes a viscoplastic term given by the functional used by Zapas and Crissman. According to this approach the total shear strain  $\gamma_{12}(t)$  induced by an arbitrary shear stress  $\tau_{12}(t)$  is given by

$$\begin{aligned} \gamma_{12}(t) = & D_0 g_0 \tau_{12}(t) + \\ & g_1 \int_{-\infty}^t \Delta D(\psi - \psi') \frac{\partial(g_2 \tau_{12}(\xi))}{\partial \xi} d\xi + \quad (2) \\ & \left\{ C \int_{-\infty}^t [\tau_{12}(\psi)]^N d\psi \right\}^n \end{aligned}$$

where  $D_0$  is the shear elastic compliance,  $\Delta D(t)$  the shear linear creep compliance,  $\psi, \psi'$  reduced times given by

$$\psi = \int_0^t \frac{d\xi'}{a_D} \quad , \quad \psi' = \int_0^s \frac{d\xi'}{a_D} \quad (3)$$

where  $g_0$ ,  $g_1$ ,  $g_2$  and  $a_D$  are stress-dependent nonlinearizing parameters. The  $C$ ,  $N$  and  $n$  parameters are stress-independent but temperature-dependent material constants of the viscoplastic term. The shear linear compliance was modelled using the Prony's series since the exponential form was numerically advantageous

$$\Delta D(t) = \sum_{i=1}^m D_i \left( 1 - e^{-\frac{t}{\tau_i}} \right) \quad (4)$$

where  $D_i$ ,  $\tau_i$  are positive constants and  $\tau_i$  are called retardation times.

The first term on the right-hand side of Equation (2) represents the nonlinear elastic strains, the second term represents the nonlinear viscoelastic strains and the last one represents the nonlinear viscoplastic strains. When the applied stress is sufficiently small  $g_0 = g_1 = g_2 = a_D = 1$ , and Equation (2) reduces to the Boltzmann superposition integral for linear viscoelastic behaviour with a flow term. The  $a_D$  parameter can be assumed as a stress shift factor similar to the temperature shift factor  $a_T$  used in the time-temperature superposition principle. As Schapery (1969) referred the  $a_D$  coefficient is assumed to depend only on the stress. The only thermodynamic restriction is that this coefficient must be positive for stable materials.

The constitutive models described above were combined with the classical lamination theory to obtain predictions for general multi-angle laminates. The formulation was developed to solve all sort of problems related with creep, relaxation and rate dependent stress/strain behaviour for in-plane and flexural loads. The method was described in detail elsewhere (Guedes, 1997) and was developed as a FORTRAN computer program called LAMFLU.

### 3 MATERIAL PROPERTIES CALCULATION

The material properties were obtained through a series of creep/creep-recovery tests. The stress history in a creep/creep-recovery consists of a constant stress ( $\sigma_0$ ) applied during the creep phase followed by removing the total applied stress during the creep-recovery phase of the test. During creep time ( $0 \leq t \leq t_a$ ) the strain response is given by

$$\begin{aligned} \epsilon_{\text{creep}}(t) = & D_0 g_0 \sigma_0 + \\ & g_1 g_2 \sum_{i=1}^m D_i \left( 1 - e^{-\frac{t}{\tau_i a_D}} \right) \sigma_0 + \\ & \{C \sigma_0^N t\}^n \end{aligned} \quad (5)$$

During the recovery time ( $t > t_a$ ) the response is given by

$$\begin{aligned} \epsilon_{\text{recovery}}(t) = & g_2 \sum_{i=1}^m D_i \left[ e^{-\frac{t-t_a}{\tau_i}} \left( 1 - e^{-\frac{t_a}{\tau_i a_D}} \right) \right] \sigma_0 + \\ & \{C \sigma_0^N t_a\}^n \end{aligned} \quad (6)$$

Data collected from creep/creep-recovery tests at several stress levels in combination with a fully numerical procedure were used to obtained the materials properties.

In this method the problem was "linearized" by prescribing the  $\{\tau_i\}_{i=1,2,\dots,M}$  parameters. The first step is the estimation of the irrecoverable viscoplastic strain induced during creep at various stress levels. The recovery curves given by Equation (6) can be rewritten in the following compact form

$$\epsilon_{\text{recovery}}(t) = A_0 + \sum_{i=1}^m A_i e^{-\frac{t-t_a}{\tau_i}} \quad (7)$$

where  $A_0, A_i$  are parameters to be determine for each stress level. Equation (7) is numerically curve fit to the recovery data using one time constant per decade of time. From the previous formulation it is possible to extrapolate the recovery curves for very long times, calculating the limit

$$\lim_{t \rightarrow \infty} \epsilon_{\text{recovery}}(t) = A_0 = \{C \sigma_0^N t_a\}^n \quad (8)$$

The product  $N \cdot n$  is determined by curve fitting of Equation (8). From the lower stress level, assumed to be a linear level, the values of the linear viscoelastic compliance are determined using Equations (6) and (7) as

$$D_i = \frac{A_i}{\sigma_0 \left( 1 - e^{-\frac{t_a}{\tau_i}} \right)} \quad (9)$$

The nonlinear stress levels are then used to determine the parameters  $g_2$  and  $a_D$  as

$$A_i - g_2 \sigma_0 D_i \left( 1 - e^{-\frac{t_a}{a_D \tau_i}} \right) = 0 \quad (10)$$

The values for  $D_0$ ,  $C$  and  $n$  are evaluated by fitting Equation (6) to the linear recovery data. Finally the parameters  $g_0$  and  $g_1$  are evaluated by fitting Equation (5) to the nonlinear creep data.

The linear viscoelastic creep compliance and the viscoplastic flow are the only time-dependent material properties in the present model. Other material properties depend on the stress. Lou and Schapery (1971) have shown that the material properties can be expressed as functions of the octahedral shear stress in the matrix.

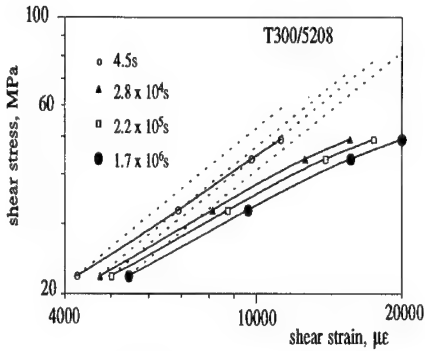


Figure 1. Isochronous stress-strain relation for  $[ \pm 45^\circ ]$  T300/5208.

### 3.1 Test of $[ \pm 45^\circ ]$ specimen

Tests were conducted at shear stress levels ranging from 22.15 MPa to 48.95 MPa. The static transverse tensile strength value for the T300/5208 laminate found in literature is around 68 MPa.

The linear viscoelastic limitation can be determined by examining the isochronous stress-strain plotted in Figure 1. The dashed lines correspond to the linear viscoelastic criterion at each instant. The creep behaviour of T300/5208 composite is highly nonlinear from the beginning of the test.

Shear direction compliance values:

$$D_0 = 0.18998 \times 10^{-3} \text{ MPa}^{-1}$$

$$D_1 = 0.82350 \times 10^{-5} \text{ MPa}^{-1} \quad \tau_1 = 0.05 \text{ hrs}$$

$$D_2 = 0.82390 \times 10^{-5} \text{ MPa}^{-1} \quad \tau_2 = 0.50 \text{ hrs}$$

$$D_3 = 0.11433 \times 10^{-4} \text{ MPa}^{-1} \quad \tau_3 = 5.00 \text{ hrs}$$

$$D_4 = 0.46191 \times 10^{-5} \text{ MPa}^{-1} \quad \tau_4 = 50.00 \text{ hrs}$$

$$D_5 = 0.22054 \times 10^{-4} \text{ MPa}^{-1} \quad \tau_5 = 500.00 \text{ hrs}$$

Nonlinear parameters:

$$\tau_c = 18.1883 \text{ MPa}$$

$$g_0 = 1.0 \quad \text{for } \tau_{\text{oct}} \leq \tau_c$$

$$g_0 = 1.0 + 0.10327 \times 10^{-1} (\tau_{\text{oct}} - \tau_c) \quad \text{for } \tau_{\text{oct}} > \tau_c$$

$$g_1 = 1.0 \quad \text{for } \tau_{\text{oct}} \leq \tau_c$$

$$g_1 = 1.0 + 0.97975 \times 10^{-2} (\tau_{\text{oct}} - \tau_c) \quad \text{for } \tau_{\text{oct}} > \tau_c$$

$$g_2 = 1.0 \quad \text{for } \tau_{\text{oct}} \leq \tau_c$$

$$g_2 = e^{-(\tau_{\text{oct}} - \tau_c)/23.087} \quad \text{for } \tau_{\text{oct}} > \tau_c$$

$$a_D = 1.0$$

Viscoplastic coefficients :

$$C^n = 0.87819 \times 10^{-10}$$

$$n = 0.4890$$

$$N = 7.3649$$

## 4 RESULTS

Predictions based on the time-dependent constitutive model in combination with the LAMFLU program have been compared with measurements obtained during different type of tests, cyclic creep/creep-recovery, multiple relaxation and constant strain rate tests.

### 4.1 Creep/Creep-Recovery

The T300/5208  $[ \pm 45^\circ ]$  laminates were subjected to cyclic creep/creep-recovery tests at room temperature. In Figures 2 and 3 the shear strain for the test data and the LAMFLU predictions are plotted together for four different tests. The specimens were tested for a total time of 10176 hours, representing approximately 14 months.

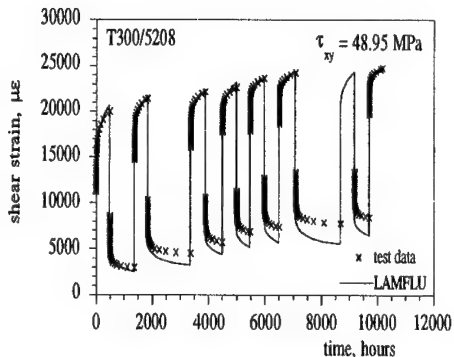


Figure 2. Measured and LAMFLU predictions of the shear strain of a laminate subjected to a cyclic creep/creep-recovery test at room temperature.

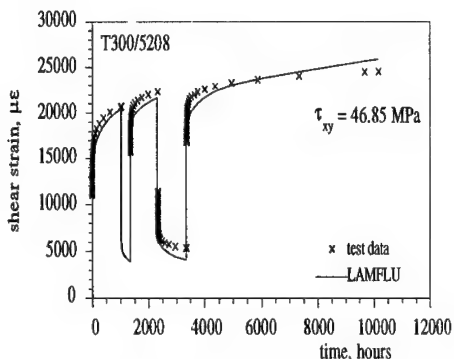


Figure 3. Measured and LAMFLU predictions of the shear strain of a laminate subjected to a cyclic creep/creep-recovery test at room temperature.

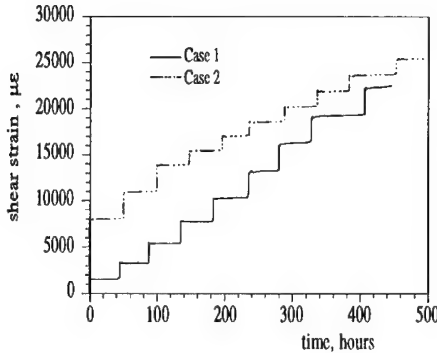


Figure 4. Shear strain imposed in the two multiple-step relaxation tests.

A very good agreement between the prediction and measured data over the entire tests was obtained. In Figure 3 one can observe that material deformed in an asymptotic form, which signifies a behaviour change from glassy to rubbery.

#### 4.2 Multiple relaxation tests

The multiple-step relaxation test consisted on maintaining a step-displacement while the load relaxed. After the load relaxation approaches the asymptotic level, another step-displacement was superimposed on the previous one and maintained while the load relaxed. The specimens were loaded by displacement conditions. The displacement rate for each step was nominally constant at 0.02cm/s and the holding time was approximately 50 hours. The two strain programs used are plotted in Figure 4.

In Figures 5 and 6 the relaxation shear stress data for both multiple-step relaxation tests is plotted with the LAMFLU predictions.

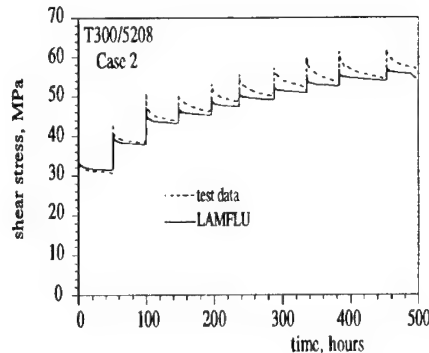


Figure 6. Multiple-step relaxation test data for Case 2 with the one predicted with LAMFLU.

Good agreement between the test and predicted data was observed. After the third step some discrepancies were found between the prediction and experimental results at the beginning of each step-displacement, but still the relaxed shear stresses become very close.

#### 4.3 Constant rate strain tests

The specimens were loaded by displacement conditions (not strained controlled), and the displacement rates were nominally constant. The deviations from constant rates were greatest at slowest cross-head rates. In any case, it would be inappropriate to interpret the data as constant strain rate and so the reported records of the actual strain-time histories were used in the LAMFLU program. In Figures 7, 8 and 9 test data and the respective plastic shear strain calculated by Equation (1) are plotted for three different shear strain rates of  $0.125\mu\epsilon/s$ ,  $12.5\mu\epsilon/s$  and  $1250\mu\epsilon/s$ , respectively with the LAMFLU predictions.

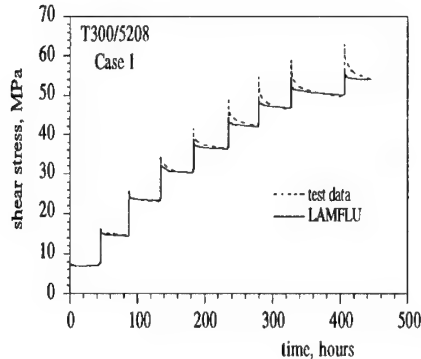


Figure 5. Multiple-step relaxation test data for Case 1 with the one predicted with LAMFLU.

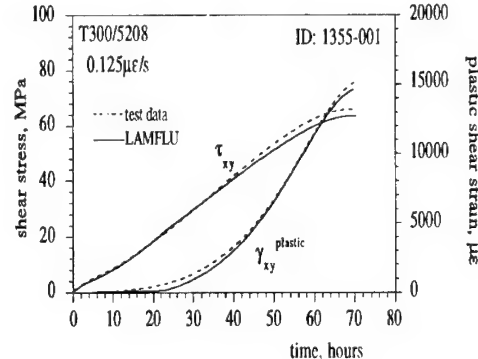


Figure 7. Constant shear strain rate test of T300/5208  $[\pm 45^\circ]$  laminate at room temperature, with the one predicted with LAMFLU.

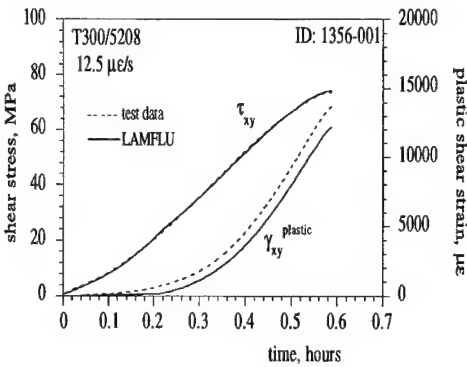


Figure 8. Constant shear strain rate test of T300/5208 [ $\pm 45^\circ$ ] laminate at room temperature, with the one predicted with LAMFLU.

Comparisons between the experimental results and the curves based on the theoretical relationship show an excellent agreement at both high and low strain rates.

## 5 CONCLUSIONS

A mechanical behaviour characterisation procedure was presented and applied to the T300/5208 composite. In the procedure it was imposed the restriction  $a_D \leq 1$ , in order to obtain a coherent model. In this case, without that restriction, the parameter  $a_D$  tended to be larger than unity and increased with the stress. Including the restriction, the parameter  $a_D$  became in this case constant and equal to unity.

With the nonlinear viscoelastic-viscoplastic model one obtains good predictions for long cyclic creep loading and ramp loading tests. Some discrepancies

were found for the model predictions with the multi-step relaxation loading tests.

The validation of the interconversion, between creep and relaxation for uniaxial nonlinear viscoelasticity, needs to be confirmed with more experimental tests. The thermodynamic model developed by Schapery (1969) allows us to express the materials properties in terms of either stress or strain. As Schapery stated, if nonlinearity is weak, both representations are acceptable. However in this case the nonlinearity could not be considered weak as one concluded from the isochronous curve of [ $\pm 45^\circ$ ] T300/5208 composite plotted in Figure 1.

## ACKNOWLEDGEMENTS

We are grateful to JNICT (Junta Nacional de Investigação Científica e Tecnológica) for providing financial support of this work under the Grant BD 706.

## REFERENCES

- Findley, W. N., J. S. Lai & K. Onaran 1989. *Creep and Relaxation of Nonlinear Viscoelastic Materials*. Dover Publications, Inc., New York.
- Guedes, Rui Miranda 1997. Time Life Prediction of Polymeric Matrix Composite Materials. *PhD Dissertation* (in portuguese). Department of Mechanical Engineering and Industrial Management, Faculty of Engineering, University of Porto.
- Lou, Y. C. & R. A. Schapery 1971. Viscoelastic Characterization of a Nonlinear Fiber-Reinforced Plastic. *J. Composite Materials*, April, Vol. 5, pp. 208-234.
- Schapery, R. A. 1969. On the Characterization of Nonlinear Viscoelastic Materials. *Polymer Engineering and Science*, Vol. 9, n° 4, 295-310.
- Tuttle, Mark E., Arun Pasricha & Ashley F. Emery, 1995. The Nonlinear Viscoelastic-Viscoplastic Behaviour of IM7/5260 Composites Subjected to Cyclic Loading. *Journal of Composite Materials*, Vol. 29, No. 15, pp. 2025-2046.
- Wu, Edward M., Nhan Q. Nguyen & Richard L. Moore 1982. Matrix-Dominated Time-Dependent Deformation and Damage of Graphite/Epoxy Composite Experimental Data Under Ramp Loading. *AFWAL-TR-82-3076 report*, California.
- Wu, Edward M., Nhan Q. Nguyen & Richard L. Moore 1983a. Matrix-Dominated Time-Dependent Deformation and Damage of Graphite/Epoxy Composite Experimental Data Under Multiple-Step Relaxation. *AFWAL-TR-83-3056 report*, California.
- Wu, Edward M., Roberto J. Sanches & N.Q. Nguyen 1983b. Matrix-Dominated Time-Dependent Deformation and Damage of Graphite/Epoxy Composite Experimental Data Under Creep and Recovery. *AFWAL-TR-83-3066 report*, California.
- Zapas, L.J. & J.M. Crissman 1984. Creep and Recovery Behaviour of Ultra-High Molecular-Weight Polyethylene at Small Uniaxial Deformations. *Polymer*, Vol 25, pp. 57-62.

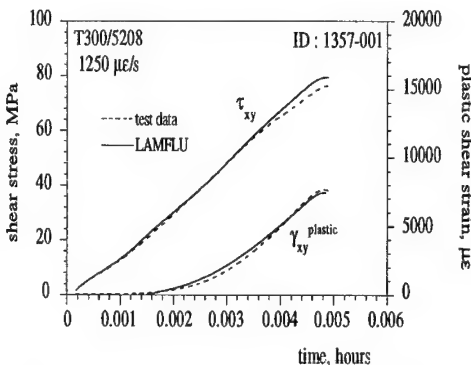


Figure 9. Constant shear strain rate test of T300/5208 [ $\pm 45^\circ$ ] laminate at room temperature, with the one predicted with LAMFLU.

## Reliability-based optimization of a laminated cylinder subject to a given axial load and pressure

A. Béakou

LaRAMA/IFMA, Campus des Cézeaux, Aubière, France

**ABSTRACT:** This paper proposes a method for the design of a  $[\pm\alpha]_n$  laminated cylinder based on reliability evaluation. As each lamina has the same limit state function, the two bounds of the probability of failure coincide and the resulting reliability system is therefore simple. Numerical results show an optimal fiber orientation angle which maximizes the reliability index  $\beta$ . The corresponding value of  $\beta$  can be adjusted to achieve a specified reliability level. Then partial safety factors can be deduced for a semi-probabilistic design.

### 1 INTRODUCTION

The mechanical design of a structure is essentially performed by one of these methods. The deterministic design, the traditional and the most widely used one, introduces an empirical global safety factor to take into account the imponderables in manufacturing, loads and materials properties; it is assumed to be reliable though this is not quantified. In probabilistic design, the reliability of the structure is evaluated through the failure probability or the equivalent so-called Hasofer-Lind index. Finally, in semi-probabilistic design, partial safety factors calibrated by reliability methods are applied to achieve a specified level of reliability.

In the coordination working draft of the MIL-HDBK-17, reliability is defined as "the probability of a device performing its purpose adequately for the period of time intended under the operating conditions encountered". The durability is related to the intended period of time or lifetime of the structure under consideration, subject to environmental effects. Environmental factors of major importance include a combination of humidity, temperature and radiant energy. The effects on the mechanical strength distribution are the reduction of the expected value and probably the increase of the scatter (Figure 1). This effect can be taken into account in a design process by adjusting the strength distribution to coincide with the environmental extremes and by assum-

ing them to be invariant during the lifetime of the structure.

The aim of this work is the optimisation of a  $[\pm\alpha]_n$  laminated cylinder, subject to a given axial load and internal pressure. Bending and buckling load cases have been studied by several authors (Kogiso et al. 1996). Reliability methods are used because fiber-reinforced composite properties and especially ultimate strengths reveal more scatter than metallic materials. The reliability index is calculated by the First Order Reliability Method (FORM) and only material ultimate strengths are treated as random variables. The optimal fiber orientation angle of the laminated cylinder, which maximizes the reliability index, is then determined for various load cases.

### 2 PROBABILISTIC METHODS AND COMPOSITE MATERIALS

Whatever the method considered, probabilistic methods are needed in the design process with composite materials. For instance, the derivation of the design allowable properties, even for deterministic methods, is done by applying statistical analysis to the results of testing on material samples. In addition, probabilistic methods are recommended for the design of structures with composite materials because of the considerable scatter of the mechanical properties.

## 2.1 Design allowable properties

Statistical analysis performed on the results of mechanical tests produce design allowable properties which take into account the degree of scatter and are related to a specific level of confidence (King, R.L., 1987). In the aerospace industry, the usual standards are the A- and B- bases. The A-base is related to the value above which at least 99% of the population is expected to fall with 95% confidence and the B-base, to the value above which at least 90% of the population is expected to fall with the same confidence level. The different steps in the determination of the design allowable properties are:

- the choice of a statistical distribution; generally log-normal and Weibull's distributions are used for composite materials
- the estimation of the chosen law parameters from test data; maximum likelihood, regression analysis are used
- the derivation of the design allowable properties; confidence factors,  $\chi^2$  distribution or Student's t-distribution are used.

In a deterministic design method, the design allowable properties are used in a format including a global safety factor and no quantification of the reliability level is performed. In a semi-probabilistic method, partial safety factors calibrated by a probabilistic method for a specified reliability level are applied to the design allowable properties.

## 2.2 Reliability evaluation

Probabilistic design of a structure considers some of the design variables to be stochastic: material properties, loads, dimensions,... These parameters are called the basic variables  $X_i$ . Then, the design rules have to be listed from the physical, mechanical or experimental knowledge of the designer in order to avoid different kinds of failure. These rules define a limit state function  $G$  and divide the basic variables' space into two sets, the safe set  $S_s$  and the failure set  $S_f$  (Madsen et al. 1986). The failure probability  $P_f$  is calculated by the integration of the variables' density function  $f_x$  over the failure domain  $S_f$ .

$$P_f = \text{Prob}(G(X) \leq 0) = \int_{S_f} f_x dX.$$

The reliability of the structure is  $1 - P_f$ . The calculation of  $P_f$  is done by the following methods: Monte Carlo simulations, First Order Relia-

bility Method (FORM), Second Order Reliability Method (SORM) and the Importance Sampling which combine the first two methods. FORM is particularly interesting because of its efficiency and its low computational cost. Its aim is the calculation of a reliability index  $\beta$  prior to a failure probability evaluation. The reliability index is defined as the minimal distance from the origin  $O$  to the limit state function in a normalized space (Madsen et al. 1986). The point  $P^*$  which minimizes the distance is the design point and the approximation of the failure probability is given by:

$$P_f \approx \Phi(-\beta)$$

where  $\Phi$  is the standardized normal probability function. The coordinates of  $P^*$  correspond to the design values of the basic variables.

## 2.3 Calibration of partial safety factors

Partial safety factors are calculated by balancing out the design values obtained by a probabilistic method to those used in a deterministic design. The different steps in the calibration process are:

- the choice of a reliability level, i.e. a target reliability index  $\beta_{target}$ .
- the probabilist calculation and reliability optimization. After convergence, the design value of each basic variable  $X_i$  is obtained as the coordinate  $x_i^*$  of the design point  $P^*$ .
- the choice of the design allowable property or characteristic value  $x_{ik}$
- the equalization of the design value  $x_i^*$  and the characteristic value  $x_{ik}$  divided (for a strength) or multiplied (for a load) by the partial safety factor  $\gamma_i$ .

## 3 OPTIMIZATION OF A LAMINATED CYLINDER

### 3.1 Mechanical model

The structure is a  $[\pm\alpha]_n$  laminated cylinder made of graphite/epoxy which is subject to an axial load  $F$  and an internal pressure  $p$ . Its middle radius  $R$  is much greater than its thickness  $h$ . In the  $(\tilde{e}_r, \tilde{e}_\theta, \tilde{z})$  axis and taking into account the thin cylinder hypothesis  $h \ll R$ , only  $\sigma_{\theta\theta} = \frac{pR}{h}$  and  $\sigma_{zz} = \frac{F}{2\pi Rh}$  can be considered as significant stresses (Figure 2). Then Tsai-Hill's interactive criterion is used to define the limit state function  $G$  for each lamina.

$$G(\vec{X}) = h^2 - \left( \frac{N - T \cos 2\alpha}{X} \right)^2 - \left( \frac{N + T \cos 2\alpha}{Y} \right)^2 + \frac{N^2 - T^2 \cos^2 2\alpha}{XY} - \frac{T^2 \sin^2 2\alpha}{S^2}$$

where  $N = \frac{1}{2} (pR + \frac{F}{2\pi R})$ ,  $T = \frac{1}{2} (pR - \frac{F}{2\pi R})$ ,  $\vec{X} = \{X, Y, S\}^T$  and  $X, Y, S$  are ultimate lamina strengths.

### 3.2 Stochastic model

Only the ultimate strength  $X, Y, S$  are considered as uncorrelated stochastic variables and are assumed to be normally distributed to allow an analytical solution.

Because of multiple failure modes of a laminated composite two limit cases must be considered. If the failure of the laminated composite occurs by serial mode, the probability of failure is

$$P_{fs} = \text{Prob} \left( \bigcup_{k=1}^{2n} G_k(X) \leq 0 \right)$$

where  $G_k$  is the limit state function of the  $k_{th}$  lamina and  $2n$  is the number of plies.

Otherwise, if the failure of the laminated composite occurs by parallel mode, the probability of failure is

$$P_{fp} = \text{Prob} \left( \bigcap_{k=1}^{2n} G_k(X) \leq 0 \right).$$

These two limit cases give the bounds of the complex phenomena that occur during the failure of a laminated composite. Usually, the lower bound is considered to correspond to the worst case. When a  $[\pm\alpha]_n$  laminated cylinder is considered, the two bounds coincide as  $G_k(X) = G(X) \forall k$ .

See below the features of the random variables.

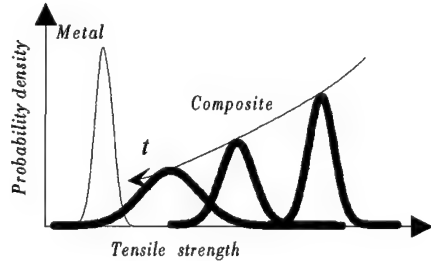


Figure 1: Variation of composite strength.

var.	exp. val.(MPa)	CV in %	law type
X	1500	0.06	normal
Y	40	0.06	normal
S	70	0.06	normal

### 3.3 Optimization problem

After appropriate transformations of the basic variables, the limit state surface is represented in the standardized space. The reliability index  $\beta$  is obtained by minimizing the origin-to-surface distance  $d$ . The optimization problem can be formulated by: for a given thickness  $h$  and a given load case  $(N, T)$ , find  $\alpha$  subject to  $0 < \alpha < \frac{\pi}{2}$  such that the reliability index  $\beta$  is at its highest value.

## 4 NUMERICAL RESULTS

A program has been created to solve the previous optimization problem. The results are validated by STRUREL, a structural reliability analysis program. It is found that the reliability index  $\beta$  is sensitive to the fiber orientation  $\alpha$  when  $N \ll T$ . Numerical simulations are performed for  $h = 0.05m$  and  $T = 2MN/m$ . For each load case defined by  $r = \frac{N}{T}$ , Figure 3 shows an optimal fiber orientation angle  $\alpha_m$  which maximizes the reliability index  $\beta$ . For example,  $\alpha_m = 62$  degrees for  $r = 0.1$ . The corresponding value of  $\beta$  can be adjusted by varying the thickness  $h$  to achieve a specified reliability level. By taking the expected values of  $X, Y$  and  $S$  to be the characteristic values, the calculated partial safety factors in this load case are:

$$\begin{cases} \gamma_X = 1.00 \\ \gamma_Y = 1.11 \\ \gamma_S = 1.8 \end{cases}$$

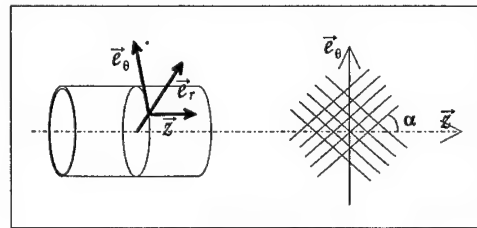


Figure 2: The structure's description.

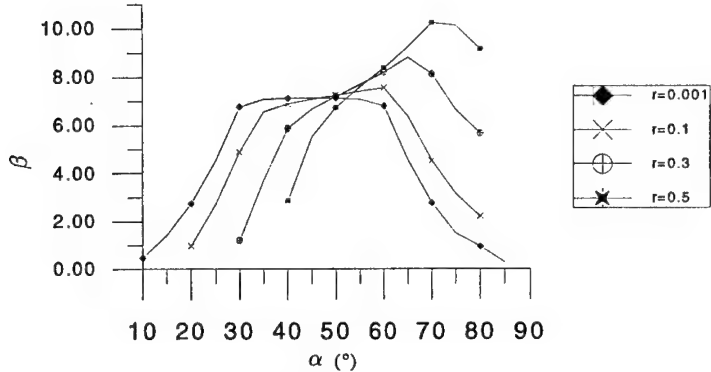


Figure 3: The change in the reliability index against the fiber orientation for various load cases.

These values are given as an illustration since they do not take into account the other design parameter variations.

## 5 CONCLUSION

This work gives a suitable method to determine the optimal fiber orientation angle for a  $[\pm\alpha]_n$  laminated cylinder. Moreover, semi-probabilistic methods can be deduced by assigning values to partial safety factors in order to achieve a specified reliability level at the optimal point. This is very useful for many designers who are not familiar with reliability methods. The model which is presented here as an illustration can easily be extended to take into account elastic modulus, dimensions and load variations.

## 6 REFERENCES

Boyer, C., Béakou, A., Lemaire, M. 1997, Design of a composite structure to achieve a specified reliability level, *Reliability Engineering and System Safety*, 56:273-283.

King,R. L. 1987, The determination of the design allowable properties for advances composite materials. *Gec Journal of Research*, 5:76-87.

Kogiso, N., Shao, S. & Morotsu, Y. 1996, Reliability-based optimization of a symmetric laminated composite plate subject to buckling load, *7th IFIP WG 7.5 Working Conference, 2-4 April 1996, Boulder, Colorado, USA*.

Madsen, H.O., Krenk, S. & Lind, N.C. 1996, *Methods of structural safety*, Prentice-Hall.

MIL-HDBK-17-3E 1996, Structural Reliability in *Polymer matrix composites*, Vol.3, Chapter 6 Department of Defense, Washington D.C. 20025.

## Comparison of methodologies for prediction of long-term properties of GRP pipes

A.Torres Marques

*Faculdade de Engenharia da Universidade do Porto (INEGI/DEMEGI/FEUP), Portugal*

F.Martins de Brito

*Laboratório Nacional de Engenharia Civil (LNEC), Lisbon, Portugal*

**ABSTRACT:** This paper presents the approaches to be used in a European research project intended to develop new (*and so far as possible short-term*) test methods to estimate the long-term behaviour of glass-reinforced plastic (GRP) pipes for water under pressure and sewerage applications. The new methods will be validated by comparison with the results obtained using the presently specified (*very*) long-term ones, the replacement of which is the main objective of the work. The starting of the work is previewed for the beginning of 1988 and so no results could be given now. Nevertheless, the authors have considered that the presentation of the methodology adopted in the research and the correlated topics could contribute for the discussion of the strategy to be followed for the study of the durability of high-diffusion composites.

### 1. INTRODUCTION

Glass reinforced thermosetting plastic (GRP) pipes are a family of quite distinct products depending on the manufacturing technologies used, each one giving laminates with quite different compositions and properties. For the transportation of water under pressure and for sewerage applications, three main cases have to be considered:

- classical filament wound pipes that could be described as angle-ply laminates with some interleaving of the adjacent layers;
- continuously manufactured filament wound pipes having a sandwich construction with hoop reinforced layers and a core in which the resin is mixed with short fibres and small size silicious sand;
- centrifugal cast pipes consisting of several layers build up mixing the resin with short fibres, small size silicious sand and calcium carbonate fillers.

In the European standardization work for GRP pipes it has been decided to specify the determination of four *very* long-term properties (tests during at least 14 months, but usually about two years) in order to assure a confident utilization of the material during the expected life previewed for the pipelines (normally, 50 years). Such strong requirements are related to the fact that the pipes

cover a wide range of diameters (up to 3 meters or even more) being responsible for pipelines which failure could render considerable economical losses and important social difficulties.

But such requirements represent also a quite difficult obstacle to the industrial improvement and innovation of the products. Furthermore, this long testing time also prevents the end users from performing confirmation tests to determine these long-term properties on the pipes really designed and manufactured for each application. This is particularly relevant for the construction of very sensitive pipelines responsible for essential social services or transporting dangerous liquids.

These facts have been recognized by CEN (European Committee for Standardization) and a special "Call for Proposals" in the scope of the Standards Measurements and Testing European Commission Research Programme have been open. The objective was the development of alternative short-term test methods for the determination of these long-term properties assuring an equal level of safety to be validate by comparison of their results with the obtained using the presently specified ones.

A research proposal involving the cooperation of a group of ten partners of six different European countries have been presented and approved. This paper will describe their fundament and strategy.

## 2. ANALYSIS OF THE STANDARDIZED METHODS

### 2.1 Existing standards

The existing European test methods for prediction of long-term behaviour of GRP pipes are:

- a) EN 1447 Plastics piping systems - Glass-reinforced thermosetting plastics (GRP) pipes - Determination of the long-term resistance to internal pressure.
- b) prEN 1227 Plastics piping systems - glass-reinforced thermosetting plastics (GRP) pipes - Determination of the long-term ultimate relative ring deflection under wet conditions.
- c) EN 1225 Plastics piping systems - Glass-reinforced thermosetting plastics (GRP) pipes - Determination of the creep factor under wet conditions and calculation of the long-term specific ring stiffness.
- d) EN 1120 Plastics piping systems - Glass-reinforced thermosetting plastics (GRP) pipes and fittings - Determination of the resistance to the chemical attack from inside of a section in a deflected condition.

They have been prepared by CEN/TC155/WG14 following the work done by ISO TC 138/SC6 during more than 20 years. The methods are essentially of empirical nature, "trying to simulate in laboratory the service loading and environmental conditions", although some general principles on the long-term behaviour of the polymer matrix composite materials have been taken into account at a qualitative level.

Note that the long-term design of buried GRP pipelines is essentially an one-dimensional problem in which only the stresses and strains the hoop direction have to be considered. The use of flexible joints prevents or considerably reduces the existence of axial stresses being enough to deal with them in a short-term basis.

For strength predictions, both internal pressure (tensile) and ring deflection (bending) tests are included because the material is seen as an homogeneous one over the wall thickness.

Long-term modulus is only important to be known in bending to avoid excessive deflections.

The last test is a special chemical ageing check and since it is not linked to the material creep and other ageing aspects of the long-term material behaviour it will be not analyzed here.

### 2.2 General discussion of their capabilities

The label *empirical* shall not be taken with the negative charge sometimes associated to the approaches of this nature. In fact the referred methods, although assuming a linear or 2<sup>nd</sup> order polynomial in a log-log scale, are supported by a consistent regression analysis. The statistical model behind kept the estimations inside a predefined confidence level for an extrapolation of not more than 1.5 decades in time taken in hours.

Furthermore, a model like this could be easily incorporated in (semi-)probabilistic reliability design methodology following the philosophy behind the Construction EuroCodes. All the uncertainties associated with loading conditions, structural analysis, *in situ* construction parameters and the scatters of material properties could be incorporated in a coherent statistical model for the definition of a minimum safety factor.

On the other hand, both creep and ageing are considered. In water supply or sewerage systems the loss of properties of the material is essentially a consequence of the creep of the material, the swelling, the slightly plasticization and the very slow hydrolysis (with scission) of the resin, and of the slow attack of the liquid to the fiber/resin interfaces. This is clearly recognized by the existing tests since they specify the constant loading of specimens immersed in the liquid:

- tests referred in a) and b) try to estimate the long term strength of the material, respectively in tensile and in bending stress conditions, being the consideration of both indispensable due to laminated nature of the material. For these creep to failure tests, at least 18 specimens shall be used with times to failure fulfilling a specified balanced distribution in the interval 10-10000 hours. The extrapolation for the expected life for the pipe is done by a linear regression analysis in a log-log plot, the statistical validity of the data being checked by two criteria: suitability for regression analysis and for extrapolation.
- the test mentioned in c) is a bending creep test at low deflection level used in order to be possible the estimation of the long term deflection of the pipe in a buried installation; based on the data of the deflection vs time up to 10 000 hours, the extrapolation of the stiffness for the life expected for the pipe is done using a 2<sup>nd</sup> order polynomial.

However, the existing methods do not take into account a fundamental characteristic of the influence of the liquid environment: the slowness of the liquid diffusion at room temperature. Depending of the composition of the material and of the thickness of the pipe wall the saturation of the specimens could only be obtained after several months. Then:

- thinking in a expected life of 50 years, only the data obtained after several thousands of hours can take into account (and probably, in a insufficient way) the effect of the liquid environment;
- the effects of the liquid in the material affects, in a quite distinct way, the data obtained at different times of testing and this circumstance increases the scatter of the data to be used in the extrapolation.

For the tests mentioned in a) and b), this last aspect introduces some disturbance in the expected shape of the regression curve. The same influence is quite evident in the low deflection creep test mentioned in c) where the available experimental sets of data normally shows a "S shape" curve in log-log plot which could be difficult to be dealt with the specified 2<sup>nd</sup> order polynomial.

In the tests which results are based in an extrapolation using failure points of several specimens (tests referred in a) and b)) it is also quite difficult to accommodate the intrinsic material variability in a regression analysis without using a very large number of specimens. Ideally, the same number of points should be used in each time period, being this number sufficiently high to allow the characterization of the measurements scatter in each time interval. To avoid this hard way of testing, it is preferably, from a statistical point of view, to select alternative corresponding properties that could be measured in the same specimens during all the time of testing.

The experimental evidence of the curve scatters found in the available data has been the main reason to extend the specified periods of testing over 10 000 hours. In a logarithmic time scale this period of time is close to 50 years (1.5 decade distant) and for the Standardization Group this was thought to be the way to assure an adequate level of safety in the extrapolation.

The reducing of the curve scatters and the modification of the methods to solve the mentioned weaknesses of the existing methods have been strong lines in the research strategy. But other methodologies have also been considered, as well as some possible accelerating techniques, as discussed in the next chapter.

### 3. DISCUSSION ON METHODOLOGIES FOR LIFE PREDICTION OF GRP PIPES

#### 3.1 Mandatory constrains

The obligation of preparing new test standards that have to be applicable to all the described types of GRP pipes is one of the main constrains conditioning the strategy of the research. The implications of this restriction are quite hard:

- the material have to be seen as a "*blind*" homogeneous one also over the thickness, being impossible to incorporate in the analysis the laminate lay-up;
- as a consequence, both tensile and bending behaviours have to be considered separately for long-term strength prediction.

A second mandatory constrain is the implicit simplicity of the system. For the standardization of high diffusion products sophisticated analytical models and/or heavy numeric calculations are interdict. Both the tests and the corresponding data analysis are intended to be performed at the factory and to be checked by the end users and by the Certification Bodies with the current tools used by practical engineers.

A third constrain is the need to evaluate the uncertainty of the long-term estimation claiming for statistical approaches.

#### 3.2 General methodologies for composites

In last years, several general methodologies have been purposed for life prediction of composite laminates (Brison-Dillard<sup>1</sup>, Tuttle<sup>2</sup>, Talreja<sup>3</sup>, Ladevèze<sup>4</sup>, Reifsnider<sup>5</sup>, etc.).

In the two first mentioned approaches emphasis is given to the estimation of the strain evolution using a Schapery based equation being strength predictions made independently using empirical criterion (Zurkov) or a short-term failure criterion with time dependent strengths. The possibility of using such approaches is quite limited for the following reasons:

- Schapery equation could be used with a great number of linear viscoelastic and non-linear viscoelastic-viscoplastic components. The strain curve so obtained could virtually be considered adequate to any set of experimental creep data, but how could be standardized a so open equation? Does make sense to have to determine experimentally all material dependent parameters and to deal with a complex model (from the point of view of the statistical analysis

to evaluate the uncertainty of predictions) just to analyze a creep evolution? We feel that such hard work could only be justified in case of a more complicated load history. However, if a dynamic loading fatigue approach could be used as an accelerating technique (see 3.4), the use of a method like this could be adequate.

- For strength predictions the empirical model is the same used in the existing standardized methods.

In the other mentioned approaches the main concern is to create a coherent procedure to "measure" the material damage and their influence on the evolution of the material moduli and strengths. Despite their intention to introduce, so far as possible, continuum damage mechanics concepts, their application to real cases always needs to use assumptions on the laminate lay-up and also frequently on the ply micromechanics and fracture modes. However the Reifsneider residual strength concept and the kinetic equations developed are sufficient general to be a frame for a research approach.

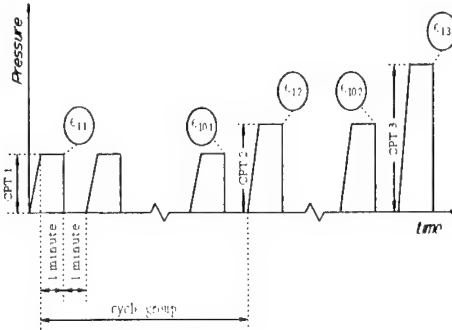
### 3.3 Specific research on GRP pipes

The results of the specific research on long-term properties of GRP pipes done in the last 20 years (some examples are: Meiras<sup>6</sup>, Carswell<sup>7</sup>, Hull<sup>8</sup>, Lenain<sup>9</sup>, Jones<sup>10</sup>, Ghorbel<sup>11,12</sup>) give relevant information but the conclusions could only be applied to one type of GRP pipes (classical filament wound one) since all the experiments have been only performed on it.

In particular, the recent work of Ghorbel gives a quite important contribution on some important issues, namely: the particularities of the use of a Schapery equation (without a viscoplastic component), the damage growth in the material and on the influence of the aging effects on the pipe long-term behaviour. All the work have been done using only an internal pressure biaxial loading condition (end thrust is included) and the life prediction criteria is restricted to the use of the pipe in water under pressure at the temperature of 60°C. The work also confirms that the creep failure always occurs at the same extension, independently of the load and that the strength evolution follows a linear (Zurkov like) equation.

### 3.4 Accelerating techniques for creep

The potential accelerating factors available for reducing the testing time are the increasing of the



temperature and the use of a dynamic loading instead of a static one.

For the first case the use of the so called Time Temperature Superposition Principle (TTSP) have been widely used, often without a sufficiently safe experimental validation. We decide not to use such approach due to the following reasons:

- the hard experimental work needed to confirm its applicability during minimum time periods and temperature ranges that could render confident long-term properties predictions;
- some types of pipe are cured at room temperature, without any type of post-cure treatment, and so the real properties could be modified in a high temperature test condition.

The use of a fatigue test could be an interesting potential alternative to avoid long creep test times. However its applicability is conditioned to the following requirements:

- a good experimental correlation leading to greatly reduced failure times is obtained and could be justified by consistent viscoelastic model;
- the fatigue failed specimens keep the same fracture morphology as the creep ones.

### 3.5 Other alternative methods

During the discussion of the strategy for the research two other alternatives have been purposed.

One is the so called *Ultimate Elastic Wall Stress (UEWS)* method used in some countries for filament wound epoxy pipes. A schematic description of the method is shown in the picture above. The idea behind the method is the evaluation of an "elastic limit" for the material over which it is assumed that permanent deformations are obtained and the material creep rate considerably increases.

For this purpose, series of trapezoidal loading cycles are performed in successive increasing loading steps (ten equal cycles at each load level) being measured the maximum strains obtained in the first and the tenth cycle of each step. The difference between these two strains is used to verify if the elastic limit have been reached. To be possible to use a method like this it have to be demonstrated that the creep rate is negligible under this "elastic limit".

Another alternative called *Strain at Failure Method* consists in creep tests that are performed using a load level slightly higher than that corresponding to the pipe service conditions, being both related by a "reduction" factor to be determined based on the statistical variability the material properties. The measured strain evolution is used to estimate the strain for the specified pipe life, being this value compared with the "*strain at failure*" of the material determined independently.

A more detailed explanation is required to show what this "strain at failure" means and how it could be determined. Historically the research on creep behaviour of polymeric materials and polymer matrix composites have been carried out treating independently the strain and strength evolutions as function of the time. The information taken from creep curves is not used for strength predictions due to the lack of a failure criterium formulated on a strain basis. To be possible to cover both creep and relaxation behaviours such criterium have to be formulated on a energetical basis.

No much research has been done on this perspective, an exception is the work done by Brüller<sup>13</sup>. The author considers that under creep conditions the work done by the external forces is transformed into a stored strain energy  $W_{sto}$  and a dissipated energy  $W_{dis}$  being both always equal. It is also assumed that the failure occurs when the time dependent stored energy reaches a certain value which is a material constant. Then the strain at failure at a constant load  $\sigma_0$  could be predicted by the equation:

$$\epsilon_{failure} = W_{tot} / \sigma_0 + \epsilon_{elastic}$$

in which,

$$W_{tot} = W_{sto} + W_{dis} = 2 W_{dis}$$

could be computed from any creep curve up to failure, including a high load level one giving a short time to failure.

A similar approach will be used but using less restrictive assumptions. In particular, the total time dependent strain energy  $W_{tot}$  is not considered to be

necessarily a material constant because, physically, such hypothesis is equivalent to suppose that the damage mechanisms has to be the same for all load levels. An assumption like this needs to be verified for each material and loading condition.

In these circumstances, and for the one-dimensional creep problem the strain at failure is assumed to be an unknown function of the load to be determined experimentally by a set of creep tests at different load levels.

### 3.6 Ageing

For pipes used with water or for sewerage and excluding the chemical action of some types of sewerage to be analyzed by other means, as stated before, ageing means the influence of the water in material behaviour.

The experience of utilization of GRP pipes and the results of accelerated tests at higher temperatures show that the physical ageing (resin plasticization) is more important than the chemical one for a time corresponding to the expected life for pipes. For strength predictions chemical ageing will not be explicit considered being open a possibility to take it into account as a reduction factor to be used in design. For long-term ring stiffness estimation, however, the load and consequently the creep rate are very low and its relative importance could not be neglected.

In the past a so called  $\alpha\beta$  method has been used in some European countries consisting in the determination of two independent factors - one related to the creep behaviour ( $\alpha$  factor) and the other measuring the effect of the liquid ( $\beta$  factor) - both to be applied to the short term stiffness value. The creep factor is determined in a 1000 hours dry creep test and the ageing one is measured by the reduction of stiffness after a conditioning period of 1000 hours in water at 50°C.

During the discussion of the research project a modification of this method have been foreseen as an eventually better technique comparing the time for saturation with the expected pipe life. The idea is to try a *Creep of saturated specimens method*, similar to  $\alpha\beta$  one but performed in sequence using the same specimens: conditioning in the liquid environment followed by a wet or a dry creep test.

The possibility of using a *Relaxation method* similar to the previous one but using relaxation instead creep will seems also an interesting possibility since the limited available experimental data seems to show that the precision obtained in the measurement of the load could be better than that achieved in the measurement of the deflection.

#### 4. STRATEGY TO BE FOLLOWED

Following the precedent discussion, the following strategy have been defined for the research project:

- a) Performing the standardized tests not only to be used for validation purposes but also, measuring additionally strains at failure, to get fundamental information for the strain at failure approach.
- b) For long-term strength predictions, the *UEWS* and *strain at failure* approaches will be analyzed in parallel for both ring deflection and internal pressure. *Dynamic loading* approach will also be tried for ring deflection loading condition.
- c) For long-term stiffness predictions, the referred  $\alpha\beta$ , *creep of saturated specimens* and *relaxation* approaches will be tried.

The selected short-term test alternative methods fulfill the requirements resulting from the analysis done on section 2:

- only saturated test specimens will be used (an additional task to study the diffusion of water at different temperatures will be done to assure the compliance to this requirement);
- if applicable, the new methods will try to originate, as much as possible, similar long-term failure mechanisms compared to those happening in real service conditions;
- the specimens will be used during all the stages of the testing procedure in order to avoid the perturbations resulting from the material variability.

Then it could be expected that the long-term curves will present a well defined and clear shape allowing extrapolations based in shorter times.

In addition, the material variability will be introduced by a complete characterization of the short-term failures distribution of the pipe (for example, determining initial ring deflection or tensile strength) performed over a very large number of specimens taken during a significative manufacturing period. The determined variability could be easily introduced as a reduction factor to be applied to the long term value obtained for the property to be measured or to be directly included in the loading conditions of the tests.

#### REFERENCES

- <sup>1</sup> Dillard,D.A. & Brinson,H.F. 1983. A numerical procedure for predicting creep and delayed failures in laminate composites. *In ASTM - STP813, T.K. O'Brien (edt), Baltimore.*
- <sup>2</sup> Tuttle, M.E. 1996. A framework for long-term durability predictions of polymer composites. *In Progress in Durability Analysis of Composite Systems, Cardon, Fukuda & Reifsnider (eds), Rotterdam, Balkema*
- <sup>3</sup> Talreja,R. 1996. A synergistic damage mechanics approach to durability of composite systems. *In Progress in Durability Analysis of Composite Systems, Cardon, Fukuda & Reifsnider (eds), Rotterdam, Balkema*
- <sup>4</sup> Ladevèze,P. 1996. A damage computational approach for composites: Basic aspects and micromechanics strength/stiffness indicators. *In Progress in Durability Analysis of Composite Systems, Cardon, Fukuda & Reifsnider (eds), Rotterdam, Balkema*
- <sup>5</sup> Reifsnider,K.L., Case,S. & Xu,Y.L. 1996. A micro-kinetic approach to durability analysis: The critical element method. *In Progress in Durability Analysis of Composite Systems, Cardon, Fukuda & Reifsnider (eds), Rotterdam, Balkema*
- <sup>6</sup> Meiras,H.J. 1973. Irreversible creep of filament-wound glass-reinforced resin pipes, Plastic and Polymers. *Plastics and Polymers, April*:86-89.
- <sup>7</sup> Carswell,W.S. 1976. The behaviour of glass filament wound pipes under internal pressures. *In Proc. 2<sup>nd</sup> Int. Conf. on Comp. Mat., New York*: 472-483.
- <sup>8</sup> Hull,D., Legg,M.J. & Spencer, B. 1978. Failure of glass/polyester filament wound pipes". *Composites, January*:17-24.
- <sup>9</sup> Lenain,J.C. & Bunsell,A.R. 1978. The behaviour of GRP pipes under cyclic pressurization. *Composites, April*:77-82.
- <sup>10</sup> Jones,F.R., Rock,J.W. & Wheatley, A.R. 1983. Stress corrosion cracking and its implications for the long-term durability of E-glass fiber composites. *Composites, March*:262-269.
- <sup>11</sup> Ghorbel,I. & Spiteri,P. 1996. Durability of closed-end pressurized GRP pipes under hygrothermal conditions. Part I: Monotonic Tests. *Journal of Composite Materials* 30(14):1562-1580.
- <sup>12</sup> Ghorbel, I. 1996. Durability of closed-end pressurized GRP pipes under hygrothermal conditions. Part II: Creep tests. *Journal of Composite Materials* 30(14):1581-1595.
- <sup>13</sup> Brüller,O.S. 1996. Creep and failure of fabric reinforced thermoplastics. *In Progress in Durability Analysis of Composite Systems, Cardon, Fukuda & Reifsnider (eds), Rotterdam, Balkema*

## Evaluation of damage accumulation of glass fibre reinforced chemically bonded ceramics (CBC) using the resonalyser technique

P.Bauweraerts, J.Wastiels, X.Wu, S.Faignet & A.Edelstein  
*Civil Engineering Laboratory, Mechanics of Materials and Constructions, Vrije Universiteit Brussel, Belgium*

**ABSTRACT:** This paper gives a summary of tests performed on laminates consisting of an inorganic phosphate cement (called IPC), developed at VUB, and unidirectional continuous glass fibres. Tests with limited loading/unloading cycles at different stress levels are performed. During the tests, Young's modulus and residual strain can be measured. The goal of the research is to find a non-destructive 'tool' to describe the 'state' of the examined composites. For this purpose the specimens were examined using a non-destructive mixed numerical/experimental technique developed at the department of Structural Analysis of the VUB, the so called 'Resonalyser' technique.

### 1 INTRODUCTION

Based on the well-established ACK theory for brittle matrix composites using continuous aligned fibre reinforcement, the tensile behaviour of laminates can be modelled (Aveston et al. 1971, 1975, Keer 1981). The mechanical behaviour of these laminates can be described in three stages of the tensile stress versus strain curve: a) elastic zone, up to first cracking b) multiple cracking c) fibre stretching. Also, the unloading/reloading behaviour can be modelled (Aveston et al. 1971, Keer 1981). Unloading can be considered from within, or beyond the multiple cracking region and the resulting residual strain can be calculated. Figure 1 shows the idealised stress versus strain curve for a brittle matrix composite with multiple fracture and some theoretical unloading/reloading cycles. The parameter  $\alpha$  used in Figure 1 is calculated as follows:

$$\alpha = \frac{E_m V_m}{E_f V_f} \quad (1)$$

As it can be seen on Figure 1, the theory suggests that the residual strains reach a maximum value (Keer 1981). However, previous authors (Keer 1981) already showed that practically there is no tendency to reach a maximum residual strain. The ACK theory does not take into account the damage evolution occurring during cyclic loading of composite materials. For future applications it is important to quantify this phenomenon and import

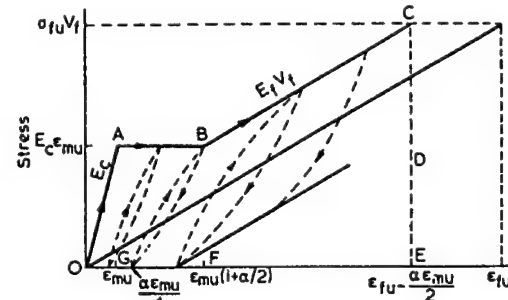


Figure 1. Theoretical tensile stress versus strain curve for multiple fracture (UD fibre reinforced brittle matrix) (Keer 1981) ( $E_c$ ,  $E_f$  = modulus of composite, fibre;  $V_f$  = volume fraction fibres;  $\sigma_{fu}$  = fibre failure stress;  $\epsilon_{mu}$ ,  $\epsilon_{fu}$  = matrix, fibre failure strain)

it into the existing behaviour models. The goal of current research is to find a non-destructive 'tool' to describe the 'state' of the examined composites. This 'state' may be determined not only by the constitutive behaviour as predicted by the ACK theory, but also by additional phenomena.

### 2 MATERIALS

For the present research, 2 continuous aligned glass fibre reinforced brittle matrix laminate plates (plates A and B) were produced.

The matrix used in this investigation is an inorganic phosphate cement (called IPC), developed

at Vrije Universiteit Brussel (VUB). These inorganic materials present some attractive properties: they are hardening out at low temperatures and they reach a high compression strength. But the main benefit of this material, compared to other inorganic materials, is the feasibility to introduce glass fibres into the material. Since alkaline conditions are not occurring before, during, and after the hardening of IPC, glass fibres are not attacked. Like other inorganic brittle materials, the IPC has a low tensile failure strain of about 0.03% and a Young's modulus of about 25 GPa.

The laminates were produced by hand lay up, eight layers were used. After curing at 60°C for one day, 6 test specimens were cut from each plate. The length of the specimens is about 250 mm, the width is about 16 mm. Because more matrix was used for plate A, the volume fraction of fibres is different for the two plates. The specimens of plate A have an average volume fraction ( $V_f$ ) of about 11.9 %, plate B 13.5%. After cutting, the specimens were post-cured at 40°C for 3 days.

### 3 RESONALYSER TECHNIQUE

For this research the specimens were examined using a non-destructive mixed numerical/experimental technique developed at the department of Structural Analysis of the VUB (Sol et al. 1991a, b, 1994). The method -the so called 'Resonalyser' technique- is based on the observation of the vibration behaviour of test structures with a very simple geometry (rectangular or circular, thin plates and beams). The material properties in a numerical model of the test structure are updated in such a way that the model reproduces the observed behaviour as good as possible. Using this technique the four complex engineering constants of thin orthotropic plates and laminates can be determined. The elastic behaviour as well as the damping of the material can be examined without inducing damage to the material.

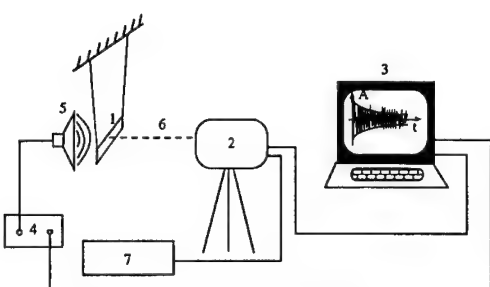


Figure 2. Resonalyser test set-up. (1 = specimen; 2 = Laser Doppler Vibrometer; 3 = PC; 4 = amplifier; 5 = loudspeaker; 6 = laser beam; 7 = power supply) (Sol et al. 1991a, b, 1994)

Figure 2 shows the Resonalyser test set up used in the present study. In this study, only beams are examined by the Resonalyser. The fundamental frequency of the beam is measured in a free boundary condition situation. From this measured frequency  $f$  the longitudinal Young's modulus  $E$  of the beam can be calculated using the theory of Bernoulli :

$$E = 0.946 \frac{f^2 \rho L^4}{t^2} \quad (2)$$

where  $E$  = Young's modulus;  $f$  = measured fundamental frequency;  $\rho$  = material density;  $L$  = length of specimen; and  $t$  = thickness of specimen.

The damping properties of the beams are determined with an acoustical excitation technique: a sinusoidal signal with the previously measured resonant frequency of the beams is generated and fed into a loudspeaker to bring the beams acoustically in resonance. After stopping the excitation, the beams vibrate freely and the decaying signal is measured using a Laser Doppler Vibrometer. The free damped vibrations of a single degree of freedom system can be expressed by the following function:

$$w(t) = A e^{-\xi \omega t} \sin(\omega t - \phi) \quad (3)$$

where  $\xi$  = modal damping ratio;  $A$  = modal displacement or amplitude;  $\phi$  = phase angle; and  $\omega$  = circular resonant frequency.

The damping ratio  $\xi$  associated with the selected resonant frequency is computed by curve-fitting the measured signal.

The main question is if the measured modulus and damping ratio can serve as the wanted 'tool' for describing the 'state' of the specimen.

### 4 TEST PROGRAM

An artificial 'state' is created in four specimens of each plate by applying a loading/unloading cycle on each specimen. Four stress levels, all beyond the multiple cracking stress, are examined: 25, 50, 75 and 100 MPa. All specimens (plate A and B) are loaded twice. Before, between and after these two cycles, the specimens are examined by the Resonalyser: the fundamental frequency (thus the Young's modulus) and the damping ratio are measured. For the specimens of plate A, additional 8 cycles are applied followed by a new Resonalyser test.

During tests in the past (Edelstein 1997) it appeared that the measured properties (especially the damping measurements) of the loaded specimens are very sensitive to environmental conditions.

Also, after loading to a certain stress level, the measured properties show an evolution in time, due

to 'accommodation' of the specimens. After unloading, although the overall stress of the specimen is zero, local stress concentrations are still present within the specimen, due to fibre stretching and matrix-fibre interactions. These stress concentrations are not constant in time, and they have a clear influence on the Resonalyser measurements after loading.

Because of these phenomena the specimens are stored at a constant temperature and humidity for five days, before the resonant frequencies and damping ratios are measured.

An additional tensile test is performed on one specimen of each plate, and a fixed cycle program is applied on the remaining specimens.

The test program, as described above, is summarised in Table 1.

can be calculated (assuming Young's modulus of the matrix,  $E_m$ , equals 25 GPa)

Table 2. Tensile test results

	Plate	A	B
Ultimate composite stress $\sigma_{cu} = \sigma_{fu}V_f$ (MPa)		117.3	130.8
Modulus of post-cracking zone* $E_fV_f$ (GPa)		7.8	8.7
Parameter $\alpha$		2.8	2.5
Equation (1)			
Initial modulus $E_c = E_fV_f + E_mV_m$ (GPa)		29.9	30.4

\*  $E_fV_f$  is determined by linear regression over 70-90 MPa stress interval

Table 1. Overview of test program

spec. nr.	plate A & B		plate A	
	nr. cycles x stress level (MPa)	nr. cycles x stress level (MPa)	nr. cycles x stress level (MPa)	
1	1x25	1x25	8x25	
2	1x50	R	1x50	R
3	1x75	*	1x75	*
4	1x100		8x75	*
5	1x25-1x50-1x75-1x100-till failure			
6	till failure			

\* Resonalyser test : measurement of fundamental frequency f and damping ratio  $\xi$  after 5 days (stored at 25°C, 60% RH)

The Young's modulus determined by the Resonalyser test is an average of 10 measurements on 1 specimen. For each measured fundamental frequency, the damping ratio is determined twice, resulting in 20 values. Further on in this paper, the measured damping ratios are given by the average of these 20 values together with the standard deviation of these measurements.

The loading cycles are performed on an Instron 1195 testing bench. The cycles were displacement controlled at a rate of 1 mm/min. The load of the specimen is recorded during the cycles, as well as the strain, using an averaging strain extensometer with a 50 mm gauge length.

## 5 RESULTS AND DISCUSSION

### 5.1 Ultimate tensile stress

The results of the tensile tests of specimen 6 of each plate is shown in Table 2. From the measured modulus of the post-cracking zone and equation (1), the parameter  $\alpha$  and the initial composite modulus  $E_c$

### 5.2 Cyclic test at different stress levels

The stress versus strain curve of specimen 5 (plate A) is plotted in Figure 3.

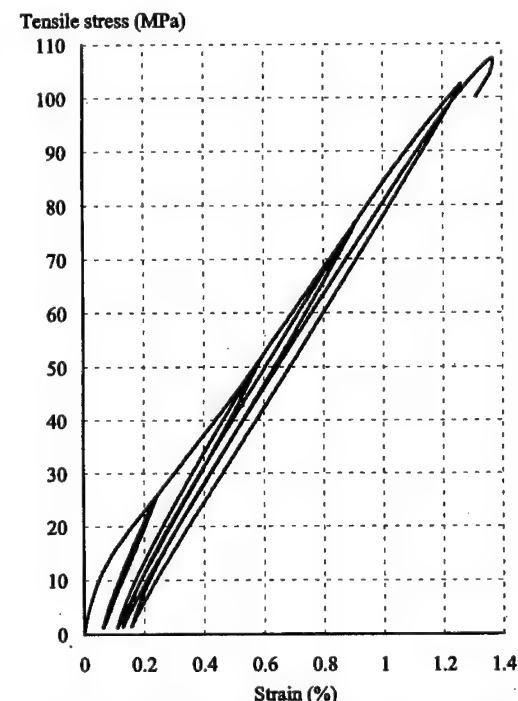


Figure 3. Static cyclic stress versus strain curve of a 8 layers glass fibre reinforced IPC specimen (plate A) (unloading at 25, 50, 75 and 100 MPa)

The experimental stress versus strain curve differs from the ACK curve: the multiple cracking zone AB from Figure 1 can not be distinguished. Instead of

this, there is a gradual and smooth S-shaped transition between the elastic behaviour and the fibre stretching zone. These phenomena can be explained by the specific structure of the composite. The elastic region of the curve is very small compared to the post cracking region. Because  $\alpha \approx 2.8$ , it is clear from Figure 1 that the multiple cracking zone and the elastic region are about the same size. As a consequence, the multiple cracking region is difficult to distinguish experimentally. The 'virgin' test beams already show some small primary cracks due to the preparation procedure, shrinkage, and the test procedure (clamping of the specimens). Also the presence of some transversal fibres is important. These fibres (16% of the total amount of fibres) affect the properties of the matrix material resulting in a varying tensile strength of the cross-section over the specimen length. There is also evidence of a crack stabilising effect of the fibres: it is obvious from Figure 3 that when the non reinforced tensile strength (about 8 MPa) and ultimate strain (about 0.03%) of the matrix are reached, no immediate multiple cracking occurs, but only a gradual cracking up to much higher stress levels. This results in the S-shaped transition curve.

At higher stress levels, the post cracking curve in Figure 3 is not a straight line due to early fibre rupture.

From the tests performed on specimens 5 of plate A (Figure 3) and plate B, the unloading modulus and the residual strains after each cycle can be calculated. These results are shown in Table 3:

Table 3. Unloading modulus and residual strains of a 4-cycles test at different stress levels.

	Stress level (MPa)	Unloading modulus (GPa)*	Residual strain (%)
A	25	14.3	0.056
	50	10.9	0.101
	75	9.9	0.115
	100	9.4	0.143
B	25	17.4	0.044
	50	12.4	0.096
	75	11.0	0.122
	100	10.2	0.151

\* unloading modulus is determined by linear regression at the maximum stress level (interval:  $\sigma_{\max} - 0.8 \sigma_{\max}$ )

The unloading results are quite different from what the ACK theory predicts. In the theory (when loaded over the multiple cracking stress) the unloading modulus varies from  $E_c$  at the unloading stress, till  $E_f V_f$  at zero stress. In our composite, the unloading curve is almost a straight line, and the unloading modulus is lower when the unloading

stress level is higher. Also, the residual strain does not reach a maximum as the theory suggests. The higher the stress level, the higher the residual strain will be.

An explanation of this phenomenon can be found in the physical background of the theory. The theory starts from the assumption that, when unloading starts, there is no slipping back of the fibres into the cracked matrix. Only when the overall stress diminishes, the fibres are able to slip back, causing a decrease of the unloading modulus. Drawing the line further to our composite, one can assume that there is a continuous slip of the fibres back into the matrix, from the unloading stress till almost zero stress. At zero stress, Figure 3 clearly shows that the unloading modulus is increasing again, indicating that slipping of some fibres stopped. However, these micromechanical phenomena are not the topic of this paper, and are presently under study.

### 5.3 Cyclic test at constant stress level

Ten load cycles at a constant stress level are performed on four specimens of plate A (Table 1). The results of the measured unloading moduli and residual strains of one specimen (specimen 3 - loaded at 75 MPa) are shown in Table 4. One has to keep in mind that, after the first and the second cycle, the specimens were removed from the testing bench for the Resonalyser measurement. For each time the specimen was placed back for another cycle, the recorded strains start from zero. The last 8 cycles were performed one after the other, without removing the specimen from the testing bench.

Table 4. Unloading modulus and residual strain of one specimen (plate A) loaded 10 times at 75 MPa

	maximum stress (MPa)	*unloading modulus (GPa)	residual strain ( $\mu$ strain)
1	76.6	10.1	1210
2	75.3	9.89	65.8
3	75.2	9.90	7.1
4	74.9	9.92	15.8
5	75.2	9.83	21.7
6	75.1	9.84	27.0
7	75.2	9.81	30.4
8	75.3	9.80	33.2
9	75.1	9.79	36.1
10	75.2	9.78	39.9

\* unloading modulus was measured by linear regression over the interval 60-75 MPa

Table 4 indicates that, although the specimen is tested at a constant stress level, the material undergoes additional damage. Indeed, the unloading

modulus is slowly decreasing without an increase of the maximum stress level. Also the residual strain is increasing continuously.

For the specimens tested at 25 and 50 MPa, similar conclusions can be made, although the evolution is less clear because of the small amount of cycles. Specimen 4 is tested at 100 MPa, which is only 15% below the ultimate tensile stress. Fibre failure for this specimen is the main cause of damage.

#### 5.4 Resonalyser test results

Knowing the results from previous paragraphs, the question is now whether the Resonalyser tests can give an indication about the 'state' of the specimens that were loaded at different stress levels.

Table 5 (Plate A) and Table 6 (Plate B) show the damping ratio results, Table 7 (Plate A) and Table 8 (Plate B) present the measured Young's moduli.

For unloaded specimens, the link between the damping properties and the modulus is clear. A lower initial modulus means more initial cracks, and more cracks means a higher energy loss due to friction between crack surfaces during vibration, thus a higher damping. When the 'virgin' specimens are loaded, the damping ratio increases. This increase is more pronounced for the specimens subjected to a lower stress level. For the specimens loaded at the higher stress levels, the influence of glass damping becomes more important resulting in a lower damping ratio.

Table 5. Resonalyser test results: damping ratios ( $10^{-5}$ ) of plate A specimens

Stress level (MPa)	25	50	75	100
Unloaded	298±4	329±4	431±2	413±2
1 cycle*	586±5	559±8	443±7	414±4
2 cycles*	660±6	614±15	482±6	452±6
10 cycles*	656±12	532±14	504±13	444±6

\* After loading, and before the Resonalyser test, the specimens were stored at 25°C and 60% RH for 5 days

Table 6. Resonalyser test results: damping ratios ( $10^{-5}$ ) of plate B specimens

Stress level (MPa)	25	50	75	100
Unloaded	322±3	310±3	249±1	262±8
1 cycle*	610±7	631±18	390±6	362±5
2 cycles*	632±6	658±23	614±8	408±4

\* After loading, and before the Resonalyser test, the specimens were stored at 25°C and 60% RH for 5 days

Tables 7 and 8 clearly indicate that the modulus measured before the start of the cycle program is an indication of the initial laminate 'state' as discussed in a previous paragraph. After one cycle there is a large drop in modulus due to completion of the multiple cracking. After 2 cycles and more a continuous decrease of the modulus is clear, but less pronounced indicating a damage increase in the composite. This may be due to additional matrix cracks, early fibre rupture, stress concentrations because of imperfections in fibre alignment, loss of matrix material (no stress transfer) and debris wedging cracks.

Table 7. Resonalyser test results: Young's moduli (GPa) of plate A specimens

Stress level (MPa)	25	50	75	100
Unloaded	25.4	24.6	22.4	22.9
1 cycle*	19.8	17.7	17.2	17.4
2 cycles*	18.8	17.0	16.9	17.0
10 cycles*	18.7	17.6	16.6	16.5

\* After loading, and before the Resonalyser test, the specimens were stored at 25°C and 60% RH for 5 days

Table 8. Resonalyser test results: Young's moduli (GPa) of plate B specimens

Stress level (MPa)	25	50	75	100
Unloaded	26.2	26.2	27.5	26.5
1 cycle*	21.2	18.7	20.8	20.0
2 cycles*	20.4	17.8	18.2	19.2

\* After loading, and before the Resonalyser test, the specimens were stored at 25°C and 60% RH for 5 days

#### 5.5 Comparison between the calculated and measured moduli

In this paragraph, a comparison is made between the initial Young's moduli obtained from the Resonalyser test, and the moduli obtained by the stress versus strain curve recorded during loading.

Table 9 summarises these moduli for the unloaded specimens. For the unloaded case, a comparison can be made with the calculated composite moduli from Table 2. It seems that all the measured moduli are lower than the calculated ones. This is what was expected because of the initial cracked 'state' of the 'virgin' specimens. This initial 'state' also explains the differences between the results obtained from the Resonalyser and the tensile tests. Indeed, the initial cracks of the specimens are not uniformly distributed over the specimen. During the Resonalyser test, the beams are vibrated in the bending mode. In the

testing bench, the specimens are uniformly stressed. Therefore the outer layers of the test beams have more influence on the Resonalyser results than those obtained during the tensile test.

Table 9. Overview of calculated and measured initial Young's moduli (GPa) for unloaded specimens

	Calculated (Table 2)	Measured (Resonalyser)	Measured (Tensile test)
A	29.9	1 25.4	29.4
		2 24.6	30.5
		3 22.5	26.5
		4 23.0	-
B	30.4	1 26.2	26.9
		2 26.2	25.9
		3 27.5	29.3
		4 26.5	28.1

The moduli measured after one load cycle in Table 10 confirms this. After one load cycle, the cracks are uniformly distributed over the test specimens, and the results of both test procedures are similar. The small differences may be due to the different crack state at the end of the specimens caused by clamping of the beams in the testing bench.

Table 10. Overview of measured initial Young's moduli (GPa) after one load cycle

	plate A		plate B	
	Resonalyser	Tensile test	Resonalyser	Tensile test
1	19.8	19.0	21.2	21.4
2	17.7	17.1	18.7	18.8
3	17.2	17.0	20.8	18.4
4	17.4	17.6	20.0	20.9

## 6 CONCLUSIONS

A series of tests were performed on laminates consisting of an inorganic phosphate cement (called IPC), developed at VUB, and unidirectional continuous glass fibres. The laminates were loaded at different stress levels. It was examined whether the Young's modulus and damping ratio of the laminates, measured by the Resonalyser technique, could serve as a 'tool' for describing the 'state' of the laminates.

\* The Young's modulus of unloaded specimens, measured by the Resonalyser, is an indication of the initial laminate 'state'.

\* The damping tests are very sensitive to stress concentrations and to storing and environmental conditions. Therefore the specimens need to be

controlled very strictly, resulting in a laborious test procedure.

\* The damping ratio of the beams increases after loading at specific stress levels. The increase is more significant for lower stress levels. For higher stress levels, the damping of the glass fibres has more influence resulting in a lower damping ratio.

\* The combination of Young's modulus and damping ratio can provide a good insight in the 'state' of the composite. The advantage of the Resonalyser is that no additional damage is induced to the material.

\* The stress versus strain curve, and the unloading/reloading curves of the examined composites are different from the curves predicted by the ACK theory for brittle matrix composites. Only two instead of three stages of the stress versus strain curve can be distinguished due to the initial crack state of the specimens. The unloading curve is different from the ACK model because the physical background of the model is not valid for the examined material.

## 7 ACKNOWLEDGEMENTS

The authors wish to acknowledge the funding of the study by the Research Council (OZR) of the Vrije Universiteit Brussel. The authors also wish to thank the staff of the lab for their help during the research: especially ir. I. Peeters, dr. ir. J. De Visscher and ing. F. Boulpaep.

## 8 REFERENCES

- Aveston, J., G.A. Cooper & A. Kelly 1971. Single and multiple fracture. *The Properties of Fibre Composites*: 15-24. London: IPC Science & Technology Press Ltd.
- Aveston, J., R.A. Mercer & J.M. Sillwood 1975. The Mechanism of Fibre Reinforcement of Cement and Concrete. Interim Report. National Physical Laboratory
- Edelstein, A. 1997. Schadebeschrijving van het postscheurgedrag voor vezelversteigde IPC. Thesis, Brussels: Vrije Universiteit Brussel (VUB)
- Keer, J.G. 1981. Behaviour of cracked fibre composites under limited cyclic loading. *The International Journal of Cement Composites* 3(3): 179-186. Construction Press
- Sol, H., J. De Visscher & J. Vantomme 1991. Measurement of Complex Moduli of Composite Materials and Discussion of Some Results. In A. Vautrin & H. Sol (eds), *Mechanical Identification of Composites*: 16-29. London New York: Elsevier Science Publishers

---

Sol, H., J. De Visscher & J. Vantomme 1991. Mixed Numerical/Experimental techniques for the characterisation of Polymer Matrix Composite Laminates. In A.H. Cardon & G. Verchery (eds), *Durability of Polymer Based Composite Systems for Structural Applications*: 514-523. London New York: Elsevier Science Publishers

Sol, H., J. De Visscher & W.P. De Wilde 1994. Identification of the complex moduli of orthotropic plates using a mixed numerical/experimental method. In W.R. Blain & W.P. De Wilde (eds), *Computer Aided Design in Composite Material Technology IV*: 365-372. Southampton Boston: Computational Mechanics Publications

## Prediction of tensile fatigue life for unidirectional CFRP

Yasushi Miyano, Masayuki Nakada & Hiroshi Kudoh

*Materials System Research Laboratory, Kanazawa Institute of Technology, Ohgigaoka Nonoichi Ishikawa, Japan*

Rokuro Muki

*Civil and Environmental Engineering Department, University of California, Los Angeles, Calif., USA*

**ABSTRACT:** A prediction method of fatigue strength of polymer composites under an arbitrary frequency, stress ratio and temperature is proposed. The method is based upon the four hypotheses: (A) same failure mechanism for static, creep and fatigue failure, (B) same time-temperature superposition principle for all failure strengths, (C) linear cumulative damage law for monotone loading and (D) linear dependence of fatigue strength upon stress ratio. Tensile static, creep and fatigue tests at various temperatures were conducted in the longitudinal direction of unidirectional CFRP. The validity of the prediction method and the applicability of the hypotheses for the tensile fatigue strength for this unidirectional CFRP are discussed.

### 1 INTRODUCTION

The mechanical behavior of polymer resins exhibits time and temperature dependence, called viscoelastic behavior, not only above the glass-transition temperature  $T_g$  but also below  $T_g$ . Thus, it can be presumed that the mechanical behavior of FRP using polymer resins as matrices also depends on time and temperature even below  $T_g$  which is within the normal operating-temperature range. These examples are shown by Aboudi et al., Sullivan and Gates, Miyano et al and Nakada et al.

The time-temperature dependence of the flexural static, creep and fatigue strengths of various CFRP laminates has been studied by Miyano et al, McMurray et al and Mohri et al. It was observed that the fracture modes are almost identical for the three types of loading over a wide range of time and temperature. Similar results were also reported by Karayaka et al for room temperature. The literature survey indicates the validity of the two hypotheses for CFRP: the same failure mechanism and the same time-temperature superposition principle for static, creep, and fatigue failure.

In our previous paper, we add two additional hypotheses: the linear cumulative damage law for monotone loading and the linear dependence of fatigue strength upon stress ratio. A prediction method based on these four hypotheses was proposed for fatigue strength of CFRP under arbitrary frequency, stress ratio and temperature. The validity of the method and the hypotheses was confirmed by three-point bending tests of satin-woven CFRP laminates.

In this paper, we apply this prediction method to

the tensile fatigue strength of unidirectional CFRP and confirm its validity by the split disk tensile fatigue tests. Our proposed approach leads to a simpler estimate of life of polymer composites than the traditional S-N approach and may be extended to life-prediction of polymer-composite structure under combined loading and temperature histories.

### 2 PREDICTION PROCEDURE OF FATIGUE STRENGTH

The prediction method for fatigue strength of polymer composites under arbitrary frequency, stress ratio and temperature requires the data of static tests at several constant loading-rates and various temperatures, and of fatigue tests at a single frequency and several temperatures. The method rests on the four hypotheses, (A) same failure mechanism for static, creep and fatigue failure, (B) same time-temperature superposition principle for all failure strengths, (C) linear cumulative damage law for monotone loading and (D) linear dependence of fatigue strength upon stress ratio.

When these hypotheses are met, the fatigue strength for an arbitrary combination of frequency, stress ratio and temperature can be determined based on the following test results: (a) master curve of static strength and (b) master curve of fatigue strength for zero stress ratio. The master curve of static strength is constructed from the test results at several constant loading-rates for various temperatures. On the other hand, the master curve of fatigue strength for zero stress ratio can be constructed from tests at a single

frequency for various temperatures using the time-temperature superposition principle in which the static strength is regarded as the fatigue strength at  $N_f=1/2$ .

The outline of this method is shown schematically in Fig.1 together with definitions of some notations. The detail of the method will be presented with experimental results.

### 3 EXPERIMENTAL PROCEDURE

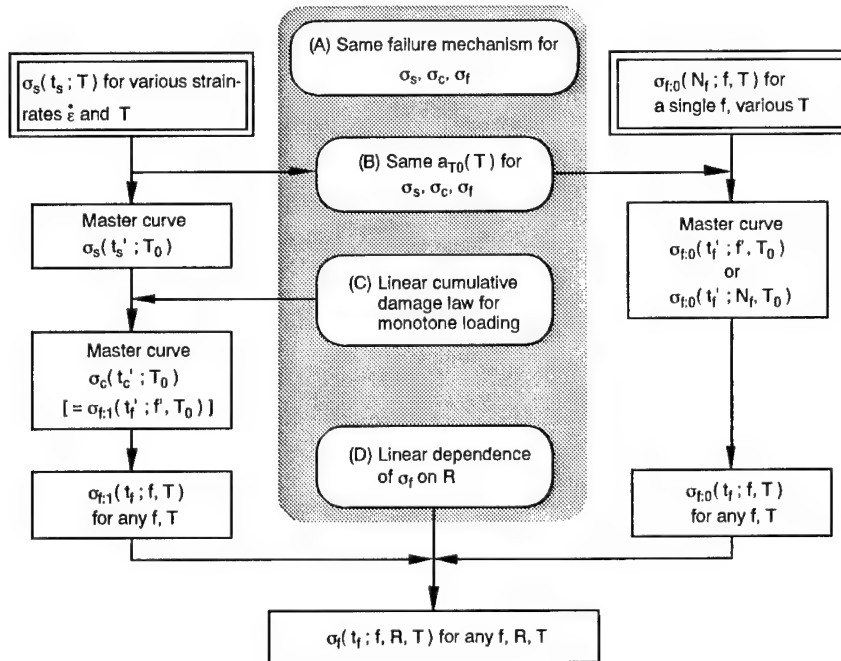
#### 3.1 Preparation of specimen

The unidirectional carbon fiber/epoxy composites ring (CF/Ep ring) produced by filament winding method

consists of high strength carbon fibers, T400-3K (TORAY, brand name TORAYCA) and a general purpose epoxy resin (YUKA SHELL EPOXY, brand name EPIKOTE 828). The CF/Ep ring is cured at 70°C for 12 hours and postcured at 150°C for 4 hours and then at 190°C for 2 hours. The glass transition temperature  $T_g$  of the epoxy resin is 112°C. The fiber volume fraction of CF/Ep ring was approximately 60 %. The diameter and thickness of CF/Ep ring are 200mm and 1mm, respectively.

#### 3.2 Test procedures

Two kinds of tests were carried out, one is the tests



- $T, T_0$  : temperature, reference temperature
- $f, f'$  : frequency, reduced frequency
- $t_s, t_c, t_f$  : time to failure under constant strain-rate, creep and fatigue loadings
- $t'_s, t'_c, t'_f$  : reduced time to failure
- $a_{T0}(T)$  : time-temperature shift factor ( $a_{T0}(T) = t_s/t'_s = t_c/t'_c = t_f/t'_f = f/f'$ )
- $R$  : stress ratio ( $R = \sigma_{min}/\sigma_{max}$ )
- $N_f$  : number of cycles to failure ( $N_f = f t_f$ )
- $\sigma_s, \sigma_c, \sigma_f$  : static, creep, and fatigue strengths
- $\sigma_{f,0}, \sigma_{f,1}$  :  $\sigma_f$  for  $R=0$  and  $R=1$

Fig.1 Prediction procedure of fatigue strength of polymer composites under arbitrary frequency, stress ratio and temperature

according to the proposed methodology and the other is the tests for confirming the validity of this methodology as shown in Table 1.

The tensile test specimens of CF/Ep ring were prepared according to ASTM D 2290 as shown in Fig.2. The tensile static tests were conducted at 6 testing temperatures between 50 and 150°C, by using an Instron type testing machine. Loading rates (cross-head speeds) were 0.01, 1 and 100mm/min.

Specimens with the same dimensions were used for tensile creep and fatigue tests. The creep tests were conducted at 3 testing temperatures by using creep testing machine. The fatigue tests were conducted by using an electro-hydraulic servo testing machine with a constant temperature chamber. The tests were conducted at 3 loading frequencies of  $f=2$ , 0.2 and 0.02Hz at several testing temperatures. Stress ratio  $R$  (minimum stress/maximum stress) was 0.01. Additionally, the fatigue tests were also conducted at  $f=0.2\text{Hz}$ ,  $R=0.5$  for several testing temperatures.

## 4 RESULTS AND DISCUSSION

### 4.1 Fractographs

The static, creep and fatigue failure occur instantly and all these specimens are failed in fine pieces. Therefore we consider that the failure mechanisms are the same for static, creep and fatigue loadings.

### 4.2 Master curve of static strength

The left side of Fig.3 shows the tensile static strength  $\sigma_s$  versus time to failure  $t_s$  at various temperatures  $T$ , where  $t_s$  is defined as the time period from initial loading to maximum load in constant loading-rate tests. The graphs on the left show the dependence of strength  $\sigma_s$  on  $t_s$  and  $T$ . The master curve was constructed by shifting  $\sigma_s$  at various constant temperatures along the log scale of  $t_s$  so they overlapped each other as shown in the right side of Fig.3. Since  $\sigma_s$  at various temperatures can be superimposed smoothly, the time-temperature superposition principle is applicable for  $\sigma_s$ .

The time-temperature shift factor  $a_{T_0}(T)$  is defined by

$$a_{T_0}(T) = \frac{t_s}{t_s'} \quad (1)$$

where,  $t_s'$  is reduced time to failure and  $T_0$  is the reference temperature. Figure 4 shows the time-temperature shift factors  $a_{T_0}(T)$  obtained experimentally for the master curve of the tensile static strength. All of these shift factors are quantitatively

Table 1 Conditions for tensile static, creep and fatigue tests

Loading type	Cross-head speed [mm/min]	Frequency [Hz]	Stress ratio $\sigma_{min}/\sigma_{max}$	Temperature [°C]
Static	0.01	—	—	50, 70, 90,
	1			110, 130, 150
Creep *	—	—	1	50, 110, 150
Fatigue I	—	0.2	0.01	50, 110, 150
Fatigue II *	—	2 0.02	0.01	110, 150 86, 130
Fatigue III *	—	0.2	0.5	50, 110, 150

\*:Test for confirming the validity of this methodology

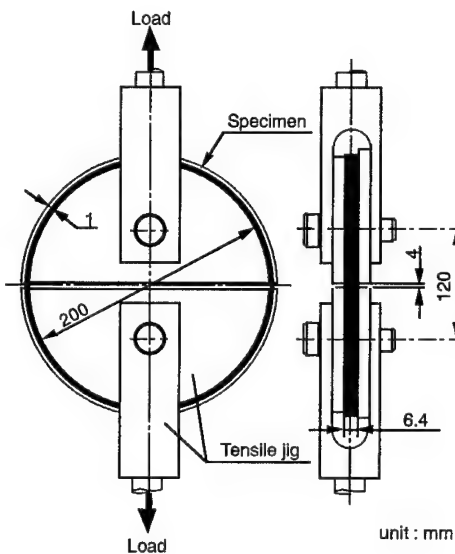


Fig.2 Tensile test procedure for CFRP ring

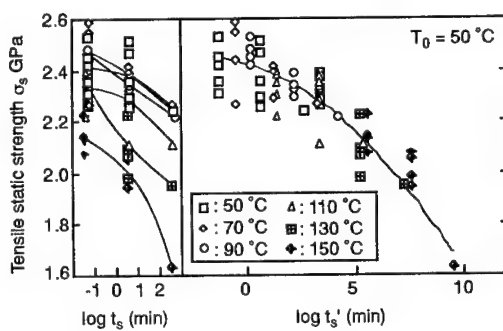


Fig.3 Master curve of tensile static strength

in good agreement with two Arrhenius' equations with different activation energies.

$$\log a_{T_0}(T) = \frac{\Delta H}{2.303R} \left( \frac{1}{T} - \frac{1}{T_0} \right) \quad (2)$$

where,  $\Delta H$  is activation energy [kJ/mol], R is gas constant  $8.314 \times 10^{-3}$  [kJ/(K·mol)].

The shift factor  $a_{T_0}(T)$  for the tensile static strength of CF/Ep ring agrees well with that for the storage modulus of matrix resin indicated by dotted lines in this figure. Therefore, the time and temperature dependence of the tensile static strength of CF/Ep ring is controlled by the viscoelastic behavior of matrix resin.

#### 4.3 Master curve of creep strength

A prediction method of creep strength  $\sigma_c$  from the master curve of static strength using the linear cumulative damage law was proposed in our previous paper. Let  $t_s(\sigma)$  and  $t_c(\sigma)$  be the static and creep failure time for the stress  $\sigma$ . Suppose that the material experiences a monotone stress history  $\sigma(t)$  for  $0 \leq t \leq t^*$  where  $t^*$  is the failure time under this stress history. The linear cumulative damage law states

$$\int_0^{t^*} \frac{dt}{t_c[\sigma(t)]} = 1 \quad (3)$$

when  $\sigma(t)$  is equal to constant stress  $\sigma_0$ , the above formula implies  $t^* = t_c(\sigma_0)$ .

Figure 5 displays the creep strength  $\sigma_c$  versus time to failure  $t_c$ ; the left side shows the experimental data, while the right side exhibits the data shifted to the reference temperature  $T_0=50^\circ\text{C}$  using the shift factors for the static strength. Since  $\sigma_c$  at various temperatures can be superimposed smoothly, the time-temperature superposition principle is also applicable for  $\sigma_c$ .

The right side of this figure also displays the master curve of static strength drawn by a dotted line. The creep strength calculated by equation (3) using the master curve of static strength is shown by a solid curve. The predicted master curve captures reasonably well the experimental data, therefore, the hypotheses (B) and (C), on which this prediction method was constructed, are valid for the creep strength.

#### 4.4 Master curve of fatigue strength

We regard the fatigue strength  $\sigma_f$  either as a function of the number of cycles to failure  $N_f$  or of the time to failure  $t_f = N_f/f$  for a combination of f, R, T and denote

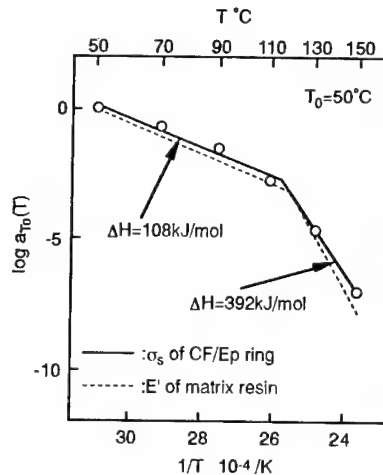


Fig.4 Time-temperature shift factors

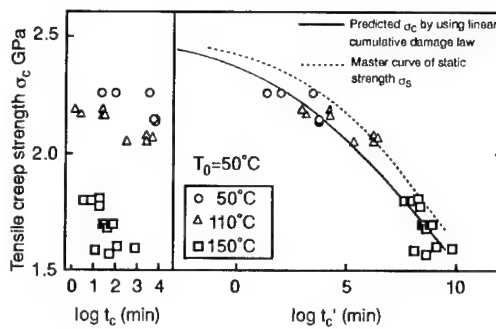


Fig.5 Prediction of tensile creep strength based on the linear cumulative damage law

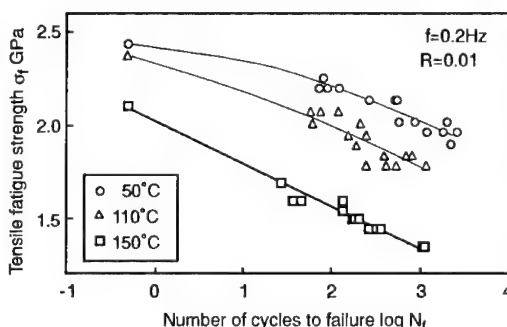


Fig.6 Tensile fatigue strength vs. number of cycles to failure ( $f=0.2\text{Hz}$ )

them by  $\sigma_f(N_f; f, R, T)$  or  $\sigma_f(t_f; f, R, T)$ . Further, we consider that the static strength  $\sigma_s(t_f; T)$  is equal to the fatigue strength at  $N_f=1/2$  and  $R=0$  by choosing  $t_f=1/(2f)$ . At this point, we introduce special symbols for fatigue strength at zero and unit stress ratios by  $\sigma_{f,0}$  and  $\sigma_{f,1}$  where the latter corresponds to creep strength.

To describe the master curve of  $\sigma_{f,0}$ , we need the reduced frequency  $f'$  in addition to the reduced time  $t_f'$ , each defined by

$$t_f' = \frac{t_f}{a_{T_0}(T)} = \frac{N_f}{f'} , \quad f' = f \cdot a_{T_0}(T) \quad (4)$$

Thus, the master curve for zero stress ratio has two alternative expressions,  $\sigma_{f,0}(t_f'; f, T_0)$  and  $\sigma_{f,0}(t_f'; N_f, T_0)$ . In the latter expression, the explicit reference to frequency is suppressed in favor of  $N_f$ . Recall that the master curve of fatigue strength at  $N_f=1/2$  reduces to the master curve of static strength.

The fatigue strength  $\sigma_f$  versus the number of cycles to failure  $N_f$  ( $\sigma_f-N_f$  curve) at a frequency  $f=0.2\text{Hz}$ , stress ratio  $R=0.01$  are shown in Fig.6. The upper side of Fig.7 shows  $\sigma_f$  versus reduced time to failure  $t_f'$  curves for three frequencies and the master curve of static strength in dashed curve. These  $\sigma_f-t_f'$  curves at  $T_0=50^\circ\text{C}$  can be obtained from  $\sigma_f-N_f$  curves by use of the time-temperature superposition principle for the static strength. Connecting the points of the same  $N_f$  on these curves, the master curves of  $\sigma_f$  for constant  $N_f$  are constructed as shown in the lower side of Fig.7.

The  $\sigma_f-N_f$  curves at  $f=2$  and  $0.02\text{Hz}$  are shown in Fig.8. These curves in this figure show the predicted  $\sigma_f-N_f$  curves at  $f=2$  and  $0.02\text{Hz}$  by using the master curves of  $\sigma_f$  as shown in the lower side of Fig.7. Since the predicted and experimental  $\sigma_f-N_f$  curves agree well with each other, the time-temperature superposition principle for the static strength also holds for the fatigue strength, and the hypothesis (B) is valid for fatigue strength.

#### 4.5 Prediction of fatigue strength for arbitrary frequency, stress ratio and temperature

We have the master curve for creep strength  $\sigma_c(t_c'; T_0)$  from which follows the creep strength at any temperature  $T$ . The creep strength, in turn, may be regarded as the fatigue strength  $\sigma_{f,1}(t_f; f, T)$  at unit stress ratio  $R=1$  and arbitrary frequency  $f$  with  $t_c=t_f$ . Further, from the master curve for fatigue strength at zero stress ratio, we can deduce the fatigue strength  $\sigma_{f,0}(t_f; f, T)$  at zero stress ratio for any frequency  $f$  and temperature  $T$ .

Implementing hypothesis (D), we propose a formula to estimate the fatigue strength  $\sigma_f(t_f; f, R, T)$  at an arbitrary combination of  $f, R, T$  by

$$\sigma_f(t_f; f, R, T) = \sigma_{f,1}(t_f; f, T)R + \sigma_{f,0}(t_f; f, T)(1-R) \quad (5)$$

Figure 9 displays the experimental data of  $\sigma_f-t_f$  for  $f=0.2\text{Hz}$ ,  $R=0.5$  and  $T=50, 110, 150^\circ\text{C}$ . The curve for  $R=0.01$  represents the least squares fit for experimental

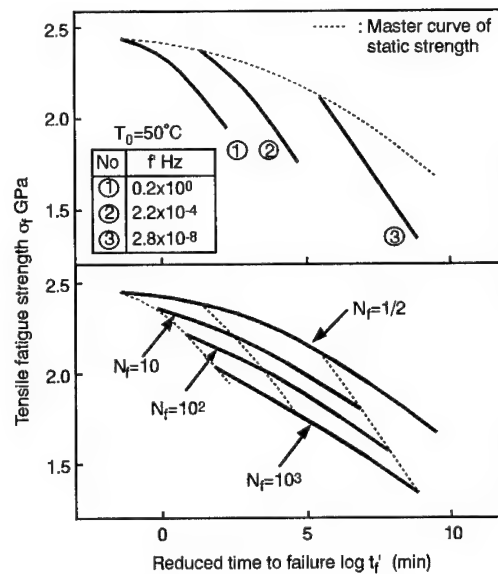


Fig.7 Master curves of tensile fatigue strength

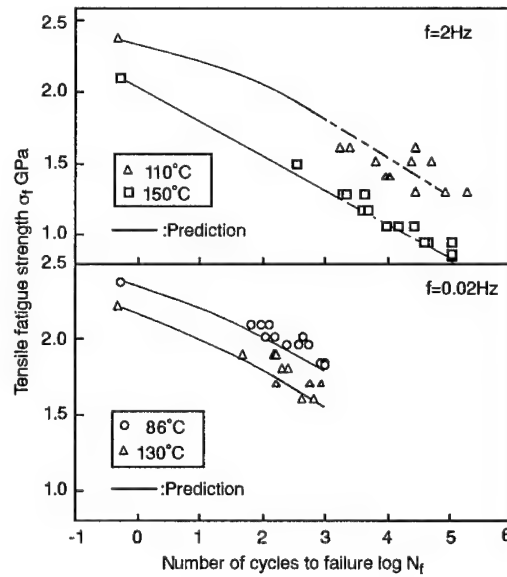


Fig.8 Tensile fatigue strength vs. number of cycles to failure ( $f=2$  and  $0.02\text{Hz}$ )

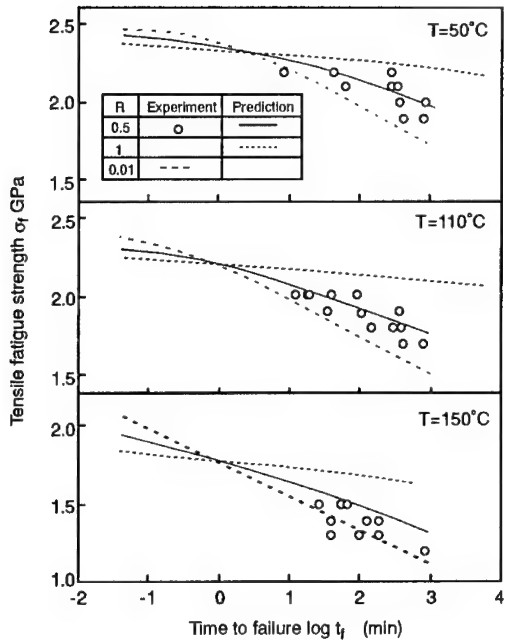


Fig.9 Tensile fatigue strength vs. time to failure for three stress ratios

data of fatigue test for  $R=0.01$ . The curve of  $R=1$  represents predicted creep strength as shown in Fig.5. The curve of  $R=0.5$  is calculated from equation (5) on the basis of the curves for  $R=0.01$  and  $R=1$ . As can be seen, the predictions correspond with the experimental data. We can predict  $\sigma_f-t_f$  relation for given  $R$ ,  $f$  and  $T$  from equation (5) if  $\sigma_{f,1}(t_f; f, T)$  and  $\sigma_{f,0}(t_f; f, T)$  are known.

## 5 CONCLUSION

We proposed, in our 1997 paper, a prediction method for the fatigue strength of polymer composites under an arbitrary frequency, stress ratio and temperature. The method is based upon the four hypotheses: (A) same failure mechanism for static, creep and fatigue failure, (B) same time-temperature superposition principle for all failure strengths, (C) linear cumulative damage law for monotone loading and (D) linear dependence of fatigue strength upon stress ratio. The validity of the prediction method and the hypotheses are confirmed for tensile fatigue tests of unidirectional CFRP.

## REFERENCES

- Aboudi J. and G. Cederbaum, 1989. Analysis of Viscoelastic Laminated Composite Plates, *Composite Structures*, 12: 243-256.
- Sullivan J., 1990. Creep and Physical Aging of Composites, *Composite Science and Technology*, 39: 207-232.
- Gates T., 1992. Experimental Characterization of Nonlinear Rate Dependent Behavior in Advanced Polymer Matrix Composites, *Experimental Mechanics*: 68-73.
- Miyano Y., M. Kanemitsu, T. Kunio and H. Kuhn, 1986. Role of Matrix Resin on Fracture Strengths of Unidirectional CFRP, *Journal of Composite Materials*, 20: 520-538.
- Nakada M., M. K. McMurray, N. Kitade, M. Mohri and Y. Miyano, 1993. Role of Matrix Resin on the Flexural Fatigue Behavior of Unidirectional Pitch Based Carbon Fiber Laminates, *Proc. International Conference on Composite Materials 9*, Vol.4: 731-738.
- Miyano Y., M.K. McMurray, J. Enyama and M. Nakada, 1994. Loading Rate and Temperature Dependence on Flexural Fatigue Behavior of a Satin Woven CFRP laminate, *Journal of Composite Materials*, 28: 1250-1260.
- McMurray M.K., J. Enyama, M. Nakada and Y. Miyano, 1993. Loading Rate and Temperature Dependence on Flexural Fatigue Behavior of a Satin Woven CFRP Laminate, *Proc. 38th SAMPE*, No.2: 1944-1956.
- Enyama J., M.K. McMurray, M. Nakada and Y. Miyano, 1993. Effects of Stress Ratio on Flexural Fatigue Behavior of a Satin Woven CFRP Laminate, *Proc. 3rd Japan SAMPE*, Vol.2: 2418-2421.
- Karakaya M. and P. Kurath, 1994. Deformation and Fatigue Behavior of Woven Composites Laminates, *Journal of Engineering Materials and Technology*, 116: 222-232.
- Miyano Y., M. Nakada, M.K. McMurray and R. Mukai, 1997. Prediction of Flexural Fatigue Strength of CFRP Composites under Arbitrary Frequency, Stress Ratio and Temperature, *Journal of Composite Materials*, 31: 619-638.

## Effect of acid-base properties of sized carbon fibers on fiber/epoxy matrix adhesion

N.Dilsiz & J.P.Wightman

*Virginia Polytechnic Institute and State University, Blacksburg, Va., USA*

**ABSTRACT:** The acid-base character of unsized Zoltek® carbon fibers was investigated using dynamic contact angle analysis. The surface acid-base properties were characterized by calculating the work of acid-base interaction according to Fowkes' and Good's models. To evaluate the effect of sizing on carbon fiber surface properties, Ultem® (polyimide) and polyurethane sized fibers were studied and compared with unsized fibers. It was found that the sizing on the carbon fibers tended to reduce the surface energy and cover acid-base sites. The surfaces of unsized and sized carbon fibers were also analyzed by XPS to investigate changes in surface chemistry. XPS analysis indicated that hydroxyl groups on the fiber surface decreased with both sizings. These changes in chemistry were reflected in a decrease in both the polar and basic components of the surface energy of the fibers. Single fiber fragmentation testing of unsized and Ultem® and polyurethane sized fibers in an epoxy matrix showed that there is a direct effect of the surface chemical changes on fiber/matrix adhesion.

### 1 INTRODUCTION

The interface between reinforcing fibers and polymeric matrices in composite materials is the controlling factor in obtaining optimum mechanical properties from composites (Yumitroji et al. 1994). It has been recognized that the function of the interface is to transmit stress from the matrix to the reinforcing fiber.

For good bonding and stress transfer, fibers are generally sized or coated with thin polymer films after surface treatment that removes weak boundary layers (Drzal et al. 1983). Sizing has a wetting promotion function but is particularly important for facilitating fiber handling during composite manufacture acting as a lubricant to prevent fiber damage. The effectiveness of the sizing is confirmed by the off-axis strength which is usually close to the strength of the polymer (Piggott, 1989). It has been also reported that the presence of sizing may improve the wetting of the fiber by the matrix resin and protect its reactivity (Hultinger & Krekel, 1991).

Wetting is a prerequisite for good adhesion (Bradley et al. 1993). However, good adhesion also requires functional groups, vis-a-vis Lewis acidic and basic sites in the interfacial region between the fiber and the matrix resin. The concepts proposed by Fowkes (Fowkes 1987)

regarding the short-range hydrogen bonding interactions important in adhesion, make it possible to assess the acid-base character of the surfaces using contact angle measurements. The acid-base nature of the fiber surface is a significant factor in determining the degree of adhesion of these fibers in a given resin matrix. If the acid-base properties of the matrix resin are also determined, it should be possible to choose a fiber/matrix pair to maximize adhesion. The adhesion strength of the interface depends on the thermodynamic work of adhesion that is closely related to the surface energy of the fiber and matrix (Tsutsumi et al. 1996). Surface energies of fibers have been determined quantitatively by measurement of the contact angles using the Wilhelmy plate technique (Chan et al. 1991).

The present study was done to evaluate the influence of polyurethane and polyetherimide sizing on both the acid-base components and the polar dispersive component of the surface energy of Zoltek® carbon fibers. The surfaces of unsized and sized fibers were also analyzed by XPS to determine changes in the elemental composition of the fiber surface. The work of adhesion at the interface between the fiber and epoxy resin matrix was calculated and compared with the interfacial shear strength measured by the fragmentation test.

## 2 EXPERIMENTAL

### 2.1. Materials

Zoltek® carbon fibers were used without and with polyetherimide (Ultem®) and polyurethane (PU) sizings. An amine cured epoxy system was selected as the matrix resin. A difunctional epoxy, diglycidyl ether of bisphenol - A (DGEBA), Epon 828® was cured with a stoichiometric amount of an aromatic amine, 1,3 phenylene diamine (mPDA).

### 2.2. Fiber surface analysis

The surfaces of Zoltek® carbon fibers and the neat polymers were analyzed using a Perkin Elmer PHI 5400 x-ray photoelectron spectrometer (XPS). The spectra were collected using a Mg K $\alpha$  x-ray source (1253.6 eV) and operated at 14 kV and 300 W with an emission current of 25 mA. The pressure inside the chamber was held below  $5 \times 10^{-7}$  Torr during analysis. Both survey and high resolution XPS spectra were recorded at a 45° take-off angle. A Gaussian function was used for curve fitting the C 1s photopeaks. The C 1s electron binding energy was referenced at 285.0 eV.

### 2.3. Contact angle measurements

Contact angles were measured by using a Wilhelmy plate technique with a Cahn dynamic contact angle analyzer. A single carbon fiber was fixed to a nichrome wire with a fast curing cyanoacrylate adhesive. The fiber was then suspended from the microbalance. Wetting force data were recorded at 1 second intervals at a speed of 20  $\mu\text{m}/\text{min}$ . The advancing wetting forces were used to calculate carbon fiber surface energies. The perimeter of the fiber was determined using the wetting force measured for silicone oil which was assumed to give a zero contact angle with the fiber. Twenty separate carbon fibers were measured to get average values.

Methylene iodide was used as the probe liquid for Lifshitz-van der Waals interactions; ethylene glycol, formamide and glycerol were used to probe for acid-base interactions.

The contact angles of liquids against the cured epoxy resin were measured by the sessile drop method with a Rame-Hart 100-00115 NRL contact angle goniometer. Five microliter drops of liquid were carefully placed on the substrate using a microliter syringe. The contact angles of both sides of each drop were measured. Six separate measurements were done to obtain an average value for the contact angle.

### 2.4. Tensile strength measurements

The tensile strengths of single carbon fibers were measured at a gauge length of 20 mm at a cross-head speed of 3  $\mu\text{m}/\text{sec}$ . The fibers were glued to paper tabs at both ends using a cyanoacrylate adhesive. After the adhesive cured, one of the tabs was hung to a Mettler PM 300 balance and the other tab was gripped by a microvise which could be moved vertically by an adjustable motor controlled elevator. The strips of paper were cut and the fiber was pulled in tension. The force was measured by the balance. Twenty data points were collected for each fiber type.

### 2.5. Single fragmentation test

The capacity of the fiber/matrix interface to transfer stress from the matrix to the fiber through the interface can be reflected by the critical length in terms of interfacial shear strength. The strength of the interface and the fracture strength of the embedded fiber determine the length of the fiber fragments obtained. The shear-lag model developed by Kelly-Tyson (Kelly & Tyson 1965) gives the interfacial shear strength, ( $\tau$  or IFSS) according to the following equation:

$$\tau = \sigma_c d / 2 L_c$$

where  $d$  is the fiber diameter, and  $\sigma_c$  is the fiber tensile strength at the critical length of fragments,  $L_c$ .

The fiber/matrix interfacial shear strengths (IFSS) for the unsized and sized carbon fibers were determined by the single fragmentation test. A single carbon fiber was embedded along the center line of a silicone rubber mold with a dog-bone shaped cavity and strained uniaxially along the fiber axis. Epoxy resin was degassed under vacuum and carefully poured into the cavity and filled to the level of mold. The resin was cured at 75°C for 2 hours and postcured at 125°C for 2 hours. The specimen was then removed from the mold and stored in a desicator until testing. The specimen was pulled in tension with 5 % specimen strain at a speed of 1 mm/min. The fragments lengths were measured using a transmission optical microscope.

## 3 RESULTS AND DISCUSSION

### 3.1. Surface composition

The surface composition of unsized and Ultem® and polyurethane sized carbon fibers is presented in Table I. Values of the binding energy (B.E.) and the atomic concentration (A.C.) are listed for

each photopeak. Unsized, Ultem® and polyurethane sized carbon fibers contain carbon, oxygen, nitrogen and sodium.

Table I. XPS surface composition of unsized and sized carbon fibers

Carbon Fiber	Photopeaks			
	C1s	O1s	N1s	Na1s
Unsized	B.E. 285.0 (eV)	533.5	401.4	1073.7
	A.C. 91.2 (%)	6.2	1.2	1.3
Ultem® sized	B.E. 285.0 (eV)	532.5	400.8	1072.2
	A.C. 83.6 (%)	12.6	2.6	1.2
PU sized	B.E. 285.0 (eV)	532.8	399.3	1071.4
	A.C. 76.1 (%)	20.6	2.4	0.9

The identification of functional groups (-COH, -C=O and -COOH) on the unsized and sized carbon fibers was obtained by curve fitting the C1s photopeaks. The percentage of carboxyl (-COOH) and carbonyl (-C=O) functional groups on the surface of the fiber does not change with sizing. However, the hydroxyl group (-C-OH) concentration decreased by nearly a factor of two for polyurethane sized fiber compared to the unsized fiber. For Ultem® sized fiber, the hydroxyl group concentration decreased only slightly from 20 to 16 %.

### 3.2. Surface energy

The contact angles ( $\theta$ ) of the fibers were calculated from wetting forces (F) of each liquid according to the following equation:

$$F = P \gamma_L \cos \theta$$

where P is perimeter of the fiber measured from the wetting force in silicone oil,  $\gamma_L$  is the surface energy of liquid used. The contact angles were higher after sizing with both Ultem® and polyurethane compared to the unsized fibers. This result suggests that high energy sites on the fiber surface are being blocked by the sizing. A similar result was reported for epoxy sizing by Fitzer and Weiss (Fitzer & Weiss 1987).

The results of the determination of the acidic and basic components of surface energy are summarized in Table II. The  $\gamma_s^{LW}$  component of the fiber surface energy was calculated using methylene iodide. The acid-base surface interaction term was determined using polar liquids.

The basic component ( $\gamma^-$ ) of the surface energy decreased from 32 mJ/m<sup>2</sup> for the unsized fiber to 20 mJ/m<sup>2</sup> and to 15 mJ/m<sup>2</sup> for the Ultem® and polyurethane sizings, respectively. The surface of the unsized fiber showed more basic character than Ultem® and polyurethane sized fibers. The surface acidity of the fibers slightly increased with polyurethane sizing. But, it is not possible to assess the acidity or basicity of these fibers from the XPS results since the nature of the C-OH and -C=O groups is not known. It is important to note that the -COOH functional group is clearly acidic. However, this may not be true for the hydroxyl group, R-OH. The -OH group can be acidic if R is a phenyl group or basic if R is an aliphatic group. Similarly, the -C=O is generally slightly basic, but if there is an alpha hydrogen, such as CH-C=O, this hydrogen atom is acidic. The strongly acidic carboxylic groups exhibit a stronger interaction with a basic resin than other groups present on the fiber surface and thus are the ones principally responsible for adhesion to basic polymers (Chan et al. 1991). The total surface energy of the carbon fibers decreased in the order unsized > Ultem® > polyurethane.

The polar and dispersive components of the surface energy of the fibers and the epoxy resin were also determined. Sizing the fibers resulted primarily in a decrease of the polar component of the surface energy ( $\gamma^P$ ) from 9 mJ/m<sup>2</sup> for unsized fiber to 6 mJ/m<sup>2</sup> for the Ultem® and polyurethane sized fibers whereas their dispersive component ( $\gamma^d$ ) did not vary with sizing. This decrease is assumed to be partially due to a decrease in the percentage of -OH functional groups but may also be dependent on the nature of the polymer. The reported value of the surface energy of epoxy resin in the solid state is ~47 mJ/m<sup>2</sup>; the experimentally measured value in the present work was ~51 mJ/m<sup>2</sup>. The surface energy of the epoxy resin was higher than that of the fibers (~40 mJ/m<sup>2</sup>) and also the surface of the epoxy resin showed a strong basic character. The acidic, basic and Lifshitz-van der Waals components of the surface surface energy for epoxy resin were  $\gamma_s^+ = 0$ ,  $\gamma_s^- = 66.8$ ,  $\gamma_s^{LW} = 46.7$  mJ/m<sup>2</sup>.

The changes in surface energy are closely related to the concentration of surface hydroxyl functional group determined by XPS analysis of the fiber surfaces as shown in Figure 1. Both the

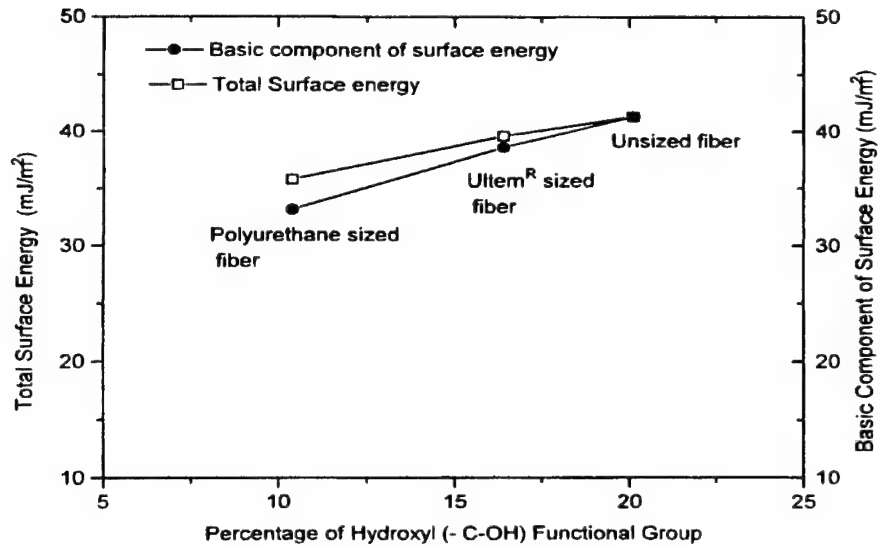


Figure 1. Basic components of surface energy and total surface of unsized, Ultem® sized and polyurethane sized carbon fibers as a function of concentration of hydroxyl groups on the fiber surfaces.

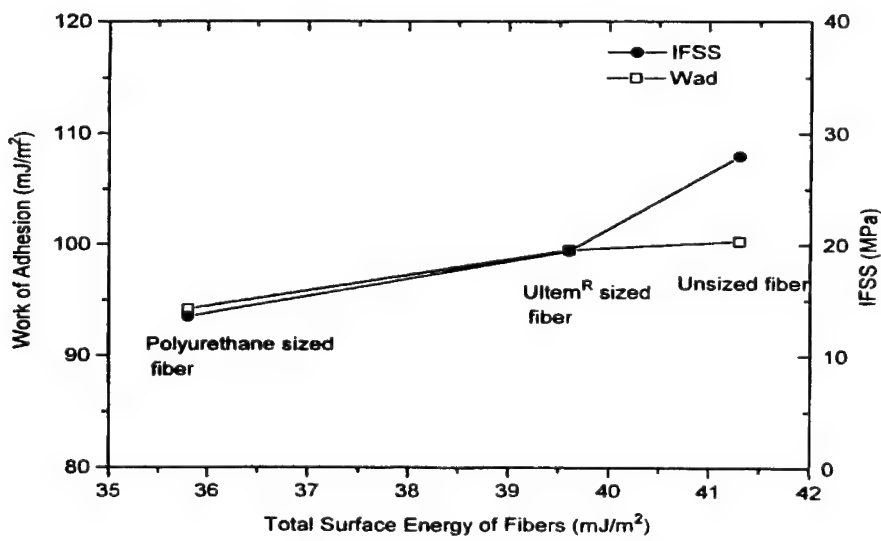


Figure 2. The relationships between interfacial shear strength (IFSS) and work of adhesion as a function of the total surface energy of fibers.

Table II. Acid-base surface energy components (in mJ/m<sup>2</sup>) of unsized Zoltek® carbon fibers as calculated by the three liquid approach

	Unsized				Ultem® sized				Polyurethane sized			
	$\gamma_s^{LW}$	$\gamma_s^-$	$\gamma_s^+$	$\gamma_s^T$	$\gamma_s^{LW}$	$\gamma_s^-$	$\gamma_s^+$	$\gamma_s^T$	$\gamma_s^{LW}$	$\gamma_s^-$	$\gamma_s^+$	$\gamma_s^T$
Ethylene glycol /Formamide	41.	28.	0.	41.	39.	16.	0.	40.	33.	16.	0.1	36.
Ethylene glycol /Glycerol	41.	34.	0.	41.	39.	20.	0.	40.	33.	15.	0.1	36.
Formamide /Glycerol	41.	35.	0.	41.	39.	25.	0.	39.	33.	15.	0.1	36.
Average	41.	32.	0.	41.	39.	20.	0.	40.	33.	15.	0.1	36.

Table III. Results of IFSS and tensile strength measurements on unsized and sized fibers

Carbon Fiber	$\gamma_s^T$ (mJ/m <sup>2</sup> )	$\sigma_t$ Tensile Strength (GPa)	$\tau$ IFSS (MPa)	$L_c$ (mm)	d ( $\mu\text{m}$ ) from SEM
Unsized	41.	3.2	28.0 $\pm$ 6.	0.44 $\pm$ 0.1	7.4 $\pm$ 1.1
Ultem® sized	40.	2.6	19.4 $\pm$ 3.	0.58 $\pm$ 0.1	8.3 $\pm$ 0.1
Polyurethane sized	36.	2.5	13.5 $\pm$ 2.	0.85 $\pm$ 0.1	9.0 $\pm$ 1.2

basic components and the total surface energy of the fibers increased with increasing hydroxyl functional group concentration. Hydroxyl functional groups may increase surface polarity and acid-base reactive sites on the fiber surface. From the surface energy data it is concluded that the (C-OH, C=O and COOH) functional groups contribute to the basic nature of the fiber surface. The unsized fiber showed the highest overall functionality and basic surface energy component in comparison to the sized fibers.

### 3.3. Interfacial shear strength

The results of the single fragmentation test and tensile strengths of the unsized and sized fibers are summarized in Table III. The tensile strength of the fibers gradually decreased from 3.2 GPa for the unsized fibers to 2.5 GPa for the sized fibers. This decrease may due to fiber damage during the sizing process.

Figure 2 shows the relationships between the interfacial shear strength (IFSS) and the work of

adhesion as a function of the total surface energy of fibers. The work of adhesion and IFSS decreased with a decrease in the total surface energy of fibers. As expected, polyurethane sized fiber showed a lower IFSS (13.5 MPa) compared to the unsized fiber (28 MPa). The decrease in the work of adhesion may result from a decrease in the basic character and the polar component of the surface energy and hydroxyl functional groups and therefore in the total surface energy of the fiber.

It is obvious that the changes in the surface properties of the fiber affect the measured IFSS and work of adhesion. Changes in interfacial shear strength and work of adhesion are related to an increase in the total surface energy of fibers. Similar results have been reported for carbon fibers by Schultz and co-workers (Schultz et al. 1987) and by Drzal and co-workers (Drzal et al. 1994).

---

#### 4 SUMMARY

The surface energy of the epoxy resin ( $51 \text{ mJ/m}^2$ ) was higher than that of the fibers ( $\sim 40 \text{ mJ/m}^2$ ) and in addition, the surface of the epoxy resin was basic. The surface energy components of the fibers slightly decreased with sizing. Unsized fibers showed a more basic character than the sized fibers. The atomic percentage of hydroxyl groups on the unsized fibers as determined by XPS was higher than on the Ultem® and polyurethane sized fibers. The atomic percentage of other functional groups did not change with sizing. The work of adhesion between carbon fibers and epoxy resin correlated well with the measured interfacial shear strength (IFSS). The tensile strength and IFSS of single fiber both decreased gradually with sizing (Ultem® and polyurethane) compared to the unsized fiber.

#### ACKNOWLEDGMENTS

We would like to acknowledge the support of the NSF Science and Technology Center for High Performance Polymeric Adhesives and Composites under grant #DMR-9120004 at Virginia Tech. We would like to thank Frank Cromer for his help with the XPS measurements.

#### REFERENCES

1. Yumitroji, S., D. Wang and F.R. Jones, 1994. *Composites* 25(7): 698-705.
2. Drzal, L.T., R.J. Micheal, M.F. Koenig and P.F. Lloyd, 1983. *J. Adhesion*, 16, 133-152.
3. Piggott, M.R., 1989. *Carbon*, 27(5), 657-662.
4. Huttinger, K.J. and G. Krekel, 1991. *Carbon*, 29(8), 1065-1070.
5. Bradley, R. H., X. Ling and I. Shutherland, 1993. *Carbon* 31(7), 1115.
6. Fowkes, F. M. 1987. *J. Adhesion. Sci. Tech.*, 1, 7.
7. Tsutsumi, K., K. Ban, K. Shibata, S. Okazaki and Kogoma, 1996. *J. Adhesion*, 57, 45.
8. Chan, D., M. A. Hozbor, E. Bayramli and R. L. Powell, 1991. *Carbon*, 29(8), 1091.
9. Kelley, A. and W.R.V. Tyson, 1965. *J. Mech. Phys. Solids*, 13, 329.
10. Fitzer, E. and R. Weiss, 1987. *Carbon*, 25(4), 455-467.
11. Schultz, J., L. Lavielle, C. Martin, 1987. *J. Adhesion*, 23, 45.
12. Drzal, L.T., M. Madhukar, M.C. Waterbury, 1994. *Composite Structures*, 27, 65-71.

## Prediction of long term behaviour of graphite-bismaleimide composites: Assessment of residual stresses

A.Vinet, D.Gamby & M.C.Lafarie-Frenot

*Laboratoire de Mécanique et Physique des Matériaux, ENSMA, Suresnes, France*

**ABSTRACT:** This paper presents a model to predict the long term creep behaviour of graphite-bismaleimide (T800H-F655-2) composites, particularly introducing the effects of residual stresses created by cooling down. This model is a combination between the Schapery and Zapas-Crissman's model to describe the viscoelastic and the "pseudoplastic" strain on the laminate. The experimental results of the curvature of an asymmetric laminate (0<sub>4</sub>/90<sub>4</sub>) during thermal creep at 120°C during five months were compared with the calculations performed on program PREVISCO. The numerical results demonstrate that the evolution of the curvature of the specimens is well predicted and validate at the same time the transverse model function identified by short term creep recovery tests. This model also permits us to validate the correct stress level field in each ply of a laminate.

### 1 INTRODUCTION

The development of aeronautical composite laminates in supersonic structures used under severe loading conditions requires a better understanding of the mechanisms involved in the long-term durability of the material. It is out of the question to perform real-time measurements over a period of ten years and it would be unrealistic to reproduce or to multiply experimental tests for many multi-angle laminates. This implies that assessment of long-term durability must be based on the development of numerical prediction methods relying on short-term tests with a duration of a few days or weeks. The constitutive parameters involved in a non-linear viscoelastic-viscoplastic behaviour, such as aging effects, residual stresses effects, mechanical degradation etc... are usually coupled.

### 2 LONG TERM PREDICTION

Here, the nonlinear viscoelastic behaviour is modeled using the Schapery integral while the modified Zapas and Crissman's model is used to represent the permanent strain. The total strain induced by a prescribed thermomechanical loading is the sum of the viscoelastic and the « pseudoplastic » strains. For a unidirectional representation, the isothermal constitutive equation is given by :

$$\varepsilon(t) = g_0 D_0 \sigma + g_1 \int_0^t \Delta D(\psi(t) - \psi(\tau)) \frac{d(g_2 \sigma(\tau))}{d\tau} d\tau + \phi \left( \int_0^t g(\sigma(\xi(\tau))) d\tau \right) \quad (1)$$

where  $D_0$  and  $\Delta D(t)$  are the instantaneous and transient compliances

$g_0, g_1, g_2$  and  $a_\sigma$  are the non-linear functions of Schapery's model

and  $\psi(\tau) = \int_0^\tau \frac{du}{a_\sigma(\sigma(u))}$  is the reduced time

$\phi$  and  $g$  are the functionals of the viscoplastic model which involves an infinite reduced time

$$\xi(t) = \int_0^t \frac{du}{a_\infty(\sigma(u))}$$

On the ply scale, the isothermal model permits an elastic behaviour in the fiber direction and a viscoelastoplastic behaviour for the transverse and shear "flow" deformations to be simulate. The behaviour of each ply is defined by its viscoplastic function and non-linear viscoelastic functions depending on the ply stress state. Thanks to simplifying assumptions it could be demonstrated that a laminate behaves like an homogeneous equivalent non-linear viscoelastic-plastic material which maintains the existence of an accelerated behaviour and allows using the use of a time stress-

superposition principle on a laminate scale. With a view to numerical calculations, these models are superposed and combined with classical lamination theory to obtain predictions for general multi-angle laminates. Then, based on short-term creep and recovery tests performed on  $(+45)_{4s}$  laminate to characterize the shear « flow » deformation and  $(90)_{16}$  laminate to characterize the transverse « flow » deformation at  $120^{\circ}\text{C}$  for different loading levels, this approach, developed by Tuttle & al, has been used to identify all the model's parameters and to predict several mechanical loading responses, more particularly the creep response of various graphite-bismaleimide laminates (T800H/F655-2).

### 3 ASSESSMENT OF RESIDUAL STRESSES

Yet, assessing exactly the strain state of a structure in order to foresee its long-term behaviour requires the accuracy of the functions involved in the isothermal model. Based on experimental observations during laminate manufacturing, it has been realized that residual stresses generated by cooling did relax with increasing time and laminate creep. These residual stresses are to be taken into account for the prediction of long term behaviour so that a means of obtaining their value in each ply and to validate the non-linear viscoelastic and viscoplastic functions of the model by testing asymmetric laminates is presented. Between the stress free temperature and the temperature at which the model will be used, the non linear constitutive equation is unknown, so these stresses cannot be assessed exactly. Moreover, the exact residual stresses field in each ply of a  $(+45)_{4s}$  specimen are unknown, which renders it impossible to correctly determine the constitutive parameters and functions for the shear deformation. Taking into account the prestress due to the initial thermal loading changes the apparent mechanical behaviour of a laminate subjected to creep and recovery, particularly in the non linear viscoelastic range. So a method meant to approach the correct residual stresses and to validate

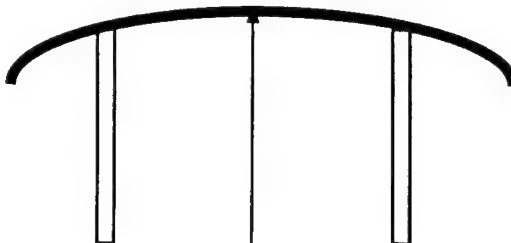


Figure 2. Measure of the specimen's curvature at  $24^{\circ}\text{C}$

the model's function identified by short-term creep and creep-recovery tests is proposed. The experimental method consists in measuring the curvature of five  $(0/90)$  specimens during thermal creep at  $120^{\circ}\text{C}$ .

### 4 EXPERIMENTAL METHOD

The effective measurement at  $120^{\circ}\text{C}$  was not possible. So, all the specimens were put in a thermal chamber at  $120^{\circ}\text{C}$  and their curvature was measured at  $24^{\circ}\text{C}$ .

We consider that the thermal cyclic approach of the specimen's curvature measurement doesn't affect the exact values, controlling the cooling and heating speed of each cycle. The values of the curvature at  $120^{\circ}\text{C}$  were obtained through the values at  $24^{\circ}\text{C}$  which were shifted with an elastic model. We have verified that between  $24^{\circ}\text{C}$  and  $120^{\circ}\text{C}$  the evolution of the curvature behaves in an elastic manner. Then, we compare the results of experimental testings with the simulation in which the residual stresses have been incorporated. Figure 3 presents a numerical simulation together with an experimental comparison of the x-axis relative creep curve after a cooling test performed on a  $(0/90)$  specimens. In calculations, the cooling is supposed to be performed suddenly from the stress free temperature and the model automatically incorporates the residual stresses at  $120^{\circ}\text{C}$ . Experimental testings were performed on several  $(0/90)$  specimens. The first two specimens 3 and 5 were submitted to 8 thermal cycles corresponding to 8 measurements at  $24^{\circ}\text{C}$  whereas another specimen 8 was submitted to 5 thermal cycles. In a first approach, the results show that the number of thermal cycles doesn't affect the curvature's measures too much.

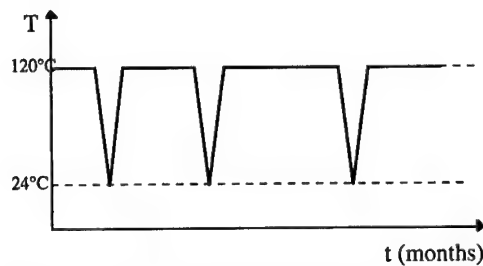


Figure 1. Thermal cyclic approach of the curvature's measure

In spite of a reduced creep for this type of composite material, we notice a common agreement between the results of the experimental testing and those of the numerical simulation, considering testings errors

and the detrimental effect of moisture for the first measurements. Moreover, the testing was not performed as soon as the specimens were elaborated. We realise that during the drying time these specimens could creep at 24°C much more than supposed. The difference in the slopes of the experimental and simulated curves can be explained by the first creep stage of the specimens during the drying at 24°C. In fact, these curves only characterize functions of the transverse « flow » deformation. In all plies, the shear stress field is zero. The decrease

of the x-axis curvature with time is associated with the relaxing of the stress state in each ply which evolves according to the same law. In each ply, only the stresses in the fiber and transverse direction exist and relax with increasing time (Figure 4). Figure 4 presents the simulation of the x-axis stress evolution in the first ply at 0°. The stress levels are different in all the plies of the (0<sub>4</sub>/90<sub>4</sub>) specimen. The elastic solution is represented on this figure in order to compare with the viscoelastic-plastic solution.

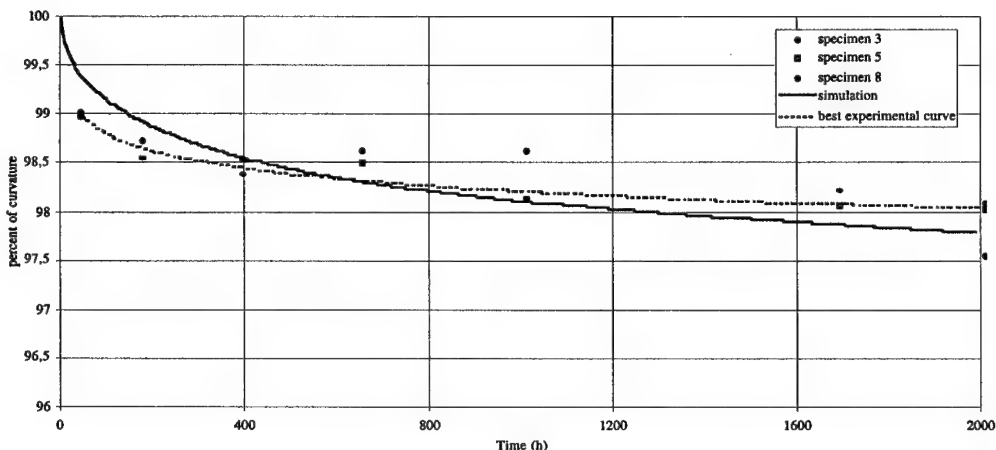


Figure 3. X-axis curvature relative evolution in a (0<sub>4</sub>/90<sub>4</sub>) laminate comparing testing and simulation at 120°C

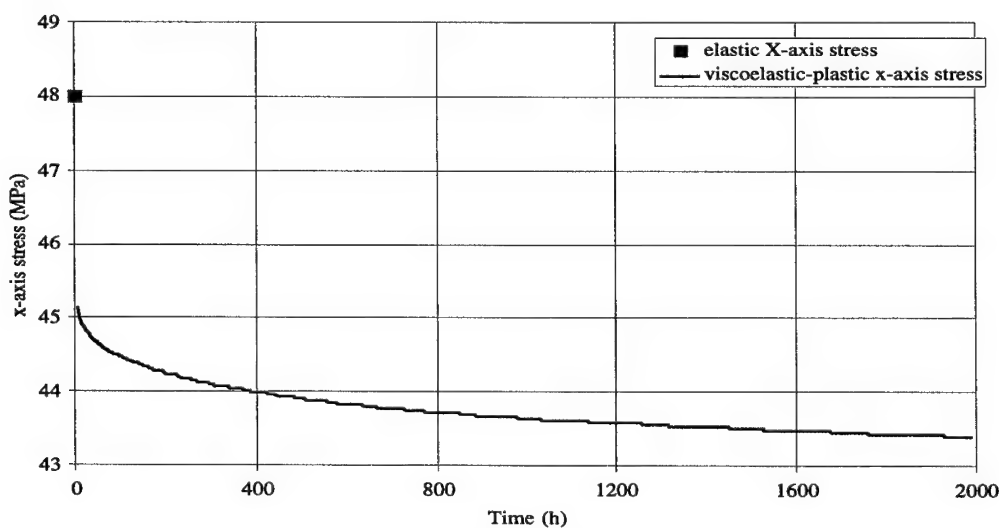


Figure 4. Numerical prediction of x-axis stresses in (0<sub>4</sub>/90<sub>4</sub>) specimen for the outer ply

---

Obviously, it is verified that an elastic approach over estimates the calculation of residual stress fields in the laminates. The relaxation of the stresses is as important as the creep of the specimens.

## 5 CONCLUSIONS

A model dedicated to solve the problem of long term prediction is proposed which incorporates the residual stresses. The method used to characterize at the same time the correct residual stresses and to check the exact constitutive parameters and functions at 120°C identified by short term creep and recovery tests relies on the measurement of the curvature's evolution of an asymmetric composite laminate (04/904) just after a cooling down from the stress free temperature. By simulating a level of the residual stresses induced by cooling down considering the anisotropy of the material and the difference between the dilatation coefficients of the fiber and the matrix, it has been possible to estimate the residual stress field and its evolution and to validate the viscoelastic-plastic functions of the isothermal model at the same time.

## REFERENCES

- Schapery, R.A. 1995. Proceedings of the international conference Duracosys Bruxelles *Characterization of non-linear time dependent polymers and polymeric composites for durability analysis*. 21-38
- PasrichaA., Tuttle M.E. & Emery A.F 1995. *Time dependent response of IM7/5260 composites subjected to cyclic thermo-mechanical loading*. Composites Sciences and Technology 55:49-56
- Zapas L.J. and Crissman J.M. 1884 *Creep and recovery behaviour of ultra-high molecular weight polyethylene in the region of small uniaxial deformations*. Polymer 25

## Life prediction for continuous fiber reinforced composites under stochastic fatigue loading based on the Critical Element Concept

R.Carmine & N.Himmel

*Institute for Composite Materials Ltd, University of Kaiserslautern, Germany*

**ABSTRACT:** The fatigue life simulation model described in this paper is based on the Critical Element Concept which allows life prediction for multiple layer laminates under multiaxial loading. This modeling philosophy combines the phenomena of stiffness reduction and residual strength degradation during cyclic fatigue loading in a physically sensible way.

A stochastic time signal can be prepared for fatigue life simulation by the rainflow cycle counting method and the Haigh diagram where use is made of curves of constant cycles to failure. The described simulation software for life prediction allows the consideration of arbitrary load signals represented by forces, moments, moisture and temperature and includes several failure criteria, namely those of Hashin and Puck. For multiaxial stress states a comparison of fatigue life time prediction based on different failure criteria can be performed.

### 1. INTRODUCTION

During the last twenty years numerous studies on fatigue life prediction of laminates made from fiber reinforced polymers have been carried out. Despite of the great number of experiments and time effort only a few test rows are available which cover a larger spectrum of geometries, stacking sequences, load histories and materials. As a consequence, a multitude of life prediction models exist which are fitted to special test conditions, but which do not provide a general applicability to other loadings, geometries or materials.

The methodology based on the Critical Element Concept is more general and offers the possibility to use few basic experimental data for a large number of simulation runs under various conditions.

For the fatigue life simulation some input data have to be prepared: the measurement data of the S-N curve for a unidirectional 0° laminate and the stiffness degradation of cross-ply laminates under various load amplitudes have to be brought into a mathematically suitable form.

In order to treat stochastic loading in the life prediction simulation - actually representing the real situation in practice - on the one hand the simulation algorithm has to be extended. On the other hand the stochastic time signals have to be prepared to make them available for the simulation based on the Critical Element Concept. Those extensions and the involved data preprocessing are described in this paper.

### 2. CRITICAL ELEMENT CONCEPT

The classical laminated plate theory which allows the determination of the state of plane stress in all layers under forces, moments, moisture and temperature, is the basis for the numerical treatment of continuous fiber reinforced composites with arbitrary stacking sequence. Following the Critical Element Concept developed by Reifsnider and Stinchcomb (1986), the composite is observed in a representative volume where failure under cyclic fatigue loading is to be expected. Two types of elements are imbedded within this volume: First, there are subcritical elements which are continuously damaged under cyclic fatigue loading in several damage modes. The damage process is modeled by a continuous stiffness degradation, whereas total failure is not initiated in these elements. On the other hand, critical elements carry most part of the load and their failure causes total failure of the complete composite. The stiffness reduction produces stress redistribution in the representative volume and - since the internal stress state is continuously changing - the effective stress in the critical elements is a function of the number of cycles.

The degradation equation for the critical elements can be written in the form of an evolution integral:

$$S_r(n_e) = 1 - \int_0^{n_e/N} K [1 - F_d(n)] \left( \frac{n}{N(n)} \right)^{K-1} d \left( \frac{n}{N(n)} \right) \quad (1)$$

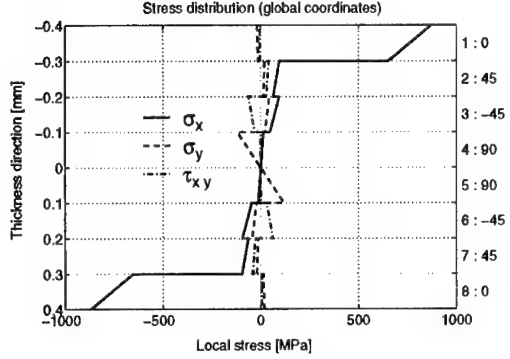


Figure 1: Stress distribution over thickness in a multidirectional laminate under bending load

where  $n$  is the number of cycles,  $S(n_e)$  the normalized residual strength after  $n_e$  cycles,  $F_a(n)$  the dynamic material effort due to a suitable failure criterion,  $N(n)$  the number of cycles to failure which changes with  $F_a(n)$ , and  $K$  an exponent describing the strength degradation.  $F_a(n)$  is a quantity derived from a suitable failure criterion, which allows to compare a general state of stress to the material strengths  $X_{ij}$  in the different directions  $F_a = F_a(\sigma_{ij}, X_{ij})$ .

While the failure criteria of Tsai-Hill, Norris and Tsai-Wu are formulated in a closed analytical form, the criteria of Hashin (1980) and Puck (1969, 1992) assign a mathematical condition to each distinct failure mode. While Hashin's criteria indicate the four failure modes tensile fiber rupture, compressive fiber failure, tensile matrix crack and compressive matrix failure, Puck set up a criterion which - beside the first two failure modes - indicates the shear failure of the matrix between the fibers.

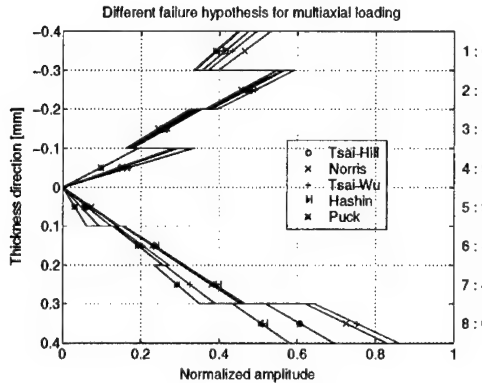


Figure 2: Normalized amplitude over thickness in a multidirectional laminate under bending load

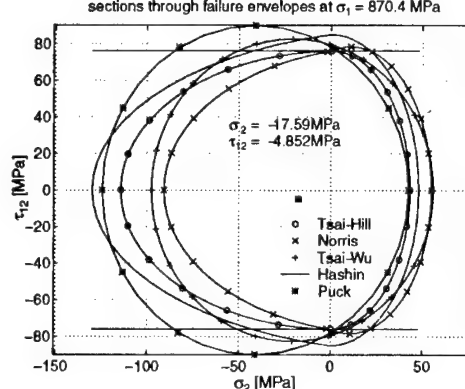


Figure 3 : Failure envelopes of different failure criteria in layer 1 at the upper surface of a multidirectional laminate under bending load

While in Figure 1 the stress distribution in a multidirectional laminate under bending load is displayed, in Figure 2 the corresponding normalized amplitudes according to the five failure hypotheses are shown for this laminate. In the Figures 3 and 4 the sections through the failure envelopes for the five criteria can be seen for cyclic bending load for the peak loads of constant amplitude test.

The normalized amplitude is written in Table 1 in accordance with the failure criteria where this is possible. It can clearly be seen that the different failure hypotheses lead to different normalized amplitudes which represent an important quantity in the life prediction calculation with the Critical Element Concept.

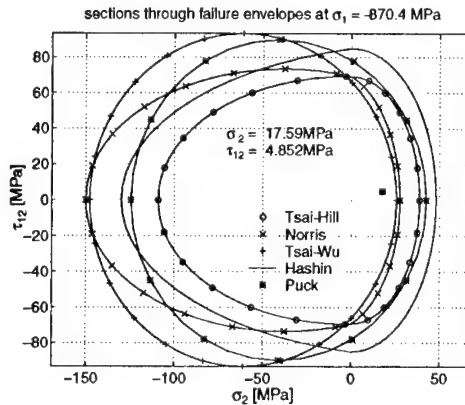


Figure 4: Failure envelopes of different failure criteria in layer 8 at the lower surface of a multidirectional laminate under bending load

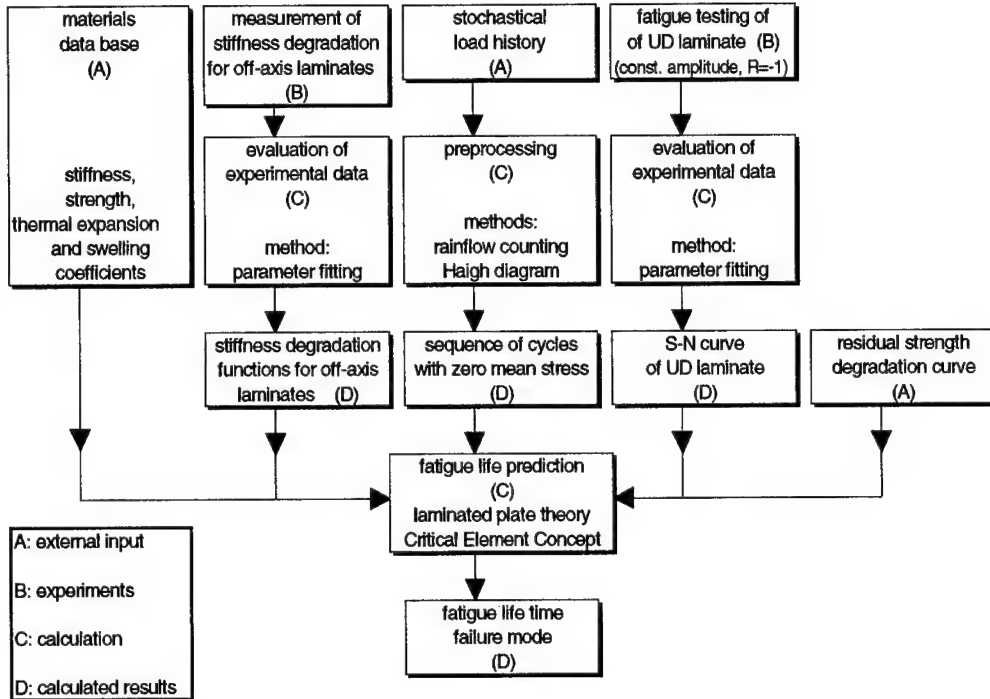


Figure 5: Overview of data preprocessing for fatigue life prediction

### 3. DATA PREPROCESSING

The input for fatigue life prediction consists of experimental data and preprocessed data values and functions. In Figure 5 all input data and their preprocessing for a simulation run are shown schematically.

While the elasticity constants, the static strength values and the hygrothermal constants often may be found in materials data bases, the stiffness degradation function and the S-N curve for the unidirectional laminate have to be determined by experimental testing.

Table 1: Normalized stress amplitudes for the turning points of cyclic bending load in layer 1 and 8 of a multidirectional laminate

	normalized stress Amplitude	
failure criterion	tension	Pressure
Tsai-Hill	0.4742	0.6936
Norris	0.5303	0.8288
Tsai-Wu	0.4946	0.8597
Hashin	0.4500 tensile fiber rupture	0.5803 compressive fiber failure
Puck	0.4463 tensile fiber rupture	0.5803 compressive fiber failure

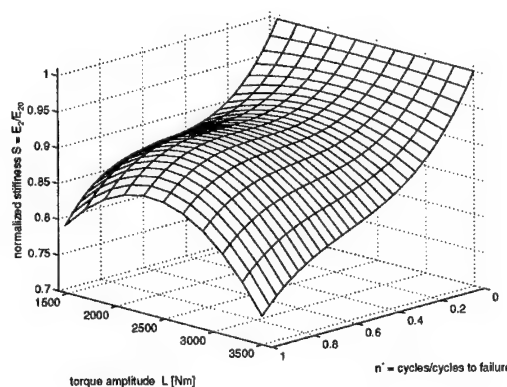


Figure 6: Transverse stiffness ( $E_2$ ) degradation obtained function from a polynomial parameter fit of experimental data as a function of loading amplitude and normalized fatigue cycle number

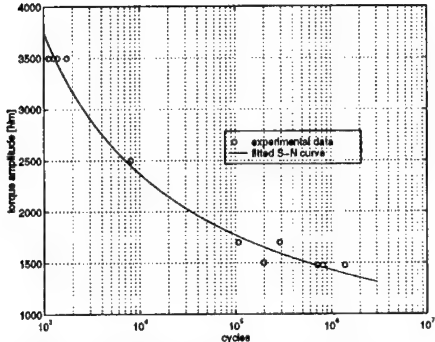


Figure 7: Three parameter S-N curve fit

The experimental data of both stiffness degradation and fatigue strength versus number of cycles to failure have to be prepared by parameter fitting algorithms. While for S-N curves there exists in literature a small amount of functions with two, three or four free parameters, a polynomial fit has to be carried out due to the absence of a given parametric curve for the stiffness degradation curves. In Figure 6 the result of such a polynomial fit is shown. For the S-N curves an automatic search algorithm for the best fit is provided by calculating the least mean square sum as a goodness of fit

measure for the different functions.

Figure 7 shows a three parameter fit

$$\log N = a - b S^c \quad (2)$$

of the S-N curve set up by Reifsneider which was found as the best fit among eight approximation functions. For the residual strength degradation with respect to the cycle number the shape of the curve was approximated by a power function given by Reifsneider and Stinchcomb (1986) with K as defined in eq.(1) equal to 1.2 .

In order to deal with stochastic loading in the fatigue life simulation it is necessary to preprocess the time signals. The rainflow counting algorithm described by de Jonge (1982) and Clormann and Seeger (1986) in a slightly modified form offers a possibility of data preprocessing and data reduction and is explained in more detail in the following.

As shown in Figure 8 a , a stochastical time signal is given. First the time signal is transformed by minimum-maximum filtering with a given hysteresis filter width into a sequence of reversals (Figure 8 b). Then the online rainflow counting algorithm is applied to this sequence, which recognizes closed hysteresis loops, extracts them from the sequence and stores the time values of the reversals. The hysteresis loops - the closed cycles - can be meshed into each other in any order, which can clearly be seen in Figure 8 c.

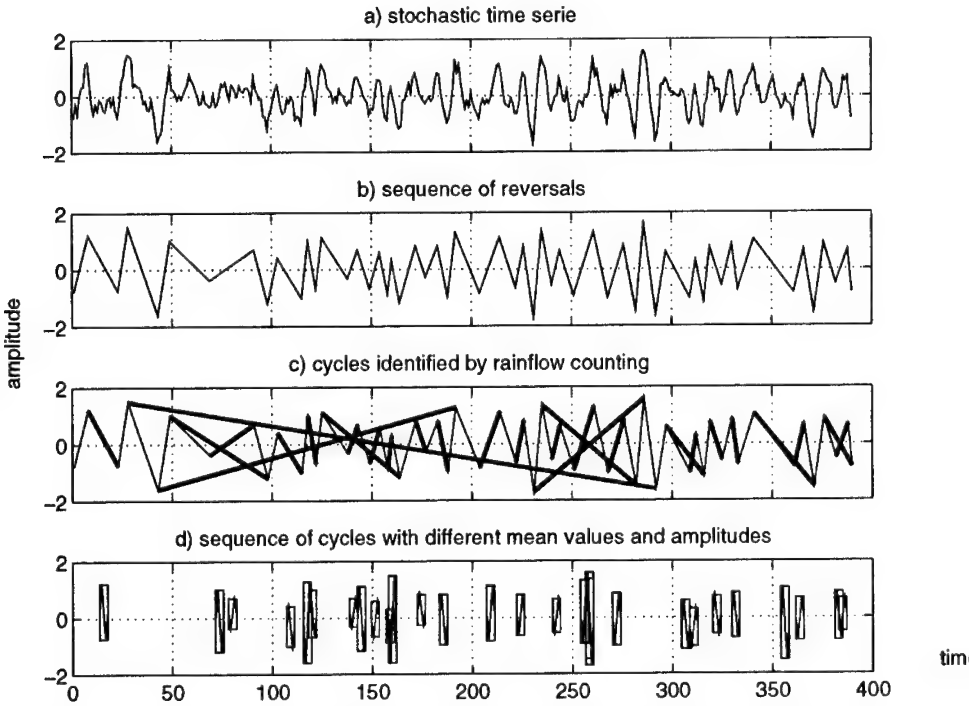


Figure 8: Preprocessing of stochastical load histories by the rainflow counting algorithm

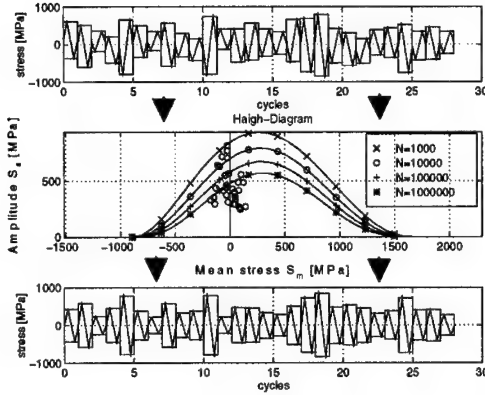


Figure 9: Calculation of the equivalent amplitude with non-zero mean stress using the Haigh diagram

Finally, the identified closed hysteresis loops are sorted in accordance to the mean time value of the two participated reversals in the original time signal

representing the input for the life prediction simulation (Figure 8 d). Using a Haigh diagram and a five parameter formula for the bell-shaped curves of constant cycles to failure as set up by Harris (1995), the amplitude can be converted into an equivalent amplitude with zero mean stress, for which the correspondent S-N curve is available in the simulation system (Figure 9).

#### 4. LIFE PREDICTION SIMULATION

A seven layer laminate of carbon fiber reinforced epoxy is investigated as shown in the upper right corner of Figure 10. The loading (upper left) consists of six blocks of different amplitudes with zero mean force (tension-compression). The result of the simulation is shown in the lower part of Figure 10, where the local state of stress, the S-N curve and the residual strength degradation in the critical element are plotted versus the number of cycles together with the predicted fatigue life cycle number.

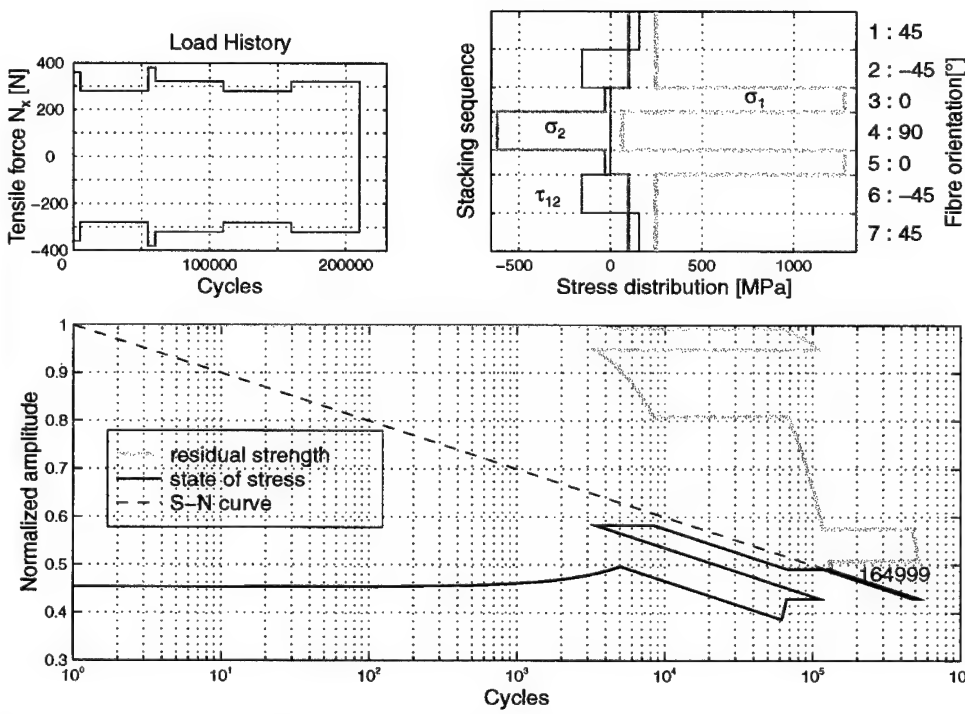


Figure 10: Load history (upper left), peak stress distribution of the first block (upper right), as well as normalized amplitude, S-N curve and residual strength in the critical element versus number of cycles together with predicted fatigue life cycle number (below)

## 5. CONCLUSION

In this paper the procedure of data preprocessing is described for the fatigue life prediction of fiber reinforced composites under cyclic loading which is based on the Critical Element Concept.

Starting from experimental data of the stiffness degradation in cross-ply laminates and of the S-N curves for unidirectional laminates representing the critical elements, a simulation of the damage development and a life time prediction can be performed. The real load histories are decomposed into single cycles by the rainflow counting scheme, which are input into the life simulation algorithm in chronological order. Applying a five parameter function to describe the stress amplitude/mean stress dependence (Haigh diagram), the non-zero mean stress amplitudes are converted into equivalent mean stress free amplitudes.

The procedure presented in this paper allows a life time prediction for stochastic load histories. The single steps of the procedure are realized as software tools.

Reifsnider, K.L. & W.W. Stinchcomb 1986. The Critical Element Model: A Modeling Philosophy. *Engineering Fracture Mechanics* 25, No 5/6 : 739-749.

## ACKNOWLEDGEMENT

The work presented in this paper was realized with the support of the Stiftung Rheinland-Pfalz für Innovation which is gratefully acknowledged.

## 5. REFERENCES

- Clormann, U.H. & T. Seeger 1986. Rainflow -HCM- Ein Zählverfahren für Betriebsfestigkeitsnachweise auf werkstoffmechanischer Grundlage. *Stahlbau* 55, Vol.3 : 65-71.
- de Jonge, J.B. 1982. The analysis of load time histories by means of counting methods, *ICAF document* 1309. National Aerospace Laboratory.
- Harris, B., N. Gathercole, H. Reiter & T. Adam 1996. Constant-stress fatigue response and life-prediction for carbon-fibre. In: A.H. Cardon, H. Fukuda & K. Reifsnider (eds), *Progress in Durability Analysis of Composite System* : 63-73. Rotterdam: Balkema.
- Hashin Z. 1980. Failure criteria for unidirectional fiber composites. *Journal of Applied Mechanics* 47 : 329-334.
- Puck, A. 1969. Festigkeitsberechnung an Glasfaser/Kunststoff-Laminaten bei zusammengesetzter Beanspruchung. *Kunststoffe* 59, No 11.
- Puck, A. 1992. Praxisgerechte Bruchkriterien für hochbeanspruchte Faser-Kunststoff-Verbunde. *Kunststoffe* 82, No.2.

## Probabilistic approach for residual compressive strength of CFRP laminates, following low velocity impact

G.C.Papanicolaou, A.V.Pournaras & D.E.Mouzakis

*Composite Materials Group, Mechanical and Aeronautical Engineering Department, University of Patras, Greece*

J.Karger-Kocsis

*Institute for Composite Materials, Materials Science Division, University of Kaiserslautern, Germany*

D.A.Bofilos

*INASCO Hellas Co., The INtegrated Aerospace Sciences COrporation, TR&D Departments, Galatsi, Greece*

**ABSTRACT:** The impact sensitivity of FRP laminates constitutes a major concern to designers, as it may result in substantial reduction of both tensile and compressive strength, without warning. In particular, for CFRP laminates used primarily in the aerospace industry, reliable predictive tools are required to allow optimized damage tolerant designs. This work presents an elaboration of a model earlier developed by one of the authors which has proven to have extended applicability to CFRPs. Probabilistic definitions of the prepreg material properties, on which model predictions are strongly dependent are embedded in the definition of the bending mismatching coefficient, a fundamental dimensionless quantity of the model. The predictions yielded by the model are based on a previously experimentally obtained nomograph, accounting for the influence of 0°, ±45° and 90° prepreg plies volume contents on the laminate impact energy absorption capacity. Deterministic and probabilistic predictions are compared against experimental residual compressive strength results for UD, angle ply, quasi-isotropic and cross-ply laminates made of the BASF Rigidite 5212 material system. The quality of both prediction types and practical aspects of the probabilistic approach are discussed.

### 1 INTRODUCTION

Sub-perforation impact caused by low velocity projectiles has been found to result in substantial reduction of both tensile and compressive strength of polymeric matrix continuous fiber reinforced laminated plate structural components, since the 1970s. Substantial research efforts have been made to model strength degradation, concerned with tensile strength initially and focusing on compressive strength in the 1980s, particularly with the widespread use of CFRP laminates in aerospace applications. The latter have exhibited a marked sensitivity to low velocity impact; in most cases of laboratory investigations interior damage has been undetectable by external inspection methods. Expensive techniques such as ultrasonic C-scan and X-ray radiography have revealed its extent and allowed to explain the observed reduction in strength. This type of damage poses a challenge to designers, as they have to take it into account in modern durability/damage tolerant requirements for composite structures. Predictive models for strength degradation as a function of impact energy can prove a valuable tool in the design processes, as they can offer some insight to the potential impact risk assessment.

### 2 THEORETICAL BACKGROUND

Originally, predictive models have been based on linear elastic fracture mechanics (LEFM) concepts. The aim has been to derive notched laminates subjected to tension equivalent to the impact damaged ones (Husman et al. 1975). Subsequently, research interest has shifted to post impact compressive behavior and energy based predictive models have become the focus of attention (Caprino 1984).

The model adopted herein belongs to this category and it is based on the so-called bending mismatching coefficient  $M$  (Liu 1988). Delamination is assumed to be the prevailing impact-induced damage mode resulting in a marked drop in compressive/tensile strength, once the total impact energy exceeds a certain threshold value denoted as  $U_0$ . This threshold value is determined for any laminate of practical interest having finite dimensions by performing only one set of impact-compression after impact (I-CAI) laboratory tests on a specimen of the same material system, stacking sequence, thickness, according to the DIN (or Boeing) standard, using a consistent methodology.

Prepreg material system elastic properties and presence of interleaves of varying thickness are accounted for in the expression yielding the dimensionless ratio  $m$ :

$$m = \frac{\sum_{k=1}^N (\bar{M}_k)_o (\bar{Q}_{11})_k (z_k^3 - z_{k-1}^3)}{\sum_{k=1}^N (\bar{Q}_{11})_k (z_k^3 - z_{k-1}^3)} \quad (1)$$

where  $k$  = the index referring to plies/layers (integer pure number),  $N$  = total number of distinct plies and interleaf layers if any (pure number),  $(\bar{M}_k)_o$  = the refined average bending mismatching coefficient defined as:

$$(\bar{M}_k)_o = \frac{(M_{k-1,k})_o + (M_{k,k+1})_o}{2} \quad (2)$$

$(\bar{Q}_{11})_k$  = the  $k$ -lamina transformed reduced stiffness matrix element 11 (GPa),  $z_{k-1}$  = the  $z$ -coordinate of the interface between layer  $k-1$  and  $k$ , in  $m$ ,  $z_k$  = the  $z$ -coordinate of the interface between layer  $k$  and  $k+1$ , in  $m$ )

The terms in the numerator of relation (2) are the evolution of an original concept termed bending mismatching coefficient (Liu 1988), referring to the interfaces between laminate prepreg plies. The new elaborate definition is as follows:

$$(M_{k,k+1})_o = \frac{D_{11,o}(\theta_k) - D_{11,o}(\theta_{k+1})}{D_{11,max} - D_{11,min}} \quad (3)$$

where  $D_{11,o}(\theta_k)$  = the  $k$ -layer bending stiffness matrix element 11 ( $Nm$ ),  $D_{11,o}(\theta_{k+1})$  = the  $k+1$ -layer bending stiffness matrix element 11 ( $Nm$ ),  $\theta_k$  = the  $k$ -layer fiber orientation angle ( $^\circ$ ),  $\theta_{k+1}$  = the  $k+1$ -layer fiber orientation angle ( $^\circ$ ); for interleaf layers it may be taken as either  $0^\circ$  or  $90^\circ$ ,  $D_{11,max}$  = the  $\max\{D_{11,o}(\theta_k)\}$ ,  $k = 1, 2, \dots, N$ ,  $D_{11,min}$  = the  $\min\{D_{11,o}(\theta_k)\}$ ,  $k = 1, 2, \dots, N$ .

It is noted that the bending stiffness matrix terms refer to individual layers, based on Classical Laminated Plate Theory (CLT) notions.

Obviously, the properties of the prepreg material are crucial for the quality of any structural component as much as the laminate manufacturing process. Furthermore the material system building block itself i.e. the unidirectional prepreg tape is the product of another manufacturing process invisible to

the end-users. Due to various shortcomings in the process and taking into account the presence of inevitable flaws in the raw material (fibers and polymeric matrix), it may be deduced that the material properties of the prepreg tape exhibit a distribution of values around a mean value. Within the framework of this work the elastic modulus along the reinforcing fibers direction is examined; it is deemed to be the most important material constant in view of the post-impact behavior under consideration and the predictive model which is focused on the laminate bending stiffness matrix element  $D_{11}$ .

Elaboration over the last years (Papanicolaou & Stavropoulos 1995), (Stavropoulos & Papanicolaou 1997) has led to a compact predictive equation (Papanicolaou & Pournaras 1997).

$$\frac{\sigma_r}{\sigma_o} = \begin{cases} 1 & , U \leq U_o \\ \exp^{-1}\left(\frac{h}{mN} \frac{U - U_o}{U}\right) & , U > U_o \end{cases} \quad (4)$$

where  $h$  = the total laminate thickness ( $m$ ),  $U$  = any non-negative total impact energy value ( $J$ ),  $U_o$  = the low velocity impact damage energy threshold value ( $J$ ).

Due to the definitions contained in relations (1-3), the variation in the longitudinal modulus, a dominant property for both tensile and compressive material behavior, is reflected in the ultimate predictive relation.

Additionally, for the broad category of laminates termed as generalized UD, including all  $0^\circ$ , or  $\theta$ , or  $90^\circ$ , or a  $+\theta / -\theta$  lay-up at any stacking sequence Equation (5) simplifies to (Papanicolaou & Pournaras 1997):

$$\frac{\sigma_r}{\sigma_o} = \begin{cases} 1 & , U \leq U_o \\ \exp^{-1}\left(\frac{2h}{N} \frac{U - U_o}{U}\right) & , U > U_o \end{cases} \quad (5)$$

The above relation is derived from (4), since it can be proven analytically that the  $m$  value is at all instances equal to 0.5. However, probabilistic definitions of material constants do not appear any more; thus the quality of prediction is not regulated by the former. It becomes dependent on the material geometrical dimension variation (ply thickness), as well as the proper determination of the impact damage threshold value.

Last but not least, the influence of  $0^\circ$ ,  $\pm 45^\circ$  and  $90^\circ$  prepreg plies volume contents on the laminate impact energy absorption capacity is quantified through a semi-empirical relationship embedded in relations (4) and (5), through the determination procedure of  $U_o$ , once more (Papanicolaou & Pournaras 1997).

Table 1. Laminate data for both tested and simulated specimens.

ID	No. of plies	Stacking sequence	Ply thickness (mm)
UD	16	[0 <sub>16</sub> ]T	0.125
AP	16	[(+45) <sub>4</sub> ]s	0.125
QI	16	[0 <sub>2</sub> /±45 <sub>2</sub> /90 <sub>2</sub> ]s	0.125
CP	16	[0 <sub>4</sub> /90 <sub>4</sub> ]s	0.125

### 3 EXPERIMENTAL PROCEDURE

All experimental work has been carried out at the laboratory facilities of the Institute for Composite Materials of the University of Kaiserslautern. Throughout the testing program, Rigidite 5212 has been the CFRP material system tested, a tough carbon fiber/thermosetting epoxy resin, supplied by BASF. 300mmx300mm 16-ply laminated plates have been produced in the autoclave from different prepreg material batches, adhering strictly to the supplier's instructions for the curing cycle. The stacking sequences considered within the framework of the present work are shown in Table 1, together with other relevant data.

Flat laminate specimens (Figure 1) having in-plane dimensions close to the ones prescribed by the DIN standard have been obtained using a diamond-tooth rotating disk-saw.

Several series of impact tests at various energy levels have been conducted, using a falling-dart CEAST computer-controlled impact testing machine. Subsequently both undamaged and impact damaged specimens have been subjected to static compression until failure; GFRP end blocks have been glued to all

specimens prior to compression testing, in order to avoid premature failure starting at the edges as well as enable proper load transmission. The use of undamaged specimens has been necessitated by the fact that the reference compression strength had to be determined for each configuration in terms of stacking sequence separately.

### 4 SIMULATION & MODELING

The prepreg material system elastic properties and the presence of interleaves of varying thickness determine the material sensitivity to impact-induced damage. Simultaneously, they influence the quality of the prediction, being a primary input data in the analytical yet automated predictive formulation. The variability in these property values, imposed by the deficiencies of every manufacturing process demands an even more critical evaluation of the prepreg material that is eventually transformed in a finished commercial product.

The Gamma distribution for  $E_{11}$  is assumed, being the most suitable to express variation in material elastic properties (Bury 1975) in the form:

$$F(x) = \begin{cases} 1 - e^{-\frac{x}{\beta}} \sum_{j=0}^{\alpha-1} \frac{1}{j!} \left(\frac{x}{\beta}\right)^j & \text{if } x > 0 \\ 0 & \text{otherwise} \end{cases} \quad (5)$$

The shape factor  $\alpha$  is taken equal to the  $E_{11}$  value quoted on the material supplier's technical data sheet, while the scale parameter  $\beta$  is taken equal to 1. Choice of the shape parameter alters the dispersion of the generated values at an interval including the manufacturer's  $E_{11}$ . If values measured by the prepreg supplier is made available, the choice of  $\alpha$  as well as  $\beta$  can be such so that we get very close to reality, and the entire approach acquire high reliability.

INASCO in-house code RAND is used to provide random numbers uniformly distributed in the interval (0, 1). Subsequently, random variables ( $E_{11}$  values) are generated obeying the probability distribution function prescribed above, using another INASCO in-house code, SIM. The *Acceptance-Rejection* method is chosen for the generation of the random variables. The simulation process is in effect a Monte-Carlo method (Bury 1975), (Bofilius & van den Ende 1992).

Last but not least, selected consecutive random values in groups of 16, are given as input to the predictive model code PACT, of the University of Patras CMG. Predictions are obtained at 0.5J energy steps. Therefore, the probabilistic material constant definition turns out to be embedded in the bending

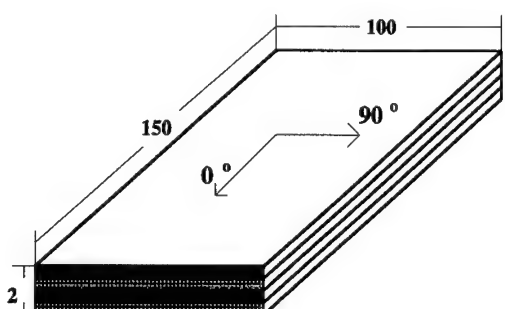


Figure 1. Laminate in-plane dimensions ( $l \times w$ ) as specified by the DIN 65561 standard;  $t$  is the one selected by the authors

mismatching coefficient and the individual lamina  $D_{11}$  values.

## 5 RESULTS & DISCUSSION

The 885 random values of prepreg longitudinal elastic modulus generated are depicted in Figure 2. Conformity with the prescribed Gamma function is visualized in Figure 3.

In the cases of unidirectional and  $\pm 45^\circ$  angle-ply symmetric laminates, designated as UD and AP respectively, the probabilistic definitions of  $E_{11}$  do not affect the quality of prediction, according to the model definition (Papanicolaou & Pournaras 1997). In other words deterministic and probabilistic predictions are identical. Thus, only single curves are shown on both Figures 4 and 5.

In the quasi-isotropic and cross-ply laminate cases, chosen to demonstrate the application of the modeling approach to laminate configurations used in practice, probabilistic definitions do make a difference. In fact, probabilistic predictive curves form a band containing the one obtained using the deterministic  $E_{11}$  value. This is a reflection of the random variable generation over an interval including the manufacturer's value.

All results refer to thin laminates having a nominal thickness of 2mm. This reflects an interest in aerospace applications where such a thickness is often met, especially for composite skins mounted on honeycomb cores, forming sandwich components. Yet, marked deviations from the nominal thickness have been measured, suggesting that the prepreg sheets had undoubtedly differences in thickness. This

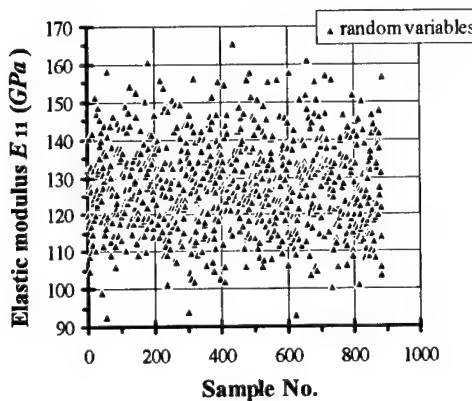


Figure 2. Prepreg tape  $E_{11}$  value distribution simulation (885 generated values)

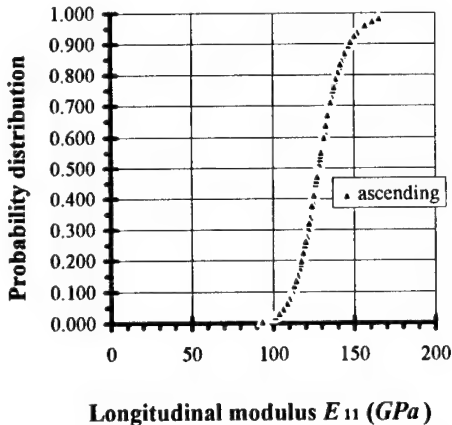


Figure 3. Cumulative probability distribution of random variables obeying the Gamma function, generated using the *Acceptance-Rejection* method

observation provides the ground to initiate a further effort to introduce probabilistic prepreg thickness definition in the model, being reflected for the generalized unidirectional laminates too, without needing to modify predictive model equation (4).

In all of the cases, experimental results are plotted together for comparison, in a qualitative way.

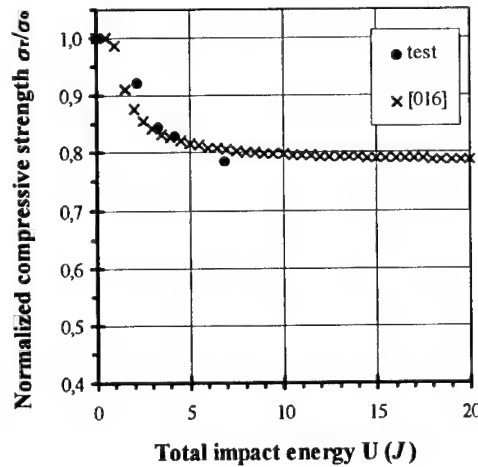


Figure 4. Strength predictions for the unidirectional laminate  $[0_{16}]_T$

For the unidirectional laminate the single curve prediction is of very good quality, regardless of the deterministic or probabilistic definition of the in-plane elastic constants (Figure 4).

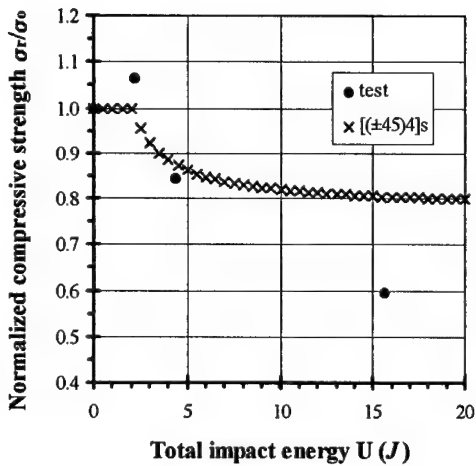


Figure 5. Strength prediction for the symmetric angle-ply laminate  $[(\pm 45)_4]_s$ .

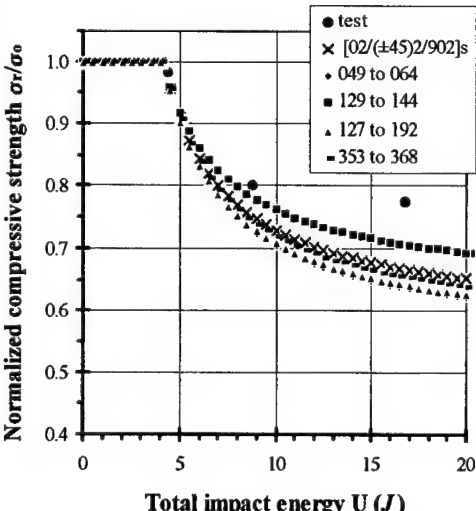


Figure 6. Strength predictions for the symmetric quasi-isotropic laminate  $[04/(\pm 45)_2/904]_s$ .

Predictive quality for the symmetric angle-ply case is mediocre (Figure 5).

For the quasi-isotropic and cross-ply laminates four groups of different random, generated  $E_{11}$  values have been chosen. Respective predictions are denoted by the three-digit numbers on the legends, corresponding to the index numbers of the values as generated by RAND code. Points denoted by the actual stacking sequence have been calculated using the elastic material properties given by the material supplier on his official Technical Data Sheets. In both cases the band of predictive curves originates from the point corresponding to exceedance of the impact damage threshold energy. Curves are not evenly spaced as they spread out with increasing energy.

For the quasi-isotropic laminate case (Figure 6) predictions prove to be more conservative than test data, while the opposite trend can be observed for the cross-ply specimens (Figure 7).

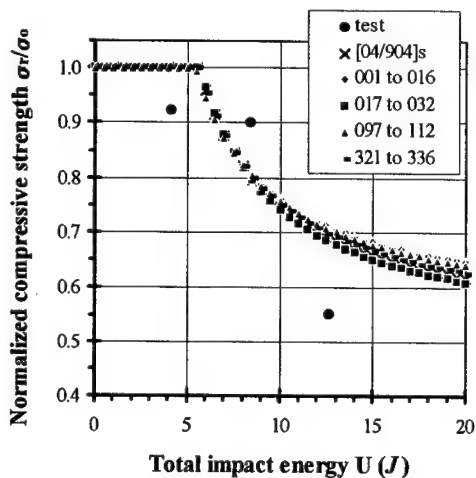


Figure 7. Strength predictions for the symmetric cross-ply laminate  $[04/904]_s$ .

Possible reasons for the deviations between the measured data and the predicted behavior may be the difference in material batches i.e. elastic property value, curing cycle deviations and hygrothermal influence; e.g. for the AP laminate family more than a month intervened between flat plate production and specimen cutting and I-CAI testing (see also Table 2).

The predictive curve shifting demonstrates that variability in elastic properties can have an effect on the prediction, a fact which explains the scattering

**Table 2. Material origin and testing information**

ID	Stacking sequence	Batch No.	Testing period
CP	[04/904] <sub>s</sub>	1	December '95
QI	[0 <sub>2</sub> /±45 <sub>2</sub> /90 <sub>2</sub> ] <sub>s</sub>	2	July '96
UD	[0 <sub>16</sub> ]T	3	December '96
AP	[(±45) <sub>4</sub> ] <sub>s</sub>	3	December '96

observed in data obtained at the laboratory, even when the same energy level is applied repetitively.

## 6 CONCLUSIONS

1. Analytical residual strength after impact predictive model has proven applicable to CFRP flat, thin (2mm) laminated plates.
2. Best approximation is eventually observed for the unidirectional (all 0°) laminate group.
3. Extension of the approach to the definitions of the remaining prepreg ply in-plane properties  $E_{22}$ ,  $G_{12}$ ,  $\nu_{12}$  seems a promising future possibility.
4. Probabilistic definition of cured laminate thickness in CAI predictive formula will render even more realistic predictions.

## 7 ACKNOWLEDGEMENTS

Experimental work has been possible thanks to the financial support of the DLR and GSRT agencies, within the frame of bilateral cooperation program between Germany and Greece, (contract No.: 6L1A6B). The authors wish to express their gratitude to the agencies, as well as to Dr. Q. Yuan of the Institute for Composite Materials Ltd., Kaiserslautern, Germany for preparing the plates and performing part of the experimental work.

## 8 REFERENCES

- Bofilios, D.A. & C.A.M. van den Ende 1992. Deformation mechanisms of continuous fibre-reinforced thermoplastic composites during manufacturing: A probabilistic approach, In ESA SP-336, *Proc. Internat. Symp. "Advanced materials for lightweight structures," ESTEC, Noordwijk, The Netherlands, 25-27 March 1992:* 173-177. Noordwijk, The Netherlands: ESA Publications Division.
- Bury, K.V. 1975. *Statistical Models in Applied Science*. New York: John Wiley & Sons.
- Caprino, G. 1984. Residual strength prediction of impacted CFRP laminates. *J.Comp.Mater.* 18: 508-518.
- Husman, G.E., J.M. Whitney, & J.C. Halpin 1975. Residual strength characterization of laminated composites subjected to impact loading. *Foreign Object Impact Damage to Composites, ASTM STP 568:* 92-113.
- Liu, D. 1988. Impact damage delamination-A view of bending stiffness mismatching, *J.Comp.Mater.* 22: 674-692.
- Papanicolaou, G.C. & C.D. Stavropoulos 1995. New approach for residual compressive strength prediction of impacted CFRP laminates. *Composites* 26(7): 517-523.
- Papanicolaou, G.C. & A.V. Pournaras 1997. Novel methodology for residual compressive strength prediction of CFRP laminates subjected to impact. *to be submitted*
- Pournaras, A.V., G. Jiga & G.C. Papanicolaou 1997. Effect of volume content of 0°, ±45° and 90° prepreg plies and stacking sequence on the prediction of the residual strength of CFRP laminates after low energy impact. In S.A. Paipetis & E.E. Gdoutos (eds), *Proc. 1st Hellenic Conf. Composite Materials and Structures, Xanthi, Greece, 2-5 July 1997:* 271-287. Thessaloniki, Greece: Kyriakidis.
- Stavropoulos, C.D. & G.C. Papanicolaou 1997. Effect of thickness on the compressive performance of ballistically impacted CFRP laminates. *J.Mater.Sci.* 32: 931-936.

## Fatigue behavior of angle-ply AS4/PEEK composite

X.R.Xiao & I.Al-Hmouz

*Concordia Center for Composites, Concordia University, Montreal, Canada*

**ABSTRACT:** The fatigue behavior of thermoplastic composite AS4/PEEK was investigated. Tensile-tensile fatigue tests were conducted at three frequencies on straight sided angle-ply specimens. The cyclic stress-strain data and temperature variation during fatigue tests were recorded. The variations of viscoelastic properties during fatigue were used for the study of the fatigue damage mechanisms in the material. The results showed that AS4/PEEK composite may display cyclic softening, hardening or combined hardening/softening behavior depending on the loading condition. Cyclic hardening or hardening/softening occurs at low stress levels and frequencies whereas softening becomes dominant at high stress levels and frequencies. Analysis shows that the transition between the two types of behavior corresponds to a specific temperature rise value, defined as the cyclic thermal softening limit.

### 1 INTRODUCTION

Because of their viscoelastic nature, polymer based composites are known to show time-dependent behavior under static and dynamic loads. The viscoelastic behavior becomes more pronounced in composites dominated by the matrix properties, such as the angle-ply composites.

One of the problems for viscoelastic materials subjected to dynamic loading is hysteretic heating. Fatigue failure resulted from hysteretic heating has been a major concern for polymers and particularly for thermoplastic polymers. Substantial hysteretic heating is also observed in thermoplastic composites. Curtis et al (1988) studied fatigue behavior of quasi-isotropic and  $\pm 45^\circ$  laminates at 0.5 Hz and 5 Hz. Ma et al (1995) compared the hysteretic loops and temperature rises between carbon/PEEK and carbon/epoxy using  $\pm 45^\circ$  laminates. Dan-Jumbo et al (1989) studied the load frequency effect for notched IM6/APC-2 composite laminates. In the above cases the temperatures recorded during fatigue tests sometimes rose to above the glass transition temperature of the PEEK resin. In contrast to carbon/epoxy composites in which hysteretic heating is moderate and fatigue lives usually increase with increasing load frequency (Reifsnider et al, 1977, Sun et al, 1979), carbon/PEEK shows a remarkably reduced fatigue life with frequency. Comparison studies (Buggy & Dillon, 1991, Curtis, 1987) between carbon/PEEK and carbon/epoxy indicated that the superior damage resistance of PEEK resin did not translate into a better fatigue resistance of the composites.

The thermal effect due to hysteretic heating could be one of the factors affecting the fatigue resistance of PEEK composites.

Thermal failure resulted from hysteretic heating has been a major concern for fatigue property of polymers and particularly for thermoplastic polymers. Studies have shown that, in many polymers, thermal failure dominates the low-cycle regime while the mechanical damage mechanisms govern the high cycle regime. Constable et al (1970) defined a cyclic thermal softening limit for this bimodal failure behavior. Lesser (1995, 1996) showed that the changes in mechanical responses of the polymer are distinctly different at these two regimes. Efforts have also been made to correlate the fatigue loading to microstructural or configuration change of the polymers. The knowledge gained on polymers can help us to better understand the effect of hysteretic heating on the fatigue behavior of thermoplastic composites.

This paper presents the results from a study which aims to understand the effect of hysteretic heating on fatigue behavior of thermoplastic composites. A semi-crystalline thermoplastic composite AS4/PEEK was selected for investigation. Tensile-tensile fatigue tests were conducted at three frequencies on straight sided angle-ply  $[\pm 45]_4s$  specimens. The cyclic stress-strain data and temperature variation during fatigue tests were recorded. The variations of viscoelastic properties during fatigue were then calculated and used for the study of the failure mechanisms of the material.

## 2 EXPERIMENTAL

### 2.1 Specimens

AS4/PEEK [±45]4<sub>S</sub> laminates of 8x8 inches were molded using a WABASH hot press following ICI's procedure. The composite laminates were molded at 380°C for 10 minutes under a pressure of 1.4 MPa and then cooled under the same pressure until the mold temperature reached 100°C. The average cooling rate was about 22°C/min between 380°C to 100°C. The straight sided ±45 specimens were then cut from the laminates. The nominal dimensions of the specimens were 200x18x2 mm with 38 mm long aluminum end tabs, which follows the specification of ASTM D3479.

### 2.2 Static tensile test

The static tensile tests were carried out using a MTS testing machine under displacement controlled mode. The cross-head speed was 2 mm/min. The measured ultimate tensile strength  $\sigma_u$  was  $338.2 \pm 5.8$  MPa and the failure strain was  $17.2 \pm 0.5\%$ .

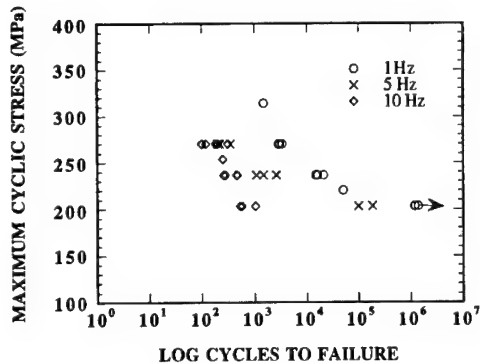


Figure 1. Stress-strain curve of AS4/PEEK ±45 laminate.

### 2.3 Fatigue test

The tensile-tensile fatigue tests were carried out using the same MTS machine under load controlled mode with sinusoidal load wave form. The stress ratio in fatigue was  $R=0.13$ . Three load

Table 1. Fatigue test results for AS4/PEEK ±45 laminate

Load Level (% of $\sigma_u$ )	Frequency (Hz)	Number of Cycles To Failure	Maximum Temperature (°C)	Failure Strain (%)
60%	1	1,400,000*	34	10.7*
		1,200,000*	32	9.83*
65%	1	50,700	-	-
70%	1	20,650	43	11.6
		16,000	40	14.4
		21,000	45	16.3
		18,800	46	-
80%	1	2,900; 3,000	45; 45	15.2, -
		3,850; 3,570	- ; 52	14.5, 13.9
93%	1	1,500	-	-
60%	5	100,000	84	19.1
		186,000	84	16.3
70%	5	2,200; 1,500	127; -	21.9, 17.2
		1,100; 2,600	135; 152	17.9,-
		2,620	127	-
75%	5	350	100	-
80%	5	200; 220	110; 97	19.2, 18.3
		200	108	18.6
60%	10	550; 575	152; 140	19.8, 22.3
		1,040; 580	-	-
70%	10	450; 260	136; 95;	17.3, 17.5
		280; 470	-; 119	17.0, 17.9
80%	10	200; 180; 315	110; 102; 135	18.4, 21.9, 19.7
		120; 100	-; 90	20.3, 10.6

\* sample did not fail

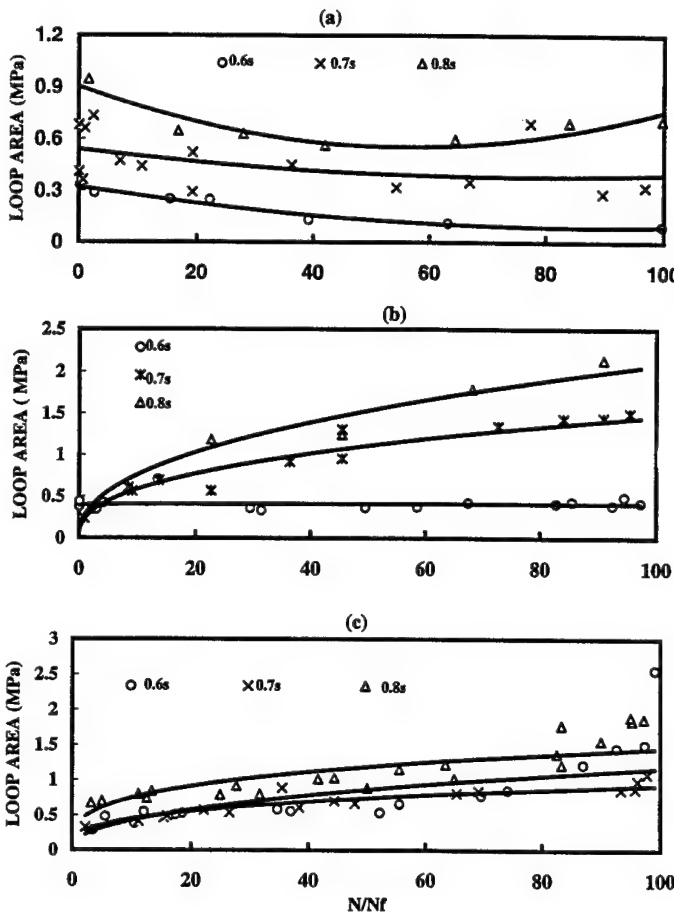


Figure 2. Hysteresis loop areas verses normalized fatigue life. (a) 1Hz, (b) 5 Hz and (c) 10 Hz.

frequencies were investigated: 1 Hz, 5 Hz and 10 Hz. At each frequency, fatigue tests were conducted at three stress levels: 60%, 70% and 80% of the ultimate tensile strength. To complete the S-N curve, few more fatigue tests were conducted at other stress levels.

During fatigue tests, the load level was monitored from the signal of the load cell while the axial strain was measured using an extensometer. The cyclic stress-strain data were collected at selected cycles. The temperatures were measured during the test using thermocouples attached to the center region of the specimen surface and recorded by a computer data acquisition system.

### 3 RESULTS

#### 3.1 S-N data

The data on fatigue strength - number of cycle to failure (S-N) obtained are summarized in Table 1.

Also presented in Table 1 are the values of the maximum temperature recorded during fatigue tests, and the fatigue failure strain.

The S-N data obtained at all frequencies are plotted in Fig.1. As seen, the data from three load frequencies follow three different curves. Increasing load frequency not only shifts the S-N curve to shorter lives but also increases the slope of the curves, suggesting that there is a change in the dominant fatigue failure mechanism.

#### 3.2 Hysteresis loop

The shape of the hysteresis loops changed gradually during fatigue and the way of its evolution depended upon the load frequency. To compare the effect of frequency and stress level on the hysteresis loop evolution, the area of hysteresis loop is plotted versus the normalized number of cycle  $N/N_f$  in Fig.2, where  $N_f$  is the fatigue life. At 1 Hz (Fig.2a), the area of hysteresis loop

decreased as the cycle number increased at 60% and 70% stress levels but initially decreased and then increased with increasing the cycle number at 80% stress level. At 5 Hz (Fig.2b), the loop area was almost constant at 60% stress level but increased with increasing cycle number at higher stress levels. At 10 Hz (Fig. 2c), the loop area increased with increasing the cycle number at all stress levels.

### 3.3 Temperature rise

The typical temperature rise during fatigue tests are

shown in Fig.3a, 3b and 3c for the three stress levels, respectively. At 1 Hz, the temperature rise reached the equilibrium for fatigue tests conducted at all stress levels and the equilibrium temperature increased with stress levels. At 5 Hz, a peak in temperature rise curve, which is similar to that reported by Curtis et al (1988), was observed at tests conducted at 60% level, as shown in Fig.3a. At higher stress levels, monotonic temperature rises were recorded. At 10 Hz, continuously rising temperatures were measured at all stress levels. The values of the maximum temperature are summarized in Table 1.

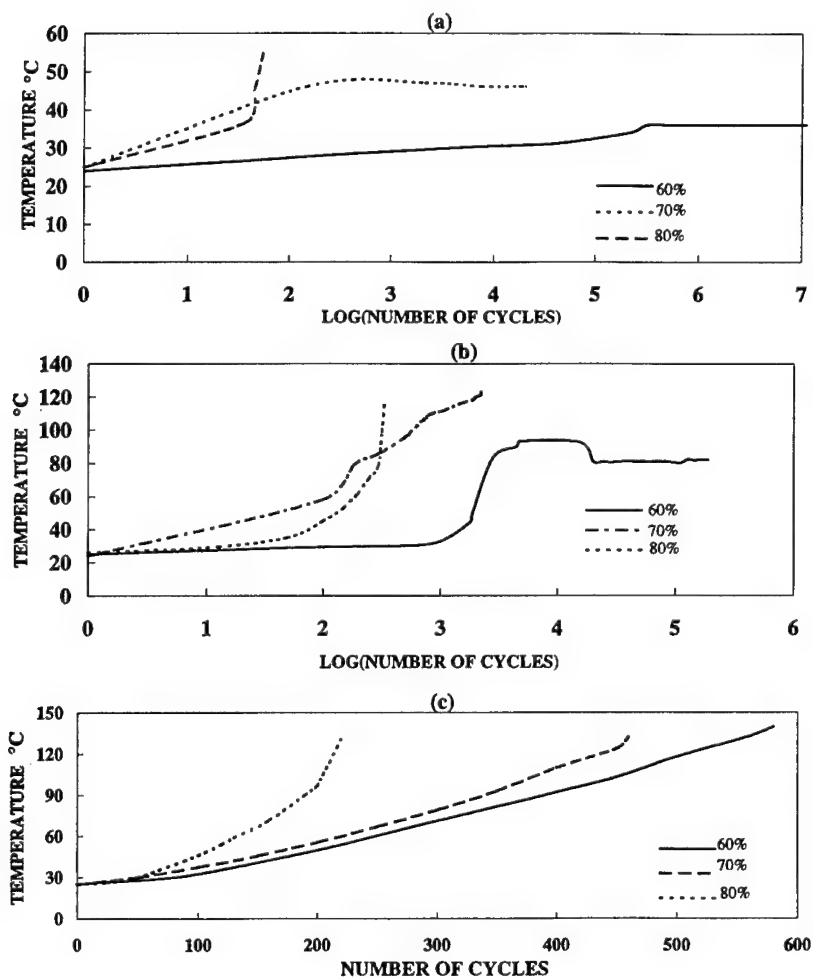


Figure 3. Temperature variation during fatigue measured at the surface of the specimens. (a) 1 Hz, (b) 5 Hz and (c) 10 Hz.

### 3.4 Failure strain

The values for the maximum strain measured at failure are summarized in Table 1. When compared with the failure strain obtained by static tests, the values appear to be lower for the samples tested at 1Hz but higher for samples tested at 5 Hz, 70% and 80% stress levels and at 10 Hz at all stress levels. In other words, the material behaved more brittle for the former case but more ductile for the latter case respect to that under static tensile loading. The tests at 1Hz, 60% was terminated before failure and hence the value is the final strain rather than failure strain.

### 3.5 Viscoelastic properties

From the cyclic stress-strain data, the storage modulus  $E'$ , loss modulus  $E''$  and loss factor  $\tan\delta$  were calculated following the definition of Read and Dean (1978), as illustrated in Fig.4.

Figs.5 and 6 plots  $E'$  and  $\tan\delta$  versus normalized number of cycles. As seen, the variation of the dynamic properties with cycle number depends upon the load frequency and stress levels. At 1 Hz,  $E'$  increased with the cycle number at 60% stress level. Increasing stress levels resulted in an almost constant  $E'$  value.  $\tan\delta$  varied in the opposite way.

At 60% stress level,  $\tan\delta$  decreased with increasing the cycle number whereas at higher stress levels  $\tan\delta$  appeared first decreased and then increased with the cycle number. The responses at 5 Hz,

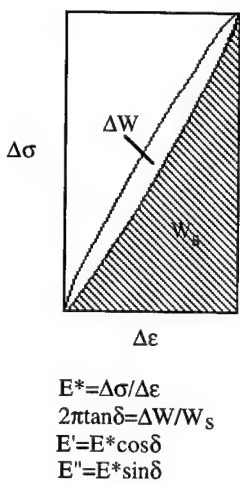


Figure 4. Calculation of dynamic properties from cyclic stress-strain data.

60% stress level were similar to those at 1Hz, 70% and 80%. At higher stress levels and at 10 Hz at all stress levels,  $E'$  generally decreased whereas  $\tan\delta$  increased with the cycle number and the extent of the variation increased with increasing the stress level.

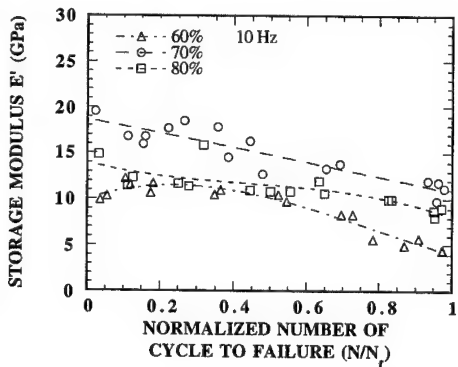
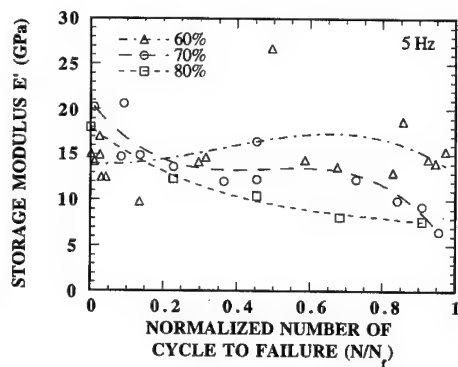
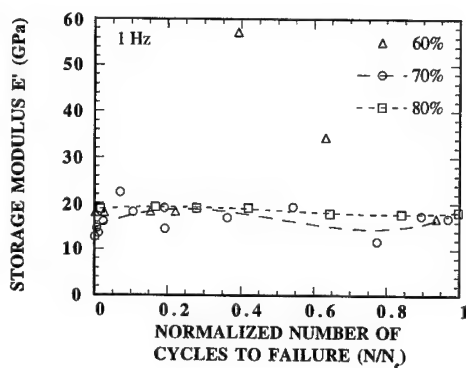


Figure 5. Variation of the storage modulus during fatigue.

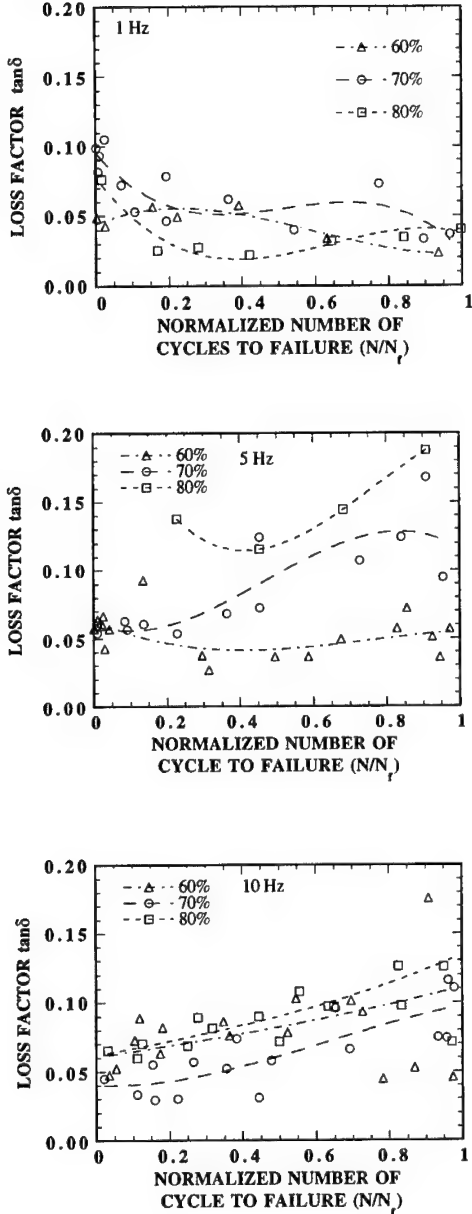


Figure 6. Variation of the loss factor during fatigue.

#### 4 DISCUSSION

The above results show that the material responses varied substantially over the range of stress level and frequency covered in this study. The first remarkable variation is the evolution of the hysteresis loops. The loop area decreased with

cycle number at low frequencies and stress levels but increased at higher frequencies and stress levels. Similar variation is seen in the viscoelastic characteristics, such as the storage modulus and loss factor. Finally, the failure strain also varied with the load frequency and stress level.

The variation in the viscoelastic characteristics and the strain response all indicate that more than one mechanisms had occurred in the material during fatigue, some of which led to cyclic hardening while others resulted in cyclic softening. The likely mechanisms for cyclic hardening are: (1) fiber rotation towards the loading direction in the angle-ply laminates (Al-Hmouz, 1997) and (2) the change of microstructure of the matrix resin, such as the volume contraction observed in amorphous polymers (Bouda et al. 1976, Lesser 1996), the change in crystallinity (Lesser, 1995) (may result in softening if the value decreases) and the reorientation of the crystallites. The softening may be related to (1) thermal softening of the material due to hysteretic heating; and (2) mechanical damage in the composite material. There are also interactions between the softening and hardening mechanisms. For example, the thermal softening of polymer matrix resin will facilitate fiber rotation and accelerate the microstructural change and damage process. Some types of microstructural change may lead to softening rather than hardening effect. Whether the material will behave cyclic softening, hardening or hardening/softening depends upon the relative contributions of each mechanism.

The above four mechanisms may all operate during fatigue process but their contributions to various properties vary with load condition. Based upon the knowledge on polymer materials, under low cyclic stress, the damping of matrix resin tends to decrease while the stiffness tends to increase because of reduced molecular mobility (Bouda et al. 1976, Kolman et al. 1982, Liu et al. 1991). This effect appears to diminish at higher stress levels. In angle-ply composites, fiber rotation also contributes to the increase in stiffness and decrease in damping but the fiber rotation angle would be small unless substantial thermal softening of the matrix occurs. On the other hands, mechanical damage and temperature rise increase with frequency and stress levels. When temperature rise is high the hardening effect of fiber rotation can be offset by thermal softening. Hence the reduced damping of stressed matrix resin may be observed only at low frequencies and stress levels and most likely at the early stage of fatigue where thermal effect due to hysteretic heating is small and substantial mechanical damage has not occurred. The temperature rise is, therefore, a key factor to determine the transition between cyclic hardening and cyclic softening behavior.

Similar to polymers, the fatigue response of the AS4/PEEK  $\pm 45$  laminate may be divided into two regimes, a mechanically dominated regime, where material exhibits some degree of cyclic hardening,

and a thermally dominated regime where cyclic softening occurs. The temperature corresponds to the transition point between the two regimes is defined as the cyclic thermal softening limit.

## 5 CYCLIC THERMAL SOFTENING LIMIT

The results on polymers (Lesser 1995, 1996) showed that the transition from mechanically dominated to thermal softening dominated failure corresponds to several distinct features. Firstly there is a transition knee on S-N curve which separates the curve into two regimes, each with a different slope. Secondly, the changes in mechanical responses of the polymer are distinctly different at these two regimes. At thermally dominated regime, the area of the hysteresis loops, the loss factor and loss modulus increase while the storage modulus decreases with the number of cycles. At mechanically dominated regime, the area of the hysteresis loop, the loss factor and loss modulus decrease slightly with the number of cycles while the storage modulus either is maintained or firstly decreases slightly and then gradually recover to its initial level.

AS4/PEEK appears to follow some of the above rules. Using a continuously declining  $E'$  and increasing  $\tan\delta$  as indications of thermal softening dominant, the cyclic thermal softening limit appears to be at a stress level above 80% of  $\sigma_u$  for 1Hz, between 60% and 70% of  $\sigma_u$  for 5 Hz and below 60% of  $\sigma_u$  for 10 Hz. These loading conditions correspond to experimentally measured maximum temperature rises to a value above 84°C. Using the slope change in S-N curve, however, will give some inconsistent temperature values. Hence the cyclic thermal softening limits is determined according to the evolution of the viscoelastic properties and the value is assumed to be 90°C. As shown by an earlier work (Xiao et al. 1994), this temperature corresponds to a change in temperature dependence of the nonlinearity in viscoelastic responses.

The temperature rise during fatigue can be estimated using thermal analysis (Xiao, 1997) and then the cyclic softening limit can be predicted for a given test condition. Fig. 7 shows such a plot generated based on thermal analysis. The dotted lines in Fig. 7 correspond to a predicted maximum temperature rise of 90°C, i.e. the cyclic thermal softening limit, over a range of stress level and load frequency at the stress ratios indicated on the curve, namely, R=0, 0.1, 0.2, 0.3 and 0.5. Also added in Fig. 7 are the experimental results obtained at R=0.13, as represented by symbols, where the open symbols correspond to the cases when the fatigue specimens behaved cyclic hardening whereas the close symbols for the cases of cyclic softening. As seen, all the open symbols fall into mechanically dominated zone while the close

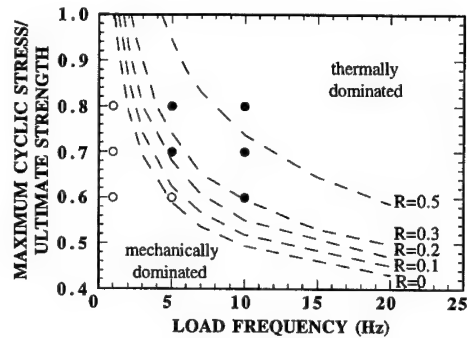


Figure 7. The cyclic thermal softening limit as a function of load frequency and stress level at stress ratios indicated on the curves. Symbols are the experimental results at R=0.13. Open circles are for specimens displayed cyclic hardening whereas close circles for cyclic softening.

symbols into thermally dominated zone. This indicates that the assumption about the thermally dominated and mechanically dominated fatigue regimes for AS4/PEEK angle-ply composite is reasonable and the transition between these two regimes can be quantitatively predicted by the cyclic thermal softening limit. In our modeling work (Xiao, 1997) the prediction based on thermal failure underestimated the fatigue life for 5 Hz, 60% condition and the assumption of thermal failure was suspected for the error. The present result confirms that 5 Hz, 60% condition is indeed in the mechanically dominated regime.

## CONCLUSIONS

The effect of hysteretic heating on fatigue behavior of thermoplastic composite AS4/PEEK was investigated through tensile fatigue tests of AS4/PEEK ±45 laminates at three frequencies. The results showed that AS4/PEEK composite may display cyclic softening, hardening or combined hardening/ softening behavior depending upon the loading condition. Similar to polymers, the fatigue response of the AS4/PEEK ±45 laminate can be divided into two regimes, a mechanically dominated regime, where material exhibits some degree of cyclic hardening, and a thermally dominated regime where cyclic softening occurs. The transition between the two regimes is determined by a specific temperature rise value, defined as the cyclic thermal softening limit. Using this parameter one can predict the service conditions for these two regimes and therefore prevent the premature failure due to thermal softening.

## ACKNOWLEDGMENT

This work is supported by National Science and Engineering Research Council of Canada. We also like to thank Mr.J.Dufour of IMI, National Research Council of Canada for the assistance in fabrication of composite plates, Mr.P.Oullette and Mr.M.El-Karmalawy of Concordia Center for Composites, for their assistance in experimental work.

## REFERENCES

- Al-Hmouz, I., The Effect of Load Frequency and Loading Level on Fatigue Behavior of Angle-ply Carbon/PEEK Thermoplastic Composites, M.A.Sc. Thesis, Concordia University, 1991.
- Bouda, V., V.Zilvar, A.J.Staverman, "The effects of cyclic loading on polymers in a glassy state", *J. Polymer Science*, Vol.14, 1976, 2113-23.
- Buggy, M., G.Dillon, "Flexural fatigue of carbon fiber-reinforced PEEK laminates", *Composites*, Vol.22, No.3, 1991, 191-198.
- Constable, I., J.G.Williams, D.J.Burns, "Fatigue and cyclic thermal softening of thermoplastics", *J. Mechanical Engineering Science*, Vol.12, 1970, 20-29.
- Curtis, D.C., D.R.Moore, B.Slater, N.Zahlan, "Fatigue testing of multi-angle laminates of CF/PEEK", *Composites*, Vol.19, No.6, 1988, 446-452.
- Curtis, P.T., "In investigation of the tensile fatigue behaviour of improved carbon fiber composite materials", *ICCM6*, Vol.4, 1987, 54-64.
- Dan-jumbo, E., S.G.Zhou, C.T.Sun, "Load-frequency effect on fatigue life of IMP6/APC-2 thermoplastic composite laminates", *ASTM STP 1044*, G.M.Newaz, Ed., 1989, 113-132.
- Kolman, H.J., K.Ard, C.L.Beatty, "Variation of dynamic mechanical properties of polycarbonate as a result of deformation", *Polymer Engineering and Science*, Vol.22, 950-954, 1982.
- Lesser, A., "Effective volume changes during fatigue and fracture of polyacetal", *Polymer Engineering and Science*, 1996, Vol.36, 2366-74.
- Lesser, A., "Changes in mechanical behaviour during fatigue of semicrystalline thermoplastics", *J. Applied polymer Science*, Vol.58, 869-879, 1995.
- Liu, L.B., A.F.Yee, D.W.Gidley, "Effect of cyclic stress on enthalpy relaxation in polycarbonate", *J. Polymer Science, Part B: polymer physics*, Vol.30, 221-230, 1991.
- Ma, C.C., S.H.Lin, N.H.Tai, J.F.Wu, G.Y.Wu, C.L.Ong, Y.C.Chang, M.F.Sheu, Y.R.Yang, "Fatigue behaviour of carbon fiber reinforced thermoplastic and thermoset polymer composites (I) [ $\pm 45^\circ$ ]4s laminates under tension-tension loading", *ICCM10*, 1995, 569-576.
- Read, B.E., G.D.Dean, "The determination of dynamic properties of polymers and composites", Adam Hilger, 1978.
- Reifsnider, K.L., W.W.Stinchcomb, T.K.O'Brien, "Frequency effects on a stiffness based fatigue criterion in flawed composite specimens", *Fatigue of Filamentary Composite Materials. ASTM STP 636*, K.L.Reifsnider and K.N.Lauraitis, Eds., ASTM, 1977, 171-184.
- Sun, C.T., W.S.Chan, "Frequency effect on the fatigue life of a laminated composite", *Composite Materials: Testing and Design, ASTM STP 674*, Ed. S.W.Tsai, 1979, 418-430.
- Xiao, X.R., C.C.Hiel, A.H.Cardon, "Characterization and modelling of nonlinear viscoelastic response of PEEK resin and PEEK composite", *Composite Engineering*, Vol. 4, No.7, 1994, 681-702.
- Xiao, X.R., "Modeling of load frequency effect on fatigue of thermoplastic composites", submitted to *J. Composite Materials*.

## Moisture detection in composite materials using infrared thermography

J.C. Kneip, X.J. Gong & S. Aivazzadeh

*Laboratoire de Recherche en Mécanique des Transports, Institut Supérieur de l'Automobile et des Transports,  
Nevers, France*

**ABSTRACT:** This paper presents the results obtained by a non-destructive evaluation method, developed in our laboratory, to detect absorbed moisture in composite materials. We use the particular dielectric properties of water molecules under microwave excitation, to create local heating in the material and detect it by an infrared thermography camera. With appropriate numerical processing, thermograms are analysed and used to locate moisture containing zones. We have applied it to damaged glass-fibre composite plates exposed to humid environments.

### 1 INTRODUCTION

For many years, conceptors of structures have been aware of the effects of hygrothermal conditions on the mechanical behaviour of composite materials. Many papers have been published in this field and enable some understanding of the absorption phenomena in these materials. Because of their heterogeneity, models cannot always completely describe absorption, and particularly in damaged structures (Cardon, 1996).

Then the use of non destructive evaluation (NDE) techniques can be of great interest to evaluate the state of a structure. Among these, the infrared thermography method is actually used in many laboratories for inspecting damaged composite materials. This is generally based on the flash method and consists in observing the response of a sample to a thermal spike and linking the thermal delay to its internal structure.

However, very few papers have been published concerning the detection of absorbed moisture. We try to show in this paper why this method is not well adapted to moisture detection in composite materials. Then, we explain the principles and show the possibilities of our technique based on microwave excitation and an infrared thermography observation.

Results are presented for both epoxy and polyester resin plate samples, containing known water content. In addition data is provided on glass

fibre epoxy matrix samples that we have examined in the damaged state.

### 2 INFRARED THERMOGRAPHY NDE

Infrared thermography technique is actually frequently used in many laboratories for inspecting damaged composite materials. Its principal advantage is its multifunctionality. Moreover it enables observation of the thermal state of material or structure to be made very quickly, without contact or perturbation of the structure during the inspection. Primarily, the use of infrared thermography for non destructive testing of materials has been based on the use of photothermal techniques (Parker (1961), Balageas (1993)), in which we analyse the thermal response of a sample to an external thermal flux, with an infrared thermography camera. In every case, the principle of these techniques is based on the observation and interpretation of thermal diffusion delays during the transmission or the reflection of the thermal excitation. Then, we can see here the two principal problems of this technique. Firstly, because of the low penetration power of infrared radiation, samples have to be thin to obtain good results (just a few millimetres). Secondly, defects have to slow down sufficiently the diffusion of the thermal spike to be detectable. Then, the higher the resistance of the defect versus the structure is, the more important the thermal contrast on the surface of the sample

becomes. Hence these techniques are essentially used to detect and characterise delaminated zones in thin polymeric laminates.

However, little work has been published in the field of moisture detection using infrared thermography techniques (Platonov's (1988), Denel's (1989)). These studies showed that detection of moisture was possible only for particular cases, for example when moisture concentrations were very high (several tens of percentage for porous materials) or with completely water-filled alveoli for honeycomb sandwich structures. We showed in a previous work (Kneip, 1997) that absorbed moisture by polymeric materials could not modify sufficiently its thermal characteristics. Thus we looked for another way to excite our humid polymeric samples capable of creating heat detectable by an infrared thermography system.

### 3 MOISTURE DETECTION SYSTEM

Our moisture detection system uses microwave excitation to create heat in the water present in the material. The principle action of microwaves on matter is indeed based on the conversion of electromagnetic energy into thermal energy, due to the interaction between electrical charges which are present in the material under the influence of an external electrical field. This process, using dielectric hysteresis, is used with dielectric liquid or solid materials, containing polar molecules, and characterised by its permittivity  $\epsilon'$  and its dipolar relaxation constant  $\epsilon''$ . Dissipated energy in the material can be directly related to these two constants.

Unlike infrared heating (with photothermal methods, in our case), microwave heating takes place directly inside the sample, because of its wave-length and its important penetration power in mainly polymeric materials. Effectively, this type of material is generally almost transparent to microwave radiation, and therefore cannot generate heating of the sample.

Unlike polymeric materials, because of its high asymmetrical configuration, the water molecule presents an exceptional polarity and makes it the ideal material for this type of heating. (Thuery, 1989). Preliminary tests on polyester and epoxy resins (Kneip, 1997) showed that absorbed moisture could have a great influence on their electrical characteristics even if the concentration was very low (Figure 1). We used this phenomenon to create local

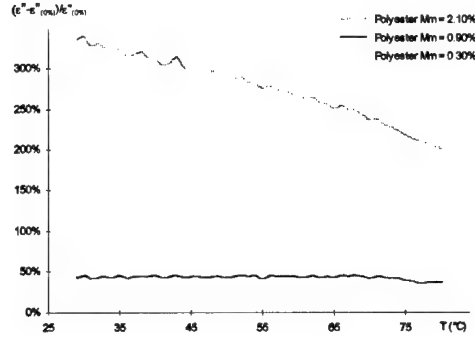


Figure 1. Polyester resin. Relative variations of the relaxation constant  $\epsilon''$  for different moisture concentrations as a function of temperature.

heating in materials in which we expect to find absorbed moisture.

Our solicitation system is formed by a microwave heating system including a variable power microwave generator (0-2 kW at 2.45 GHz ( $\lambda=12.4$  cm in vacuum)). The wave applicator is a oversized monomode wave-guide developed by CNRS (Bertaud, 1982), as we can see in Figure 2. A wave-guide enables electromagnetic energy to be carried and coupled to the sample. The dimensions of the microwave applicator were defined to cover the maximum heating surface. This system is used in the progressive wave state, which gives less efficient but more homogeneous heating than in the stationary wave state. The absorption of the radiation at the end of the applicator is done through a water load. This system works in the transverse electric 01 mode ( $TE_{01}$ ). In the material the electric fields are influenced by the dielectric and geometrical characteristics of the sample.

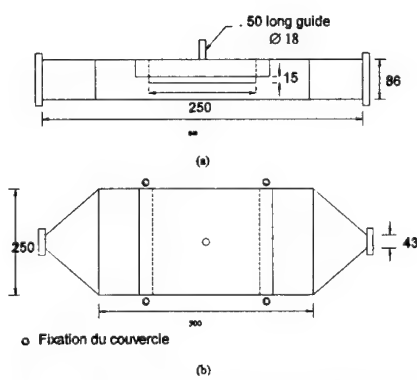


Figure 2. Schematic representation of oversized monomode applicator used

The second part of the system is formed by an infrared thermography camera (AGEMA TH880 Swb), with quantic monodetector, liquid nitrogen-cooled (77 K). It deals with a short wave camera, using the infrared atmospheric transmission band 3-3.5 mm. A recording system enables data to be saved and viewed in real time on a PC compatible, with a resolution of 128 x 64 pixels, at 6.25 pictures/second.

By infrared thermography and numerical models, we attempted to determine the characteristics (position and size) of the heating source, corresponding to the zones of concentrated water. The difficulty is that each application needs the development of a specific applicator, as a function of the sample's geometry and the kind of heating required.

A test sample is firstly exposed to microwave solicitations. It is placed in the wave guide on a polypropylene support, which is transparent to microwave excitation. The necessary time of the microwave solicitation to obtain sufficient heating was determined to avoid any vaporisation of the moisture present. Immediately after heating, the sample is placed on a support to allow its observation by infrared thermography camera. An infrared mirror, placed behind the sample, allowed a thermal view of the front and the back of the sample simultaneously.

#### 4 RESULTS AND DISCUSSION

A first step of our work was realised on both epoxy or polyester resin plate samples, containing known water content. Its dimensions were of 70 x 70 mm<sup>2</sup> for a thickness from 4 to 12 mm. Humid blotting paper was placed inside each sample during its realisation. After microwave excitation a thermal response of each tested sample (Figure 3), located on concentrated water areas was observed.

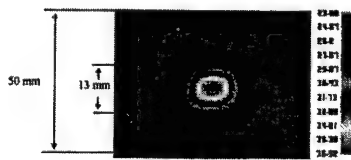


Figure 3. Thermogram of a polyester resin sample (70x70x5 mm), containing a humid insert (15x15x0.2 mm). Observation 20 seconds after microwave excitation.

These first results were particularly interesting because they showed that a detection was possible even if the sample was thick. This was an advantage over the photothermal technique classically used in non destructive testing of composite materials.

As we explained in part 3, microwave heating takes place directly inside the sample because of the wave-length and the important penetration power of microwave radiation. Thus, thermal modelisation of heat becomes easier than in the photothermal process. Inside the material, the main process is thermal diffusivity, and outside there is just a thermal exchange by convection.

After we tried to modelise these phenomena in order to determine position and size of humid inserts. For our samples, we used a two dimensional finite differences model.

Firstly we determined the thermal characteristics of our samples :  $\rho$  density,  $\lambda$  thermal conductivity,  $C$  calorific capacity and  $h$  the global thermal exchange coefficient. Then, our process consisted in recording the thermal response on both main sides of the tested sample, and adjusting parameters of our model to obtain the same thermal response.

This technique allowed us to determine size and position of the heating source corresponding to water concentrations. We present in Figure 4 comparison between the recorded and calculated thermal response of an polyester resin sample of 70x70x5.3 mm, with a humid insert of 15x15x0.2 mm placed at 1.9 mm of one side. With the numerical process, we evaluated its position to  $1.9 \pm 0.3$  mm and its size to  $13 \times 13 \pm 0.2 \times 0.2$  mm<sup>2</sup>. However there

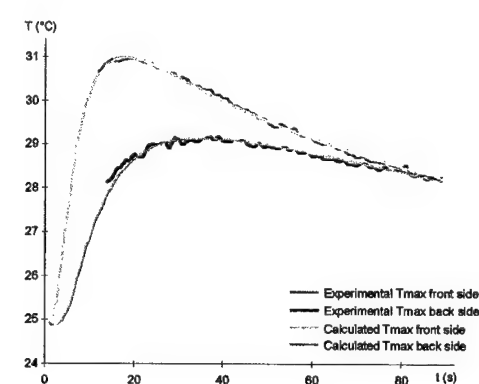


Figure 4. A comparison of the evolution of experimental and calculated maximum temperature on front and back sides of a polyester resin sample.

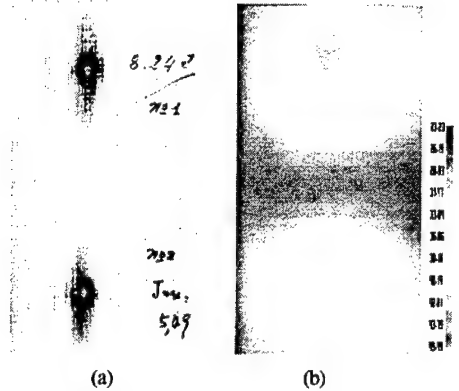


Figure 5. Test on glass fibre epoxy matrix composite sample. (a) after double impacts. (b) thermogram obtained with infrared thermography camera after microwave excitation.

was no data on the thickness of the humid insert and on the moisture concentration.

In the second part, we tested damaged glass fibre epoxy matrix samples. Dimensions were of 150 x 100 mm<sup>2</sup> with a thickness of 2.1 mm. We created initial damage on these samples using an impacting system. We present in Figure 5a a photograph of a tested sample with two impacts.

These samples were dried during 3 weeks. A first test was realised with our moisture detection system and showed that it had no effect on dry materials. Afterwards this sample was immersed in water at a temperature of 60 °C during 1 month.. Then we tested again the wet sample, and we observed immediately after microwave excitation a large temperature rise located in the impacted areas (Figure 5b). Thus, our technique allows of quick detection of abnormal moisture absorption zones.

However, we cannot actually determine any information about the moisture distribution in the material because the characteristics of the heating source is very difficult to be described by a model. In observing infrared thermography records, it is seen that maximum heats, i.e. the maximum moisture concentration, correspond to impact areas.

## 5 CONCLUSION

In this paper we presented an original non-destructive technique allowing of the detection of absorbed moisture in polymeric materials. Its principle is based on the use of microwave excitation combined to an infrared thermography inspection of the thermal response of the sample.

We have shown that this technique was particularly well adapted to the detection of absorbed moisture, in comparison of classical photothermal techniques. Its main advantages are its possibilities to locate very quickly concentrated water areas and to enable investigation of thick samples.

By infrared thermography and numerical models, we determined in simple cases the characteristics (position and size) of the heating source corresponding to the zones of concentrated water with good agreement.

In the case of damaged composite materials we showed that this technique enabled the detection of concentrated water areas. Thus, we think that this technique could be used indirectly to detect damaged areas, by observing the anomalous presence of absorbed moisture, for example.

The limitations of this technique are actually on the one hand the difficulty of evaluating moisture concentration in the sample, and on the other hand the necessity of adapting the form of the wave-guide to the geometry of the sample.

## REFERENCES

- Balageas D., 1993, Contrôle non destructif des matériaux composites par thermographie IR, *Revue des Laboratoires d'essais*, N°35, mai 1993, p 12-18.
- Cardon A.H., Fukuda H. & Reifsneider K.L., 1996, Progress in durability analysis of composite systems, *Proceedings of the international Conference Duracosys 95*, Edited by Cardon A.H., Fukuda H. & Reifsneider K.L., 1996, Brussels.
- Denel A.K. Golubev A.J. & Zhalnin A.P., 1989, Complex thermal testing of honey-comb panels, *Sov. J. of NDT (Defectoscopy)*, 1989, N° 9, p 55-56.
- Kneip J.C., 1997, Application de la thermographie infrarouge à la détection de l'humidité dans les polymères et matériaux composites, *Thèse de l'Université de Bourgogne*, Janvier 1997.
- Parker W.J., Jenkins R.J., Buttler G.P. & Abbott G.L., 1961, *J. of Applied Phys.*, vol. 32, N°9, 1961.
- Platonov V.V., 1988, Ellipsometry in defectoscopy, *Sov. J. of NDT (Defectoscopy)*, N° 11, 1988, p 3-8.
- Thuery J., 1989, Les micro-ondes et leurs effets sur la matière, CDIUPA, Tech&Doc, Ed. Lavoisier.

## Crack growth prediction in composites using the dual boundary element method

P.Sollero & S.G.Mendonça

*Department of Computational Mechanics, State University of Campinas, Brazil*

M.H.Aliabadi

*Damage Tolerance Division, Wessex Institute of Technology, Ashurst, Southampton, UK*

**ABSTRACT:** This paper presents a predictive technique for evaluating the crack growth path in composites and anisotropic materials. This technique is based on the strain energy density criterion and was implemented in the DELA, the dual boundary element code to perform crack propagation analysis in anisotropic media. Numerical examples are presented to validate this procedure for predicting the propagation path for cracks in unidirectional composites. This work is supported by the Fundação de Amparo à Pesquisa do Estado de São Paulo (FAPESP).

### 1 INTRODUCTION

Failure modes in composites were observed by experimental works as fiber breakage, matrix separation and interface debonding. The complex behavior of the progressive failure in composites is very difficult to be modelled successfully by a predictive technique. However, crack growth analysis is the basis of damage tolerance design and a very useful tool for fault inspection assessment.

Two major approaches are found in the literature to scale the continuum element as function of the crack size and microstructure of the composite. The first assumes a global nonhomogeneous anisotropic medium where the crack tip is present in just one phase of the composite, the matrix or the fiber (Servadurai 1990). The second considers a global homogeneous anisotropic continuum where the crack propagates in an idealized material which properties are determined by the proportion of the composite constituents (Ellyin & El Kadi 1990). Sih (Sih 1991) compared the results obtained from these two analytical models and experimental data, in order to evaluate the behavior of brittle fracture of unidirectional fiber/matrix composites, and found close values for the critical stress as a function of the crack angle for the two models and the laboratory data. The second approach is used in this work.

According to Sih's strain energy density criterion, crack initiation occurs in a direction determined by the relative minimum of the strain energy density factor and unstable crack growth is reached whenever this minimum factor reaches a critical value.

An incremental crack growth analysis is carried

out in this work to predict the crack path, which is assumed piece-wise straight. After each increment a dual boundary element analysis is performed in the anisotropic medium and the mixed mode stress intensity factors are computed by the  $J$ -integral and the ratio of relative displacements at crack faces, in a single region stress analysis (Sollero & Aliabadi 1995). The strain energy density criterion is equated and the solution for the propagation angle is obtained numerically by bracketing and the golden section search.

Due to intrinsic features of the dual boundary element method, remeshing is kept to a minimum, as the original mesh is preserved, apart the element that is added to the crack tip in the propagation direction. The system of equation is solved by an incremental LU decomposition scheme that is performed adding the new rows and new columns to the coefficient matrix, which is an efficient and accurate procedure. Remeshing is a major difficulty when applying finite element methods for the solution of crack growth problems, requiring sophisticated and time-consuming algorithms (Boone et al. 1987).

Numerical examples of this implementation of the strain energy density criterion is presented and compared with those established in the literature. A computational simulation of crack propagating from a hole in a unidirectional composite specimen and the resulting crack path is presented.

### 2 THE DUAL BOUNDARY ELEMENT METHOD FOR LINEAR ANISOTROPIC ELASTICITY

The dual boundary element method is based on the

use of two boundary integral equations, namely the displacement and the traction equation. General crack problems can be solved in a single domain formulation by applying the displacement equation on one crack surface and the traction equation on the other. A detailed formulation of this method applied to anisotropic materials is found in (Sollero 1994).

In the absence of body forces the boundary integral equation for the displacements at an internal point  $z'$  of an anisotropic domain can be derived from Betti's reciprocal work theorem and given by the Somigliana's identity as

$$u_i(z') + \int_{\Gamma} T_{ij}(z', z) u_j(z) d\Gamma(z) = \int_{\Gamma} U_{ij}(z', z) t_j(z) d\Gamma(z) \quad (1)$$

where  $i,j=1,2$ ;  $T_{ij}$  and  $U_{ij}$  are the anisotropic fundamental solution for tractions and displacements respectively and the displacements  $u_j$  and the tractions  $t_j$  are computed on the boundary  $\Gamma$ . The points  $z'$  and  $z$  are the source and field points defined by

$$z' = \begin{cases} z_1 \\ z_2 \end{cases} = \begin{cases} x_1 + \mu_1 x_2 \\ x_1 + \mu_2 x_2 \end{cases} \quad (2)$$

and

$$z = \begin{cases} z_1 \\ z_2 \end{cases} = \begin{cases} x_1 + \mu_1 x_2 \\ x_1 + \mu_2 x_2 \end{cases} \quad (3)$$

where  $\mu_k$  are the complex roots of the characteristic equation of the anisotropic material, with  $k=1,2$ , see (Sollero & Aliabadi 1993).

The displacement boundary integral equation is obtained by the limit transition when the source point in equation (1) is taken to the boundary, resulting

$$c_{ij}(z') u_j(z') + \int_{\Gamma} T_{ij}(z', z) u_j(z) d\Gamma(z) = \int_{\Gamma} U_{ij}(z', z) t_j(z) d\Gamma(z), \quad (4)$$

where  $\int$  stands for the Cauchy principal-value integral and the constant  $c_{ij}(z')$  is given by  $\frac{1}{2}\delta_{ij}$  for smooth boundaries.

The displacement gradient tensor  $u_{i,k}$  for an internal point can be calculated from equation (1) by differentiation at  $z'$  to give

$$u_{ij}(z') = \int_{\Gamma} T_{ij,k}(z', z) u_k(z) d\Gamma(z) - \int_{\Gamma} U_{ij,k}(z', z) t_k(z) d\Gamma(z), \quad (5)$$

where the fundamental solution derivatives  $T_{ij,k}$  and  $U_{ij,k}$  are given in (Sollero & Aliabadi 1993). The stresses  $\sigma_{ij}(z')$  at an internal point can be obtained from the definition of the tensorial strain at  $z'$  and the application of the generalized Hooke's law resulting

$$\sigma_{ij}(z') + \int_{\Gamma} S_{kij}^a(z', z) u_k(z) d\Gamma(z) = \int_{\Gamma} D_{kij}^a(z', z) t_k(z) d\Gamma(z), \quad (6)$$

where the kernels  $S_{kij}^a$  and  $D_{kij}^a$  are functions of the compliance matrix of the material and the derivatives of the fundamental solution.

Taking the source point to a smooth boundary, in the limit, the stress boundary integral equation is given by

$$\frac{1}{2} \sigma_{ij}(z') + \int_{\Gamma} S_{kij}^a(z', z) u_k(z) d\Gamma(z) = \int_{\Gamma} D_{kij}^a(z', z) t_k(z) d\Gamma(z), \quad (7)$$

where  $\int$  stands for the Hadamard principal value integral. Applying the Cauchy stress transformation, on a smooth boundary, the traction boundary integral equation is given by

$$\frac{1}{2} t_i(z') + n_i(z') \int_{\Gamma} S_{kij}^a(z', z) u_k(z) d\Gamma(z) = n_i(z') \int_{\Gamma} D_{kij}^a(z', z) t_k(z) d\Gamma(z), \quad (8)$$

where  $n_i$  denotes the  $i$ -th component of the unit outward normal to the boundary at the source point.

Equations (4) and (8) are the basic equations of the dual boundary element method for linear anisotropic fracture problems.

### 3 STRAIN ENERGY DENSITY CRITERION

The strain energy density criterion is a theory built in the framework of fracture mechanics that predicts the onset of failure as crack instability, or rapid crack propagation, through the critical density factor (Sih 1991):

$$S_c = r_c \left( \frac{dW}{dV} \right)_c \quad (9)$$

with  $r_c$  being the radius of a core region surrounding the crack tip and  $dW/dV$  is the strain energy density function.

For a homogeneous anisotropic material this function is given by

$$\frac{dW}{dV} = \frac{1}{2}(\sigma_{11}\epsilon_{11} + \sigma_{22}\epsilon_{22} + 2\sigma_{12}\epsilon_{12}) \quad (10)$$

where  $\sigma_{ij}$  are the components of a stress field surrounding the crack tip at a distance  $r$  and direction  $\theta$ , as shown in Figure 1, see (Sih et al. 1965).

Equation (10) yields an expression involving  $1/r$ , the coefficient of which is the strain energy density factor

$$S(\theta) = \frac{1}{\pi}(A_{11}K_I^2 + 2A_{12}K_I K_{II} + A_{22}K_{II}^2), \quad (11)$$

where  $K_I$  and  $K_{II}$  are the stress intensity factors and

$$\begin{aligned} A_{11} &= \frac{1}{4}[a_{11}A^2 + a_{22}C^2 + a_{66}E^2 + 2a_{12}AC + 2a_{16}AE + 2a_{26}CE], \\ A_{12} &= \frac{1}{4}[a_{11}AB + a_{22}CD + a_{66}EF + a_{12}(AD + BC) \\ &\quad + a_{16}(AF + BE) + a_{26}(CF + DE)], \\ A_{22} &= \frac{1}{4}[a_{11}B^2 + a_{22}D^2 + a_{66}F^2 + 2a_{12}BD + 2a_{16}BF + 2a_{26}DF], \end{aligned} \quad (12)$$

where  $a_{ij}$  are the coefficients of the compliance matrix and

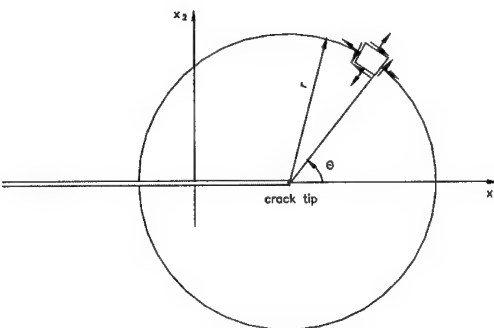


Figure 1: Region surrounding the crack tip.

$$\begin{aligned} A &= \operatorname{Re} \left[ \frac{\mu_1 \mu_2}{\mu_1 - \mu_2} \left( \frac{\mu_2}{\sqrt{\cos \theta + \mu_2 \sin \theta}} - \frac{\mu_1}{\sqrt{\cos \theta + \mu_1 \sin \theta}} \right) \right], \\ B &= \operatorname{Re} \left[ \frac{1}{\mu_1 - \mu_2} \left( \frac{\mu_2^2}{\sqrt{\cos \theta + \mu_2 \sin \theta}} - \frac{\mu_1^2}{\sqrt{\cos \theta + \mu_1 \sin \theta}} \right) \right], \\ C &= \operatorname{Re} \left[ \frac{1}{\mu_1 - \mu_2} \left( \frac{\mu_1}{\sqrt{\cos \theta + \mu_2 \sin \theta}} - \frac{\mu_2}{\sqrt{\cos \theta + \mu_1 \sin \theta}} \right) \right], \\ D &= \operatorname{Re} \left[ \frac{1}{\mu_1 - \mu_2} \left( \frac{1}{\sqrt{\cos \theta + \mu_2 \sin \theta}} - \frac{1}{\sqrt{\cos \theta + \mu_1 \sin \theta}} \right) \right], \\ E &= \operatorname{Re} \left[ \frac{\mu_1 \mu_2}{\mu_1 - \mu_2} \left( \frac{1}{\sqrt{\cos \theta + \mu_1 \sin \theta}} - \frac{1}{\sqrt{\cos \theta + \mu_2 \sin \theta}} \right) \right], \\ F &= \operatorname{Re} \left[ \frac{1}{\mu_1 - \mu_2} \left( \frac{\mu_1}{\sqrt{\cos \theta + \mu_1 \sin \theta}} - \frac{\mu_2}{\sqrt{\cos \theta + \mu_2 \sin \theta}} \right) \right] \end{aligned} \quad (13)$$

According to the strain energy density theory unstable crack growth takes place in the radial direction  $\theta_c$  along which  $S$  becomes minimum, or

$$\frac{\partial S}{\partial \theta} = 0 \text{ and } \frac{\partial^2 S}{\partial \theta^2} > 0. \quad (14)$$

The classical method for obtaining the minimum value of equation (11) (taking its first derivative to  $\theta$  equal to zero and checking the sign of the second derivative) appears not to have a simple analytical solution. As a consequence, a numerical solution was implemented using bracketing and the golden section search technique (Press et al. 1992).

Other criteria for the onset of crack propagation in anisotropic materials include those proposed by Zhang, Jang, Valaire and Suhling (Zhang et al. 1989), named *Z*-criterion, and by Theocaris and Philippidis (Theocaris & Philippidis 1991), named *T*-criterion. However, these criteria presented increased difficulty for the application in an incremental crack growth analysis by the dual boundary element method and would require expensive computational implementation.

#### 4 NUMERICAL RESULTS

The results obtained by the incremental crack growth analysis can be summarized in a crack path diagram. This path was obtained by adding an element to the previous crack tip element, in the

direction evaluated by the minimum strain energy density criterion.

A validation of the results obtained by the present implementation of the strain energy density criterion is initially presented, comparing the results for the crack initiation angle  $\theta$  to those obtained by Sih (Sih 1991). The numerical results of equation (11) obtained by the golden section search were compared to a solution of the same equation using MATHEMATICA obtaining results with a difference smaller than 0.1%. Figure 2 shows a comparison of the present results to those obtained by Sih for a central slant crack forming an angle  $\beta$  to the tensile load axis. The fibers of the unidirectional composite were aligned to the crack axis. The material is a Modulite II 5206 composite with the gross mechanical properties are:  $E_1 = 158.0$  GPa,  $E_2 = 15.3$  GPa,  $G_{12} = 5.52$  GPa and  $\nu_{12} = 0.34$ .

The results show a small difference (under 3%) between the present values of the crack initiation angle and those found by Sih for  $\beta$  smaller than  $60^\circ$ . For larger values of the crack angle there is an increasing difference between these implementations, reaching 12%.

An application of the present technique is presented for the specimen shown in Figure 3, which was designed for the analysis of crack propagating from a circular hole. The material is a graphite-epoxy unidirectional laminate, with the fibers rotated at  $70^\circ$  and the orthotropic properties are:  $E_1 = 144.8$  GPa,  $E_2 = 11.7$  GPa,  $G_{12} = 9.65$  GPa and  $\nu_{12} = 0.21$ .

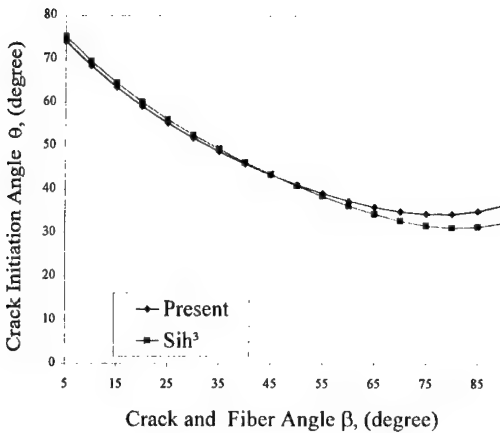


Figure 2: Crack initiation angle for different initial crack angles.

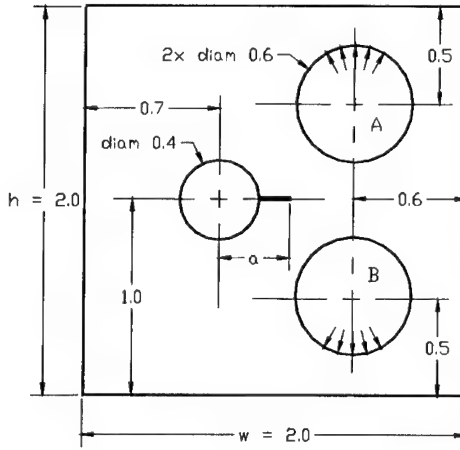


Figure 3: Crack from a hole specimen.

The incremental crack growth analysis was performed with an initial crack length to width ratio  $a/w = 0.15$ . The crack path is shown in figure 4. As the stress and displacements fields produced by holes A and B are symmetric to the initial crack, the crack propagates in the direction dictated by the minimum strain energy density criterion, in fiber breakage mode. As the crack approaches hole B, the path is affected by the stress field of this hole and tend to approach it.

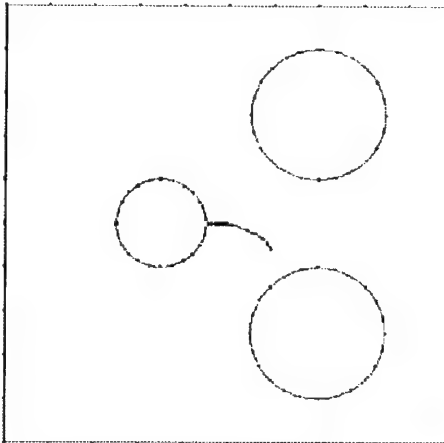


Figure 4: Crack growth path for the crack from a hole specimen.

## 5 CONCLUSIONS

A predictive technique for crack growth analysis in composites and anisotropic materials was presented. The direction of crack propagation was evaluated by the minimum strain energy density criterion and implemented in the dual boundary element code. This analysis is performed in order to predict the crack propagation path, which was assumed piecewise straight.

The implementation of the minimum strain energy density criterion was compared with a numerical example of the literature for evaluating the direction of crack initiation in a unidirectional composite. A small difference was found for the major extension in the range of crack and fiber angles. A crack from a hole specimen was used to analyze the crack propagation path in a unidirectional laminate. The propagation path indicated failure by fiber breakage and was influenced by a loading hole in the specimen.

## ACKNOWLEDGEMENTS

The first author acknowledges the Fundação de Amparo à Pesquisa do Estado de São Paulo (FAPESP) and the Fundo de Apoio ao Ensino e à Pesquisa (FAEP) of the State University of Campinas for supporting this work. The second author acknowledges the Conselho Nacional de Desenvolvimento Científico e Tecnológico (CNPq) for supporting this work through the program PIBIC-CNPq-UNICAMP.

## REFERENCES

- Selvadurai,A.P.S. 1990. Fracture mechanics of a reinforced solid: a boundary element approach, in *Advances in BEM in Japan and USA, Topics in Engineering 7*, (M. Tanaka, C.A. Brebbia and R. Shaw, Eds.), Proc. Int. Conf., Computational Mechanics, Southampton, 107-117.
- Ellyin,F. and El Kadi,H. 1990. Predicting crack growth direction in unidirectional composite laminae, *Engng. Fracture Mechanics* 36, 27-37.
- Sih,G.C. 1991. *Mechanics of Fracture Initiation and Propagation*, Kluwer Academic, Dordrecht.
- Sollero,P. and Aliabadi,M.H. 1995. Anisotropic analysis of cracks in composite laminates using the dual boundary element method, *Composite Structures* 31, 229-233.
- Sollero,P. 1994. *Fracture Mechanics Analysis of Anisotropic Laminates by the Boundary Element Method*, Ph.D. thesis, Wessex Institute of Technology, Southampton.
- Boone,T.J., Wawrynek,P.A. and Ingraffea,A.R. 1987. Finite element modelling of fracture propagation in orthotropic materials, *Engng. Fracture Mech.* 26, 185-201.
- Sollero,P. and Aliabadi,M.H. 1993. Fracture mechanics analysis of anisotropic plates by the boundary element method, *Int. J. Fracture* 64, 269-284.
- Sih,G.C., Paris,P.C. and Irwin,G.R. 1965. On cracks in linear anisotropic bodies, *Int. J. Fracture Mechanics* 3, 189-203.
- Press,W.H., Teukolsky,S.A. Vetterling,W.T. and Flannery,B.P. 1992. *Numerical Recipes in Fortran*, Second ed., Cambridge Univ. Press, Cambridge.
- Zhang,S.Q., Jang,B.Z., Valaire,B.T. and Suhling,J.C. 1989. A new criterion for composite material mixed mode fracture analysis, *Engng. Fracture Mech.* 34, 749-769.
- Theocaris,P.S. and Philippidis,T.P. 1991. Mixed-mode fracture mechanics of anisotropic plates by means of the T-criterion, *Int. J. Fracture* 52, 223-237.

## Estimation of carrying capacity of aviation engine parts from composite materials

T.D.Karimbayev, A.A.Lupov, D.I.Nicolayev & A.N.Zavyalov  
*Central Institute of Aviation Motors (CIAM), Moscow, Russia*

### ABSTRACT:

When analyzed phenomena are changed on distances, comparable to the sizes of structural heterogeneity of composite materials, the mathematical models of higher levels than the homogeneous anisotropic body model are used. In this connection the main relationships of the proposed two-component theory of composite materials linear deformability are discussed. On the basis of proposed approach the estimation of the carrying capacity of the blade root is given and the fatigue damage of the cantilever boraluminium beam at bending vibration on natural frequencies is researched.

### 1. INTRODUCTION

The model of homogeneous anisotropic linearly-deformable medium is widely used in engineering practice of structure designing from modern composite materials. It, being a powerful tool of the solution of engineering problems, unfortunately, does not permit to describe the phenomena, the characteristic changes of which occur on distances, comparable to the sizes structural heterogeneity of composite materials, for example, on the distances between fibres, lamina and so on. In a number of applied problems the mentioned situation takes place. For example, an origin of a damage is characterized by local effects and it takes place in the one of the constituent of composite heterogeneous medium ( in a filling material or a matrix material or an interface debonding ). This situation requires to pay attention to new mathematical models of composite material deformability of the higher level than the homogeneous anisotropic body model. In connection with this the principal directions of the calculated model development are briefly discussed below and in more detailed considered

- the main relationships of the proposed two-component theory of composite materials linear deformability;

- the development of the boundary value problem solution techniques in the above variant of the deformation structural theory;
- the estimation of the carrying capacity of the blade root and of the analysis results of the fatigue damage of the cantilever boraluminium beam at bending vibration on natural frequencies.

### 2. THE TWO-COMPONENT MODEL OF COMPOSITE MATERIAL DEFORMATION

On the basis of the general assumptions and thermodynamic approaches the principal equations of the connected thermoelasticity for two-component medium is developed. The general equations for the isothermal deformable medium consist of

- kinematic relations

$$\varepsilon_{ij}^{\alpha}=0.5(u_{i,j}^{\alpha}+u_{j,i}^{\alpha}) \quad (1)$$

- physical dependencies

$$\sigma_{ij}^{\alpha}=c_{ijmn}^{\alpha\beta}\varepsilon_{mn}^{\beta} \quad (2)$$

- equations of equilibrium

$$\sigma_{ij,j}^{\alpha}+X_i^{\alpha}=\rho^{\alpha\beta}u_i^{\beta}+g_{ij}^{\alpha\beta}(u_j^{\beta}-u_i^{\alpha}) \quad (3)$$

Here and below the superscripts determine the belonging to the constituent of composite materials of parameter (the filling, if  $\alpha, \beta=1$  or the matrix, if  $\alpha, \beta=2$ ). The subscripts correspond to the axes of rectangular coordinate system with value 1, 2 and 3. The representative volume element in the developed model of the composite material deformation theory figures as the compose point  $P(x_i, t)$  (see Fig.1.), in which the projections  $u_i^\alpha$  of the displacement vector on axis  $x_i$ , stresses  $\sigma_{ij}$ , deformations  $\varepsilon_{ij}^\alpha$  and components  $X_j$  of mass force for every constituent of composite materials are introduced. The parameters  $c_{ijmn}^{\alpha\beta}$  are the elasticity characteristics of composite materials constituent at  $\beta=1$  and the characteristic of "the coupling stiffness" at  $\beta\neq1$ . The parameters  $\rho^\alpha, g_{ij}^\alpha$  are the characteristics of the inertial and mechanical interaction between the composite material constituent at  $\alpha\neq1$  and at  $\alpha=1$ ; the parameters  $\rho^\alpha$  are determined by density of composite material constituents [1]. At last, here well-known tensor symbolism is used. In [1] - [6] original ways of analytical and experimental definition of the two-component medium parameters are described.

### 3. THE BOUNDARY VALUE PROBLEM FORMULATION AND THE DETERMINATION TECHNIQUE OF THE STRUCTURE STRESS-STRAIN STATE

The features of the boundary value problem formulation and of the stress-strain state calculation technique within the limits of the suggested structural model of composite material deformation theory are described on an example of the compressor blade-root calculation, which has a dovetail form. Cross section of one is given on Fig.2. The blade-root is loading by forces from the blade profile part and centrifugal forces of the blade-root material mass. Herewith

$$X_1^\alpha = \rho^{\alpha\alpha} \omega^2 x_1, \quad X_2^\alpha = X_3^\alpha = 0 \quad (4)$$

Here the parameter  $\rho^\alpha$  is a material density, the value  $\omega$  is a circular frequency. A load  $\sigma$  from blade profile part at blade-root tip  $x=h$  is distributed proportionally to stiffness of composite material constituent

$$\sigma_{11}^\alpha = \sigma^\alpha v_\alpha E^\alpha / (v_1 E^1 + v_2 E^2) \quad \text{and} \quad \sigma_{12}^\alpha = \sigma_{13}^\alpha = 0 \quad (5)$$

Here the parameter  $F$  is a blade-root cross-section area, the values  $v$  and  $E$  are the volume contents and the elasticity moduli of the composite material constituent. The stresses on the blade-root foot  $x=0$  and on end faces of its are absent, that is

$$\begin{aligned} \sigma_{11}^\alpha &= \sigma_{12}^\alpha = \sigma_{13}^\alpha = 0 & \text{at } x_1 = 0 \\ (6) \quad \sigma_{33}^\alpha &= \sigma_{32}^\alpha = \sigma_{31}^\alpha = 0 & \text{at } x_2 = 0, x_3 = L \end{aligned}$$

The displacements on blade-root lateral faces  $x_2 = \pm kx_1 + b$  are fixed, this is

$$u_i^\alpha = 0. \quad (7)$$

The contact boundary value problem takes place in reality. The used conditions (7) result in some high stress that goes in the strength margin.

The solution of the equation system (1)-(3) are looked for at formulated conditions (4)-(7). The feature of the boundary value problem mathematical formulation consists in assignment of stresses or of displacements or of their combination for composite material each constituent at a body boundary. In connection with this the boundary value problem types for two-component medium are more various than homogeneous body.

All modern model of calculation can be used for solution of the formulated boundary value problem. Below an extension of finite element methods to the two-component medium is proposed and used. The usual solution procedure of the derived resolvent equations by finite element technique for the proposed two-component model of composite material deforming results to relationship

$$K^{\alpha\beta}\{U\}^\beta = \{R\}^\alpha \quad (8)$$

Here the matrices  $K^\alpha$  are the matrix of the filling material stiffness at  $\alpha=1$  and of the matrix material stiffness at  $\alpha=2$  and at  $\alpha\neq\beta$ . The matrix  $K^\alpha$  is the "coupling stiffness" matrix of the composite material constituent. Vector  $\{U\}^\alpha$  is a unknown displacement vector of finite element nodes and the vector  $\{R\}^\alpha$  is the prescribed forces vector, acting on constituent of composite material in node points. In order to use the developed ready computer program the iterative model of calculation was used

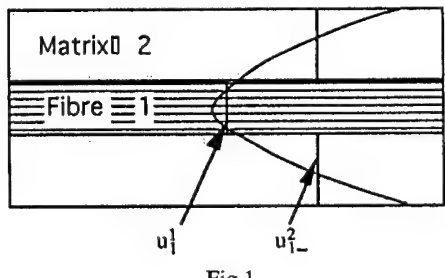
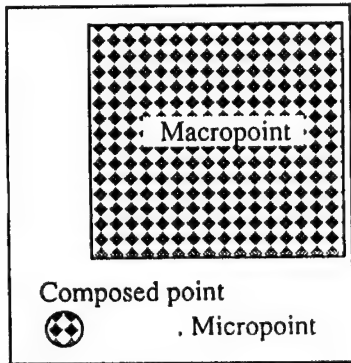


Fig.1

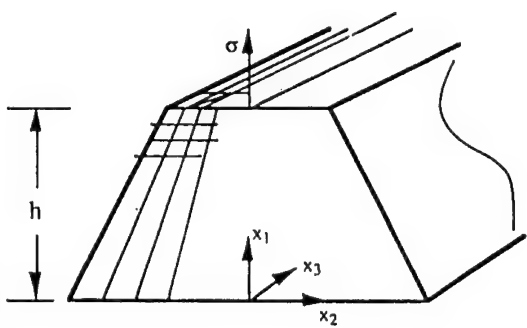


Fig.2

at equation (8) solution. In this case, the two matrix equation system

$$\begin{aligned} K^{\alpha\alpha}\{U\}^\alpha &= \{R^*\}^\alpha \\ \{R^*\}^\alpha &= \{R\}^\alpha - \{K\}^{\alpha\beta}\{U\}^\beta \end{aligned} \quad (9)$$

is solved sequentially, at the each of which is used an algorithm developed for homogeneous medium. Only right parts  $\{R^*\}^\alpha$  of equation (9), due to the displacement  $\{U\}$  vector, are found at the

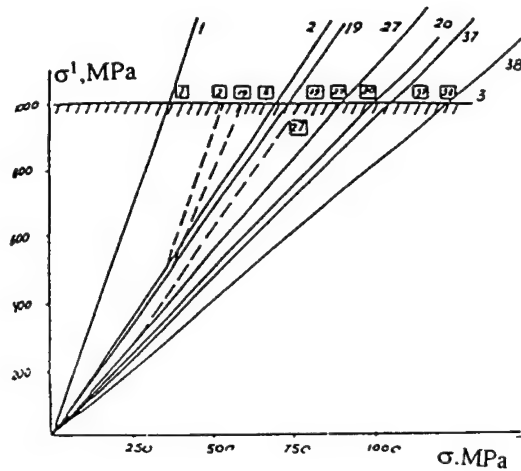


Fig.3a Dependences of "effective" stresses  $\sigma^1$  from the stress nominal value  $\sigma$  in different finite elements.

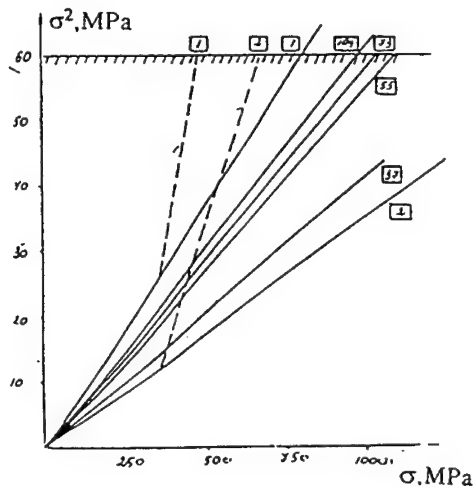


Fig.3b Dependences of "effective" stresses  $\sigma^2$  from the stress nominal value  $\sigma$  in different finite elements.

iteration previous stage and were refined from iteration to iteration. The sequential iterations are continued so long as difference of displacement value in two next iterations in all nodes simultaneously did not become less prescribed precisely. It would notice the convergence is stipulated by the "coupling stiffness" parameters  $C_{ijmn}^{\alpha\beta}$  ( $\alpha \neq \beta$ ), and for solution of boundary value problem it was usually sufficiently 4-6 iterations at precision 10-6.

#### 4. THE FAILURE CRITERION

As a result of the boundary value problem solution (1)-(7) the displacements  $u_i^\alpha$ , the strains  $\epsilon_{ij}^\alpha$  and stresses  $\sigma_{ij}$  in each of composite material constituent are determined. It permits to calculate the generalized parameters for two-component medium [5]

$$\begin{aligned} C^\alpha &= \Pi_{ij}^\alpha \sigma_{ij}^\alpha + (\Pi_{ijmn}^\alpha \sigma_{ij}^\alpha \sigma_{mn}^\alpha)^{0.5} \\ C^a &= \Pi_{ij}^a \sigma_{ij}^a + (\Pi_{ijmn}^a \sigma_{ij}^a \sigma_{mn}^a)^{0.5}, \quad (10) \\ \sigma_{ij}^a &= \sigma_{ij}^1 - \sigma_{ij}^2 \end{aligned}$$

if strength tensor components  $\Pi_{ij}^\alpha$ ,  $\Pi_{ijm}^\alpha$  of composite material separate constituent and the adhesive strength tensor components  $\Pi_{ij}^a$ ,  $\Pi_{ijm}^a$  are known. If the parameter  $C^\alpha$  is become equal 1 or exceed 1 in some point of structure then it is consider that the filling failure at  $\alpha=1$  or the matrix failure  $\alpha=2$  takes place in this point. The fiber-matrix interfacial debonding will take place, if the parameter  $C$  is reach or exceed a value, equal 1. The formulated criterion of the local failure is reasonably common and contains practically important private cases, which were used at estimation of the different structure carrying capacity. The criterion application permits to establish not only place of the failure onset but also the failure character. Cohesive failure takes place at the matrix or filling failure and adhesive failure takes place at the interface debonding.

The development and growth of initiating crack is the gradual and nonlinear process of alternated further failure of the composite material constituent or the interface debonding. The failure unstable process, connected with complete loss of the structure carrying capacity, begins at determined stage of loading. An analysis technique of nonlinear process of the carrying capacity exhaustion by linear equations (1)-(10) was developed. The results of this method using are demonstrated at the blade-root carrying capacity estimation. The stress dependencies in the composite material separate constituent of finite elements from nominal value stress  $\sigma$ , prescribed on root section  $x=h$  of blade are given on Fig.3. The results are derived on the basis of the equations (1)-(9) solution by described earlier manner. From analysis of derived results it can see the filling material is the most loading in the first

finite element ( a finite element number are given on Fig.2.). In further calculation the power form of limiting relationship (10) as for filling material  $\alpha=1$  as matrix material  $\alpha=2$  is accepted

$$C^\alpha \sigma_b^\alpha = S_{ij}^\alpha S_{ij}^\alpha$$

$$S_{ij}^\alpha = \sigma_{ij}^\alpha - S^\alpha \delta_{ij}, \quad S^\alpha = \frac{1}{3} S_{ij}^\alpha \delta_{ij}$$

Here the parameter  $\sigma_b^\alpha$  is the constituent strength. If to accept  $\sigma=1$  GPa and  $\sigma=60$  MPa the failure of the filling material in first finite element will take place already at the stress nominal value  $\sigma$ , equal 350 MPa. Further on the basis of equations (8) the blade-root stress-strain state calculations without the taking part of the first finite element filling material are continued at further increasing of the nominal stress  $\sigma$ . The calculation results are indicated by dashed lines in Fig.3. It is seen, the stress redistribution takes place and the stress dependence linear character from the stress nominal value  $\sigma$  is changed. The matrix material stress in first finite element reaches the limit value at nominal stress  $\sigma$  about 430 MPa. The further calculation was carried out at refined values of stiffness matrix, derived without the taking part of the first finite element matrix material. It is shown the filling material stress in second finite element reaches the limit value at the stress value equal 470 MPa. Like that the calculations are performed to the exhaustion of blade-root carrying capacity. The present calculations were conducted as soon as nominal stress  $\sigma$  reached a level 510 MPa. As qualitative character of the failure process as the carrying capacity quantitative estimation of glass fiber blade-root are satisfactorily agreed experimental data. The strength margin was set a value equal 1.5, at which the designed blade-root carrying capacity was guaranteed [7].

#### 5. THE FATIGUE FAILURE BORALUMINIUM.

The results of experimental analysis of fatigue damage of metal-matrix composite cantilever beam were described in [6]. The specimen of rectangular section by length l had the packing different angle of fibres. The tests were carried out at the first bending normal mode vibration. The vibration amplitude A of cantilever beam free end was automatically maintained constant. The natural frequency was

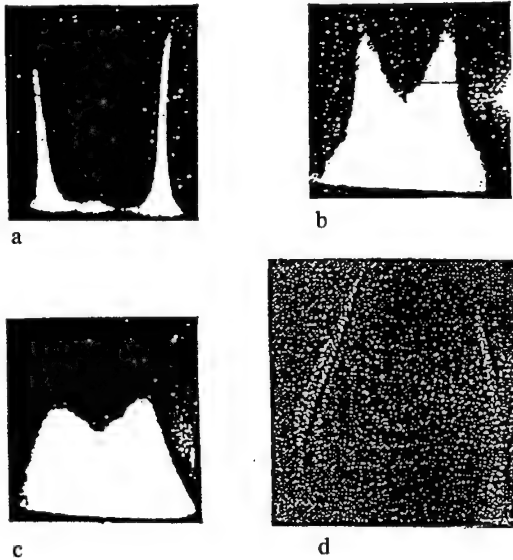


Fig.4 Common torsional normal mode vibration of carbon-aluminium aspecimens at different natural vibration frequency.

$$\begin{array}{ll} \text{a. } 0-f^1 = 1124 \text{Hz}, & \text{c. } \pm 45-f^1 = 3546 \text{Hz}, \\ \text{b. } 0-f^2 = 4473 \text{ Hz} & \text{d. } 45-f^2 = 5790 \text{ Hz} \end{array}$$

decreased as the damage was accumulated. The specimens are considered to be destroyed as soon as the natural frequency was decreased of 10% in comparison with input value. The results of testing are given on the Fig.5 and Table.

The analysis of the cantilever beam vibration on the basis of equations (1)-(3) of the two-component medium linear elasticity permits to derive the characteristic relationship

$$(\Omega^2 - \Omega_1^2)(\Omega^2 - \Omega_2^2) - B(\Omega^2 - \Omega_0^2) = 0 \quad (11)$$

Here the unknown parameter  $\Omega$  is a required value of the eigenvalue, the parameter  $\Omega$  is eigenvalue, corresponding to eigenvalue of the cantilever beam from homogeneous material. Parameter B depends from parameters of mechanical  $g_{ij}^\alpha$  and inertial  $\rho^\alpha$  interaction of the composite material constituents

$$B = g_{11}^{12} \frac{\rho}{(\rho^{11}\rho^{22} - (\rho^{12})^2)} / k \Omega \quad (12)$$

The vibration amplitudes A of filling and matrix materials are connected by dependence

$$A_n^2 = A_h G^1 / G^2, \\ G^{\alpha\beta} = \alpha^{\alpha\beta} - \rho^{\alpha\beta} F \Omega_0^2 (-1)^{\alpha+\beta} g_{11}^{12} / k$$

Evidently, first term of characteristic equation (11) and simultaneously of the first two terms of amplitude dependence (12) can be neglected at strong mechanical interaction (the parameter  $g_{ij}^\alpha$  is large) or at low normal mode vibration, when wave number  $k$  is small and hence wave length is large. Then the vibration amplitudes of the matrix  $A_n$  and filling  $A_h$  materials coincides. That means the vibration phases as matrix as filling are same. At this the characteristic equation (11) has the one only root  $\Omega$  and the first bending natural frequency of cantilever beam will be equalled

$$2\pi l^2 f_n = k_n^2 \sqrt{\frac{I[v_1(\lambda^1 + \mu^1) + v_2(\lambda^2 + \mu^2) + 2c_{11}^{12}]}{(\rho F)}}$$

Here the values  $I$  and  $F$  are the inertia moment and the area of the beam cross-section, the parameters  $\lambda$ ,  $\mu$  are the parameters of Lame of the composite material constituent. If the parameter of "coupling stiffness"  $c_{11}^{12}$  is known, it can calculate natural frequency  $f_n$ . If the results of vibration testing are have, it can find the "coupling stiffness" parameters  $c_{11}^{12}$  by means of the last relation. This is the one of possible experimental manners of determination of "coupling stiffness" parameters  $c_{11}^{12}$ .

If the high normal modes are considered, when wave number  $k$  is large and hence wave length is small and compared with dimension of the composite material structural non-homogeneity, or the mechanical interaction is weak (parameter  $g_{ij}^\alpha$  is small) or, at last, the combination of this case takes place then the characteristic equation (11) has two real root at one and the same normal mode vibration. This effect was observed experimentally. Two natural frequency, corresponding only common torsional normal mode of the metal-matrix composite specimens with the fiber packing different angle is shown on the Fig. 4 [1].

The developed analytical approach was used to estimate fatigue failure of metal-matrix composite material. The results of calculating analysis is given on the last three columns of table. It is shown [6] the material of matrix is destroyed from the first. The



Fig.5.c.



Fig.5.d.

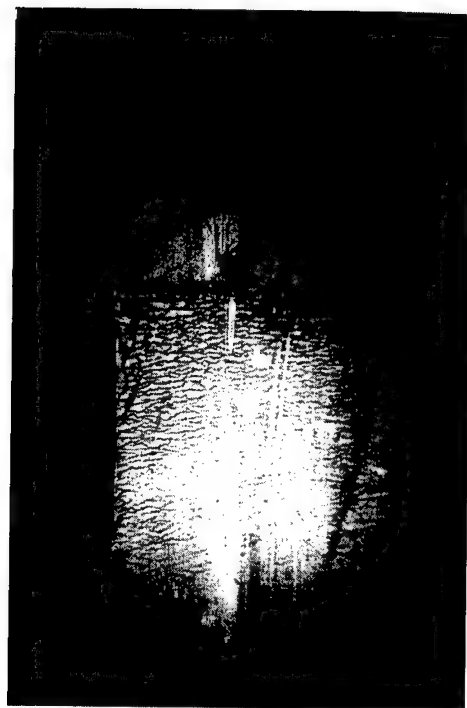


Fig.5.a.



Fig.5.b.

Sam ple №	Pack ing Angle	Wind th b, (mm)	Thick ness h, (mm)	Mass of Weight mgr	Experimental				Calculated		
					$f_1$	2A	$\sigma^{-1}$	$\sigma^{-1} \ast$	$c^2$	$c^1$	$c^a$
					(Hz)	(mm)	(MPa)	(GPa)	(GPa)	(GPa)	(GPa)
7	0								31.1	171	69
8	0	20.1	1.5	11.8	225	13.0	423	76.0			
13	$\pm 15$	20.1	2.0	11.8	136	18.1	337	36.8	30.3	169	70
14		20.1	1.9	20.5	76	16.0	299	34.8			
15		20.1	2.0	20.5	84	17.0	318	36.8			
30	$\pm 30$	19.3	1.8	20.5	77	18.0	128	24.6	29.4	168	70
40		19.3	1.8	11.8	140	9.0	114	27.2			
32		19.1	1.8	11.8	146	10.0	163	32.4			
28	$\pm 45$	19.8	1.7	11.8	180	6.3	80	26.0	26.7	167	70
25		20.25	1.6	11.8	182	8.0	100	27.4			

calculating values of the fatigue parameter at  $c$  are confirmed by experimental data the only for specimens with the fibre packing angle  $\pm 15$ ,  $\pm 30$ ,  $\pm 45$  but not for unidirectional specimens with the 0 fibre packing angle. Moreover, the test character of fatigue failure (the damage is developed along of material matrix, see Fig.5; b, c, d.) is coincided with calculating predictions too. It is necessary to remind the experimental data correspond the case, when natural frequency of specimen is decreased on 10%. Such level of the natural frequency decrease is connected with interfacial debonding fatigue failure, which is determinant factors in this case though the origin damage takes place in the matrix material on the specimen outside surfaces. The thankful analysis of the fatigue failure character of experimental specimens showed really the interfacial debonding determines the fatigue damage of the beam metal-matrix composite material (see Fig.5.a.). As a matter of fact and the calculating value of the fatigue parameter at  $c$  is well agreed with experimental data.

## 6. CONCLUSIONS

The proposed two-component mathematical model of composite material linear deformation and failure is used

- for estimation of the blade-root carrying capacity and determination of the crack origin and description of its development;
- for analysis of the vibration and fatigue damage of beam metal-matrix composite material.

The description analytic technique of the carrying capacity exhaustion non-linear process by proposed linear equations (1)-(7) is developed. The qualitative and quantitative calculating results were performed on the basis of this technique is well agreed with experimental data.

The experimentally discovered phenomenon of the existing two natural frequency corresponding the only common normal mode of composite material beam is described analytical technique. The analysis results of beam fatigue strength derived on the basis of proposal approach are confirm experimental data qualitatively and quantitatively.

## REFERENCES

1. Karimbayev T. D. 1985 *The basic relationships of the two-component medium mechanics and the definition manners of their parameters*. CIAM Transaction, Numb.1119, 23 p. (in Russian )
2. Green A. E., Naghdi I. M. 1968 *The theory of mixes. Mechanics*. Numb.4 (110), p.109-127 ( in Russian )

- 
3. Horoshun L. P. 1982 *About force of the interface interaction in elasticity theory*. Prikladnaja mechanika., Vol.13, Numb.5, p.23-29 ( in Russian ).
  4. Mc Niven H. D., Mengi Y. A 1979. *Mathematical model for the linear dynamic behavior of two phase periodic materials* Int. J. Solids and Structure., Vol.15, Numb. 2, p.271-280
  5. Karimbayev T. D. 1980 *The failure estimation of the composite material constituent* In book "Problems of strength and dynamic in engines". CIAM Transaction, Numb. 887. p.151-161 ( in Russian ).
  6. KarimbayevT. D., Aphanasov V. N.1993 *Structural analysis of boraluminium fatigue damage*. Sc. and Eng. of Composite Material. Vol.2, Numb. 4, p.227-235
  7. Karimbayev T. D. 1992 *The statistical nature of the standardized value of the strength margin*. Proceeding 3 Conference "Brittle matrix composite" Warsaw, p.107-111.

## Author index

- Aivazzadeh, S. 339  
Al-Hmouz, I. 331  
Aliabadi, M. H. 343  
Amigó, V. 167  
Andersons, J. 143  
Anifantis, N.K. 129  
Aniskevich, K. 143  
Bathias, C. 103  
Bauweraerts, P. 295  
Béakou, A. 285  
Belcher, J.R. 41  
Berglund, L.A. 137  
Bloem, C. 167  
Bofilios,D.A. 325  
Bowles, K.J. 71  
Bradley, W.L. 3  
Butkus, L.M. 77  
Caprino, G. 51  
Cardon, A.H. 249, 279  
Carmine, R. 319  
Case, S. 11  
Chafra, M. 87  
Chatawanich, C.S. 3  
Chevalier, Y. 87  
Choqueuse, D. 19  
Chow, C.L. 111  
Clair, T.L.St. 227  
Cunningham, R.A. 63  
Dal Maso, F. 185  
D'Amore, A. 51  
Davies, P. 19  
Dillard, D.A. 227  
Dilsiz, N. 309  
Ebersole,A. 11  
Edelstein, A. 295  
Faignet, S. 295  
Ferrer, C. 167  
Foch, B.J. 63  
Furrow, A.P.C. 227  
Gamby, D. 315  
Gamstedt, E.K. 137  
Garcia, K. 173  
Garrett, J. 11  
Gaynes, M.A. 241  
Gentry, J.R. 211  
Gittleson, R. 11  
Gong, X.J. 339  
Gudmundson, P. 263  
Guedes, R.M. 249, 279  
Hamelin, P. 153  
Hayes, M.D. 173  
Himmel, N. 319  
Hinkley, J. 227  
Hood, D. 11  
Houël, P. 103  
Johnson, W.S. 77  
Kakavas, P.A. 129  
Kalman, M.D. 41  
Kardos, J.L. 235  
Karger-Kocsis, J. 325  
Karimbayev, T.D. 349  
Khomami, B. 235  
Kneip, J.C. 339  
Kobayashi, A. 95  
Korsgaard, J. 143  
Kranbuehl, D. 11  
Kudoh, H. 303  
Lafarie-Frenot, M.C. 315  
Le Gorju, K. 103  
Lesko, J.J. 173  
Leterrier, Y. 219  
Loos, A. 11  
Louzar, M. 87  
Luppov, A.A. 349  
MacLellan, P.T. 211  
Månsen, J.-A.E. 219  
Marino, G. 51  
Marques, A.T. 31, 279, 289  
Martins de Brito, F. 289  
Maugin, G.A. 87  
Mazéas, F. 19  
McManus, H.L. 63  
Mendonça, S.G. 343  
Meyer, A. 11  
Miyano, Y. 303  
Morais, J.J.L. 31  
Mouzakis, D.E. 325  
Muki, R. 303  
Nakada, M. 303  
Newby-Mahler, W. 11  
N'Faly Bérété, Y. 103  
Nicolais, L. 51  
Nicolayev, D.I. 349  
Odru, P. 185  
Ogihara, S. 95, 255  
Papanicolaou, G.C. 129, 271,  
331  
Parvatareddy, H. 227  
Peijs, T. 137, 203  
Perreux, D. 159  
Pournaras, A.V. 325

- |                       |                    |                    |
|-----------------------|--------------------|--------------------|
| Pratt, B.A. 3         | Sollero, P. 343    | Weitsman, Y.J. 25  |
| Qin, Y. 249           | Spalik, J.M. 241   | Wightman, J.P. 309 |
| Ramachandran, P. 235  | Suri, C. 159       | Wood, C.A. 3       |
| Reifsnider, K. 11     | Takeda, N. 95, 255 | Wu, X. 295         |
| Rogozinski, J. 11     | Talreja, R. 119    | Wyser, Y. 219      |
| Salvador, M. 167      | Tamuzs, V. 143     | Xiao, X.R. 331     |
| Schrauwen, B.A.G. 203 | Valentin, R.V. 77  | Yang, B. 235       |
| Seferis, J.C. 193     | Vergheese, N. 173  | Yang, F. 111       |
| Segovia, F. 167       | Vinet, A. 315      | Zaoutsos, S.P. 271 |
| Shaukatullah, H. 241  | Warner, J. 11      | Zavyalov, A.N. 349 |
| Shepard, R. 235       | Wastiels, J. 295   | Zureick, A. 181    |